NATIONAL TECHNICAL UNIVERSITY OF ATHENS
School of Chemical Engineering
NATIONAL CENTER FOR SCIENTIFIC RESEARCH
"DEMOKRITOS"
Institute of Nanoscience and Nanotechnology

Development and Application of Computational Algorithms and Thermodynamic Models for Multiphase, Multicomponent Chemical Systems

PhD Thesis

of

Ilias K. Nikolaidis

Athens, July 2019

Development and Application of Computational Algorithms and Thermodynamic Models for Multiphase, Multicomponent Chemical Systems

A dissertation

by

Ilias K. Nikolaidis

to

the School of Chemical Engineering

in partial fulfillment of the requirements for the degree of

Doctor of Philosophy

in

Chemical Engineering

National Technical University of Athens

Athens, Greece

July 2019

The approval of this PhD dissertation by the School of Chemical Engineering of the National Technical University of Athens does not imply the acceptance of the author's opinions (Law 5343/32 Article 202 § 2).

Η έγκριση της διδακτορικής διατριβής από την Ανωτάτη Σχολή Χημικών Μηχανικών του Εθνικού Μετσόβιου Πολυτεχνείου δεν υποδηλώνει αποδοχή των απόψεων του συγγραφέα (Ν. 5343/32 Άρθρο 202 § 2).

Abstract

Development and Application of Computational Algorithms and Thermodynamic Models for Multiphase, Multicomponent Chemical Systems

PhD Thesis by Ilias K. Nikolaidis

Supervisor: Professor Ioannis G. Economou

Supervising Committee: Professor Andreas G. Boudouvis
Professor Ioannis G. Economou
Professor Epaminondas C. Voutsas

Fossil fuels are by far the most widely used energy source accounting for approximately 80% of the total worldwide. The demand for coal experienced some stagnation in recent years while oil and natural gas demand continues to increase with the latter exhibiting by far the fastest growing demand among the three. Natural gas is considered "the cleanest" fossil fuel source of energy. Closely related to the need for cleaner energy sources is also the role of natural gas in chemical conversion processes to ultraclean fuels and other added-value products used by the chemical industry.

To respond to the increased demand for natural gas and oil products, more than 3.5 million km of pressurized pipelines have been constructed worldwide to transport huge amounts of hydrocarbons. Furthermore, significant amount of research has been conducted for the development of new technologies that aim to reduce the levels of carbon dioxide (CO_2) in the atmosphere, with the most mature being the Carbon Capture and Sequestration (CCS). An important part of the CCS process is the transportation of a CO_2-rich stream from the capture site to the sequestration site and in most cases this is done via pipelines. The two factors that have contributed to this extensive use of pipelines are safety and cost effectiveness. Despite the fact that pipelines are considered to be the safest mode for transportation of gas mixtures, they present significant safety challenges related to their operation and maintenance.

Preliminary and detailed design, simulation and optimization of a transport process require, among others, accurate knowledge of the physical properties of the chemical system involved as functions of temperature, pressure and composition. Quite often, the system exists in more than one phase (*i.e.*, liquid, vapor and/or solid) and as a

result process design calculations have to take into account the phase equilibrium conditions and also the composition of the relevant phases and the respective physical property values. Furthermore, rigorous mathematical tools can be used to accurately assess and improve the safety of high pressure transportation pipelines. These mathematical tools entail the development of a pipeline rupture outflow model in the form of computational fluid dynamics (CFD) simulations. Development of reliable pipeline rupture mathematical models that account for single and multi-phase heterogeneous flows rely heavily on the accurate knowledge of various physical properties of the fluid(s) involved and the phase equilibrium conditions.

Calculation of the physical properties and phase equilibria of mixtures is typically performed with Equations of State (EoS). The two challenges that arise here are the accurate prediction or correlation of the physical properties of the system and the conditions in which the system splits into two or more coexisting phases. Furthermore, calculation of phase equilibria itself using EoS presents various computational challenges and the need for robust algorithms has driven a wealth of mathematical formulations for the phase equilibrium problem. Finally, coupling complex EoS with CFD simulators entails the challenge of providing the physical properties of the chemical system involved and the calculation of phase equilibrium at a specific state, without significant increase of the computational cost and at same time retaining the robustness of the differential equation solver.

In this PhD thesis, the development, application and evaluation of thermodynamic models for the accurate prediction of two-phase / multiphase (solid, liquid, vapor) equilibria and physical properties of complex chemical mixtures, with significant interest in industrial and environmental applications, were studied. The mixtures under study included binary and multicomponent mixtures of CO_2 associated with CCS processes and oil-natural gas derived mixtures with the main components being methane (CH_4) and ethylene (C_2H_4). The CH_4 mixtures are mainly asymmetric hydrocarbon mixtures which are extracted from high pressure-high temperature (HPHT) oil reservoirs, while the C_2H_4 mixtures studied occur from its production process by ethane steam cracking. The models applied for the fluid phases include cubic (Soave-Redlich-Kwong, SRK, Peng-Robinson, PR) and Statistical Associating Fluid Theory (SAFT) based EoS (Perturbed Chain-SAFT, PC-SAFT, SAFT with the Mie potential of variable range, SAFT-VR Mie), while several approaches for the solid phase were utilized and further developed, including different reference state models and a solid-phase EoS

for CO_2. Two-phase (vapor-liquid, liquid-liquid, solid-liquid, solid-gas) and three-phase (vapor-liquid-liquid, solid-liquid-liquid, solid-liquid-gas) equilibria of mixtures were studied, while physical properties, important for pipeline design and operation, such as density, speed of sound, Joule-Thomson coefficient etc. were considered. Furthermore, efficient and robust algorithms for the direct calculation of saturation points, as well as, the sequential construction of phase diagrams of binary and multicomponent mixtures were developed and an efficient technique for rapid and robust coupling of thermodynamic calculations with CFD models for pipeline decompression simulations was proposed.

Several useful conclusions are drawn from this work, while the methods proposed here are expected to be of immense importance for the oil & gas industry in the near future. The new algorithms for direct saturation point calculations tackle successfully the problem of the multiplicity of solutions in the retrograde regions of phase diagrams and proved to be efficient and robust tools, even in very challenging conditions. New Euler-Newton predictor-corrector methods were proposed that are capable of handling different types of phase behavior and trace common phase diagrams as well as more unusual cases like open-ended dew lines with multiple critical points, double retrograde behavior etc.

The cubic and SAFT based EoS considered in this work, predict / correlate with similar accuracy the vapor-liquid equilibrium (VLE) of CO_2, CH_4 and C_2H_4 – the three major components considered in this thesis – binary mixtures with other gases and low molecular weight hydrocarbons that occur in the respective processes. The vapor phase composition of these mixtures is correlated better with the cubic EoS in the region where the pressure maximum of the P-x,y phase diagram corresponds to a critical point. SAFT type EoS correlate more accurately the liquid phase composition, in expense of the critical point overshooting and the deterioration of the vapor phase description. The VLE of binary CH_4 mixtures with long-chain normal alkanes (*n*-alkanes) was also studied and Gibbs Ensemble Monte Carlo simulations (GEMC) were combined with EoS to develop a predictive methodology for the calculation of the VLE of multicomponent hydrocarbon mixtures with high asymmetry. It was observed that, with increasing asymmetry, PC-SAFT EoS is more successful in correlating the low temperature binary VLE data and cubic EoS the high temperature data. Overall, the EoS binary interaction parameters (BIPs) regressed from GEMC simulation data lead to equally accurate modeling results for multicomponent mixtures, compared to those regressed from

experimental binary mixture data. Furthermore, the solid-liquid-gas equilibrium (SLGE) study of the respective binary mixtures showcased the effect of various terms of the combined models (solid-phase model coupled with a fluid-phase EoS) considered in this work, which led to targeted modifications and very accurate modeling results, even at high pressures.

Most of the physical properties of pure C_2H_4 are predicted with relatively high accuracy by PC-SAFT and SAFT-VR Mie EoS, with none being clearly superior to the other. Both SAFT EoS are more accurate than PR in predicting the pure C_2H_4 physical properties overall.

A technique for the rapid interpolation of thermodynamic properties of mixtures for the purposes of simulating two-phase flow was initially developed to simulate the experimental decompression of CO_2-rich mixtures. This technique was extended to handle the critical and supercritical region of multicomponent mixtures, while retaining accuracy and computational efficiency. The extension was a prerequisite for performing numerical simulations of pipeline decompression for a ternary ethylene mixture with impurities and results were validated against full-bore rupture experimental data.

In conclusion, this thesis referred to the development, validation and application of robust algorithms and thermodynamic models for phase equilibrium calculations of binary and multicomponent mixtures with emphasis to gas mixtures.

Keywords

Carbon Capture and Sequestration, oil and gas, pipeline transportation, equations of state, phase equilibrium, physical properties, interpolation of thermodynamic properties

Abstract in Greek

Ανάπτυξη και Εφαρμογή Υπολογιστικών Αλγορίθμων και Θερμοδυναμικών Μοντέλων για Πολυφασικά, Πολυσυστατικά Χημικά Συστήματα

Διδακτορική Διατριβή Ηλία Κ. Νικολαΐδη

Επιβλέπων: Καθηγητής Ιωάννης Γ. Οικονόμου

Επιβλέπουσα Επιτροπή: Καθηγητής Ανδρέας Γ. Μπουντουβής
Καθηγητής Ιωάννης Γ. Οικονόμου
Καθηγητής Επαμεινώνδας Χ. Βουτσάς

Τα ορυκτά καύσιμα είναι μακράν η πιο διαδεδομένη πηγή ενέργειας, καλύπτοντας περίπου το 80% του παγκόσμιου συνόλου. Η ζήτηση για γαιάνθρακα εμφάνισε στασιμότητα τα τελευταία χρόνια, ενώ η ζήτηση πετρελαίου και φυσικού αερίου συνεχίζει να αυξάνεται με το δεύτερο να εμφανίζει μακράν την ταχύτερα αυξανόμενη ζήτηση ανάμεσα στα τρία. Το φυσικό αέριο θεωρείται η «καθαρότερη» πηγή ενέργειας προερχόμενη από την κατηγορία των ορυκτών καυσίμων. Στενά συνδεδεμένος με την ανάγκη για καθαρότερες πηγές ενέργειας είναι και ο ρόλος του φυσικού αερίου σε διεργασίες χημικής μετατροπής σε υπερκαθαρά καύσιμα και άλλα προϊόντα υψηλής προστιθέμενης αξίας τα οποία χρησιμοποιούνται από τη χημική βιομηχανία.

Για την κάλυψη της υψηλής απαίτησης προϊόντων φυσικού αερίου και πετραλαίου, περισσότερα από 3.5 εκατομμύρια km αγωγών υψηλής πίεσης έχουν κατασκευαστεί παγκοσμίως για τη μεταφορά τεράστιων ποσοτήτων υδρογονανθράκων. Επιπλέον, σημαντική έρευνα έχει πραγματοποιηθεί για την ανάπτυξη νέων τεχνολογιών με στόχο τη μείωση των επιπέδων διοξειδίου του άνθρακα (CO_2) στην ατμόσφαιρα, με την πιο ώριμη τεχνολογία να είναι η Δέσμευση και Γεωλογική Αποθήκευση του άνθρακα (Carbon Capture and Sequestration, CCS). Ένα σημαντικό κομμάτι της διεργασίας του CCS είναι η μεταφορά ενός ρεύματος πλούσιο σε CO_2 από τις μονάδες δέσμευσης στα σημεία αποθήκευσης, και η οποία στις περισσότερες περιπτώσεις γίνεται μέσω αγωγών. Οι δύο παράγοντες που έχουν συνεισφέρει σε αυτή την εκτεταμένη χρήση αγωγών είναι η ασφάλεια και το χαμηλό κόστος. Όμως, παρόλο που οι αγωγοί θεωρούνται το ασφαλέστερο μέσο μεταφοράς μειγμάτων αερίων, παρουσιάζουν σημαντικές προκλήσεις ασφάλειας οι οποίες σχετίζονται με τη λειτουργία και τη συντήρησή τους.

Ο προκαταρκτικός και αναλυτικός σχεδιασμός, η προσομοίωση και βελτιστοποίηση μιας διεργασίας μεταφοράς απαιτούν, μεταξύ άλλων, ακριβή γνώση των φυσικοχημικών ιδιοτήτων του εμπλεκόμενου χημικού συστήματος ως συναστήσεις της θερμοκρασίας, της πίεσης και της σύστασης. Αρκετά συχνά, το σύστημα συνυπάρχει σε παραπάνω από μία φάσεις (π.χ. υγρή, ατμώδης και/ή στερεή), με αποτέλεσμα οι υπολογισμοί για το σχεδιασμό της διεργασίας να πρέπει να λάβουν υπόψη τις συνθήκες ισορροπίας φάσεων, τη σύσταση των σχετικών φάσεων, καθώς επίσης και τις αντίστοιχες φυσικοχημικές ιδιότητες. Επιπλέον, προηγμένα μαθηματικά εργαλεία μπορούν να χρησιμοποιηθούν για την ακριβή αξιολόγηση και βελτίωση της ασφάλειας των αγωγών υψηλής πίεσης. Τέτοια μαθηματικά εργαλεία περιλαμβάνουν την ανάπτυξη ενός μοντέλου εκροής λόγω ρήξης του αγωγού με τη μορφή προσομοιώσεων υπολογιστικής ρευστοδυναμικής (CFD). Η ανάπτυξη αξιόπιστων μαθηματικών μοντέλων προσομοίωσης ρήξεων σε αγωγούς τα οποία λαμβάνουν υπόψη την ύπαρξη μονοφασικών και πολυφασικών ροών, βασίζονται σε μεγάλο βαθμό στην ακριβή γνώση των διάφορων φυσικοχημικών ιδιοτήτων των εμπλεκόμενων ρευστών και των συνθηκών ισορροπίας φάσεων.

Ο υπολογισμός των φυσικοχημικών ιδιοτήτων και της ισορροπίας φάσεων μειγμάτων πραγματοποιείται τυπικά με Καταστατικές Εξισώσεις (ΚΕ). Οι προκλήσεις οι οποίες προκύπτουν είναι η ακριβής πρόβλεψη ή συσχέτιση των φυσικοχημικών ιδιοτήτων του συστήματος και των συνθηκών στις οποίες το σύστημα διαχωρίζεται σε δύο ή και περισσότερες συνυπάρχουσες φάσεις. Επιπλέον, ο ίδιος ο υπολογισμός της ισορροπίας φάσεων με χρήση ΚΕ παρουσιάζει διάφορες υπολογιστικές προκλήσεις και η ανάγκη για αξιόπιστους αλγορίθμους έχει οδηγήσει σε μια πληθώρα μαθηματικών διατυπώσεων του προβλήματος. Τέλος, η σύζευξη σύνθετων ΚΕ με προσομοιωτές CFD πρέπει να πραγματοποιείται με τέτοιο τρόπο, ώστε η παροχή των φυσικοχημικών ιδιοτήτων του συστήματος και ο υπολογισμός ισορροπίας φάσεων να μην αυξάνει σημαντικά το υπολογιστικό κόστος, ενώ ταυτόχρονα να διατηρείται η αξιοπιστία του αλγορίθμου επίλυσης των διαφορικών εξισώσεων.

Σε αυτή τη διδακτορική διατριβή πραγματοποιήθηκε η ανάπτυξη, εφαρμογή και αξιολόγηση θερμοδυναμικών μοντέλων για την ακριβή πρόβλεψη της διφασικής και πολυφασικής (στερεή, υγρή, ατμώδης) ισορροπίας και των φυσικοχημικών ιδιοτήτων σύνθετων χημικών μειγμάτων, τα οποία παρουσιάζουν ιδιαίτερο ενδιαφέρον σε βιομηχανικές και περιβαλλοντικές εφαρμογές. Τα μείγματα τα οποία εξετάστηκαν περιλαμβάνουν δυαδικά και πολυσυστατικά μείγματα CO_2 τα οποία συναντώνται σε διεργασίες CCS και μείγματα προερχόμενα από πετρέλαιο και φυσικό αέριο με κύρια συστατικά το μεθάνιο (CH_4) και το

αιθυλένιο (C_2H_4). Τα μείγματα μεθανίου είναι κυρίως ασύμμετρα μείγματα υδογονανθράκων τα οποία εξορύσσονται από ταμιευτήρες υψηλής πίεσης και υψηλής θερμοκρασίας, ενώ τα μείγματα αιθυλενίου που εξετάστηκαν προκύπτουν από τη διεργασία παραγωγής του μέσω ατμοπυρόλησης αιθανίου. Τα μοντέλα που εφαρμόστηκαν για τις ρευστές φάσεις περιλαμβάνουν κυβικές (Soave-Redlich-Kwong, SRK, Peng-Robinson, PR) ΚΕ, καθώς επίσης και ΚΕ βασισμένες στη στατιστική μηχανική (Perturbed Chain-Statistical Associating Fluid Theory, PC-SAFT, SAFT with the Mie potential of variable range, SAFT-VR Mie), ενώ παράλληλα χρησιμοποιήθηκαν και αναπτύχθηκαν περεταίρω αρκετές προσεγγίσεις για τη στερεή φάση, οι οποίες περιλαμβάνουν μοντέλα με διαφορετικές καταστάσεις αναφοράς και μία ΚΕ στερεής φάσης για CO_2. Μελετήθηκε η διφασική (υγρού-ατμού, υγρού-υγρού, στερεού-υγρού, στερεού-αερίου) και τριφασική (υγρού-υγρού-ατμού, στερεού-υγρού-υγρού, στερεού-υγρού-αερίου) ισορροπία μειγμάτων, όπως επίσης και φυσικοχημικές ιδιότητες, σημαντικές για το σχεδιασμό και τη λειτουργία αγωγών, όπως η πυκνότητα, η ταχύτητα του ήχου, ο συντελεστής Joule-Thomson κλπ. Επίσης, αναπτύχθηκαν αποδοτικοί και αξιόπιστοι αλγόριθμοι για τον απευθείας υπολογισμό σημείων ισορροπίας φάσεων, όπως επίσης και για την διαδοχική κατασκευή διαγραμμάτων φάσης δυαδικών και πολυσυστατικών μειγμάτων. Τέλος, προτάθηκε μία αποδοτική τεχνική για την ταχεία και αξιόπιστη σύζευξη θερμοδυναμικών υπολογισμών με μοντέλα CFD για την προσομοίωση της διεργασίας αποσυμπίεσης αγωγών μετά από τυχαία ρήξη.

Πολλά χρήσιμα συμπεράσματα εξάγονται από αυτή τη διατριβή, ενώ οι μέθοδοι που προτείνονται αναμένεται να έχουν μεγάλη σημασία για τη βιομηχανία πετρελαίου και φυσικού αερίου στο εγγύς μέλλον. Οι νέοι αλγόριθμοι για τον απευθείας υπολογισμό σημείων ισορροπίας φάσεων αντιπετωπίζουν με επιτυχία το πρόβλημα της πολλαπλότητας λύσεων στις περιοχές αναστροφής (παλινδρομικής συμπύκνωσης) των διαγραμμάτων φάσης και αποδείχθηκαν αποτελεσματικά και αξιόπιστα εργαλεία ακόμα και σε πολύ δύσκολες συνθήκες. Νέες μέθοδοι Euler-Newton predictor-corrector προτάθηκαν, οι οποίες μπορούν να χρησιμοποιηθούν σε πολλούς διαφορετικούς τύπους φασικής συμπεριφοράς και να κατασκευάσουν κοινά διαγράμματα φάσεων, αλλά και να διαχειριστούν πιο ασυνήθιστες περιπτώσεις όπως καμπύλες σημείων δρόσου ανοιχτής μορφής με πολλαπλά κρίσιμα σημεία, καμπύλες με διπλή παλινδρομική συμπύκνωση κλπ.

Οι κυβικές και τύπου SAFT ΚΕ οι οποίες χρησιμοποιήθηκαν σε αυτή τη διατριβή, προβλέπουν / συσχετίζουν με παρόμοια ακρίβεια την ισορροπία υγρού-ατμού δυαδικών μειγμάτων CO_2, CH_4 και C_2H_4 – τα τρία κύρια συστατικά που εξετάστηκαν σε αυτή τη διατριβή – με άλλα αέρια και υδρογονάνθρακες μικρού μοριακού βάρους τα οποία

προκύπτουν στις αντίστοιχες διεργασίες. Η σύσταση της ατμώδους φάσης αυτών των μειγμάτων συσχετίζεται καλύτερα από τις κυβικές ΚΕ στην περιοχή όπου το μέγιστο της πίεσης του διαγράμματος πίεσης - σύστασης αντιστοιχεί σε κρίσιμο σημείο. Οι ΚΕ τύπου SAFT συσχετίζουν με μεγαλύτερη ακρίβεια τη σύσταση της υγρής φάσης, με τίμημα την υπέρβαση του κρίσιμου σημείου και τη χειρότερη περιγραφή της σύστασης της ατμώδους φάσης. Επιπλέον, μελετήθηκε η ισορροπία υγρού - ατμού δυαδικών μειγμάτων CH_4 με κανονικά αλκάνια (*κ*-αλκάνια) μακριάς αλυσίδας και προσομοιώσεις Monte Carlo στο στατιστικό σύνολο Gibbs (GEMC) συνδυάστηκαν με ΚΕ για την ανάπτυξη μίας μεθοδολογίας πρόβλεψης της ισορροπίας υγρού - ατμού πολυσυστατικών μειγμάτων υδρογονανθράκων με υψηλή ασυμμετρία. Παρατηρήθηκε ότι, με αύξηση της ασυμμετρίας, η ΚΕ PC-SAFT συσχετίζει με μεγαλύτερη επιτυχία τα δεδομένα ισορροπίας φάσεων των αντίστοιχων δυαδικών μειγμάτων σε χαμηλές θερμοκρασίες, ενώ οι κυβικές ΚΕ τα δεδομένα σε υψηλές θερμοκρασίες. Συνολικά, οι δυαδικές παράμετροι αλληλεπίδρασης από προσαρμογή των ΚΕ σε δεδομένα προσομοιώσεων GEMC οδηγούν σε αποτελέσματα μοντελοποίησης πολυσυστατικών μειγμάτων, ισοδύναμης ακρίβειας με αυτά από χρήση παραμέτρων που προκύπτουν από προσαρμογή σε πειραματικά δεδομένα. Η μελέτη της ισορροπίας στερεού-υγρού-αερίου των αντίστοιχων δυαδικών μειγμάτων έδειξε την επίδραση διαφόρων όρων των συνδυασμένων μοντέλων (μοντέλο στερεής φάσης συζευγμένο με ΚΕ ρευστής φάσης) που χρησιμοποιήθηκαν σε αυτή τη διατριβή, κάτι το οποίο οδήγησε στην πραγματοποίηση στοχευμένων τροποποιήσεων και τελικών αποτελεσμάτων πολύ υψηλής ακρίβειας, ακόμα και σε πολύ υψηλές πιέσεις.

Οι περισσότερες από τις φυσικοχημικές ιδιότητες του καθαρού C_2H_4 προβλέπονται με σχετικά υψηλή ακρίβεια από τις ΚΕ PC-SAFT και SAFT-VR Mie, με καμία από τις δύο να είναι σαφώς ανώτερη από την άλλη. Και οι δύο SAFT ΚΕ είναι πιο ακριβείς από την PR για την πρόβλεψη των φυσικοχημικών ιδιοτήτων καθαρού C_2H_4 συνολικά.

Τέλος, αναπτύχθηκε μία τεχνική για την ταχεία παρεμβολή θερμοδυναμικών ιδιοτήτων μειγμάτων για την πραγματοποίηση προσομοιώσεων διφασικής ροής. Η τεχνική αυτή χρησιμοποιήθηκε αρχικά για την προσομοίωση αποσυμπίεσης αγωγού μεταφοράς μειγμάτων πλούσια σε CO_2, ενώ τα αποτελέσματα συγκρίθηκαν με αντίστοιχα πειραματικά δεδομένα. Η τεχνική αυτή επεκτάθηκε στη συνέχεια έτσι ώστε να μπορεί να διαχειριστεί την κρίσιμη και υπερκρίσιμη περιοχή πολυσυστατικών μειγμάτων, διατηρώντας την αρχική ακρίβεια και υπολογιστική απόδοση. Η επέκταση αυτή ήταν απαραίτητη για την πραγματοποίηση αριθμητικών προσομοιώσεων αποσυμπίεσης αγωγού μεταφοράς τριαδικού

μείγματος αιθυλενίου με άλλα συστατικά σε πολύ μικρές ποσότητες. Τα αποτελέσματα των προσομοιώσεων συγκρίθηκαν με πειραματικά δεδομένα πλήρους ρήξης αγωγού.

Συμπερασματικά, η διατριβή αυτή πραγματεύεται την ανάπτυξη, σύγκριση και εφαρμογή αποδοτικών αλγορίθμων και θερμοδυναμικών μοντέλων για τον υπολογισμό ισορροπίας φάσεων δυαδικών και πολυσυστατικών μειγμάτων με έμφαση σε μείγματα αερίων.

Λέξεις κλειδιά

Δέσμευση και Αποθήκευση άνθρακα, πετρέλαιο και αέριο, μεταφορά με αγωγούς, καταστατικές εξισώσεις, ισορροπία φάσεων, φυσικοχημικές ιδιότητες, παρεμβολή θερμοδυναμικών ιδιοτήτων

Αφιερωμένο στην οικογένειά μου
και στους ανθρώπους που με
στήριξαν και σε αυτό το ταξίδι

Acknowledgements

… and the long journey of the PhD is finally over. A journey filled with plenty of experiences and certainly many moments of joy, sadness, satisfaction, disappointment, relief, discomfort, fatigue and creativity. Having completed this journey, I would like to dedicate this part of my thesis to the people that shared the good and bad moments with me, supported and guided me for longer or shorter periods of time.

First and foremost, I am sincerely grateful to my supervisor, Professor Ioannis Economou, for giving me the opportunity to join his research group, collaborate with excellent scientists and work on very interesting projects in a friendly environment. He has always shown me his support, even when I used to come up with my own ideas that didn't really follow the original plans we had set, kept me motivated and encouraged me to be creative. His advice and vast experience on being a supervisor and a scientist were invaluable for my continuous self-improvement. Furthermore, I would like to especially thank him for giving me the opportunity to spend one year in total in Doha, as a visiting PhD student in Texas A&M University at Qatar.

I would like to give special thanks to my supervising committee members, Professor Andreas Boudouvis and Professor Epaminondas Voutsas for the constructive discussions we had and their willingness to promptly help me with any issue. Although we were not collaborating on a daily basis, they were always interested in my progress and their scientific advice and suggestions were incredibly helpful.

I am deeply indebted and thankful to my senior colleagues and friends from NCSR "Demokritos", Dr. Loukas Peristeras and Assistant Professor Georgios Boulougouris, with whom we worked closely to carry out the CO_2QUEST project initially and continued to collaborate during all my PhD years. I would like to thank them for the time they dedicated to help me and answer my countless questions, especially at the beginning of my PhD, and for the constructive, mind challenging and probably loud discussions. Furthermore, I would like to thank them for their support and encouragement, as well as their willingness to discuss and advise me in a personal level. Moreover, I would like to thank my colleagues and friends from the Molecular Thermodynamics and Modeling of Materials Laboratory in NCSR "Demokritos" for the friendly environment and fun time we spent together.

I would also like to express my sincere gratitude to my colleagues and friends from Texas A&M University at Qatar, Assistant Professor Othonas Moultos, Dr. Vasileios Michalis and Dr. Panagiotis Krokidas, who made my stay in Doha a nice experience, helped me in everyday life and were always eager to help me both scientifically and personally. Their friendship and support were crucial, so that I could adapt in a very different environment

and deal with every challenge. I want to especially thank Othonas Moultos for our scientific collaboration and for giving me the chance to spend one month in the Netherlands, as a visiting PhD student in TU Delft. I am sincerely thankful to him and Sofia for their friendship and for always treating me as a member of the family.

During these years of the PhD, I had the chance to work with professors and researchers from Texas A&M University at Qatar, Delft University of Technology and University College London. I want to offer my special thanks to them for the interesting discussions and excellent collaboration; Professor Thijs Vlugt, Professor Marcelo Castier, Assistant Professor Luis Franco and Dr. Sergey Martynov.

I would like to express my gratitude for the financial support from the 7th European Commission Framework Program for Research and Technological Development "Impact of the Quality of CO_2 on Storage and Transport, CO_2QUEST" (Project No.: 309102). I am sincerely thankful to Texas A&M University at Qatar for a visiting student assistantship and for the financial support from the NPRP grant number 8-1339-2-569 "Quantitative Safety Assessment of Hydrocarbon Transportation Pipelines" from the Qatar National Research Fund (a member of the Qatar Foundation). I want to thank also the European Union Horizon 2020 Research and Innovation Programme "Maximizing the EU shale gas potential by minimizing its environmental footprint, ShaleXenvironmenT" (Project No.: 640979) for the financial support. Furthermore, I am grateful to the General Secretariat for Research and Technology Hellas (GSRT) and the Hellenic Foundation for Research and Innovation (HFRI) for awarding me a PhD scholarship (Contract code: 745) and to TU Delft for financing my visit in the Netherlands.

It would have been impossible for me to finish this endeavor without the support of my dearest people and friends in my hometown and here in Athens, my second home. A million thanks to my dear Nefeli for the understanding, patience and huge everyday support. Finally, I want to thank my dear family; my parents Kostas and Lemonia and my sister Marina who continuously strive to help, support and encourage me to follow my dreams, as well as give me all the prerequisites to continue on.

For all that…
my sincere thanks,

Ilias Nikolaidis
Athens, July 2019

Imagination is more important than knowledge. Knowledge is limited.
Imagination encircles the world.

Albert Einstein (1879 - 1955)

Table of Contents

Abstract i

Abstract in Greek v

Acknowledgements xiii

Table of Contents xvii

List of Tables xxiii

List of Figures xxv

List of Abbreviations xliii

List of Symbols xlv

1. Introduction 1

1.1. Motivation 1

1.2. Key Mixtures of Interest 4

1.3. Objectives 7

1.4. Structure of Thesis 8

2. Literature Review 11

2.1. Calculation of Saturation Points and Phase Diagrams 11

2.2. Phase Equilibria of CO_2 Mixtures 19

2.3. Phase Equilibria of Asymmetric CH_4 Mixtures 20

2.4. Phase Equilibria and Physical Properties of C_2H_4 Mixtures 27

2.5. Coupling Thermodynamic Calculations with Flow Models 28

3. Thermodynamic Models 31

3.1. Equations of State for Fluids 31

3.1.1. Cubic Equations of State 31

3.1.2. SAFT Equations of State 33

3.2. Thermodynamic Models for the Solid Phase 38
3.2.1. Approach of McHugh 39
3.2.2. Approach of Seiler 39
3.2.3. Gibbs Free Energy Eos for Solid CO_2 42
4. Methods for Direct Saturation Point Calculations 45
4.1. Introduction 45
4.2. Working Equations Derivation 47
4.3. Computational Algorithms 52
4.3.1. Bubble / Upper Dew Points 53
4.3.2. Lower Dew Points 58
4.4. Implementation 60
4.4.1. Initialization and Stability (Block A) 64
4.4.2. Trust Region Modification (Block B) 65
4.4.3. Pressure Correction (Block C) 67
4.5. Results and Discussion 69
4.6. Conclusions 84
5. Sequential Construction of Phase Diagrams 85
5.1. Introduction 85
5.2. Constant Composition Phase Envelopes 85
5.2.1. Working Variables and Equations 85
5.2.2. Initialization 87
5.2.3. Linear Extrapolation 87
5.2.4. Temperature and Pressure Maxima 88
5.2.5. Results and Discussion 89
5.3. Phase Diagrams of Binary Mixtures 96
5.3.1. Working Variables and Equations 96

5.3.2. Results and Discussion 98
5.4. Conclusions 109
6. Solid-Fluid Equilibrium of CO_2 mixtures 111
6.1. Introduction 111
6.2. Results and Discussion 113
6.2.1. Solid-Fluid Equilibrium of Pure CO_2 114
6.2.2. Solid-Liquid-Gas Equilibrium of CO_2 mixtures 115
6.3. Conclusions 125
7. Vapor-Liquid Equilibrium of Asymmetric CH_4 mixtures 127
7.1. Introduction 127
7.2. Results and Discussion 130
7.2.1. Monte Carlo Simulation 130
7.2.2. Equation of State Modeling 132
7.2.3. Comparison of Calculations from the Various Methods 133
7.3. Conclusions 144
8. Solid-Liquid-Gas Equilibrium of CH_4 - *n*-Alkane Mixtures 145
8.1. Introduction 145
8.2. Solid-Phase Models 146
8.2.1. Basic Solid-Phase Model 146
8.2.2. Advanced Solid-Phase Model 146
8.2.3. Advanced-Fit Solid-Phase Model 147
8.3. Results and Discussion 149
8.3.1. Basic Solid-Phase Model: Effect of BIPs 150
8.3.2. Advanced Solid-Phase Model: Liquid-Phase Poynting Correction 165
8.3.3. Correlation of BIPs: A Predictive Approach 168
8.3.4. Advanced Fit Solid-Phase Model 170

8.3.5. Global Phase Diagrams 173
8.4. Conclusions 177
9. Vapor-Liquid Equilibrium and Physical Properties of C_2H_4 Mixtures 179
9.1. Introduction 179
9.2. Results and Discussion 179
9.2.1. Pure Component Properties 179
9.2.2. Vapor-Liquid Equilibrium of Binary Mixtures 186
9.2.3. Vapor-Liquid Equilibrium of Ternary Mixtures 196
9.3. Conclusions 201
10. Efficient Coupling of Thermodynamic Calculations with Models for Two-Phase Flow Simulation 203
10.1. Introduction 203
10.2. Pipeline Releases of CO_2 Mixtures 203
10.2.1. Interpolation Technique 203
10.2.2. Interpolation Technique Consistency 206
10.2.3. Full-Bore Rupture Simulation of CO_2 Pipeline 210
10.3. Pipeline Releases of C_2H_4 Mixtures 212
10.3.1. Physical Properties of the Chemical System 212
10.3.2. Construction and Accuracy of the Interpolation Grids 214
10.3.3. Full-bore Rupture Simulation of C_2H_4 pipeline 220
10.4. Conclusions 223
11. Conclusions 225
12. Future Work 229
Appendix A: Flowcharts and Supporting Information for the Methods Presented in Chapter 4 231

Appendix B: Equations and Jacobian Matrices for the Methods Presented in Chapter 5 239

Appendix C: Pure Component Parameters 253

Appendix D: Monte Carlo Simulation Details and Results 257

Appendix E: CH_4 - *n*-Alkane Mixtures VLE and SLGE 271

Appendix F: Supporting Information for Chapter 9 283

References 285

Short CV 313

Publications 315

List of Tables

Table 3.1: Expressions for the energy ($\alpha(T)$) and co-volume (b) parameters for the cubic equations of state used in this work. 32

Table 6.1: Experimental binary SLGE data from the literature modeled in this work. . 115

Table 6.2: % AARD between experimental SLGE data for the equilibrium pressure and model calculations for the CO_2 - N_2 mixture and corresponding kij values. 116

Table 6.3: % AARD between experimental SLGE data for the equilibrium pressure and model calculations for the CO_2 - H_2 mixture and corresponding kij values. 116

Table 6.4 : % AARD between experimental SLGE data for the equilibrium pressure and model calculations for the CO_2 - CH_4 mixture and corresponding kij values... 117

Table 7.1: Experimental binary VLE data of CH_4 - *n*-alkane mixtures examined in this work. 128

Table 7.2: %AARD between experimental VLE data and EoS calculations for the mixture bubble pressure and corresponding kij values. 134

Table 7.3: %AARD between GEMC simulation VLE data and EoS calculations for the mixture bubble pressure and corresponding kij values regressed from Monte Carlo simulation data..... 135

Table 7.4: Composition in mole fractions of the synthetic gas condensates studied in this work. 142

Table 8.1: Experimental binary VLE data of CH_4 - *n*-alkane mixtures from the literature, used for the regression of kij values. 151

Table 8.2: Experimental binary SLGE data of CH_4 - *n*-alkane mixtures from the literature. 152

Table 8.3: %AARD between experimental VLE data and EoS calculations for the mixture bubble pressure and corresponding kij values regressed from experimental measurements. 155

Table 8.4: %AARD between experimental SLGE data and model predictions calculated for the equilibrium temperature or pressure of each mixture. 156

Table 8.5: %ARD between the liquid molar volumes of Table C.4 and the predicted volumes of the untranslated cubic and PC-SAFT EoS at the reported temperature and pressure conditions (normal melting point of pure components). 166

Table 8.6: %AARD between experimental SLGE data and correlations with the advanced-fit solid-phase model calculated for the equilibrium temperature of each mixture. 172

Table 9.1: %AARD between experimental data at saturated conditions taken from NIST [261] and EoS predictions for C_2H_4. The ideal gas heat capacity is calculated using a correlation from DIPPR [175]. 182

Table 9.2: %AARD between experimental data at supercritical conditions taken from NIST [261] and EoS predictions for C_2H_4. The ideal gas heat capacity is calculated using a correlation from DIPPR [175]. 183

Table 9.3: Experimental binary VLE data from literature modeled in this work. 187

Table 9.4: %AARD between experimental VLE data and EoS calculations for the mixture bubble pressure and corresponding kij values. 188

Table 9.5: %AARD between experimental VLE data and EoS calculations for the mixture bubble pressure and corresponding kij values, calculated as a temperature dependent function. 189

Table 9.6: Experimental ternary VLE data from literature modeled in this work. 196

List of Figures

Figure 3.1: Schematic representation of the formation of a pure fluid within the PC-SAFT framework. 34

Figure 3.2: Thermodynamic cycle for the calculation of the solid-phase fugacity, based on the hypothetical, pure, subcooled melt reference state. Figure taken from Seiler et al. [162]. 40

Figure 4.1: Constant composition VLE phase envelope of a 94.3% (mole) CH_4 - 2.7% C_2H_6 - 0.74% C_3H_8 - 0.49% *n*-C_4H_{10} - 0.27% *n*-C_5H_{12} - 0.10% *n*-C_6H_{14} - 1.4% N_2 mixture (mix1). Calculations were performed with SRK EoS and $kij = 0$. 61

Figure 4.2: Flow diagram of the implementation algorithm for method 1U. 62

Figure 4.3: Flow diagram of the implementation algorithm for method 3U. 63

Figure 4.4: Convergence comparison of the three (1U, 2U, 3U) different methods for an upper dew point calculation at T= 240 K for mix1. Initialization was done at P= 1 MPa. The calculations were performed with SRK EoS and $kij = 0$. Top panels: Solid lines correspond to the error with respect to pressure and dashed lines correspond to the error with respect to the mole number of the component presented in the bottom panels. 70

Figure 4.5: Convergence comparison of the three (1L, 2L, 3L) different methods for a lower dew point calculation at T= 240 K for mix1. Initialization was done at P= 8 MPa. The calculations were performed with SRK EoS and $kij = 0$. Top panels: Solid lines correspond to the error with respect to pressure and dashed lines correspond to the error with respect to the mole number of the component presented in the bottom panels. 71

Figure 4.6: Convergence comparison of the three (1U, 2U, 3U) different methods for an upper dew point calculation at T= 450.05 K for mix2. Initialization was done at P= 1 MPa. The calculations were performed with SRK EoS and kij parameters taken from Novak et al. [92] and Nikolaidis et al. [169]. Top panels: Solid lines correspond to the error with respect to pressure and dashed lines correspond to the error with respect to the mole number of the component presented in the bottom panels. 72

Figure 4.7: Convergence comparison of the three (1H, 2H, 3H) different methods for a high temperature dew point calculation at P= 20.0 MPa for mix2. Initialization was done at T= 500 K. The calculations were performed with SRK EoS and kij parameters taken from Novak et al. [92] and Nikolaidis et al. [169]. Top panels: Solid lines correspond to the error with respect to temperature and dashed lines correspond to the error with respect to the mole number of the component presented in the bottom panels. 73

Figure 4.8: Convergence comparison of the three (1C, 2C, 3C) different methods for a low temperature dew point calculation at P= 7 MPa for mix1. Initialization was done at T= 240 K. The calculations were performed with SRK EoS and $kij = 0$. Top panels: Solid lines correspond to the error with respect to temperature and dashed lines correspond to the error with respect to the mole number of the component presented in the bottom panels. 74

Figure 4.9: Effect of the initial pressure on the convergence behavior for an upper dew point calculation at T= 325.0 K for mix2. The calculations were performed with method 3U, SRK EoS and kij parameters taken from Novak et al.[92] and Nikolaidis et al. [169]. Top panels: Solid lines correspond to the error with respect to pressure and dashed lines correspond to the error with respect to the mole number of the component presented in the bottom panels..... 75

Figure 4.10: Number of iterations for bubble point pressure calculations. Pressure - composition VLE phase diagram for the CH_4 - *n*-$C_{36}H_{74}$ mixture (mix3) at T= 373 K. The calculations were performed with (a) method 3U, (b) partial Newton's method (Eqs. 2.1 - 2.5) and (c) full Newton's method (Eqs. 2.14 - 2.15). PC-SAFT EoS was used with $kij = 0.0282$ taken from Nikolaidis et al. [170]. 76

Figure 4.11: Reduced Gibbs free energy of mixing and reduced TPD function for the CH_4 - *n*-$C_{36}H_{74}$ mixture (mix3) at T= 373 K. The reduced TPD function is calculated using as feed phase composition z_{CH4}= 0.924 (mole fraction). The calculations were performed with PC-SAFT EoS and $kij = 0.0282$. Top panels refer to the results for P = 98 MPa and bottom panels refer to the results for P= 20 MPa. The black dot corresponds to the feed phase composition..... 78

Figure 4.12: Reduced Gibbs free energy of mixing and reduced TPD function for the CH_4 - *n*-$C_{36}H_{74}$ mixture (mix3) at T= 373 K. The reduced TPD function is calculated using as feed phase composition z_{CH4}= 0.924 (mole fraction). The calculations were performed with PC-SAFT EoS and $kij = 0.0282$. Top panels refer to the results for P = 6 MPa and bottom panels refer to the results for P= 0.2 MPa. The black dot corresponds to the feed phase composition..... 79

Figure 4.13: Number of iterations for bubble point pressure, dew point pressure and dew point temperature calculations. Constant composition VLE phase envelope of mix4. The calculations were performed with methods 3U, 3L, 3H, SRK EoS and $kij = 0$..... 80

Figure 4.14: Number of iterations for dew point pressure and dew point temperature calculations. Constant composition VLE phase envelope of mix2. The calculations were performed with methods 3U, 3L, 3H, SRK EoS and kij parameters taken from Novak et al. [92] and Nikolaidis et al. [169]..... 81

Figure 4.15: Number of iterations for bubble point pressure and dew point pressure calculations. Constant composition VLE phase envelope of a 50% (mole) CH_4 - 50% H_2S mixture (mix5). The calculations were performed with methods 3U, 3L, SRK EoS and $kij = 0.08$ taken from Nikolaidis et al. [62]. 82

Figure 4.16: Calculation of multiple solutions (3 dew point pressure solutions) with methods 3U and 3L at T= 208 K for mix5. The calculations were performed with SRK EoS and $kij = 0.08$ taken from Nikolaidis et al. [62]. 83

Figure 5.1: Constant composition VLE phase envelopes of mix1, mix2, mix3 and mix4, calculated with method X1U and SRK EoS..... 91

Figure 5.2: Condition number of the Jacobian matrix for each method, calculated at the solution, along the VLE phase envelope of mix 1. The calculations were performed with SRK EoS and $kij = 0$. The dashed line corresponds to the pressure - temperature projection of the VLE envelope and the open circle corresponds to the critical point..... 92

Figure 5.3: Condition number of the Jacobian matrix for each method, calculated at the solution, along the VLE phase envelope of mix 2. The calculations were performed with SRK EoS and kij parameters taken from Novak et al. [92] and

Nikolaidis et al. [169]. The dashed line corresponds to the pressure - temperature projection of the VLE envelope. 93

Figure 5.4: Condition number of the Jacobian matrix for each method, calculated at the solution, along the VLE phase envelope of mix 3. The calculations were performed with SRK EoS and $kij = 0$. The dashed line corresponds to the pressure - temperature projection of the VLE envelope. 94

Figure 5.5: Condition number of the Jacobian matrix for each method, calculated at the solution, along the VLE phase envelope of mix 4. The calculations were performed with SRK EoS and $kij = 0.08$. The dashed line corresponds to the pressure - temperature projection of the VLE envelope and the open circles correspond to the critical points. 95

Figure 5.6: Pressure - composition VLE phase diagrams for the CH_4 - *n*-$C_{36}H_{74}$ mixture at (a) T= 373 K, (b) T= 700 K, calculated with the SRK EoS and $kij = 0$. Pressure - composition VLE phase diagram for the CH_4 - CO_2 mixture at (c) T= 241.5 K, calculated with the SRK EoS and $kij = 0$. Pressure - composition VLE / LLE phase diagram for the CO_2 - H_2O mixture at (d) T= 298 K, calculated with the PC-SAFT EoS and kij taken from Diamantonis et al. [172]. 99

Figure 5.7: Condition number of the Jacobian matrix for each method, calculated at the solution, along the pressure - composition phase diagrams presented in Figure 5.6. Solid black lines correspond to method 1mV, solid red lines to method 2mV, solid green lines to method 3m and solid blue lines to method 4mV. Dotted black lines correspond to method 1mL, dotted red lines to method 2mL and dotted blue lines to method 4mL 100

Figure 5.8: Variation of pressure along the P-x,y phase diagram of the CH_4 - *n*-$C_{36}H_{74}$ mixture at T= 700 K (SRK EoS and $kij = 0$), with various specification variables. 101

Figure 5.9: Variation of pressure along the P-x,y phase diagram of the CH_4 - CO_2 mixture at T= 241.5 K (SRK EoS and $kij = 0$), with various specification variables. ... 102

Figure 5.10: Variation of pressure along the P-x,y phase diagram of the CO_2 - H_2O mixture at T= 298 K (PC-SAFT EoS and kij taken from Diamantonis et al. [172]), with various specification variables. 103

Figure 5.11: Variation of pressure along the P-x,y phase diagram of the CO_2 - H_2O mixture at T= 298 K (PC-SAFT EoS and kij taken from Diamantonis et al. [172]), with various specification variables (detail). 103

Figure 5.12: Pressure - composition VLE phase diagram for the CH_4 - CO_2 mixture at T= 180 K, calculated with the SRK EoS and $kij = 0.1$. 104

Figure 5.13: Variation of pressure along the P-x,y phase diagram of the CH_4 - CO_2 mixture at T= 180 K (SRK EoS and $kij = 0.1$), with various specification variables. 105

Figure 5.14: Variation of pressure along the P-x,y phase diagram of the CH_4 - CO_2 mixture at T= 180 K (SRK EoS and $kij = 0.1$), with various specification variables (detail). 106

Figure 5.15: Temperature - composition VLE phase diagrams for the CH_4 - *n*-C_6H_{14} mixture at (a) P= 2.5 MPa, (b) T= 10 MPa, calculated with the PC-SAFT EoS and $kij = 0$. 107

Figure 5.16: Condition number of the Jacobian matrix for each method, calculated at the solution, along the temperature - composition phase diagrams presented in Figure 5.15. Solid black lines correspond to method 1mV, solid red lines to method 2mV, solid green lines to method 3m and solid blue lines to method 4mV. Dotted black lines correspond to method 1mL, dotted red lines to method 2mL and dotted blue lines to method 4mL. 107

Figure 5.17: Variation of temperature along the T-x,y phase diagram of the CH_4 - *n*-C_6H_{14} mixture at P= 2.5 MPa (PC-SAFT EoS and $kij = 0$), with various specification variables. 108

Figure 5.18: Variation of temperature along the T-x,y phase diagram of the CH_4 - *n*-C_6H_{14} mixture at P= 10 MPa (PC-SAFT EoS and $kij = 0$), with various specification variables. 109

Figure 6.1: Pure CO_2 SVE: Comparison of Empirical Correlation, Thermodynamic Integration model and Jäger and Span EoS, coupled with PC-SAFT EoS..... 114

Figure 6.2: Pure CO_2 SLE: Comparison of Empirical Correlation, Thermodynamic Integration model and Jäger and Span EoS, coupled with PC-SAFT EoS..... 115

Figure 6.3: Prediction ($kij = 0$) of the SLGE of the CO_2 - N_2 mixture. Results with three different solid-phase models: (a) Thermodynamic Integration model, (b) Empirical Correlation model, (c) Jäger and Span EoS, coupled with three fluid-phase EoS. Experimental data [176] are represented by data points and calculations by lines: $(-)$ SRK, $-\cdot-$PR, $(---)$ PC-SAFT. 118

Figure 6.4: Pressure - composition VLE phase diagram for the CO_2 - N_2 mixture at T= 218.15 K. Experimental data [176] are represented by data points and correlations ($kij \neq 0$) by lines: (−) SRK, $(-\cdot-)$ PR, $(---)$ PC-SAFT. 119

Figure 6.5: Prediction of the SLGE of the CO_2 - N_2 mixture when kij parameters fitted to experimental binary VLE data at low temperature are used. Results with three different solid-phase models: (a) Thermodynamic Integration model, (b) Empirical Correlation model, (c) Jäger and Span EoS, coupled with three fluid-phase EoS. Experimental data [176] are represented by data points and calculations by lines: $(-)$ SRK, $-\cdot-$PR, $(---)$ PC-SAFT. 120

Figure 6.6: Prediction ($kij = 0$) of the SLGE of the CO_2 - H_2 mixture. Results with three different solid-phase models: (a) Thermodynamic Integration model, (b) Empirical Correlation model, (c) Jäger and Span EoS, coupled with three fluid-phase EoS. Experimental data [176] are represented by data points and calculations by lines: $(-)$ SRK, $-\cdot-$PR, $(---)$ PC-SAFT. 121

Figure 6.7: Pressure - composition VLE phase diagram for the CO_2 - H_2 mixture, at T= 218.15 K. Experimental data [176] are represented by data points and correlations ($kij \neq 0$) by lines: (−) SRK, $(-\cdot-)$ PR, $(---)$ PC-SAFT. 122

Figure 6.8: Prediction of the SLGE of the CO_2 - H_2 mixture when kij parameters fitted to experimental binary VLE data at low temperature are used. Results with three different solid-phase models: (a) Thermodynamic Integration model, (b) Empirical Correlation model, (c) Jäger and Span EoS, coupled with three fluid-phase EoS. Experimental data [176] are represented by data points and calculations by lines: $(-)$ SRK, $-\cdot-$PR, $(---)$ PC-SAFT. 122

Figure 6.9: Prediction ($kij = 0$) of the SLGE of the CO_2 - CH_4 mixture. Results with three different solid-phase models: (a) Thermodynamic Integration model, (b) Empirical Correlation model, (c) Jäger and Span EoS, coupled with three fluid-

phase EoS. Experimental data [177, 178] are represented by data points and calculations by lines: (−) SRK, −·−PR, (− − −) PC-SAFT. 123

Figure 6.10: Prediction of the SLGE of the CO_2 - CH_4 mixture when $\boldsymbol{kij}$ parameters fitted to experimental binary VLE data from Diamantonis et al. are used. Results with three different solid-phase models: (a) Thermodynamic Integration model, (b) Empirical Correlation model, (c) Jäger and Span EoS, coupled with three fluid-phase EoS. Experimental data [177, 178] are represented by data points and calculations by lines: (−) SRK, −·−PR, (− − −) PC-SAFT. 124

Figure 6.11: P-T projection of the SLGE and LG critical locus of the CO_2 - CH_4 mixture when $\boldsymbol{kij}$ parameters fitted to experimental binary VLE data are used [13]. Calculations with the Thermodynamic Integration model coupled with the PR EoS..... 125

Figure 7.1: Pressure - composition VLE for the CH_4 - n-$C_{24}H_{50}$ mixture at various temperatures; (a) T= 330 K, (b) T= 350 K, (c) T= 374.05 K, (d) T= 523.15 K. Experimental data [208-210] are represented by black data points and GEMC simulation data by red squares. 132

Figure 7.2: % AARD vs carbon number of the long-chain hydrocarbon for binary CH_4 mixtures. Left panel shows the % AARD when $\boldsymbol{kij}$ parameters are fitted to experimental data. Right panel shows the % AARD when $\boldsymbol{kij}$ parameters are fitted to GEMC simulation data. Black lines correspond to SRK, red to PR and blue to PC-SAFT EoS..... 136

Figure 7.3: Pressure - composition VLE phase diagrams for the CH_4 - n-$C_{10}H_{22}$ mixture at various temperatures; (a) T= 244.26 K, (b) T= 310.93 K, (c) T= 450 K, (d) T= 583.05 K. Experimental data [189, 192, 194] are represented by black data points. GEMC simulation data are represented by red data points. Calculations with EoS are represented by lines and are performed with $\boldsymbol{kij}$ parameters fitted to GEMC simulation data. Black lines correspond to SRK, red to PR and blue to PC-SAFT EoS..... 138

Figure 7.4: Pressure - composition VLE phase diagrams for the CH_4 - n-$C_{12}H_{26}$ mixture at various temperatures; (a) T= 303.15 K, (b) T= 373.2 K, (c) T= 450 K, (d) T= 550 K. Experimental data [191, 196] are represented by black data points. GEMC simulation data are represented by red data points. Calculations with EoS are

represented by lines and are performed with kij parameters fitted to GEMC simulation data. Black lines correspond to SRK, red to PR and blue to PC-SAFT EoS..... 139

Figure 7.5: Pressure - composition VLE phase diagrams for the CH_4 - *n*-$C_{16}H_{34}$ mixture at various temperatures; (a) T= 340 K, (b) T= 500 K, (c) T= 600 K, (d) T= 623.15 K. Experimental data [198, 202] are represented by black data points. GEMC simulation data are represented by red data points. Calculations with EoS are represented by lines and are performed with kij parameters fitted to GEMC simulation data. Black lines correspond to SRK, red to PR and blue to PC-SAFT EoS..... 140

Figure 7.6: Pressure - composition VLE phase diagrams for the CH_4 - *n*-$C_{20}H_{42}$ mixture at various temperatures; (a) T= 323.15 K, (b) T= 500 K, (c) T= 600 K, (d) T= 700 K. Experimental data [206] are represented by black data points. GEMC simulation data are represented by red data points. Calculations with EoS are represented by lines and are performed with kij parameters fitted to GEMC simulation data. Black lines correspond to SRK, red to PR and blue to PC-SAFT EoS..... 141

Figure 7.7: Pressure - composition VLE phase diagrams for the CH_4 - *n*-$C_{24}H_{50}$ mixture at various temperatures; (a) T= 330 K, (b) T= 374.05 K, (c) T= 500 K, (d) T= 750 K. Experimental data [208, 210] are represented by black data points. GEMC simulation data are represented by red data points. Calculations with EoS are represented by lines and are performed with kij parameters fitted to GEMC simulation data. Black lines correspond to SRK, red to PR and blue to PC-SAFT EoS..... 141

Figure 7.8: Constant composition phase envelopes for the synthetic gas condensate mixtures (SGC1, SGC2, SGC3, SGC4, SGC5, SGC6, SGC7) studied in this work. The compositions of the mixtures are listed in Table 7.4. Experimental data [88, 236-238] are represented by points and calculations by lines. Solid lines correspond to calculations with kij parameters fitted to experimental binary VLE data. Dashed lines correspond to calculations with kij parameters fitted to GEMC simulation binary VLE data. Black lines correspond to SRK, red to PR and blue to PC-SAFT EoS..... 143

Figure 8.1: Enthalpy of melting of *n*-alkanes with carbon number. Black data points correspond to even carbon number *n*-alkanes and blue data points to odd carbon number *n*-alkanes [175]. 150

Figure 8.2: Prediction of the SLGE curve of the CH_4 - *n*-C_6H_{14} mixture. Experimental data [244, 245] are represented by data points and calculations by lines. Black lines correspond to SRK, red to PR and blue to PC-SAFT EoS. Left panels show predictions with the basic solid-phase model and $kij = 0$, while right panels show predictions with the basic solid-phase model and kij parameters fitted to experimental binary VLE data. The *n*-C_6H_{14} mole fraction refers to the liquid phase along the SLGE curve. 157

Figure 8.3: Prediction of the SLGE curve of the CH_4 - *n*-C_7H_{16} mixture. Experimental data [246] are represented by data points and calculations by lines. Black lines correspond to SRK, red to PR and blue to PC-SAFT EoS. Left panels show predictions with the basic solid-phase model and $kij = 0$, while right panels show predictions with the basic solid-phase model and kij parameters fitted to experimental binary VLE data. The *n*-C_7H_{16} mole fraction refers to the liquid phase along the SLGE curve. 158

Figure 8.4: Prediction of the SLGE curve of the CH_4 - *n*-C_8H_{18} mixture. Experimental data [242, 247] are represented by data points and calculations by lines. Black lines correspond to SRK, red to PR and blue to PC-SAFT EoS. Left panels show predictions with the basic solid-phase model and $kij = 0$, while right panels show predictions with the basic solid-phase model and kij parameters fitted to experimental binary VLE data. The *n*-C_8H_{18} mole fraction refers to the liquid phase along the SLGE curve. 159

Figure 8.5: Prediction of the SLGE curve of the CH_4 - *n*-$C_{10}H_{22}$ mixture. Experimental data [193, 248] are represented by data points and calculations by lines. Black lines correspond to SRK, red to PR and blue to PC-SAFT EoS. Left panels show predictions with the basic solid-phase model and $kij = 0$, middle panels show predictions with the basic solid-phase model and kij parameters fitted to experimental binary VLE data, while right panels show predictions with the advanced solid-phase model and kij parameters fitted to experimental binary VLE data. The *n*-$C_{10}H_{22}$ mole fraction refers to the liquid and vapor phases along the SLGE curve. 160

Figure 8.6: Prediction of the SLGE curve of the CH_4 - *n*-$C_{16}H_{34}$ mixture. Experimental data [198] are represented by data points and calculations by lines. Black lines correspond to SRK, red to PR and blue to PC-SAFT EoS. Left panels show predictions with the basic solid-phase model, while right panels show predictions with the advanced solid-phase model. Both calculations include kij parameters fitted to experimental binary VLE data. The *n*-$C_{16}H_{34}$ mole fraction refers to the liquid and vapor phases along the SLGE curve. 161

Figure 8.7: Prediction of the SLGE curve of the CH_4 - *n*-$C_{17}H_{36}$ mixture. Experimental data [24] are represented by data points and calculations by lines. Black lines correspond to SRK, red to PR and blue to PC-SAFT EoS. Left panels show predictions with the basic solid-phase model, while right panels show predictions with the advanced solid-phase model. Both calculations include kij parameters fitted to experimental binary VLE data. The *n*-$C_{17}H_{36}$ mole fraction refers to the liquid and vapor phases along the SLGE curve. 161

Figure 8.8: Prediction of the SLGE curve of the CH_4 - *n*-$C_{20}H_{42}$ mixture. Experimental data [206] are represented by data points and calculations by lines. Black lines correspond to SRK, red to PR and blue to PC-SAFT EoS. Left panels show predictions with the basic solid-phase model, while right panels show predictions with the advanced solid-phase model. Both calculations include kij parameters fitted to experimental binary VLE data. The *n*-$C_{20}H_{42}$ mole fraction refers to the liquid and vapor phases along the SLGE curve. 162

Figure 8.9: Prediction of the SLGE curve of the CH_4 - *n*-$C_{24}H_{50}$ mixture. Experimental data [208] are represented by data points and calculations by lines. Black lines correspond to SRK, red to PR and blue to PC-SAFT EoS. Left panels show predictions with the basic solid-phase model, while right panels show predictions with the advanced solid-phase model. Both calculations include kij parameters fitted to experimental binary VLE data. The *n*-$C_{24}H_{50}$ mole fraction refers to the liquid and vapor phases along the SLGE curve. 162

Figure 8.10: Prediction of the SLGE curve of the CH_4 - *n*-$C_{30}H_{62}$ mixture. Experimental data [20] are represented by data points and calculations by lines. Black lines correspond to SRK, red to PR and blue to PC-SAFT EoS. Left panels show predictions with the basic solid-phase model, while right panels show predictions with the advanced solid-phase model. Both calculations include kij parameters

fitted to experimental binary VLE data. The *n*-$C_{30}H_{62}$ mole fraction refers to the liquid and vapor phases along the SLGE curve. 163

Figure 8.11: Prediction of the SLGE curve of the CH_4 - *n*-$C_{36}H_{74}$ mixture. Experimental data [249] are represented by data points and calculations by lines. Black lines correspond to SRK, red to PR and blue to PC-SAFT EoS. Left panels show predictions with the basic solid-phase model, while right panels show predictions with the advanced solid-phase model. Both calculations include kij parameters fitted to experimental binary VLE data. The *n*-$C_{36}H_{74}$ mole fraction refers to the liquid and vapor phases along the SLGE curve. 163

Figure 8.12: Prediction of the SLGE curves of various binary CH_4 mixtures with kij parameters calculated from the proposed correlations. Experimental data [24, 193, 198, 242, 244-248] are represented by data points and calculations by lines. Black lines correspond to SRK, red to PR and blue to PC-SAFT EoS. Top panels show predictions with the basic solid-phase model, while bottom panels show predictions with the advanced solid-phase model. 169

Figure 8.13: Prediction of the SLGE curves of various binary CH_4 mixtures with kij parameters calculated from the proposed correlations and the advanced solid-phase model. Experimental data [20, 206, 208, 249] are represented by data points and calculations by lines. Black lines correspond to SRK, red to PR and blue to PC-SAFT EoS. 170

Figure 8.14: Correlation of the SLGE curve with the advanced-fit solid phase model and kij parameters fitted to experimental binary VLE data. Experimental data [24, 198] are represented by data points and calculations by lines. Black lines correspond to SRK, red to PR and blue to PC-SAFT EoS. Left panels show the correlation of the CH_4 - *n*-$C_{16}H_{34}$ mixture, while right panels show the correlation of the CH_4 - *n*-$C_{17}H_{36}$ mixture. The mole fraction refers to the liquid and vapor phases along the SLGE curve. 171

Figure 8.15: Correlation of the SLGE curve with the advanced-fit solid phase model and kij parameters fitted to experimental binary VLE data. Experimental data [20, 206, 208] are represented by data points and calculations by lines. Black lines correspond to SRK, red to PR and blue to PC-SAFT EoS. Left panels show the correlation of the CH_4 - *n*-$C_{20}H_{42}$ mixture, middle panels show the correlation of

the CH_4 - *n*-$C_{24}H_{50}$ mixture and right panels show the correlation of the CH_4 - *n*-$C_{30}H_{62}$ mixture. The mole fraction refers to the liquid and vapor phases along the SLGE curve. 172

Figure 8.16: Global phase diagram of the CH_4 - *n*-C_6H_{14} mixture. Experimental SLGE data [244, 245] are represented by blue data points. Experimental VLE / GLE critical points [254, 255] are represented by black points. Experimental LCEP and UCEP are represented by red data points. Red lines correspond to PR and blue to PC-SAFT EoS. All calculations were performed with kij parameters fitted to experimental binary VLE data. Solid lines correspond to pure component vapor pressure calculations. Dashed lines correspond to VL / GL critical point calculations. Dash-dot lines correspond to VLLE / GLLE calculations. Dotted lines correspond to SLGE calculations. SLGE calculations were performed with the basic solid-phase model..... 174

Figure 8.17: Global phase diagram of the CH_4 - *n*-C_7H_{16} mixture. Experimental SLGE data [246] are represented by blue data points. Experimental VLE / GLE critical points [256, 257] are represented by black points. Red lines correspond to PR and blue to PC-SAFT EoS. All calculations were performed with kij parameters fitted to experimental binary VLE data. Solid lines correspond to pure component vapor pressure calculations. Dashed lines correspond to VL / GL critical point calculations. Dash-dot lines correspond to VLLE / GLLE calculations. Dotted lines correspond to SLGE and SLLE calculations. SLGE and SLLE calculations were performed with the basic solid-phase model..... 175

Figure 8.18: Global phase diagrams of various binary CH_4 mixtures. Experimental SLGE data [193, 198, 206, 242, 247, 248] are represented by blue points. Experimental VLE / GLE critical points [194, 242, 251, 258] are represented by black points. Red lines correspond to PR and blue to PC-SAFT EoS. All calculations were performed with kij parameters fitted to experimental binary VLE data. Solid lines correspond to pure component vapor pressure calculations. Dashed lines correspond to VL / GL critical point calculations. Dotted lines correspond to SLGE calculations. The CH_4 - *n*-C_8H_{18} SLGE was calculated with the basic solid-phase model. The CH_4 - *n*-$C_{10}H_{22}$ SLGE was calculated with the advanced solid-phase model. The CH_4 - *n*-$C_{16}H_{34}$ and CH_4 - *n*-$C_{20}H_{42}$ SLGE were calculated with the advanced-fit solid-phase model..... 176

Figure 9.1: Speed of sound along the saturation curve of C_2H_4. NIST data [261] are represented by data points and calculations by lines. Red lines correspond to PR, blue lines to PC-SAFT and black lines to SAFT-VR Mie EoS..... 181

Figure 9.2: Joule-Thomson coefficient along the saturation curve of C_2H_4. NIST data [261] are represented by data points and calculations by lines. The color code is the same as in Figure 9.1..... 183

Figure 9.3: Saturated and supercritical density of C_2H_4. Supercritical temperature range (from right to left: $1.027T_r$, $1.062T_r$, $1.133T_r$, $1.204T_r$, $1.345T_r$, $1.434T_r$) spans $1.027T_r$ to $1.434T_r$. NIST data [261] are represented by data points and calculations by lines. The color code is the same as in Figure 9.1..... 184

Figure 9.4: Supercritical speed of sound of C_2H_4. Supercritical temperature range spans $1.027T_r$ to $1.434T_r$. NIST data [261] are represented by data points and calculations by lines. The color code is the same as in Figure 9.1..... 185

Figure 9.5: Supercritical Joule-Thomson coefficient of C_2H_4. Supercritical temperature range spans $1.027T_r$ to $1.434T_r$. NIST data [261] are represented by data points and calculations by lines. The color code is the same as in Figure 9.1. 185

Figure 9.6: Pressure - composition VLE phase diagrams for the H_2 - C_2H_4 mixture at temperatures from 114.15 to 166.15 K. Experimental data [265] are represented by data points and calculations by lines. The color code is the same as in Figure 9.1. Calculations were performed with temperature-dependent $\boldsymbol{kij}$..... 190

Figure 9.7: Pressure - composition VLE phase diagrams for the H_2 - C_2H_4 mixture at temperatures from 175.15 to 247.15 K. Experimental data [265] are represented by data points and calculations by lines. The color code is the same as in Figure 9.1. Calculations were performed with temperature-dependent $\boldsymbol{kij}$..... 191

Figure 9.8: Pressure - composition VLE phase diagrams for the CH_4 - C_2H_4 mixture at various temperatures. Experimental data [264, 267] are represented by data points and calculations by lines. The color code is the same as in Figure 9.1. Calculations were performed with $\boldsymbol{kij} \neq \boldsymbol{0}$..... 191

Figure 9.9: Pressure - composition VLE phase diagrams for the C_2H_4 - CO_2 mixture at various temperatures. Experimental data [268, 270] are represented by data points and calculations by lines. The color code is the same as in Figure 9.1. Top panels

show predictions ($kij = 0$), while bottom panels show correlations ($kij \neq 0$). 192

Figure 9.10: Pressure - composition VLE phase diagrams for the C_2H_4 - C_3H_8 mixture at various temperatures. Experimental data [276] are represented by data points and calculations by lines. The color code is the same as in Figure 9.1. Calculations were performed with $kij \neq 0$..... 193

Figure 9.11: Pressure - composition VLE phase diagrams for the C_2H_4 - C_3H_6 mixture at various temperatures. Experimental data [277-279] are represented by data points and calculations by lines. The color code is the same as in Figure 9.1. Calculations were performed with $kij \neq 0$..... 194

Figure 9.12: Pressure - composition VLE phase diagrams for the C_2H_4 - *1*-C_4H_8 mixture at various temperatures. Experimental data [117, 278] are represented by data points and calculations by lines. The color code is the same as in Figure 9.1. Calculations were performed with $kij \neq 0$. 195

Figure 9.13: Ternary phase diagrams for the H_2 - CH_4 - C_2H_4 mixture at (a) T= 123.15 K and P= 2.0265 MPa, (b) T= 198.15 K and P= 8.106 MPa and (c) T= 248.15 K and P= 8.106 MPa. Experimental data [264] are represented by data points and calculations by lines. The color code is the same as in Figure 9.1. Calculations were performed with $kij \neq 0$..... 197

Figure 9.14: Ternary phase diagram for the H_2 - C_2H_4 - C_2H_6 mixture at T= 198.15 K and P= 2.0265 MPa. Experimental data [264] are represented by data points and calculations by lines. The color code is the same as in Figure 9.1. Calculations were performed with $kij \neq 0$..... 198

Figure 9.15: Ternary phase diagram for the H_2 - C_2H_4 - C_3H_8 mixture at T= 248.15 K and P= 2.0265 MPa. Experimental data [280] are represented by data points and calculations by lines. The color code is the same as in Figure 9.1. Calculations were performed with $kij \neq 0$..... 199

Figure 9.16: Ternary phase diagrams for the CH_4 - C_2H_4 - C_2H_6 mixture at (a) T= 169.15 K and P= 0.50663 MPa and (b) T= 273.15 K and P= 5.06625 MPa. Experimental data [281] are represented by data points and calculations by lines. The color code is the same as in Figure 9.1. Calculations were performed with $kij \neq 0$..... 200

Figure 10.1: Sampling the T, P grid and evaluating the corresponding ρ, e, or another property pair ($s, htot$ for example) (Step 1). Reinterpret the grid to return the inverse maps $P(\rho, e)$ and $T(\rho, e)$ (Step 2). 204

Figure 10.2: ρ, e grid distribution with a uniform sampling for the binary 95.96% (vol./vol) CO_2 - 4.04% N_2 mixture. Calculations were performed with the PC-SAFT EoS. 207

Figure 10.3: ρ, e grid distribution with the proposed adaptive sampling for the binary 95.96% (vol./vol) CO_2 - 4.04% N_2 mixture. Calculations were performed with the PC-SAFT EoS. 207

Figure 10.4: T, P grid distribution with the proposed adaptive sampling for the binary 95.96% (vol./vol) CO_2 - 4.04% N_2 mixture. Calculations were performed with the PC-SAFT EoS. 208

Figure 10.5: The temperature and pressure interpolation errors, ΔT and ΔP, due to a mismatch between the (To, Po) data corresponding to the interpolation point $(\rho o, eo)$ and the results of the interpolation (T, P). 208

Figure 10.6: %AARD interpolation errors observed in (a) pressure and (b) temperature across the relevant region in the P-T phase diagram for the binary mixture. Calculations were performed with the PC-SAFT EoS..... 209

Figure 10.7: %AARD interpolation errors observed in (a) pressure and (b) temperature across the relevant region in the P-T phase diagram for the 5-component mixture. Calculations were performed with the PC-SAFT EoS. 209

Figure 10.8: Comparison of the predicted and measured variation of pressure with time at the closed end of the pipeline following the initiation of decompression for the binary mixture. 210

Figure 10.9: Thermodynamic trajectory of the decompression relative to the binary mixture phase envelope at the closed end of the pipeline following the initiation of decompression. 211

Figure 10.10: P-T phase envelope for the 99.5% (mole) C_2H_4 - 0.2% CH_4 - 0.3% N_2 mixture. The red line marks the VLE boundary for the mixture, while the green dashed line represents the VLE boundary for pure C_2H_4. The dots on the VLE

boundaries represent the critical points. Calculations were performed with the PC-SAFT EoS. 213

Figure 10.11: Density-specific internal energy phase diagram for the 99.5% (mole) C_2H_4 - 0.2% CH_4 - 0.3% N_2 mixture. The red line marks the VLE boundary for the mixture, while the green dashed line represents the VLE boundary for pure C_2H_4. The dots on the VLE boundaries represent the critical points. Calculations were performed with the PC-SAFT EoS..... 213

Figure 10.12: The entropy-total sonic enthalpy phase diagram for the 99.5% (mole) C_2H_4 - 0.2% CH_4 - 0.3% N_2 mixture. The red line marks the VLE boundary for the mixture, while the green dashed line represents the VLE boundary for pure C_2H_4. The dots on the VLE boundaries represent the critical points. Calculations were performed with the PC-SAFT EoS..... 214

Figure 10.13: The P-T diagram of the 99.5% (mole) C_2H_4 - 0.2% CH_4 - 0.3% N_2 mixture with 150 × 150 points sampled in T-P space. Results are shown with the non-uniform sampling and smoothening procedures. Calculations were performed with the PC-SAFT EoS. 216

Figure 10.14: The ρ-e diagram of the 99.5% (mole) C_2H_4 - 0.2% CH_4 - 0.3% N_2 mixture with 150 × 150 points sampled in T-P space. Results are shown with the non-uniform sampling and smoothening procedures. Calculations were performed with the PC-SAFT EoS. 216

Figure 10.15: The s-$htot*$ diagram of the 99.5% (mole) C_2H_4 - 0.2% CH_4 - 0.3% N_2 mixture with 150 × 150 points sampled in T-P space. Results are shown with the non-uniform sampling and smoothening procedures. Calculations were performed with the PC-SAFT EoS..... 217

Figure 10.16: % AARD interpolation errors observed in pressure as functions of the grid size. 217

Figure 10.17: % AARD interpolation errors observed in temperature as functions of the grid size. 218

Figure 10.18: The density and internal energy errors, $\Delta\rho$ and Δe, resulting from propagation of interpolation errors carried from T, P data, into (ρ, e) data predicted using the PC-SAFT EoS. 218

Figure 10.19: % AARD interpolation errors observed in density as functions of the grid size, using the interpolated temperature and pressure input data..... 219

Figure 10.20: % AARD interpolation errors observed in specific internal energy as functions of the grid size, using the interpolated temperature and pressure input data..... 219

Figure 10.21: The time variation of pressure, as predicted by the decompression model at different locations on the pipeline (PT1, PT2, PT3, PT4), in comparison with the measurements from the pipeline discharge experiment. Experimental data are represented by data points and model predictions by lines..... 221

Figure 10.22: The time variation of temperature, as predicted by the decompression model at different locations on the pipeline (PT1, PT2, PT3, PT4), in comparison with the measurements from the pipeline discharge experiment. Experimental data are represented by data points and model predictions by lines..... 221

Figure 10.23: The thermodynamic trajectories plotted in T-P space, as predicted by the decompression model at different locations on the pipeline (PT1, PT2, PT3, PT4), in comparison with the measurements from the pipeline discharge experiment. Experimental data are represented by data points. Solid orange lines correspond to the P-T phase envelope of the 99.5% (mole) C_2H_4 - 0.2% CH_4 - 0.3% N_2 mixture, calculated with the PC-SAFT EoS. Dash-dot lines correspond to the decompression model predictions and dotted lines correspond to isentropes, calculated with the PC-SAFT EoS..... 222

List of Abbreviations

% AARD	Percentage Average Absolute Deviation
% ARD	Percentage Absolute Relative Deviation
BH	Barker-Henderson
BIPs	Binary Interaction Parameters
CBMC	Configurational Bias Monte Carlo
CCS	Carbon Capture and Sequestration
CFCMC	Continuous Fractional Component Monte Carlo
CFD	Computational Fluid Dynamics
DIPPR	Design Institute for Physical Properties
EoS	Equation of State
EoS-CG	Equation of State with Group Contribution
EoS/G^E	Equation of State coupled with excess Gibbs energy model through advanced mixing rules
FBR	Full-Bore Rupture
GE	Excess Gibbs energy model
GEMC	Gibbs Ensemble Monte Carlo
GERG	Groupe Européen de Recherches Gazières
Gibbs-NPT	Gibbs Ensemble at constant number of molecules, pressure and temperature
GLLE	Gas-Liquid-Liquid Equilibrium
HEM	Homogeneous Equilibrium Model
HPHT	High Pressure High Temperature
LCEP	Lower Critical End Point
LCVM	Linear Combination Vidal Michelsen
LJ	Lennard-Jones
LLE	Liquid-Liquid Equilibrium
n-alkane	normal alkane
PC-SAFT	Perturbed Chain-Statistical Associating Fluid Theory
PR	Peng - Robinson
PPR78	Predictive 1978 Peng-Robinson
SAFT	Statistical Associating Fluid Theory
SAFT-VR Mie	SAFT with the Mie potential of variable range

SBWR	Soave modified Benedict-Webb-Rubin
SGC	Synthetic Gas Condensate
SFE	Solid-Fluid Equilibrium
SLE	Solid-Liquid Equilibrium
SLGE	Solid-Liquid-Gas Equilibrium
SLLE	Solid-Liquid-Liquid Equilibrium
SLVE	Solid-Liquid-Vapor Equilibrium
sPC-SAFT	Simplified Perturbed Chain-Statistical Associating Fluid Theory
SRK	Soave-Redlich-Kwong
SS	Successive Substitution
SSE	Solid-Solid Equilibrium
SSLGE	Solid-Solid-Liquid-Gas Equilibrium
STLL	Stability Test Limit Locus
SVE	Solid-Vapor Equilibrium
SW	Square-Well
TPD	Tangent Plane Distance
TraPPE-UA	Transferable Potentials for Phase Equilibria-United Atom
TraPPE-EH	Transferable Potentials for Phase Equilibria-Explicit Hydrogen
TPT1	Thermodynamic Perturbation Theory of order 1
UCEP	Upper Critical End Point
UMR-PRU	Universal Mixing Rules-PR UNIFAC
vdW	Van der Waals
vdW1f	van der Waals one-fluid
VLE	Vapor-Liquid Equilibrium
VLLE	Vapor- Liquid-Liquid Equilibrium

List of Symbols

Latin Letters

$A^{RESIDUAL}$	Residual Helmholtz free energy
$A^{HARD-CHAIN}$	Hard-chain contribution to the residual Helmholtz free energy
$A^{DISPERSION}$	Dispersion forces contribution to the residual Helmholtz free energy
$A^{ASSOCIATION}$	Association contribution to the residual Helmholtz free energy
$\tilde{a}$	Helmholtz free energy per mole
b	Co-volume parameter for the cubic equations of state
c_P	Isobaric heat capacity per mole
C	Number of components in a mixture
e	Internal energy per mass
$\boldsymbol{e}$	Error vector
d_i	Temperature-dependent diameter in SAFT-based EoS
$\hat{f}_i^F$	Fugacity of component i in phase F
g_{ij}^{hs}	Radial distribution function of hard spheres of component i at contact
g	Gibbs free energy per mole
$g^{(k)}$	Equation value at iteration k
g_i^U	Equation i in a nonlinear set of equations
G	Gibbs free energy
h	Enthalpy per mole
h_{tot}^*	Sonic enthalpy per mass
H_{ij}	Element of an Hessian matrix
J_{ij}	Element of a Jacobian matrix
k	Iteration counter
k_B	Boltzmann's constant
k_T	Isothermal compressibility
k_{ij}	Binary interaction parameter in the attractive term

K_i	Ratio of the incipient phase mole number / mole fraction over feed phase mole number / mole fraction of component i
$\overline{K_i}$	Ration of Ξ_i of the incipient phase over the feed phase
l_{ij}	Binary interaction parameter in the repulsive term
M_i	Number of association sites per molecule of species i
$\overline{m}$	Number of spherical segments in a chain in SAFT-based EoS
n_i	Number of moles of component i
N	Number of molecules
P	Pressure
P^+	Reference pressure
P_c	Critical pressure
P_{tr}	Triple point pressure
$P_{0i}^{sat}(T)$	Saturation pressure of component i at temperature T
Q_1	Modified tangent plane distance function of Michelsen
Q_1^m	Modified tangent plane distance function proposed in this work
R	Universal gas constant
s	Entropy per mass
S	Specification variable value
T	Temperature
T_c	Critical temperature
T_{tr}	Triple point temperature
T_{0i}^{SL}	Melting temperature of pure solid former i
T_{0i}^{SV}	Sublimation temperature of pure solid former i
v	Molar volume
v_{0i}^{S}	Pressure, temperature independent pure solid molar volume
$v_{0i}^{L^*}$	Molar liquid volume at the solid-liquid transition
v^k	Value of a variable in iteration k
v^∞	Value of a variable at the solution
w_i	Incipient phase mole fraction of component i
W_i	Incipient phase mole number of component i

x_i	Liquid phase mole fraction of component i
X^{A_i}	Fraction of molecules of species i that are not hydrogen bonded at site A
X_S	Specification variable
y_i	Vapor phase mole fraction of component i
z_i	Feed phase mole fraction of component i
Z	Compressibility factor
Z_i	Feed phase mole number of component i

Greek Letters

$\alpha(T)$	Temperature dependent function for the attractive term of cubic EoS
α_C	Critical value of Soave's alpha function
β	Vapor fraction
$\hat{\beta}$	Proportionality coefficient
δ_{ij}	Kronecker delta
ε	Dispersion energy parameter used by PC-SAFT EoS
$\varepsilon^{A_iB_i}$	Association energy
ζ_k	Zeta function
η_1	Relaxation parameter
η_2	Positive constant used to turn a matrix positive definite
ϑ	Reduced temperature
θ	Bond angle
$\kappa^{A_iB_i}$	Association volume
$\kappa_2(\boldsymbol{A})$	Condition number of a matrix $\boldsymbol{A}$ based on $\|\boldsymbol{A}\|_2$
λ_{min}	Minimum eigenvalue of a matrix
λ_r	Repulsive exponent in the Mie potential
λ_a	Attractive exponent in the Mie potential
μ_i	Chemical potential of component i
μ_{JT}	Joule-Thomson coefficient
π	Reduced pressure
ρ	Molar density

$\hat{\rho}$	Number density of molecules
σ	Segment diameter parameter used by PC-SAFT
v_s	Speed of sound
φ	Dihedral angle
$\hat{\varphi}_i^F$	Fugacity coefficient of a component i in phase F
ω	Acentric factor

Subscripts and Superscripts

ASSOC	Association
DISP	Dispersion
E	Excess
HC	Hard Chain
HS	Hard Sphere
L	Liquid
sat	Saturation
tr	triple
V	Vapor

1. Introduction

1.1. Motivation

The significant energy needs in recent years have led to an extensive consumption of fossil fuels, which account for more than 80% of the total worldwide. The growth of the global energy need abruptly increased in 2017, driven by economic growth but also by the slowdown in the improvement of energy efficiency. The most significant part in the increased energy need is attributed to the power sector, accounting for over 40% of the primary energy consumption [1]. Despite the appearance and adoption of new and more environmentally friendly technologies, fossil fuels are still the most widely used sources for power and heat generation and they are also used in heavy industrial manufacturing operations. This can be attributed to the lower efficiency and higher costs that occur – as compared to the exploitation of fossil fuels – due to the low level of maturity of the new technologies. Coal demand has remained stagnant in recent years, while oil and natural gas demand is increasing [1]. Natural gas is considered "the cleanest" fossil fuel source of energy and exhibits by far the fastest growing demand among the three. Closely related to the need for cleaner energy sources is also the role of natural gas in chemical conversion processes to ultraclean fuels and other added-value products used by the chemical industry [2].

The extensive consumption of fossil fuels contributes significantly to the increased levels of greenhouse gases in the atmosphere, which subsequently leads to environmental problems such as global warming. The most important greenhouse gas, in terms of quantity and impact, is carbon dioxide (CO_2). As the global energy demand has increased, CO_2 levels have risen significantly, from the preindustrial levels of 280 ppm to 413 ppm in June 2019 [3]. Moreover, fossil fuels will continue to play an important role in power and heat generation and also be used in large industrial operations in the foreseeable future [4-7]. Unless major measures are taken for the reduction of CO_2 emissions, the CO_2 concentration is projected to rise even more over the next 25 years as global demands for energy are anticipated to increase [8].

To respond to the increased demand for natural gas and oil products, more than 3.5 million km of pressurized pipelines have been constructed worldwide to transport huge amounts of hydrocarbons [9]. Globally, the total length of hydrocarbon

transportation pipelines has increased a 100 fold in the past 50 years with over 32,000 km of new pipelines being constructed every year. Furthermore, significant amount of research has been conducted for the development of new technologies that aim to reduce the levels of CO_2 in the atmosphere. The most mature technology today is Carbon Capture and Sequestration (CCS), which is the process of capturing CO_2 from the flue gas of a large point source (typically a power plant), transporting it to a sequestration site and then depositing it to a geological formation, which can be a saline aquifer or a depleted oil well. The CCS process can be divided into three main parts: CO_2 capture, transport and storage. An important part of the CCS process is the transportation of a CO_2-rich stream from the capture plant to the sequestration site and in most cases this is done via pipelines. The two factors that have contributed to this extensive use of pipelines are safety and cost effectiveness.

Although pipelines are considered to be the safest mode for transportation of hydrocarbon products, they present significant challenges related to their operation and maintenance. More than 250 pipeline rupture incidents occur globally every year, with some resulting in serious consequences, such as fatalities, injuries and damage to assets [10]. The most common types of incidents are pipeline material failure (corrosion), impact failure during excavating work, human errors and other external events [11]. Another emerging safety challenge is due to the fact that a significant part of the currently used pressurized pipelines has been in operation for more than 30 years. To ensure their continued safe operation, diligent maintenance and regular inspection are of paramount importance. As for the new generation pipelines, these are being made of higher strength steel materials but thinner walls to reduce costs. For such new pipelines very little historical data is available regarding their reliability in the long term.

Regarding the construction and operation of CO_2 pipelines; CO_2 possesses some unusual physical properties which make its release behavior challenging to predict. CO_2 has a triple point pressure and temperature of 5.18 bar and 216.58 K respectively, and at atmospheric pressure it exists in either a solid or gaseous state, with a sublimation temperature of 194.25 K. This means that there is likely to be complex phase-transition when CO_2 decompresses from an initial dense-phase state in the pipeline (*i.e.* as a supercritical or liquid fluid) into a solid and gaseous state at atmospheric pressure [12]. Moreover, CO_2 pipelines may be crossing in the close proximity of populated areas. CO_2 is a colorless and odorless gas under ambient conditions and is toxic if inhaled in air at concentrations around 5%, and likely to be fatal at concentrations of around 10%. As a

result, a more thorough investigation, regarding the hazards of CO_2 pipeline construction should be performed.

Preliminary and detailed design, simulation and optimization of an uninterrupted transport process require, among others, accurate knowledge of the physical properties of the chemical system involved. In real-life industrial applications, most of the fluid streams consist of binary or multicomponent mixtures and as a result, the physical properties of the fluids have to be known as functions of temperature (T), pressure (P), and composition. Furthermore, depending on the conditions, the system may split into two or more coexisting phases (*i.e.*, liquid, vapor and/or solid) and as a result process design calculations have to take into account these conditions. For example, it is not always possible to maintain pipeline temperatures above the cricondentherm point (maximum temperature above which liquid cannot be formed, regardless of pressure) of the relevant mixture. It is, therefore, important to ensure pressure drops are managed and pipeline pressures are kept above certain limits to maintain a single dense phase flow, avoid liquid slugs, solid-phase precipitations and other operational problems. Moreover, rigorous mathematical tools can be used to accurately assess and improve the safety of high pressure hydrocarbon transportation pipelines. These mathematical tools entail the development of a pipeline rupture outflow model in the form of computational fluid dynamics (CFD) simulations. Development of reliable pipeline rupture mathematical models that account for single and multi-phase heterogeneous flows rely heavily on the accurate knowledge of various physical properties of the fluid(s) involved. In the case of a sudden decompression of a pipeline, the initially single phase fluid splits into two or more coexisting phases. The challenge is the accurate prediction of the composition of the phases as well as the respective physical properties.

Prediction or correlation of the physical properties and phase equilibria of mixtures is typically performed with Equations of State (EoS), which offer a good balance between accuracy and computational efficiency. Moreover, the calculation of phase equilibria itself using EoS presents various computational challenges and robust algorithms are needed for stand-alone calculations and even more importantly when thermodynamic calculations must be incorporated in process and CFD simulators. Finally, coupling complex EoS with CFD simulators entails the challenge of providing the physical properties of the chemical system involved and performing phase equilibrium calculations, while retaining the robustness of the differential equation solver and not significantly increasing the computational cost.

1.2. Key Mixtures of Interest

The chemical systems studied in this thesis are of particular interest for the oil & gas industry, since they are encountered in important industrial and environmental applications. They include binary and multicomponent mixtures of CO_2 associated with CCS processes and oil-natural gas derived mixtures with the main components being methane (CH_4) and ethylene (C_2H_4). The CH_4 mixtures are mainly asymmetric hydrocarbon mixtures which are extracted from high pressure-high temperature (HPHT) oil reservoirs, while the C_2H_4 mixtures studied occur from its production process by ethane steam cracking.

Regarding the study of CO_2 mixtures, the contribution of this PhD thesis was based on the previous work of Diamantonis et al. [13-15]. These authors evaluated the performance of cubic, Statistical Associating Fluid Theory [16, 17] (SAFT) and Perturbed Chain-SAFT [18, 19] (PC-SAFT) EoS in predicting the physical properties and vapor-liquid equilibrium (VLE) of pure CO_2 and its mixtures with components occurring as impurities (N_2, CH_4, O_2, Ar, SO_2, H_2S, H_2) during the transport process of CCS. Although significant amount of research has been conducted for the experimental determination and modeling of the VLE of CO_2-rich mixtures with the compounds mentioned previously, relatively little work has been performed to measure and predict solid-fluid equilibrium (SFE) of CO_2 mixtures, which is critical to the design and operation of CO_2 pipelines and storage facilities. Hazard assessment studies associated with CO_2 transport include scenarios of accidental releases with sharp expansion, where solid-vapor (SVE) as well as solid-liquid (SLE) equilibria may occur [12].

The significant progress and development in the drilling technology has made possible the exploitation of deep, HPHT oil reservoirs for hydrocarbon production [20]. Due to the depletion of conventional resources, the oil and gas industry is driven to explore and extract petroleum fluids from geological formations and wells located in the deep crust, which differ significantly from the conventional ones with respect to temperature, pressure and composition [20]. The temperature in such reservoirs can vary from 150 to 260 °C and the pressure from 70 to 200 MPa [21]. The fluid composition can be very asymmetric, with CH_4 being the dominant component, mixed with long-chain normal alkanes (*n*-alkanes) [20, 22]. The asymmetric nature of these reservoir fluids results in a more complex phase behavior, compared to those extracted from conventional wells. A class of hydrocarbon mixtures that are present in HPHT reservoirs are the so-called gas condensate mixtures. The phase behavior of these systems differs

from the phase behavior of conventional natural gas, because liquid can be condensed from the gas with pressure reduction at the temperature of the reservoir. As a result, the pressure decrease upon depletion of the reservoir can lead to significant loss of valuable product via liquid condensation, if precautions are not taken [23].

Furthermore, a common problem during the production and process of such fluids is the formation of solid phases which are comprised mainly of long-chain *n*-alkanes (paraffins), also known as waxes. Paraffin precipitation is caused mainly due to changes in temperature and pressure conditions, during the extraction of the hydrocarbon fluid, with temperature being the most important parameter. However, pressure can also have a significant effect on wax formation, especially for CH_4-rich mixtures under HPHT conditions, taking also into account the retrograde behavior of the phase boundary [24, 25]. Furthermore, oil and gas processes that are performed under low temperature conditions involve the risk of solid-phase precipitations. Small amounts of long-chain hydrocarbons are present even in natural gas mixtures and form solid phases because of their relatively high melting temperatures; solid formation often occurs in heat exchangers, pipes and valves which results in equipment damage and blockage. Replacement or treatment of damaged equipment and blocked pipelines from waxy deposits is well known to induce significant operational costs. Wax deposition on pipelines and other equipment is controlled by several physical mechanisms [26]. However, the thermodynamic conditions of phase instability and in this case solidification dictate the initiation of such processes. Therefore, accurate knowledge of the VLE and SFE boundaries is necessary for the detailed design and optimal operation of industrial processes that involve CH_4-rich paraffinic mixtures.

C_2H_4 is one of the most important compounds for the chemical and petrochemical industry, since it has found extensive use in the production of polymers, functionalized hydrocarbons and many other basic and intermediate products. As a result, significant amounts of C_2H_4 are being transported, mainly through pipelines, from the site of production to the relevant industrial areas for exploitation and conversion to products of higher value.

The most widespread process for C_2H_4 production is ethane steam cracking. The process itself is a high-temperature pyrolysis in the presence of diluting steam. Typical feedstocks are various grades of naphtha and components of natural gas, with naphtha being the main feedstock in Western Europe and Japan, while in Middle East the feedstock basis has shifted to ethane in the last decade, thus leading to attractive

production costs [27]. In this process, the ethane feed is preheated and diluted in high temperature steam and then is fed in high temperature, low pressure tube reactors. The typical conversion is 50 - 60% [27, 28]. Froment et al. [29] performed pilot plant experiments of the thermal cracking of ethane under conditions representative of the industrial process. They measured the composition of the products after the cracking process and compared with an analysis from a real industrial plant, obtaining very good agreement between the experimental set up and the industrial measurements. The compounds with the highest concentration were C_2H_4 (approx. 49.0 wt %) and C_2H_6 (approx. 39.0 wt %), as expected, while there were a number of impurities containing gaseous components like H_2 and CO_2 and several different hydrocarbons. The impurity with the highest concentration was H_2 (3.71 wt %), followed by CH_4 (~3.0 wt %) while other compounds (CO_2, C_2H_2, C_3H_6, C_3H_8, C_4H_6, *1*-C_4H_8, *n*-C_4H_{10}, C_5+) varied from 0.2 to 1.5 wt %. These measurements are also in relatively good agreement with the specifications reported by Shokrollahi et al. [30].

After the cracking process, the stream containing the products is fed into a separation train, so that C_2H_4 can be isolated from the other compounds. The target is to obtain high purity C_2H_4 and the most widely applied process is low temperature distillation [31]. Although the C_2H_4 transported is of high purity, it does contain small amounts of impurities. Knowledge of the various physical properties (density, heat capacity, speed of sound, Joule-Thomson coefficient, isothermal compressibility coefficient) of C_2H_4 and the VLE of C_2H_4 mixtures with the relevant impurities is a key aspect for the accurate safety assessment of the transportation pipeline, using numerical simulations.

1.3. Objectives

The main objectives of this dissertation were the following:

- Development of efficient and robust algorithms for direct saturation point calculations of binary and multicomponent mixtures.
- Development of Euler-Newton predictor-corrector methods for the construction of phase envelopes of binary and multicomponent mixtures.
- Based on the previous work of Diamantonis et al. [13-15], extension of the cubic (Soave-Redlich-Kwong [32], SRK, Peng-Robinson [33], PR) and PC-SAFT EoS to predict the SFE of pure CO_2 and CO_2 mixtures, by combining them with different models for the solid phase.
- Development of a predictive methodology for the calculation of the VLE of highly asymmetric CH_4 mixtures with *n*-alkanes, by combining Gibbs Ensemble Monte Carlo (GEMC) simulations with EoS (SRK, PR, PC-SAFT).
- Prediction of the solid-liquid-gas equilibrium (SLGE) of binary CH_4 mixtures with *n*-alkanes, by combining fluid-phase EoS (SRK, PR, PC-SAFT) with different solid-phase models.
- Investigate the accuracy of PR, PC-SAFT and SAFT with the Mie potential of variable range [34] (SAFT-VR Mie) EoS towards the prediction of physical properties and VLE of C_2H_4 and C_2H_4 mixtures.
- Development of an efficient technique for rapid and robust coupling of thermodynamic calculations with CFD models for pipeline decompression simulations.
- Application of the developed and validated methods and models to simulate the experimental decompression of CO_2 and C_2H_4 mixtures.

1.4. Structure of Thesis

In this section, the way the thesis is structured will be described, in order to briefly present the topics discussed and guide the reader.

The motivation, the mixtures of interest and the objectives are presented in Chapter 1 in order to set the boundaries of the studied area in this thesis. The following two chapters are dedicated to the literature review and the theoretical background of the work. The results and discussion are presented in Chapters 4, 5, 6, 7, 8, 9, 10. The final chapters are the conclusions and the proposals for further work.

More specifically, Chapter 2 provides an extensive literature review of the existing methods for saturation point calculations and the construction of phase diagrams. Furthermore, experimental measurements and existing modeling research studies for the key mixtures of interest in this work are discussed. Finally, the challenges in coupling thermodynamic calculations with flow models are presented and various approaches presented in the open literature are discussed.

In Chapter 3 the models for the fluid and the solid phase that were used and further developed in this work are presented. Their mathematical formalism is given, as well as some details regarding their derivation.

Chapters 4, 5 present the newly developed methods for direct saturation point calculations and for the sequential construction of phase diagrams of binary and multicomponent mixtures. Detailed derivation of the governing equations is given, implementation details and application results for various simple and complex mixtures.

Chapter 6 contains the work regarding the SFE modeling of CO_2 mixtures with components associated with CCS processes. The various models presented in Chapter 3 for the solid phase are coupled with different fluid-phase EoS and the results are compared against experimental SLGE data.

Chapter 7 discusses the development of a predictive methodology for the calculation of the VLE of asymmetric hydrocarbon mixtures by combining MC simulations with EoS.

Chapter 8 presents the application of existing models for the solid phase and the development of new ones for the modeling of the SLGE of binary CH_4 mixtures with *n*-alkanes. The solid-phase models are coupled with various EoS and the low and high pressure SLGE of the binary mixtures considered is modeled.

Chapter 9 contains the work on validating the cubic and the SAFT-based EoS considered in this thesis against experimental physical property and VLE data for pure C_2H_4 and C_2H_4 mixtures.

Chapter 10 discusses the development of a new technique for the efficient coupling of thermodynamic calculations in CFD simulators. The implementation details are discussed and the accuracy of the method is assessed in various examples. Finally the newly developed technique is incorporated in combination with the PC-SAFT EoS in a CFD simulator to model the experimental full-bore rupture releases from pipelines that contain CO_2-rich and C_2H_4-rich mixtures.

The conclusions from this thesis are collectively presented in Chapter 11 and Chapter 12 contains suggestions for further work.

2. Literature Review

2.1. Calculation of Saturation Points and Phase Diagrams

As it has already been mentioned in Chapter 1, accurate knowledge of the bubble and dew point boundaries of binary and multicomponent mixtures is of great importance for many applications and processes in chemical industry. Of particular interest are the isoplethic VLE phase envelopes which are coexistence lines, at specified feed phase composition and phase fraction, calculated at different conditions of temperature or pressure. These P-T phase diagrams are very important for the oil and gas industry, where avoiding condensation of a single-phase petroleum fluid, during pipeline transportation, is crucial for safe and continuous operation. Another two important types of VLE phase diagrams, which are commonly used for evaluation of the performance of thermodynamic models and parameter fitting, are the constant temperature (P-x,y) or pressure (T-x,y) VLE diagrams of binary mixtures.

Calculation of the previously mentioned phase diagrams poses different challenges depending on the type and the overall complexity of the physical behavior of the mixture under study, but also on the type of the diagram itself. Most isoplethic phase envelopes present a temperature (cricondentherm) and a pressure maximum (cricondenbar), which means that the phase boundary is non-monotonic and tracing it in the vicinity of these points needs special attention due to the divergence of some thermodynamic derivatives. Furthermore, the presence of one or more critical points renders calculations in their vicinity very difficult, frequently resulting in trivial solutions (two phases with the same composition and density which are not real solutions) or divergence of the iterative procedure. Calculation of the most common constant temperature or constant pressure phase diagrams of binary mixtures is simpler, in the sense that they usually can be traced by varying monotonically only one variable; but still, high pressure calculations are difficult to perform and the presence of a critical point creates numerical difficulties. However, specific types of phase behavior in binary mixtures [35] can result in more complex phase diagrams and continuation procedures are needed, such as the one proposed by Cismondi and Michelsen [36]. A solution to the difficulty of tracing the various non-monotonic phase diagrams has been also proposed by Venkatarathnam [37-39], who suggested the use of density solely as the specification variable in an Euler-Newton predictor-corrector continuation scheme. However, if

derivatives of density with respect to some independent variables assume high values, this results in inaccurate initial estimates for a specific equilibrium point and may lead to divergence of the iterative procedure.

Gibbs was the first to formulate the thermodynamic equilibrium laws for open systems and to define the set of extensive and intensive properties which are the variables that need to be set, so that a system can be fully described [40]. The phase equilibrium relations can be derived by utilizing the first and second law of thermodynamics *i.e.* entropy, as an extensive and convex function of internal energy and volume takes a maximum value for a closed system. In general, most of the proposed phase equilibrium calculation schemes recast the entropy maximization as an optimization problem of another thermodynamic potential or as a problem of solving a nonlinear set of equations. Local and global optimization [41-47] or nonlinear system [48-51] solving methods are employed to calculate the equilibrium states.

The most important phase equilibrium calculation is probably the isothermal flash [42], *i.e.* the computation of the composition of two or more coexisting phases and the amount of each one at specified temperature, pressure and overall composition of a non-stable mixture. Fixation of both temperature and pressure, which are the natural independent variables of the Gibbs free energy, has the important effect that the correct solution corresponds to the global minimum of Gibbs free energy. As a result, very reliable and robust algorithms can be constructed to perform this calculation, but the solution has to be checked for stability, if the number of coexisting phases is not known in advance [41]. Furthermore, stability of the solution has also to be verified when local optimization algorithms are employed, because there are cases where many local minima can be present [42, 43, 45]. The isothermal flash calculation can be treated mathematically either as a set of nonlinear equations to be solved or as a Gibbs free energy minimization problem. The formulation as a nonlinear equation set can be done by solving simultaneously the equifugacity (or chemical potentials) relations, the material balances and the mole fractions summation constraints [48, 52]. In this category fall also the methods that solve the constraints (material balance, summation of mole fractions) internally, using an estimate of the K-factors and then update the K-factor values in an outer loop [42, 49, 53]. A third case of equation solving methods are those that solve the equifugacity equations, which are the components of the gradient of the total Gibbs free energy of the system with respect to the number of moles per component, but perform a change of independent variables, in order to get better convergence properties [44, 51,

54]. Gibbs free energy minimization has also been studied and used extensively as an alternative to equation solving techniques [42, 45, 47, 55, 56].

On the other hand, constructing a robust algorithm for the calculation of saturation points at specified temperature or pressure and phase fraction presents many challenges when EoS are considered. First, fixation of temperature or pressure and phase fraction (β) does not allow directly for a formulation as an optimization problem based on a thermodynamic potential. Of course, the correct solution is a minimum of a thermodynamic function but this property cannot be directly used to construct an algorithm. Furthermore, calculation of saturation points at high pressures is more difficult than a flash calculation because the number of solutions at a specified pressure (or temperature) is not known a priori [57] and also the trivial solution is much more common. Finally, the existence of multiple critical points along a phase boundary is also an important reason for trivial solutions or divergence of the iterative procedure.

As already mentioned, while the flash calculation has been formulated both as an optimization and a nonlinear equation solving problem, the calculation of bubble and dew points of binary and multicomponent mixtures has been treated as a solution of a given set of nonlinear equations [58]. The most well established methods are pressure-based, in which temperature, pressure and the molar composition ($\boldsymbol{w}$) of the incipient phase are treated as primary variables, while the EoS is solved for volume. These methods can be distinguished by the way they update the variables mentioned above. One of the first approaches for the calculation of bubble and dew point pressures of mixtures was discussed by Baker and Luks [59]. The most well-known method, which is usually applied for individual saturation point calculations was proposed by Anderson and Prausnitz [49] and was later advanced by Michelsen [60]. This method is a partial Newton's method that corrects temperature or pressure by taking into account appropriate derivatives (with respect to temperature or pressure) of the fugacity coefficients, while composition is corrected through successive substitution (SS), utilizing the fugacity coefficients calculated at the new set of conditions. A saturation point calculation is closely related to the stability test. In the most well-known stability test formulation, which was proposed by Michelsen [41], an unconstrained minimization of the tangent plane distance (TPD) function was proposed, by replacing the component mole fractions as iteration variables, with the composition variables $\boldsymbol{W}$, while $\hat{\varphi}_i(\boldsymbol{W},T,P) = \hat{\varphi}_i(\boldsymbol{w},T,P)$. These composition variables are formally treated as mole numbers, while $\sum_{i=1}^{C} W_i$ is not constrained to unity, contrary to $\sum_{i=1}^{C} w_i$. The partial

Newton's method solves only one nonlinear equation, which corresponds to the stability test outcome when the respective conditions of T and P lie exactly on the phase boundary for a mixture of feed composition $\boldsymbol{z}$. For example, a bubble-point pressure calculation for a mixture of C components takes the form:

$$g^{(k)} = \sum_{i=1}^{C} W_i^{(k)} - 1 = 0 \tag{2.1}$$

with

$$W_i^{(k)} = \frac{z_i \hat{\varphi}_i(\boldsymbol{z}, T, P)^{(k)}}{\hat{\varphi}_i(\boldsymbol{w}, T, P)^{(k)}} \tag{2.2}$$

$$w_i^{(k+1)} = \frac{W_i^{(k)}}{\sum_{i=1}^{C} W_i^{(k)}} \tag{2.3}$$

$$P^{(k+1)} = P^{(k)} - g^{(k)} \cdot \left(\frac{dg^{(k)}}{dP}\right)^{-1} \tag{2.4}$$

$$\frac{dg^{(k)}}{dP} = \sum_{i}^{C} W_i^{(k)} \cdot \left(\frac{\partial \ln \hat{\varphi}_i(\boldsymbol{z}, T, P)^{(k)}}{\partial P} - \frac{\partial \ln \hat{\varphi}_i(\boldsymbol{w}, T, P)^{(k)}}{\partial P}\right) \tag{2.5}$$

where $(\boldsymbol{z})$ is the composition of the feed phase (liquid phase in this case) and $(\hat{\varphi}_i)$ is the fugacity coefficient of component i in the respective phase. A K-value (where $K_i = \frac{W_i}{z_i}$) formulation of this method [57] is also possible by using:

$$K_i = \frac{\hat{\varphi}_i(\boldsymbol{z}, T, P)}{\hat{\varphi}_i(\boldsymbol{w}, T, P)} = \frac{W_i}{z_i} \tag{2.6}$$

The partial Newton's method shows good behavior for low pressure bubble and dew point calculations but its performance deteriorates with increasing pressure and especially near critical points. Moreover, for constant composition phase envelopes in multicomponent mixtures, divergence occurs frequently in the low temperature - high pressure retrograde part of the dew line [57], unless initial estimates are very accurate. Furthermore, a common problem in the retrograde parts of a phase diagram is the multiplicity of solutions for a specified pressure (or temperature) and even with accurate initial estimates, convergence to a different solution rather than the desired one can happen, especially for envelopes with narrow two phase region.

A solution to these difficulties is the sequential construction of the entire phase envelope, as demonstrated first by Michelsen [61]. In this formulation, the equations which are utilized are the C equifugacity relations, the mole fractions summation equation and a specification equation:

$$g_i = \ln K_i + \ln\hat{\varphi}_i(\boldsymbol{y}, T, P) - \ln\hat{\varphi}_i(\boldsymbol{x}, T, P) = 0;\ i = 1,2 \dots C \tag{2.7}$$

$$g_{C+1} = \sum_{i=1}^{C} (y_i - x_i) = 0 \tag{2.8}$$

$$g_{C+2} = X_S - S = 0 \tag{2.9}$$

where $\boldsymbol{x}$ and $\boldsymbol{y}$ are the molar compositions of the two fluid phases at equilibrium and in this case $K_i = \frac{y_i}{x_i}$. The mole fractions in each phase are retrieved using:

$$x_i = \frac{z_i}{1 - \beta + \beta K_i} \tag{2.10}$$

$$y_i = \frac{K_i z_i}{1 - \beta + \beta K_i} \tag{2.11}$$

where β is the phase fraction. Michelsen essentially proposed an Euler-Newton predictor-corrector continuation procedure to trace the entire branch of solutions for the phase equilibrium problem where the feed phase composition and the phase fraction are kept constant. In this method, the independent variables are $\boldsymbol{X} = (lnK_1, \dots, lnK_C, lnT, lnP)$ and one of them is used as the specification variable (X_S), which is set to a specified value (S). The value of β determines if a boundary (bubble, dew) or a quality line is calculated. When $\beta = 0$, then $\boldsymbol{x} = \boldsymbol{z}$ and when $\beta = 1$, then $\boldsymbol{y} = \boldsymbol{z}$. When the calculation of a VLE phase envelope is concerned, $\boldsymbol{x}$ usually represents the liquid phase and setting $\beta = 0$ corresponds to starting the calculation from a bubble point, while $\boldsymbol{y}$ represents the vapor phase and setting $\beta = 1$ corresponds to starting the calculation from a dew point. Setting β to a value in between 0 and 1 corresponds to calculating constant phase fraction lines which are not the boundary ones for a feed mixture of composition $\boldsymbol{z}$. In this case, two phases (liquid and vapor) with compositions $\boldsymbol{x}$ and $\boldsymbol{y}$ respectively are calculated, satisfying the equilibrium criteria, but both compositions are different from $\boldsymbol{z}$. Newton's method is used to solve the set of equations and initial estimates for every equilibrium point are calculated using linear extrapolation. To produce initial estimates, the derivatives of every variable with respect

to the specification are computed, while as specification variable is chosen to be the most sensitive one (the one with the numerically largest value of $\frac{\partial \boldsymbol{X}}{\partial S}$), so that infinite derivatives are avoided. The process for setting the initial estimates for each equilibrium point calculation is expressed as:

$$\frac{\partial \boldsymbol{g}}{\partial \boldsymbol{X}}\frac{\partial \boldsymbol{X}}{\partial S}+\frac{\partial \boldsymbol{g}}{\partial S}=0 \tag{2.12}$$

$$\boldsymbol{X}(S+\Delta S)=\boldsymbol{X}(S)+\frac{\partial \boldsymbol{X}}{\partial S}\Delta S \tag{2.13}$$

where $\frac{\partial \boldsymbol{g}}{\partial s}=(0,0,\dots,-1)$. A similar formulation is also applicable for the calculation of (P-x,y) or (T-x,y) phase diagrams of binary mixtures [57]. For the calculation of the boundary equilibrium lines only ($\beta=0$ or $\beta=1$), Eqs. 2.7 and 2.8 can be written as follows:

$$g_i=\ln W_i+\ln\hat{\varphi}_i(\boldsymbol{W},T,P)-\ln z_i-\ln\hat{\varphi}_i(\boldsymbol{z},T,P)=0;\ i=1,2\dots C \tag{2.14}$$

$$g_{C+1}=\sum_{i=1}^{C}W_i-1=0 \tag{2.15}$$

where $\boldsymbol{W}$ represents the incipient phase (liquid or vapor) and $\boldsymbol{z}$ again represents the feed phase. The molar composition $\boldsymbol{w}$ of the incipient phase is calculated using Eq. 2.3. At the solution, $\boldsymbol{w}=\boldsymbol{W}$. The independent variables in this case are $\boldsymbol{X}=(\ln W_1,\dots,\ln W_C,\ln T,\ln P)$, while $K_i=\frac{W_i}{z_i}$ values can be also used. For the calculation of the boundary lines, solving Eqs. 2.7 - 2.9 or Eqs. 2.14, 2.15 and 2.9 results in the same convergence properties.

An important difference between the partial Newton's method and the full Newton's method is that in the latter case the composition dependency of the incipient phase is explicitly accounted for, with the use of composition derivatives of the fugacity coefficients. The use of these derivatives renders the method significantly faster than successive substitution but the need for very accurate initial estimates is not eliminated, as Newton methods tend to be more sensitive to the quality of the initial estimates than successive substitution ones. To overcome this difficulty, the continuation procedure is applied as mentioned above – via the use of linear extrapolation for initialization – and very accurate initial estimates are provided for the calculation of every point.

Pressure-based modifications of Michelsen's method for the sequential construction of the isoplethic phase envelope have been also proposed. In the "bead

spring" method [62] for example, the specification equation Eq. 2.9 of the original method was replaced with another equation based on a "spring" that sets the slope value of the modified tangent plane distance (Q_1) function with respect to either temperature or pressure. This way, the equilibrium curve can be traversed and with a minor modification, the temperature or pressure maxima of the constant composition phase envelope can be directly determined. Venkatarathnam [37] has also shown that it is potentially preferable to alter the specification equation and use instead a variable that is not present in the independent variables vector ($\boldsymbol{X}$), in order to achieve monotonic behavior during the tracing of the phase boundary. In his implementation, the density of the feed phase is used as specification and it is varied monotonically.

An efficient alternative for phase equilibrium calculations can be the use of volume-based methods when complex EoS are utilized and the determination of the correct volume roots at specified temperature, pressure and composition, is computationally intensive. In the volume-based approach, Helmholtz free energy is the central function and the primary variables are temperature, volume and mole numbers. In this way, there is no need to solve the EoS for the volume, thus reducing the computation time for complex EoS significantly. Venkatarathnam [37] presented a volume-based version of the density marching method, in which the density of the feed phase is used as specification in a similar way to the pressure-based counterpart. A density representation for calculating phase boundaries has been proposed by Quiñones-Cisneros and Deiters [63], using as central function the Helmholtz free energy density. In this case, the incipient phase component molar densities and the total density of the feed phase are used as independent variables. The method was demonstrated for the calculation of isothermal phase diagrams of binary mixtures and constant composition phase envelopes of multicomponent mixtures. The use of component molar densities as independent variables, based on the Helmholtz free energy density, was first derived by Nagarajan et al. [64] for the formulation of a stability test method at constant T and P. Deiters [65, 66] presented also the use of ordinary differential equations for the calculation of isothermal or isobaric phase diagrams of binary mixtures and isoplethic phase envelopes of multicomponent mixtures, using the Helmholtz free energy density framework. A density-based method for the construction of constant composition phase envelopes has also been recently proposed by Nichita [67]. In this implementation, modified K-factors were used as fractions of the component molar densities in the feed and incipient phase. The set of independent variables is comprised of the modified K-

factors, the feed phase density and temperature. Volume-based methods can also be employed in order to efficiently perform the P-T flash calculation when complex EoS are used [68-71].

The constant composition phase envelopes are non-monotonic in T, P space and present retrograde behavior both for specified T or P. As a result, convergence to the lower / upper pressure or low / high temperature solution in the retrograde region depends strongly on the initial estimates. Nghiem et al. [72] presented three different formulations based on Newton's method and an accelerated successive substitution method to perform isolated saturation point calculations. The target, apart from the comparison of the computational performance of the different formulations, was also to present a methodology to calculate the multiple solutions in the retrograde parts of the phase envelope. Essentially, the methodology that was proposed is a multiple initialization method, in which two initializations (a liquid-like and a vapor-like) for the incipient phase composition are produced from a stability test calculation [41]. Depending on the type of calculation (saturation temperature or pressure), multiple initial values for temperature or pressure are generated by performing one-dimensional search to find all roots of the TPD function, using the previously initialized incipient phase compositions. In this way, the computational methods proposed, were applied in combination with the different initial estimates (up to 4) and multiple solutions were calculated, some of them being trivial solutions which lie on the stability limit curve. A more recent approach to this problem is the one proposed by Khodapanah et al. [73], but the authors dealt only with the simultaneous calculation of lower / upper pressure dew points of gas condensate mixtures at specified temperature. Their method relies on accurately interpolating the function of Eq. 2.1 with Chebyshev polynomials, so that a closed form expression can be obtained, while a pressure range is given as input to the algorithm to be able to calculate all physically meaningful roots.

To summarize, the calculation of saturation points with EoS presents significant computational challenges. Firstly, the formulation as an optimization problem of a thermodynamic potential cannot be performed in a straightforward and robust manner, because of the fixation of temperature or pressure and phase fraction. The solution of a set of algebraic equations ($\boldsymbol{g}$) can be reformulated as an optimization problem using the objective function $Q(\boldsymbol{X}) = \boldsymbol{g}^T\boldsymbol{g}$, but there are several complications with this formulation. Secondly, the calculation of saturation points entails the implication that the number of solutions (multiple solutions / no solution at all) is not known a priori at

specified conditions of pressure (or temperature) for mixtures. Furthermore, the rate of convergence becomes slow at elevated pressures and can be intolerably low in the vicinity of critical points. Finally, the most common methods employ initial estimates calculated from ideal solution approximations, such as Wilson's approximation [74], which deteriorate significantly at high pressures. This results frequently in divergence of the iterative procedure, because of extrapolation at conditions in which the EoS cannot calculate meaningful density roots or the trivial solution in which the two phases at equilibrium have the same composition and density.

2.2. Phase Equilibria of CO_2 Mixtures

VLE of CO_2 mixtures has attracted most of the attention both in terms of experimental measurements and modeling using EoS. Coquelet et al. [75] measured the VLE of the CO_2 - Ar binary mixture at six different isotherms from 233.32 to 299.21 K and pressures up to 14 MPa and modeled the data using the PR EoS. Li and Yan [76] modeled the VLE of CO_2 with various impurities, using different cubic EoS and concluded that SRK [32] and PR [33] EoS are the most accurate ones. Diamantonis et al. [13] evaluated the performance of cubic, SAFT [16, 17] and PC-SAFT [18] EoS using the standard van der Waals one fluid theory (vdW1f) mixing rules in predicting and correlating the VLE of different binary CO_2 mixtures with impurities, using isothermal experimental data reported in the literature. The authors performed also liquid density calculations and concluded that PC-SAFT is on the average the most accurate model for VLE prediction but when a binary interaction parameter (BIP) was used, the accuracy of all models was comparable. Chapoy et al. [77] reported new experimental VLE data for the CO_2 - H_2S mixture from 258.41 to 313.02 K in a pressure range from 1.0 to 5.5 MPa. The authors have shown that cubic EoS are able to provide a satisfactory description of the phase behavior when appropriate BIPs are used. Experimental measurements for the CO_2 - SO_2 and CO_2 - NO mixtures at different isotherms were also performed by Coquelet et al. [78]. Moreover, the VLE of two ternary mixtures (CO_2 - O_2 - Ar and CO_2 - SO_2 - O_2) were measured in the same work and the PR EoS was used to model the phase behavior and also to calculate the critical locus of the two binary mixtures. Westman et al. [79, 80], presented a new setup for VLE measurements of CO_2-rich mixtures and determined new isothermal VLE data for the binary CO_2 - N_2 mixture at four isotherms from 223 to 303 K and for the binary CO_2 - O_2 mixture at five isotherms

from 218 to 298 K. The authors modeled the new data using higher order EoS (GERG-2008/EOS-CG) and an EoS/G^E model. Lasala et al. [81] reported new experimental VLE data for the systems CO_2 - N_2, CO_2 - Ar and CO_2 - O_2 and presented modeling results with PR EoS combined with an advanced class of mixing rules.

The constant composition VLE phase envelopes of binary CO_2 mixtures with N_2, O_2, Ar and CH_4 were experimentally determined by Ahmad et al. [82], who used the SRK, the GERG-2008 and a group contribution EoS (EOS-CG) to model the phase behavior. Blanco et al. [83, 84] performed experimental measurements for the determination of the constant composition VLE phase envelopes of CO_2 mixtures with CO and CH_4 at different compositions. In these works, experimental measurements were performed to obtain new pressure-density-temperature data for the two mixtures. The PR, PC-SAFT and GERG EoS were used to model the VLE of CO_2 - CO mixture, while only GERG was used to model CO_2 - CH_4 mixture. The VLE of CO_2 - O_2 - Ar - N_2 mixture was experimentally determined by Chapoy et al. [85]. The densities and P-T phase diagrams of two ternary mixtures (CO_2 - Ar - N_2 and CO_2 - Ar - H_2) were measured at temperatures between 268 and 303 K by Ke et al. [86] and the data were modeled with GERG-2008/EoS-CG, gSAFT and PR EoS. An extensive work, regarding the VLE of binary mixtures associated with CCS processes was performed by Xu et al. [87].

To summarize, significant amount of research has been conducted for the experimental determination and modeling of the VLE of CO_2-rich mixtures with the compounds occurring as impurities in CCS processes. However, relatively little work has been performed to measure and predict the SFE of CO_2 mixtures, which is critical to the design and operation of CO_2 pipelines and storage facilities. CO_2 exhibits a relatively high Joule-Thomson expansion coefficient and an accidental release from a pipeline will lead to sudden depressurization and rapid cooling, and as a result, solid formation can be expected [12]. Taking this into account, it is easily understood that the formation of dry-ice resulting from SFE can largely affect the safety of CCS facilities during equipment depressurization, process shutdown or other process upsets.

2.3. Phase Equilibria of Asymmetric CH_4 Mixtures

Experimental measurements of the physical properties and phase equilibrium of real reservoir fluids are relatively scarce. The modeling of these mixtures is a challenging

task, due to the theoretical limitations in the available models and to the high uncertainties of the composition in such complex systems [22]. Current practice focuses on the experimental determination of these properties for synthetic mixtures comprised mainly of *n*-alkanes. A comprehensive review of the available experimental studies of asymmetric ternary and multicomponent hydrocarbon mixtures is given by Regueira et al. [88].

Experimental measurements for multicomponent mixtures are usually expensive and difficult to perform and do not cover the full range of working conditions. To that extent, thermodynamic models that can accurately predict the phase behavior and the physical properties of reservoir fluids are very important for the oil and gas industry, so that optimized and safe processes can be designed. Usually, the available experimental data of synthetic hydrocarbon mixtures are utilized for the assessment of existing models and the development of new ones. The agreement between model predictions and experimental data, for different mixtures, indicates how well these predictions can be extrapolated to conditions for which experimental data are not available.

There are two systematic research studies regarding the modeling of asymmetric CH_4 mixtures. Yan et al. [89] made a comparative study between cubic such as SRK, PR and higher order (simplified PC-SAFT [90], sPC-SAFT, Soave modified Benedict-Webb-Rubin [91], SBWR) EoS, to assess the performance of each model in predicting physical properties and phase equilibria of reservoir fluids. The authors considered density predictions of each EoS for pure components that typically exist in reservoir fluids, isothermal VLE of relevant binary mixtures, VLE predictions of synthetic multicomponent mixtures, and PVT properties of real reservoir fluids. It was concluded that the predictions of the four models regarding the VLE of synthetic gases are very similar, with or without the use of k_{ij} parameters, if the mixtures are not very asymmetric. Discrepancies between the models are becoming more prominent for more asymmetric mixtures, while the values of the BIPs play an important role in the accurate prediction of the phase behavior. The authors mention that the k_{ij} parameters between hydrocarbons, other than CH_4, were set equal to zero, while the most important pairs contained CH_4, N_2, CO_2 and H_2S.

In a recent study, Novak et al. [92] evaluated the performance of the SRK, PR, PC-SAFT and UMR-PRU [93] models to predict dew points and liquid dropouts of synthetic and real gas condensates. The authors concluded that, in most cases, PC-SAFT predicts higher dew-point pressures than the experimentally measured ones for the

synthetic gases, cubic EoS fail to describe the mixtures containing aromatic components, while the UMR-PRU model exhibits the lowest overall deviation from the experimental data. As a first step in their methodology, the authors evaluated the effect of the k_{ij} parameters on the calculations. It was shown that the use of k_{ij} parameters only between CH_4 and long-chain hydrocarbons (with 10 carbon atoms or more) yields practically the same results with those obtained when k_{ij} parameters for all binary pairs containing CH_4 are used. The exploitation of the complete matrix of binary pairs yields also very similar results. This finding indicates that the performance of each model in predicting the VLE of these multicomponent mixtures depends mainly on specific interaction pairs of molecules, *i.e.* between CH_4 and long-chain hydrocarbons. It is important to note that the synthetic mixtures considered by Novak et al. [92] did not include N_2, CO_2 and H_2S, which would require additional k_{ij} parameters. Finally, it was emphasized that the regression of BIPs based on the respective binary mixture data is not always possible and there may be large uncertainties regarding the values of the parameters. This is a result of insufficient experimental VLE data for binary mixtures of CH_4 with long-chain hydrocarbons, especially at high pressures.

Fitting BIPs to binary mixture VLE data that do not span a wide temperature and pressure range may lead to false assessment of the correlative ability of different models. For example, even with one temperature independent k_{ij} parameter, some EoS can correlate better a wide temperature and pressure range of binary mixture VLE than others. The use of a limited number of experimental VLE data in the fitting process may result in similar performance, in terms of correlation of the phase behavior, with different thermodynamic models. The use of BIPs fitted to limited VLE data to predict the phase equilibria of multicomponent mixtures can lead to erroneous evaluation of the predictive capabilities of the models considered.

Regarding the modeling of wax precipitation in CH_4 mixtures, the first studies that dealt with the phenomenon considered multicomponent hydrocarbon mixtures, with composition resembling crude oils, at SLE conditions. All published papers, applied the solid-phase modeling method as presented by Prausnitz et al. [94], with the additional assumption that the solid phase is a solution, and used various models for the liquid mixture. The mixing effect in the solid phase was taken into account with a simplified model (regular solution theory based) and the liquid phase mixture was modeled using regular solution theory, Excess Gibbs energy (GE) and local composition models [95-98]. Coutinho et al. [98] and Lira-Galeana et al. [99] presented also results with their

models for binary *n*-alkane mixtures of high molecular weight. Contrary to the previous studies, Lira-Galeana et al. used a cubic EoS (PR in that case) to model the fluid mixture. Furthermore, in the same work the authors stated that wax precipitation in multicomponent oil systems produces initially an unstable solid mixture, where components are miscible and then a spontaneous de-mixing occurs and multiple solid phases are formed that consist predominantly of pure components. They supported their claims based on independent experimental studies referenced in the original publication [99]. As a result, the authors modeled multicomponent oil mixtures using a model that considers multiple pure solid phases, the appearance or disappearance of which is assessed by stability analysis. For the calculation of the thermophysical properties of the components that solidify (melting temperatures and enthalpies, etc.), all the studies mentioned previously used correlations proposed by Won [95]. Coutinho and co-workers [100] presented the same year with Lira-Galeana et al., a local composition model for solid solutions, which are comprised of long-chain paraffin molecules, and validated their results against solid-solid equilibrium (SSE) experimental data. Coutinho and Ruffier-Meray [101] subsequently applied the previously proposed solid-solution model, in combination with the Flory-Huggins equation for the liquid-phase activity coefficient, in modeling mixtures of long-chain *n*-alkanes.

One common characteristic of the previously mentioned research studies, is that they only considered the modeling of mixtures at atmospheric pressure. At these conditions, the pressure effect on the fugacity coefficients of the solid and the fluid phases is negligible and the corresponding term of the solid-phase model is usually neglected. The first research study that incorporated modeling of wax formation at high pressures, is the one published by Lindeloff et al. [102]. The authors presented an Euler-Newton predictor-corrector algorithm, for the sequential calculation of multiphase equilibrium lines that can also include pure or impure solid phases. The algorithm is capable of tracing equilibrium lines at very high pressures, where convergence of an iterative procedure is very difficult. At these conditions, very accurate initial estimates for the independent variables are needed and the Euler predictor, when applied with a small step, is very efficient at providing them. The authors modeled wax precipitation from multicomponent *n*-alkane mixtures at high pressures, by applying the previously discussed solid-phase model with the addition of a term (Poynting-type correction) that takes into account the pressure dependency of the solid-phase fugacity (or equivalently the chemical potential). The inclusion of the Poynting correction induces two more

parameters that have to be supplemented to the solid-phase model, which are the solid and the fluid (liquid or vapor, depending on the reference state) molar volumes, normally calculated at the reference state and assumed pressure independent. The authors calculated the necessary liquid molar volumes using a group contribution method and the corresponding solid molar volumes using some approximations based on experimental observations. The solid phase was assumed to be a mixture of paraffins with orthorhombic crystal structure and the solid solution model of Coutinho et al. [100] was used to calculate the effect of mixing. The SRK EoS with the Twu alpha function [103] was used, in combination with a correlation for the BIPs to calculate the fluid-phase fugacities. The melting temperatures and enthalpies were treated as adjustable parameters with specific constraints, in order to improve the correlation of experimental data for the mixtures. It was concluded that the addition of the Poynting correction in the solid-phase fugacity had significant impact on the modeling results at high pressures, while caution must be exerted when cubic EoS are applied in hybrid models because of the errors in the calculated fugacity coefficients.

In order to correct some deficiencies of the approach discussed in the previous paragraph, Pauly et al. [104] used an EoS/G^E model to predict the SFE of binary, ternary and multicomponent mixtures of light gases with paraffins. The LCVM [105] mixing rule was used, combined with the SRK EoS in order to calculate more accurately the fugacity coefficients. As it has been stated by Lundgaard and Mollerup [106], accurate calculation of the fugacity coefficients is of high importance to obtain accurate modeling results when different models are adopted for the fluid and the solid phases (the same principle applies in hydrate systems). Furthermore, contrary to the previous study of Lindeloff et al., the authors did not assume pressure independent solid and liquid molar volumes in the Poynting correction of the solid-phase model, but they calculated the pressure dependency of the liquid molar volume through the fluid-phase EoS. This way, they took into account the pressure dependency of the chemical potential, in the thermodynamic integration process behind the derivation of the solid-phase model. Accurate calculation of this pressure dependency requires at least accurate representation of the liquid phase molar volume. Hence, Pauly et al. [104] adopted a Peneloux-type [107] volume translated version of the SRK EoS. The translation parameter was estimated through a group contribution method at atmospheric pressure. The solid molar volume was taken proportional to the liquid molar volume by multiplying with a proportionality coefficient (β^+), which was assumed pressure independent and equal to 0.86 (0.9 for solid mixtures),

based on experimental observations. Finally, one more term was included in the solid-phase model in a simple additive manner, which incorporated the solid-solid (SS) transition temperature and enthalpy. However, the addition of this term shifts the pure solid-former normal melting point prediction to lower temperatures. The melting and SS transition temperatures and enthalpies were calculated from correlations.

Most research studies that were published after Pauly et al. [104] and dealt with the thermodynamic modeling of wax formation at high pressures aimed at developing a more accurate representation of the Poynting correction [108-111]. A comprehensive review and analysis of the different modifications applied to mixtures of *n*-alkanes is presented by Ghanaei et al. [111] and Ameri-Mahabadian et al. [112]. The referenced research studies evaluated their high pressure models against SLE experimental data of binary, ternary and multicomponent mixtures of paraffins. All the proposed solid-phase models included melting and SS transition temperatures and enthalpies, as well as a solid-solution model to account for the mixing effect in the solid phase. The fluid phase EoS used, were translated or standard versions of SRK and PR EoS, while the Predictive 1978 Peng-Robinson (PPR78) EoS [113] has been also used [110]. Morawski et al. [108] used a simplified version of the Clausius-Clapeyron equation (constant $\frac{dP}{dT}$ and pressure independent melting enthalpy) to obtain an expression for the proportionality coefficient used by Pauly et al. [104]. In this way, the solid molar volume is still a pressure independent function of the liquid molar volume. However, an adjustable parameter needs to be fitted to melting temperatures of pure compounds for the estimation of the proportionality coefficient. Ghanaei et al. [109, 111] and Nasrifar and Fani-Khesty [110] on the other hand, essentially attempted to replace the solid and liquid molar volumes in the Poynting term, with thermophysical properties (temperatures and enthalpies) upon melting and / or SS transition, through the Clausius-Clapeyron equation. In this way, the problem of estimating pressure-dependent or independent molar volumes is transformed into accurately estimating phase change temperatures and enthalpies at low or high pressures, depending on the assumptions made by each model. The model of Ghanaei et al. [109] requires the evaluation of melting temperatures at the pressure of the system and they are calculated by a specific correlation. The model proposed by Nasrifar and Fani-Khesty involves a constant which is obtained by fitting SLE data of pure paraffins from *n*-C_8H_{18} to *n*-$C_{40}H_{82}$. The second model proposed by Ghanaei et al. [111] requires the slopes of the melting and SS transition curves of pure paraffins and average values were used after the assessment of an experimental database.

A second approach to high pressure modeling of wax systems is based on eliminating the Poynting correction, by evaluating the solid-phase fugacity and thus, the physical properties (temperature and enthalpy of melting / SS transition) needed, at high pressures. To this end, Ji et al. [114] proposed a solid-phase model, in which the reference state pressure is the actual pressure of the system, but only the melting temperature is calculated at the working conditions, with the use of a correlation the authors proposed (linear extrapolation based on the slope of the melting line of pure paraffins). Ameri-Mahabadian et al. [112] proposed two new solid-phase models, based on calculating the solid-phase fugacity at high pressures. The first one is a modification of the Ji et al. model, in which except for the melting temperature, the SS transition temperature is also calculated at the pressure of the system, using a similar linear extrapolation scheme. The second model incorporates the calculation of the melting and SS transition temperatures at the working pressure with the extrapolation scheme mentioned before, but also the melting and SS transition enthalpies at the same conditions. This is done via the Clausius-Clapeyron equation with the assumption that the slope of the equilibrium line is constant. Following Pauly et al. [104], the authors correlated the solid molar volume with the liquid one via a proportionality coefficient, which was considered pressure dependent and assumed to increase linearly with pressure. In this way, the melting and SS transition enthalpies can be calculated at the pressure of the system as a function of the respective properties at a reference pressure and the proportionality coefficient. The proportionality coefficient is calculated through a linear correlation with pressure, which includes a positive constant. In their implementation, the authors fitted this constant directly on SLGE and SLE experimental data of asymmetric binary, ternary and multicomponent *n*-alkane mixtures. In this way, a different constant was obtained for each mixture, although average values were given that resulted in satisfying modeling of the mixtures. Furthermore, it is important to note that fitting parameters of the solid-phase model to SFE data of pure components or mixtures renders the model less flexible, since a fluid-phase EoS is always involved in the calculation of fugacities and the fluid-phase equilibrium part. As a result, the use of a different fluid-phase EoS necessitates refitting of these parameters. Ameri-Mahabadian et al. [112] used the SRK EoS combined with the group contribution scheme for evaluating temperature-dependent k_{ij} parameters, as presented by Jaubert and Privat [115].

Finally, it should be stressed that all the solid-phase modeling approaches mentioned in the last three paragraphs are fundamentally equal. The same model is used

for calculating the solid-phase fugacity and different alternatives are evaluated for the estimation of the pressure effect. For example, calculating solid-phase fugacities directly at a high pressure is fundamentally equal to evaluating them at a reference pressure and then taking into account the Poynting correction. The essential difference is the existence of methodologies to accurately evaluate the emerging terms in each approach.

2.4. Phase Equilibria and Physical Properties of C_2H_4 Mixtures

As far as the thermodynamic modeling of mixtures associated with C_2H_4 pipeline transport is concerned, a unified research work that incorporates phase equilibria and physical properties modeling remains to be developed. Most of the available open literature deals with experimental VLE measurements of binary C_2H_4 mixtures and their modeling with various EoS, usually a cubic one.

To this end, Machat and Boublik [116] used the BACK EoS to correlate the VLE of 15 binary mixtures at elevated pressures to investigate the applicability of different combining and mixing rules on the calculations. Their work included two binary C_2H_4 mixtures with C_2H_6 and C_3H_8. The authors used two isotherms (263.15 and 293.15 K) for the C_2H_4 - C_2H_6 mixture and one isotherm (273.06 K) for the C_2H_4 - C_3H_8 mixture to validate their results. Laugier et al. [117] performed experimental VLE measurements of C_2H_4 mixtures with *1*-C_4H_8, *1*-C_6H_{12} and *1*-C_8H_{16} and modeling using the PR EoS. Chen et al. [118] measured gas-liquid critical properties of H_2 - C_2H_4 and H_2 - C_3H_6 mixtures and used the Predictive SRK (PSRK) EoS [119] to predict the critical points. An extensive work regarding the VLE of binary mixtures containing C_2H_4 was performed by Qian et al. [120]. The authors extended the PPR78 EoS, which combines the PR EoS with a group contribution method aimed at estimating the temperature-dependent BIPs, $k_{ij}(T)$, involved in the vdW1f mixing rules, in order to predict the VLE and liquid-liquid equilibrium (LLE) of alkene containing mixtures. Their work included experimental VLE and LLE data of 198 alkene based binary mixtures, 36 of them containing C_2H_4 with other compounds. Using specific objective functions, the authors fitted the group contribution parameters and concluded that satisfactory results can be obtained over a wide temperature and pressure range.

2.5. Coupling Thermodynamic Calculations with Flow Models

The modeling of compressible two-phase or flashing flows is encountered in many engineering applications, such as outflows from a pipe or a pressurized vessel. The accuracy of these simulations depends to a large extent on the accuracy of the physical property data of the fluids modeled, particularly when multicomponent mixtures are involved.

The physical properties of the fluids involved in such applications and the conditions in which two or more phases coexist can be provided by a suitable EoS. The common practice is that the EoS is solved for the volume, at constant temperature, pressure and composition and then, all the other properties can be determined using specific thermodynamic relations. Another, useful alternative is the volume-based approach in which the primary variables are temperature, volume and composition and in this way there is no need to solve the EoS for the volume. A practical problem arises when EoS are coupled with flow models. Their formulation contrasts with the fluid-dynamics models, where the governing conservation laws are naturally posed in terms of density (ρ) and internal energy (U). Due to this mismatch between the data available and the natural variables of the EoS, iterative algorithms are needed, so that the physical properties at a specific state can be calculated.

Furthermore, the calculation of phase equilibrium at a specified temperature and pressure of a non-stable mixture (PT flash) [41, 42] is more robust and has been the subject of more investigation than other alternatives, such as flash calculations at specified (ρ, U), (P, H) etc. Algorithms for phase equilibrium calculation using these types of specifications have been proposed in the literature [69, 121-124] but they present lower computational efficiency and more implications than the PT flash, because of the additional constraints that occur.

In the oil and gas industry, fluid flow simulators use almost exclusively cubic EoS (such as SRK and PR, Zaydullin et al. [125]), which can be solved with a relatively low computational cost. However, the higher order EoS developed in the last two decades provide improved accuracy in physical property estimations, but the computational cost is higher than the cubic ones.

Previous work to address this issue has focused on producing tables of thermodynamic properties to replace the isothermal flash [125] during the simulations. In particular, Zaydullin et al. [125] extended the compositional space adaptive tabulation

(CSAT) technique of Iranshahr et al. [126] and applied it to compositional and thermal reservoir simulations of multicomponent-multiphase systems. In this case, the generalized negative flash approach was used to first establish and then extend the set of tie-simplexes for the CSAT procedure. These tie-simplexes were then used to look up, for a particular pressure and temperature, representing the phase state of the mixture. Dumbser et al. [127] presented a method of building an interpolating function in terms of density and internal energy using adaptive mesh refinement for a single-component fluid. The technique relied on the ability to calculate isochoric-isoenergetic flashes. Fang et al. [128] applied a bilinear interpolation method based on density and energy data returned by a computational flow model, to calculate the pressure, temperature and the speed of sound to simulate the two-phase compressible flow of CO_2. The interpolation grids were built based on properties of a CO_2 fluid predicted by the Span and Wagner (SW) EoS [129]. In their implementation, an iterative procedure is used to calculate the thermodynamic properties using the density and internal energy as input variables to the EoS. The authors compared the run times of the CFD simulations in cases where the properties were calculated directly from the SW and other tested EoS, as opposed to using their interpolation method. The results showed the superior computational efficiency of the interpolation method. Wilhelmsen et al. [130] have discussed methods of integration of conservation equations involving flash calculations, emphasizing that for its practical application an interpolation method should predict properties at least as accurately as the original EoS.

While the interpolation techniques have been almost exclusively developed for the density-internal energy flash calculations, their adaptation to other flash problems can also become practically useful. In particular, modeling the discharge flow from stationary and running pipeline fractures involve pressure-entropy flash algorithms [131-133], the application of which may become very computationally demanding, especially when simulating long running fractures. Finally, although efforts have been made in developing efficient algorithms for the entropy-stagnation enthalpy flash calculations in the discharge flow modeling [123], the use of interpolation tables to speed up these calculations has not been considered yet.

3. Thermodynamic Models

3.1. Equations of State for Fluids

3.1.1. Cubic Equations of State

An EoS is a mathematical relation that typically correlates the temperature, pressure and molar volume (v) of a pure compound at a thermodynamic equilibrium state. From these three coordinates, one is always dependent on the other two, for a single phase system with one component, according to the Gibbs phase rule. The EoS can be solved for one of these variables, while the other two are set. Most EoS are pressure-explicit and as a result, the equation is solved for the volume (or for the density), at constant temperature and pressure and then all the other properties (primary and derivative) can be determined using specific thermodynamic relations [94, 134]. The most well-known EoS are the SRK [32] and PR [33], which belong to the family of cubic EoS (cubic dependency on volume) and are empirical expressions based on the pioneering work of van der Waals [135]. A cubic EoS can be expressed by the general formula [57]:

$$P = \frac{RT}{v - b} - \frac{\alpha(T)}{(v + \delta_1 b)(v + \delta_2 b)} \qquad 3.1$$

where R is the gas constant and $\alpha(T)$ and b are component-specific parameters that account for the attractive intermolecular interactions and the excluded volume of the component, respectively. These parameters are calculated based on the critical temperature (T_c), the critical pressure (P_c) and the acentric factor (ω) of a pure compound. Alternatively, they can be fitted using experimentally measured pure component physical properties, such as vapor pressure and saturated densities. For $\delta_1 = 1$ and $\delta_2 = 0$, Eq. 3.1 takes the form of SRK EoS and for $\delta_1 = 1 + \sqrt{2}$ and $\delta_2 = 1 - \sqrt{2}$, Eq. 3.1 takes the form of PR EoS. In Table 3.1, the expressions for the two cubic equations of state and their parameters, used in this work are presented.

Table 3.1: Expressions for the energy ($\alpha(T)$) and co-volume (b) parameters for the cubic equations of state used in this work.

EoS	Equation	$\alpha(T)$	α_c	b
SRK	$P = \frac{RT}{v-b} - \frac{\alpha(T)}{v(v+b)}$	$\alpha_c[1+m(1-\sqrt{T_r})]^2$ $m = 0.48 + 1.574\omega - 0.176\omega^2$	$0.42748\frac{(RT_c)^2}{P_c}$	$0.08664\frac{RT_c}{P_c}$
PR	$P = \frac{RT}{v-b} - \frac{\alpha(T)}{v(v+b)+b(v-b)}$	$\alpha_c[1+m(1-\sqrt{T_r})]^2$ $m = 0.37464 + 1.542\omega - 0.26992\omega^2$	$0.45724\frac{(RT_c)^2}{P_c}$	$0.07780\frac{RT_c}{P_c}$

Extension of the two EoS to mixtures requires suitable mixing rules for the two parameters, the energy parameter and the co-volume one. One widely used way to extend the cubic EoS to mixtures is via the so-called vdW1f mixing (quadratic composition dependency for both parameters) and combining rules, *i.e.* the geometric mean rule for the cross-energy and the arithmetic mean rule for the cross co-volume parameter [136].

$$\alpha = \sum_{i=1}^{C}\sum_{j=1}^{C} x_i x_j \alpha_{ij} \qquad \alpha_{ij} = \sqrt{\alpha_{ii}\alpha_{jj}}(1-k_{ij}) \tag{3.2}$$

$$b = \sum_{i=1}^{C}\sum_{j=1}^{C} x_i x_j b_{ij} \qquad b_{ij} = \frac{b_{ii}+b_{jj}}{2}(1-l_{ij}) \tag{3.3}$$

where x_i and x_j are the mole fractions of components i and j in a mixture comprised of C components. The k_{ij} and l_{ij} parameters are called binary interaction parameters (BIPs) and are used to optimize the EoS performance by fitting them to phase equilibrium data. Of the two interaction parameters, k_{ij} is by far the most important one and usually l_{ij} is set equal to zero [136]. As a result, the mixing rule for the co-volume parameter is simplified to:

$$b = \sum_{i=1}^{C} x_i b_{ii} \tag{3.4}$$

A temperature-independent k_{ij} is usually preferred, but there are cases (highly asymmetric, polar mixtures etc.), in which the k_{ij} is made temperature dependent, so that a satisfying correlation of the phase behavior can be obtained.

3.1.2. SAFT Equations of State

SAFT based EoS are theoretically derived EoS, based on rigorous perturbation theory [137-139]. The basis of this theory (first order thermodynamic perturbation theory, TPT1) was developed by Wertheim [140-143], who proposed a model for systems with highly directional forces, which entail a repulsive core and multiple attractive sites capable of forming chains and closed rings. In addition, molecules can form hydrogen bonds. In his work, Wertheim expanded the Helmholtz free energy in a series of integrals of molecular distribution functions and the association potential. He showed that many of these integrals are zero and as a result, a simplified expression for the Helmholtz free energy can be obtained. In this way, the Helmholtz free energy of a fluid can be described as the sum of the Helmholtz free energy of a simple reference fluid which is known accurately and a perturbation term, the development of which is the challenging part.

Many different SAFT EoS have been proposed in the literature, which differ mainly in the intermolecular potential used to model the reference fluid. The early proposed SAFT EoS used the hard sphere system as the reference fluid, based on which the perturbation terms were developed to account for dispersion forces, formation of chains and intermolecular association phenomena. Later on, reference fluids that are allowed to interact with various potentials such as square-well (SW) [144-149] and Lennard-Jones (LJ) [150-154] were employed, resulting also in different chain and association terms. In this common framework, SAFT type EoS are written as summations of Helmholtz free energy terms corresponding to different types of molecular interactions.

A SAFT model that has gained tremendous industrial popularity is the PC-SAFT EoS [18]. Gross and Sadowski derived PC-SAFT using the hard chain fluid as their reference system and applied second order Barker - Henderson (BH) perturbation theory to develop the Helmholtz free energy term that accounts for the dispersion interactions. The pair potential used is the modified square well potential, proposed by Chen and Kreglewski [155]:

$$u(r) = \begin{cases} \infty & r < (\sigma - s_1) \\ 3\varepsilon & (\sigma - s_1) \le r < \sigma \\ -\varepsilon & \sigma \le r < \lambda\sigma \\ 0 & r \ge \lambda\sigma \end{cases} \qquad 3.5$$

The chain and association terms in PC-SAFT EoS are the same as the ones used in the SAFT EoS proposed by Huang and Radosz [16, 17]. These chain and association terms

were developed by applying TPT1 on the hard sphere reference fluid. PC-SAFT is commonly written as summation of Helmholtz free energy terms and the reader can refer to the original publications [18, 19] for the exact mathematical relations:

$$\frac{A^{RESIDUAL}}{Nk_BT} = \frac{A^{HARD-CHAIN}}{Nk_BT} + \frac{A^{DISPERSION}}{Nk_BT} + \frac{A^{ASSOCIATION}}{Nk_BT} \tag{3.6}$$

where A is the Helmholtz free energy and the superscripts refer to the respective molecular interaction contributions. N is the number of molecules and k_B is the Boltzmann constant.

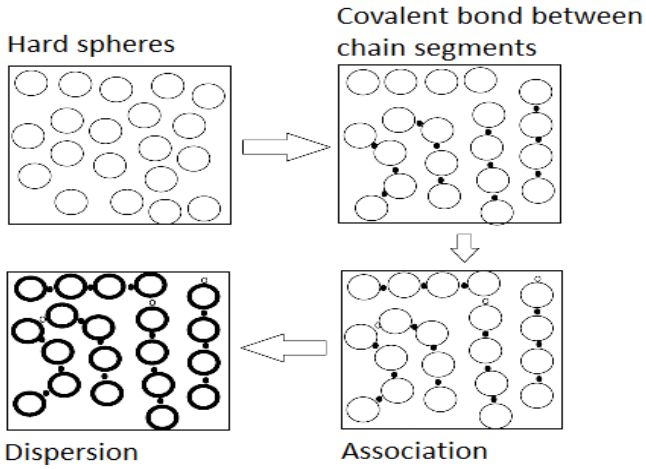

Figure 3.1: Schematic representation of the formation of a pure fluid within the PC-SAFT framework.

The expressions for the individual Helmholtz free energy terms used by PC-SAFT EoS for mixtures are presented in the following equations:

$$\frac{\tilde{a}^{HS}}{RT} = \frac{1}{\zeta_0}\left[\frac{3\zeta_1\zeta_2}{1-\zeta_3} + \frac{\zeta_2^3}{\zeta_3(1-\zeta_3)^2} + \left(\frac{\zeta_2^3}{\zeta_3^2} - \zeta_0\right)\ln(1-\zeta_3)\right] \tag{3.7}$$

$$\frac{\tilde{a}^{HC}}{RT} = \bar{m}\frac{\tilde{a}^{HS}}{RT} - \sum_i x_i\,(m_i - 1)\ln g_{ii}^{hs}(\sigma_{ii}) \tag{3.8}$$

$$\frac{\tilde{a}^{DISP}}{RT} = -2\pi\hat{\rho}I_1(\eta,\bar{m})\overline{m^2\varepsilon\sigma^3} - \pi\hat{\rho}\bar{m}C_1I_2(\eta,\bar{m})\overline{m^2\varepsilon^2\sigma^3} \tag{3.9}$$

$$\frac{\tilde{a}^{ASSOC}}{RT} = \sum_i x_i\left[\sum_{A_i}\left(lnX^{A_i} - \frac{X^{A_i}}{2}\right) + \frac{1}{2}M_i\right] \tag{3.10}$$

where $\tilde{a}$ is the molar Helmholtz free energy, while the superscripts denote the different contributions from the molecular interactions. x_i is the mole fraction of component i in

the mixture, m_i is the number of spherical segments in a chain of component i, $\overline{m}$ is the mean segment number, σ_i is the segment diameter of component i, d_i is the temperature dependent segment diameter of component i, ε_i is the dispersion energy and $g_{ii}^{hs}(d_{ii})$ is the radial pair distribution function of hard spheres of component i at contact.

$$g_{ij}^{hs}(d_{ij}) = \frac{1}{1-\zeta_3} + \left(\frac{d_i d_j}{d_i + d_j}\right)\frac{3\zeta_2}{(1-\zeta_3)^2} + \left(\frac{d_i d_j}{d_i + d_j}\right)^2 \frac{2\zeta_2^2}{(1-\zeta_3)^2} \tag{3.11}$$

$$\zeta_n = \frac{\pi}{6}\hat{\rho}\sum_i x_i m_i d_i^n \tag{3.12}$$

$$d_i = \sigma_i\left[1 - 0.12 \cdot \exp\left(-\frac{3\varepsilon_i}{k_B T}\right)\right] \tag{3.13}$$

$$X^{A_i} = \left[1 + \sum_j \sum_{B_j}^{M_i} \rho_j X^{B_j} \Delta^{A_i B_j}\right]^{-1} \tag{3.14}$$

$$\Delta^{A_i B_j} = d_{ij}^3 g_{ij}^{hs}(d_{ij}) \kappa^{A_i B_j}\left[\exp\left(\frac{\varepsilon^{A_i B_j}}{k_B T} - 1\right)\right] \tag{3.15}$$

where $\hat{\rho}$ is the number density of molecules and $I_1(\eta, \overline{m})$, $I_2(\eta, \overline{m})$ are integrals calculated by power series in reduced density $\eta = \zeta_3$. X^{A_i} is the fraction of molecules of species i not bonded at site A, M_i is the number of association sites on molecule i and $\Delta^{A_i B_j}$ is the association strength between position A of a molecule i and position B of a molecule j. $\varepsilon^{A_i B_j}$ is the association energy and $\kappa^{A_i B_j}$ is the association volume.

One of the especially attractive features of SAFT-type EoS, which stems from their theoretical origin, is that no mixing rules are needed in the chain and association terms. These terms are thus rigorously extended to mixtures. Extension of the EoS to mixture calculations requires however mixing rules for the dispersion term and the vdW1f mixing rules are usually employed (also in this work), as proposed by Gross and Sadowski [18]. Specific combining rules (Lorentz-Berthelot) are applied to calculate the segment dispersive energy and diameter parameters. Moreover, combining rules are needed for the association parameters in a mixture.

$$\overline{m^2 \frac{\varepsilon}{k_B T} \sigma^3} = \sum_{i=1}^{C} \sum_{j=1}^{C} x_i x_j m_i m_j \left[\frac{\varepsilon_{ij}}{k_B T}\right] \sigma_{ij}^3 \tag{3.16}$$

$$\overline{m^2 \left[\frac{\varepsilon}{k_B T}\right]^2 \sigma^3} = \sum_{i=1}^{C} \sum_{j=1}^{C} x_i x_j m_i m_j \left[\frac{\varepsilon_{ij}}{k_B T}\right]^2 \sigma_{ij}^3$$

$$\bar{m} = \sum_i x_i m_i \tag{3.17}$$

$$\varepsilon_{ij} = \sqrt{\varepsilon_{ii}\varepsilon_{jj}}\left(1 - k_{ij}\right) \tag{3.18}$$

$$\sigma_{ij} = \frac{\sigma_{ii} + \sigma_{jj}}{2}$$

$$\varepsilon^{A_i B_j} = \frac{1}{2}\left(\varepsilon^{A_i B_i} + \varepsilon^{A_j B_j}\right) \tag{3.19}$$

$$\kappa^{A_i B_j} = \sqrt{\kappa^{A_i B_i} \kappa^{A_j B_j}} \left(\frac{\sqrt{\sigma_{ii}\sigma_{jj}}}{\frac{1}{2}\left(\sigma_{ii} + \sigma_{jj}\right)}\right)^3 \tag{3.20}$$

A BIP was used in this work in the combining rule for the energy interaction parameter between unlike molecules to optimize the performance of the model.

The recently developed SAFT-VR Mie EoS [34] was also used in this work. The main motivation behind the development of SAFT-VR Mie was to improve the description of thermodynamic second-order derivative properties such as the isothermal compressibility and the speed of sound, as well as the prediction of critical point of pure components. Previous studies [156-158] have demonstrated that EoS based on hard-core or LJ potentials do not provide an adequate description of these properties [34]. Polishuk [159] has also reported that SAFT EoS using a temperature dependent diameter predict with much higher accuracy the thermodynamic properties than those that do not (for example SAFT-VR SW), but always in the expense of violation of the thermal stability criterion at very high pressures. In SAFT-VR Mie the pair potential utilized is the Mie potential, which is a generalized LJ potential with varying repulsive and attractive exponents:

$$u(r) = \frac{\lambda_r}{\lambda_r - \lambda_a}\left(\frac{\lambda_r}{\lambda_a}\right)^{\frac{\lambda_a}{\lambda_r - \lambda_a}} \varepsilon \left[\left(\frac{\sigma}{r}\right)^{\lambda_r} - \left(\frac{\sigma}{r}\right)^{\lambda_a}\right] \quad 3.21$$

For $\lambda_r = 12$ and $\lambda_a = 6$, the ordinary LJ potential is recovered. The Helmholtz free energy contribution from dispersive interactions in SAFT-VR Mie EoS is obtained by applying second order BH perturbation theory and extending it with a third order term, on a hard sphere reference fluid and utilizing the Mie potential as the perturbed potential. The first and second order terms are those dictated by BH perturbation theory and are obtained rigorously, while the third order term is of empirical nature. The chain and association terms are obtained with TPT1, using an approximation for the radial distribution function of a Mie fluid. In this framework, SAFT-VR Mie EoS is written as summation of Helmholtz free energy terms as follows:

$$\frac{A^{RESIDUAL}}{Nk_BT} = \frac{A^{MONOMER}}{Nk_BT} + \frac{A^{CHAIN}}{Nk_BT} + \frac{A^{ASSOCIATION}}{Nk_BT} \quad 3.22$$

$$\frac{A^{MONOMER}}{Nk_BT} = \frac{A^{HARD-SPHERE}}{Nk_BT} + \frac{A^{DISPERSION}}{Nk_BT} \quad 3.23$$

The mixing rule applied for the dispersion contribution, when mixtures are considered, is of vdW1f nature and is called MX1b [149], utilizing the radial distribution function for a single fluid and the effective packing fraction as discussed in [34, 149]. The necessary combining rules, taking also into account that the mixtures are non-conformal are the following:

$$\varepsilon_{ij} = \sqrt{\varepsilon_{ii}\varepsilon_{jj}}\frac{\sqrt{\sigma_{ii}^3\sigma_{jj}^3}}{\sigma_{ij}^3}\left(1 - k_{ij}\right)$$

$$\sigma_{ij} = \frac{\sigma_{ii} + \sigma_{jj}}{2} \quad 3.24$$

$$d_{ij} = \frac{d_{ii} + d_{jj}}{2}$$

$$\lambda_{k,ij} - 3 = \sqrt{\left(\lambda_{k,ii} - 3\right)\left(\lambda_{k,jj} - 3\right)}$$

where d_{ii} is the temperature-dependent diameter of the spherical segments of component i and $\lambda_{k,ii}$ is the repulsive (λ_r) or attractive (λ_a) exponent of the Mie potential of component i.

In summary, the general differences between PC-SAFT and SAFT-VR Mie EoS, in terms of theoretical background, are the fluid serving as reference for the BH perturbation, the order of the BH perturbation, the potential used to describe the dispersive interactions and the fluid serving as reference for the TPT1 based on which the chain and association terms are developed. In terms of application to real fluids, PC-SAFT requires the regression of three pure component parameters ($m_i, \varepsilon_{ii}, \sigma_{ii}$) for non-associating compounds which are typically fitted to vapor pressure and saturated liquid density experimental data. SAFT-VR Mie requires two additional parameters which are the repulsive and attractive exponents ($\lambda_{r,ii}, \lambda_{a,ii}$) of each component, although it is common practice to fix the attractive exponent to 6. SAFT-VR Mie parameters are obtained by fitting vapor pressure, saturated liquid density, condensed liquid density and speed of sound data. In this way, a better prediction of the different thermophysical properties is obtained, as well as, physically relevant values of the repulsive exponent [34].

3.2. Thermodynamic Models for the Solid Phase

The SFE of mixtures can be predicted by a variety of methods. Thermodynamic models in the form of EoS provide a very good balance between accuracy and computational efficiency for such calculations. However, most EoS are developed only for application in fluid phases (liquid, vapor and supercritical); EoS for solid phases are usually very complex, multi parametric and component specific. As an alternative, thermodynamically consistent models for the solid phase can be considered, in combination with fluid-phase EoS. The challenge in developing a solid-fluid (SF) model lies on selecting and combining models for each phase which are both accurate and computationally efficient for pure compounds but also for mixtures. To this end, two approaches, which are based on different thermodynamic reference states, are the most well-known. The first approach, originally proposed by McHugh et al. [160], utilizes the temperature of the system and the saturation pressure at SFE conditions of the pure solid-former, as reference state for the calculation of the solid-phase fugacity. The saturation pressure is most commonly provided by empirical correlations fitted to

experimental data under SVE or SLE conditions. The second approach, is based on applying a thermodynamic integration process, originally proposed by Prausnitz et al. [94] and later extended for high pressure calculations by various authors [102, 161, 162]. The differences between the referenced methodologies (based on thermodynamic integration) for high pressure modeling are essentially practical and not fundamental.

3.2.1. Approach of McHugh

The first approach for calculating the solid-phase fugacity of a pure component was originally proposed by McHugh et al. [160]. The approach utilizes as reference state the saturation pressure of the pure solid-former at SFE conditions at the temperature of the system. This leads to the expression:

$$\hat{f}_{0i}^{S}(T,P) = P_{0i}^{sat}(T)\hat{\varphi}_{0i}^{sat}\left(T,P_{0i}^{sat}\right)\exp\left[\frac{v_{0i}^{S}}{RT}\left(P-P_{0i}^{sat}(T)\right)\right] \qquad 3.25$$

where $P_{0i}^{sat}(T)$ is the saturation pressure at SLE of SVE conditions of the pure solid-former at the temperature T of the system, $\hat{\varphi}_{0i}^{sat}\left(T,P_{0i}^{sat}\right)$ is the fugacity coefficient of the pure solid-former calculated from a fluid-phase EoS at temperature T and pressure P_{0i}^{sat}, P is the pressure of system and v_{0i}^{S} is the temperature and pressure-independent solid molar volume of the pure solid-former. In order to use Eq. 3.25 for SFE calculations, it is necessary to couple a fluid-phase EoS with a model that provides the saturation pressure of the solid-former. This solid-phase model can be an empirical correlation fitted to experimental data at SLE or SVE conditions.

3.2.2. Approach of Seiler

An alternative way to model SFE was proposed by Seiler et al. [162]. Here, in the case of SLE, the reference state is the hypothetical, pure, subcooled melt, at system temperature and a reference pressure (P^{+}). The hypothetical, pure, superheated sublime reference state at system temperature and a reference pressure can be used to model the SVE. The reference pressure is chosen by taking into account the existence of experimentally measured (or accurately calculated) thermophysical properties at this state and usually the normal melting point of the pure solid-forming compound is used for SLE and SLGE calculations. Based on this reference state, it follows:

$$\hat{f}_{0i}^{S}(T,P) = \hat{f}_{0i}^{F^*}(T,P)\exp\left[-\frac{1}{RT}\left(\mu_{0i}^{F^*}(T,P)-\mu_{0i}^{S}(T,P)\right)\right] \qquad 3.26$$

where $\hat{f}_{0i}^{F^*}(T,P)$ and $\mu_{0i}^{F^*}(T,P)$ are the fugacity and the chemical potential of the fluid phase (liquid or vapor), used as reference. The procedure for calculating the solid-phase fugacity, using the hypothetical subcooled melt (for SLE and SLGE calculations) as reference state, will be shown here and the same principles apply when the hypothetical, pure, superheated sublime is used (for SVE calculations). Eq. 3.26 then takes the form:

$$\hat{f}_{0i}^{S}(T,P) = \hat{f}_{0i}^{L^*}(T,P)\exp\left[-\frac{1}{RT}\left(\mu_{0i}^{L^*}(T,P) - \mu_{0i}^{S}(T,P)\right)\right] \qquad 3.27$$

The difference of the chemical standard state potentials of the pure substance in Eq. equals to the Gibbs free energy change Δg^{SL^*}:

$$\mu_{0i}^{L^*}(T,P) - \mu_{0i}^{S}(T,P) = g_{0i}^{L^*}(T,P) - g_{0i}^{S}(T,P) = \Delta g_{0i}^{SL^*} \qquad 3.28$$

The Gibbs free energy change $\Delta g_{0i}^{SL^*}$ of the pure substance in Eq. 3.28 is calculated by applying a thermodynamic cycle [162]. This cycle can be divided into three steps. The starting point is represented by state A at system temperature and system pressure. In the first step, this state has to be converted isothermally to the introduced reference pressure P^+. The second step from point B (T,P^+) to point E (T,P^+) is an isobaric thermodynamic cycle, similar to the one described by Prausnitz et al. [94]. Between points B and E, steps "heating up the solid to its melting curve", "melting" and "cooling down the liquid to the hypothetical state of the subcooled melt" can be calculated. The third and final step follows, in which the isothermal change from point E at the reference pressure P^+ to point F at system pressure is considered.

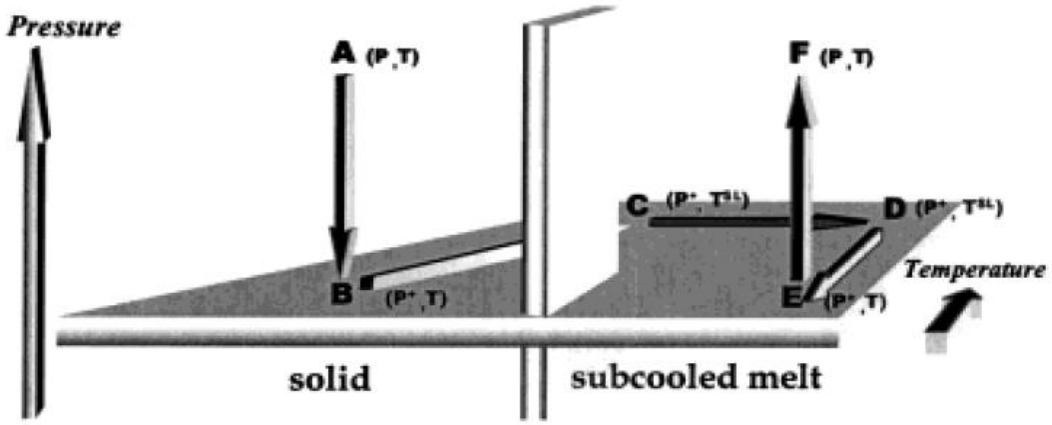

Figure 3.2: Thermodynamic cycle for the calculation of the solid-phase fugacity, based on the hypothetical, pure, subcooled melt reference state. Figure taken from Seiler et al. [162].

Step 1 (from point A to point B)

$$\Delta g_{step1} = g_{0i}^{S}(T, P^{+}) - g_{0i}^{S}(T, P) = \int_{P}^{P+} v_{0i}^{S}\, dP \tag{3.29}$$

Step 2 (from point B to point E)

$$\Delta g_{step2} = g_{0i}^{L^*}(T, P^{+}) - g_{0i}^{S}(T, P^{+}) = \Delta h_{0i}^{SL^*} - T\Delta s_{0i}^{SL^*} \tag{3.30}$$

$$\Delta g_{step2} = \Delta h_{0i}^{SL}\left(1 - \frac{T}{T_{0i}^{SL}}\right) - \int_{T}^{T_{0i}^{SL}} \Delta c_{P,0i}^{SL^*}\, dT + T\int_{T}^{T_{0i}^{SL}} \frac{\Delta c_{P,0i}^{SL^*}}{T} dT \tag{3.31}$$

Step 3 (from point E to point F)

$$\Delta g_{step3} = g_{0i}^{L}(T, P) - g_{0i}^{L^*}(T, P^{+}) = \int_{P+}^{P} v_{0i}^{L^*}\, dP \tag{3.32}$$

Applying this thermodynamic integration process, the solid-phase fugacity of the pure solid-former is retrieved:

$$\hat{f}_{0i}^{S}(T, P) = \hat{f}_{0i}^{L^*}(T, P)\exp\left[-\frac{1}{RT}\left(-\int_{P^+}^{P} v_{0i}^{S} dP + \int_{P^+}^{P} v_{0i}^{L^*} dP\right) - \frac{\Delta h_{0i}^{SL}}{RT}\left(1 - \frac{T}{T_{0i}^{SL}}\right) + \frac{1}{RT}\int_{T}^{T_{0i}^{SL}} \Delta c_{P,0i}^{SL^*} dT - \frac{1}{R}\int_{T}^{T_{0i}^{SL}} \frac{\Delta c_{P,0i}^{SL^*}}{T} dT\right] \tag{3.33}$$

where Δh_{0i}^{SL} is the enthalpy of melting at melting temperature T_{0i}^{SL}, v_{0i}^{S} and $v_{0i}^{L^*}$ are the pure solid-former solid molar volume and liquid molar volume at the solid-liquid (SL) transition and $\Delta c_{P,0i}^{SL^*}$ is the difference of the molar, isobaric heat capacities between the hypothetical subcooled melt and the solid. Assuming that the difference in the isobaric heat capacities is temperature-independent and the solid and liquid molar volumes are pressure-independent, the solid-phase fugacity is retrieved as proposed by Seiler et al. [162]:

$$\hat{f}_{0i}^{S}(T, P) = \hat{f}_{0i}^{L^*}(T, P)\exp\left[-\frac{\left(v_{0i}^{S} - v_{0i}^{L^*}\right)(P^{+} - P)}{RT} - \frac{\Delta h_{0i}^{SL}}{RT}\left(1 - \frac{T}{T_{0i}^{SL}}\right) + \frac{\Delta c_{P,0i}^{SL^*}}{RT}\left(T_{0i}^{SL} - T\right) - \frac{\Delta c_{P,0i}^{SL^*}}{R} ln\frac{T_{0i}^{SL}}{T}\right] \tag{3.34}$$

3.2.3. Gibbs Free Energy Eos for Solid CO_2

Jäger and Span [163] proposed a new EoS, that describes the thermodynamic behavior of solid CO_2, based on the Gibbs free energy. It is an empirical model which is explicit in the Gibbs free energy by using a fundamental expression for it and is fitted to experimental data (heat capacity, molar volume, expansion coefficient and compressibility) of solid CO_2.

The Gibbs free energy can be written as:

$$g(P,T) = h_0 - Ts_0 + \int_{T0}^{T} c_P(T,P_0)\,dT - T\int_{T0}^{T} \frac{c_P(T,P_0)}{T}\,dT + \int_{P0}^{P} v(P,T)\,dP \qquad 3.35$$

Jäger and Span [163] used appropriate functional forms for the heat capacity, the thermal expansion coefficient and the first derivative of the molar volume with respect to pressure, so that these quantities could be accurately fitted to experimental data. The final equation for the Gibbs free energy is:

$$\begin{aligned}\frac{g}{RT_0} = {} & g_0 + g_1\Delta\vartheta + g_2\Delta\vartheta^2 \\ & + g_3\left\{\ln\left(\frac{\vartheta^2+g_4^2}{1+g_4^2}\right) - \frac{2\vartheta}{g_4}\left[\arctan\left(\frac{\vartheta}{g_4}\right) - \arctan\left(\frac{1}{g_4}\right)\right]\right\} \\ & + g_5\left\{\ln\left(\frac{\vartheta^2+g_6^2}{1+g_6^2}\right) - \frac{2\vartheta}{g_6}\left[\arctan\left(\frac{\vartheta}{g_6}\right) - \arctan\left(\frac{1}{g_6}\right)\right]\right\} \\ & + g_7\Delta\pi\left[e^{f_\alpha(\vartheta)} + K(\vartheta)g_8\right] \\ & + g_9K(\vartheta)\left[(\pi+g_{10})^{(n-1)/n} - (1+g_{10})^{(n-1)/n}\right]\end{aligned} \qquad 3.36$$

where T_0 is the reference temperature set equal to 150 K, P_0 is the reference pressure set equal to 0.101325 MPa and $\vartheta = T/T_0$. Eq. 3.36 uses 23 adjustable parameters that are fitted to experimental data. Here, all parameters are kept to the original values proposed by Jäger and Span, except for two, namely the g_0 and g_1 parameters, which have to be retuned for every fluid-phase EoS that is coupled with the solid-phase EoS. The purpose of tuning these two parameters for every different fluid-phase EoS is to ensure that the corresponding solid-fluid model is going to be thermodynamically consistent. For more details regarding the parameters of the model, the reader can refer to the original publication of Jäger and Span [163].

When different thermodynamic models are used to describe the fluid and the solid-phase properties of a system, special consideration must be given to the thermodynamic consistency. As a result, any solid-fluid model which is going to be the

result of coupling the solid-phase and fluid-phase EoS has to be adjusted in a way, so that all properties are consistent at phase equilibria.

A thermodynamic triple point is the point where three phases are in equilibrium simultaneously. In a pure component system, three phases may be found at coexistence only at specific pairs of temperature and pressure, with no degrees of freedom; meaning that these are points in the phase diagram (triple points). A pure component triple point and its properties are of great importance to the procedure of tuning the solid-fluid model to be thermodynamically consistent. This point of coexisting phases is used to "anchor" the solid-phase and fluid-phase models.

In order to make the solid and fluid models thermodynamically consistent, parameters g_0 and g_1 are adjusted so that the Gibbs free energy of all phases (vapor, liquid and solid) is the same at the triple point, as suggested by Jäger and Span [163]. This is done by solving Eqs. 3.37 and 3.38 with respect to g_0 and g_1.

$$g_{0i}^{S}(T_{tr}, P_{tr}) = g_{0i}^{L}(T_{tr}, P_{tr}) = g_{0i}^{V}(T_{tr}, P_{tr}) \tag{3.37}$$

$$s_{0i}^{S}(T_{tr}, P_{tr}) = s_{0i}^{L}(T_{tr}, P_{tr}) - \frac{\Delta h_{0i}^{SL}}{T_{tr}} \tag{3.38}$$

The solution of these equations requires certain derivatives of the Gibbs free energy which are not presented here and the reader can refer to the original publication of Jäger and Span for more details.

The melting enthalpy at the triple point of CO_2 is set equal to 8,875 J/mole as suggested by Jäger and Span who treated it as an adjustable parameter. The triple point temperature is set equal to the experimental value of 216.58 K. The triple point pressure is predicted by every model as the "intersection" of the solid-vapor and the vapor-liquid saturation curves. In this work, the Jäger and Span EoS was coupled with PC-SAFT EoS and the resulting values for the g_0 and g_1 parameters are 7.447399 and -2.19139 respectively. Other fluid-phase EoS can be coupled with the Jäger and Span EoS but in such a case different values for g_0 and g_1 will be needed.

The calculation of the equilibrium pressure of pure CO_2 with the Jäger and Span EoS at a specified temperature at SLE or SVE conditions is performed by numerically integrating the Clausius-Clapeyron equation. The numerical integration applies a Runge-Kutta 4th order method and the enthalpy and volume differences are calculated at each point of numerical integration, using the solid-phase and the fluid-phase EoS. This ensures that Eq. 3.39 is not limited to a narrow range of conditions. The Clausius-

Clapeyron equation provides the means to evaluate the change of the phase equilibrium conditions from one equilibrium point to another. The basis behind this equation is that, at each phase equilibrium point the Gibbs free energy of each phase is the same and therefore, the differential along the equilibrium phase boundary is zero. Based on this, it can be shown that the derivative of the pressure as a function of temperature along the phase equilibrium curve is given by Eq. 3.39 and is a function of the enthalpy and volume difference between the phases in equilibrium:

$$\left.\frac{dP}{dT}\right|_{equil} = \frac{\Delta h}{T\Delta v} \tag{3.39}$$

The use of the Jäger and Span EoS in mixture calculations will be presented in Chapter 6.

4. Methods for Direct Saturation Point Calculations

4.1. Introduction

New algorithms for the calculation of bubble and dew points of binary and multicomponent mixtures are presented in this chapter. The proposed numerical methods are based on the derivation of the equations that govern phase equilibrium, by starting from the stability criterion of Gibbs and applying a modification, thus resulting in new sets of independent variables and iterative procedures. An additional change of variables is performed to obtain optimal scaling in the minimization problem which is nested in the proposed iterative schemes and thus obtain methods with improved speed and robustness. The algorithms can be applied to calculate at will the lower / upper pressure or low / high temperature bubble or dew point parts of phase diagrams, thus being robust tools when retrograde regions are considered. A simple and widely used initialization method is utilized at low and elevated pressures, while implementation guidelines are given to ensure robust iterative procedures. The proposed methodologies can be applied with or without the use of derivatives of the fugacity coefficients, although their use is strongly advised (if available), since the proposed methods become significantly faster. The new algorithms are tested by calculating saturation points of binary and multicomponent mixtures and prove to be efficient and robust, even in the near proximity of critical points in some cases.

In Chapter 2, section 2.1, the computational challenges surrounding the methods for saturation point calculations were presented. These challenges, except for the formulation as an optimization procedure, are tackled with high success by using the continuation methods which were mentioned in Chapter 2. These methods calculate in a single run the entire solution branch of saturation points for mixtures (the whole phase envelope) and their main advantage is the very accurate initial estimates produced by the predictor-corrector procedure. This also enables the use of full Newton's method which is quadratically convergent, when sufficiently close to the solution. However, algorithms for direct calculation of saturation points with EoS still need further development, as it is also noted by Michelsen [164]. The need for such algorithms is particularly important for data regression procedures, in which EoS parameters are adjusted to match sets of experimental data. Failure to converge the saturation point calculation at difficult conditions (usually elevated pressures and proximity to critical points) leads in the end to

the exclusion of data points from the regression, which results in inferior correlation ability of the model. Moreover, tracing the whole branch of solutions can be computationally expensive, especially when complex EoS are utilized, as they require the determination of a number of solutions along the path, which may not be required. In terms of coding, connecting a continuation method with regression algorithms can be also more complex than the use of a direct saturation point calculation.

In this work, the use of different sets of variables is proposed for the calculation of bubble and dew points of mixtures. The objective is to propose fast and robust algorithms for the direct calculation of saturation points. One of the targets is to use a simple and widely used initialization method (Wilson approximation), while retaining robust iterative procedures which can be initiated both at low or high pressures. As it has already been mentioned, ideal solution approximations can lead to very poor initial estimates for the incipient phase composition at high pressures and consequently the proposed algorithms must be able to tolerate these initial estimates and retain their robustness. Furthermore, a fast convergence rate is desirable, which is achieved by taking into account derivatives of specific functions, while the methods can be applied to binary and multicomponent mixtures with simple or complex EoS.

The proposed methods are based on the stability criterion of Gibbs under constant temperature and pressure and new potentials are constructed by modifying the Gibbs free energy. As a result, new sets of independent variables are derived, which can be used for saturation point calculations and algorithms that can calculate at will the lower / upper pressure or low / high temperature dew point parts of constant composition phase envelopes are constructed. The same methods can also be applied for bubble points. The basis of the methods is the modification of the thermodynamic potential based on which the equations of phase equilibrium are derived. A representative example is given here and a detailed analysis will follow. The total differential of Gibbs free energy, expressed as function of temperature, pressure and the number of moles of each component in a mixture is:

$$dG = V \cdot dP - S \cdot dT + \sum_{i=1}^{C} \mu_i dn_i \qquad 4.1$$

where (S) is the entropy, (V) the volume of the mixture, (μ_i) the chemical potential and (n_i) the number of moles of component i. Multiplying G by P and taking the total differential:

$$d\mathcal{L}^U = d(G \cdot P) = P \cdot dG + G \cdot dP \tag{4.2}$$

using Euler's theorem for homogeneous functions:

$$G = \sum_{i=1}^{C} n_i \mu_i \tag{4.3}$$

and combining Eqs. 4.1, 4.2 and 4.3:

$$d\mathcal{L}^U = P \cdot \left(V \cdot dP - S \cdot dT + \sum_{i=1}^{C} \mu_i dn_i \right) + \sum_{i=1}^{C} n_i \mu_i \cdot dP \tag{4.4}$$

$$d\mathcal{L}^U = V \cdot P \cdot dP - S \cdot P \cdot dT + \sum_{i=1}^{C} \mu_i \cdot (P dn_i + n_i dP) \tag{4.5}$$

by setting:

$$\overline{\xi}_i = n_i P \tag{4.6}$$

then Eq. 4.5 becomes:

$$d\mathcal{L}^U = V \cdot P \cdot dP - S \cdot P \cdot dT + \sum_{i=1}^{C} \mu_i d\overline{\xi}_i \tag{4.7}$$

Based on $\mathcal{L}^U$, the VLE condition of chemical potential equality at constant temperature and pressure can be written as:

$$\mu_i^V = \left. \frac{\partial \mathcal{L}^{U^V}}{\partial \overline{\xi}_i} \right|_{T,P} = \left. \frac{\partial \mathcal{L}^{U^L}}{\partial \overline{\xi}_i} \right|_{T,P} = \mu_i^L \tag{4.8}$$

4.2. Working Equations Derivation

To derive the equations for the new methods, the stability criterion of Gibbs as demonstrated by Michelsen [41, 57], is cited. When δn_i moles of a component i are transferred from a liquid to a vapor phase (the same relationship holds for any two fluid phases at equilibrium) under constant T and P, the Gibbs free energy change is given by:

$$\delta G = \left(\mu_i^V - \mu_i^L \right) \delta n_i \tag{4.9}$$

If δn_i is infinitesimally small, this change must be zero when Gibbs free energy is at the global minimum. If a phase of molar composition $\boldsymbol{z}$ and chemical potentials $\boldsymbol{\mu}(\boldsymbol{z})$ is considered and an infinitesimal molar amount δe of a new phase with composition $\boldsymbol{w}$ is formed, the change in Gibbs free energy is:

$$\delta G = \delta e \sum_{i=1}^{C} w_i(\mu_i(\boldsymbol{w}) - \mu_i(\boldsymbol{z})) \tag{4.10}$$

The original phase with composition $\boldsymbol{z}$ is stable when δG is non-negative for any positive δe and this necessary condition for stability is expressed mathematically as:

$$\sum_{i=1}^{C} w_i(\mu_i(\boldsymbol{w}) - \mu_i(\boldsymbol{z})) \geq 0 \tag{4.11}$$

for any composition $\boldsymbol{w}$. This is the tangent plane condition of Gibbs. It can be shown that this condition is also a sufficient condition for stability [57]. The reduced TPD function, if the chemical potentials are expressed as fugacities and the ideal gas reference state is used, is formulated as:

$$TPD(\boldsymbol{w}) = \sum_{i=1}^{C} w_i\big(\ln w_i + \ln\hat{\varphi}_i(\boldsymbol{w}, T, P) - \ln z_i - \ln\hat{\varphi}_i(\boldsymbol{z}, T, P)\big) \tag{4.12}$$

under the constraints:

$$\begin{gathered} w_i \geq 0;\ i = 1,2 \ldots C \\ \sum_{i=1}^{C} w_i - 1 = 0 \end{gathered} \tag{4.13}$$

Minimization of the TPD function can be formulated as a constrained minimization problem with the use of Lagrange multipliers [57]:

$$L(\boldsymbol{w}, \lambda) = \sum_{i=1}^{C} w_i\big(\ln w_i + \ln\hat{\varphi}_i(\boldsymbol{w}, T, P) - \ln z_i - \ln\hat{\varphi}_i(\boldsymbol{z}, T, P)\big) - \lambda\left(\sum_{i=1}^{C} w_i - 1\right) \tag{4.14}$$

and the stationary conditions are:

$$\frac{\partial L}{\partial w_j} = \ln w_j + \ln\hat{\varphi}_j(\boldsymbol{w}, T, P) - \ln z_j - \ln\hat{\varphi}_j(\boldsymbol{z}, T, P) + 1 - \lambda = 0;\ j = 1,2 \ldots C \tag{4.15}$$

$$\frac{\partial L}{\partial \lambda} = -\sum_{i=1}^{C} w_i + 1 = 0 \tag{4.16}$$

The reduced TPD is modified by explicitly eliminating the constraint that the mole fractions add up to 1 and using as independent variables the composition variables

$W_i = w_i \exp(1-\lambda)$. These composition variables are treated formally as mole numbers and an unconstrained formulation can be constructed:

$$Q_1(\boldsymbol{W}) = \sum_{i=1}^{C} W_i\left(\ln W_i + \ln\hat{\varphi}_i(\boldsymbol{W},T,P) - \ln z_i - \ln\hat{\varphi}_i(\boldsymbol{z},T,P)\right) + 1 - \sum_{i=1}^{C} W_i \qquad 4.17$$

The first derivatives of the modified reduced TPD (Q_1) are the equifugacity relations:

$$\frac{\partial Q_1}{\partial W_j} = \ln W_j + \ln\hat{\varphi}_j(\boldsymbol{W},T,P) - \ln z_j - \ln\hat{\varphi}_j(\boldsymbol{z},T,P);\ j = 1,2 \ldots C \qquad 4.18$$

At the minimum (stationary point, SP), Q_1 takes the value:

$$Q_1{}^{SP} = 1 - \sum_{i=1}^{C} W_i \qquad 4.19$$

At the SP, the following cases exist:

$$Q_1{}^{SP} > 0 \quad \sum_{i=1}^{C} W_i < 1 \qquad \text{One phase stable mixture} \qquad 4.20$$

$$Q_1{}^{SP} = 0 \quad \sum_{i=1}^{C} W_i = 1 \qquad \text{Two phases at equilibrium (exactly on the bubble or dew point)} \qquad 4.21$$

$$Q_1{}^{SP} < 0 \quad \sum_{i=1}^{C} W_i > 1 \qquad \text{Metastable - Unstable mixture} \qquad 4.22$$

It has to be noted that the trivial solution $\boldsymbol{W} = \boldsymbol{z}$ is also a minimum of the Q_1 function in the cases of a stable or metastable mixture. In the former case it can be the only minimum if the conditions (T, P) lie outside the stability test limit locus (STLL), or else one positive minimum will exist in addition to the trivial one. Exactly on the STLL, the non-trivial stationary point is a saddle point and not a minimum [165]. In the metastable region, in addition to the trivial solution, at least one negative minimum exists. In these cases, the matrix of second derivatives of Q_1 with respect to $\boldsymbol{W}$ (Hessian), evaluated at $\boldsymbol{W} = \boldsymbol{z}$, is positive definite. If the Hessian matrix (evaluated at $\boldsymbol{W} = \boldsymbol{z}$) has a negative eigenvalue, then the mixture is unstable and at least two negative minima exist [41].

The stability criterion can be formulated under constant T and P, based on $\mathcal{L}^U$ (Eq. 4.2) and Eqs. 4.6, 4.7:

$$\delta\mathcal{L}^U = \left(\mu_i^V - \mu_i^L\right)\delta\overline{\xi_\iota} \tag{4.23}$$

$$\delta\mathcal{L}^U = P\left(\mu_i^V - \mu_i^L\right)\delta n_i \tag{4.24}$$

$$\delta\mathcal{L}^U = \delta eP\sum_{i=1}^{C} w_i(\mu_i(\boldsymbol{w}) - \mu_i(\boldsymbol{z})) \tag{4.25}$$

$$\delta\mathcal{L}^U = P\sum_{i=1}^{C} w_i(\mu_i(\boldsymbol{w}) - \mu_i(\boldsymbol{z})) \tag{4.26}$$

Pressure is always positive and as a result Eq. 4.26 corresponds to an equivalent stability criterion as Eq. 4.11. The new reduced TPD function on this surface is written as:

$$TPD^{mU}(\boldsymbol{\xi}) = \sum_{i=1}^{C}\xi_i\left(\ln w_i + \ln\hat{\varphi}_i(\boldsymbol{w},T,P) - \ln z_i - \ln\hat{\varphi}_i(\boldsymbol{z},T,P)\right) \tag{4.27}$$

where $\xi_i = w_i P$, under the constraints:

$$\begin{gathered}\xi_i \geq 0;\ i = 1,2\ldots C \\ \sum_{i=1}^{C}\xi_i - P = 0\end{gathered} \tag{4.28}$$

The TPD^{mU} function can be modified by explicitly eliminating the constraint of Eq. 4.28 and using as independent variables $\Xi_i^U = W_i P$.

$$Q_1{}^{mU}(\boldsymbol{\Xi}^U) = \sum_{i=1}^{C}\Xi_i^U\left(\ln W_i + \ln\hat{\varphi}_i(\boldsymbol{W},T,P) - \ln z_i - \ln\hat{\varphi}_i(\boldsymbol{z},T,P)\right) + P - \sum_{i=1}^{C}\Xi_i^U \tag{4.29}$$

The equifugacity relations can be derived by taking the first derivatives of $Q_1{}^{mU}$ with respect to $\boldsymbol{\Xi}^U$.

$$\frac{\partial Q_1{}^{mU}}{\partial\Xi_j^U} = \left[\left(\ln W_j + \ln\hat{\varphi}_j(\boldsymbol{W},T,P) - \ln z_j - \ln\hat{\varphi}_j(\boldsymbol{z},T,P)\right) + \frac{1}{P}\sum_{i=1}^{C}\Xi_i^U\left(\frac{1}{W_j}\delta_{ij} + \frac{\partial\ln\hat{\varphi}_i(\boldsymbol{W},T,P)}{\partial W_j}\right)\right] - 1;\ j = 1,2\ldots C \tag{4.30}$$

$$\frac{\partial {Q_1}^{mU}}{\partial \Xi_j^U} = \left(\ln W_j + \ln\hat{\varphi}_j(\boldsymbol{W},T,P) - \ln z_j - \ln\hat{\varphi}_j(\boldsymbol{z},T,P)\right) + \sum_{i=1}^{C} W_i\left(\frac{1}{W_j}\delta_{ij} + \frac{\partial \ln\hat{\varphi}_i(\boldsymbol{W},T,P)}{\partial W_j}\right) - 1;\ j = 1,2 \dots C \quad (4.31)$$

$$\frac{\partial {Q_1}^{mU}}{\partial \Xi_j^U} = \left(\ln W_j + \ln\hat{\varphi}_j(\boldsymbol{W},T,P) - \ln z_j - \ln\hat{\varphi}_j(\boldsymbol{z},T,P)\right) + \sum_{i=1}^{C} W_i\frac{1}{W_j}\delta_{ij} + \sum_{i=1}^{C} W_i\frac{\partial \ln\hat{\varphi}_i^W}{\partial W_j} - 1;\ j = 1,2 \dots C \quad (4.32)$$

and by means of the Gibbs-Duhem equation:

$$\frac{\partial {Q_1}^{mU}}{\partial \Xi_j^U} = \ln W_j + \ln\hat{\varphi}_j(\boldsymbol{W},T,P) - \ln z_j - \ln\hat{\varphi}_j(\boldsymbol{z},T,P);\ j = 1,2 \dots C \quad (4.33)$$

At the minimum (stationary point):

$${Q_1}^{mU,SP} = P - \sum_{i=1}^{C} \Xi_i^U \quad (4.34)$$

At the SP, the following cases exist:

$${Q_1}^{mU,SP} > 0, \quad \sum_{i=1}^{C} \Xi_i^U < P \quad \text{One phase stable mixture} \quad (4.35)$$

$${Q_1}^{mU,SP} = 0, \quad \sum_{i=1}^{C} \Xi_i^U = P \quad \text{Two phases at equilibrium (exactly on the bubble or dew point)} \quad (4.36)$$

$${Q_1}^{mU,SP} < 0, \quad \sum_{i=1}^{C} \Xi_i^U > P \quad \text{Metastable - Unstable mixture} \quad (4.37)$$

The equations that were derived above are based on $d\mathcal{L}^U = d(G \cdot P)$. Another set of variables ($\Xi_i^L = W_i/P$) can be also constructed based on $d\mathcal{L}^L = d(G/P)$. The same procedure can be followed, as the one mentioned previously, and again the equifugacity relations, as written in Eq. 4.33 will be derived. In this case, the modified TPD function and the conditions at the stationary point become:

$$Q_1{}^{mL}(\boldsymbol{\Xi}^L) = \sum_{i=1}^{C} \Xi_i^L \left(\ln W_i + \ln\hat{\varphi}_i(\boldsymbol{W}, T, P) - \ln z_i - \ln\hat{\varphi}_i(\boldsymbol{z}, T, P)\right) + \frac{1}{P} - \sum_{i=1}^{C} \Xi_i^L \quad 4.38$$

$$Q_1{}^{mL,SP} = 1/P - \sum_{i=1}^{C} \Xi_i^L \quad 4.39$$

At the SP, the following cases exist:

$$Q_1{}^{mL,SP} > 0 \qquad \sum_{i=1}^{C} \Xi_i^L < 1/P \qquad \text{One phase stable mixture} \quad 4.40$$

$$Q_1{}^{mL,SP} = 0 \qquad \sum_{i=1}^{C} \Xi_i^L = 1/P \qquad \text{Two phases at equilibrium (exactly on the bubble or dew point)} \quad 4.41$$

$$Q_1{}^{mL,SP} < 0 \qquad \sum_{i=1}^{C} \Xi_i^L > 1/P \qquad \text{Metastable - Unstable mixture} \quad 4.42$$

The two sets of variables mentioned above, can be used to perform saturation pressure calculations and by taking advantage of the stability criteria derived, calculate at will the lower or upper pressure solutions at retrograde branches (bubble or dew). The exact procedure is going to be discussed in the following sections. For saturation temperature calculations, the same derivations can be applied with $d\mathcal{L}^H = d(G \cdot T)$ and $\Xi_i^H = W_i T$ or $d\mathcal{L}^C = d(G/T)$ and $\Xi_i^C = W_i/T$.

4.3. Computational Algorithms

In this section, the working equations of three different methodologies for saturation pressure calculations are going to be presented. The same equations are applied for bubble or dew point calculations. At first, the methods based on $d\mathcal{L}^U = d(G \cdot P)$ are going to be discussed. In the following subsections, the same analysis is going to be performed for methods which are based on $d\mathcal{L}^L = d(G/P)$. The implementation details for the methods are given in section 4.4.

4.3.1. Bubble / Upper Dew Points

Method 1U

Method 1U is the basic computational scheme that can be constructed, based on the variables $\Xi_i^U = W_i P$. Performing saturation pressure calculations at constant T and $\boldsymbol{z}$ (feed phase composition), requires the determination of the equilibrium pressure P and the incipient phase composition $\boldsymbol{w}$. The calculation is done in two stages. The first one is performed at constant P, while $\boldsymbol{\Xi^U}$ are updated with Newton's method. This step is an unconstrained minimization of ${Q_1}^{mU}$ with respect to $\boldsymbol{\Xi^U}$:

$$g_i^U = \frac{\partial {Q_1}^{mU}}{\partial \Xi_i^U} = \ln W_i + \ln\hat{\varphi}_i(\boldsymbol{W}, T, P) - \ln z_i - \ln\hat{\varphi}_i(\boldsymbol{z}, T, P) = 0;\ i = 1,2 \dots C \qquad 4.43$$

$$H_{ij}^U = \frac{\partial^2 {Q_1}^{mU}}{\partial \Xi_i^U \partial \Xi_j^U} = \frac{1}{P}\left(\frac{1}{W_j}\delta_{ij} + \frac{\partial \ln\hat{\varphi}_i(\boldsymbol{W}, T, P)}{\partial W_j}\right);\ i, j = 1,2 \dots C \qquad 4.44$$

$$\boldsymbol{\Xi}^{U(k+1)} = \boldsymbol{\Xi}^{U(k)} + \delta\boldsymbol{\Xi}^{U(k)} \qquad 4.45$$

$$\boldsymbol{H}^{U(k)}\delta\boldsymbol{\Xi}^{U(k)} = -\boldsymbol{g}^{U(k)} \qquad 4.46$$

where $\boldsymbol{H^U}$ is the Hessian matrix. In the second step of method 1U, the incipient phase composition and the pressure are updated by imposing the constraint expressed in Eq. 4.36:

$$P^{(k+1)} = \sum_{i=1}^{C} \Xi_i^{U(k+1)} \qquad 4.47$$

and

$$\boldsymbol{w}^{(k+1)} = \frac{\boldsymbol{\Xi}^{U(k+1)}}{P^{(k+1)}} \qquad 4.48$$

Method 1U essentially involves a Newton step, that updates $\boldsymbol{\Xi^U}$ at constant T, P and consequently, the incipient phase composition variables ($\boldsymbol{W}$). The second step is a successive substitution step, which updates pressure by imposing the constraint of Eq. 4.36. If an initialization of pressure is given inside the metastable-unstable region, then for an incipient phase composition (different from the trivial one), Eq. 4.37 dictates that $\sum_{i=1}^{C} \Xi_i^U > P$ and by applying Eq. 4.47, P is going to acquire successively higher values. By taking advantage of this behavior, this method will always calculate the upper dew point in a retrograde region or a bubble point.

If the fugacity coefficients are considered composition independent, then the first step has the rate of convergence of a SS correction, which is generally considered a safe approach. However, Heidmann and Michelsen [166] have reported a particular problem, associated with the SS method, that is present in either flash or stability calculations and consequently in saturation point calculations also. That is, the oscillatory or non-convergent behavior of SS when very strong negative deviations from ideality are observed for a mixture. When SS is applied to correct the composition, as done in stability or saturation point calculations [60], then the rate of convergence depends on the eigenvalues of the matrix $\boldsymbol{M}$:

$$M_{ij} = -\left(w_j \frac{\partial \ln \hat{\varphi}_i(\boldsymbol{w}, T, P)}{\partial w_j}\right);\ i,j = 1,2 \dots C \tag{4.49}$$

Convergence of SS requires that all eigenvalues of $\boldsymbol{M}$ at the solution are smaller in absolute value than 1. If all eigenvalues are positive and smaller in magnitude than 1, which is the case for a large number of practical applications, then SS will converge to the final solution, given tolerable initial estimates. Near the critical point, the dominant eigenvalue approaches unity and convergence becomes slow [57]. It is possible that $\boldsymbol{M}$ may have negative eigenvalues at the solution and in this case convergence becomes oscillatory and if one or more eigenvalues becomes smaller than -1, SS does not converge. Mixtures in which this behavior can be observed usually involve strong electrolytes or polymers and present strong negative deviations from ideality. In this work, Eq. 4.44 is always applied using the composition derivatives of the fugacity coefficients, which also ensures faster convergence. On the other hand, $\boldsymbol{H^U}$ may be indefinite (positive and negative eigenvalues) and/or ill-conditioned. This happens mainly in early iterations and when ideal solution approximations are used to calculate the initial incipient phase composition at high pressures. Specific treatment must be applied in these cases and details are discussed in section 4.4.

Method 2U

To reduce the number of iterations in the iterative procedure, pressure can be updated with Newton's method by choosing an appropriate equation to calculate the derivative with respect to pressure. Method 2U is again a two-step method. The first step is identical to that of method 1, *i.e.* minimization of ${Q_1}^{mU}$ with respect to $\boldsymbol{\Xi^U}$, at constant T and P. In the second step, P is corrected with Newton's method, while $\boldsymbol{\Xi^U}$ are kept constant. The equation, based on which pressure is updated, is expressed by:

$$F^{mU} = P\left(1 - \sum_{i=1}^{C} z_i \frac{\hat{\varphi}_i(\boldsymbol{z}, T, P)}{\hat{\varphi}_i(\boldsymbol{W}, T, P)}\right) \tag{4.50}$$

$$\frac{dF^{mU}}{dP} = \left(1 - \sum_{i=1}^{C} z_i \frac{\hat{\varphi}_i(\boldsymbol{z}, T, P)}{\hat{\varphi}_i(\boldsymbol{W}, T, P)}\right) + P \sum_{i=1}^{C} z_i \frac{\hat{\varphi}_i(\boldsymbol{z}, T, P)}{\hat{\varphi}_i(\boldsymbol{W}, T, P)} \left(\frac{\partial \ln \hat{\varphi}_i(\boldsymbol{W}, T, P)}{\partial P} - \frac{\partial \ln \hat{\varphi}_i(\boldsymbol{z}, T, P)}{\partial P}\right) \tag{4.51}$$

,and

$$P^{(k+1)} = P^{(k)} + \eta_1 \cdot \delta P^{(k)} \tag{4.52}$$

$$\frac{dF^{mU}{}^{(k)}}{dP} \quad \delta P^{(k)} = -F^{mU}{}^{(k)} \tag{4.53}$$

where η_1 is a relaxation factor that is used to avoid overshooting of the final solution. Guidelines for the values of η_1 are given in section 4.4. When Eqs. 4.52 and 4.53 are used to correct P, special care must be given to the sign of $\frac{dF^{mU}}{dP}$ in Eq. 4.51. Since the constraint of Eq. 4.36 is not imposed explicitly, method 2U may converge to a lower dew point in the retrograde region. Consequently, in method 2U, Eqs. 4.47 and 4.48 are used initially to update P and composition, until $\frac{dF^{mU}}{dP}$ obtains the correct sign. Specific implementation details are given in section 4.4.

Method 3U

Method 3U follows the same principles as method 2U, but a different equation is used to calculate the derivative with respect to pressure and subsequently correct the values of P during the iterative procedure. Method 3U uses the function ${Q_1}^{mU}$, as presented in Eq. 4.29 and the corresponding derivative with respect to pressure is expressed by:

$$\begin{aligned}\frac{d{Q_1}^{mU}}{dP} = &\left[\sum_{i=1}^{C} W_i\left(\ln W_i + \ln \hat{\varphi}_i(\boldsymbol{W}, T, P) - \ln z_i - \ln \hat{\varphi}_i(\boldsymbol{z}, T, P)\right) + 1 - \sum_{i=1}^{C} W_i\right] \\ &+ \sum_{i=1}^{C} \Xi_i^U \left(\frac{\partial \ln \hat{\varphi}_i(\boldsymbol{W}, T, P)}{\partial P} - \frac{\partial \ln \hat{\varphi}_i(\boldsymbol{z}, T, P)}{\partial P}\right)\end{aligned} \tag{4.54}$$

and

$$\frac{dQ_1{}^{mU(k)}}{dP}\ \delta P^{(k)} = -Q_1{}^{mU(k)} \tag{4.55}$$

Similarly to method 2U, Eqs. 4.52 and 4.53 are used initially to update P and composition, until $\frac{dQ_1{}^{mU}}{dP}$ obtains the correct sign.

Scaling and Hessian Modification

The three methods (1U, 2U, 3U) that have been discussed up till now, involve a Newton step to correct the $\boldsymbol{\Xi^U}$ variables, at constant T and P. This step is a minimization of the $Q_1{}^{mU}$ function and if a number of iterations are performed without changing the value of P, it is equivalent to a stability analysis procedure. A particularly advantageous form of this step can be formulated by performing the following variable substitution:

$$\alpha_i^U = 2\sqrt{\Xi_i^U} \tag{4.56}$$

This variable substitution has been originally proposed by Michelsen [41] ($\alpha_i = 2\sqrt{W_i}$) for stability testing. It has been also shown by Nichita [54, 68, 167] that this formulation generally results in a very fast and robust method for stability calculations and in most test cases results in the best scaling when compared to other choices of independent variables. Consequently, the first iterative loop in methods 1U, 2U and 3U is always applied with the above change of variables and the respective equations are formulated as follows:

$$\bar{g}_i^U = \frac{\partial Q_1{}^{mU}}{\partial \alpha_i^U} = \sqrt{\Xi_i^U}[\ln W_i + \ln\hat{\varphi}_i(\boldsymbol{W},T,P) - \ln z_i - \ln\hat{\varphi}_i(\boldsymbol{z},T,P)] = 0;\ i = 1,2 \dots C \tag{4.57}$$

$$\bar{H}_{ij}^U = \frac{\partial^2 Q_1{}^{mU}}{\partial \alpha_i^U \partial \alpha_j^U} = \delta_{ij} + \sqrt{W_i W_j}\frac{\partial \ln\hat{\varphi}_i(\boldsymbol{W},T,P)}{\partial W_j} + \frac{\bar{g}_i^U}{\alpha_i^U}\delta_{ij};\ i,j = 1,2 \dots C \tag{4.58}$$

The last term in Eq. 4.58 does not have significant effect on the rate of convergence, when sufficiently close to the solution, since it vanishes when $\bar{g}_i^U = 0$ [57]. However, in early iterations this last term can deteriorate the conditioning of the Hessian and cause convergence problems [167]. Consequently, in all calculations presented in this work, the last term in 4.58 is neglected. Furthermore, a trust region modification is applied to the correction vector, which restricts its magnitude to a specified value as follows:

$$\left(\bar{\boldsymbol{H}}^{U(k)} + \eta_2 \boldsymbol{I}\right) \delta \boldsymbol{\alpha}^{U(k)} = -\bar{\boldsymbol{g}}^{U(k)} \tag{4.59}$$

where $\boldsymbol{I}$ is the identity matrix, as proposed by Michelsen and Mollerup [57]. This modification of the Hessian decreases the magnitude of the correction vector but also changes its initial direction (with the unmodified Hessian) bringing it closer to a steepest descent correction. Furthermore, this modification increases the eigenvalues of the Hessian and it is a way to turn an indefinite Hessian to positive definite. In the stability analysis method presented in Michelsen and Mollerup [57] positive definiteness is also added to the requirement to restrict the magnitude of the correction vector to a prescribed value. If the Hessian is indefinite, the minimum value of η_2 to turn the matrix positive definite is:

$$\eta_2 = -\lambda_{min} + \varepsilon \tag{4.60}$$

where λ_{min} is the smallest eigenvalue of the unmodified Hessian and ε is a positive number. If ε is zero, then the matrix becomes singular. If the Hessian is highly ill-conditioned (except for being indefinite), then λ_{min} is negative and significantly higher in absolute value than the other eigenvalues. Consequently, a large number needs to be added to the diagonal elements of the Hessian. Moreover, small values of ε will result in the magnitude of the correction vector being large, because the minimum eigenvalue will be close to zero (even though the Hessian is now positive definite). In this case, a large value of ε must be also used to decrease further the magnitude of the correction vector. The result is that the diagonal elements of the Hessian become very large, compared to the off-diagonal ones, and the second-order information of the Newton method is lost. Eventually, the direction of the correction vector becomes aligned with the one of the steepest descent correction which decreases severely the convergence rate.

After a large number of numerical experiments it was observed that, for the cases in which adjustment of the correction vector magnitude is required, usually 1 or 2 eigenvalues are negative and one of them is very large in absolute value compared to the others. Consequently, the requirement of a positive definite Hessian necessitates a significant modification and the convergence rate is highly decreased. However, if the magnitude of the correction step remains in some boundaries, all eigenvalues become positive after some iterations and convergence is safeguarded. To this end, diagonal modification of the Hessian is applied only to reduce the correction vector magnitude,

without requiring at the same time positive definiteness. The specific boundaries for the correction step adjustment are discussed in section 4.4.

The trust region modification of the Hessian requires finding an appropriate value of η_2 that will reduce the correction step magnitude and bring it rapidly inside the prescribed bounds, thus avoiding a large number of matrix-vector operations. Methods that calculate exactly η_2 based on prescribed limits are described in Nocedal and Wright [168] for trust region methods which can be also applied in combined trust region Newton methods. However, these methods require an additional one-dimensional Newton search to determine η_2 and a more practical approach is desired in this work. Taking into account the previous discussion, a good choice of η_2 would be a positive multiple of the largest in absolute value eigenvalue (which is also negative) of the Hessian. This strategy involves though the determination of the matrix eigenvalues which can be an expensive calculation. A simpler and more cost efficient choice is to recall that the largest eigenvalue (in absolute value) of the matrix is bounded by its Frobenius norm, which can be easily calculated by:

$$\|\bar{\boldsymbol{H}}^U\|_F = \sqrt{\sum_{i=1}^{C}\sum_{j=1}^{C}\bar{h}_{ij}^U} \tag{4.61}$$

So, instead of determining eigenvalues, a simple double summation is used and η_2 is calculated from:

$$\eta_2 = 0.5\|\bar{\boldsymbol{H}}^U\|_F \tag{4.62}$$

The value 0.5 in Eq. 4.62 was proposed in Nocedal and Wright [168].

4.3.2. Lower Dew Points

Method 1L

Method 1L is the counterpart of method 1U to calculate lower dew points, based on the variables $\Xi_i^L = W_i/P$. The calculation is performed again in two steps, the first of which is performed at constant T and P, while $\boldsymbol{\Xi^L}$ are updated with Newton's method. This step is an unconstrained minimization of ${Q_1}^{mL}$ with respect to $\boldsymbol{\Xi^L}$:

$$g_i^L = \frac{\partial {Q_1}^{mL}}{\partial \Xi_i^L} = \ln W_i + \ln\hat{\varphi}_i(\boldsymbol{W},T,P) - \ln z_i - \ln\hat{\varphi}_i(\boldsymbol{z},T,P) = 0;\ i = 1,2\ldots C \tag{4.63}$$

$$H_{ij}^{L} = \frac{\partial^2 {Q_1}^{mL}}{\partial \Xi_i^L \partial \Xi_j^L} = P\left(\frac{1}{W_j}\delta_{ij} + \frac{\partial \ln \hat{\varphi}_i(\boldsymbol{W}, T, P)}{\partial W_j}\right);\ i, j = 1,2 \dots C \tag{4.64}$$

$$\boldsymbol{\Xi}^{L(k+1)} = \boldsymbol{\Xi}^{L(k)} + \delta \boldsymbol{\Xi}^{L(k)} \tag{4.65}$$

$$\boldsymbol{H}^{L(k)} \delta \boldsymbol{\Xi}^{L(k)} = -\boldsymbol{g}^{L(k)} \tag{4.66}$$

In the second step of method 1L, the incipient phase composition and the pressure are updated by imposing the constraint expressed in Eq. 4.41:

$$P^{(k+1)} = \frac{1}{\sum_{i=1}^{C} \Xi_i^{L(k+1)}} \tag{4.67}$$

and

$$\boldsymbol{w}^{(k+1)} = \boldsymbol{\Xi}^{L(k+1)} P^{(k+1)} \tag{4.68}$$

If an initialization of pressure is given inside the metastable-unstable region, then for an incipient phase composition (different from the trivial one), Eq. 4.42 dictates that $\sum_{i=1}^{C} \Xi_i^L > 1/P$ and by applying Eq. 4.67, P is going to acquire successively lower values. By taking advantage of this property, this method will always calculate the lower dew point in a retrograde region.

Method 2L

Method 2L is the counterpart of method 2U to calculate lower dew points, while pressure is updated with Newton's method based on the following equations:

$$F^{mL} = \frac{1}{P}\left(1 - \sum_{i=1}^{C} z_i \frac{\hat{\varphi}_i(\boldsymbol{z}, T, P)}{\hat{\varphi}_i(\boldsymbol{W}, T, P)}\right) \tag{4.69}$$

$$\frac{dF^{mL}}{dP} = -\frac{1}{P^2}\left(1 - \sum_{i=1}^{C} z_i \frac{\hat{\varphi}_i(\boldsymbol{z}, T, P)}{\hat{\varphi}_i(\boldsymbol{W}, T, P)}\right) + \frac{1}{P}\sum_{i=1}^{C} z_i \frac{\hat{\varphi}_i(\boldsymbol{z}, T, P)}{\hat{\varphi}_i(\boldsymbol{W}, T, P)}\left(\frac{\partial \ln \hat{\varphi}_i(\boldsymbol{W}, T, P)}{\partial P} - \frac{\partial \ln \hat{\varphi}_i(\boldsymbol{z}, T, P)}{\partial P}\right) \tag{4.70}$$

Since the constraint of Eq. 4.41 is not imposed explicitly, special care must be given to the sign of $\frac{dF^{mL}}{dP}$ in Eq. 4.70. Similarly to method 2U, Eqs. 4.67 and 4.68 are used initially to update P and composition, until $\frac{dF^{mL}}{dP}$ obtains the correct sign.

Method 3L

Method 3L uses the function ${Q_1}^{mL}$, as presented in Eq. 4.38, in a Newton's method to sequentially correct the values of P, while the corresponding derivative with respect to pressure is expressed by:

$$\frac{d{Q_1}^{mL}}{dP} = -\frac{1}{P^2}\left[\sum_{i=1}^{C} W_i\left(\ln W_i + \ln\hat{\varphi}_i(\boldsymbol{W},T,P) - \ln z_i - \ln\hat{\varphi}_i(\boldsymbol{z},T,P)\right) + 1 - \sum_{i=1}^{C} W_i\right] + \sum_{i=1}^{C} \Xi_i^L\left(\frac{\partial\ln\hat{\varphi}_i(\boldsymbol{W},T,P)}{\partial P} - \frac{\partial\ln\hat{\varphi}_i(\boldsymbol{z},T,P)}{\partial P}\right) \quad 4.71$$

Similarly to method 2L, Eqs. 4.67 and 4.68 are used initially to update P and composition, until $\frac{d{Q_1}^{mL}}{dP}$ obtains the correct sign.

Similarly with the methods for bubble and upper dew point calculations, the first loop of methods 1L, 2L and 3L is applied with the change of variables, as described in subsection "Scaling and Hessian Modification". In this case, the variable substitution is:

$$\alpha_i^L = 2\sqrt{\Xi_i^L} \quad 4.72$$

while the equations and the Hessian matrix have exactly the same form as presented in Eqs. 4.57 - 4.58.

4.4. Implementation

In this section, the implementation details for the methods presented in section 4.3 are going to be discussed. The case of an upper dew point pressure calculation is going to be analyzed and the same principles apply for the other types of saturation point calculations. The analysis is going to be done using as base mixture a 7-component natural gas mixture (mix1) that has been studied previously [42, 62]. The constant composition VLE phase envelope for mix1 is presented in Figure 4.1. In Figure 4.2 and Figure 4.3, the flow diagrams for methods 1U and 3U are presented respectively. The following analysis is based on these two flow diagrams, while the same principles apply for the other methods as well. Corresponding flow diagrams for the other methods (saturation pressure and saturation temperature) discussed in the previous sections are included in Appendix A. The values of tunable parameters for each method are shown in

the flow diagrams that follow and those included in Appendix A. In all calculations, MPa and Kelvin units are used for pressure and temperature respectively.

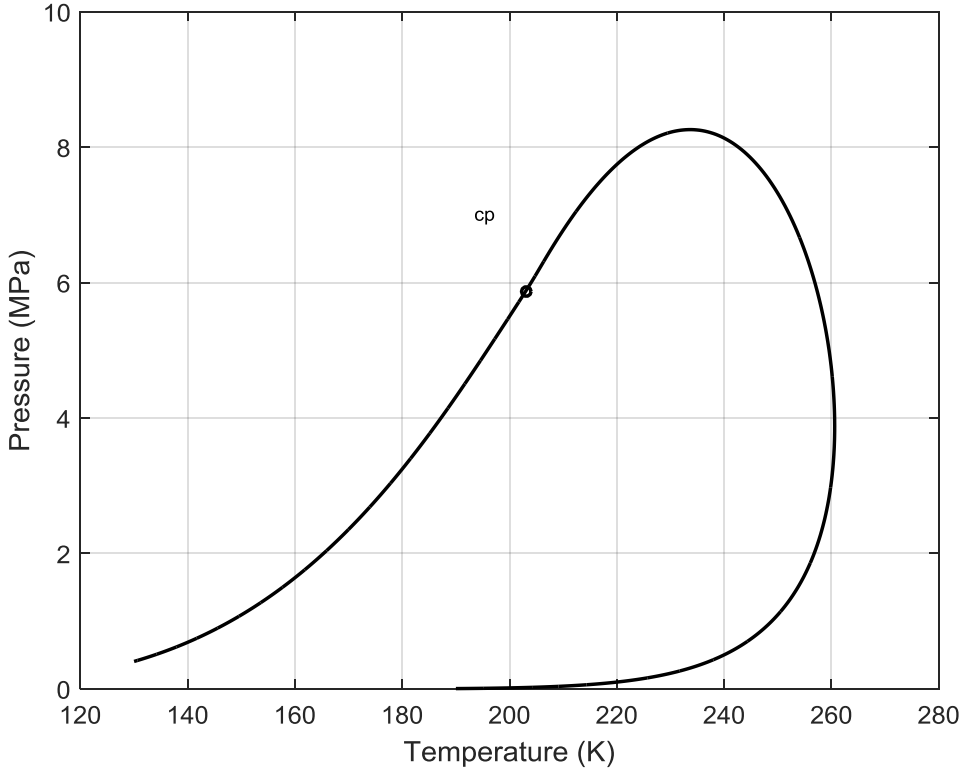

Figure 4.1: Constant composition VLE phase envelope of a 94.3% (mole) CH_4 - 2.7% C_2H_6 - 0.74% C_3H_8 - 0.49% *n*-C_4H_{10} - 0.27% *n*-C_5H_{12} - 0.10% *n*-C_6H_{14} - 1.4% N_2 mixture (mix1). Calculations were performed with SRK EoS and $k_{ij} = 0$.

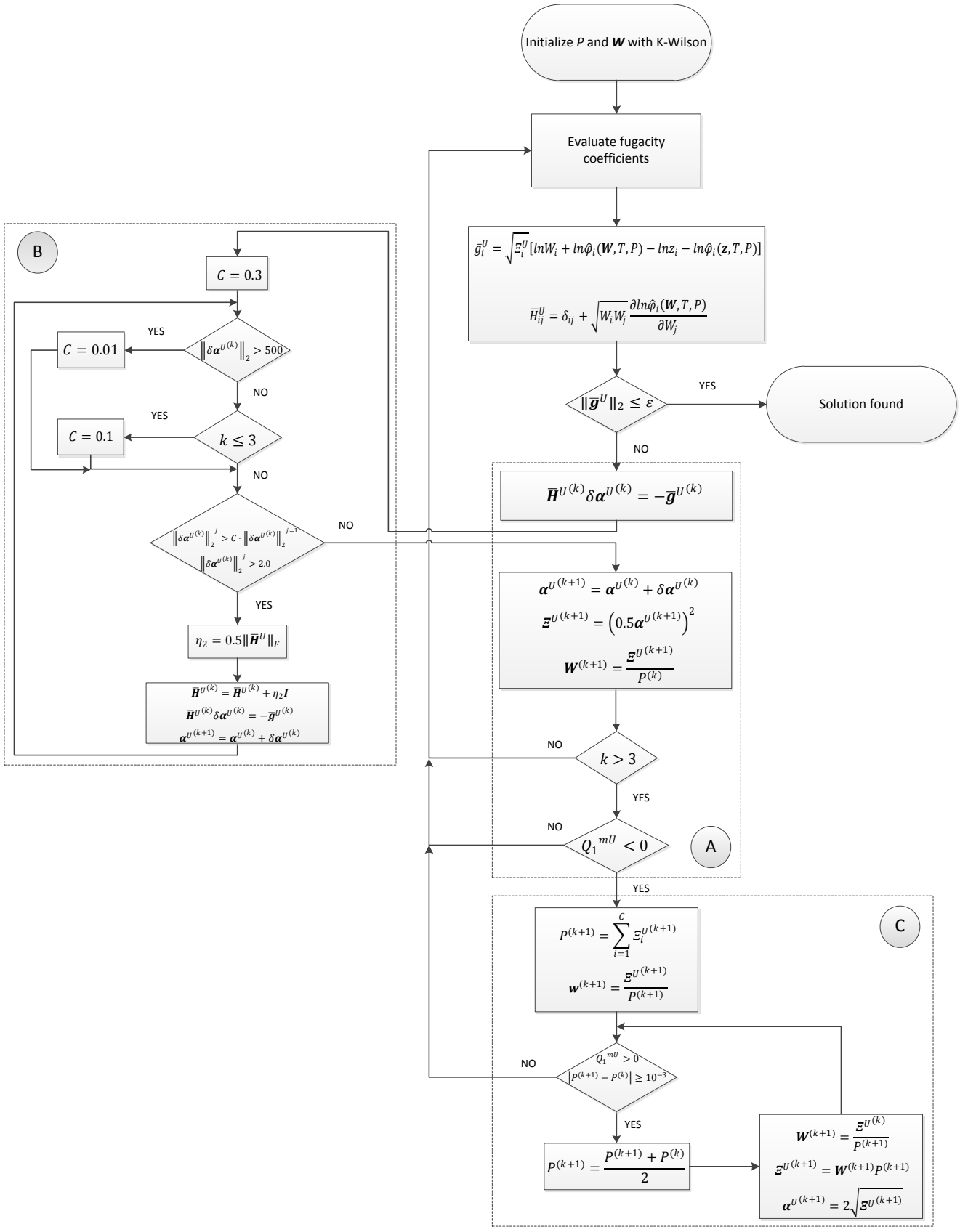

Figure 4.2: Flow diagram of the implementation algorithm for method 1U.

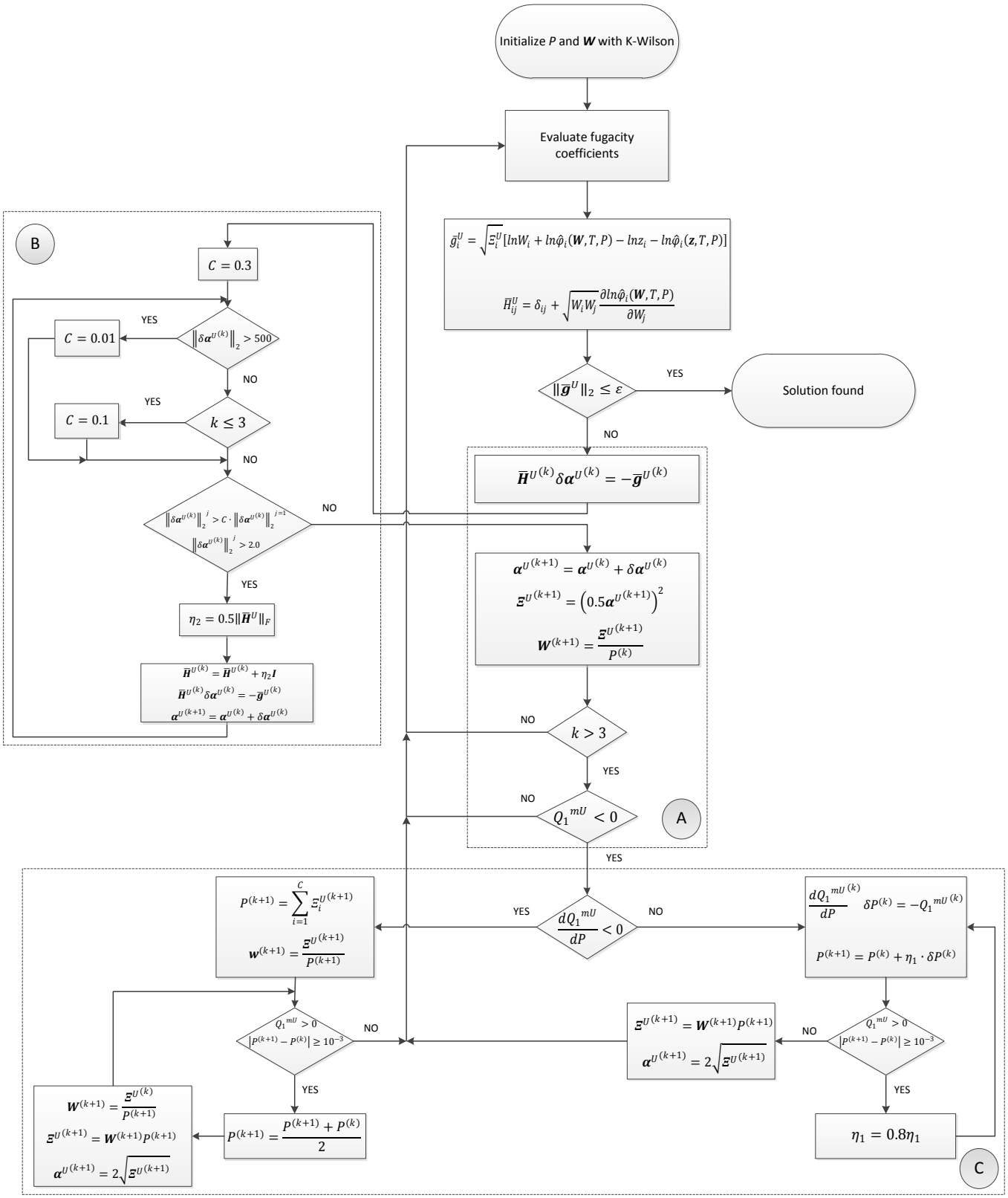

Figure 4.3: Flow diagram of the implementation algorithm for method 3U.

4.4.1. Initialization and Stability (Block A)

The initial estimates for the incipient phase composition are produced using Wilson's relation [74]:

$$K_i = \frac{P_{ci}}{P} \exp\left[5.373(1+\omega_i)\left(1-\frac{T}{T_{ci}}\right)\right] \quad 4.73$$

The initial value for pressure (or temperature for saturation temperature calculations) can be obtained by solving:

$$\sum_{i=1}^{C} z_i K_i^s(T,P) - 1 = 0 \quad 4.74$$

where $s = +1$ for bubble point calculations and $s = -1$ for dew point calculations [67].

One of the requirements that is set in this work for the initialization of the iterative procedure is that the initial conditions of temperature and pressure should be located inside the metastable or unstable region of the mixture under study, *i.e.* the region where the stability test would result in a non-trivial negative minimum (metastable, unstable) or the Hessian matrix calculated at the feed composition would have negative eigenvalues (unstable). For mix1, this region is surrounded by the phase boundary presented in Figure 4.1. Depending on the mixture under study and the temperature (for a saturation pressure calculation), the initial pressure calculated by solving Eq. 4.74 can be located outside the phase boundary. This is the usual case for high temperature dew point calculations. In this case, if a number of iterations are performed at constant T and P (essentially a stability test), $\|\boldsymbol{g}\|_2$ will eventually satisfy the convergence accuracy, but the modified TPD function (${Q_1}^{mU}$) will have a positive value. If the initial estimate lies outside the STLL, then the trivial solution is the only real solution [165].

In the proposed methodology, the target is to calculate the pressure (or temperature) at the solution by avoiding oscillations and overshooting of its final value. This is achieved by monitoring the value of ${Q_1}^{mU}$ function after every update of the $\boldsymbol{\Xi}^U$ variables and P (or T), requiring that is always negative.

A negative value of the ${Q_1}^{mU}$ function after the correction of $\boldsymbol{\Xi}^U$ ensures that the current state lies inside the phase boundary and the second loop of the iterative procedure can be applied with the strong safety that will update P towards the correct direction to the final solution. If the initial estimate for P lies inside the phase boundary, a negative value of the TPD function is expected after some updates of $\boldsymbol{\Xi}^U$. As it is shown in Figure 4.2 and Figure 4.3 (in the block abbreviated as A), the first 3 iterations

of the iterative sequence are performed at constant T and P. This is done, so that the initial composition is corrected and the value of the TPD function can be more safely calculated. For example, if the initial estimate for pressure lies outside the phase boundary, the composition generated from Wilson's relation may give a negative value of TPD instead of positive and vice versa. After a number of numerical experiments it was observed that 3 iterations are enough, so that the sign of the TPD function is safely calculated. To summarize, block A in Figure 4.2 and Figure 4.3 is the application of Newton's method at constant T and P with the use of two conditions. The first condition forces pressure to remain constant for 3 iterations, so that the ${Q_1}^{mU}$ function is safely calculated. The second condition checks if the current state lies inside the phase boundary, so that the second loop (block C) will update P monotonically towards the solution we seek. The ${Q_1}^{mU}$ function value is calculated in block A from Eq. 4.29 by using the EoS to evaluate the fugacity coefficients calculated at each $\boldsymbol{W}$, which are in turn calculated from $\boldsymbol{\Xi}^U$ and P.

In connection to the discussion in the previous paragraph, if the pressure calculated from Wilson's relation is located outside the phase boundary, then the TPD function will not acquire negative values, while $\|\boldsymbol{g}\|_2$ will satisfy the convergence criterion. In this case, the initial estimate for pressure must be increased and new K-factors must be calculated using Eq. 4.73.

4.4.2. Trust Region Modification (Block B)

Block B in Figure 4.2 and Figure 4.3 is the implementation of the trust region modification of the Hessian matrix, as proposed in this work. Block B is a sub-block inside block A. As it has already been discussed in a previous section, the Hessian matrix is modified by the addition of a positive multiple of the identity matrix. The multiple η_2 is calculated as discussed in the previous section, so that it can effectively reduce the correction step length, thus avoiding extra iterations and matrix-vector operations. Furthermore, η_2 is calculated with a low computational cost as a double summation.

The procedure for the trust region modification of the Hessian involves the prescription of specific bounds for the correction step length. These bounds however are rather empirical and they depend on the mixtures under study and on the conditions of temperature and pressure. Furthermore, depending also on the initialization, the correction step length can span large orders of magnitude. For example, a low temperature dew point calculation for a gas condensate mixture, initialized at a high

pressure with K-Wilson can result in a correction step length of an order of 10^6. Reducing this step length to an order of 10^3 for the first iterations can lead to a convergent procedure. On the other hand, even a correction step length of 10 or 50 can be significantly high and lead easily to divergence for a dew point calculation of a natural gas mixture. Consequently, just setting a low bound for the correction step length would lead to an intolerably low convergence rate for some mixtures, while a high value may cause divergence in other cases.

A more suitable approach is the reduction of the correction step length to a percent of its initial value (as calculated with the unmodified Hessian) using a factor that can be tuned accordingly. In this way, the effect of the conditions of temperature and pressure on the correction step length is taken into account and over reduction of the length of the correction vector is avoided. The value of this factor (C) is generally dependent on the initialization method, the conditions of temperature and pressure and on the mixture under study. To find a suitable value for C, an extensive number of numerical experiments were performed for upper dew point pressure calculations at different temperatures. Furthermore, the calculation at each temperature was initialized at many different pressures and the initial composition was always calculated with K-Wilson. The mixtures used for the numerical experiments included natural gas mixtures, synthetic gas condensates and an equimolar mixture of CH_4 and H_2S.

For the upper dew point pressure calculation, a value of 0.3 for C was found to be optimum for most cases examined in the numerical experiments. As shown in Figure 4.2 and Figure 4.3 two more values for C are used. A value of 0.1 is used for the first 3 iterations, so that more restricted steps are taken to correct the initial composition. Furthermore, to account for cases in which the correction vector length is really big ($\left\|\delta\boldsymbol{\alpha}^{U(k)}\right\|_2 > 500$), C is set equal to 0.01, so that $\delta\boldsymbol{\alpha}^U$ is rapidly restricted in logical bounds. Moreover, it was observed that if $\left\|\delta\boldsymbol{\alpha}^{U(k)}\right\|_2 < 2$, which can be a usual case at higher temperatures and natural gas mixtures, no modification of the Hessian is needed. These conditions are graphically described in block B of Figure 4.2 and Figure 4.3. It should be pinpointed, that the tuning of the C parameter and the exact values in the conditions described above is up to the user and the values mentioned here are not restrictive. However, these ones were found to be appropriate for a large number of mixtures at many different conditions.

Finally, it is worth mentioning that modification of the Hessian is usually needed only in the first iterations and especially when calculations are performed at challenging conditions. An example is a low temperature (320 K for example) dew point pressure calculation for a gas condensate mixture, especially when high pressure initializations are used. In these cases, the composition produced from Wilson's relation is of low quality and the composition variables ($\boldsymbol{W}$) sum highly above unity. The result is that the correction step length is really big and can easily lead to divergence of the iterative procedure in the early iterations. The procedure described above and presented in block B of Figure 4.2 and Figure 4.3 is constructed so that convergence can be safeguarded in these challenging cases. Usually, after some iterations and as the solution at the phase boundary is approached, the correction step length obtains values that guarantee convergence and no modification of the Hessian is needed.

4.4.3. Pressure Correction (Block C)

In method 1U, pressure is updated by applying Eq. 4.47 as shown in block C of Figure 4.2. This type of correction is essentially an SS update, based on the new $\boldsymbol{\Xi}^U$ values calculated at block A. After the update of P, the sign of the modified TPD function is checked again and the new value of pressure is accepted only if the ${Q_1}^{mU}$ function is negative. The correction of pressure, especially in early iterations can lead to significant extrapolations and overshooting of the value at the solution. Checking the sign of ${Q_1}^{mU}$ and requiring that is always negative is a good indication that the new pressure lies inside the phase boundary (in T, P space) and the method has not overshot the value at the solution. If the new pressure leads to a positive value of ${Q_1}^{mU}$, then a bisection scheme is used, as shown in Figure 4.2. If the bisection is applied many consecutive times, then the pressure of the previous iteration will be retrieved which will lead to a negative ${Q_1}^{mU}$.

It was observed in some cases of dew point calculations, that for certain values of pressure inside the metastable-unstable region and far away from the solution, the ${Q_1}^{mU}$ wouldn't acquire a negative value and the bisection was applied numerous times until the new pressure was practically equal to the previous one. In other words, at a certain composition and pressure during the iterative procedure, even a small change in pressure would lead to positive values of ${Q_1}^{mU}$, even though this point was inside the phase boundary. To overcome this difficulty and avoid a large number of consecutive bisections, a second condition is used in combination with the requirement of negative

${Q_1}^{mU}$, as shown in block C of Figure 4.2. That is, if the difference of the new pressure and the previous one is lower than 10^{-3} in absolute value (MPa units are used for pressure in this work), then the iterative process continues normally even if ${Q_1}^{mU}$ is positive.

It has to be noted, that if a point in temperature and pressure space lies inside the phase boundary (for example 240 K and 4 MPa in Figure 4.1), then ${Q_1}^{mU}$ must obtain a negative sign when the respective composition satisfies the equifugacity relations. However, if at a certain pressure, the respective composition calculated in the previous step (block A), is far from the one that satisfies the equifugacity criterion, then ${Q_1}^{mU}$ may have a positive sign, even at a (T, P) point inside the phase boundary. Of course, if sequential updates on the composition variables were applied, then ${Q_1}^{mU}$ would acquire the correct negative sign. This procedure however implies that a number of iterations would be wasted to find the correct composition at a pressure that may as well lie outside the phase boundary. Consequently, we chose to take more restrictive steps in pressure updates by applying bisection, if ${Q_1}^{mU}$ was found to be positive, rather than converge to full accuracy the composition at each pressure point during the total iterative procedure. In block C, the ${Q_1}^{mU}$ function value is calculated at each trial pressure by using the EoS to evaluate the fugacity coefficients and apply a successive substitution step to the composition variables using Eq. 2.2. Then, these composition variables are used to calculate the respective $\boldsymbol{\Xi}^{U}$ and with Eq. 4.29 evaluate the sign of ${Q_1}^{mU}$.

In method 3U, pressure is updated in two different ways by evaluating first the sign of the derivative of ${Q_1}^{mU}$ with respect to pressure. If $\frac{d{Q_1}^{mU}}{dP}$ is negative, then pressure is updated the same way as in method 1U. When the sign of the derivative changes to being positive, then Eqs. 4.52 and 4.55 are used to calculate the new pressure. This is a Newton's correction for pressure and results in significant acceleration of the method as compared to method 1U. If at a specific temperature two solutions for pressure exit (retrograde region), like for example at 240 K in Figure 4.1; an initialization at a low pressure inside the metastable-unstable region will probably result in $\frac{d{Q_1}^{mU}}{dP}$ being negative which will lead pressure towards the lower dew point solution. Method 3U is designed to calculate upper dew points (or bubble points) and the application of Eq. 4.47 will lead pressure towards the desired solution. As pressure changes towards higher values, the sign of $\frac{d{Q_1}^{mU}}{dP}$ will turn positive and then Newton's method can be applied with the safety that will update pressure towards the upper dew point solution. In this case, to avoid large extrapolations in pressure updates that may overshoot the solution, a

relaxation factor η_1 is used to decrease the correction δP. The relaxation factor η_1 is initially equal to 1 and if the new pressure violates the condition discussed in the previous paragraph, η_1 is successively reduced as shown in block C of Figure 4.3. The value of the reduction factor for η_1 that is shown in Figure 4.3 is based on experience and numerical experiments. This is also the case for the corresponding factor in saturation temperature calculations, presented in Appendix A.

4.5. Results and Discussion

In this section, further computational results with the methods that were discussed above are going to be presented. All the results are taken by following the implementation details as discussed in the previous section and presented in the respective flow diagrams for each method. The convergence accuracy used for all calculations was $\varepsilon = 10^{-10}$. In the top panels of Figure 4.4 - Figure 4.9 , the reduction of the natural logarithm of the error (in absolute value) with respect to specific variables is given. The error of a variable (v) in the kth iteration is defined as:

$$Error \equiv \left|\mathrm{v}^k - \mathrm{v}^\infty\right| \tag{4.75}$$

where v^∞ is the value of the variable at the solution. In all comparisons, v^∞ is the result of calculating the respective saturation point with the full Newton's method described by Eqs. 2.7 - 2.9and using accuracy $\varepsilon = 10^{-10}$.

In Figure 4.4, convergence comparison between the three methods (1U, 2U, 3U) for an upper dew point pressure calculation at T= 240 K of mix 1 is presented. The top panels show the reduction of the natural logarithm of the error with respect to pressure and with respect to the mole number of *n*-C_6H_{14} (the component with the highest molecular weight in the mixture), during the course of iterations. The middle panels show the variation of pressure with each iteration and the bottom panels show the variation of the mole number of *n*-C_6H_{14} with each iteration. All three calculations were initialized at P= 1 MPa and the composition was initialized with Wilson's relation (Eq. 4.73). The calculations were performed with the SRK [32] EoS and zero k_{ij} parameters. As shown in Figure 4.1, there are two dew point pressure solutions at T= 240 K and although the initial pressure is closer to the low pressure one, all three methods consistently determine the high pressure solution. As it is shown, the first iterations are done under constant pressure, dictated by the conditions discussed in the previous

section and shown in block A of the flow diagrams, so that corrections to the initial composition can be performed. Then, pressure is corrected by the respective equations of each method. As it is expected, methods 2U and 3U achieve convergence in a lower number of iterations as compared to method 1U, since they update pressure with Newton's method, when the derivative of the respective function obtains the correct sign. Methods 2U and 3U converge in 14 iterations. Method 1U needs 25 iterations in total to converge. It can be seen graphically, that all three methods need 10 - 12 iterations to stabilize pressure to the second decimal digit. Then, the error reduction in methods 2U and 3U is rapid, while method 1U much slower, showing the effect of the SS correction of pressure.

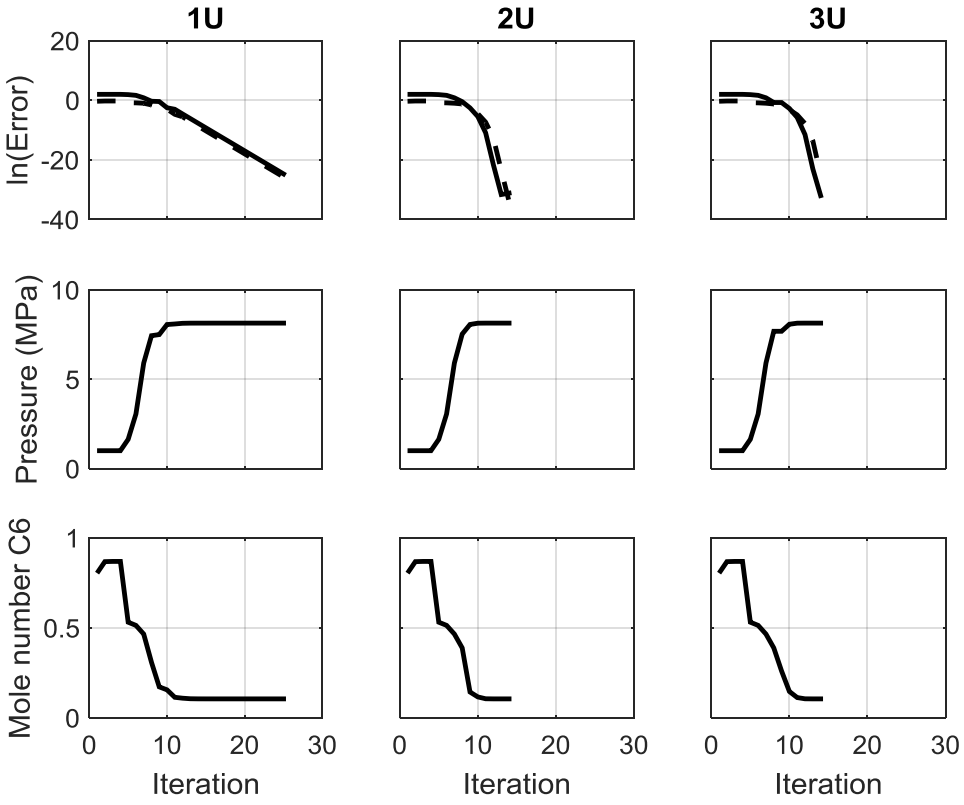

Figure 4.4: Convergence comparison of the three (1U, 2U, 3U) different methods for an upper dew point calculation at T= 240 K for mix1. Initialization was done at P= 1 MPa. The calculations were performed with SRK EoS and $k_{ij} = 0$. Top panels: Solid lines correspond to the error with respect to pressure and dashed lines correspond to the error with respect to the mole number of the component presented in the bottom panels.

Figure 4.5 presents the convergence comparison between methods 1L, 2L and 3L for the determination of the lower dew point pressure at T= 240 K of mix 1. All three calculations are initialized at P= 8 MPa which is close to the upper dew point solution in the retrograde region. In this case, a lot more iterations are needed with each method to

converge to the final solution, as compared to the previous case. This is the effect of the condition that is set in block B of the flow diagrams that sets more strict values for the length of the correction vector $\delta\boldsymbol{\alpha}^{U(k)}$ in methods 1L, 2L and 3L, as opposed to the upper saturation point methods (1U, 2U, 3U). The value in this condition is the result of a large number of numerical experiments that included many mixtures at different conditions and resulted in a robust method overall. In this case, the use of the values described in block B of methods 1U, 2U and 3U would decrease the number of iterations almost by half, but the robustness would be sacrificed for more challenging cases.

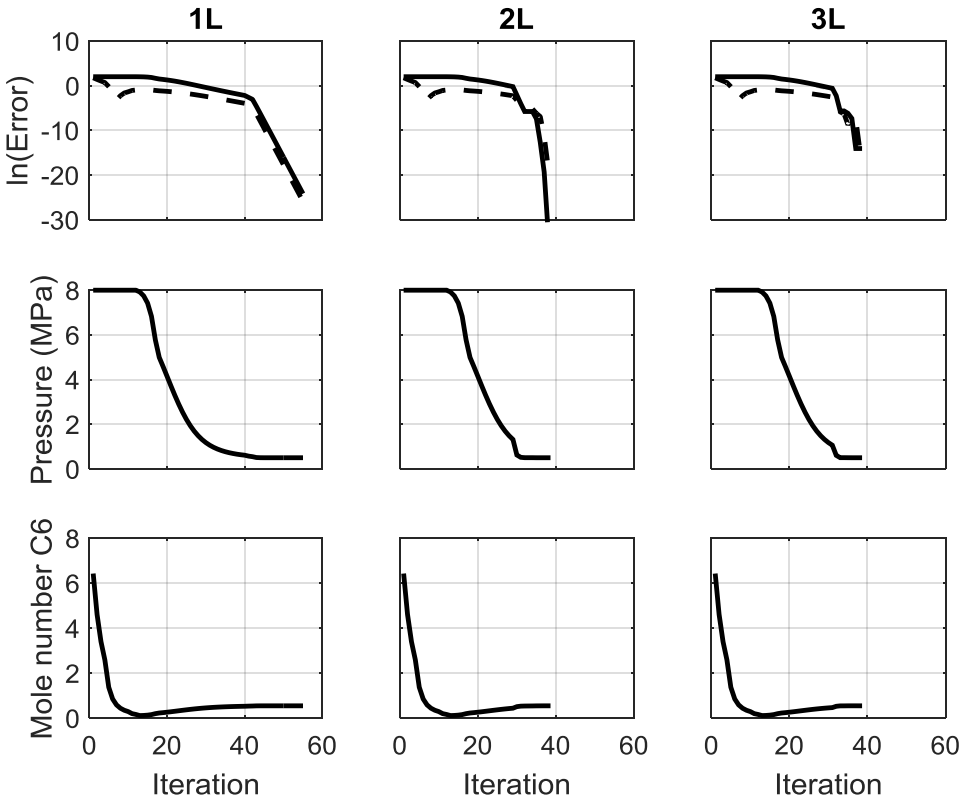

Figure 4.5: Convergence comparison of the three (1L, 2L, 3L) different methods for a lower dew point calculation at T= 240 K for mix1. Initialization was done at P= 8 MPa. The calculations were performed with SRK EoS and $k_{ij} = 0$. Top panels: Solid lines correspond to the error with respect to pressure and dashed lines correspond to the error with respect to the mole number of the component presented in the bottom panels.

In Figure 4.6, the convergence comparison for an upper dew point pressure calculation is presented. The mixture is a 6-component synthetic gas condensate (mix2) exhibiting phase equilibrium at high pressures and is comprised of 89.97% (mole) CH_4 - 3.0% *n*-C_4H_{10} - 2.97% *n*-C_8H_{18} - 2.07% *n*-$C_{12}H_{26}$ - 1.49% *n*-$C_{16}H_{34}$ - 0.5% *n*-$C_{20}H_{42}$. The calculations were performed with the SRK EoS and k_{ij} parameters taken from Novak et

al. [92] and Nikolaidis et al. [169] In this case, the dew point pressure is calculated at T= 450.05 K and the calculation is initialized at P= 1 MPa. As shown, the three methods calculate without problems the dew point, even though the initial estimate for pressure is far from the solution and the composition of this asymmetric mixture is initialized with K-Wilson. In this high pressure calculation, the significant speed up gained by using Newton's method to correct pressure in methods 2U and 3U is very prominent, compared to method 1U that uses SS. Method 3U converges in 22 iterations, while method 2U in 23. It can be seen in the middle panel of method 3U, that pressure remains constant during the iterative procedure for 6 iterations before starting to increase again. This indicates that after the update of $\boldsymbol{\Xi}^{U}$ (Figure A.1, block A), ${Q_1}^{mU}$ becomes positive and the condition that requires an always negative modified TPD function is violated. As a result, pressure remains constant and corrections are applied on the $\boldsymbol{\Xi}^{U}$ variables, until ${Q_1}^{mU}$ becomes negative again.

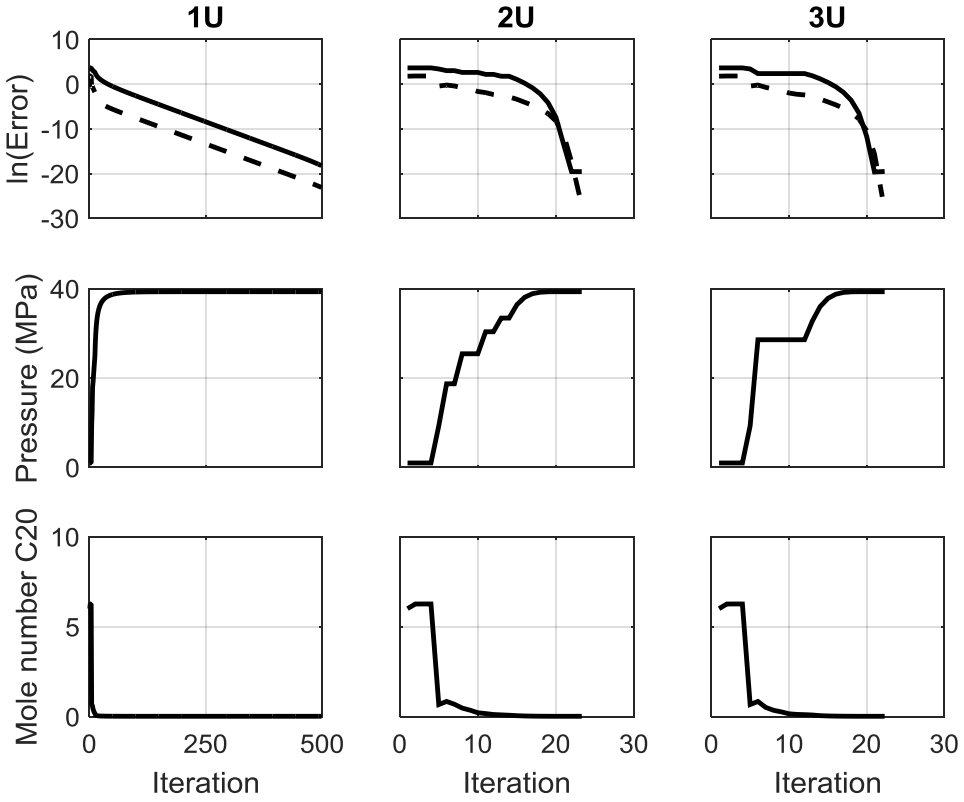

Figure 4.6: Convergence comparison of the three (1U, 2U, 3U) different methods for an upper dew point calculation at T= 450.05 K for mix2. Initialization was done at P= 1 MPa. The calculations were performed with SRK EoS and k_{ij} parameters taken from Novak et al. [92] and Nikolaidis et al. [169]. Top panels: Solid lines correspond to the error with respect to pressure and dashed lines correspond to the error with respect to the mole number of the component presented in the bottom panels.

In Figure 4.7, the three methods (1H, 2H, 3H) are compared in calculating a high temperature dew point of mix2 at P= 20 MPa. Methods 1H, 2H and 3H are designed to always calculate the high temperature saturation point of mixtures in cases where a retrograde region is present. This calculation was initialized at T= 500 K, while the saturation temperature at the solution is equal to 550.45 K. As in the previous case, the two methods (2H, 3H) that correct temperature with Newton's method are significantly faster than method 1H. The initial temperature in this case was chosen relatively close to the temperature at the solution for clarity in depicting the variation of the variables with the iterations. The three methods would converge robustly to the solution even if the calculation was initialized at a low temperature like 250 K. However, a much larger number of iterations would be needed to achieve convergence, since the initial composition generated from Wilson's relation would be significantly more erroneous.

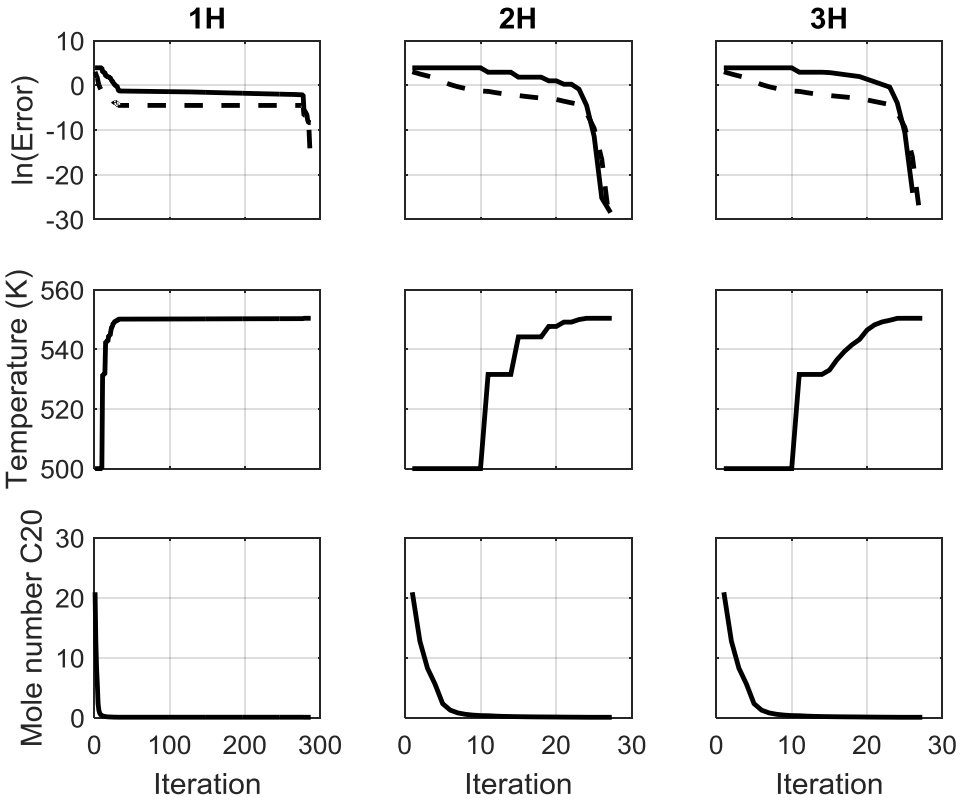

Figure 4.7: Convergence comparison of the three (1H, 2H, 3H) different methods for a high temperature dew point calculation at P= 20.0 MPa for mix2. Initialization was done at T= 500 K. The calculations were performed with SRK EoS and k_{ij} parameters taken from Novak et al. [92] and Nikolaidis et al. [169]. Top panels: Solid lines correspond to the error with respect to temperature and dashed lines correspond to the error with respect to the mole number of the component presented in the bottom panels.

The corresponding methods (1C, 2C, 3C) for low temperature saturation point calculations are compared in Figure 4.8. In this case, the low temperature dew point in the retrograde region of mix1 is calculated at P= 7 MPa. The calculation is initialized at T= 240 K and all three methods converge robustly to the correct solution. An excessive number of iterations is needed for method 1C to converge to the solution, while methods 2C and 3C converge in only 15 iterations.

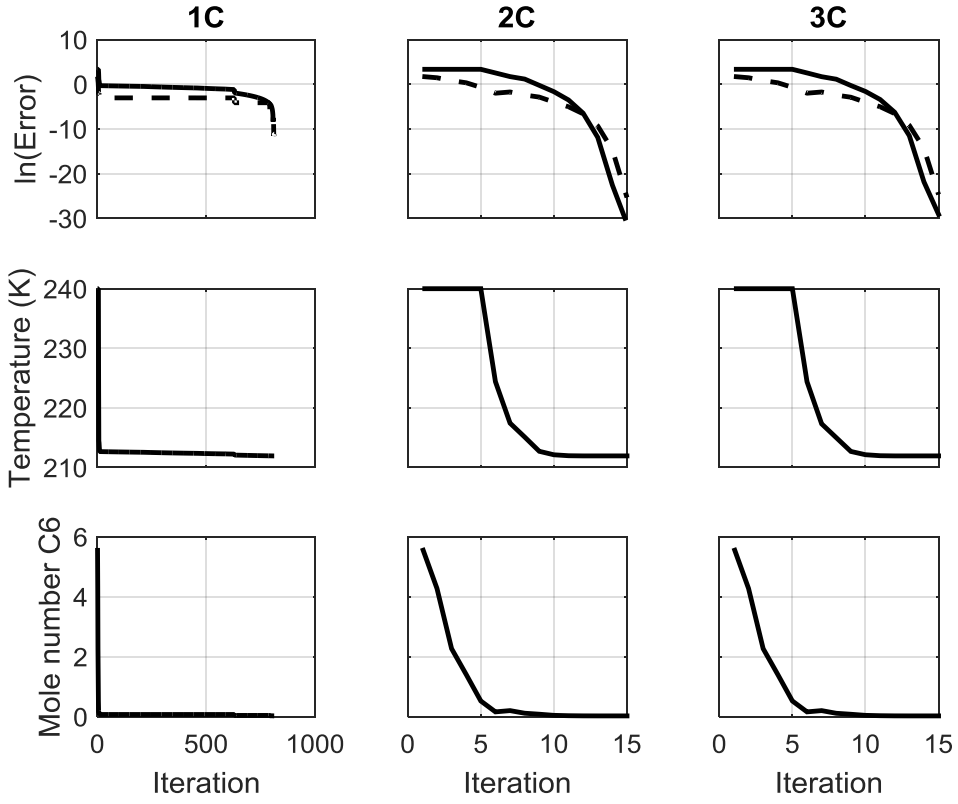

Figure 4.8: Convergence comparison of the three (1C, 2C, 3C) different methods for a low temperature dew point calculation at P= 7 MPa for mix1. Initialization was done at T= 240 K. The calculations were performed with SRK EoS and $k_{ij} = 0$. Top panels: Solid lines correspond to the error with respect to temperature and dashed lines correspond to the error with respect to the mole number of the component presented in the bottom panels.

The effect of the initialization was also investigated in various cases. In Figure 4.9, the calculation of an upper dew point pressure at T= 325 K for mix2 is presented. The method utilized is 3U and the calculation is initialized at 4 different pressures (1, 10, 20, 30 MPa). As shown, increasing the initialization pressure leads to a larger number of iterations for convergence. Method 3U requires 44 iterations to converge when pressure is initialized at 1 MPa, while 122 iterations are needed when the initial pressure is equal to 30 MPa. This trend is due to the composition generated from Wilson's relation, the error of which increases with the increase of pressure, as compared to the final solution. This

ability to handle such erroneous initializations with respect to composition is an indicator of the notable robustness that the proposed methods show.

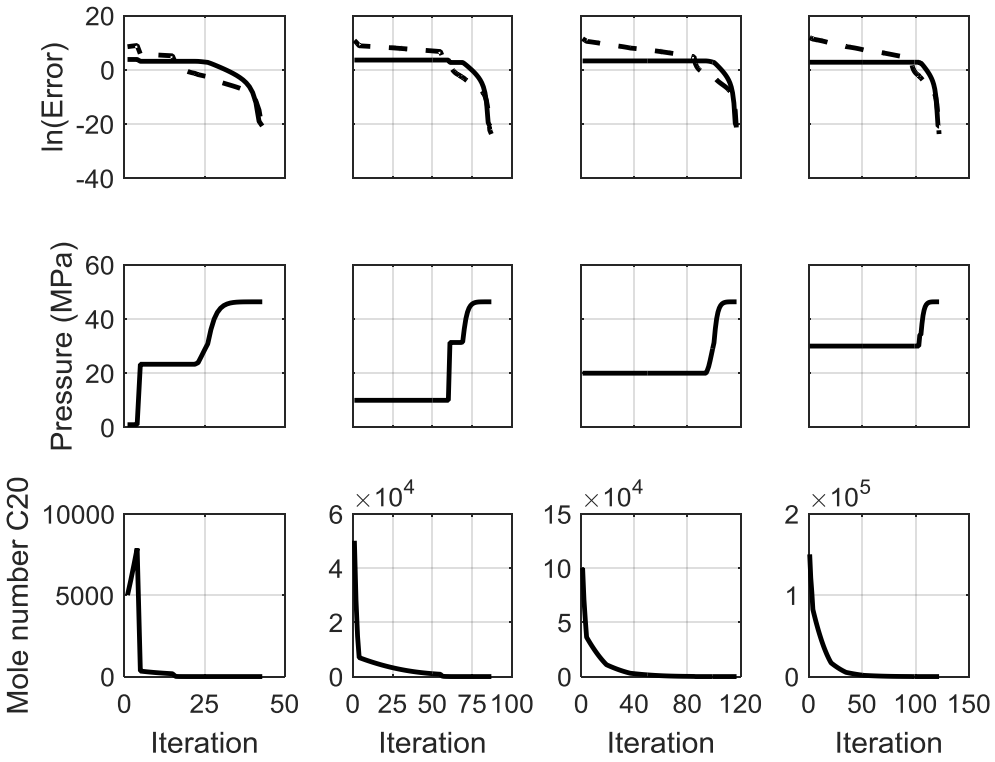

Figure 4.9: Effect of the initial pressure on the convergence behavior for an upper dew point calculation at T= 325.0 K for mix2. The calculations were performed with method 3U, SRK EoS and k_{ij} parameters taken from Novak et al.[92] and Nikolaidis et al. [169]. Top panels: Solid lines correspond to the error with respect to pressure and dashed lines correspond to the error with respect to the mole number of the component presented in the bottom panels.

Taking into account the results presented and the numerical experiments performed, it is assessed that all three methods developed for each type of saturation point calculations are robust alternatives. However, the methods that update pressure with SS, rather than Newton's method, are significantly slower and can lead to really low convergence rates and large number of iterations in certain cases. Consequently, if pressure or temperature derivatives of the fugacity coefficients are available for an EoS, the use of methods 2 (U, L, H, C) or 3 (U, L, H, C) is strongly advised. Comparing these two methods, method 3 needs a lower number of iterations for convergence in some cases but the difference in performance with method 2 is not really significant. In terms of coding, since method 3 utilizes the $Q_1{}^m$ function to assess stability but also update pressure or temperature with Newton's method, requires less programming effort than

method 2 which requires also the respective values for the F^m function. Therefore, the methods 3U, 3L, 3H and 3C are preferred.

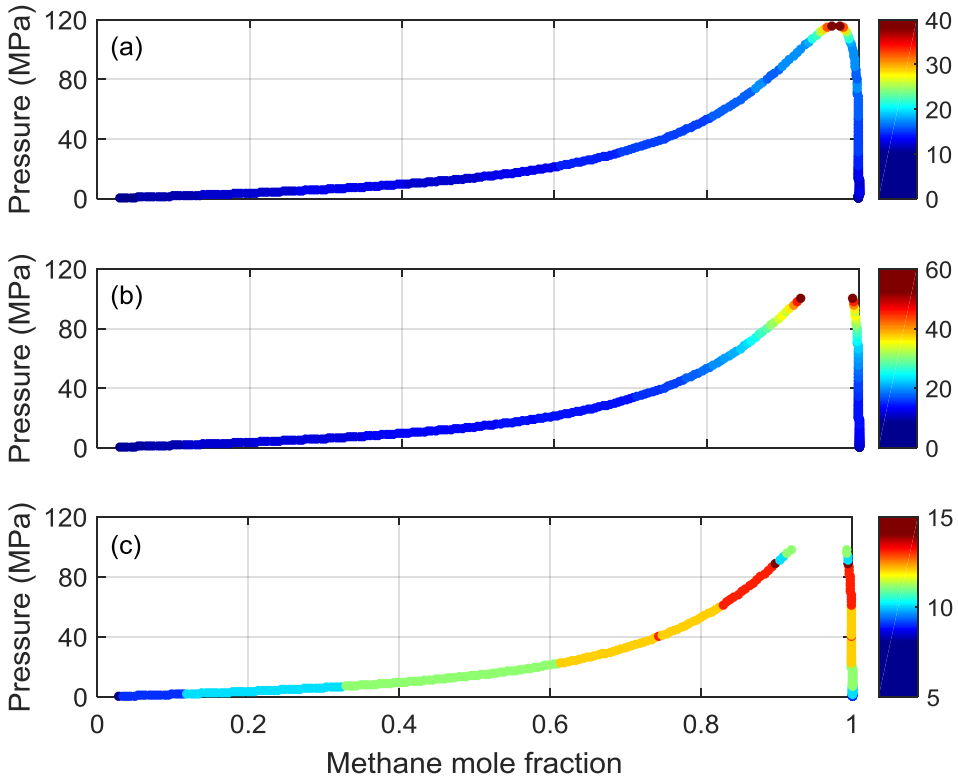

Figure 4.10: Number of iterations for bubble point pressure calculations. Pressure - composition VLE phase diagram for the CH_4 - n-$C_{36}H_{74}$ mixture (mix3) at T= 373 K. The calculations were performed with (a) method 3U, (b) partial Newton's method (Eqs. 2.1 - 2.5) and (c) full Newton's method (Eqs. 2.14 - 2.15). PC-SAFT EoS was used with $k_{ij} = 0.0282$ taken from Nikolaidis et al. [170].

The complete pressure - composition VLE phase diagram, for the binary CH_4 - n-$C_{36}H_{74}$ mixture (mix3) was calculated with method 3U (bubble point pressure calculation) at T= 373 K and different feed phase (liquid phase) compositions. The same phase diagram was calculated with the partial Newton's method (Eqs. 2.1 - 2.5) and the full Newton's method (Eqs. 2.14 - 2.15), so that the computational performance of the three methods can be compared. The higher order PC-SAFT [18] EoS was used with $k_{ij} = 0.0282$ taken from Nikolaidis et al. [170]. The number of iterations for the calculation of each bubble pressure point with the three methods is presented in Figure 4.10. The calculation of each point was initialized at P= 0.2 MPa and using Wilson's relation for the vapor phase composition. At the feed phase composition z_{CH4}= 0.904 and until close to the critical composition, the calculation was initialized at P= 6.0 MPa. As shown in Figure 4.10, method 3U is very efficient and robust in calculating all bubble

points, even very close to the critical point. As expected, the number of iterations increases with increasing pressure at the solution when the same initial point (in terms of initial pressure) is used.

For some of the compositions between z_{CH4}= 0.904 and the critical one, initialization at pressures lower than 6 MPa leads the method to calculate the trivial solution at the initial T and P state, although the state lies inside VLE phase envelope and normally a negative value of ${Q_1}^{mU}$ is expected. A tangent plane analysis must be used to explain this behavior. In Figures Figure 4.11 and Figure 4.12, the reduced Gibbs free energy of mixing and the reduced TPD function (Eq. 4.12), calculated at z_{CH4}= 0.924 and using PC-SAFT EoS with $k_{ij} = 0.0282$, are presented. The two functions are calculated at T= 373 K and four different pressures (98, 20, 6 and 0.2 MPa, respectively). Method 3U (bubble point pressure calculation) converges without problems to the final solution for z_{CH4}= 0.924 if initialized at either P= 98, 20 or 6 MPa. It can be observed in Figures Figure 4.11 and Figure 4.12, that for the three pressures which can be used as initialization and convergence is achieved, the feed phase composition (z_{CH4}= 0.924) is located at either the metastable region of the "heavier" phase (P= 98 MPa) or at the unstable region of the "heavier" (P= 20 MPa) or "lighter" (P= 6 MPa) phase. In these three cases, by initializing the incipient phase as a vapor with K-Wilson ("lighter" phase than the feed which is a liquid), a composition that leads to a negative TPD can be calculated. For the case of P= 98 MPa, the feed mixture is metastable and a negative minimum with composition richer in CH_4 than the feed exists. For the cases of P= 20 MPa and P= 6 MPa, the feed mixture is unstable and two negative minima exist, one of them leading to a composition richer in CH_4 than the feed phase composition. On the other hand, at P= 0.2 MPa (Figure 4.12, bottom panels), the feed mixture is located in the metastable region of the "lighter" phase, being essentially the vapor and no phase richer in CH_4 can be determined to lead to a negative value of the TPD function. As a result, method 3U is led to the trivial solution at the initial state. In this case, as proposed for the case in which the initial state lies on the stable region, an increase of the initialization pressure is needed and new K-factors must be calculated using Eq. 4.73.

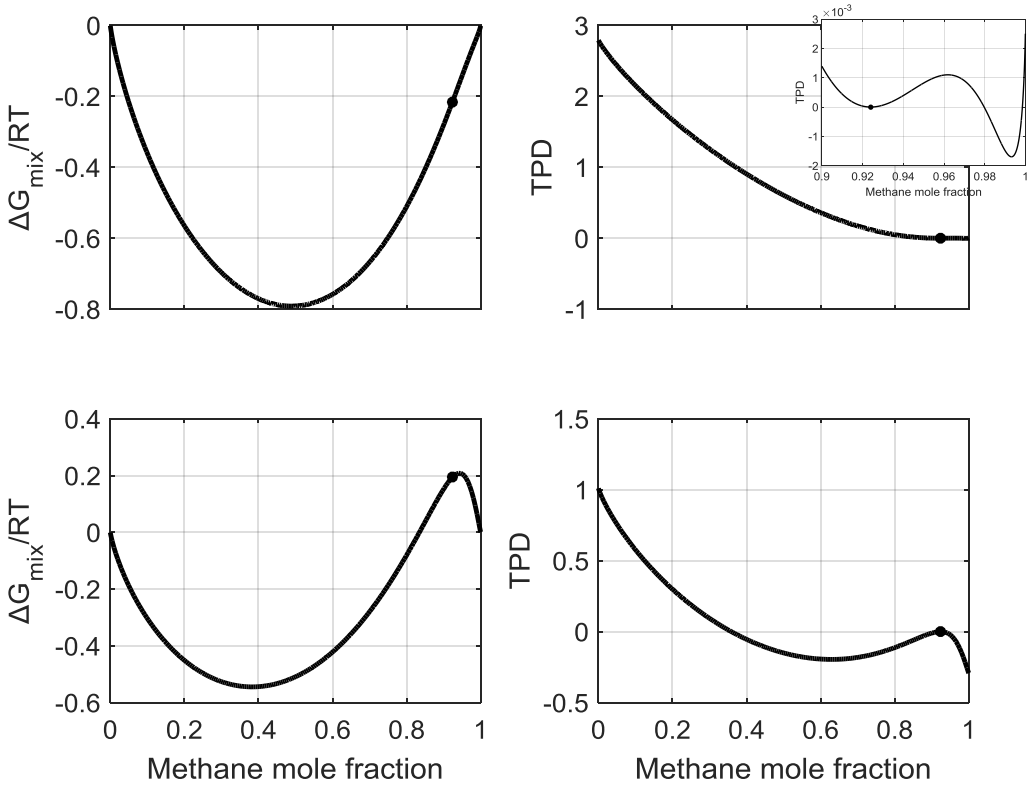

Figure 4.11: Reduced Gibbs free energy of mixing and reduced TPD function for the CH_4 - *n*-$C_{36}H_{74}$ mixture (mix3) at T= 373 K. The reduced TPD function is calculated using as feed phase composition z_{CH4}= 0.924 (mole fraction). The calculations were performed with PC-SAFT EoS and $k_{ij} = 0.0282$. Top panels refer to the results for P = 98 MPa and bottom panels refer to the results for P= 20 MPa. The black dot corresponds to the feed phase composition.

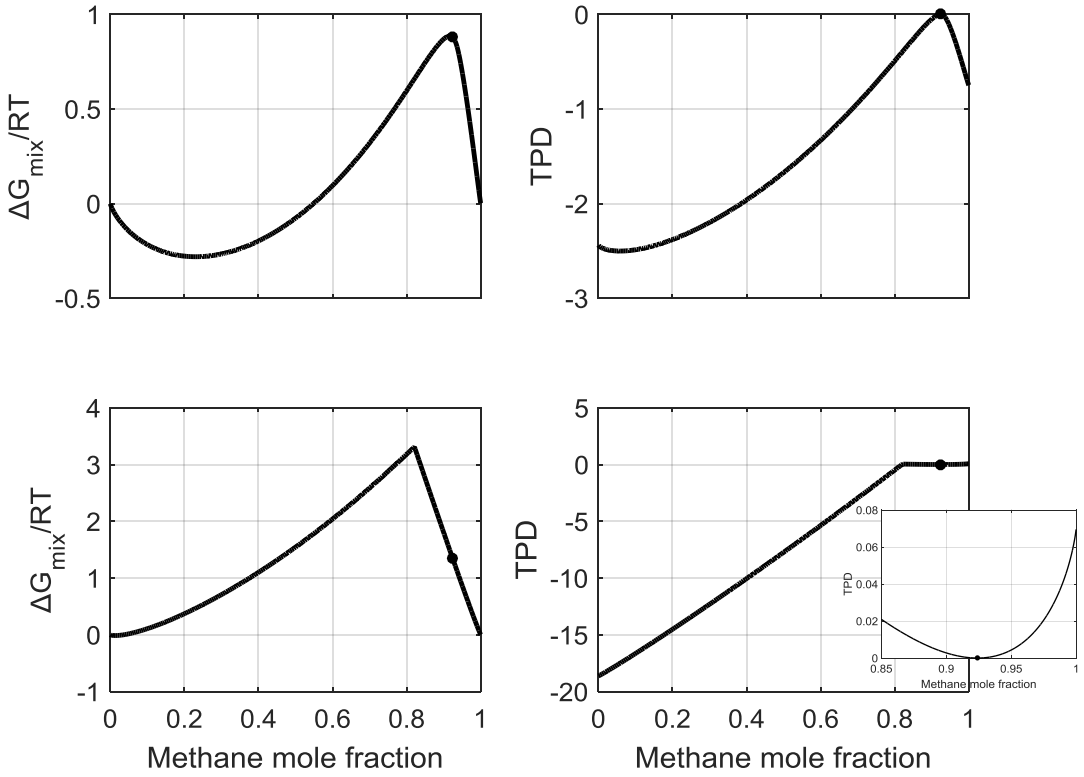

Figure 4.12: Reduced Gibbs free energy of mixing and reduced TPD function for the CH_4 - *n*-$C_{36}H_{74}$ mixture (mix3) at T= 373 K. The reduced TPD function is calculated using as feed phase composition z_{CH4}= 0.924 (mole fraction). The calculations were performed with PC-SAFT EoS and $k_{ij} = 0.0282$. Top panels refer to the results for P = 6 MPa and bottom panels refer to the results for P= 0.2 MPa. The black dot corresponds to the feed phase composition.

When compared with the partial Newton's method and the full Newton's method, method 3U is able to determine bubble points until very close to the critical point, while the two other methods fail at z_{CH4}= 0.929 and z_{CH4}= 0.924 (and for all compositions until the critical one) respectively. In the low pressure region and until around P= 40 MPa, the three methods have similar performance. At z_{CH4}= 0.744 (P= 40.22 MPa), the full Newton's method requires 13 iterations for convergence, method 3U requires 15, while the partial Newton's method requires 16. This behavior is expected, since the full Newton's method corrects all variables in a single step (derivatives of all equations with respect to all variables are used), while method 3U performs the calculation in 2 steps. The partial Newton's method has the lowest rate of convergence, since composition is updated with SS. Furthermore, the effect of the composition derivatives is becoming more pronounced with the increase of pressure. At z_{CH4}= 0.919 (P= 98.25 MPa), the full Newton's method requires 11 iterations for

convergence, while method 3U requires 17. The partial Newton's method which is the slowest requires 45 iterations.

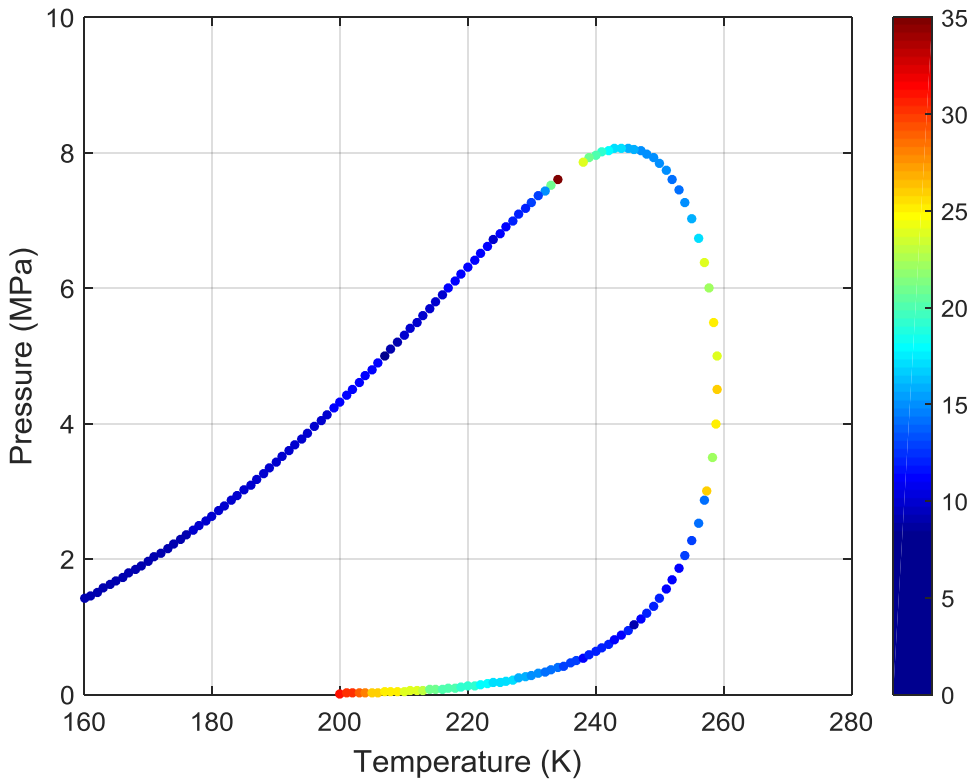

Figure 4.13: Number of iterations for bubble point pressure, dew point pressure and dew point temperature calculations. Constant composition VLE phase envelope of mix4. The calculations were performed with methods 3U, 3L, 3H, SRK EoS and $k_{ij} = 0$.

In Figure 4.13, the constant composition VLE phase envelope of a 69.114% (mole) CH_4 - 2.62% *n*-C_2H_6 - 0.423% *n*-C_3H_8 - 0.105% *i*-C_4H_{10} - 0.104% *n*-C_4H_{10} - 0.034% *i*-C_5H_{12} - 0.023% *n*-C_5H_{12} - 0.11% *n*-C_6H_{14} - 1.559% N_2 - 25.908% CO_2 synthetic natural gas mixture [171] is presented. The bubble points from T= 160 - 234 K and the upper dew points from T= 238 - 257 K were calculated with method 3U (at different specified temperatures). The lower dew points from T= 200 - 257 K were calculated with method 3L (at different specified temperatures). The dew points close to the cricondentherm were calculated with the saturation temperature method 3H from P= 3 - 6 MPa (at different specified pressures). The SRK EoS was used with zero k_{ij} parameters. The bubble point calculations from T= 160 - 206 K were initialized at P= 1 MPa, while the higher temperatures were initialized at P= 5 MPa. Initializing the calculation at lower pressures than P= 5 MPa at the higher temperature range, led to the trivial solution for the same reasons discussed in the previous paragraph. All the upper

and lower dew point pressure calculations were initialized at P= 3 MPa and the saturation temperature calculations were initialized at T= 230 K. All bubble points were calculated efficiently with maximum 9 - 12 iterations for convergence. The number of iterations is increasing close to the critical point of the mixture with the maximum iterations presented, being 35 at ~3 K before the critical temperature. Two more bubble points very close to the critical point were calculated but are not presented here for clarity reasons in the colormap of the diagram. At 236 K, the number of iterations for the bubble point pressure calculation increased to 295. A higher number of iterations was required for the upper and lower dew point pressure calculations performed, ranging from 10 to 30. The dew point temperature calculations were also very robust and required 22 to 26 iterations.

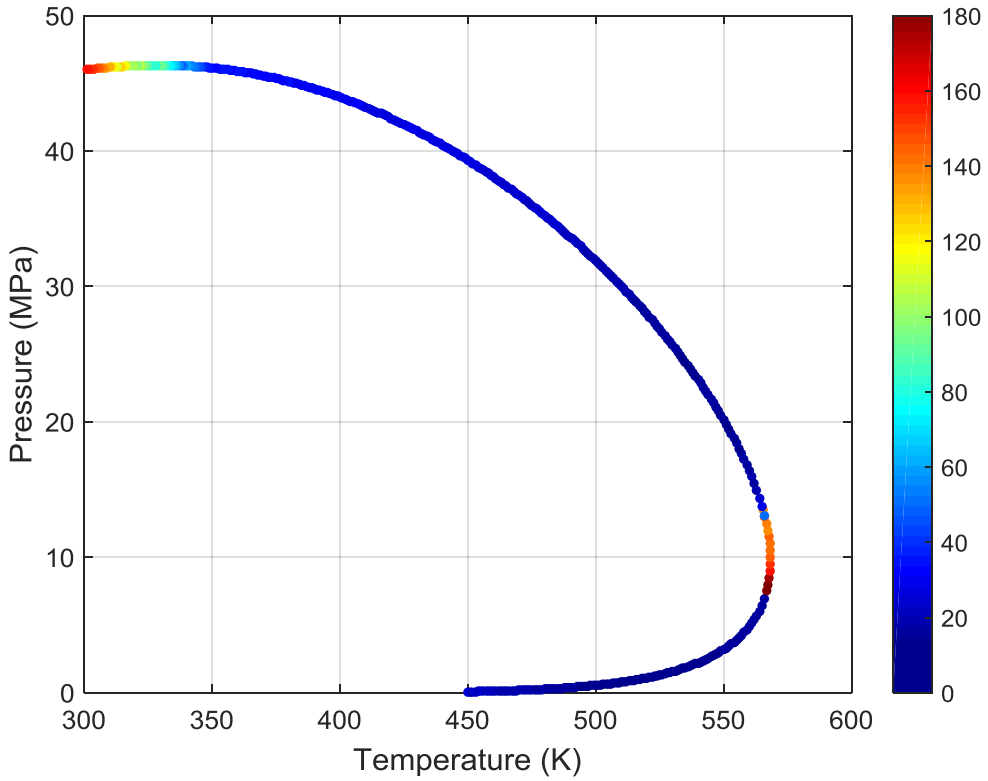

Figure 4.14: Number of iterations for dew point pressure and dew point temperature calculations. Constant composition VLE phase envelope of mix2. The calculations were performed with methods 3U, 3L, 3H, SRK EoS and k_{ij} parameters taken from Novak et al. [92] and Nikolaidis et al. [169].

The constant composition VLE phase envelope for the synthetic gas condensate mixture (mix2) was also calculated, using SRK EoS and k_{ij} parameters taken from Novak et al. [92] and Nikolaidis et al. [169]. The results are presented in Figure 4.14. It has to be noted, that all saturation points in this envelope are dew points. The methods

3U and 3L were used for the calculation of upper and lower dew points respectively, by specifying different temperatures (from lower temperatures to higher ones), while the saturation points close to the cricondentherm were calculated using method 3H at different specified pressures (7.5 - 13.5 MPa). The lower and upper dew point pressure calculations were initialized at P= 7 MPa, while the dew point temperature calculations were initialized at T= 350 K. In every case, the composition was initialized with Wilson's relation. The 3U and 3L methods were able to calculate all saturation points in a robust manner requiring 12 - 23 iterations in the temperature range 450 - 566 K. At lower temperatures, the upper dew point pressure calculation requires gradually more iterations to determine the solution. At the lowest temperature in which a dew point was calculated (T= 300 K), the iteration count is 161 with the composition being almost critical. Method 3H requires 137 - 183 iterations to converge to the solution, starting from a very low initial temperature and a considerably erroneous initial mixture composition as discussed above. If these dew point temperature calculations were initialized at T= 500 K, 25 - 30 iterations would be enough for convergence.

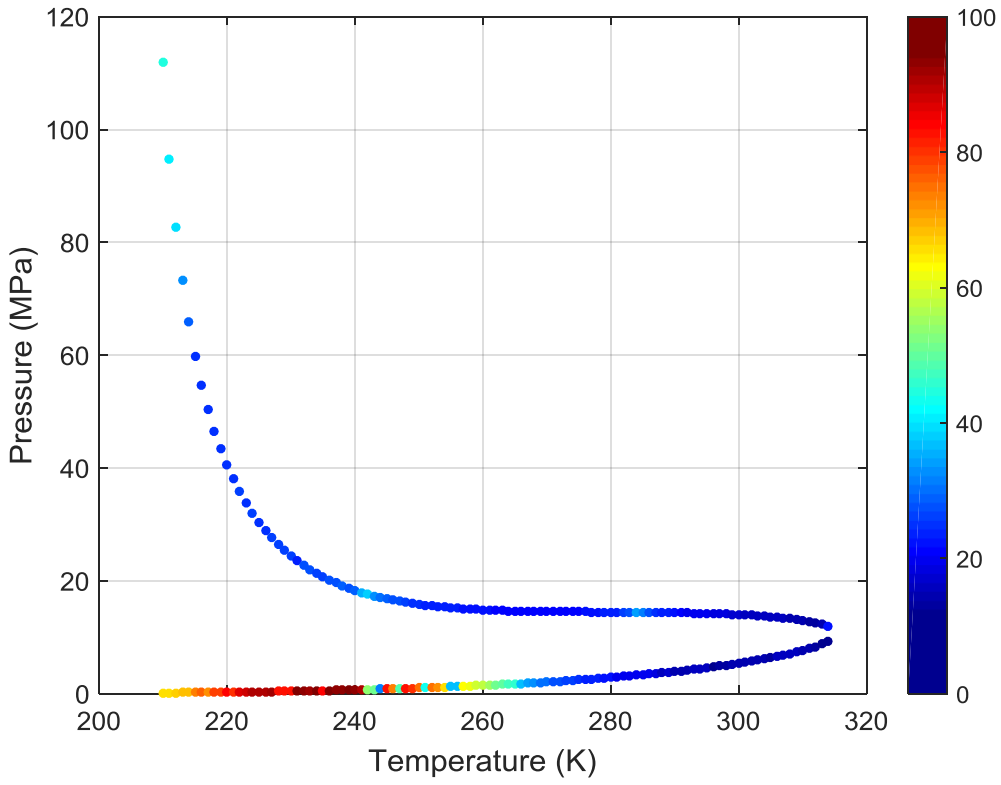

Figure 4.15: Number of iterations for bubble point pressure and dew point pressure calculations. Constant composition VLE phase envelope of a 50% (mole) CH_4 - 50% H_2S mixture (mix5). The calculations were performed with methods 3U, 3L, SRK EoS and $k_{ij} = 0.08$ taken from Nikolaidis et al. [62].

The last mixture studied is a 50% (mole) CH_4 - 50% H_2S mixture (mix5), which exhibits an open-ended constant composition phase envelope with two critical points. The phase envelope was calculated using the SRK EoS and $k_{ij} = 0.08$ taken from Nikolaidis et al. [62]. The two critical points are located at approximately T= 284.242 K, P= 14.45 MPa and T= 241.811 K, P= 17.716 MPa. In between these two critical points, the calculation is a bubble point pressure calculation and in all other conditions a dew point pressure calculation. Method 3U was used for the upper dew point pressure and bubble point pressure calculations, while method 3L was used for the lower dew point pressure calculations at different specified temperatures, starting from 210 K and until 314 K. All calculations were initialized at P= 10 MPa. As shown in Figure 4.15, all upper dew points and bubble points are calculated efficiently requiring 14 - 45 iterations, while in the proximity of the two critical points, the iteration count lies around 40 iterations. A larger number of iterations is required in the low temperature region of the lower dew point branch, which decreases gradually as the maximum dew point temperature of the mixture is approached.

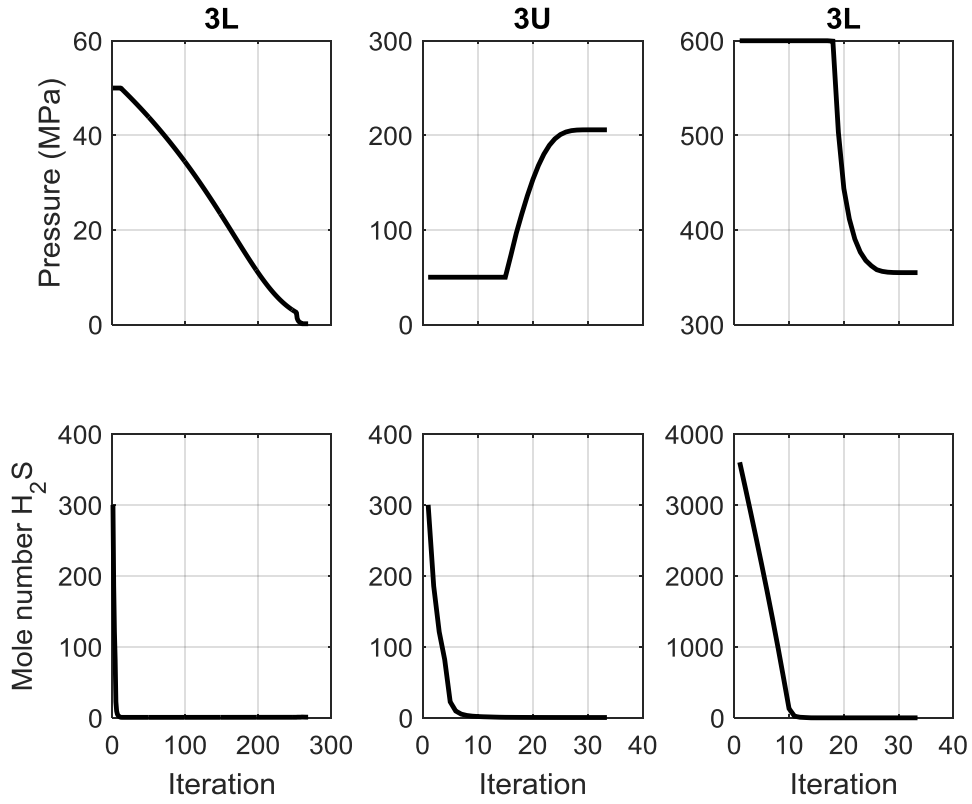

Figure 4.16: Calculation of multiple solutions (3 dew point pressure solutions) with methods 3U and 3L at T= 208 K for mix5. The calculations were performed with SRK EoS and $k_{ij} = 0.08$ taken from Nikolaidis et al. [62].

If the phase envelope of mix5 is extended to very high pressures, then the pressure - temperature line exhibits a positive slope and another retrograde is presented. Figure A.7 shows the envelope of mix5 extended to such high pressures. This behavior results to 3 dew point pressure solutions existing at a specified temperature. The proposed methods for saturation pressure calculations can be used to determine the multiple solutions, using an appropriate initialization. Figure 4.16 presents the calculation of 3 dew point pressure solutions at T= 208 K, using methods 3U and 3L. The lower and intermediate dew point pressures are determined with methods 3L and 3U respectively, with both calculations initialized at P= 50 MPa. The 3rd solution that is present because of the second retrograde, is determined with method 3L, initialized at P= 600 MPa (inside the meta-unstable region). The 3 solutions are determined efficiently and robustly, taking also into consideration that the incipient phase composition is initialized with Wilson's relation, utilized at very high pressures.

4.6. Conclusions

Efficient and robust methods were presented for the calculation of bubble and dew points of binary and multicomponent mixtures. The stability criterion of Gibbs was employed and new independent variables and iterative procedures were derived for saturation point calculations. An additional change of variables was applied to obtain optimal scaling in the minimization problem that is nested in all the methods presented. The problem of multiplicity of solutions in the retrograde region of phase diagrams was targeted by designing each method to be able to calculate only one of the possible solutions. A simple and widely used initialization method was used in all calculations presented and specific guidelines and implementation details were given for each type of calculation. The proposed methods are not dependent on the EoS employed and can be used with simple or higher order ones. The use of the derivatives of the fugacity coefficients is strongly advised, so that a high convergence rate is achieved, but it is not mandatory. The proposed methods were tested in calculating saturation points of binary and multicomponent mixtures using cubic and non-cubic EoS at challenging conditions and proved to be very efficient and robust.

5. Sequential Construction of Phase Diagrams

5.1. Introduction

In this Chapter, new algorithms for the calculation of constant composition phase envelopes of binary and multicomponent mixtures and constant temperature (P-x,y), constant pressure (T-x,y) phase diagrams of binary mixtures are presented. The proposed numerical methods are Euler-Newton predictor-corrector methods that sequentially trace the entire family of solutions (phase diagrams), corresponding to given specifications. The variable sets that were proposed in Chapter 4 for direct saturation point calculations are used here for the sequential calculation of constant composition phase envelopes of mixtures and the resulting methods are compared. The variable set that shows the best behavior in terms of efficiency, robustness and conditioning is utilized subsequently in constructing new methods that trace phase diagrams of binary mixtures at constant temperature or pressure. In this case, the methods are based on different combinations of thermodynamic equations and are evaluated with respect to the condition number of the corresponding Jacobian matrix and the ability to trace different types of phase diagrams.

5.2. Constant Composition Phase Envelopes

5.2.1. Working Variables and Equations

The combination of the equifugacity relations with Eq. 4.36 and Eq. 2.9 forms a nonlinear set of equations that defines a saturation point. Using as independent, the variables $\boldsymbol{X}^U = (\ln\Xi_1^U, \dots, \ln\Xi_C^U, \ln T, \ln P)$, the nonlinear equation set takes the form:

$$g_i^U = \ln\Xi_i^U + \ln\hat{\varphi}_i(\boldsymbol{W}, T, P) - \ln z_i - \ln\hat{\varphi}_i(\boldsymbol{z}, T, P) - \ln P = 0;\ i = 1,2 \dots C \qquad 5.1$$

$$g_{C+1}^U = \sum_{i=1}^{C} \Xi_i^U - P = 0 \qquad 5.2$$

$$g_{C+2}^U = X_S^U - S = 0 \qquad 5.3$$

Eq. 5.1 is derived from Eq. 2.14 by adding and subtracting $\ln P$. Eqs. 5.1 - 5.3 can be solved with Newton's method, with one of the independent variables being used as

specification variable. The elements of the Jacobian matrix of the equation set mentioned above are:

$$J_{ij}^{U} = \frac{\partial g_i^U}{\partial \ln \Xi_j^U} = \delta_{ij} + W_j \frac{\partial \ln \hat{\varphi}_i(\boldsymbol{W}, T, P)}{\partial W_j};\ i,j = 1,2 \dots C \tag{5.4}$$

$$J_{i,C+1}^{U} = \frac{\partial g_i^U}{\partial \ln T} = T\left(\frac{\partial \ln \hat{\varphi}_i(\boldsymbol{W}, T, P)}{\partial T} - \frac{\partial \ln \hat{\varphi}_i(\boldsymbol{z}, T, P)}{\partial T}\right);\ i = 1,2 \dots C \tag{5.5}$$

$$J_{i,C+2}^{U} = \frac{\partial g_i^U}{\partial \ln P} = P\left(\frac{\partial \ln \hat{\varphi}_i(\boldsymbol{W}, T, P)}{\partial P} - \frac{\partial \ln \hat{\varphi}_i(\boldsymbol{z}, T, P)}{\partial P}\right) - 1;\ i = 1,2 \dots C \tag{5.6}$$

$$J_{C+1,j}^{U} = \frac{\partial g_{C+1}^U}{\partial \ln \Xi_j^U} = \Xi_j^U;\ j = 1,2 \dots C \tag{5.7}$$

$$J_{C+1,C+1}^{U} = \frac{\partial g_{C+1}^U}{\partial \ln T} = 0 \tag{5.8}$$

$$J_{C+1,C+2}^{U} = \frac{\partial g_{C+1}^U}{\partial \ln P} = -P \tag{5.9}$$

$$J_{C+2,j}^{U} = \frac{\partial g_{C+2}^U}{\partial X_j^U} = \delta_{jS};\ j = 1,2 \dots C+2 \tag{5.10}$$

The Newton iteration becomes:

$$\boldsymbol{X}^{U(k+1)} = \boldsymbol{X}^{U(k)} + \delta \boldsymbol{X}^{U(k)} \tag{5.11}$$

$$\boldsymbol{J}^{U(k)} \delta \boldsymbol{X}^{U(k)} = -\boldsymbol{g}^{U(k)} \tag{5.12}$$

Mole numbers are then retrieved by:

$$\boldsymbol{W}^{(k+1)} = \frac{\boldsymbol{\Xi}^{U(k+1)}}{P^{(k+1)}} \tag{5.13}$$

The presented method, which combines the variables $\boldsymbol{X}^U$ with Eqs. 5.1 - 5.3 and the corresponding Jacobian matrix will be abbreviated as method X1U. The corresponding equations and Jacobian matrices for the other sets of variables (*i.e.* $\boldsymbol{X}^L, \boldsymbol{X}^H$ and $\boldsymbol{X}^C$) are presented in Appendix B and are abbreviated as methods X1L, X1H and X1C respectively.

5.2.2. Initialization

The construction of the constant composition phase envelope is initiated by calculating first a saturation point (bubble or dew point) at a specified temperature or pressure in which convergence is easily achieved. Usually this corresponds to a low pressure equilibrium point, since high pressure calculations are more prone to the trivial solution or divergence of the iterative procedure. The initial estimates for the incipient phase composition are produced using Eq. 4.73.

The first saturation point can be determined by solving Eqs. 5.1 - 5.3 directly (if $\boldsymbol{\Xi}^U$ variables are used; else the respective counterparts for the other variable sets are used), using the initial estimates from Eqs. 4.73 and 4.74. Another approach could be the use of a method less sensitive to the initial estimates for the first iterations (such as the ones presented in Chapter 4) and then use of the full set of equations for final convergence. In the test cases that follow, the first saturation point is always calculated using the full Newton's method.

5.2.3. Linear Extrapolation

As proposed by Michelsen [61], linear extrapolation (Euler predictor) is used to provide accurate initial estimates for a subsequent equilibrium point along the phase boundary, using information from the previously calculated one. Then Newton's method (Newton corrector) is used to solve the nonlinear system of equations and in this stepwise fashion the phase envelope is traced. The continuation method is formed by combining Eqs. 5.1 - 5.3 (or the equations corresponding to variable sets other than $\boldsymbol{X}^U$) for the determination of each equilibrium point and Eqs. 2.12 and 2.13 for calculating the initial estimates. $\frac{\partial \boldsymbol{g}}{\partial \boldsymbol{X}}$ in Eq. 2.12 is the Jacobian matrix of each equation set, calculated at the solution. If an LU decomposition is used for solving the linear system involved in Newton's method during the iterations, only a back substitution is needed to determine $\frac{\partial \boldsymbol{X}}{\partial S}$ from Eq. 2.12. Michelsen [61] proposed also the use of cubic polynomials for extrapolations when at least two equilibrium points along the envelope are calculated. In this work, only linear extrapolations are performed.

The specification variable at each point is automatically selected as the one having the numerically largest value of $\frac{\partial \boldsymbol{X}}{\partial S}$. In this way, very large values of $\frac{\partial \boldsymbol{X}}{\partial S}$, which would render extrapolations inaccurate and inapplicable at turning points are avoided, while all the elements of the sensitivity vector are limited in magnitude to about 1.

Variable step lengths are used based on prescribed number of iterations for convergence. Bigger steps can be taken if a small number of iterations is needed for convergence, while the step size is reduced if the iterations exceed the predetermined limit. An increased iteration count can be due to low quality initial estimates or due to inherently difficult conditions, such as calculations in the vicinity of critical points. In this work, tracing of the phase envelope is tuned, so that convergence is achieved in 2 - 4 iterations for each equilibrium point, using as convergence criterion $\|\boldsymbol{g}\|_2 \leq 10^{-10}$.

5.2.4. Temperature and Pressure Maxima

Michelsen [60] has shown that the slope of the phase envelope of a mixture in the T, P plane can be calculated exactly, using only temperature and pressure derivatives of the modified TPD function. Applying the variables and the respective TPD functions of this work, the slope of the phase boundary can be calculated as:

$$\frac{dP}{dT} = -\frac{\left(\frac{\partial {Q_1}^{mU}}{\partial T}\right)_P}{\left(\frac{\partial {Q_1}^{mU}}{\partial P}\right)_T} \tag{5.14}$$

Eq. 5.14 can be used to provide the necessary relations for the determination of the temperature and pressure maxima of a phase boundary. At the pressure maximum (cricondenbar), $\frac{dP}{dT} = 0$ which leads to:

$$\left(\frac{\partial {Q_1}^{mU}}{\partial T}\right)_P = 0 \tag{5.15}$$

while at the temperature maximum (cricondentherm), $\frac{dT}{dP} = 0$ which leads to:

$$\left(\frac{\partial {Q_1}^{mU}}{\partial P}\right)_T = 0 \tag{5.16}$$

where

$$\left(\frac{\partial {Q_1}^{mU}}{\partial T}\right)_P = \sum_{i=1}^{C} \Xi_i^U \left(\frac{\partial \ln\hat{\varphi}_i(\boldsymbol{W},T,P)}{\partial T} - \frac{\partial \ln\hat{\varphi}_i(\boldsymbol{z},T,P)}{\partial T}\right) \tag{5.17}$$

and

$$\left(\frac{\partial {Q_1}^{mU}}{\partial P}\right)_T = \sum_{i=1}^{C} W_i\left(\ln W_i + \ln\hat{\varphi}_i(\boldsymbol{W},T,P) - \ln z_i - \ln\hat{\varphi}_i(\boldsymbol{z},T,P)\right) + 1 - \sum_{i=1}^{C} W_i + \sum_{i=1}^{C} \Xi_i^U \left(\frac{\partial \ln\hat{\varphi}_i(\boldsymbol{W},T,P)}{\partial P} - \frac{\partial \ln\hat{\varphi}_i(\boldsymbol{z},T,P)}{\partial P}\right) \quad 5.18$$

The corresponding relations for the other sets of variables are presented in Appendix B.

The temperature and pressure maxima of the constant composition phase envelope are of considerable interest for industrial applications, such as the transportation of mixtures with pipelines. These two points can be indirectly determined by tracing the entire phase boundary and simultaneously monitoring the signs of the functions in Eqs. 5.17 and 5.18. When there is a sign change, the corresponding extremum can be approximated by interpolation. A direct calculation of these extrema is also possible by replacing Eq. 5.3 (specification equation) with Eq. 5.17 or 5.18 in the system of nonlinear equations (the same independent variables are used) and solution with Newton's method. In this case, additional partial derivatives are needed for the last row of the Jacobian matrix. A two-step formulation, in which the $\boldsymbol{\Xi}$ variables are corrected first and T, P values are updated in a second iterative loop is also possible.

5.2.5. Results and Discussion

The proposed methods are used in this section for the sequential calculation of constant composition phase envelopes of various binary and multicomponent mixtures that exhibit different types of phase behavior. The comparison between the methods is based on the condition number of the corresponding Jacobian matrix at the solution. Other properties like iteration count for convergence and convergence radius cannot be systematically compared, since the calculations are performed in a sequential manner and the number of iterations can be tuned by the step selection. Furthermore, keeping a low iteration count by choosing the step length accordingly prevents also breakdown from poor initial estimates.

Conditioning is a property of the numerical problem at hand. A problem is well conditioned if its solution is not affected greatly by small perturbations in the data that define it [168]. If small changes in the data impose significant changes to the results, then the problem is ill conditioned. The conditioning of a problem is quantified by the use of condition numbers. The condition number is most commonly associated with the solution of a linear system of equations of the form $\boldsymbol{Ax} = \boldsymbol{b}$ and it is a measure of how

close the numerical solution approximates the exact solution after solving the system. One of the most widely used condition numbers is:

$$\kappa_2(\boldsymbol{A}) = \|\boldsymbol{A}\|_2 \|\boldsymbol{A}^{-1}\|_2 \tag{5.19}$$

and

$$\|\boldsymbol{A}\|_2 = \sqrt{\rho(\boldsymbol{A}^T\boldsymbol{A})} \tag{5.20}$$

where $\rho(\boldsymbol{A}) = max_{1\le i\le n}|\lambda_i|$ is the spectral radius of matrix $\boldsymbol{A}$ with dimensions *(n × n)* and $\lambda_i(\boldsymbol{A})$ is an eigenvalue of the matrix (also denoted as just λ_i).

$$\|\boldsymbol{A}^{-1}\|_2 = \sqrt{\rho(\boldsymbol{A}^{-1}\boldsymbol{A}^{-T})} = \frac{1}{\sqrt{\lambda_{min}(\boldsymbol{A}^T\boldsymbol{A})}} \tag{5.21}$$

From Eqs. 5.19 - 5.21 we get:

$$\kappa_2(\boldsymbol{A}) = \sqrt{\frac{\lambda_{max}(\boldsymbol{A}^T\boldsymbol{A})}{\lambda_{min}(\boldsymbol{A}^T\boldsymbol{A})}} \tag{5.22}$$

For a symmetric matrix Eq. 5.22 becomes:

$$\kappa_2(\boldsymbol{A}) = \frac{\max_i|\lambda_i|}{\min_i|\lambda_i|} \tag{5.23}$$

If the inputs $\boldsymbol{A}$ and $\boldsymbol{b}$ of the original system are perturbed and become $\widetilde{\boldsymbol{A}}$, $\widetilde{\boldsymbol{b}}$ and $\widetilde{\boldsymbol{x}}$ is the solution of the perturbed system, it can be shown that [168]:

$$\frac{\|\boldsymbol{x}-\widetilde{\boldsymbol{x}}\|_2}{\|\boldsymbol{x}\|_2} \approx \kappa_2(\boldsymbol{A})\left[\frac{\|\boldsymbol{A}-\widetilde{\boldsymbol{A}}\|_2}{\|\boldsymbol{A}\|_2} + \frac{\|\boldsymbol{b}-\widetilde{\boldsymbol{b}}\|_2}{\|\boldsymbol{b}\|_2}\right] \tag{5.24}$$

Hence, a large value of $\kappa_2(\boldsymbol{A})$ indicates that the problem is ill conditioned, since small perturbations in the input data alter the solution significantly, while a modest value indicates well conditioning. It can be also shown that $\kappa_2(\boldsymbol{A})$ is always ≥ 1, while a problem is optimally conditioned when the equality holds (*i.e.* $\kappa_2(\boldsymbol{A}) = 1$). Truncation and round off errors during computer operations are usual perturbations in the data of the problem, which are transferred to the solution and are amplified by a large condition number. If we set the error vector $\boldsymbol{e} = \boldsymbol{x} - \boldsymbol{x}^{\infty}$, where $\boldsymbol{x}^{\infty}$ is the exact solution and $\tilde{\boldsymbol{r}} = \widetilde{\boldsymbol{A}}\boldsymbol{x} - \widetilde{\boldsymbol{b}}$ the residual for some value of $\boldsymbol{x}$ of the numerical problem, then for an ill conditioned problem, a low value of the residual doesn't necessarily imply a low value for the error. Furthermore, if an iterative method for the solution of the linear system is used, a large condition number will decrease significantly the convergence rate and

preconditioning must be used. However, the vast majority of the published methods dealing with phase equilibrium calculations, solve the linear systems involved in the nonlinear problem with direct methods, such as LU or Cholesky decomposition.

The discussion above isn't limited to linear systems of equations, but also applies to nonlinear, optimization, differential equations problems etc. In this case, the solution procedure is iterative and one or more linear systems are solved at every iteration. In phase equilibrium calculations (nonlinear problem), a linear system of the form presented in Eq. 5.12 is solved several times until the solution is found. If the Jacobian matrix is ill conditioned, truncation and round off errors that occur during the factorization or even in the calculation of Jacobian itself will result in the calculation of a correction step that is different from the exact one. This usually results in an increased number of iterations for convergence and many times in divergence of the iterative procedure as in the case of close proximity to a critical point, where the Jacobian is almost singular and the condition number obtains extremely high values. The condition number is affected the numerical formulation of the physical problem (*i.e.* the choice of independent variables and thermodynamic equations). Consequently, the aforementioned methods present different conditioning and this is the basis for the following discussion.

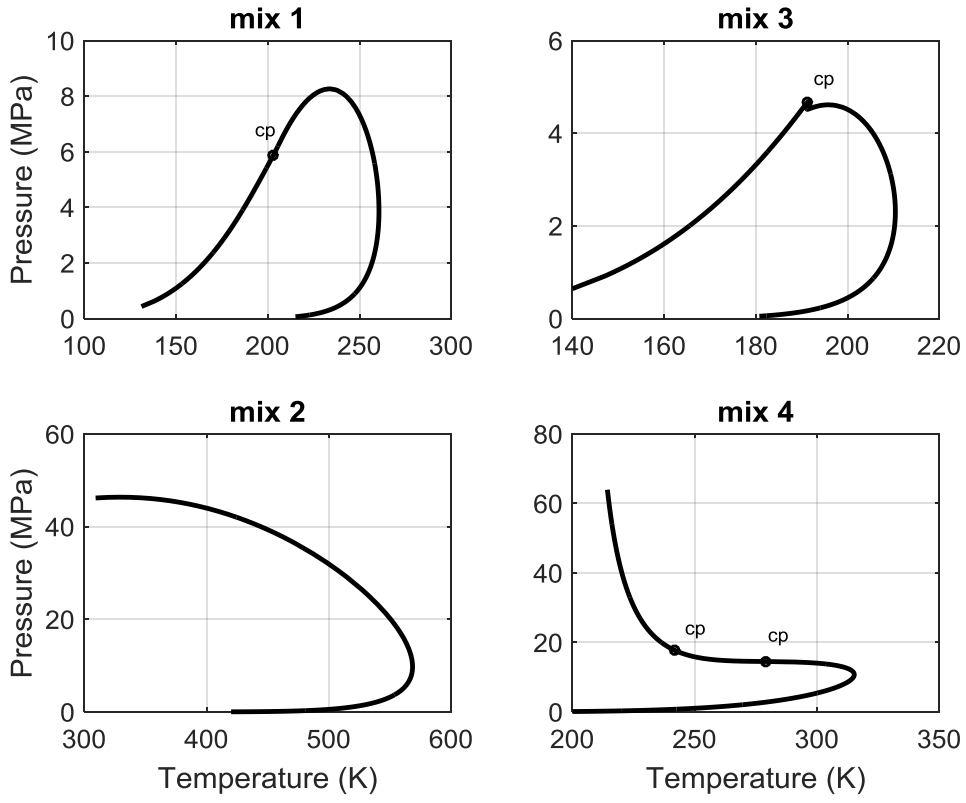

Figure 5.1: Constant composition VLE phase envelopes of mix1, mix2, mix3 and mix4, calculated with method X1U and SRK EoS.

In Figure 5.1, the constant composition phase envelopes of 4 different mixtures are presented. The calculations were performed with method X1U. Mix 1 is the 7-component natural gas mixture comprised of 94.3% (mole) CH_4 - 2.7% C_2H_6 - 0.74% C_3H_8 - 0.49% *n*-C_4H_{10} - 0.27% *n*-C_5H_{12} - 0.10% *n*-C_6H_{14} - 1.4% N_2 [42] that was presented in Chapter 4. Mix 2 is a 6-component synthetic gas condensate exhibiting phase equilibrium at high pressures and is comprised of 89.97% (mole) CH_4 - 3.0% *n*-C_4H_{10} - 2.97% *n*-C_8H_{18} - 2.07% *n*-$C_{12}H_{26}$ - 1.49% *n*-$C_{16}H_{34}$ - 0.5% *n*-$C_{20}H_{42}$. Mix 3 is a 99.95% (mole) CH_4 - 0.05% *n*-C_5H_{12} binary mixture that exhibits double retrograde behavior and mix 4 is 50% (mole) CH_4 - 50% H_2S mixture, which exhibits an open-ended constant composition phase envelope with two critical points. All calculations in Figure 5.1 were performed with SRK EoS and zero k_{ij} parameters for mix 1 and mix 3. For mix 2, k_{ij} parameters were taken from Novak et al. [92] and Nikolaidis et al. [169]. For mix 4 one $k_{ij} = 0.08$ was used.

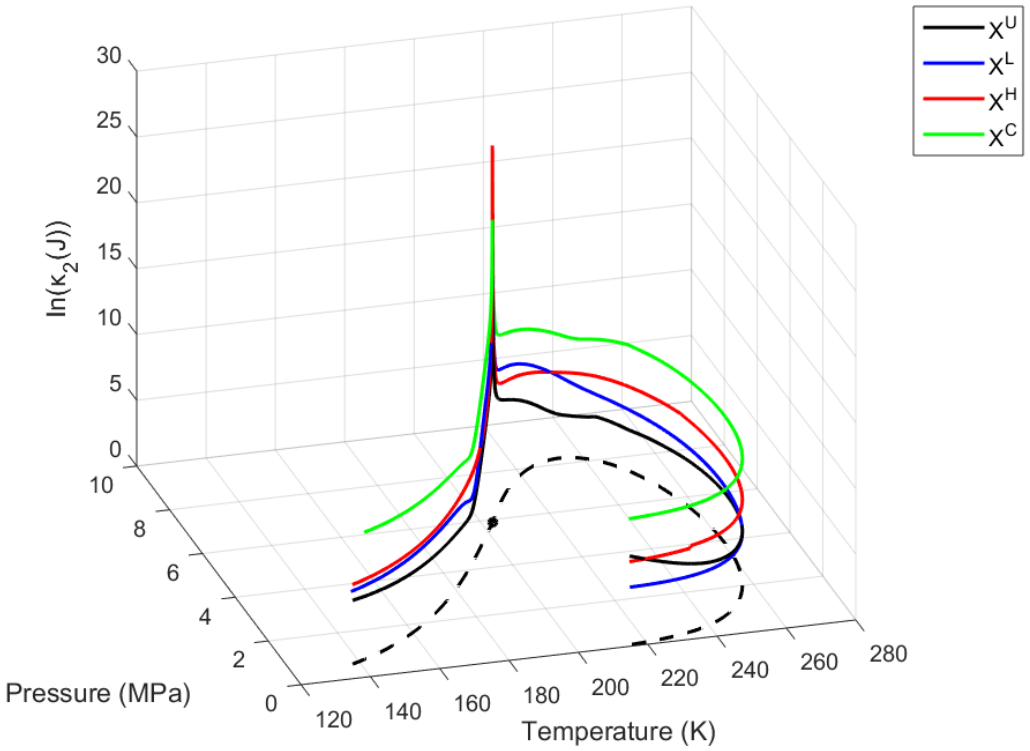

Figure 5.2: Condition number of the Jacobian matrix for each method, calculated at the solution, along the VLE phase envelope of mix 1. The calculations were performed with SRK EoS and $k_{ij} = 0$. The dashed line corresponds to the pressure - temperature projection of the VLE envelope and the open circle corresponds to the critical point.

In Figure 5.2, the condition number of the Jacobian matrix of each method (X1U, X1L, X1H, X1C) - calculated at the solution - along the phase envelope of mix 1 is presented. The calculation of the VLE envelope with each method was initiated from a low temperature - low pressure bubble point and was carried out sequentially as described in the previous section. As shown in Figure 5.2, method X1U has the lowest $\kappa_2(\boldsymbol{J})$ along the envelope as compared to the other methods, except for the low pressure region in the dew line in which method X1L shows the best condition number. The highest $\kappa_2(\boldsymbol{J})$ is shown by method X1C systematically. As expected, the condition number of all methods increases abruptly when the critical point is approached and exactly on the critical point becomes infinite, since the Jacobian matrix is singular. The location of the critical point is at T= 203.05 K, P= 5.88 MPa approximately. All methods are able to trace the phase envelope and pass the critical point without problems, while the iteration count at each point is tuned by the step length selection in the linear extrapolation part. On passage of the critical point, the incipient phase becomes the heavier one and the feed becomes the lighter phase, since the calculation was initiated from a bubble point.

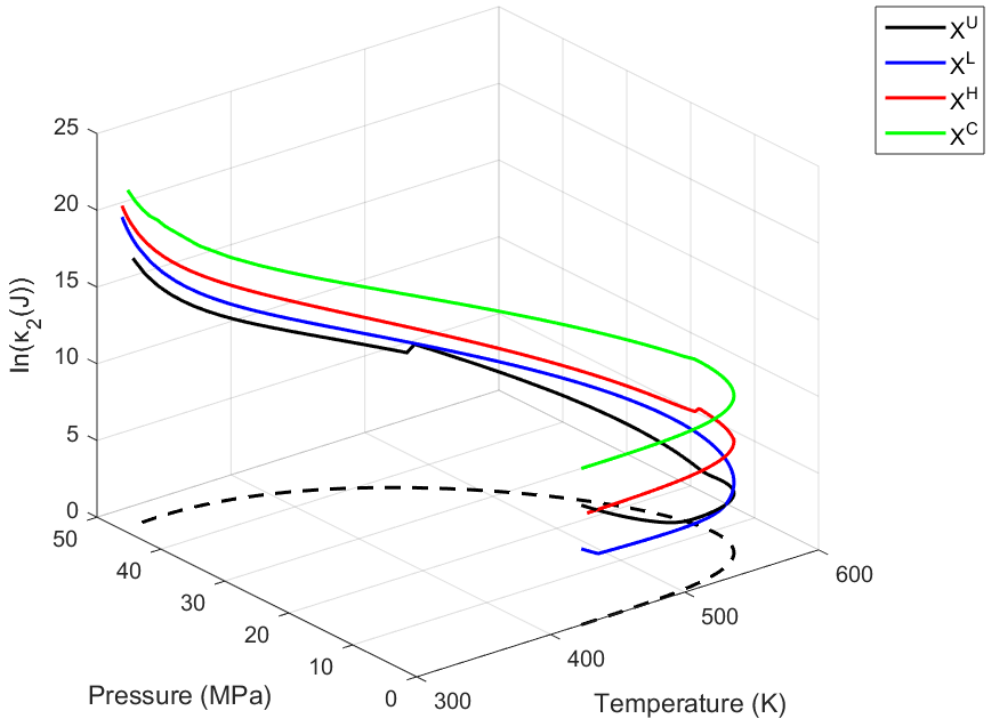

Figure 5.3: Condition number of the Jacobian matrix for each method, calculated at the solution, along the VLE phase envelope of mix 2. The calculations were performed with SRK EoS and k_{ij} parameters taken from Novak et al. [92] and Nikolaidis et al. [169]. The dashed line corresponds to the pressure - temperature projection of the VLE envelope.

In Figure 5.3, the condition numbers of the proposed methods along the phase envelope of mix 2 are compared. Mix 2 is a synthetic gas condensate and the phase envelope shown is exclusively a dew point line. The calculation with each method was initiated from a low temperature - low pressure dew point. The trend shown is the same as in the previous case of mix 1, with method X1U showing the lowest values for $\kappa_2(\boldsymbol{J})$ along the entire envelope, except for the low pressure region, in which method X1L shows the best conditioning. The sharp variations of the condition number, presented by methods X1U and X1H are caused by the change of the specification variable at that point on the phase envelope.

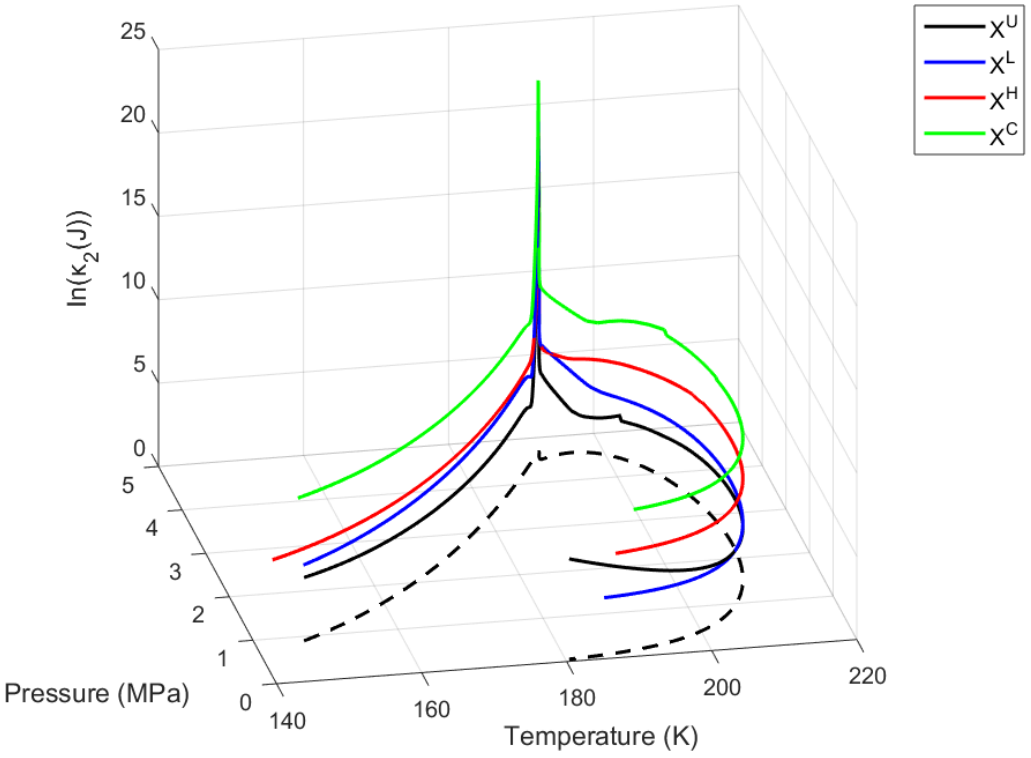

Figure 5.4: Condition number of the Jacobian matrix for each method, calculated at the solution, along the VLE phase envelope of mix 3. The calculations were performed with SRK EoS and $k_{ij} = 0$. The dashed line corresponds to the pressure - temperature projection of the VLE envelope.

The same trend between the $\kappa_2(\boldsymbol{J})$ values of the proposed methods is also followed for the calculation of the constant composition VLE envelope of mix 3. Mix 3 exhibits a double retrograde behavior and has one critical point approximately at T= 191.31 K, P= 4.67 MPa (where the condition numbers increase abruptly). The calculation in this case was initiated from a bubble point and all methods are able to pass to critical point and trace the VLE envelope, with method X1U showing the lowest values of

$\kappa_2(\boldsymbol{J})$, except for the low pressure region in the dew line, where method X1L is better conditioned.

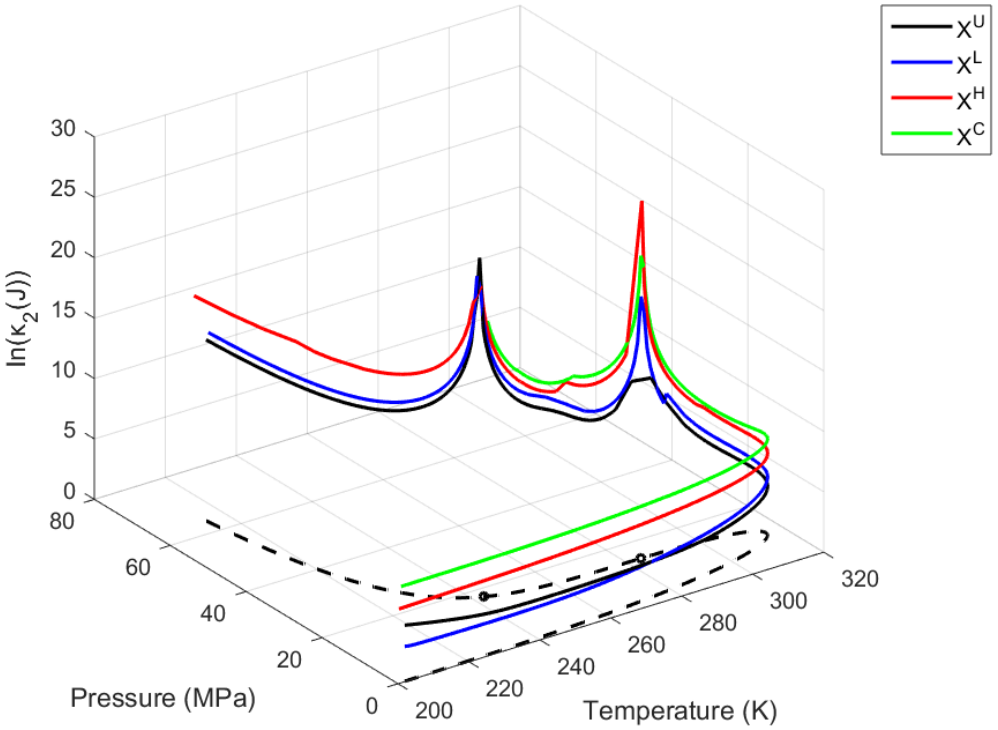

Figure 5.5: Condition number of the Jacobian matrix for each method, calculated at the solution, along the VLE phase envelope of mix 4. The calculations were performed with SRK EoS and $k_{ij} = 0.08$. The dashed line corresponds to the pressure - temperature projection of the VLE envelope and the open circles correspond to the critical points.

The last constant composition phase envelope examined is the one presented in Figure 5.5. Mix 4 exhibits an open-ended phase envelope with two critical points that are located approximately at T= 284.24 K, P= 14.45 MPa and T= 281.81 K, P= 17.72 MPa. In this case the calculations were initiated from a low temperature - low pressure dew point. As shown, the same trend between the proposed methods is again followed as in the previous cases. The condition number values of each method peak at the two critical points, while some sharp changes of $\kappa_2(\boldsymbol{J})$ along the envelope are caused again from the change of the specification variable. It has to be noted that this case was the most challenging one in tuning the step length to ensure passing the critical points and avoiding the trivial solution. Passing the second critical point (T= 281.81 K, P= 17.72 MPa) could not be performed with method X1C, even after trying many different step lengths, and the result was always the trivial solution or divergence of the iterative method.

Overall, the method X1U has shown the lowest condition numbers along the phase envelopes of the mixtures examined. Therefore, the variables incorporated in the $\boldsymbol{X}^{U}$ vector are going to be used in the next section to formulate methods for the calculation of the constant temperature (P-x,y) and constant pressure (T-x,y) phase diagrams of binary mixtures.

5.3. Phase Diagrams of Binary Mixtures

5.3.1. Working Variables and Equations

In this section, the $\boldsymbol{\Xi}^{U}$ variables are going to be used to formulate methods for the calculation of P-x,y and T-x,y phase diagrams of binary mixtures. The various methods are formulated by choosing different nonlinear sets of equations to be solved and different independent variables. The occurring formulations are compared based on the condition number of the corresponding Jacobian matrix at the solution and the ability to handle different types of phase behavior. The Jacobian matrices for each method are included in Appendix B. In this section, only the various equation sets and respective vectors of independent variables are presented.

Method 1m

The first method (method 1m) for the calculation of P-x,y phase diagrams utilizes as independent variables the vector $\boldsymbol{X}^{m1} = (\ln\Xi_1^{UW}, \ln\Xi_2^{UW}, \ln W_1, \ln W_2, \ln Z_1, \ln Z_2, \ln P)$, while temperature is constant. W_i and Z_i are the composition variables (formally treated as mole numbers) of each component at the two phases (vapor-liquid, liquid-liquid). Contrary to the constant composition phase envelope case, the compositions of the two phases both change during the iterations and the mole numbers of each component are used as independent variables. Similarly, $\hat{\varphi}_i(\boldsymbol{W}, T, P) = \hat{\varphi}_i(\boldsymbol{w}, T, P)$ and $\hat{\varphi}_i(\boldsymbol{Z}, T, P) = \hat{\varphi}_i(\boldsymbol{z}, T, P)$, while the mole fractions for both phases are retrieved from Eq. 2.3. $\Xi_i^{UW} = W_i P$ at the initialization and the solution. For the calculation of T-x,y phase diagrams the vector $\boldsymbol{X}^{m1} = (\ln\Xi_1^{UW}, \ln\Xi_2^{UW}, \ln W_1, \ln W_2, \ln Z_1, \ln Z_2, \ln T)$ is used, while pressure is constant. The same equation set is used for both types of calculations but the corresponding Jacobian matrices are different. The nonlinear equation set is:

$$g_i^{m1} = \ln\Xi_i^{UW} + \ln\hat{\varphi}_i(\boldsymbol{W}, T, P) - \ln Z_i - \ln\hat{\varphi}_i(\boldsymbol{Z}, T, P) - \ln P = 0;\ i = 1, C \quad (5.25)$$

$$g_{C+i}^{m1} = \Xi_i^{UW} - W_i P = 0;\ i = 1, C \quad (5.26)$$

$$g_{2C+1}^{m1} = W_1 + W_2 - 1 = 0 \quad (5.27)$$

$$g_{2C+2}^{m1} = Z_1 + Z_2 - 1 = 0 \quad (5.28)$$

$$g_{2C+3}^{m1} = X_S^{m1} - S = 0 \quad (5.29)$$

The initialization and linear extrapolation steps have the same form as in the case of constant composition phase envelopes. However, in method 1m, only $\ln\Xi_1^{UW}, \ln\Xi_2^{UW}$ and either $\ln P$ or $\ln T$ are used as specification variables in Eq. 5.29.

Method 2m

Method 2m incorporates the same independent variables with method 1m ($\boldsymbol{X^{m2} \equiv X^{m1}}$) for the calculation of P-x,y and T-x,y phase diagrams and the same equation set, except for Eq. 5.27. In method 2m, Eq. 5.27 is replaced with:

$$g_{2C+1}^{m2} = \Xi_1^{UW} + \Xi_2^{UW} - P = 0 \quad (5.30)$$

Method 3m

$\boldsymbol{X}^{m3} = (\ln\Xi_1^{UW}, \ln\Xi_2^{UW}, \ln\Xi_1^{UZ}, \ln\Xi_2^{UZ}, \ln W_1, \ln W_2, \ln Z_1, \ln Z_2, \ln P)$ is the vector of independent variables of method 3m for the calculation of P-x,y phase diagrams, when temperature is constant. In this case, the number of equations and variables is increased by C compared to the two previously mentioned methods. Furthermore, the Ξ_i^{UZ} variables are introduced, which are the counterparts of Ξ_i^{UW} for the phase with composition $\boldsymbol{z}$. For the calculation of T-x,y diagrams, $\ln P$ is substituted with $\ln T$ in the independent variables vector. In method 3m, $\ln\Xi_1^{UW}, \ln\Xi_2^{UW}, \ln\Xi_1^{UZ}, \ln\Xi_2^{UZ}$ and either $\ln P$ or $\ln T$ are used as specification variables. The nonlinear set of equations is:

$$g_i^{m3} = \ln\Xi_i^{UW} + \ln\hat{\varphi}_i(\boldsymbol{W}, T, P) - \ln\Xi_i^{UZ} - \ln\hat{\varphi}_i(\boldsymbol{Z}, T, P) = 0;\ i = 1, C \quad (5.31)$$

$$g_{C+i}^{m3} = \Xi_i^{UW} - W_i P = 0;\ i = 1, C \quad (5.32)$$

$$g_{2C+i}^{m3} = \Xi_i^{UZ} - Z_i P = 0;\ i = 1, C \quad (5.33)$$

$$g_{3C+1}^{m3} = \Xi_1^{UW} + \Xi_2^{UW} - P = 0 \quad 5.34$$

$$g_{3C+2}^{m3} = \Xi_1^{UZ} + \Xi_2^{UZ} - P = 0 \quad 5.35$$

$$g_{3C+3}^{m3} = X_S^{m3} - S = 0 \quad 5.36$$

Method 4m

Method 4m utilizes as independent variables for the calculation of P-x,y phase diagrams, the vector $\boldsymbol{X}^{m4} = (\ln\overline{K_1}, \ln\overline{K_2}, \ln\Xi_1^{UW}, \ln\Xi_2^{UW}, \ln\Xi_1^{UZ}, \ln\Xi_2^{UZ}, \ln P)$. In this method, the $\overline{K_\iota}$ variables are introduced which are equal to $\frac{\Xi_i^{UW}}{\Xi_i^{UZ}}$ at the initialization and the solution. The mole numbers W_i and Z_i are retrieved after each iteration from Eq. 5.13. For the calculation of T-x,y phase diagrams $\ln P$ is substituted with $\ln T$ in the independent variables vector. In this method, $\ln\overline{K_1}, \ln\overline{K_2}$ and either $\ln P$ or $\ln T$ are used as specification variables. The nonlinear equation set is:

$$g_i^{m4} = \ln\overline{K_\iota} + \ln\hat{\varphi}_i(\boldsymbol{W}, T, P) - \ln\hat{\varphi}_i(\boldsymbol{Z}, T, P) = 0;\ i = 1, C \quad 5.37$$

$$g_{C+i}^{m4} = \Xi_i^{UW} - \overline{K_\iota}\Xi_i^{UZ} = 0;\ i = 1, C \quad 5.38$$

$$g_{2C+1}^{m4} = \Xi_1^{UW} + \Xi_2^{UW} - P = 0 \quad 5.39$$

$$g_{2C+2}^{m4} = \Xi_1^{UZ} + \Xi_2^{UZ} - P = 0 \quad 5.40$$

$$g_{2C+3}^{m4} = X_S^{m4} - S = 0 \quad 5.41$$

5.3.2. Results and Discussion

In the previous type of calculations for isoplethic phase envelopes, the composition of the feed phase ($\boldsymbol{z}$) remains constant and the incipient phase ($\boldsymbol{w}$) composition is determined along with T and P. On passing the critical point, the only essential difference is that the character of the phases is interchanged, so that the properties of a vapor and a liquid phase are properly assigned. For the calculation of P-x,y and T-x,y diagrams, the compositions of both phases are unknown and there is no need to alter the character of the phases, since the calculation is usually terminated at a pure component vapor pressure, a critical point or the phase equilibrium curve extends to infinite pressures (or very low temperatures).

Because of their formulation, the phase assignment (vapor or liquid in VLE) to $\boldsymbol{w}$ and consequently to $\boldsymbol{\Xi}^{UW}$ and the other variables as well, affects the condition number of the Jacobian in methods 1m, 2m and 4m and their ability to trace specific types of phase diagrams. The formulation of method 3m and the resulting structure of its corresponding Jacobian matrix results in the condition number not being affected by the assignment of phases. Consequently, the calculation of binary phase diagrams was performed twice with methods 1m, 2m and 4m. For convenience, when $\boldsymbol{w}$ represents the vapor phase (or second liquid phase), the methods will be referred to as 1mV, 2mV and 4mV and when $\boldsymbol{w}$ represents the liquid phase, the methods will be referred to as 1mL, 2mL and 4mL.

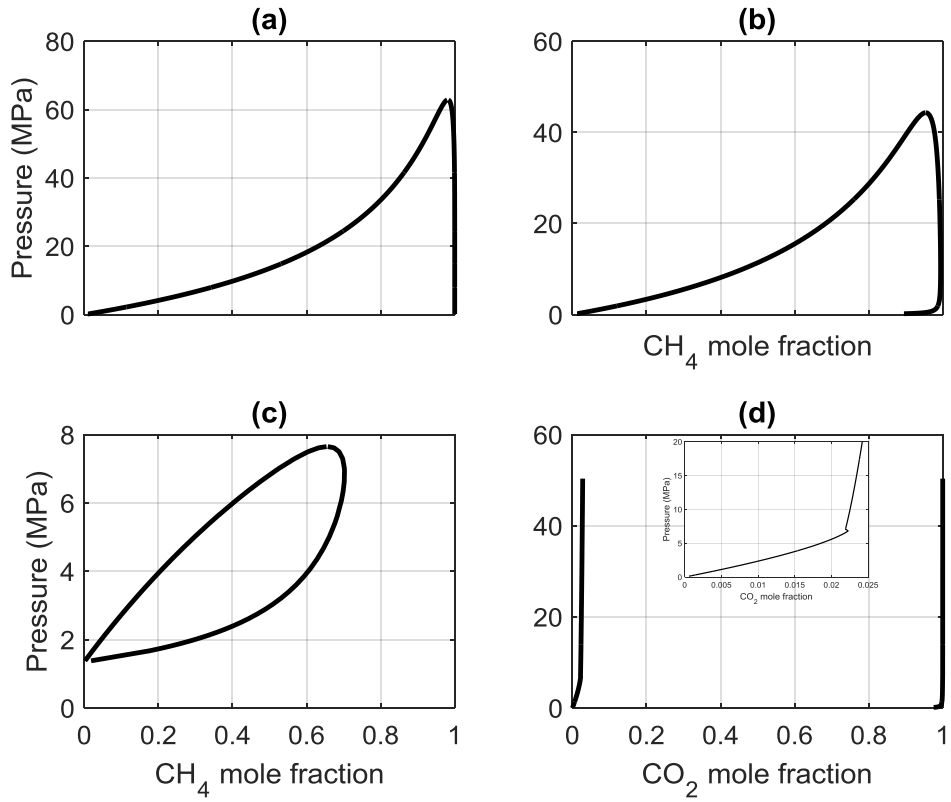

Figure 5.6: Pressure - composition VLE phase diagrams for the CH_4 - n-$C_{36}H_{74}$ mixture at (a) T= 373 K, (b) T= 700 K, calculated with the SRK EoS and $k_{ij} = 0$. Pressure - composition VLE phase diagram for the CH_4 - CO_2 mixture at (c) T= 241.5 K, calculated with the SRK EoS and $k_{ij} = 0$. Pressure - composition VLE / LLE phase diagram for the CO_2 - H_2O mixture at (d) T= 298 K, calculated with the PC-SAFT EoS and k_{ij} taken from Diamantonis et al. [172].

In Figure 5.6, the constant temperature (P-x,y) phase diagrams of 3 different binary mixtures are presented. The top panels (a), (b) of Figure 5.6 show the P-x,y phase diagrams of the CH_4 - n-$C_{36}H_{74}$ mixture at T= 373 K and T= 700 K respectively, calculated with the SRK EoS and $k_{ij} = 0$. Figure 5.6(c) presents the VLE phase diagram

for the CH_4 - CO_2 mixture at T= 241.5 K, calculated with the SRK EoS and $k_{ij} = 0$. Figure 5.6(d) presents the VLE / LLE phase diagram for the CO_2 - H_2O mixture at T= 298 K, calculated with the PC-SAFT EoS. In this case, CO_2 was modeled as a non-associating compound and H_2O as a 4-associating site molecule (4C in the terminology of Huang and Radosz) with a $k_{ij} = -0.0033$ taken from Diamantonis et al. [172]. The phase diagram of this mixture starts from low pressures with VLE until approximately P= 6.8 MPa, where the type of equilibrium changes to LLE.

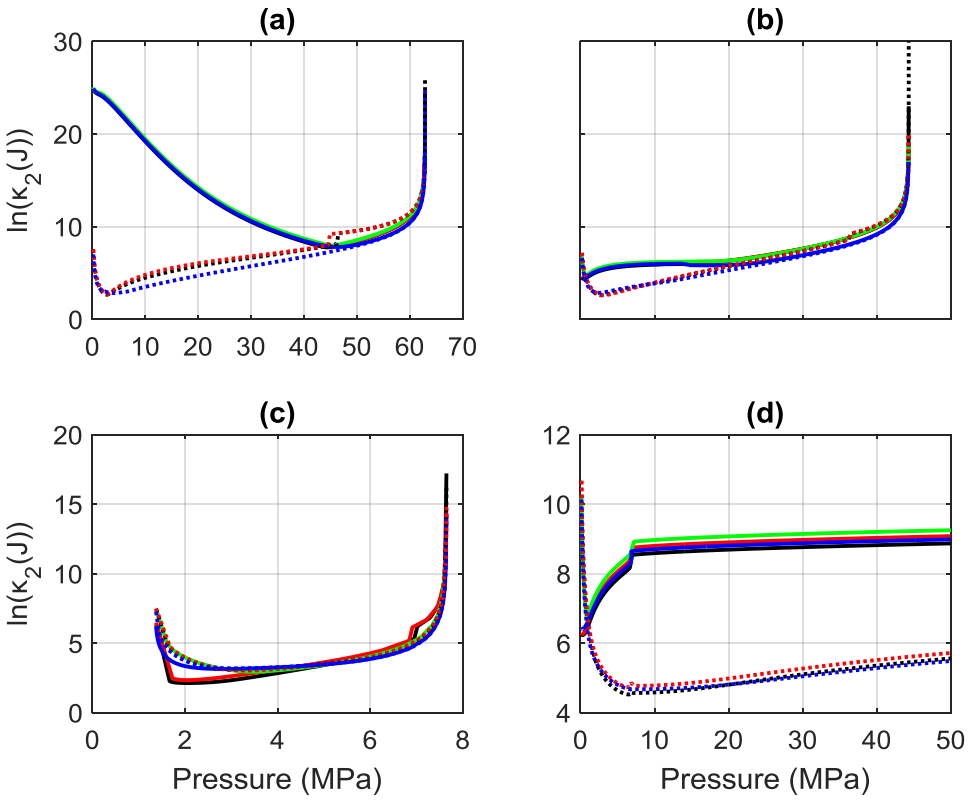

Figure 5.7: Condition number of the Jacobian matrix for each method, calculated at the solution, along the pressure - composition phase diagrams presented in Figure 5.6. Solid black lines correspond to method 1mV, solid red lines to method 2mV, solid green lines to method 3m and solid blue lines to method 4mV. Dotted black lines correspond to method 1mL, dotted red lines to method 2mL and dotted blue lines to method 4mL.

Figure 5.7 presents the condition number of the Jacobian matrix of each method - calculated at the solution - along the phase diagrams plotted in Figure 5.6. It can be observed that the differences between the 4 methods are generally small, when the same phase assignment is used. Methods 1mL, 2mL and 4mL show much lower condition numbers, as compared to their counterparts (1mV, 2mV, 4mV) in the low pressure region of Figure 5.7(a), while the difference is not that significant in Figure 5.7(b). This behavior is attributed to the vapor phase composition of the CH_4 - n-$C_{36}H_{74}$ mixture at

T= 373, which is comprised of CH_4 completely, except for pressures very close to the critical point. All methods, regardless of phase assignment, show small differences in terms of conditioning for the CH_4 - CO_2 mixture at T= 241.5 K (Figure 5.7(c)). In this mixture, the two phases have distinct compositions, but the immiscibility gap is smaller than the previous case and consequently, the region where one or both phases are comprised practically of only one component is very small. It can be observed that for pressures between the CO_2 vapor pressure and until 3 - 4 MPa, methods 1mV, 2mV, 3m and 4mV show lower condition numbers than their counterparts (1mL, 2mL, 4mL), since in this region the vapor phase is a mixture that includes both components, while the liquid phase is comprised mainly of CO_2. Generally, though, all methods show similar conditioning. It has to be noted, that method 3m follows more closely the trend of methods 1mV, 2mV and 4mV regarding the $\kappa_2(\boldsymbol{J})$ variation. The condition number of all methods increases abruptly, when the critical point is approached and another peak is always present in the limit of the pure component vapor pressure. From Figure 5.7(d), it can be observed that methods 1mL, 2mL and 4mL show much lower condition numbers than methods 1mV, 2mV, 3m and 4mV along the CO_2 - H_2O mixture phase diagram, except for the low pressure region. A sharp increase of the condition number in methods 1mV, 2mV, 3m and 4mV is the point in which VLE changes to LLE.

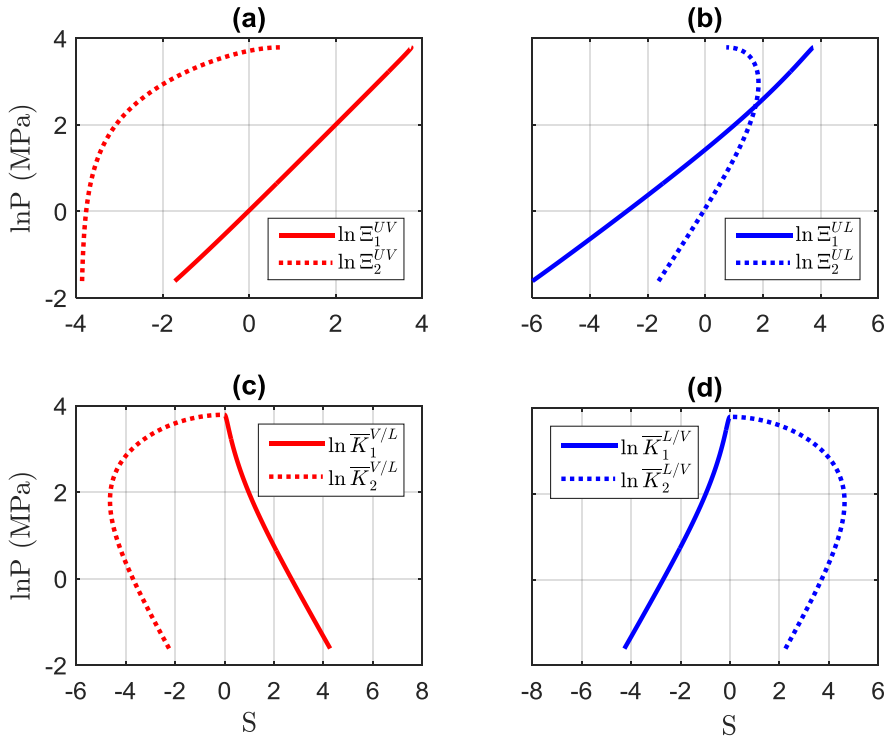

Figure 5.8: Variation of pressure along the P-x,y phase diagram of the CH_4 - n-$C_{36}H_{74}$ mixture at T= 700 K (SRK EoS and $k_{ij} = 0$), with various specification variables.

Figure 5.8 presents the variation of pressure along the P-x,y phase diagram of the CH_4 - n-$C_{36}H_{74}$ mixture at T= 700 K (Figure 5.6(b)) with variables that are used as specifications in the proposed methods. Figure 5.8(a) is associated with methods 1mV, 2mV and Figure 5.8(c) is associated with method 4mV in which $\boldsymbol{w}$ represents the vapor phase. Figure 5.8(b) is associated with methods 1mL, 2mL and Figure 5.8(d) with method 4mL in which $\boldsymbol{w}$ represents the liquid phase. Method 3m by construction utilizes both sets of variables ($\Xi_1^{UV}, \Xi_2^{UV}, \Xi_1^{UL}, \Xi_2^{UL}$) that are presented in Figure 5.8(a) and Figure 5.8(b). Subscript (1) in the presented graphs corresponds always to the more volatile component in each mixture. In Figure 5.8 corresponds to CH_4 for example. The first point in every diagram is calculated with pressure being the first specification and then, the continuation procedure, as described in section "Linear Extrapolation", is applied. After the calculation of the first point on the phase diagram, the automatic selection will set as specification variable the one having the numerically largest value of $\frac{\partial \boldsymbol{X}}{\partial s}$. As shown in Figure 5.8(a), when method 1mV is applied which utilizes $\Xi_1^{UV}, \Xi_2^{UV}, P$ as specification variables, Ξ_1^{UV} has the numerically largest variation with respect to pressure initially and it is chosen as the next specification. Around 10 MPa, Ξ_2^{UV} derivative with respect to Ξ_1^{UV} becomes greater than 1 and the phase diagram is eventually traced until the critical point using Ξ_2^{UV} as specification variable. It is important to note that all variables present smooth variations until the critical point, thus no problems are encountered during the extrapolation procedure.

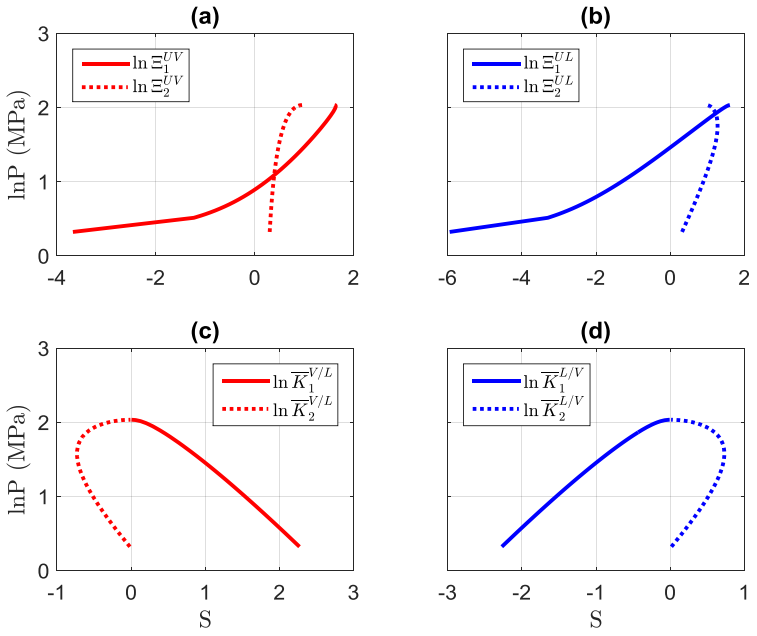

Figure 5.9: Variation of pressure along the P-x,y phase diagram of the CH_4 - CO_2 mixture at T= 241.5 K (SRK EoS and $k_{ij} = 0$), with various specification variables.

Figure 5.9 presents the same variable variations along the P-x,y phase diagram of the CH_4 - CO_2 mixture at T= 241.5 K. Again the specifications vary smoothly in every case, making them all suitable for tracing the phase diagram.

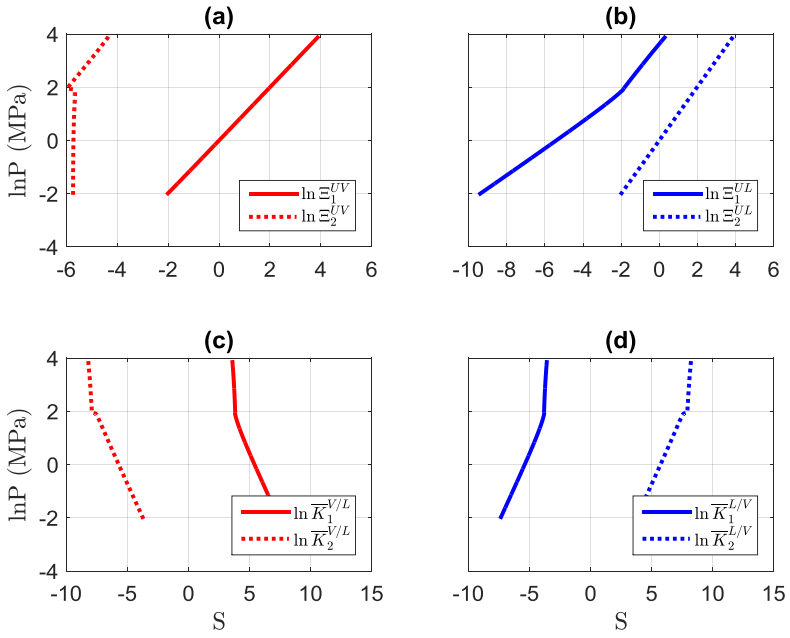

Figure 5.10: Variation of pressure along the P-x,y phase diagram of the CO_2 - H_2O mixture at T= 298 K (PC-SAFT EoS and k_{ij} taken from Diamantonis et al. [172]), with various specification variables.

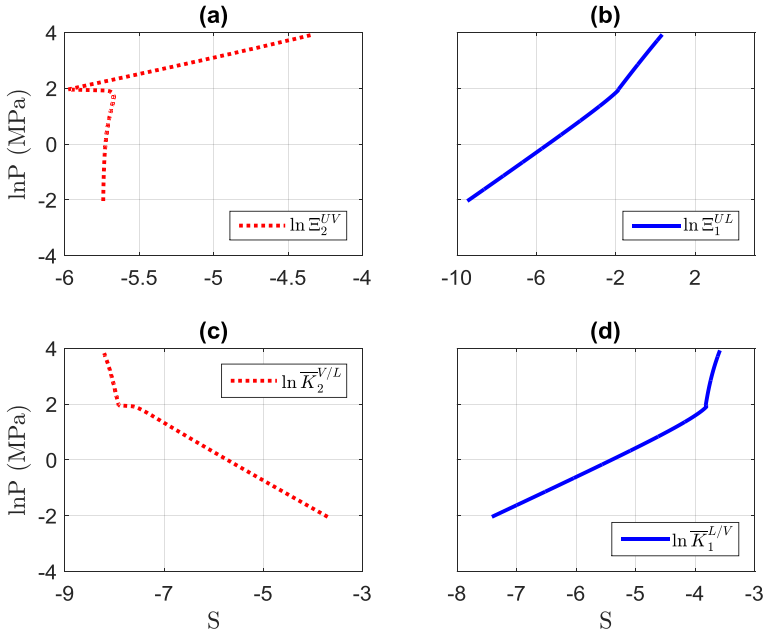

Figure 5.11: Variation of pressure along the P-x,y phase diagram of the CO_2 - H_2O mixture at T= 298 K (PC-SAFT EoS and k_{ij} taken from Diamantonis et al. [172]), with various specification variables (detail).

Figure 5.10 presents the variation of pressure along the P-x,y phase diagram of the CO_2 - H_2O mixture at T= 298 K (Figure 5.6(d)) with variables that are used as specifications in the proposed methods. Figure 5.11 presents the same variation in more detail, focusing on the low pressure - low specification variables' values region. The CO_2 - H_2O mixture presents a small retrograde part at the point where VLE changes to LLE, as shown in Figure 5.6(d). This results in a non-smooth variation of the variables $\overline{K_1}^{V/L}$, $\overline{K_2}^{V/L}$, $\overline{K_1}^{L/V}$, $\overline{K_2}^{L/V}$ and Ξ_2^{UV}. The automatic selection in methods 4mV and 4mL uses pressure as specification variable and around 5 MPa, the specification changes to $\overline{K_2}^{V/L}$ and $\overline{K_2}^{L/V}$ respectively, which results in a breakdown at the point where VLE is converted to LLE. To trace this specific phase diagram with methods 4mV and 4mL, it was necessary to set pressure as a sole specification variable and use small steps in order to calculate the retrograde part. In methods 1mV and 2mV, Ξ_1^{UV} is chosen automatically as specification variable and very close to the retrograde, the specification changes to Ξ_2^{UV} and very quickly again to Ξ_1^{UV}. Although a breakdown doesn't occur in this case, it results in overstepping the retrograde region, if really small steps are not taken on Ξ_2^{UV}. Using Ξ_1^{UV} as sole specification variable results in a smooth and non-problematic calculation of the phase diagram with methods 1mV and 2mV. In methods 1mL, 2mL and 3m, Ξ_1^{UL} is the resulting specification variable from the automatic selection and the calculation proceeds without any problems through the retrograde region.

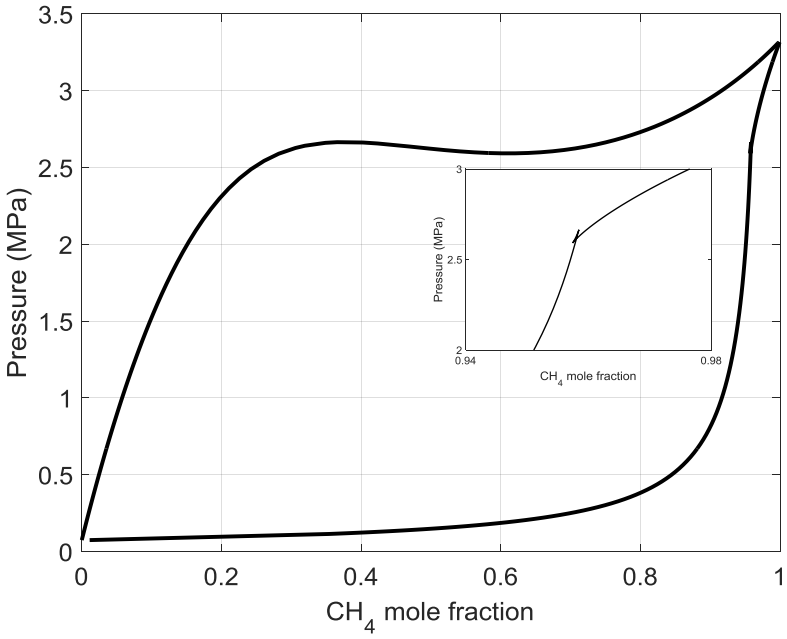

Figure 5.12: Pressure - composition VLE phase diagram for the CH_4 - CO_2 mixture at T= 180 K, calculated with the SRK EoS and $k_{ij} = 0.1$.

Figure 5.12 presents the P-x,y phase diagram of the CH_4 - CO_2 mixture at T= 180 K, calculated with SRK EoS and $k_{ij} = 0.1$. The value of the k_{ij} parameter was adjusted by hand in order to reproduce the behavior presented in Figure 5.12. The phase diagram presented is a typical case of an unstable VLE solution that occurs after a point, which indicates the existence of VLLE. The Px line shows two extrema in pressure, while the Py line intersects itself and forms two cusps. The point of intersection is where VLLE is exhibited and from that point and towards higher pressures, two sets of equilibrium lines – LLE and VLE – extend. Calculation of this specific phase behavior is problematic with methods 1mV and 2mV because of non-smooth variation of the specification variables along the phase diagram.

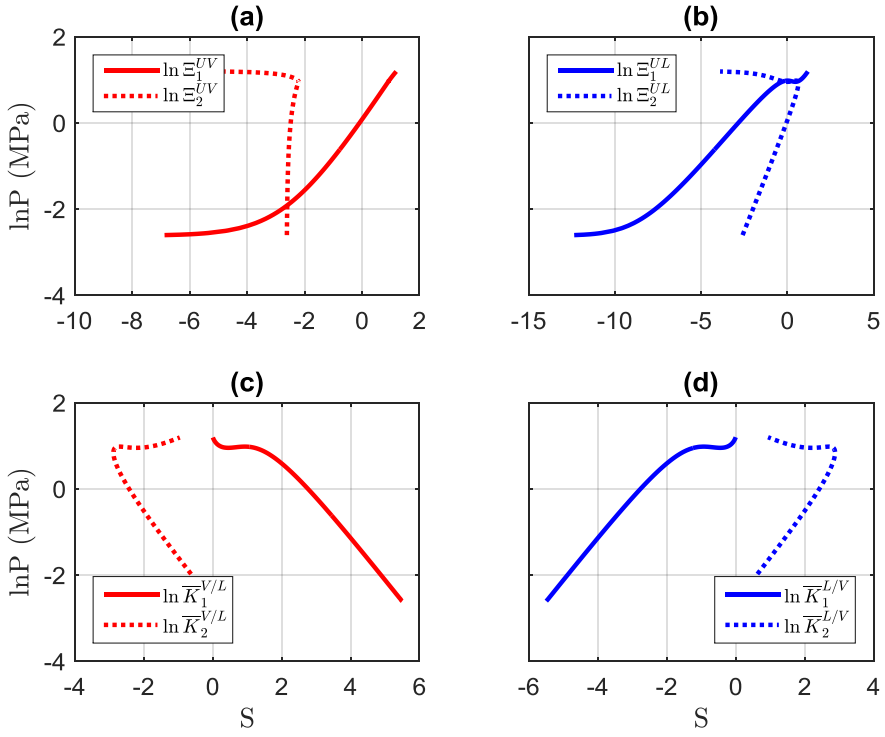

Figure 5.13: Variation of pressure along the P-x,y phase diagram of the CH_4 - CO_2 mixture at T= 180 K (SRK EoS and $k_{ij} = 0.1$), with various specification variables.

This can be observed from Figure 5.13 and Figure 5.14 which present these variations. The variables Ξ_1^{UV} and Ξ_2^{UV}, as shown in Figure 5.14(a) and Figure 5.14(b), present very sharp changes and intersections in the metastable part of Figure 5.12, rendering the linear extrapolation part and extension of the curve problematic. On the other hand, as shown in Figure 5.13, the variables Ξ_1^{UL} and Ξ_2^{UL} that are used by methods 1mL, 2mL and 3m vary smoothly and the P-x,y diagram can be traced without any

problems. Methods 4mV and 4mL also trace this specific phase diagram without any issue.

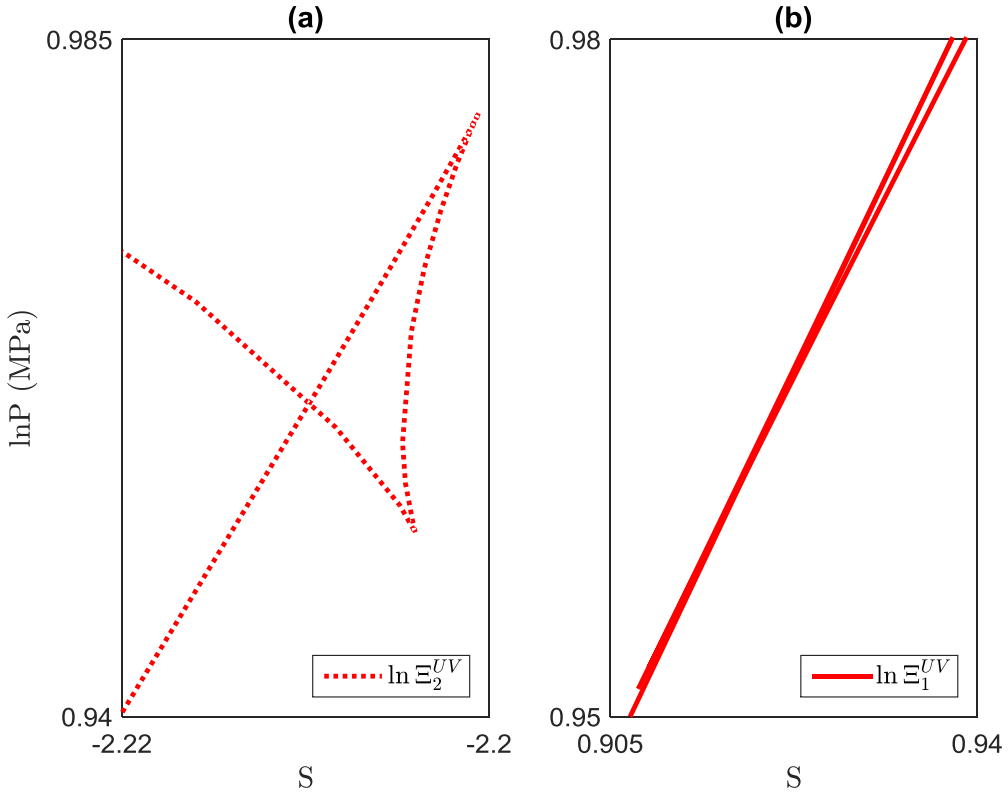

Figure 5.14: Variation of pressure along the P-x,y phase diagram of the CH_4 - CO_2 mixture at T= 180 K (SRK EoS and $k_{ij} = 0.1$), with various specification variables (detail).

Figure 5.15 presents the T-x,y phase diagrams for the CH_4 - *n*-C_6H_{14} mixture at (a) P= 2.5 MPa, (b) P= 10 MPa, calculated with the PC-SAFT EoS and $k_{ij} = 0$. The pressure - temperature projection, global phase diagram of this mixture, calculated with PC-SAFT EoS can be found in Nikolaidis et al. [170]. The phase diagram at P= 2.5 MPa starts and terminates at a pure component saturation temperature, while at P= 10 MPa, the lowest and highest temperatures correspond to critical points. The calculation of the phase diagram in Figure 5.15(a) was initiated from the higher saturation temperature and was traced towards the lower one. The phase diagram in Figure 5.15(b) was traced in two runs. The calculation was initialized at an intermediate temperature and was directed firstly towards higher temperatures until the critical point and towards lower ones in the second run.

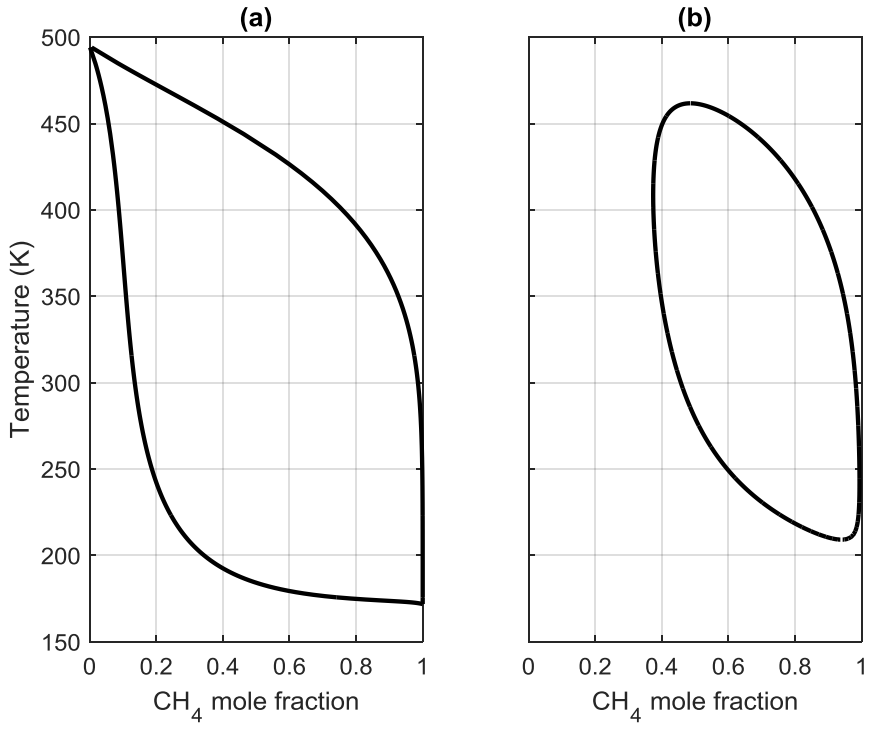

Figure 5.15: Temperature - composition VLE phase diagrams for the CH_4 - n-C_6H_{14} mixture at (a) P= 2.5 MPa, (b) T= 10 MPa, calculated with the PC-SAFT EoS and $k_{ij} = 0$.

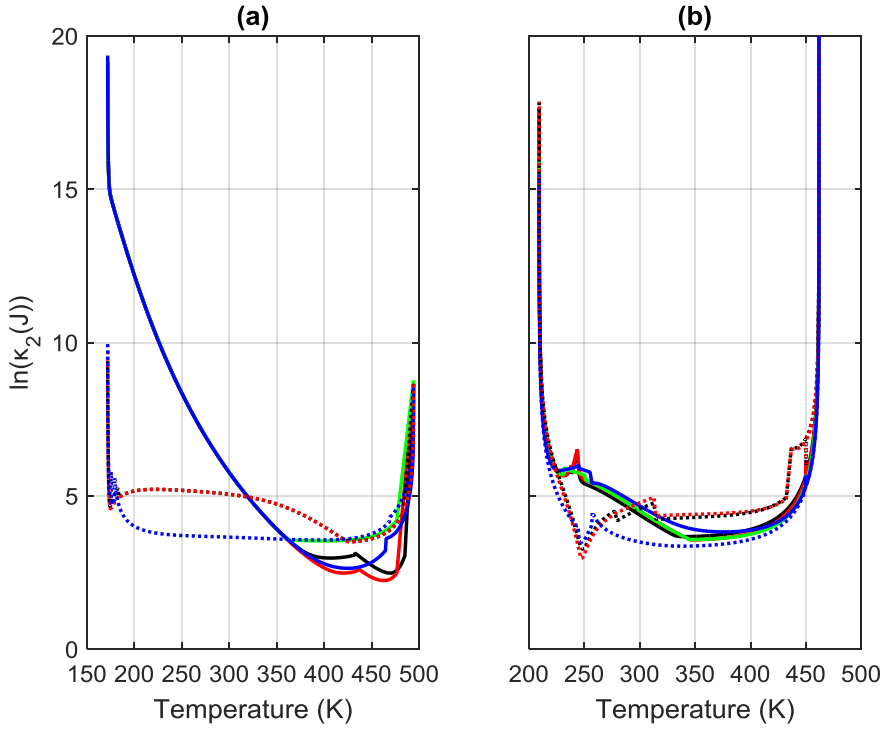

Figure 5.16: Condition number of the Jacobian matrix for each method, calculated at the solution, along the temperature - composition phase diagrams presented in Figure 5.15. Solid black lines correspond to method 1mV, solid red lines to method 2mV, solid green lines to method 3m and solid blue lines to method 4mV. Dotted black lines correspond to method 1mL, dotted red lines to method 2mL and dotted blue lines to method 4mL.

Figure 5.16 presents the condition number of the Jacobian matrix of each method - calculated at the solution - along the phase diagrams plotted in Figure 5.15. Regarding the phase diagram in Figure 5.15(a), methods 1mV, 2mV and 4mV show a bit lower condition numbers than their counterparts in the high temperature region, while from T= 350 K and lower, methods 1mL, 2mL and 4mL are better conditioned. Method 4mL shows the most stable values for the condition number in the entire temperature range, while the condition numbers for all methods peak at the two pure component limits. The two peaks in Figure 5.16(b) are the two critical points of the T-x,y phase diagram in Figure 5.15(b). Methods 1mV, 2mV, 3m and 4mV present very similar condition number values, while method 4mL shows the lowest values generally.

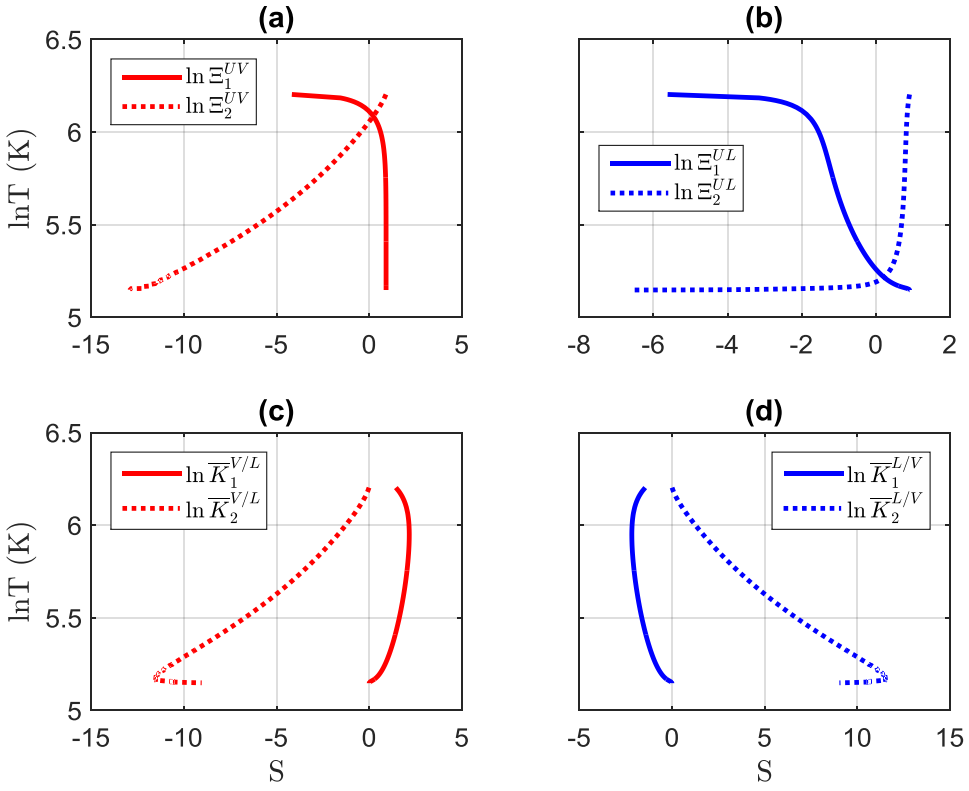

Figure 5.17: Variation of temperature along the T-x,y phase diagram of the CH_4 - *n*-C_6H_{14} mixture at P= 2.5 MPa (PC-SAFT EoS and $k_{ij} = 0$), with various specification variables.

Figure 5.17 and Figure 5.18 show the variation of temperature with the different specification variables along the T-x,y phase diagrams presented in Figure 5.15(a) and Figure 5.15(b) respectively. All variables change smoothly along the phase diagrams and no computational problems were encountered with any of the proposed methods during the tracing of the equilibrium curves.

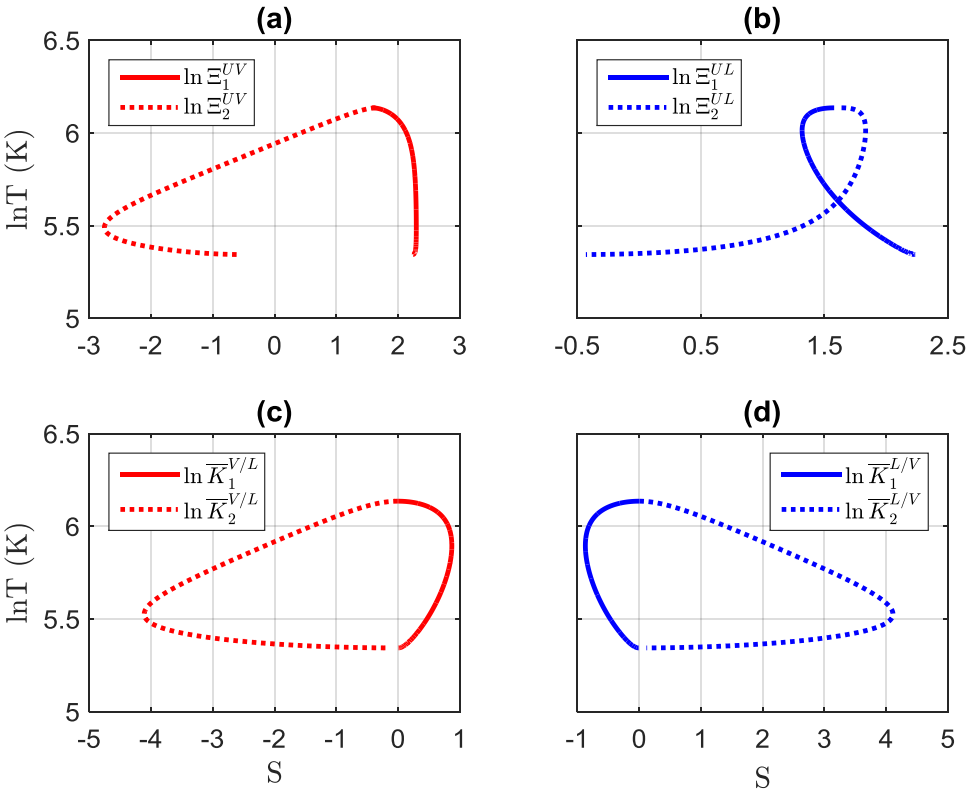

Figure 5.18: Variation of temperature along the T-x,y phase diagram of the CH_4 - *n*-C_6H_{14} mixture at P= 10 MPa (PC-SAFT EoS and $k_{ij} = 0$), with various specification variables.

5.4. Conclusions

New Euler-Newton predictor-corrector methods were presented for the sequential construction of constant composition phase envelopes of binary and multicomponent mixtures and P-x,y, T-x,y phase diagrams of binary mixtures. Different sets of independent variables were used and in most cases all the proposed methods were able to trace the constant composition phase envelopes of various mixtures. The test cases included mixtures with similar composition to natural gas and gas condensate mixtures that are of interest to the oil and gas industry, as well as unusual phase envelopes exhibiting double retrograde behavior or open-ended phase envelopes extending to high pressures. The proposed methods were compared based on the conditioning that each one exhibited along the calculated phase envelopes and method X1U proved to be the better conditioned. Based on the variables utilized by method X1U, new methods were proposed for the calculation of P-x,y and T-x,y phase diagrams of binary mixtures. Several combinations of equations were proposed, each one possessing different independent and specification variables. The comparison between

the methods was based on the conditioning of each method and the ability to trace different types of binary mixture phase diagrams. In that regard, different choices of phase assignment in the variables involved and the effect on the condition numbers, as well as the ability to handle different types of phase behavior were investigated. It was shown, that methods 1mL, 2mL and 4mL are better conditioned than their counterparts in most cases, while methods 1mL and 2mL encountered no problems in tracing any of the test cases examined. Method 3m is able to trace all the phase diagrams examined with no computational problems as well.

6. Solid-Fluid Equilibrium of CO_2 mixtures

6.1. Introduction

In this Chapter, solid-phase thermodynamic models of different complexity are applied to model the SFE of pure CO_2 and CO_2 mixtures with other compounds. These models include the approach of McHugh et al. [160] coupled with an empirical correlation for the CO_2 saturation pressure at SFE (abbreviated as empirical correlation model), the approach of Seiler et al. [162] (abbreviated as thermodynamic integration model) and the solid-phase EoS, proposed by Jäger and Span [163] for pure CO_2. The different models are coupled with three fluid-phase EoS (SRK, PR and PC-SAFT) and the performance of each combined model is evaluated for various binary mixtures. In total, 7 different models are examined *i.e.* the empirical correlation and the thermodynamic integration models each one coupled with SRK, PR and PC-SAFT EoS and the PC-SAFT EoS coupled with the Jäger and Span EoS.

Calculation of the two-phase SFE of a mixture requires the equilibration of the chemical potentials of each component between the two coexisting phases (S: solid phase, F: fluid phase) at the same temperature and pressure.

$$\mu_i^S(T,P,\boldsymbol{x}^S) = \mu_i^F(T,P,\boldsymbol{x}^F) \tag{6.1}$$

In many cases, the solid phase is comprised of only one component (solid former) and thus, calculation of the SFE requires solution of only one equation; the chemical potential equality of the solid-forming compound between the two phases:

$$\mu_{0i}^S(T,P) = \mu_i^F(T,P,\boldsymbol{x}^F) \tag{6.2}$$

Eq. 6.2 can be replaced by the equifugacity relation:

$$\hat{f}_{0i}^S(T,P) = \hat{f}_i^F(T,P,\boldsymbol{x}^F) \tag{6.3}$$

where $\hat{f}_i^F(T,P,\boldsymbol{x}^F)$ is the fugacity of the solid-forming compound in the fluid mixture and it is calculated with a fluid-phase EoS. The solid-phase fugacity is calculated with one of the solid-phase thermodynamics models, presented in Chapter 3.

The approach of McHugh et al. [160] can be used for calculating the solid-phase fugacity in Eq. 6.3, combined with an empirical correlation for the saturation pressure of pure CO_2 at SLE or SVE conditions. Two correlations for pure CO_2 – one for SLE and

one for SVE – taken from Span and Wagner [129] are used and are presented in Table C.5, Appendix C.

The parameters for the thermodynamic integration model, when the hypothetical subcooled melt is used as reference state for the solid-phase fugacity (applied to SLE calculations) are presented in Table C.4. The difference of the molar, isobaric heat capacities between the hypothetical subcooled melt and the solid, for pure CO_2 is $\Delta c_{P,0i}^{SL^*} = 20.205$ (J/mol K) [173]. For SVE calculations, a modification was applied to the model proposed by Seiler et al. [162]. In this case, the assumption of pressure independent vapor volume is unrealistic and can lead to high errors. The corresponding term in the equation can be calculated from the Gibbs free energy change using a fluid-phase EoS. The solid-phase fugacity now is calculated as:

$$\hat{f}_{0i}^{S}(T,P) = \hat{f}_{0i}^{V^*}(T,P)\exp\left[-\frac{\left(v_{0i}^{S}\right)(P^+ - P)}{RT} - \ln\left(\frac{\hat{f}_{0i}^{V^*}(T,P)}{\hat{f}_{0i}^{V}(T,P^+)}\right) - \frac{\Delta h_{0i}^{SV}}{RT}\left(1 - \frac{T}{T_{0i}^{SV}}\right) + \frac{\Delta c_{P,0i}^{SV^*}}{RT}\left(T_{0i}^{SV} - T\right) - \frac{\Delta c_{P,0i}^{SV^*}}{R}\ln\frac{T_{0i}^{SV}}{T}\right] \quad 6.4$$

where Δh_{0i}^{SV} (equal to 26,300 J/mol for CO_2 [174]) is the enthalpy of sublimation at sublimation temperature T_{0i}^{SV} (equal to 194.5 K for CO_2), v_{0i}^{S} is the pure solid former solid molar volume (equal to 29.069 cm^3/mol for CO_2 [175]) and $\Delta c_{P,0i}^{SV^*}$ is the difference of the molar, isobaric heat capacities between the hypothetical superheated sublime and the solid (equal to -23.611 J/mol K for CO_2). The solid-phase heat capacity value for CO_2 is taken from DIPPR [175]. The vapor-phase heat capacity is calculated from PC-SAFT EoS, because there are no available experimental data. The ideal gas heat capacity is calculated using a DIPPR correlation and the residual part is calculated using PC-SAFT. The reference pressure P^+ in this case is equal to 0.1 MPa.

The application of Jäger and Span EoS is done using the approach of McHugh for calculating the solid-phase fugacity, but in this case the pure CO_2 saturation pressure at SLE or SVE is not given by an empirical correlation, but is calculated from the solid-phase EoS, as described in Chapter 3.

Calculation of SLVE (SLGE) requires a VLE (GLE) and an SLE or SVE (SGE) to exist at the same conditions of temperature and pressure. This is expressed by the equality of chemical potentials for each component between the three phases:

$$\mu_i^S(T,P,\boldsymbol{x}^S) = \mu_i^L(T,P,\boldsymbol{x}^L) = \mu_i^V(T,P,\boldsymbol{y}^V) \quad 6.5$$

Eq. 6.5 requires satisfaction of two independent equations, either

$$\mu_i^S(T,P,\boldsymbol{x}^S) = \mu_i^L(T,P,\boldsymbol{x}^L)$$
$$\mu_i^L(T,P,\boldsymbol{x}^L) = \mu_i^V(T,P,\boldsymbol{y}^V) \quad 6.6$$

or:

$$\mu_i^S(T,P,\boldsymbol{x}^S) = \mu_i^V(T,P,\boldsymbol{y}^V)$$
$$\mu_i^L(T,P,\boldsymbol{x}^L) = \mu_i^V(T,P,\boldsymbol{y}^V) \quad 6.7$$

Of course, there is no fundamental difference between Eqs. 6.6 and 6.7, but in terms of application, choosing Eq. 6.6 usually implies that the solid-phase chemical potential will be calculated using as reference phase the liquid one and the respective thermophysical properties, while Eq. 6.7 the vapor (gaseous) one. Furthermore, if the thermophysical properties of one of the fluid phases are known more accurately, this will have an impact on the final calculations. In SLGE calculations, it is more common to relate the solid-phase chemical potential to the liquid-phase one.

6.2. Results and Discussion

The first step is the evaluation of every model for the description of pure CO_2 SLE and SVE. In this way, the performance of a solid-phase model, coupled with different EoS, is tested and the agreement between the different models is assessed. Moreover, an accurate description of the SFE behavior of the pure solid-former is a good basis for subsequent two phase and three phase SLGE mixture calculations. It will be shown here that accurate description of the triple point of the pure solid-forming compound is crucial for the overall performance of a model for SLGE calculations of binary mixtures.

Because of lack of experimental data for two-phase SFE for CO_2 mixtures relevant to CCS applications, the performance of the different models is evaluated for SLGE calculations, and compared to experimental data from literature. Three CO_2 mixtures with N_2, H_2 and CH_4 were modeled.

6.2.1. Solid-Fluid Equilibrium of Pure CO_2

Table C.1 and Table C.2 summarize the pure component parameters for the cubic and the PC-SAFT EoS used to model the fluid phases. Table C.4 and Table C.5 summarize the parameters used by the solid-phase models.

In Figure 6.1, calculation of the pure CO_2 SVE from the three different solid-phase models is presented. PC-SAFT was used to calculate the vapor-phase properties. The empirical correlation is fitted to experimental SVE data of pure CO_2 and is valid in the range 154 - 216.59 K. Consequently, it can be used as a basis to assess the performance of the other two models. The results show that the empirical correlation and the Jäger - PCSAFT models completely coincide, whereas the thermodynamic integration model coupled with PC-SAFT deviates at temperatures higher than 200 K.

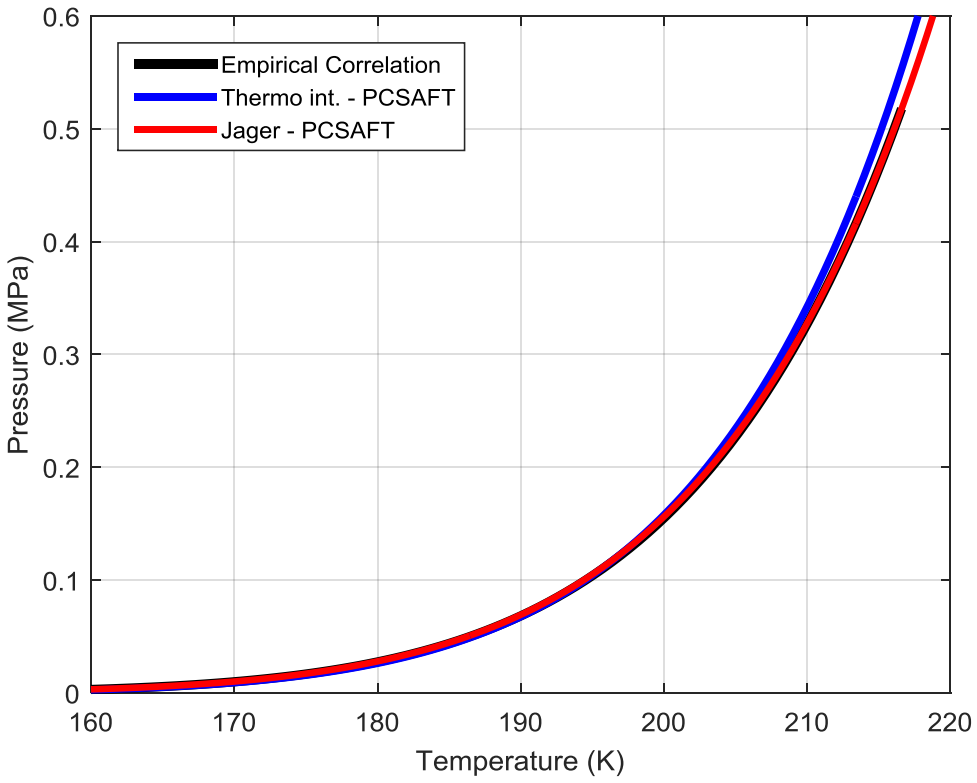

Figure 6.1: Pure CO_2 SVE: Comparison of Empirical Correlation, Thermodynamic Integration model and Jäger and Span EoS, coupled with PC-SAFT EoS.

Similar calculations were performed for the SLE of pure CO_2 and results are presented in Figure 6.2. The validity range of the empirical correlation for the melting pressure of pure CO_2 is 216.59 - 270 K. In this case, all three models are in excellent agreement at low temperatures up to 226 K; at higher temperatures the Jäger - PCSAFT model deviates from the other two which remain in excellent agreement to each other.

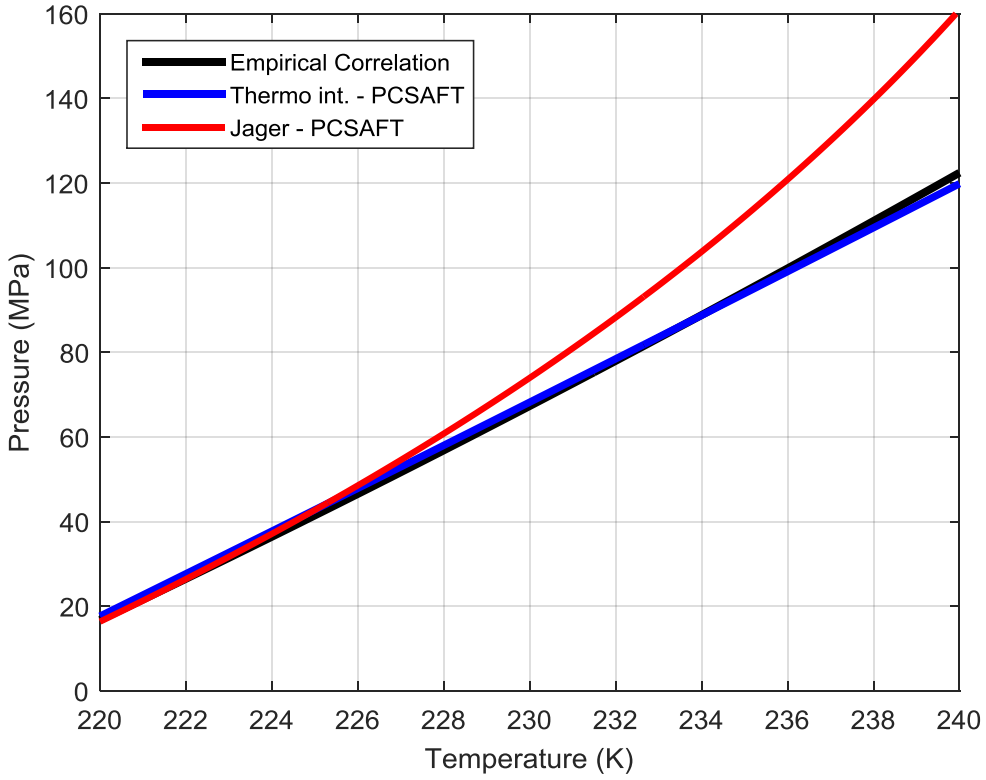

Figure 6.2: Pure CO_2 SLE: Comparison of Empirical Correlation, Thermodynamic Integration model and Jäger and Span EoS, coupled with PC-SAFT EoS.

6.2.2. Solid-Liquid-Gas Equilibrium of CO_2 mixtures

In Table 6.1, the experimental SLGE data sets for the mixtures modeled are presented. In Table 6.2, Table 6.3 and Table 6.4, the Percentage Average Absolute Relative Deviation (% AARD) between experimental SLGE data and model calculations for each mixture and the corresponding k_{ij} values are presented.

Table 6.1: Experimental binary SLGE data from the literature modeled in this work.

Pressure (MPa)	Ref	Temperature (K)	Ref
CO_2 - N_2		CO_2 - CH_4	
4.8 - 13.01	[176]	194.53 - 215.37	[177]
CO_2 - H_2		97.39 - 211.56	[178]
4.3 - 13.7	[176]		

Table 6.2: % AARD between experimental SLGE data for the equilibrium pressure and model calculations for the CO_2 - N_2 mixture and corresponding k_{ij} values.

		% AARD		
EoS	k_{ij}	Correlation model	Thermodynamic Integration model	Jäger and Span EoS
SRK	0	41.28 (1)[a]	19.76	-
	-0.0172	28.58	2.80	-
PR	0	20.92	2.85	-
	-0.0026	22.48	3.53	-
PC-SAFT	0	7.41	8.09	8.07
	0.00575	4.06	5.58	3.13

NP: Number of experimental data points

$$\%AARD = \frac{100}{NP}\sum_{i=1}^{NP}\left|\frac{P_i^{calculated} - P_i^{experimental}}{P_i^{experimental}}\right|$$

[a] 1 data point was not included in the calculation of % AARD

Table 6.3: % AARD between experimental SLGE data for the equilibrium pressure and model calculations for the CO_2 - H_2 mixture and corresponding k_{ij} values.

		% AARD		
EoS	k_{ij}	Correlation model	Thermodynamic Integration model	Jäger and Span EoS
SRK	0	5.41	37.07	-
	0.1106	17.80	9.70	-
PR	0	(3)[a]	84.80	-
	0.1684	43.55	9.70	-
PC-SAFT	0	18.04	25.54	13.31
	0.05984	3.18	13.52	0.99

NP: Number of experimental data points

$$\%\ AARD = \frac{100}{NP}\sum_{i=1}^{NP}\left|\frac{P_i^{calculated} - P_i^{experimental}}{P_i^{experimental}}\right|$$

[a] All 3 data points were excluded from the calculation of % AARD

Table 6.4 : % AARD between experimental SLGE data for the equilibrium pressure and model calculations for the CO_2 - CH_4 mixture and corresponding k_{ij} values.

		% AARD		
EoS	k_{ij}	Correlation model	Thermodynamic Integration model	Jäger and Span EoS
SRK	0	13.67	12.82	-
	0.103	2.75	2.90	-
PR	0	13.97	13.21	-
	0.100	2.19	1.67	-
PC-SAFT	0	14.49	14.10	14.79
	0.061	2.93	2.82	3.07

NP: Number of experimental data points

$$\%\ AARD = \frac{100}{NP}\sum_{i=1}^{NP}\left|\frac{P_i^{calculated} - P_i^{experimental}}{P_i^{experimental}}\right|$$

For SLGE calculations with the thermodynamic integration model, the pure subcooled melt reference state was used. Judging by the results of the model for the pure CO_2, the model is more accurate in the SLE case, because the fitted enthalpy, proposed by Jäger and Span [163] is used and the enthalpic term has the major impact on the results [162]. If the SV thermodynamic integration model was used, the calculations would be less accurate because the model fails to describe very accurately the pure CO_2 SVE curve. In the calculations presented here, the terms corresponding to the difference between solid and liquid isothermal heat capacities were truncated because they cancel out each other, thus having practically no impact on the results.

When SLGE calculations with the use of an empirical correlation that provides the saturation pressure are concerned, one has to choose between using a correlation for the SVE or the SLE curves. Normally, these empirical correlations are accurate only within the range of fitting which means that an SVE correlation should be used for temperatures lower and up to the triple temperature of the pure solid former, whereas an SLE correlation should be used for temperatures greater than the triple temperature. The P-T projection of the SLGE curve for many compounds is located at temperatures lower than the triple temperature of the pure solid former. For these cases, using an SVE correlation is the valid choice. There are systems though, where the SLGE equilibrium curve lies at temperatures greater than the triple temperature of the pure solid-former. In

this case, an SLE correlation should be used. All the mixtures studied in this work exhibit SLGE curves that lie at temperatures lower than the pure solid-former triple temperature, except for the case of the CO_2 - H_2 mixture. The same approach used for fitted correlations is also used when SLGE calculations with the Jäger and Span solid-phase EoS are concerned.

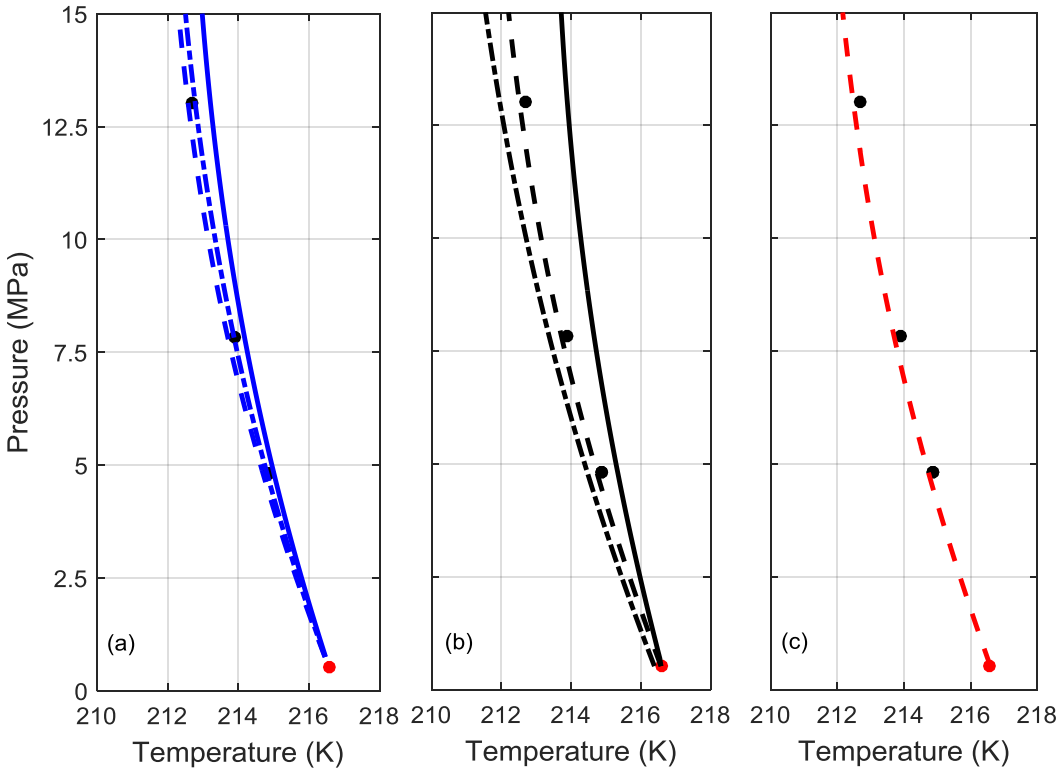

Figure 6.3: Prediction ($k_{ij} = 0$) of the SLGE of the CO_2 - N_2 mixture. Results with three different solid-phase models: (a) Thermodynamic Integration model, (b) Empirical Correlation model, (c) Jäger and Span EoS, coupled with three fluid-phase EoS. Experimental data [176] are represented by data points and calculations by lines: $(-)$ SRK, $(- \cdot -)$PR, $(- - -)$ PC-SAFT.

For the case of the CO_2 - N_2 mixture presented in Figure 6.3, the thermodynamic integration model coupled with PR EoS gives the most accurate predictions with an % AARD = 2.85. Coupling all fluid-phase EoS with the empirical correlation model results in higher deviations, ranging from 7.41 to 41.28 % AARD. Coupling this solid-phase model with cubic EoS results in a poorer reproduction of the pure CO_2 triple point but also a different trend of the SLGE line which causes the higher deviations observed with this model. PC-SAFT in this case successfully predicts it, providing the most accurate results with this model, but in general less accurate than the thermodynamic integration model. At this point is has to be noted that all fluid-phase EoS reproduce accurately the

pure CO_2 triple point when coupled with the thermodynamic integration model because the triple temperature is an input parameter in this modeling approach, since the reference pressure is very close to the triple point of the pure solid-former and as a result all the input parameters are taken at this point. Finally, the Jäger and Span EoS coupled with PC-SAFT results in very similar predictions with the thermodynamic integration model (% AARD = 8.07).

If the assumption of a pure solid phase is valid, the SLGE prediction of a model is a combination of the accuracy of the solid-phase model to describe the pure solid-former SVE or SLE and the accuracy of the EoS to describe the fluid phases. Driven by this fact, instead of regressing BIPs from the SLGE data, a different methodology was adopted to improve the performance of the models. Experimental VLE data at 218.15 K [176] were used to regress BIPs for the three fluid-phase EoS.

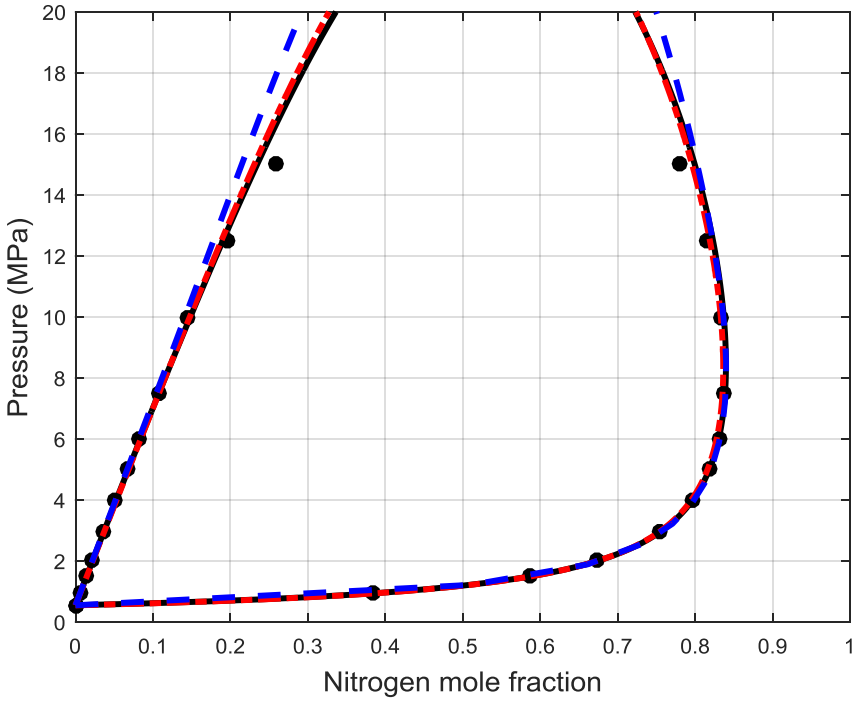

Figure 6.4: Pressure - composition VLE phase diagram for the CO_2 - N_2 mixture at T= 218.15 K. Experimental data [176] are represented by data points and correlations ($k_{ij} \neq 0$) by lines: (—) SRK, (— · —) PR, (— — —) PC-SAFT.

VLE predictions for the CO_2 - N_2 mixture (not shown here) from PR EoS are the most accurate, while PC-SAFT is slightly less accurate, which is in agreement with the SLGE modeling results when a solid-phase model that accurately predicts the pure solid former triple point is used. In Figure 6.4, experimental data and VLE model correlations

are presented. All three models provide accurate correlation of the data with SRK being the most accurate at high pressure.

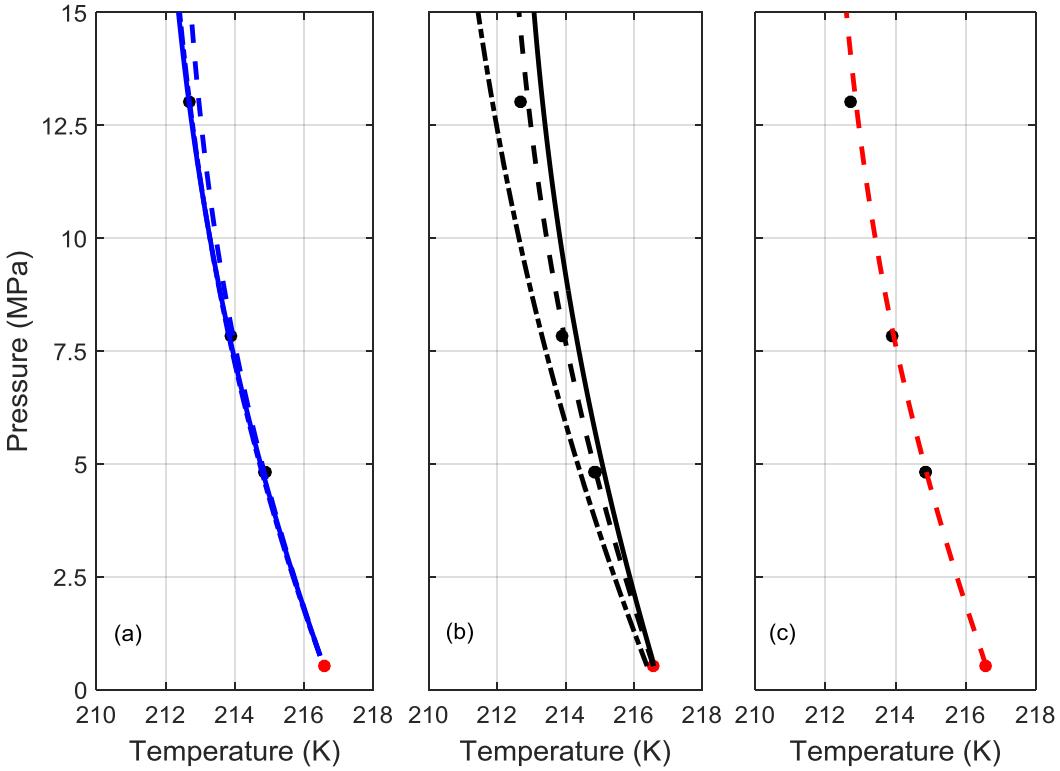

Figure 6.5: Prediction of the SLGE of the CO_2 - N_2 mixture when k_{ij} parameters fitted to experimental binary VLE data at low temperature are used. Results with three different solid-phase models: (a) Thermodynamic Integration model, (b) Empirical Correlation model, (c) Jäger and Span EoS, coupled with three fluid-phase EoS. Experimental data [176] are represented by data points and calculations by lines: $(-)$ SRK, $(-\cdot-)$PR, $(--)$ PC-SAFT.

SLGE calculations with k_{ij} fitted to VLE data for the CO_2 - N_2 mixture are shown in Figure 6.8. The use of the regressed BIPs results in an accurate prediction of the SLGE behavior with every solid-phase model coupled with SRK and PC-SAFT EoS, since the description of the composition of the fluid phases is improved. In the case of PR EoS, the use of a BIP slightly improves the vapor phase correlation and deteriorates the liquid phase correlation of the VLE. This results in poorer prediction of the SLGE behavior with BIPs compared to the pure prediction when all k_{ij} parameters are zero. It has to be noted that in the case of PC-SAFT EoS, the use of a BIP improves the correlation of the liquid phase composition and deteriorates the vapor phase description, but the overall prediction of the SLGE is improved. The most accurate model in this case is the thermodynamic integration model coupled with SRK EoS (% AARD = 2.80),

consistent with the fact that SRK provides also the most accurate correlation of the VLE behavior of this mixture.

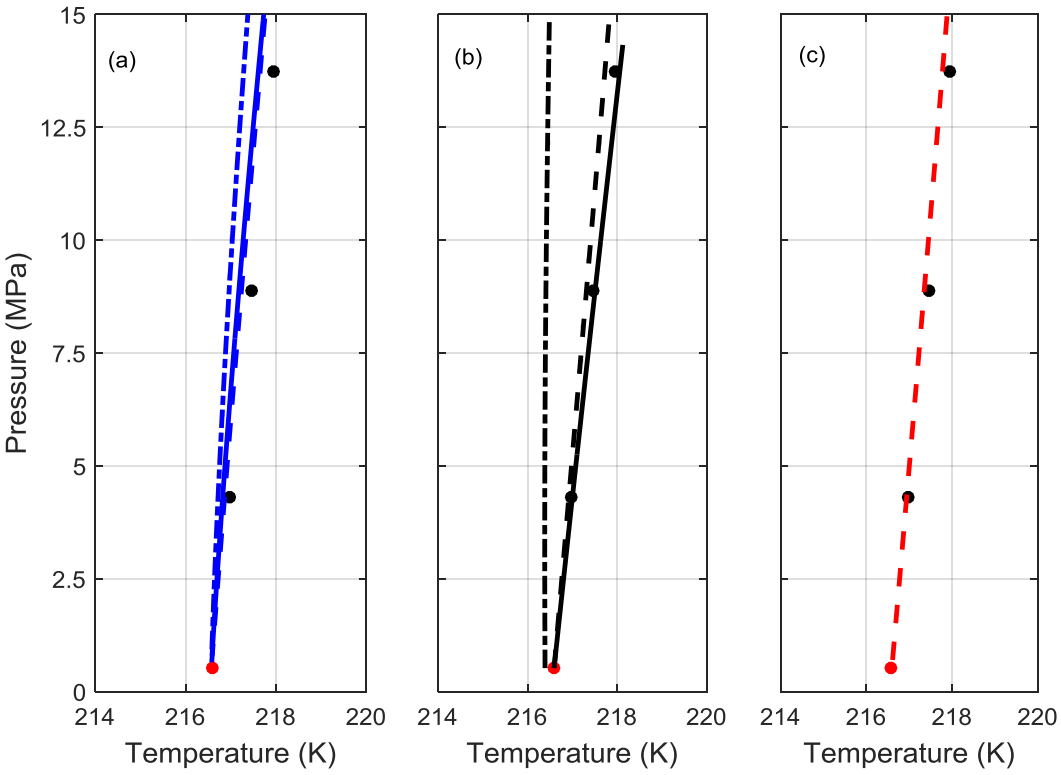

Figure 6.6: Prediction ($k_{ij} = 0$) of the SLGE of the CO_2 - H_2 mixture. Results with three different solid-phase models: (a) Thermodynamic Integration model, (b) Empirical Correlation model, (c) Jäger and Span EoS, coupled with three fluid-phase EoS. Experimental data [176] are represented by data points and calculations by lines: $(-)$ SRK, $(-\cdot-)$PR, $(---)$ PC-SAFT.

The same approach was also adopted for the CO_2 - H_2 mixture. In this mixture, when no BIPs are used, the empirical correlation model is generally more accurate than the thermodynamic integration model, except for the case of the PR EoS. When using the thermodynamic integration model which accurately reproduces the pure CO_2 triple point, PC-SAFT predicts the SLGE line more accurately than the other EoS and this is in agreement with the more accurate prediction of the VLE behavior at the low temperature from PC-SAFT. The Jäger and Span EoS coupled with PC-SAFT predicts more accurately the SLGE (% AARD = 13.31), than the corresponding empirical correlation model but still the latter one coupled with SRK is the most accurate (% AARD = 5.41).

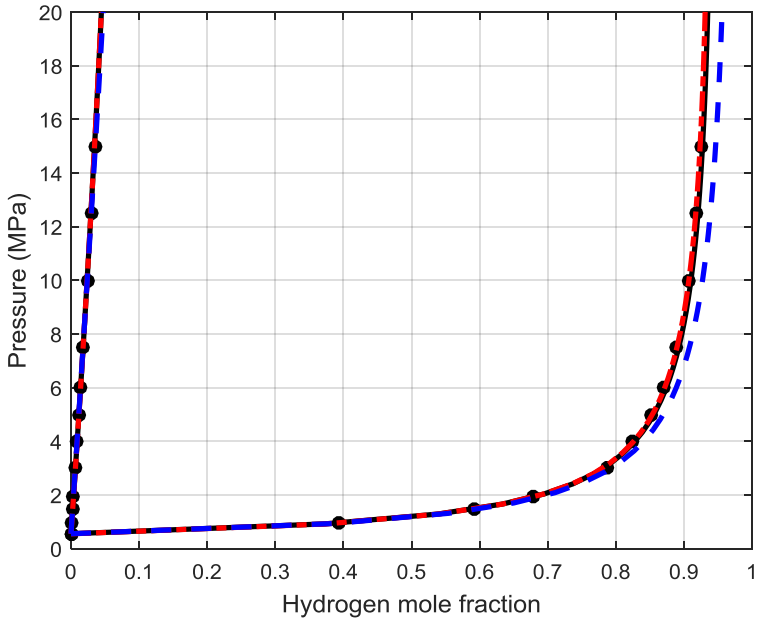

Figure 6.7: Pressure - composition VLE phase diagram for the CO_2 - H_2 mixture, at T= 218.15 K. Experimental data [176] are represented by data points and correlations ($k_{ij} \neq 0$) by lines: (—) SRK, (— · —) PR, (— — —) PC-SAFT.

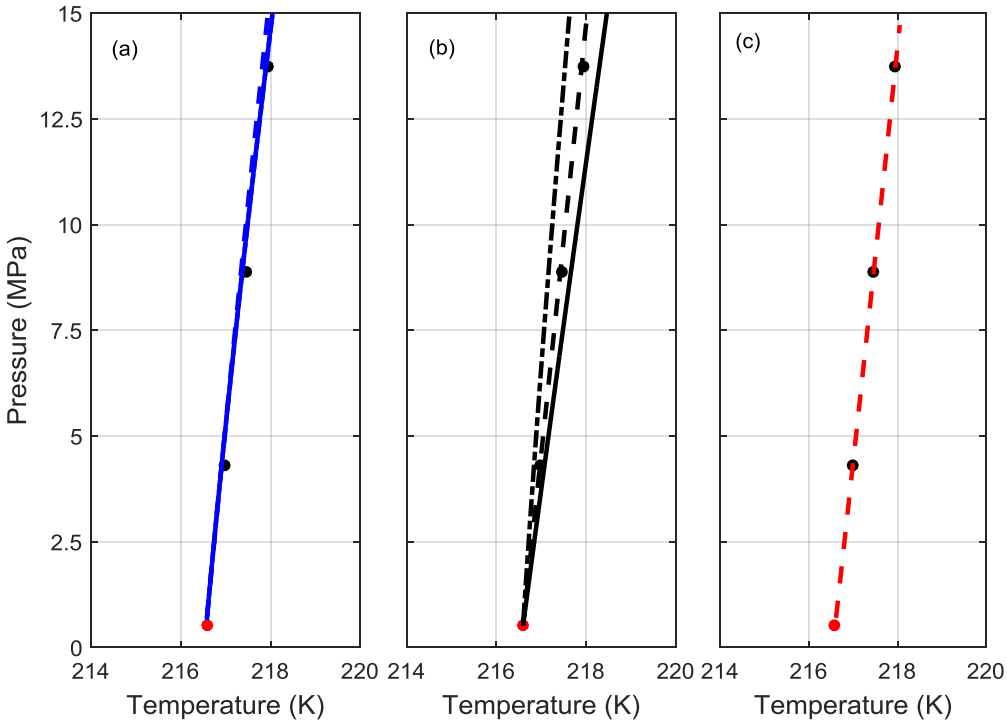

Figure 6.8: Prediction of the SLGE of the CO_2 - H_2 mixture when k_{ij} parameters fitted to experimental binary VLE data at low temperature are used. Results with three different solid-phase models: (a) Thermodynamic Integration model, (b) Empirical Correlation model, (c) Jäger and Span EoS, coupled with three fluid-phase EoS. Experimental data [176] are represented by data points and calculations by lines: (—) SRK, (— · —)PR, (— — —) PC-SAFT.

For the CO_2 - H_2 mixture, k_{ij} parameters were also regressed from experimental binary VLE data [176] at low temperature (T= 218.15 K). The use of BIPs, improves the prediction of the SLGE with all models except for the case of the empirical correlation model, coupled with SRK EoS, while very low deviation is achieved with the Jäger and Span EoS (% AARD = 0.99).

Another important impurity associated with CO_2 transport is CH_4. All the solid-phase models and the fluid-phase EoS were used for the modeling of the SLGE behavior of this mixture.

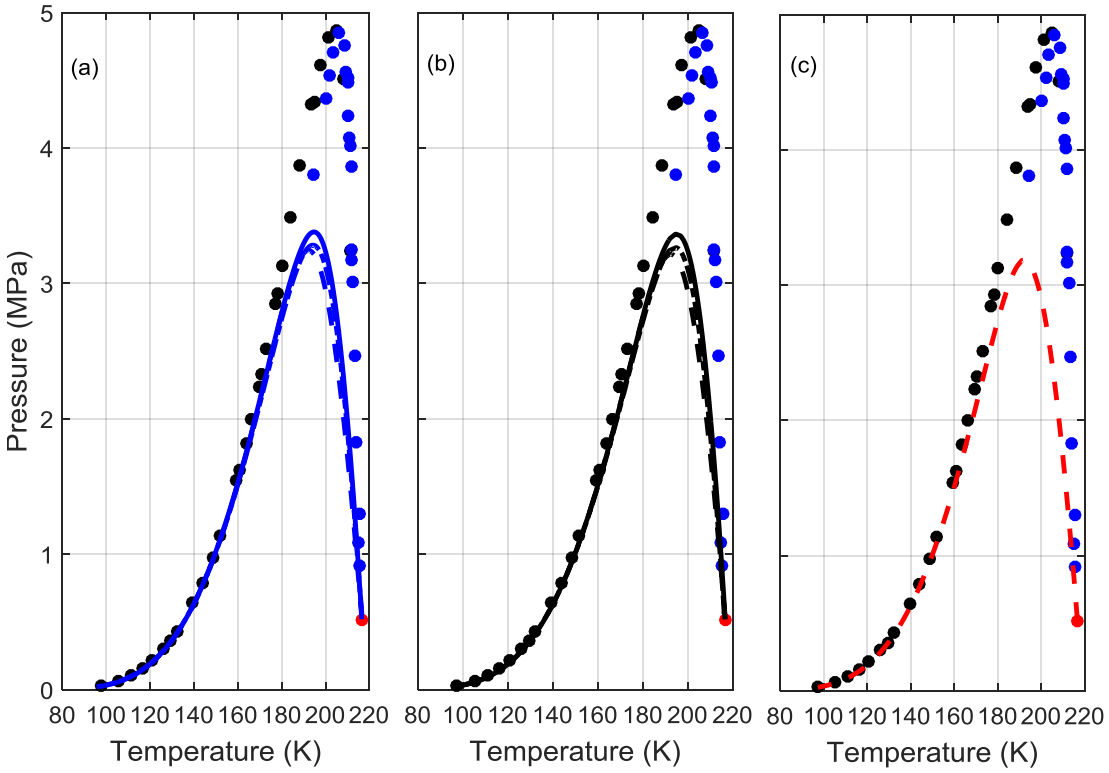

Figure 6.9: Prediction ($k_{ij} = 0$) of the SLGE of the CO_2 - CH_4 mixture. Results with three different solid-phase models: (a) Thermodynamic Integration model, (b) Empirical Correlation model, (c) Jäger and Span EoS, coupled with three fluid-phase EoS. Experimental data [177, 178] are represented by data points and calculations by lines: $(-)$ SRK, $(-\cdot-)$PR, $(---)$ PC-SAFT.

The prediction of the low temperature data is very accurate but the models fail to reproduce the high temperature, high pressure range of the SLGE locus. In general, the performance of all models is similar with deviations varying from 12.82 to 14.79 %. In Figure 6.9, the calculations when all BIPs are set equal to zero are presented. To obtain a more accurate prediction of the SLGE locus, k_{ij} parameters, regressed from experimental CO_2 - CH_4 VLE data over a wide temperature range from Diamantonis et

al. [13] were used. The use of the BIPs results in a very accurate prediction of the SLGE behavior with very low deviations varying in the range of 1.67 to 3.07 %. The most accurate model is the thermodynamic integration coupled with the PR EoS. In Figure 6.10, calculations are compared to experimental data.

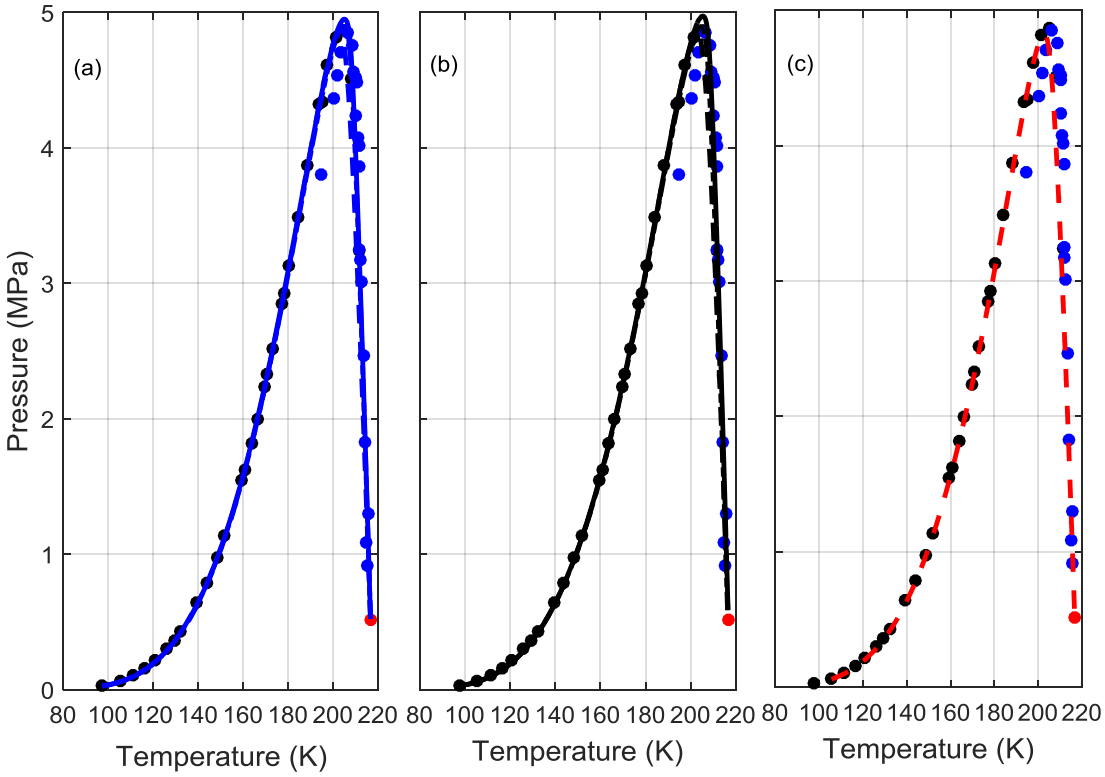

Figure 6.10: Prediction of the SLGE of the CO_2 - CH_4 mixture when k_{ij} parameters fitted to experimental binary VLE data from Diamantonis et al. are used. Results with three different solid-phase models: (a) Thermodynamic Integration model, (b) Empirical Correlation model, (c) Jäger and Span EoS, coupled with three fluid-phase EoS. Experimental data [177, 178] are represented by data points and calculations by lines: $(-)$ SRK, $(-\cdot-)$PR, $(--)$ PC-SAFT.

The use of BIPs regressed over a wide temperature range permits a unified description of both the VLE and SLGE behavior of this mixture. Figure 6.11 provides the SLGE calculations with the thermodynamic integration model coupled with PR EoS and the calculated liquid-gas (LG) critical locus of the binary mixture. Both calculations were performed with the same k_{ij} parameters and an excellent agreement is obtained compared to the experimentally measured LG critical locus [177, 179, 180].

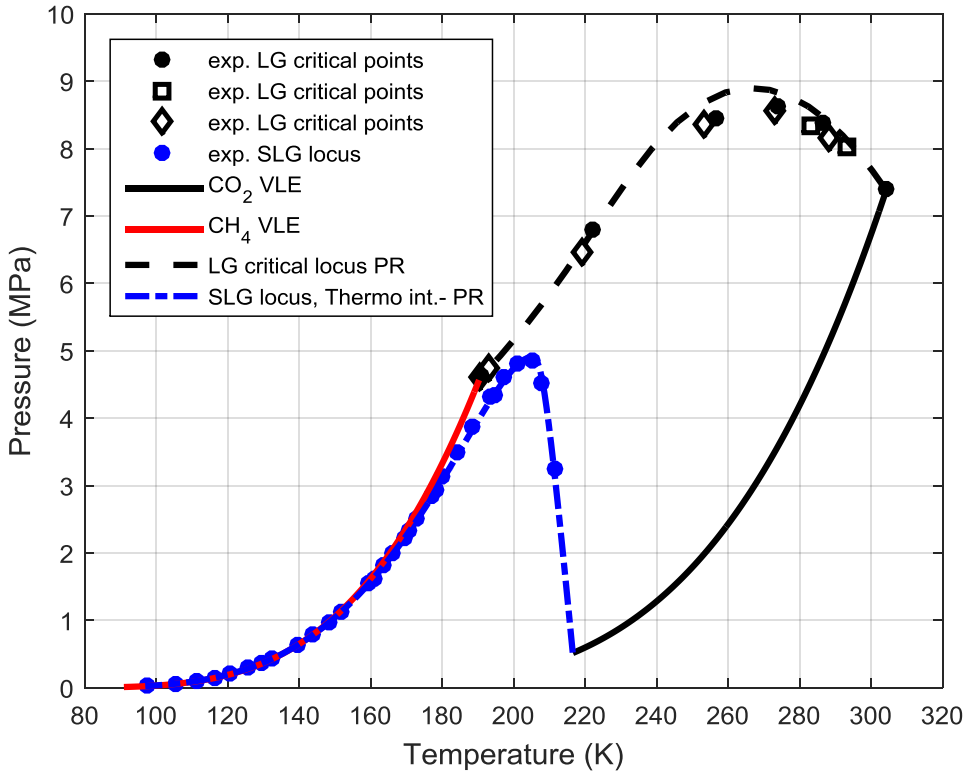

Figure 6.11: P-T projection of the SLGE and LG critical locus of the CO_2 - CH_4 mixture when k_{ij} parameters fitted to experimental binary VLE data are used [13]. Calculations with the Thermodynamic Integration model coupled with the PR EoS.

6.3. Conclusions

Three solid-phase thermodynamic models of different complexity were coupled with three fluid-phase EoS to model the SFE of pure CO_2 and binary mixtures of CO_2 with other compounds. Scarcity of experimental data for two-phase SFE of CO_2 mixtures relevant to CCS applications, led to the evaluation of the performance of each combined model on SLGE experimental data from literature.

The results show that a model that successfully reproduces the pure solid-former triple or normal melting point will predict more accurately the SLGE locus of the mixture. In this context, the thermodynamic integration model and the Jäger and Span EoS provide in general better predictions of the SLGE, when all BIPs are zero for the mixtures of CO_2 with N_2 and H_2. For these two mixtures, the empirical correlation model is comparable to the other two models only when coupled with PC-SAFT EoS which accurately reproduces the pure CO_2 triple point. The use of BIPs, regressed from binary VLE data at low temperature, significantly improves the prediction of the SLGE behavior for most models. All models provide very similar results for the mixture of CO_2

with CH_4 and very low deviations are achieved with the use of BIPs regressed from binary VLE data over a wide temperature range. The use of these BIPs results also to a successful unified description of both the SLGE and the LG critical locus of the mixture with PR EoS.

7. Vapor-Liquid Equilibrium of Asymmetric CH_4 mixtures

7.1. Introduction

In Chapter 2, the challenges associated with the experimental determination and the modeling of the VLE of asymmetric CH_4 mixtures were highlighted. The phase equilibria of CH_4 binary mixtures with *n*-alkanes up to *n*-$C_{10}H_{22}$ are well studied in terms of experimental measurements. The mixture of CH_4 with *n*-$C_{16}H_{34}$ constitutes a very well-studied benchmark that is used also for the validation of experimental apparatuses. However, experimentally measured VLE data for mixtures with lower asymmetry, such as CH_4 - *n*-$C_{12}H_{26}$ and CH_4 - *n*-$C_{14}H_{30}$ are much scarcer and the available experimental data do not cover the full temperature and pressure range of conditions which are encountered in multicomponent applications. In cases of mixtures with higher asymmetry, the reported experimental data are also not sufficient. Table 7.1 summarizes the available VLE experimental data from literature for binary CH_4 - *n*-alkane mixtures. As the asymmetry of a mixture increases, so does the temperature and pressure range where VLE is exhibited. Thus, experimental measurements have to be carried out at very high temperatures and pressures, which significantly increases the difficulty and the cost.

Molecular simulation is a powerful tool for the accurate prediction of phase equilibria and transport properties of pure components and binary mixtures [181-184]. During the past three decades, the rapid development of computers and statistical mechanics enabled the development of accurate potentials representing the intermolecular interactions and the simulation of the phase equilibria of various complex systems [181, 185]. Monte Carlo simulation in the Gibbs Ensemble (GEMC) is the primary tool for calculating the phase coexistence of pure components and mixtures [186, 187]. In the GEMC, two phases are simulated explicitly in two different simulation boxes without an interface. Molecules in the same simulation box interact with each other, but there are no interactions between molecules of different simulation boxes. Equilibrium is obtained by variation of the volume of each box, molecule exchange between the boxes and random displacement of the molecules. Although GEMC provides a straightforward route to determine accurate coexistence densities, the computation of critical parameters is not always easy [188].

Table 7.1: Experimental binary VLE data of CH_4 - *n*-alkane mixtures examined in this work.

Temperature (K)	Pressure (MPa)	Ref
	CH_4 - *n*-$C_{10}H_{22}$	
244.26 - 277.59	1.56 - 6.90	[189]
263.15 - 303.15	1.60 - 36.53	[190]
310.90 - 410.90	1.04 - 8.65	[191]
423.15 - 583.05	3.04 - 18.68	[192]
237.15 - 423.15	0.053 - 10.13	[193]
310.93 - 510.93	0.14 - 36.20	[194]
293.15 - 472.47	11.30 - 35.98	[195]
	CH_4 - *n*-$C_{12}H_{26}$	
263.15 - 303.15	1.41 - 49.48	[196]
323.2 - 373.2	1.33 - 10.38	[191]
374.05	9.97 - 40.79	[197]
	CH_4 - *n*-$C_{16}H_{34}$	
290.00 - 360.00	2.15 - 70.35	[198]
293.15 - 313.15	2.09 - 69.55	[199]
303.20 - 323.20	0.06 - 0.51	[200]
324.00 - 413.20	7.60 - 31.90	[201]
462.45 - 703.55	2.05 - 25.26	[202]
623.10	2.50 - 18.00	[203]
	CH_4 - *n*-$C_{20}H_{42}$	
313.15	0.10 – 6.08	[204]
323.20 - 423.20	0.95 - 10.69	[205]
323.15 - 353.15	0.41 - 83.40	[206]
373.35 - 573.15	1.01 - 5.05	[207]
	CH_4 - *n*-$C_{24}H_{50}$	
325.00 - 425.00	1.93 - 104.05	[208]
373.15 - 573.15	1.01 - 5.07	[209]
374.05	20.10 - 84.30	[210]

To that end, alternative simulation methods such as the histogram reweighting in the grand-canonical ensemble [211, 212], the Gibbs-Duhem integration technique [213, 214] and the iterative Monte Carlo scheme [215] (SPECS) can be very efficient, provided that the number of components is limited and the acceptance probability for insertions/deletions of molecules is sufficiently high. Nevertheless, GEMC combined with advanced techniques such as the configurational-bias Monte Carlo (CBMC) [216-218] or continuous fractional component Monte Carlo (CFCMC) [219-222], which increase the acceptance probability of the molecule exchange trial move, is still a very reliable and efficient tool for the phase equilibria calculation of hydrocarbon mixtures.

In this Chapter, a methodology for the prediction of the VLE of multicomponent gas condensate mixtures is developed by combining molecular simulation with thermodynamic models in the form of an EoS. Monte Carlo simulations in the Gibbs Ensemble with the TraPPE-UA force field [182] are used for the calculation of VLE data for various binary CH_4 - *n*-alkane mixtures. In total, 5 binary mixtures are investigated: the mixtures of CH_4 with *n*-$C_{10}H_{22}$, *n*-$C_{12}H_{26}$, *n*-$C_{16}H_{34}$, *n*-$C_{20}H_{42}$ and *n*-$C_{24}H_{50}$. Initially, the GEMC simulation results are validated against the available experimental data and subsequently new calculations are performed at conditions in which no experimental measurements exist. Two sets of k_{ij} parameters for two cubic (SRK, PR) and one higher order (PC-SAFT) EoS are then regressed; one from the available experimental VLE data for the 5 binary mixtures and a second one using the GEMC simulation results. The aim is to compare the variation of the k_{ij} values when fitted to experimental data at the available range of conditions versus the respective k_{ij} values fitted to GEMC simulation data which span an extensive temperature and pressure range. The ability of each EoS to correlate the VLE data depending on the available range of conditions is also assessed. Finally, the EoS considered are used to predict the VLE of multicomponent gas condensate mixtures with both sets of k_{ij} parameters and a comparison between the models is performed.

The gas condensate mixtures considered in this study consist mainly of *n*-alkanes. Although multicomponent mixtures including components like CO_2 and N_2, or even sour gases with high concentration of H_2S (and / or CO_2), better resemble reservoir fluids, the scope of this work is to concentrate on mixtures of alkanes, only. For the five binary CH_4 - *n*-alkanes mixtures studied in this work, an extensive number of MC simulations is required to cover the wide range of temperatures and pressures for the accurate prediction. The consideration of CO_2, N_2 and H_2S would require a significant

number of additional MC simulations to validate and extend the binary mixture data. In addition, molecular simulation studies of hydrocarbons with polar molecules often require modifications of the binary interaction parameters used, mainly due to deficiencies in the force fields of the polar components [223-228].

7.2. Results and Discussion

7.2.1. Monte Carlo Simulation

Monte Carlo simulations were performed in the Gibbs-NPT ensemble to compute the VLE of mixtures [181, 186, 187]. In the Gibbs-NPT ensemble, the volume of the two boxes can be changed independently and different kinds of MC moves are performed to satisfy the equilibrium conditions, *i.e.*, the equality of temperature, pressure, and chemical potential of each component in the coexisting phases. In each MC step, a trial move is selected at random to displace, regrow, rotate or exchange a chosen hydrocarbon chain or change the volume of a randomly selected box. GEMC relies on a sufficient number of molecule exchanges between the simulation boxes. Unfortunately, the acceptance probabilities for these exchanges can be close to zero for the case of long molecules or when densities are high (*e.g.*, a liquid phase at low temperature).

Although GEMC has been used to study a wide range of mixtures, simulation data for asymmetric mixtures of hydrocarbons are scarce. This should be attributed, among others, to the low acceptance probability for the exchange of the long-chain hydrocarbons. At these conditions, advanced simulation techniques such as CBMC [216-218] or CFCMC [219, 220] are used to increase the acceptance probability of the molecule exchange trial move. Details for these simulation techniques are given in Appendix D. In this work, all simulations were performed using the CBMC method, while the CFCMC method was used to verify the results for systems where the exchange of molecules between the boxes is expected to be more difficult (*e.g.* CH_4 - *n*-$C_{20}H_{42}$ and CH_4 - *n*-$C_{24}H_{50}$ at low temperatures and high pressures).

The TraPPE united atom (TraPPE-UA) force field was used for all the *n*-alkanes [182]. In the TraPPE-UA, CH_4, CH_3 and CH_2 groups are modeled as pseudo-atoms with no charges. The non-bonded intra- and intermolecular interactions between the pseudo-atoms are represented by the 12-6 Lennard-Jones (LJ) potential. The LJ parameters used in this study can be found in the work by Martin and Siepmann [182]. Force field and

computational details for the MC simulations are given in Appendix D. All GEMC simulations were carried out with RASPA [229, 230].

The computed VLE from the GEMC simulations depends heavily on the accuracy of the force fields used. As already mentioned, TraPPE-UA was used in all simulations. The choice of this force field was based on various reasons: Siepmann and coworkers reported the VLE of pure alkanes up to *n*-$C_{12}H_{26}$ [182], showing that the TraPPE-UA force field is sufficiently accurate in reproducing the VLE of these hydrocarbons. In addition, the use of united atom force fields is advantageous due to the significant reduction of interaction sites compared to their full atom counterparts (*e.g.*, TraPPE-EH [231]). One of the drawbacks of the TraPPE-UA force field is the tendency to slightly overestimate the vapor pressures and densities [182]. However, the saturated liquid densities and critical temperatures are predicted accurately [182]. Therefore, since the liquid phase properties at high temperatures are represented well by the TraPPE-UA force field, it is expected that the k_{ij} parameters, which are typically fitted to bubble-point data, will not be affected by the deficiency of the model to accurately describe the gas-phase.

To validate the TraPPE-UA force field, the VLE of binary mixtures of CH_4 with different long-chain *n*-alkanes were computed in the Gibbs-NPT ensemble and compared with available experimental data. In Figure 7.1, the simulated VLE data for the most asymmetric mixture (*i.e.*, CH_4 - *n*-$C_{24}H_{50}$) at temperatures ranging from 330 K to 523.15 K are plotted against the available experimental data. Excellent agreement between the two sets of data is observed, even at conditions close to the critical points. Similarly, good agreement is observed for all the mixtures considered, justifying the choice of the TraPPE-UA force field. Relevant comparisons between experiments and simulations can be found in Appendix D (Figure D.1, Figure D.2, Figure D.3, Figure D.4).

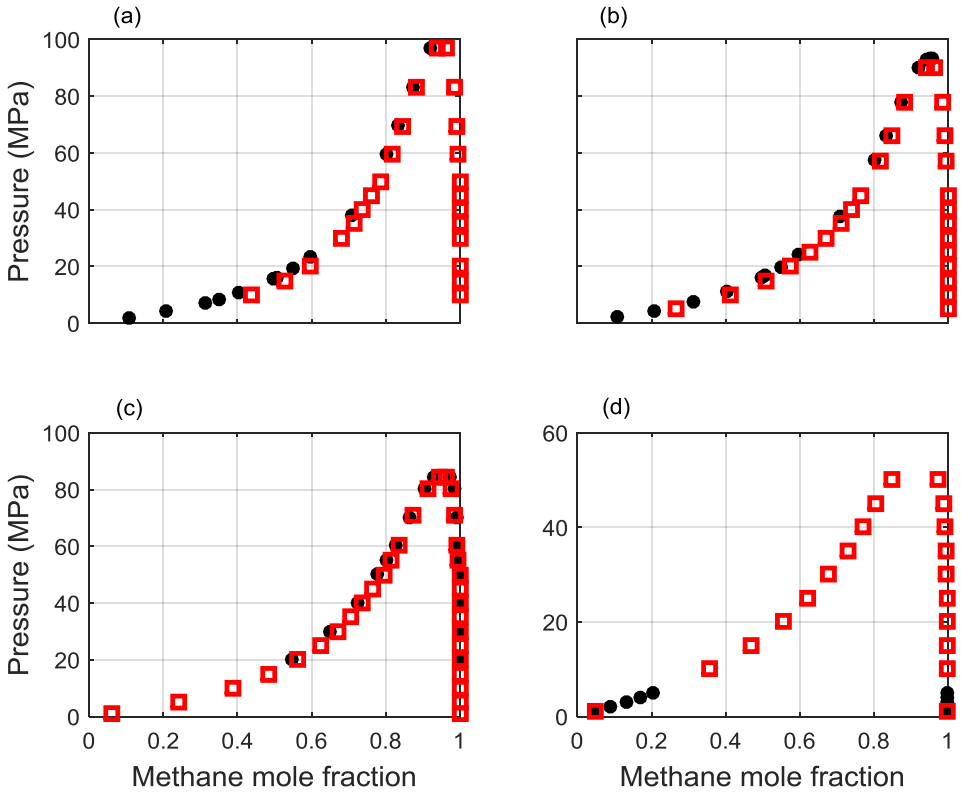

Figure 7.1: Pressure - composition VLE for the CH_4 - *n*-$C_{24}H_{50}$ mixture at various temperatures; (a) T= 330 K, (b) T= 350 K, (c) T= 374.05 K, (d) T= 523.15 K. Experimental data [208-210] are represented by black data points and GEMC simulation data by red squares.

7.2.2. Equation of State Modeling

The accurate phase equilibrium modeling of asymmetric hydrocarbon mixtures with EoS relies heavily on the BIPs between CH_4 and long-chain hydrocarbons [92]. In this work, temperature independent k_{ij} parameters are used in the combining rules of the adopted EoS. A different model selection would require the use of different BIPs, *e.g.*, energetic interactions in Excess Gibbs Energy models, interactions between groups in group contribution schemes, etc.[113, 232, 233]. Except for the thermodynamic model itself, the number of BIPs, their temperature dependency, etc. affects the general correlative ability of the model.

Table C.1 and Table C.2 summarize the pure component parameters used for the cubic and PC-SAFT EoS respectively. The critical properties and the acentric factor for the cubic EoS were taken from the DIPPR [175] database, while the PC-SAFT EoS parameters were taken from Gross and Sadowski [18] except for the *n*-$C_{24}H_{50}$ parameters, which were taken from the MAPS platform v4.0 [234].

7.2.3. Comparison of Calculations from the Various Methods

A major aim in this work is to evaluate k_{ij} parameters by fitting the EoS to GEMC simulation data generated here, and to experimental data available in the literature. As shown in the previous section, GEMC simulations can provide accurate VLE predictions for the binary mixtures considered. In this work, GEMC simulations were also performed at conditions where no experimental data are available. The aim was to cover the entire temperature range from the normal melting temperature to the critical temperature of the long-chain *n*-alkane in every mixture. The target is to show that molecular simulation based on accurate force fields is a powerful tool that can be used to complement experiments and provide useful insight at conditions in which measurements are difficult to be carried out (e.g., high temperature and pressures). The pressure range examined in the simulations spans from low values up to approximately the binary mixture critical point. To avoid conditions where solidification may occur, the lowest isotherm is approximately 10 K higher than the normal melting point and the highest one is approximately 50 K lower than the critical temperature of the long-chain *n*-alkane, respectively.

Two sets of k_{ij} parameters were obtained: One by minimizing the root-mean-square deviation between the bubble pressure values calculated by the EoS and experimental data and the second one by minimizing the same deviation between EoS calculations and GEMC data. Table 7.2 summarizes the % AARD between experimental VLE data and EoS calculations for each mixture and the corresponding k_{ij} values. Table 7.3 summarizes the % AARD and the respective k_{ij} values for the case where GEMC simulation VLE data were used. In the rest of this Chapter, the % AARD and k_{ij} parameters calculated from the experimental VLE data will be referred to as % AARD-EXP and k_{ij}^{EXP}, while those calculated from GEMC simulations as % AARD-MC and k_{ij}^{MC}, respectively. As a general trend, it should be pointed out that the k_{ij} values are relatively small in all cases, and EoS predictions are in reasonable agreement with both experimental and GEMC data, even when $k_{ij} = 0$. An assessment of these calculations is shown in Table 7.2 and Table 7.3.

Table 7.2: %AARD between experimental VLE data and EoS calculations for the mixture bubble pressure and corresponding k_{ij} values.

EoS			CH_4 - *n*-$C_{10}H_{22}$	CH_4 - *n*-$C_{12}H_{26}$	CH_4 - *n*-$C_{16}H_{34}$	CH_4 - *n*-$C_{20}H_{42}$	CH_4 - *n*-$C_{24}H_{50}$
SRK	Pr.	%AARD	9.37	17.49	13.06	13.26	17.49
	Cor.	%AARD	4.30	5.92	4.81	13.62	14.58
		k_{ij}	0.0349	0.0421	0.0565	0.0392	0.0428
PR	Pr.	%AARD	10.13	19.63	14.14	14.45	19.23
	Cor.	%AARD	4.01	5.81	4.96	15.06	16.23
		k_{ij}	0.0389	0.0461	0.0595	0.0421	0.0494
PC-SAFT	Pr.	%AARD	12.85	18.15	21.51	21.64	25.29
	Cor.	%AARD	5.55	5.31	8.47	4.94	5.69
		k_{ij}	0.0208	0.0213	0.0364	0.0375	0.0408
NP			87	40	59	49	67

$$\%\ AARD = \frac{100}{NP}\sum_{i=1}^{NP}\left|\frac{P_i^{calculated} - P_i^{experimental}}{P_i^{experimental}}\right|$$

NP is the number of experimental data points and P_i is the bubble pressure.

"Pr." refers to predictions ($k_{ij} = 0$), whereas "Cor." refers to correlations (calculations with $k_{ij} \neq 0$).

Table 7.3: %AARD between GEMC simulation VLE data and EoS calculations for the mixture bubble pressure and corresponding k_{ij} values regressed from Monte Carlo simulation data.

EoS			CH_4 - *n*-$C_{10}H_{22}$	CH_4 - *n*-$C_{12}H_{26}$	CH_4 - *n*-$C_{16}H_{34}$	CH_4 - *n*-$C_{20}H_{42}$	CH_4 - *n*-$C_{24}H_{50}$
SRK	Pr.	%AARD	16.44	10.62	11.97	13.06	15.52
	Cor.	%AARD	3.93	4.34	7.31	8.38	12.41
		k_{ij}	0.0379	0.0368	0.0526	0.0436	0.0355
PR	Pr.	%AARD	18.30	11.84	12.12	14.95	17.52
	Cor.	%AARD	3.79	3.90	7.30	8.93	12.66
		k_{ij}	0.0416	0.0406	0.0538	0.0497	0.0434
PC-SAFT	Pr.	%AARD	13.52	15.16	18.27	20.49	21.85
	Cor.	%AARD	3.79	6.26	7.28	8.68	8.97
		k_{ij}	0.0150	0.0237	0.0332	0.0344	0.0343
NP			53	64	54	69	86

$$\%\ AARD = \frac{100}{NP}\sum_{i=1}^{NP}\left|\frac{P_i^{calculated} - P_i^{experimental}}{P_i^{experimental}}\right|$$

NP is the number of experimental data points and P_i is the bubble pressure.

"Pr." refers to predictions ($k_{ij} = 0$), whereas "Cor." refers to correlations (calculations with $k_{ij} \neq 0$).

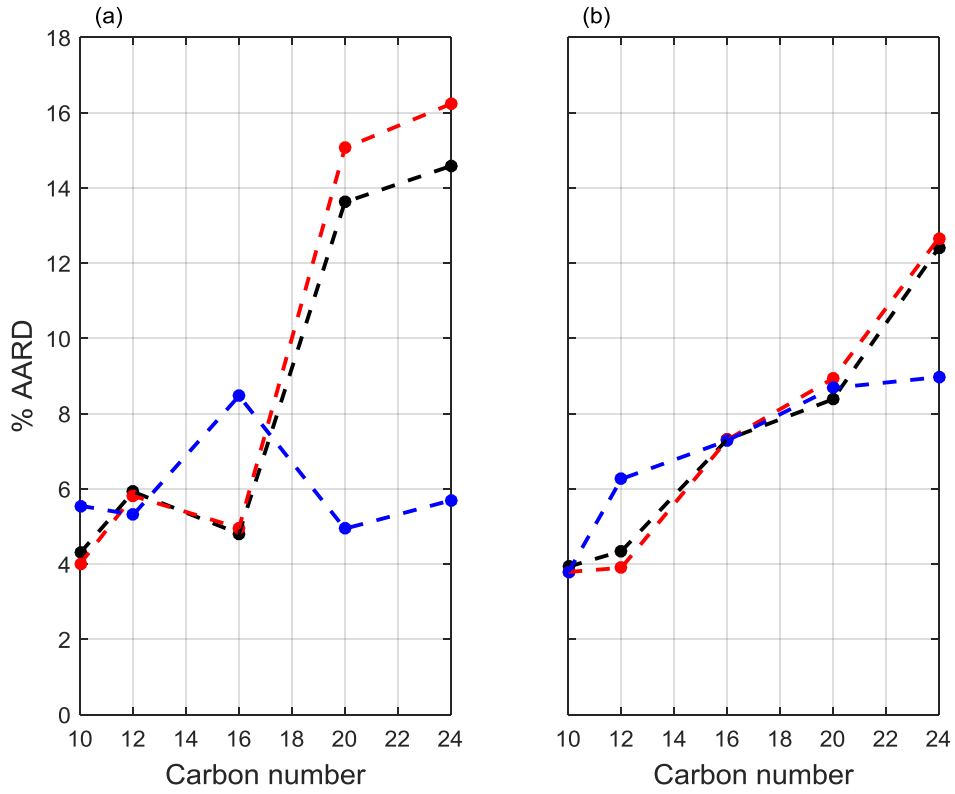

Figure 7.2: % AARD vs carbon number of the long-chain hydrocarbon for binary CH_4 mixtures. Left panel shows the % AARD when k_{ij} parameters are fitted to experimental data. Right panel shows the % AARD when k_{ij} parameters are fitted to GEMC simulation data. Black lines correspond to SRK, red to PR and blue to PC-SAFT EoS.

In Figure 7.2, the variation of % AARD-EXP and % AARD-MC with the carbon number of the long-chain *n*-alkane in each binary mixture is presented. All the binary mixtures considered in this work include only *n*-alkanes and one might expect that the % AARD will increase as the asymmetry of each mixture increases, *i.e.*, with the carbon number. However, this is not always the case here. The two cubic EoS essentially deviate from the expected behavior because of the % AARD-EXP value of CH_4 - *n*-$C_{16}H_{34}$ mixture, which has a lower value compared to CH_4 - *n*-$C_{12}H_{26}$ mixture. The most prevalent deviation from the expected behavior is presented by PC-SAFT EoS which correlates with almost the same accuracy in terms of % AARD-EXP values (approximately 5.3%) the VLE of CH_4 mixtures with *n*-$C_{10}H_{22}$, *n*-$C_{12}H_{26}$, *n*-$C_{20}H_{42}$ and *n*-$C_{24}H_{50}$. A distinctively higher value (% AARD-EXP = 8.47) is presented for the CH_4 - *n*-$C_{16}H_{34}$ mixture. The relative constant k_{ij} can be attributed partly to the strong theoretical basis of PC-SAFT that captures accurately the properties of long-chain hydrocarbon molecules.

The same trend presented for the % AARD-EXP of the cubic EoS in this work is also followed by the respective values reported by Yan et al. [89], while the absolute values are also similar. The k_{ij}^{EXP} values regressed in this work are in very good agreement with those reported by Novak et al. [92] that also used the DIPPR [175] database for the pure component parameters of the cubic EoS and the Gross and Sadowski [18] ones for PC-SAFT. Taking into account the possible differences in tolerance values for the fitting of BIPs, the calculation procedure for the VLE and the exact experimental data used by the various authors, it can be assessed that the agreement with prior work is sufficiently good.

As it can be observed from Figure 7.2(b), the % AARD-MC for all three EoS always increases with the carbon number, following the expected behavior. The three EoS present similar % AARD-MC values for the mixtures of CH_4 with *n*-$C_{10}H_{22}$, *n*-$C_{16}H_{34}$ and *n*-$C_{20}H_{42}$, while PC-SAFT presents two distinct values for the CH_4 - *n*-$C_{12}H_{26}$ and CH_4 - *n*-$C_{24}H_{50}$ mixtures when compared to the cubic EoS. The two cubic EoS present very similar % AARD-MC values for all the binary mixtures considered. Comparing the % AARD-MC values to the respective % AARD-EXP, it is observed that the CH_4 - *n*-$C_{10}H_{22}$ value remains almost constant for the cubic EoS, while others change significantly resulting in a totally different assessment between the three models. A more detailed analysis for each mixture and the correlative ability of the EoS considered is presented below.

Figure 7.3 through Figure 7.7 refer to P-x,y phase diagrams for the binary mixtures considered at various temperatures, with the three EoS using k_{ij} parameters regressed from GEMC simulation data. Experimental and GEMC simulation data are plotted together (when available) at the selected temperatures, showing the very good agreement between the two datasets. Figure 7.3 shows the P-x,y diagrams for the CH_4 - *n*-$C_{10}H_{22}$ mixture at temperatures from 244.26 to 583.05 K. All EoS correlate accurately the two datasets with the % AARD-MC being almost equal for the cubic and PC-SAFT. Furthermore, the % AARD-EXP for the cubic EoS is similar to % AARD-MC, while a higher difference is presented for PC-SAFT. This higher variation of the % AARD value for PC-SAFT is attributed to the VLE data at 244.26 K. The k_{ij} parameters of PC-SAFT EoS generally show higher sensitivity to the dataset used for the regression, compared to the respective ones of cubic EoS [89, 235]. However, similar sensitivity of the k_{ij} parameters for the three EoS is shown when high temperature VLE GEMC simulation

data are added. This indicates that the higher sensitivity of the BIPs of PC-SAFT may be attributed mainly to the low temperature VLE correlation.

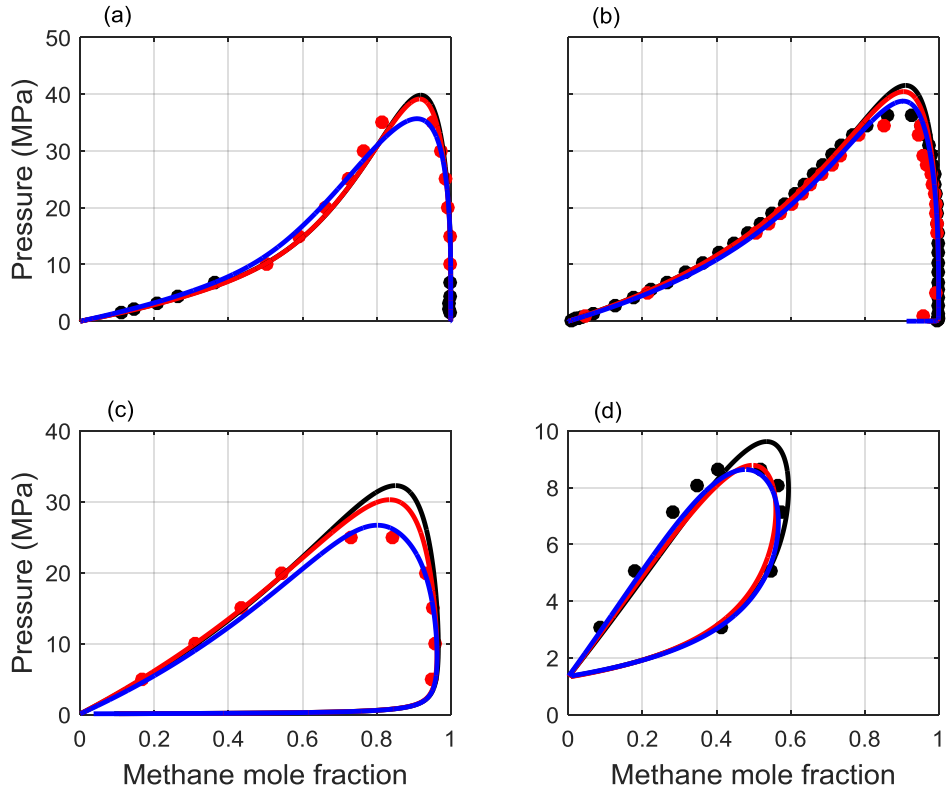

Figure 7.3: Pressure - composition VLE phase diagrams for the CH_4 - *n*-$C_{10}H_{22}$ mixture at various temperatures; (a) T= 244.26 K, (b) T= 310.93 K, (c) T= 450 K, (d) T= 583.05 K. Experimental data [189, 192, 194] are represented by black data points. GEMC simulation data are represented by red data points. Calculations with EoS are represented by lines and are performed with k_{ij} parameters fitted to GEMC simulation data. Black lines correspond to SRK, red to PR and blue to PC-SAFT EoS.

In Figure 7.4, the VLE correlation results for the CH_4 - *n*-$C_{12}H_{26}$ mixture are presented with the three EoS. The isotherms at 303.15 and 373.2 K are correlated almost with the same accuracy by the three EoS. At higher temperatures (450 and 550 K), cubic EoS correlate slightly more accurately the equilibrium pressure away from the critical point compared to PC-SAFT, in expense of a more significant critical point over prediction. It is prevalent even at 373.2 K, that SRK presents the most significant over prediction of the critical point, with PR following and with PC-SAFT being the most accurate. Comparing the % AARD-EXP and % AARD-MC values for this mixture, it can be assessed that the addition of high-temperature VLE data for the regression shifts the % AARD to lower values for the cubic EoS, since they are more successful in correlating the high temperature VLE and to a higher value for PC-SAFT which correlates better the low temperature data. Note that the available experimental VLE

data for this mixture are in the range of 263.15 - 373.2 K, while the critical temperature of *n*-$C_{12}H_{26}$ is 650 K. GEMC simulations were performed at isotherms from 283 to 600 K to obtain a wider range of pseudo-experimental data for CH_4 - *n*-$C_{12}H_{26}$. Results are plotted in Figure 7.5 for the CH_4 - *n*-$C_{16}H_{34}$ mixture with calculations from the three EoS and k_{ij}^{MC}. In this case, the difference between the three EoS in the critical point prediction becomes even more pronounced with the increase of temperature.

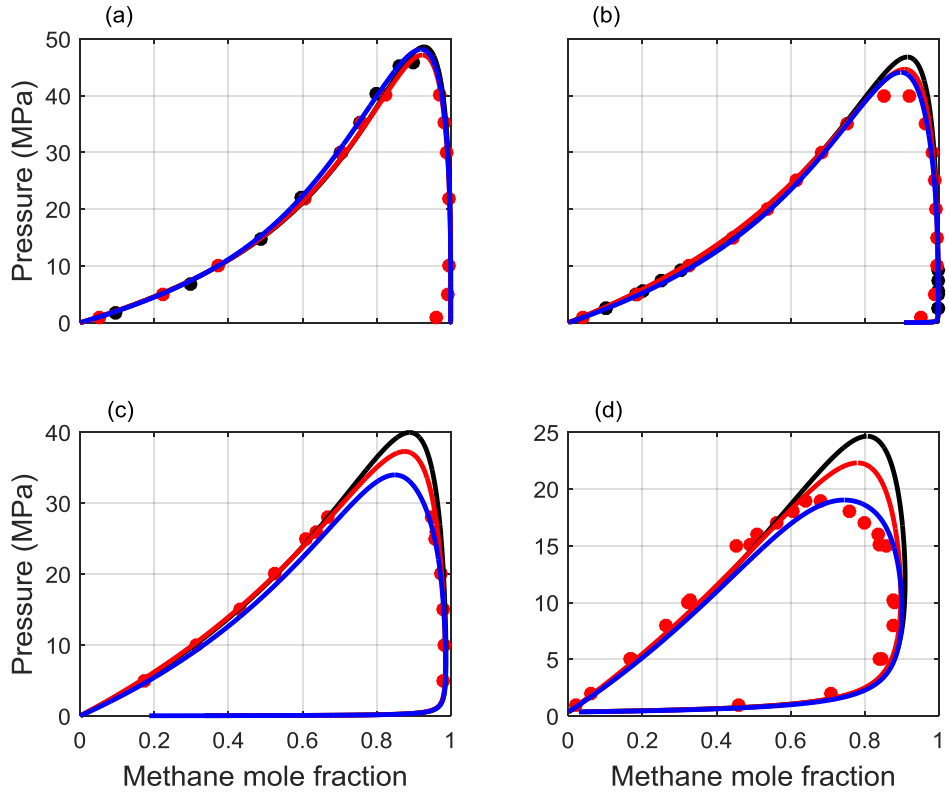

Figure 7.4: Pressure - composition VLE phase diagrams for the CH_4 - *n*-$C_{12}H_{26}$ mixture at various temperatures; (a) T= 303.15 K, (b) T= 373.2 K, (c) T= 450 K, (d) T= 550 K. Experimental data [191, 196] are represented by black data points. GEMC simulation data are represented by red data points. Calculations with EoS are represented by lines and are performed with k_{ij} parameters fitted to GEMC simulation data. Black lines correspond to SRK, red to PR and blue to PC-SAFT EoS.

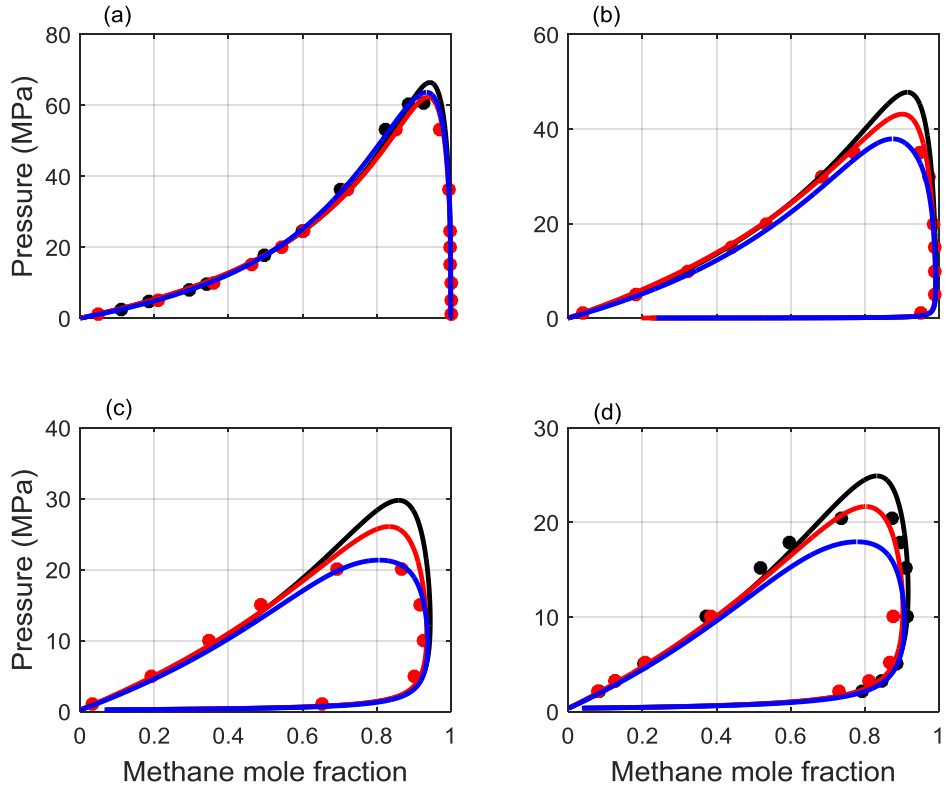

Figure 7.5: Pressure - composition VLE phase diagrams for the CH_4 - *n*-$C_{16}H_{34}$ mixture at various temperatures; (a) T= 340 K, (b) T= 500 K, (c) T= 600 K, (d) T= 623.15 K. Experimental data [198, 202] are represented by black data points. GEMC simulation data are represented by red data points. Calculations with EoS are represented by lines and are performed with k_{ij} parameters fitted to GEMC simulation data. Black lines correspond to SRK, red to PR and blue to PC-SAFT EoS.

Figure 7.6 and Figure 7.7 show the VLE results for the mixtures of CH_4 with *n*-$C_{20}H_{42}$ and *n*-$C_{24}H_{50}$. For these two mixtures, the improved correlation of the VLE behavior at low temperatures (323.15 and 330 K respectively) with PC-SAFT EoS is more pronounced. At high temperatures, especially from 500 K and higher, cubic EoS correlate more accurately the equilibrium pressure than PC-SAFT. As with the previous mixtures, SRK EoS predicts the highest critical pressures, while PC-SAFT EoS predicts the lowest ones. At temperatures close to the normal melting temperature of the long-chain *n*-alkane of every mixture, the two cubic EoS predict almost the same critical pressure. The experimental data for the CH_4 - *n*-$C_{20}H_{42}$ mixture span from 323.15 to 573.15 K, while GEMC simulation data cover a temperature range from 323 to 700 K. The respective range for the CH_4 - *n*-$C_{24}H_{50}$ mixture is 330 - 573.15 K for the experiments and 330 - 750 K for the GEMC simulation data.

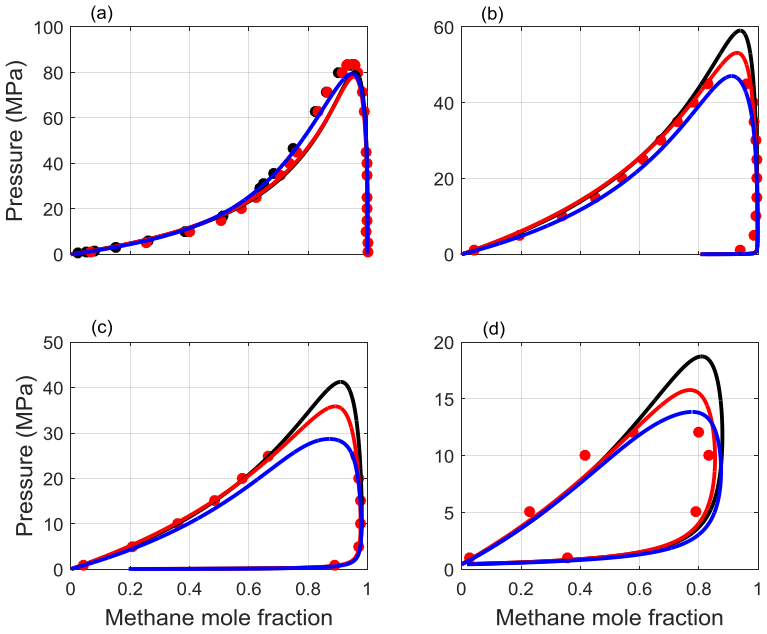

Figure 7.6: Pressure - composition VLE phase diagrams for the CH_4 - n-$C_{20}H_{42}$ mixture at various temperatures; (a) T= 323.15 K, (b) T= 500 K, (c) T= 600 K, (d) T= 700 K. Experimental data [206] are represented by black data points. GEMC simulation data are represented by red data points. Calculations with EoS are represented by lines and are performed with k_{ij} parameters fitted to GEMC simulation data. Black lines correspond to SRK, red to PR and blue to PC-SAFT EoS.

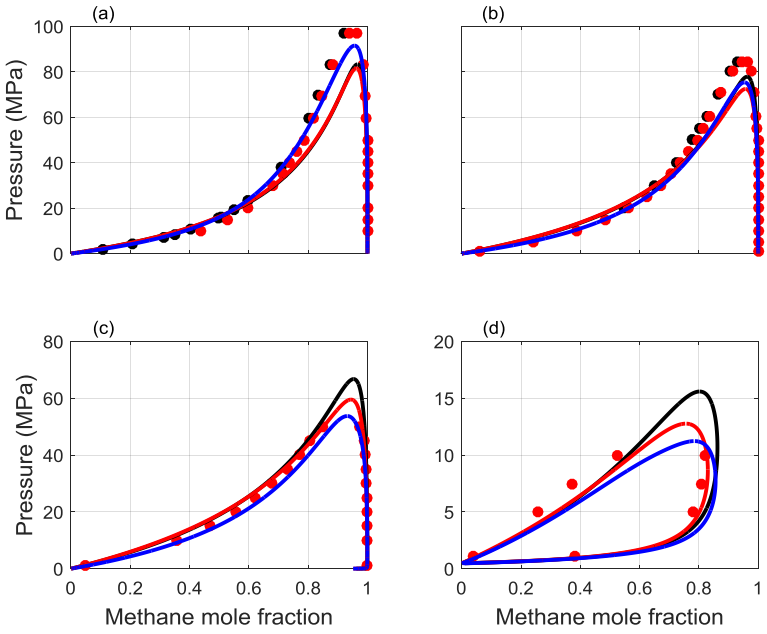

Figure 7.7: Pressure - composition VLE phase diagrams for the CH_4 - n-$C_{24}H_{50}$ mixture at various temperatures; (a) T= 330 K, (b) T= 374.05 K, (c) T= 500 K, (d) T= 750 K. Experimental data [208, 210] are represented by black data points. GEMC simulation data are represented by red data points. Calculations with EoS are represented by lines and are performed with k_{ij} parameters fitted to GEMC simulation data. Black lines correspond to SRK, red to PR and blue to PC-SAFT EoS.

The two sets of k_{ij} parameters were used for the calculation of constant composition VLE of asymmetric multicomponent mixtures, comprised mainly of *n*-alkanes. The compositions of the mixtures studied are summarized in Table 7.4. The k_{ij} parameters between CH_4 and alkanes with lower molecular weight than *n*-$C_{10}H_{22}$ were taken from Novak et al. [92]. Alternatively the interaction parameter values for these binary pairs could have been set equal to zero and almost the same modeling results would have been obtained, since their effect is negligible, as shown by Novak et al.

Table 7.4: Composition in mole fractions of the synthetic gas condensates studied in this work.

Compound	SGC1	SGC2	SGC3	SGC4	SGC5	SGC6	SGC7
CH_4	0.8119	0.8512	0.7000	0.8997	0.7905	0.8232	0.8205
C_3H_8						0.0871	0.0895
n-C_4H_{10}	0.1385	0.0991	0.1200	0.0300			
i-C_5H_{12}					0.0023		
n-C_5H_{12}					0.1999	0.0505	0.0500
n-C_6H_{14}					0.0023		
n-C_8H_{18}			0.0700	0.0297			
n-$C_{10}H_{22}$	0.0496					0.0198	0.0199
n-$C_{12}H_{26}$		0.0497	0.0499	0.0207			
n-$C_{16}H_{34}$			0.0301	0.0149		0.0194	0.0201
n-$C_{20}H_{42}$			0.0300	0.0050			
n-$C_{24}H_{50}$					0.0050		

In Figure 7.8, the results for the multicomponent mixtures considered are presented, with the two cubic and PC-SAFT EoS. The difference between calculations with the two sets of k_{ij} parameters is practically negligible. The highest deviations between the two sets of calculations are presented with PC-SAFT EoS for the synthetic gas condensates (SGCs) 4, 5, 6 and 7. For SGC4, the deviations in the calculated equilibrium pressure start close to 280 K and are approximately 1 MPa. For SGCs 5, 6 and 7 the deviations appear close to 290 K and vary from 1 to 2.5 MPa. Both cubic EoS are much more insensitive to the choice of the set of k_{ij} parameters for the mixtures mentioned. Very low sensitivity to the choice of BIPs is manifested in SGC3 mixture with all three EoS. It should be noticed that the composition of SGC3 in terms of high molecular weight *n*-alkanes is higher compared to SGC4. This results in the equilibrium measurements being bubble points instead of dew points, as opposed to all the other mixtures studied. This is the only mixture in which PC-SAFT EoS is clearly more accurate than the cubic ones.

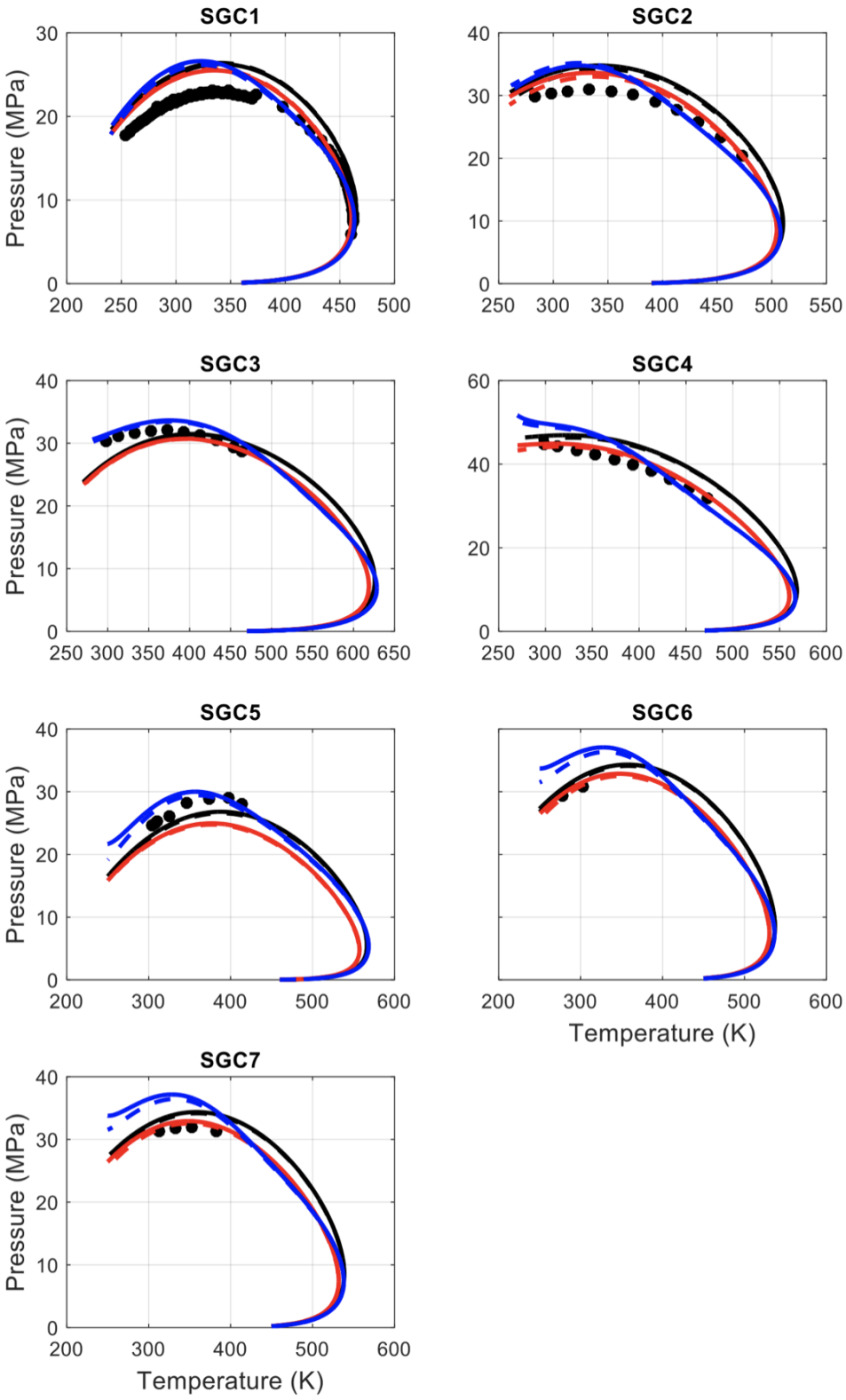

Figure 7.8: Constant composition phase envelopes for the synthetic gas condensate mixtures (SGC1, SGC2, SGC3, SGC4, SGC5, SGC6, SGC7) studied in this work. The compositions of the mixtures are listed in Table 7.4. Experimental data [88, 236-238] are represented by points and calculations by lines. Solid lines correspond to calculations with k_{ij} parameters fitted to experimental binary VLE data. Dashed lines correspond to calculations with k_{ij} parameters fitted to GEMC simulation binary VLE data. Black lines correspond to SRK, red to PR and blue to PC-SAFT EoS.

7.3. Conclusions

A predictive methodology was developed for the calculation of the VLE of multicomponent hydrocarbon mixtures with high asymmetry, combining molecular simulations and EoS. MC simulations in the Gibbs Ensemble were used for the calculation of the VLE of binary CH_4 mixtures with *n*-alkanes, to be used as a pseudo-experimental dataset, for a consistent fitting of the BIPs of the thermodynamic models. Two cubic (SRK, PR) and one higher order (PC-SAFT) EoS were used to correlate the binary-mixture VLE data and subsequently predict the multicomponent mixture VLE. GEMC simulations with the TraPPE-UA force field were validated with experimental VLE data for the binary mixtures considered. It is shown that accurate predictions can be retrieved even in very asymmetric mixtures. It is assessed that GEMC simulations can be carried out with high accuracy at temperatures and pressures in which no experimental VLE data exist, thus covering a wide range of conditions, suitable for fitting BIPs of thermodynamic models. k_{ij} parameters with the three EoS were regressed from both experimental and GEMC simulation data. It is shown that the use of a dataset that spans a wide range of temperatures and pressures consistently affects the k_{ij} values. It is also observed that for the CH_4 - *n*-$C_{10}H_{22}$ mixture the three EoS correlate with equal accuracy the VLE behavior, while with increasing asymmetry, PC-SAFT EoS is more successful in correlating the low temperature data and cubic EoS the high temperature data. Finally, the BIPs regressed from GEMC simulation data lead to equally accurate modeling results for multicomponent mixtures, compared to those regressed from experimental binary mixture data. Consequently, molecular simulations using accurate force fields can be used to generate precise VLE data for binary mixtures of CH_4 with *n*-alkanes, in the absence of experimental data.

8. Solid-Liquid-Gas Equilibrium of CH_4 - *n*-Alkane Mixtures

8.1. Introduction

In this Chapter, the accuracy of widely used by industry and academia fluid-phase EoS (SRK, PR, PC-SAFT), in combination with a solid-phase model, is investigated towards the prediction and correlation of the SLGE behavior of binary CH_4 mixtures with *n*-alkanes. The approach proposed by Seiler et al. [162] is adopted for the calculation of the solid-phase fugacity. A detailed analysis regarding the methodology itself was presented in Chapter 3. The use of the McHugh et al. [160] approach for calculating the solid-phase fugacity was avoided, because it does not always reproduce the pure solid-former normal melting point (or triple point), but it depends on the fluid-phase EoS used. As shown in Chapter 6 and in other studies [134, 239], a model (solid-phase modeling approach combined with a fluid-phase EoS) that successfully reproduces the pure solid-forming compound normal melting (or triple) point, will predict more accurately the SLGE line of a mixture. In this context, the method proposed by Seiler et al. [162] reproduces accurately the normal melting point since it is an input parameter for this approach. Furthermore, if the normal melting point prediction is very poor, which is not unusual with the McHugh approach, the overall description of the SLGE line will be very poor also [134, 239].

In total, 10 binary mixtures are investigated, starting from the CH_4 - *n*-C_6H_{14} mixture, while the most asymmetric one is the CH_4 - *n*-$C_{36}H_{74}$ mixture. The predictive capabilities of each combined model are validated against available experimental data. BIPs are regressed from binary mixture VLE data and their effect in the prediction of the SLGE behavior is assessed. Furthermore, various modifications on the basic solid-phase model are applied step by step, in order to evaluate the effect of each term and in this way enhance the performance of each combined model. The target is to obtain a simple and accurate combined model that also retains a predictive nature (no direct fitting on the SLGE data). Moreover, a specific volume translation strategy is adopted for the cubic EoS, in order to describe more accurately the pressure dependency of the liquid molar volume in the Poynting correction. A correlation of the k_{ij} parameters with the carbon number of *n*-alkanes is proposed for each fluid-phase EoS, which can be used as an alternative to fitting k_{ij} parameters for other similar mixtures at this range of conditions. Moreover, a new approach is presented, that incorporates the pressure dependent

proportionality coefficient - $\hat{\beta}$ - between the solid and the liquid molar volumes in the solid-phase fugacity coefficient equation, as proposed by Ameri-Mahabadian et al. [112]. This method essentially combines the Poynting correction approach of Pauly et al. [104] with the pressure dependent $\hat{\beta}$ that Ameri-Mahabadian et al. proposed. However, in the latter approach, $\hat{\beta}$ is used to calculate the thermophysical properties of the solid-phase model at high pressures. In this work, it is used in the Poynting correction, the fluid part of which is calculated through the fluid-phase EoS. It has to be noted that the proposed method, following Ameri-Mahabadian et al., requires direct fitting on the SLGE experimental data and thus it is not fully predictive. Finally, taking into account that each binary mixture examined included only CH_4 and an *n*-alkane, a pure solid phase was assumed in all cases which consisted of the heavy *n*-alkane.

8.2. Solid-Phase Models

8.2.1. Basic Solid-Phase Model

The basic solid-phase model adopted in this work is the one proposed by Seiler et al. [162], discussed in Chapter 3 and is based on a thermodynamic integration process. As already mentioned in Chapter 6, if the thermophysical properties of one of the fluid phases (liquid or vapor) that can be used as reference for the solid-phase fugacity are known more accurately, this will have an impact on the final calculations. In SLGE calculations, it is more common calculate the solid-phase fugacity based on the pure, subcooled melt reference state. Furthermore, the terms that correspond to the difference between the solid and the liquid isobaric heat capacities tend to cancel out each other and thus they have practically no impact on the calculations. Consequently, they were truncated and the basic solid-phase model, takes the form:

$$\hat{f}_{0i}^{S}(T,P) = \hat{f}_{0i}^{L^*}(T,P)\exp\left[-\frac{\left(v_{0i}^{S}-v_{0i}^{L^*}\right)(P^{+}-P)}{RT}-\frac{\Delta h_{0i}^{SL}}{RT}\left(1-\frac{T}{T_{0i}^{SL}}\right)\right] \qquad 8.1$$

8.2.2. Advanced Solid-Phase Model

A first modification on the basic solid-phase model was applied by taking into account the pressure dependency of the liquid molar volume in Eq. 3.33. The respective integral is substituted by fugacities at the corresponding pressures (P^{+}, P), calculated with the fluid-phase EoS that is coupled with the solid-phase model in each case. The terms that include the isobaric heat capacities were again truncated, so that:

$$\hat{f}_{0i}^{S}(T,P) = \hat{f}_{0i}^{L^*}(T,P)\exp\left[-\frac{\left(v_{0i}^{S}\right)(P^{+}-P)}{RT} - \ln\left(\frac{\hat{f}_{0i}^{L^*}(T,P)}{\hat{f}_{0i}^{L^*}(T,P^{+})}\right) - \frac{\Delta h_{0i}^{SL}}{RT}\left(1-\frac{T}{T_{0i}^{SL}}\right)\right] \quad 8.2$$

Eq. 8.2 can be considered as a step in between the Seiler et al. [162] and the Pauly et al. [104] approaches. In the first approach, the solid and the liquid molar volumes are considered pressure-independent, whereas in the latter one, both volumes depend on pressure. In the work of Pauly et al. [104], the solid molar volume pressure dependency is taken into account by correlating it with the liquid molar volume through a proportionality coefficient:

$$v_{0\mathrm{i}}^{\mathrm{S}} = \hat{\beta}^{+} v_{0\mathrm{i}}^{\mathrm{L}^*} \quad 8.3$$

The proportionality coefficient $\hat{\beta}^{+}$ is assumed to be pressure-independent and equal to 0.86, based on experimental observations of volume change data at SLE conditions of pure paraffins [104]. However, keeping v_{0i}^{S} constant with pressure can be a good approximation even at high pressures. Furthermore, if the two volumes are correlated with Eq. 8.3, inaccuracies in the calculation of the liquid molar volume pressure dependency from the fluid-phase EoS, are transferred in the solid-phase Poynting term. It has to be noted though, that apart from the liquid molar volume prediction at the normal melting point of the pure solid-forming compound, the accuracy of the fluid-phase EoS in predicting this pressure dependency cannot be directly assessed at higher pressures, in the temperature range where SLGE is exhibited. This is a result of the solid-phase model reference state, which is a hypothetical one. Therefore, it is important to alter initially only the liquid-phase Poynting term and keep the solid-phase one unaltered, in order to systematically assess the performance of each combined model against the experimental SLGE data.

8.2.3. Advanced-Fit Solid-Phase Model

A new solid-phase model is proposed. The new model combines the approaches of Pauly et al. [104] and Ameri-Mahabadian et al. [112], who proposed that the proportionality coefficient between v_{0i}^{S} and $v_{0i}^{L^*}$ should depend on pressure. This assumption is based on the fact that, upon pressurization, the liquid volume decreases faster than the solid one. The authors assumed that the proportionality coefficient increases linearly with pressure, because this way the simplest dependency can be retrieved, but there is no experimental evidence that justifies the assumption. Therefore,

the approach can be considered as an engineering alternative that lacks strong theoretical basis, but leads to more accurate calculations at high pressures. Furthermore, an adjustable positive parameter is fitted directly to experimental SFE data, which renders the model less predictive. The proportionality coefficient at the pressure of the system is given by:

$$\hat{\beta}(\mathrm{P}) = \hat{\beta}^{+} + \hat{a}(P - P^{+}) \tag{8.4}$$

and

$$v_{0i}^{S} = \hat{\beta}(P) v_{0i}^{L^*} \tag{8.5}$$

Ameri-Mahabadian et al. combined correlations (linear extrapolation) for the melting and SS transition temperatures at the system pressure with the Clausius-Clapeyron equation and Eqs. 8.4 - 8.5 in order to calculate the corresponding enthalpies at the pressure of the system. In this way, they proposed a solid-phase model without the need of a Poynting correction. Implementation of the model requires direct fitting of the $\hat{a}$ parameter on mixture SFE data and thus it is fluid-phase EoS specific and mixture specific. However, the authors presented average values of $\hat{a}$ that resulted in satisfying correlation of the data considered in their work.

The pressure dependent $\hat{\beta}$ can also be used in a solid-phase model that incorporates a Poynting term, such as the one used by Pauly et al. Starting from Eq. 3.33, neglecting the isobaric heat capacity terms and combing with Eqs. 8.4 - 8.5 we get:

$$\hat{f}_{0i}^{S}(T,P) = \hat{f}_{0i}^{L^*}(T,P)\exp\left[-\frac{1}{RT}\left(-\int_{P^+}^{P}\left(\hat{\beta}^{+} + \hat{a}(P - P^{+})\right)v_{0i}^{L^*}dP + \int_{P^+}^{P} v_{0i}^{L^*}dP\right) - \frac{\Delta h_{0i}^{SL}}{RT}\left(1 - \frac{T}{T_{0i}^{SL}}\right)\right] \tag{8.6}$$

By splitting the first integral, grouping the resulting terms and calculating the liquid molar volume integral as fugacity difference between the two pressure states we arrive at:

$$\hat{f}_{0i}^{S}(T,P) = \hat{f}_{0i}^{L^*}(T,P)\exp\left[\ln\left(\frac{\hat{f}_{0i}^{L^*}(T,P)}{\hat{f}_{0i}^{L^*}(T,P^{+})}\right)\left(\hat{\beta}^{+} - \hat{a}P^{+} - 1\right) + \frac{\hat{a}}{RT}\int_{P^+}^{P} P v_{0i}^{L^*}dP - \frac{\Delta h_{0i}^{SL}}{RT}\left(1 - \frac{T}{T_{0i}^{SL}}\right)\right] \tag{8.7}$$

The integral in Eq. 8.7 can be replaced with an integral of the compressibility factor with pressure and as a result the final equation for the solid-phase fugacity is formulated:

$$\hat{f}_{0i}^{S}(T,P) = \hat{f}_{0i}^{L^*}(T,P)\exp\left[\ln\left(\frac{\hat{f}_{0i}^{L^*}(T,P)}{\hat{f}_{0i}^{L^*}(T,P^+)}\right)\left(\hat{\beta}^+ - \hat{a}P^+ - 1\right) + \hat{a}\int_{P^+}^{P} Z_{0i}^{L^*}dP - \frac{\Delta h_{0i}^{SL}}{RT}\left(1 - \frac{T}{T_{0i}^{SL}}\right)\right] \quad 8.8$$

The remaining integral can be calculated with numerical integration. In this work, the Simpson integration method was chosen, while the smoothness of the function inside the integral allowed the use of a relatively small number of nodes. For example, increment of the number of nodes from 10 to 50 over the entire pressure range examined in each case resulted in a change of the equilibrium temperature in the sixth decimal digit.

8.3. Results and Discussion

One of the main targets of this work is to obtain a simple and at the same time accurate model for the prediction of the SLGE behavior of the mixtures considered. Therefore, a systematic study that enables the assessment of the effect of the various terms involved is a prerequisite. Consequently, the first step in the approach is the evaluation of the simplest model of those considered, i.e. the basic solid-phase model combined with the fluid-phase EoS without the use of BIPs, against the available experimental SLGE data. Subsequently, predictions of the same combined models are compared to the ones when k_{ij} parameters regressed from experimental binary VLE data are employed. It will be shown, that the use of k_{ij} parameters is essential for each combined model, so that the correct type of phase behavior is predicted. Furthermore, using the regressed BIPs, the advanced solid-phase model is applied and the effect of a pressure-dependent liquid molar volume in the Poynting term is going to be presented. At this point, the adoption of a specific volume translation strategy for the cubic EoS is crucial to obtain accurate results. A correlation of the regressed BIPs with carbon number is proposed for each fluid-phase EoS and results are presented for each mixture. Finally, the newly-proposed advanced-fit solid-phase model is implemented and correlation of the SLGE data is presented with PR and PC-SAFT EoS.

8.3.1. Basic Solid-Phase Model: Effect of BIPs

The pure component parameters, required by the cubic and PC-SAFT EoS, as well as the physical properties required for the implementation of the solid-phase model are summarized in Table C.1, Table C.2 and Table C.4 in Appendix C. The melting enthalpy of *n*-$C_{17}H_{36}$ was not available in the DIPPR database and was calculated via interpolation of values for other odd carbon number *n*-alkanes. In Figure 8.1, the melting enthalpies of *n*-alkanes are plotted versus the carbon number. As shown, the melting enthalpies of even carbon number *n*-alkanes follow a different trend than the odd ones. Consequently, the melting enthalpy of *n*-$C_{17}H_{36}$ was linearly interpolated using data of odd carbon number *n*-alkanes from 9 until 19 carbon atoms.

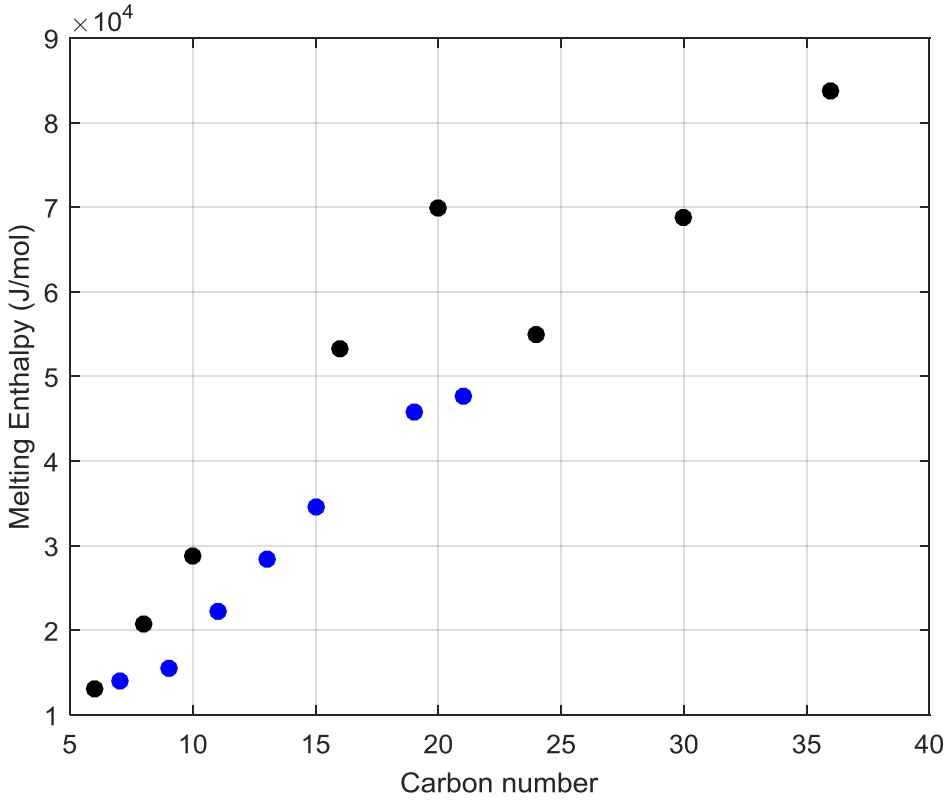

Figure 8.1: Enthalpy of melting of *n*-alkanes with carbon number. Black data points correspond to even carbon number *n*-alkanes and blue data points to odd carbon number *n*-alkanes [175].

Table 8.1: Experimental binary VLE data of CH_4 - *n*-alkane mixtures from the literature, used for the regression of k_{ij} values.

Temperature (K)	Pressure (MPa)	Ref
	CH_4 - *n*-C_6H_{14}	
182.46	0.14 - 3.55	[240]
	CH_4 - *n*-C_7H_{16}	
183.15	0.69 - 3.45	[241]
	CH_4 - *n*-C_8H_{18}	
223.15	1.01 - 7.09	[242]
	CH_4 - *n*-$C_{10}H_{22}$	
244.26	1.60 - 6.90	[189]
	CH_4 - *n*-$C_{16}H_{34}$	
300	2.15 - 67.86	[198]
	CH_4 - *n*-$C_{17}H_{36}$	
300	4.20 - 74.12	[24]
	CH_4 - *n*-$C_{20}H_{42}$	
~310	0.40 - 86.73	[206]
	CH_4 - *n*-$C_{24}H_{50}$	
~323	5.05 - 104.06	[208]
	CH_4 - *n*-$C_{30}H_{62}$	
338 - 350	1.64 - 116.40	[20]
	CH_4 - *n*-$C_{36}H_{74}$	
373	5.90 - 109.60	[243]

As it has already been mentioned, the first step in our approach is the evaluation of the effect of the BIPs in the prediction of the SLGE behavior of the mixtures considered. In order to retain the predictive nature of the models, k_{ij} parameters were regressed from experimental binary VLE data for each fluid-phase EoS, instead of directly fitting them to the experimental SLGE data. The latter approach would also mean that inaccuracies of the solid-phase model to describe the SLGE behavior would be fine-tuned by the fitting process. However, this does not imply that the second approach would also lead to more accurate results, especially in mixtures which exhibit SLGE at very high pressures. Regression of the BIPs from experimental VLE / GLE data results in a more accurate description of the fluid phases involved. Therefore,

experimental VLE / GLE data at temperatures close to the normal melting point of each solid-forming compound were used for the corresponding binary mixtures. Table 8.1 and Table 8.2 summarize the temperature and pressure ranges for the experimental VLE / GLE and SLGE data considered in this work, respectively.

Table 8.2: Experimental binary SLGE data of CH_4 - *n*-alkane mixtures from the literature.

Temperature (K)	Pressure (MPa)	Number of PT points	Number of liquid phase composition points	Number of gas phase composition points	Ref
		CH_4 - *n*-C_6H_{14}			
162.89 - 177.81	0.0003 - 1.95	10	10	0	[244]
138 - 164	0.59 - 1.72	14	14	0	[245]
		CH_4 - *n*-C_7H_{16}			
131 - 181	0.37 - 2.19	26	26	0	[246]
		CH_4 - *n*-C_8H_{18}			
165.56 - 216.43	0.10 - 7.14	15	8	0	[242]
156 - 191.15	1.36 - 4.65	19	19	0	[247]
		CH_4 - *n*-$C_{10}H_{22}$			
228.22 - 245	0.15 - 26.15	8	0	0	[248]
236.77 - 243.48	0.10 - 7.10	14	14	0	[193]
		CH_4 - *n*-$C_{16}H_{34}$			
284.71 - 289.98	2.06 - 71.17	13	10	3	[198]
		CH_4 - *n*-$C_{17}H_{36}$			
286.25 - 292.45	4.09 - 78.33	11	7	4	[24]
		CH_4 - *n*-$C_{20}H_{42}$			
304.55 - 309.65	0.37 - 88.95	44	15	8	[206]
		CH_4 - *n*-$C_{24}H_{50}$			
318.32 - 322.77	1.73 - 104.2	23	0	0	[208]
		CH_4 - *n*-$C_{30}H_{62}$			
333.67 - 340.28	3.97 - 123.68	12	10	2	[20]
		CH_4 - *n*-$C_{36}H_{74}$			
346.27 - 348.98	0.10 - 7.77	10	10	0	[249]

The k_{ij} parameters were fitted by minimizing the root-mean-square deviation of the bubble pressure values between experimental VLE / GLE data and EoS calculations. The corresponding k_{ij} values and the Percentage Average Absolute Relative Deviation (% AARD) between the experimental VLE / GLE data and EoS calculations are summarized in Table 8.3 for each mixture. Only the experimental bubble pressure values were considered in the calculation of % AARD, since the mole fractions of the vapor phase were unavailable for most mixtures. Experimental VLE data and calculations are presented in Figure E.1 - Figure E.10.

With respect to the VLE correlation (calculations with the regressed k_{ij} parameters) for the mixtures of CH_4 with *n*-C_6H_{14}, *n*-C_7H_{16}, *n*-C_8H_{18} and *n*-$C_{10}H_{22}$, the three EoS exhibit very similar % AARD values while for the CH_4 - *n*-C_7H_{16} mixture the two cubic EoS are distinctly more accurate than PC-SAFT. However, from CH_4 - *n*-$C_{16}H_{34}$ mixture and on, PC-SAFT becomes increasingly more accurate as the asymmetry of the mixture rises. An observed trend for these mixtures is that PC-SAFT tends to slightly under-predict the binary mixture critical point, while cubic EoS present a more significant over-prediction of it. It is interesting also to note that the pure VLE predictions ($k_{ij} = 0$) from PC-SAFT are systematically more accurate for all the mixtures up to CH_4 - *n*-$C_{17}H_{36}$. For the remaining mixtures, cubic EoS exhibit lower % AARD values than PC-SAFT, except for the mixture of CH_4 with *n*-$C_{36}H_{74}$.

It has to be noted, that some of the k_{ij} parameters presented in Table 8.3 are not the optimum ones, as produced from the VLE fitting process. Specifically, the k_{ij} values of the cubic EoS for the CH_4 - *n*-C_6H_{14} were adjusted to lower values than the optimum ones with respect to the experimental VLE data from which they were regressed. The fitting process for this mixture returned k_{ij} values equal to 0.0376 for SRK and 0.0443 for PR EoS. However, with these values the two EoS predict the wrong type of SLGE phase diagram. Van Konynenburg and Scott [35] reported CH_4 - *n*-C_6H_{14} to be a type V mixture or effectively a type IV with the lower VLLE / GLLE line being hidden by solidification. However, the authors focused on classifying the binary mixtures based on their fluid-phase behavior. Addition of solid phases results in different connectivity of univariant lines even in the same type of fluid-phase behavior and can create confusion about the classification of a binary mixture. Quinteros and Llovell [250] also agreed with a type IV classification reporting that soft-SAFT predicts LLE below the crystallization temperature of *n*-C_6H_{14}. On the other hand, Cismondi et al. [251] and Polishuk et al. [252] classified the mixture as a type V without performing any solid-phase calculations

and both mentioned the uncertainty of the type because of the solidification phenomena. In our opinion, the correct classification of this mixture is a type V phase behavior, which can be seen theoretically in Figure 2 in the work of Garcia and Luks [253]. The SLGE line in this type of behavior is smooth without abrupt changes in the liquid phase composition. Furthermore, a separate GLLE line extends from a lower critical end point (LCEP, type L point where L=L,G) to an upper critical end point (UCEP, type K point where L,L=G). A type IV phase behavior corresponds to Figure 4 from Garcia and Luks and involves a quadruple point (Q point) from which 4 other lines extend (SL_1GE, SL_2GE, SL_1L_2E, GL_1L_2E). Furthermore, a second separate GLLE line extends from an LCEP to a UCEP. The existence of a Q point results in an abrupt change of the liquid-phase composition and a sharp peak at the highest pressure point on the P-T projection graph, which does not agree with the SLGE experimental data for the CH_4 - *n*-C_6H_{14} mixture [244, 245]. Using the k_{ij} values as produced from the fitting process for the two cubic EoS, resulted in a type III phase behavior for this mixture with the major critical line extending to high pressures until it is connected to an SLLE line. Consequently, their values were adjusted to the closest values with respect to the optimum ones that reproduced a type V behavior. A similar case is encountered in CH_4 - *n*-C_7H_{16} mixture with PC-SAFT. The optimum k_{ij} value from the regression with respect to the VLE data is equal to 0.0, but with this value the model is unable to reproduce the type III phase behavior of the mixture. Consequently, the parameter value was adjusted to the lowest one that enabled the model to qualitatively predict the behavior.

Finally, the k_{ij} parameters of the cubic EoS for the CH_4 - *n*-$C_{36}H_{74}$ mixture were adjusted to lower values than those produced from the fitting process, because of an inconsistency with the experimental VLE data. Specifically, the regressed k_{ij} parameters resulted in an isothermal P-x,y graph with no critical point and the bubble and dew lines extending to high pressures with opposite slopes. In order to avoid this behavior, the values of the BIPs were adjusted to the highest ones that predicted a critical point for the binary mixture. Some characteristic global phase diagrams, calculated with the adopted models in this work, are given in the last section of this Chapter.

Table 8.3: %AARD between experimental VLE data and EoS calculations for the mixture bubble pressure and corresponding k_{ij} values regressed from experimental measurements.

EoS			CH_4 - *n*-C_6H_{14}	CH_4 - *n*-C_7H_{16}	CH_4 - *n*-C_8H_{18}	CH_4 - *n*-$C_{10}H_{22}$	CH_4 - *n*-$C_{16}H_{34}$	CH_4 - *n*-$C_{17}H_{36}$	CH_4 - *n*-$C_{20}H_{42}$	CH_4 - *n*-$C_{24}H_{50}$	CH_4 - *n*-$C_{30}H_{62}$	CH_4 - *n*-$C_{36}H_{74}$
SRK	Pr.	%AARD	22.0	27.5	25.6	22.4	28.5	32.0	25.5	27.9	22.7	32.5
	Cor.	%AARD	7.3	3.3	1.6	2.1	5.7	8.0	12.0	10.6	18.0	10.7
		k_{ij}	0.0280[a]	0.0446	0.0476	0.0496	0.0561	0.0549	0.0548	0.0529	0.0454	0.0580[c]
PR	Pr.	%AARD	26.0	31.3	29.3	25.8	30.8	34.5	27.0	30.7	23.9	36.5
	Cor.	%AARD	7.8	2.2	2.1	1.7	4.8	7.4	11.7	10.7	17.5	15.4
		k_{ij}	0.0340[a]	0.0507	0.0531	0.0555	0.0603	0.0590	0.0592	0.0581	0.0548	0.0550[c]
PC-SAFT	Pr.	%AARD	6.3	9.0	12.6	10.1	25.6	30.0	27.0	31.6	27.7	25.3
	Cor.	%AARD	6.3	10.4	1.6	2.7	4.5	4.2	6.5	4.8	3.5	5.1
		k_{ij}	0	0.0080[a]	0.0126	0.0112	0.0306	0.0328	0.0337	0.0372	0.0386	0.0282
NP			10	5	7	5	10	7	15[b]	12[b]	10[b]	16

$$\%\,AARD = \frac{100}{NP}\sum_{i=1}^{NP}\left|\frac{P_i^{calculated} - P_i^{experimental}}{P_i^{experimental}}\right|$$

where NP is the number of experimental data points and P_i is the bubble pressure.

"Pr." refers to predictions ($k_{ij} = 0$), whereas "Cor." refers to correlations (calculations with $k_{ij} \neq 0$).

[a] Adjusted value, so that the model predicts the correct type of global phase behavior.

[b] Different temperatures close to the normal melting temperature were used for the fitting process.

[c] Adjusted value, so that the model predicts the correct type of isothermal VLE behavior.

Table 8.4: %AARD between experimental SLGE data and model predictions calculated for the equilibrium temperature or pressure of each mixture.

EoS		CH_4 - *n*-C_6H_{14}	CH_4 - *n*-C_7H_{16}	CH_4 - *n*-C_8H_{18}	CH_4 - *n*-$C_{10}H_{22}$	CH_4 - *n*-$C_{16}H_{34}$	CH_4 - *n*-$C_{17}H_{36}$	CH_4 - *n*-$C_{20}H_{42}$	CH_4 - *n*-$C_{24}H_{50}$	CH_4 - *n*-$C_{30}H_{62}$	CH_4 - *n*-$C_{36}H_{74}$
SRK	Bsc.	15.4	18.2	1.3, 1.2	0.6	-	-	-	-	-	-
	Bsc. k_{ij}	4.0	4.7	1.4, 0.3	0.4	0.2	0.4	0.2	0.7	0.2	0.3
	Adv. k_{ij}	-	-	-	0.3	0.2	1.1	0.1	0.2	0.4	0.3
PR	Bsc.	18.4	20.7	1.1, 1.6	0.8	-	-	-	-	-	-
	Bsc. k_{ij}	4.0	4.8	1.2, 0.3	0.4	0.3	0.3	0.2	0.7	0.1	0.3
	Adv. k_{ij}	-	-	-	0.4	0.2	0.8	0.1	0.3	0.4	0.3
PC-SAFT	Bsc.	7.0	6.9	1.0, 0.1	0.3	-	-	-	-	-	-
	Bsc. k_{ij}	-	12.3	1.0, 0.6	0.5	0.5	0.4	0.16	0.4	0.5	0.13
	Adv. k_{ij}	-	-	-	0.4	0.2	0.7	0.06	0.1	1.0	0.05
NP		23	26	34	22	8	9	33	19	7	10

$$\%\ AARD = \frac{100}{NP}\sum_{i=1}^{NP}\left|\frac{X_i^{calculated} - X_i^{experimental}}{X_i^{experimental}}\right|$$

where NP is the number of experimental data points and X_i is the equilibrium temperature or pressure.

"Bsc." refers to predictions with the basic solid-phase model and $k_{ij} = 0$.

"Bsc. k_{ij}" refers to predictions with the basic solid-phase model and $k_{ij} \neq 0$.

"Adv. k_{ij}" refers to predictions with the advanced solid-phase model and $k_{ij} \neq 0$.

% AARD is calculated for the equilibrium pressure in the mixtures CH_4 - *n*-C_6H_{14}, CH_4 - *n*-C_7H_{16}, CH_4 - *n*-C_8H_{18} (first number). For all the other mixtures and CH_4 - *n*-C_8H_{18} (second number) is calculated for the equilibrium temperature.

Table 8.4 summarizes the % AARD between experimental SLGE data and model calculations for each mixture. For the mixtures of CH_4 with *n*-C_6H_{14}, *n*-C_7H_{16}, *n*-C_8H_{18} and *n*-$C_{10}H_{22}$, the use of k_{ij} parameters with the cubic EoS, coupled with the basic solid-phase model results in significant increase of accuracy in the SLGE prediction. Experimental data and model calculations for these mixtures are presented in Figure 8.2 through Figure 8.5. PC-SAFT coupled with the basic solid-phase model and with a k_{ij} equal to 0.0 predicts very accurately the CH_4 - *n*-C_6H_{14} SLGE, while cubic EoS predictions are comparable with PC-SAFT only with the adjusted BIPs. The use of the adjusted k_{ij} of PC-SAFT EoS in the CH_4 - *n*-C_7H_{16} mixture results in worse prediction when compared to the basic solid-phase model with k_{ij}= 0.0 in terms of % AARD, but in the latter case the correct type of phase behavior (type III) is not reproduced. This can be seen graphically by the absence of the sharp peak in the P-T graph and the smooth change of the liquid-phase composition in the left panels of Figure 8.3 as calculated by the model. The regressed k_{ij} parameters of the cubic EoS result in excellent prediction of the SLGE of the CH_4 - *n*-C_7H_{16} mixture, while PC-SAFT is less accurate.

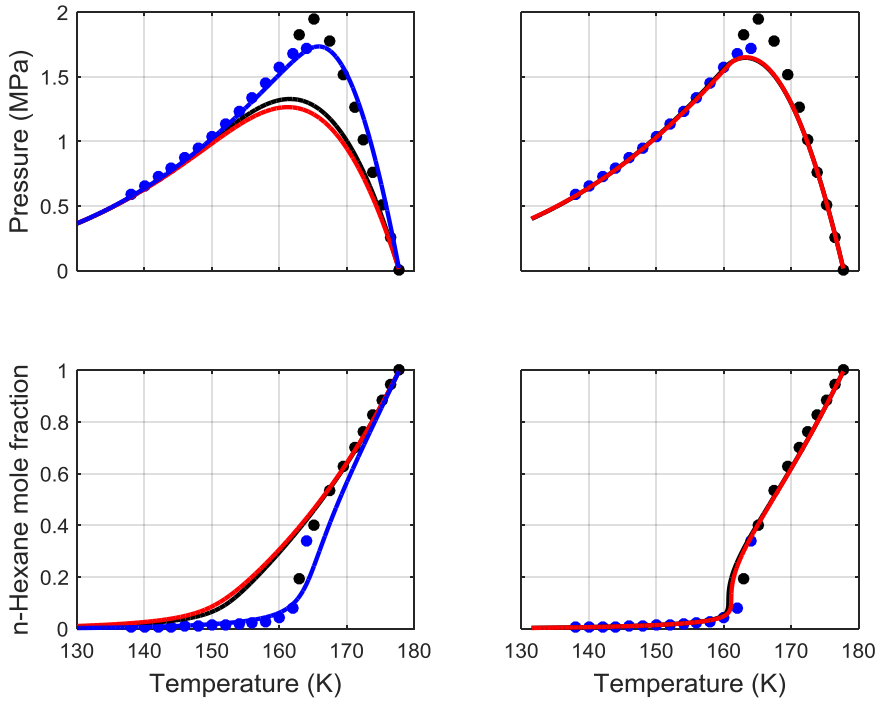

Figure 8.2: Prediction of the SLGE curve of the CH_4 - *n*-C_6H_{14} mixture. Experimental data [244, 245] are represented by data points and calculations by lines. Black lines correspond to SRK, red to PR and blue to PC-SAFT EoS. Left panels show predictions with the basic solid-phase model and $k_{ij} = 0$, while right panels show predictions with the basic solid-phase model and k_{ij} parameters fitted to experimental binary VLE data. The *n*-C_6H_{14} mole fraction refers to the liquid phase along the SLGE curve.

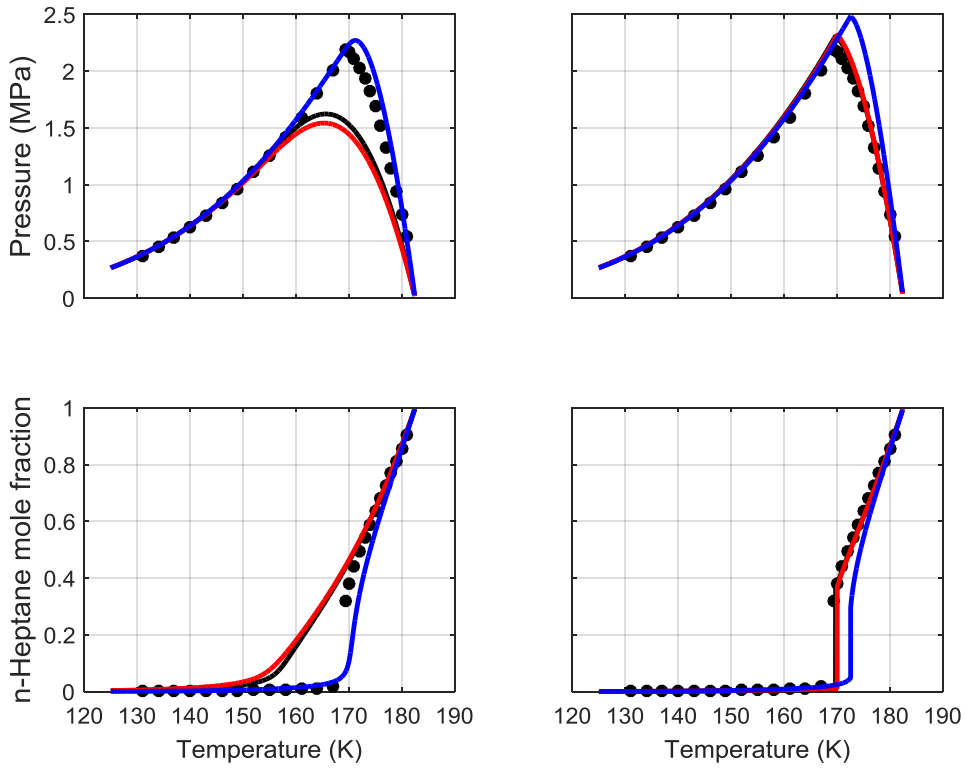

Figure 8.3: Prediction of the SLGE curve of the CH_4 - *n*-C_7H_{16} mixture. Experimental data [246] are represented by data points and calculations by lines. Black lines correspond to SRK, red to PR and blue to PC-SAFT EoS. Left panels show predictions with the basic solid-phase model and $k_{ij} = 0$, while right panels show predictions with the basic solid-phase model and k_{ij} parameters fitted to experimental binary VLE data. The *n*-C_7H_{16} mole fraction refers to the liquid phase along the SLGE curve.

The CH_4 - *n*-C_8H_{18} mixture presents another possibility of type III phase behavior, which is also exhibited by the more asymmetric mixtures to be discussed. In this case, the SLGE line does not intersect with a low temperature GLLE line to create a Q point as in the CH_4 - *n*-C_7H_{16} mixture (see Figure 8.4). Instead, two SLGE lines exist (considering the solidification of the heavier compound only), one stemming from the pure *n*-C_8H_{18} melting point which extends to high pressures until it intersects the major critical line and one stemming from low temperatures (from an $S_1S_2L_2G$ point) and lies closely to the pure CH_4 VLE line. Calculation of the CH_4 - *n*-C_8H_{18} mixture SLGE using the regressed BIPs with the cubic EoS results in a more accurate prediction when compared to calculation without k_{ij} parameters. The opposite happens with PC-SAFT EoS which predicts with excellent accuracy the SLGE when k_{ij} is equal to 0.0, while this accuracy diminishes when the regressed BIP is used. The same trend is also evident in the calculations for the CH_4 - *n*-$C_{10}H_{22}$ mixture.

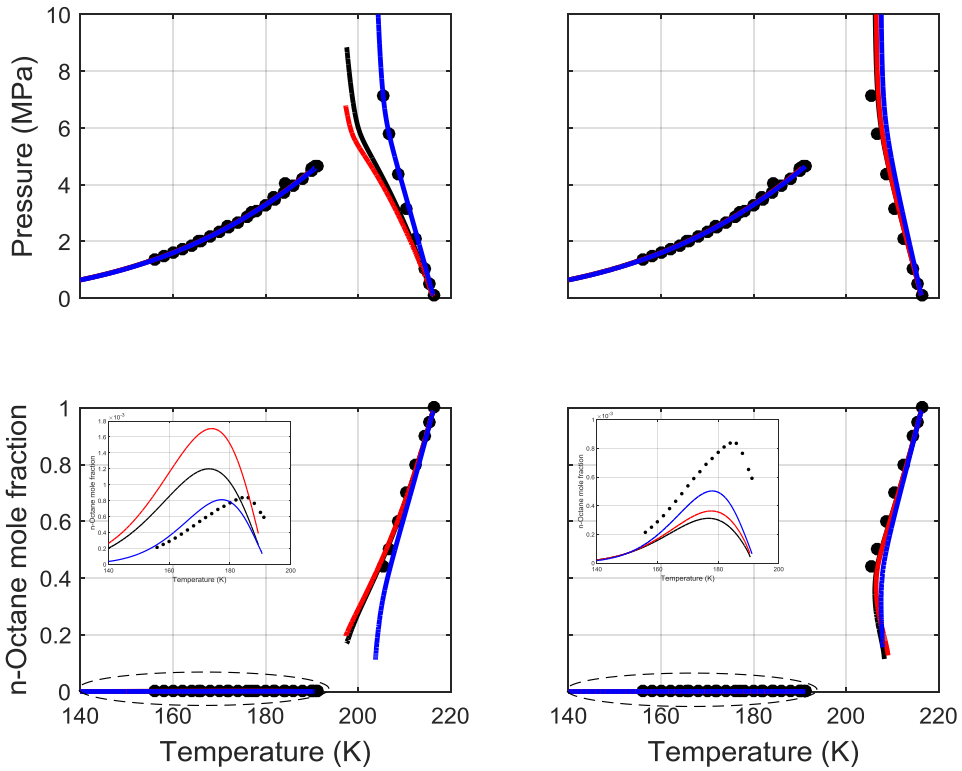

Figure 8.4: Prediction of the SLGE curve of the CH_4 - *n*-C_8H_{18} mixture. Experimental data [242, 247] are represented by data points and calculations by lines. Black lines correspond to SRK, red to PR and blue to PC-SAFT EoS. Left panels show predictions with the basic solid-phase model and $k_{ij} = 0$, while right panels show predictions with the basic solid-phase model and k_{ij} parameters fitted to experimental binary VLE data. The *n*-C_8H_{18} mole fraction refers to the liquid phase along the SLGE curve.

A distinct characteristic of the type III SLGE behavior is the retrograde presented in the equilibrium temperature which is initially reduced to a minimum value and subsequently starts increasing with pressure. The first mixture exhibiting this behavior is CH_4 - *n*-C_8H_{18} and the phenomenon becomes more pronounced as the asymmetry of each mixture rises. From the mixtures considered in this work, CH_4 - *n*-$C_{16}H_{34}$ is the first mixture in which the phenomenon is clearly more evident, because of the SLGE being exhibited at very high pressures. Apart from the CH_4 - *n*-C_7H_{16} case, the SLGE of the mixtures that have already been discussed is qualitatively reproduced by the basic solid-phase model coupled with all EoS even without the use of k_{ij} parameters. A doubt should be kept for the CH_4 - *n*-$C_{10}H_{22}$ mixture because of the limited experimental data available (see Figure 8.5).

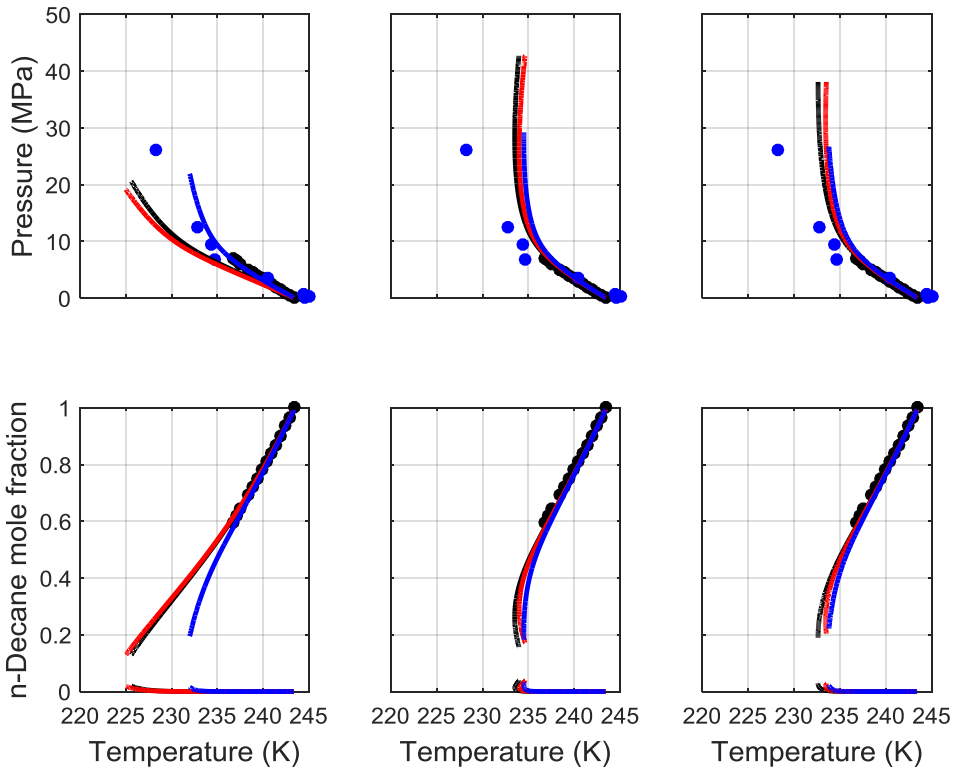

Figure 8.5: Prediction of the SLGE curve of the CH_4 - *n*-$C_{10}H_{22}$ mixture. Experimental data [193, 248] are represented by data points and calculations by lines. Black lines correspond to SRK, red to PR and blue to PC-SAFT EoS. Left panels show predictions with the basic solid-phase model and $k_{ij} = 0$, middle panels show predictions with the basic solid-phase model and k_{ij} parameters fitted to experimental binary VLE data, while right panels show predictions with the advanced solid-phase model and k_{ij} parameters fitted to experimental binary VLE data. The *n*-$C_{10}H_{22}$ mole fraction refers to the liquid and vapor phases along the SLGE curve.

However, from CH_4 - *n*-$C_{16}H_{34}$ and on, without the use of regressed k_{ij} parameters, no combined model can reproduce the retrograde behavior of the SLGE, which leads to very poor predictions, with the highest deviations between the experimental and calculated equilibrium temperatures ranging from 7 to 9 K. Furthermore, the calculated liquid-phase composition along the equilibrium curve presents the opposite trend from the experimental one, resulting in a very low pressure UCEP. The % AARD for these cases were not calculated. The results are presented in Figure E.11 through Figure E.16. The only exception is the CH_4 - *n*-$C_{36}H_{74}$ mixture SLGE, when calculated with the basic solid-phase model combined with PC-SAFT and a k_{ij} equal to 0.0.

Using the regressed k_{ij} parameters with all fluid-phase EoS results in significant increase of accuracy for each combined model both qualitatively and quantitatively.

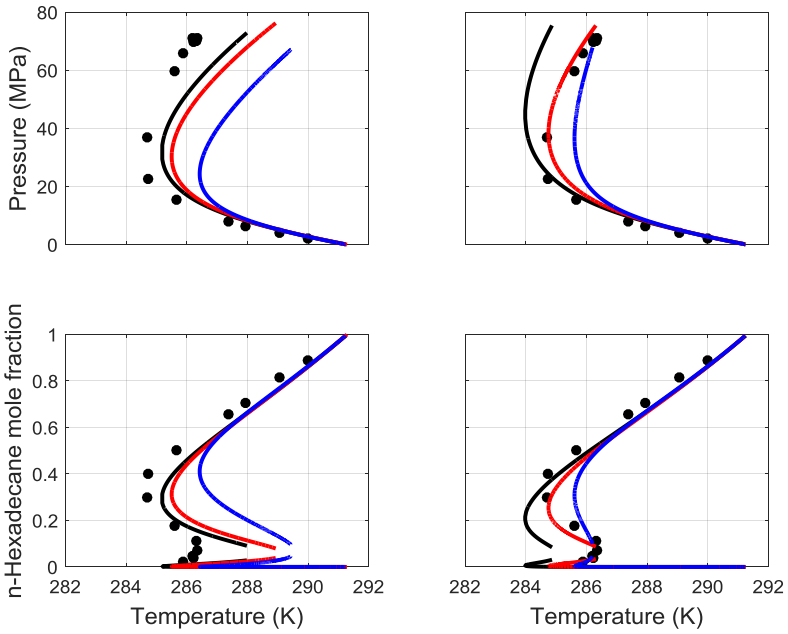

Figure 8.6: Prediction of the SLGE curve of the CH_4 - *n*-$C_{16}H_{34}$ mixture. Experimental data [198] are represented by data points and calculations by lines. Black lines correspond to SRK, red to PR and blue to PC-SAFT EoS. Left panels show predictions with the basic solid-phase model, while right panels show predictions with the advanced solid-phase model. Both calculations include k_{ij} parameters fitted to experimental binary VLE data. The *n*-$C_{16}H_{34}$ mole fraction refers to the liquid and vapor phases along the SLGE curve.

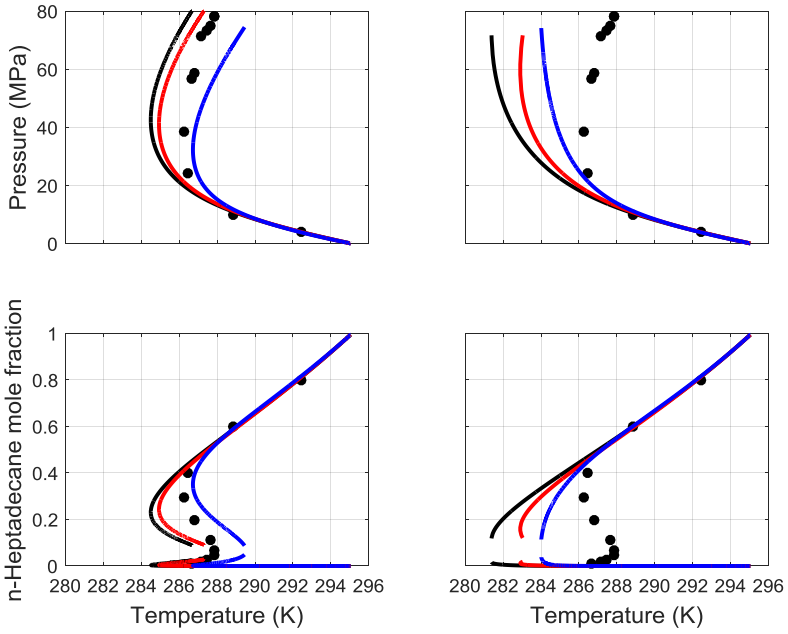

Figure 8.7: Prediction of the SLGE curve of the CH_4 - *n*-$C_{17}H_{36}$ mixture. Experimental data [24] are represented by data points and calculations by lines. Black lines correspond to SRK, red to PR and blue to PC-SAFT EoS. Left panels show predictions with the basic solid-phase model, while right panels show predictions with the advanced solid-phase model. Both calculations include k_{ij} parameters fitted to experimental binary VLE data. The *n*-$C_{17}H_{36}$ mole fraction refers to the liquid and vapor phases along the SLGE curve.

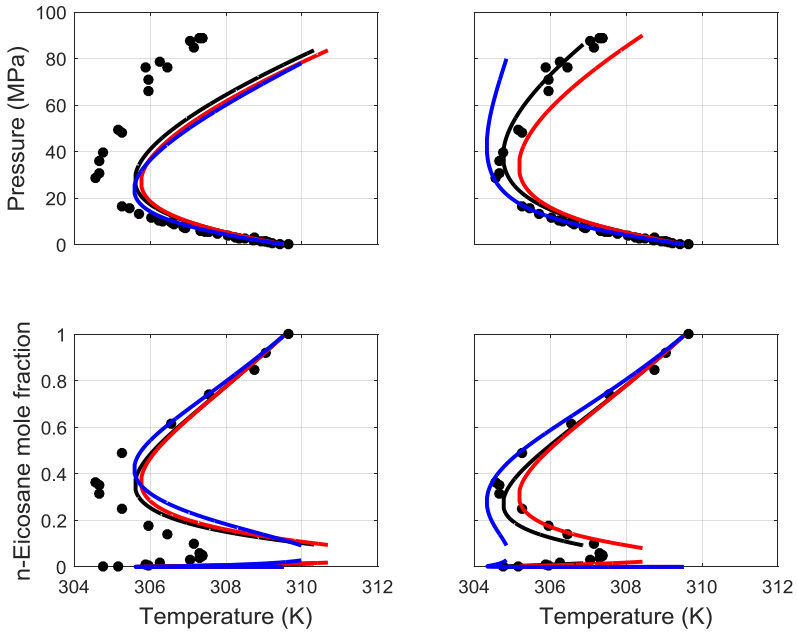

Figure 8.8: Prediction of the SLGE curve of the CH_4 - *n*-$C_{20}H_{42}$ mixture. Experimental data [206] are represented by data points and calculations by lines. Black lines correspond to SRK, red to PR and blue to PC-SAFT EoS. Left panels show predictions with the basic solid-phase model, while right panels show predictions with the advanced solid-phase model. Both calculations include k_{ij} parameters fitted to experimental binary VLE data. The *n*-$C_{20}H_{42}$ mole fraction refers to the liquid and vapor phases along the SLGE curve.

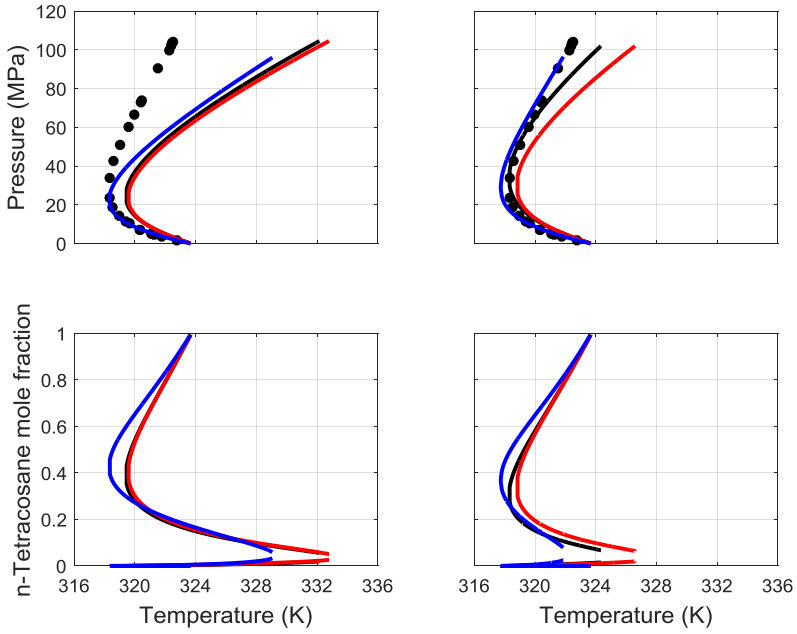

Figure 8.9: Prediction of the SLGE curve of the CH_4 - *n*-$C_{24}H_{50}$ mixture. Experimental data [208] are represented by data points and calculations by lines. Black lines correspond to SRK, red to PR and blue to PC-SAFT EoS. Left panels show predictions with the basic solid-phase model, while right panels show predictions with the advanced solid-phase model. Both calculations include k_{ij} parameters fitted to experimental binary VLE data. The *n*-$C_{24}H_{50}$ mole fraction refers to the liquid and vapor phases along the SLGE curve.

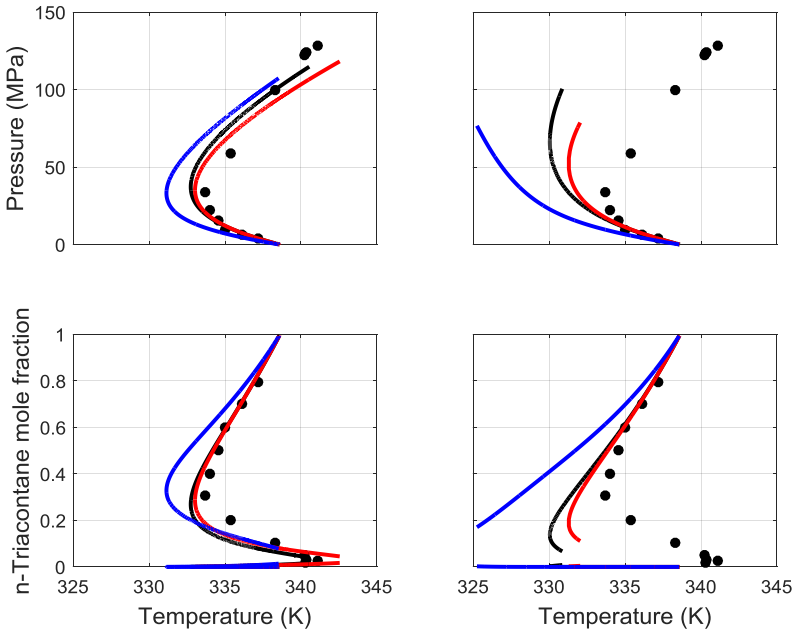

Figure 8.10: Prediction of the SLGE curve of the CH_4 - *n*-$C_{30}H_{62}$ mixture. Experimental data [20] are represented by data points and calculations by lines. Black lines correspond to SRK, red to PR and blue to PC-SAFT EoS. Left panels show predictions with the basic solid-phase model, while right panels show predictions with the advanced solid-phase model. Both calculations include k_{ij} parameters fitted to experimental binary VLE data. The *n*-$C_{30}H_{62}$ mole fraction refers to the liquid and vapor phases along the SLGE curve.

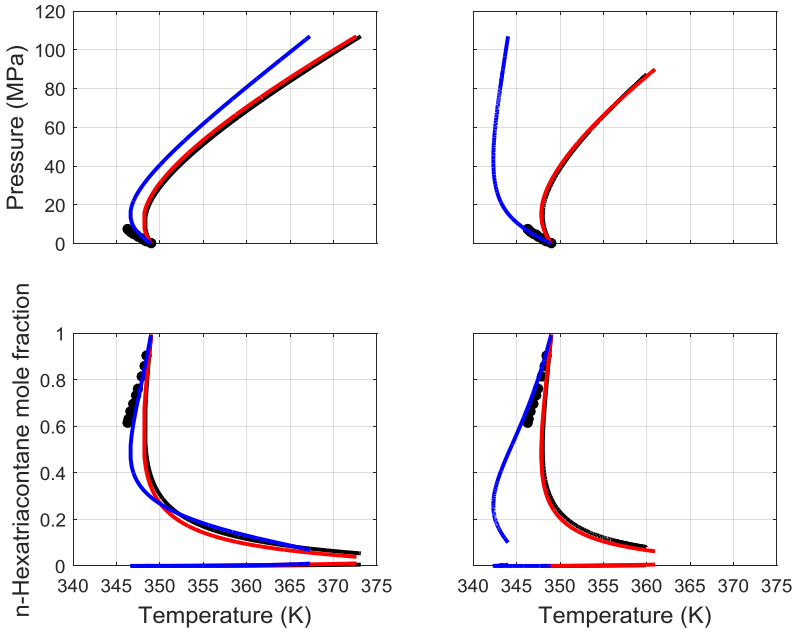

Figure 8.11: Prediction of the SLGE curve of the CH_4 - *n*-$C_{36}H_{74}$ mixture. Experimental data [249] are represented by data points and calculations by lines. Black lines correspond to SRK, red to PR and blue to PC-SAFT EoS. Left panels show predictions with the basic solid-phase model, while right panels show predictions with the advanced solid-phase model. Both calculations include k_{ij} parameters fitted to experimental binary VLE data. The *n*-$C_{36}H_{74}$ mole fraction refers to the liquid and vapor phases along the SLGE curve.

The calculations with the basic solid-phase model and each EoS are presented in the left panels of Figure 8.6 through Figure 8.11. As it can be seen, every combined model now reproduces the retrograde behavior of the SLGE curve and the experimental trend of the liquid-phase composition. With respect to the % AARD values, there is no EoS combined with the basic solid-phase model that is systematically more accurate than the others. The highest deviations are presented in the high pressure region and vary in the range of 3 to 4 K for the mixtures of CH_4 with *n*-$C_{16}H_{34}$, *n*-$C_{17}H_{36}$ and *n*-$C_{20}H_{42}$. The highest deviation observed is presented by PR EoS in the CH_4 - *n*-$C_{24}H_{50}$ mixture at 104.2 MPa and is equal to 10 K. Generally the use of the regressed k_{ij} parameters renders the combined models very accurate until pressures around 20 MPa. After that point, deviations from experiments start to increase. Furthermore, an observed trend is that the use of the fitted BIPs results also in a systematic over-estimation of the equilibrium temperature, in the region where the models deviate from experiments, for the mixtures of CH_4 with *n*-$C_{16}H_{34}$, *n*-$C_{20}H_{42}$, *n*-$C_{24}H_{50}$ and *n*-$C_{36}H_{74}$. The only exception is the CH_4 - *n*-$C_{30}H_{62}$ mixture and the calculations with the two cubic EoS for the CH_4 - *n*-$C_{17}H_{36}$ mixture. This inconsistency may be attributed to the relevant uncertainty of the critical properties, vapor pressure and saturated liquid density data of pure *n*-$C_{30}H_{62}$ which may have an impact on the pure component EoS parameters. Furthermore, the melting enthalpy used for *n*-$C_{17}H_{36}$ was interpolated and the relevant uncertainty may also result in the non-systematic behavior.

Comparing the modeling results between the CH_4 - *n*-$C_{16}H_{34}$ and CH_4 - *n*-$C_{17}H_{36}$ mixtures, it is clearly evident that in the first case there is a much higher overestimation of the equilibrium temperature with each EoS than the latter one, which is not justified taking into account the similarity of the two mixtures. Eventually, PC-SAFT results in lower over-estimation of the experimentally measured equilibrium temperatures, while the two cubic EoS under-estimate them.

In summary, the use of a k_{ij} parameter is imperative for the correct qualitative prediction of the SLGE for almost all the binary mixtures considered. To retain a predictive nature for all the combined models and improve the description of the fluid phases involved, BIPs are preferably fitted on experimental VLE / GLE data at temperatures close to the SLGE conditions of every mixture. Only in two cases the k_{ij} values had to be adjusted by hand in order to predict the correct type of phase behavior. For the mixtures of CH_4 with *n*-C_6H_{14}, *n*-C_7H_{16}, *n*-C_8H_{18} and *n*-$C_{10}H_{22}$ very accurate modeling results are achieved with the basic solid-phase model and the reported BIPs

with all three fluid-phase EoS. The lowest deviations in these 4 mixtures are systematically given by SRK EoS, while PR EoS predictions are very similar. For the more asymmetric type III mixtures, the use of k_{ij} parameters increases significantly the performance of each combined model and until approximately 20 MPa the maximum deviations with respect to the equilibrium temperature range between 2 and 2.5 K. For these mixtures, no EoS combined with the basic solid-phase model is systematically more accurate than the others. A general remark is that the predictions of the SRK and PR EoS with the reported BIPs are very similar for all the mixtures and practically identical until pressures around 20 - 25 MPa. Hereafter, all SLGE calculations are based on the use of k_{ij} parameters.

8.3.2. Advanced Solid-Phase Model: Liquid-Phase Poynting Correction

As it has already been discussed, the use of the reported k_{ij} parameters with the basic solid-phase model results in very accurate prediction of the SLGE for the mixtures of CH_4 with *n*-C_6H_{14}, *n*-$C_7H_{16,}$ *n*-C_8H_{18} and *n*-$C_{10}H_{22}$. The same models give also reliable predictions for the more asymmetric mixtures until approximately 20 - 25 MPa. A first attempt to increase the accuracy of the combined models is with the use of Eq. 8.2, instead of Eq. 8.1, for the calculation of the solid-phase fugacity. The advanced solid-phase model takes into account the pressure dependency of the liquid molar volume in the Poynting correction and this dependency is calculated through the fluid-phase EoS. At this point, the solid molar volume is kept constant with pressure which can be a good approximation, even at high pressures, and this way the effect of the liquid molar volume pressure dependency on the modeling results can be systematically assessed.

Successful implementation of the advanced solid-phase model, in combination with the fluid-phase EoS considered in this work, depends heavily on the correct description of the liquid molar volume pressure dependency. However, because of the hypothetical reference state used for the calculation of the solid-phase fugacity, the accuracy of each EoS can only be directly assessed by predicting the liquid molar volume at the normal melting point of the pure solid-forming compound. PC-SAFT EoS is known to reproduce accurately the saturated liquid molar volumes of pure compounds, as the pure component parameters are typically regressed from vapor pressure and saturated liquid density data. On the other hand, cubic EoS do not provide accurate volume predictions. Table 8.5 summarizes the % Absolute Relative Deviation (% ARD) between EoS predictions of liquid molar volumes at the normal melting point of *n*-

alkanes from *n*-$C_{10}H_{22}$ until *n*-$C_{36}H_{74}$. All volume predictions of PC-SAFT present values of ARD below 1% when compared to DIPPR volumes, except for *n*-$C_{36}H_{74}$, in which the ARD is equal to 5.2%. SRK prediction of the liquid molar volume of *n*-$C_{10}H_{22}$ results in ARD = 23.5 % and it increases with carbon number up to 77.9 for *n*-$C_{36}H_{74}$. The same happens for PR EoS which starts from ARD = 10.3 % for *n*-$C_{10}H_{22}$ and reaches 59.7 % for *n*-$C_{36}H_{74}$.

Table 8.5: %ARD between the liquid molar volumes of Table C.4 and the predicted volumes of the untranslated cubic and PC-SAFT EoS at the reported temperature and pressure conditions (normal melting point of pure components).

Component	T (K)	P (MPa)	SRK	PR	PC-SAFT
n-$C_{10}H_{22}$	243.510	0.1	23.5	10.3	0.4
n-$C_{16}H_{34}$	291.308	0.1	36.0	21.6	0.2
n-$C_{17}H_{36}$	295.134	0.1	36.4	22.0	0.5
n-$C_{20}H_{42}$	309.580	0.1	38.9	24.3	0.6
n-$C_{24}H_{50}$	323.750	0.1	44.1	29.1	1.1
n-$C_{30}H_{62}$	338.650	0.1	48.1	32.8	0.6
n-$C_{36}H_{74}$	349.050	0.1	77.9	59.7	5.2

In this work, calculations were performed with Eq. 8.1 (basic solid-phase model) combined with each fluid-phase EoS, but the experimental liquid molar volume was replaced with the one predicted from each EoS. Because of the low pressure conditions in the mixtures of CH_4 with *n*-C_6H_{14}, *n*-C_7H_{16}, *n*-C_8H_{18}, the Poynting correction has no actual effect and thus the results were practically unaltered. Of course, the same happens if the advanced solid-phase model (Eq. 8.2) is used to calculate the solid-phase fugacity for these mixtures. On the other hand, for the mixtures of CH_4 with *n*-$C_{16}H_{34}$, *n*-$C_{17}H_{36}$, *n*-$C_{20}H_{42}$, *n*-$C_{24}H_{50}$, *n*-$C_{30}H_{62}$ and *n*-$C_{36}H_{74}$, because of the high pressure conditions encountered, the Poynting correction affects the results significantly. If the experimental liquid molar volume is replaced with the predicted one from the cubic EoS in these mixtures, the modeling results with the basic solid-phase model are very poor with the equilibrium temperature being significantly over-predicted (17 - 20 K). In this case, the advanced solid-phase model also gives very poor results. On the other hand, PC-SAFT predictions with the basic solid-phase model are very similar because of the accurate reproduction of the liquid molar volume at the reference state. These calculations are not presented in this work.

In order to get accurate results with the advanced solid-phase model combined with the cubic EoS, a Peneloux-type [107] volume translation scheme was adopted. In this work, the translation parameter was calculated, so that the cubic EoS reproduce exactly the liquid molar volume of each paraffin at the corresponding normal melting point. In this way, if the basic solid-phase model were to be used with the predicted volumes from the translated cubic EoS, the results would be the same with those presented in the previous section. Furthermore, the pressure dependency of the liquid molar volume in Eq. 8.2 is expected to be more accurate than the one calculated from an un-translated EoS. The volume translation parameters for SRK and PR EoS are summarized in Table E.1. Of course, PC-SAFT can be used in its original form since the volume predictions of the EoS are accurate. Hereafter, predictions of the advanced solid-phase model combined with cubic EoS refer to their translated versions, as adopted in this work.

Predictions with the advanced solid-phase model and the fluid-phase EoS considered in this work are presented in the right panels of Figure 8.5 through Figure 8.11. The % AARD between experimental SLGE data and model calculations are summarized in Table 8.4. The mixture of CH_4 with *n*-$C_{10}H_{22}$ is the first mixture in which the advanced solid-phase model shows a small difference in the final results when compared to the basic solid-phase model. Differences between the two models are becoming more prominent from the mixture of CH_4 with *n*-$C_{16}H_{34}$ and on and for pressures higher than approximately 15 to 20 MPa. The use of Eq. 8.2 for the solid-phase fugacity, systematically leads to a lower equilibrium temperature when compared to the basic solid-phase model predictions and a different slope of the SLGE line at high pressures. As a result, because of the over-estimation of the equilibrium temperature with the basic solid-phase model and the regressed BIPs, the modeling results are systematically more accurate with the advanced solid-phase model. Very low % AARD values are achieved, especially for the mixtures of CH_4 with *n*-$C_{20}H_{42}$ and *n*-$C_{24}H_{50}$. The two exceptions again are the mixtures of CH_4 with *n*-$C_{17}H_{36}$ and *n*-$C_{30}H_{62}$ which presented a non-systematic behavior as discussed in the previous section. In these two cases, the advanced solid-phase model is less accurate than the basic one. Similar to the calculations with the previous solid-phase model, no fluid-phase EoS is systematically more accurate than the others.

In summary, the advanced solid-phase model is able to provide accurate results for the high pressure SLGE of asymmetric CH_4 mixtures with *n*-alkanes. The pressure

dependency of the liquid molar volume is taken into account through the fluid-phase EoS and is becoming prominent for pressures higher than 15 - 20 MPa. This way, an already accurate prediction of the low pressure SLGE region remains unaltered and the high pressure region is described more accurately. Implementation of the model with cubic EoS requires the use of volume-translated versions of them as proposed in this work, so that accurate results are obtained. PC-SAFT EoS in its original form in terms of parameterization provides accurate low and high pressure modeling results for the SLGE of the mixtures discussed. The highest deviations between model predictions and experimental SLGE data are approximately 2 - 3 K, except for the two cases of non-systematic behavior, in which the maximum deviations are approximately 6 (CH_4 - *n*-$C_{17}H_{36}$) and (CH_4 - *n*-$C_{30}H_{64}$) 10 K.

8.3.3. Correlation of BIPs: A Predictive Approach

The k_{ij} parameters reported in Table 8.3 for each fluid-phase EoS, were correlated with the carbon number of the solid-forming paraffin for every binary mixture considered in this work. A quadratic dependency of the BIPs was established with each fluid-phase EoS and the resulting coefficients are summarized in Table E.2. The correlations are presented in Figure E.17. It has to be noted that the k_{ij} values of the cubic EoS for the CH_4 - *n*-$C_{36}H_{74}$ mixture were not included in the fitting process for the correlation, since the reported value shows a particular scattering from the others. As it has already been discussed, cubic EoS showed a problematic behavior in the fitting process for the k_{ij} parameter in this mixture, by not predicting a critical point at the respective isotherm. The adjusted k_{ij} value reported in Table 8.3 reproduces the experimental behavior by achieving the lowest % AARD between experimental GLE data and model calculations. However, this value deviates from the quadratic trend that the other BIPs seem to follow. On the other hand, the corresponding k_{ij} of PC-SAFT EoS is in very good agreement with a quadratic variation with the carbon number.

The proposed correlations were used for the calculation of k_{ij} parameters for the PR and PC-SAFT EoS to showcase the results of this predictive approach on the mixtures considered in this work. The basic solid-phase model is used for the mixtures of CH_4 with *n*-C_6H_{14}, *n*-C_7H_{16} and *n*-C_8H_{18}, since the advanced solid-phase model will yield the same results because of the low pressures encountered, and the advanced solid-phase model is used for the remaining asymmetric mixtures. The results are presented in Figure 8.12 and Figure 8.13, while Table E.3 summarizes the % AARD between experimental

SLGE data and model predictions. As it can be seen from the % AARD values and the graphical results, the correlated BIPs give very similar predictions of the SLGE for all the mixtures considered with those reported in Table 8.3. The only exception is the CH_4 - *n*-C_6H_{14} mixture in which the correlated k_{ij} results in a wrong type of phase behavior. A sharp peak can be seen on the highest pressure point of the P-T graph for this mixture which results in an abrupt change of the liquid-phase composition, which is not in agreement with experiments. The adjusted k_{ij} value reported in Table 8.3 for the cubic EoS should be the upper limit for this mixture, in order to predict the correct type of phase behavior. Apart from this exception, the SLGE of all the other mixtures is reliably predicted. In summary, the proposed correlations can be used as an alternative for the calculation of k_{ij} parameters for mixtures of CH_4 with *n*-alkanes with reliable accuracy at a relevant range of conditions.

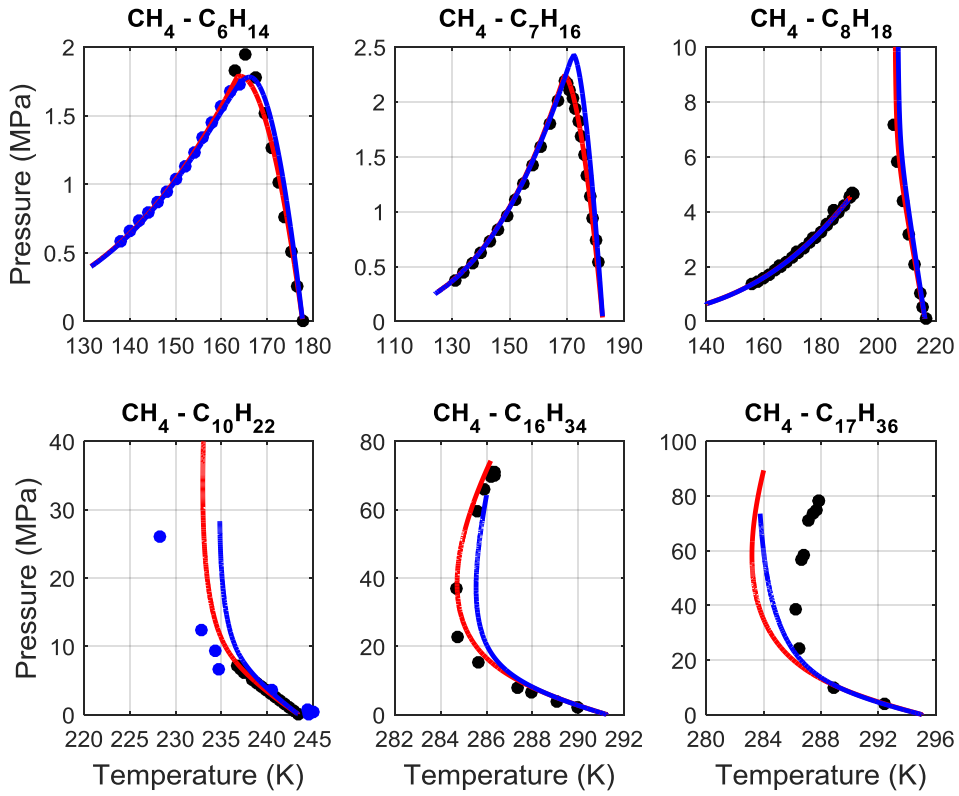

Figure 8.12: Prediction of the SLGE curves of various binary CH_4 mixtures with k_{ij} parameters calculated from the proposed correlations. Experimental data [24, 193, 198, 242, 244-248] are represented by data points and calculations by lines. Black lines correspond to SRK, red to PR and blue to PC-SAFT EoS. Top panels show predictions with the basic solid-phase model, while bottom panels show predictions with the advanced solid-phase model.

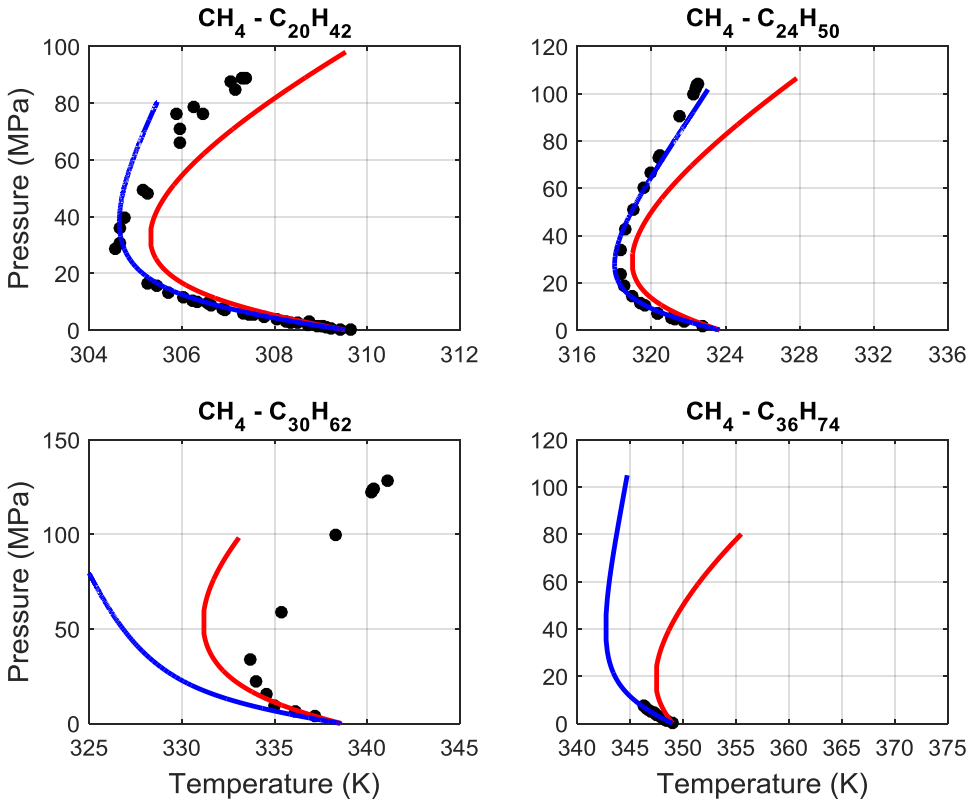

Figure 8.13: Prediction of the SLGE curves of various binary CH_4 mixtures with k_{ij} parameters calculated from the proposed correlations and the advanced solid-phase model. Experimental data [20, 206, 208, 249] are represented by data points and calculations by lines. Black lines correspond to SRK, red to PR and blue to PC-SAFT EoS.

8.3.4. Advanced Fit Solid-Phase Model

The newly proposed advanced-fit solid-phase model combines the approach of Pauly et al. [104], which incorporates a Poynting solid-phase model, with the approach of Ameri-Mahabadian et al. [112] which correlates the solid molar volume with the liquid one, through a pressure dependent proportionality coefficient, as shown in Eqs. 8.4 and 8.5. However, in the latter approach, a no-Poynting solid-phase model is used and the correlation between the two volumes is employed for the calculation of the solid-phase thermophysical properties at high pressures. By combining the two approaches, Eq. 8.8 is proposed for the calculation of the solid-phase fugacity. Following Ameri-Mahabadian et al., the adjustable parameter ($\hat{a}$) in Eq. 8.4, is fitted directly to the experimental SLGE data.

Results with the new model, coupled with PR and PC-SAFT EoS are presented in Figure 8.14 and Figure 8.15 for mixtures in which experimental SLGE data are available at high pressures. The k_{ij} parameters reported in Table 8.3 are used for each

fluid-phase EoS and the same volume translation scheme, as discussed in a previous section, is applied to PR. The values for the adjustable parameter of the advanced-fit solid-phase model and the % AARD between experimental SLGE data and model calculations are summarized in Table 8.6. The new solid-phase model was not coupled with SRK EoS because very similar results with PR EoS would have been obtained. Moreover, the emphasis in this section is to showcase the new solid-phase model, rather than presentation of an extensive comparison between the different fluid-phase EoS.

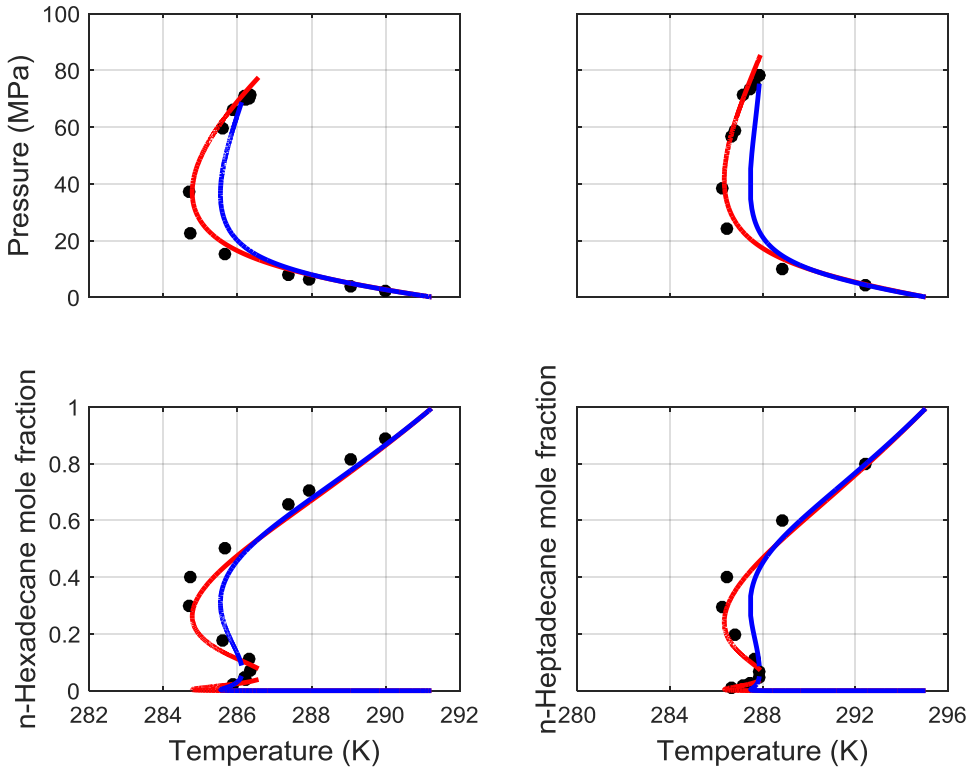

Figure 8.14: Correlation of the SLGE curve with the advanced-fit solid phase model and k_{ij} parameters fitted to experimental binary VLE data. Experimental data [24, 198] are represented by data points and calculations by lines. Black lines correspond to SRK, red to PR and blue to PC-SAFT EoS. Left panels show the correlation of the CH_4 - *n*-$C_{16}H_{34}$ mixture, while right panels show the correlation of the CH_4 - *n*-$C_{17}H_{36}$ mixture. The mole fraction refers to the liquid and vapor phases along the SLGE curve.

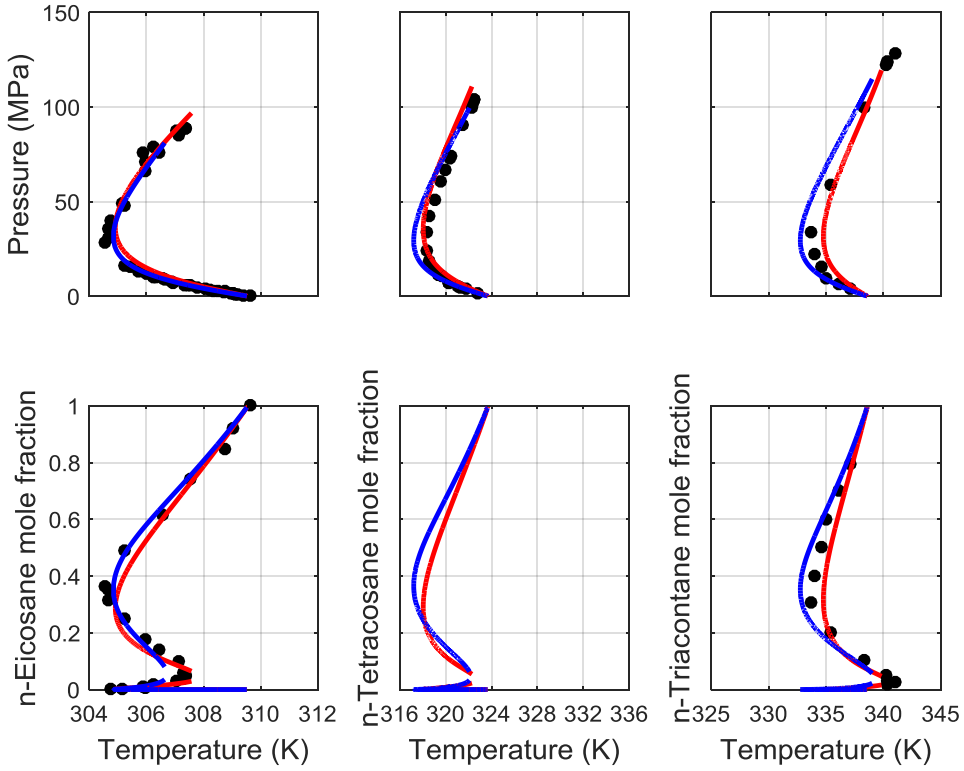

Figure 8.15: Correlation of the SLGE curve with the advanced-fit solid phase model and k_{ij} parameters fitted to experimental binary VLE data. Experimental data [20, 206, 208] are represented by data points and calculations by lines. Black lines correspond to SRK, red to PR and blue to PC-SAFT EoS. Left panels show the correlation of the CH_4 - *n*-$C_{20}H_{42}$ mixture, middle panels show the correlation of the CH_4 - *n*-$C_{24}H_{50}$ mixture and right panels show the correlation of the CH_4 - *n*-$C_{30}H_{62}$ mixture. The mole fraction refers to the liquid and vapor phases along the SLGE curve.

Table 8.6: %AARD between experimental SLGE data and correlations with the advanced-fit solid-phase model calculated for the equilibrium temperature of each mixture.

EoS		CH_4 - *n*-$C_{16}H_{34}$	CH_4 - *n*-$C_{17}H_{36}$	CH_4 - *n*-$C_{20}H_{42}$	CH_4 - *n*-$C_{24}H_{50}$	CH_4 - *n*-$C_{30}H_{62}$
PR	$\hat{a}$	2.7×10^{-4}	5.6×10^{-4}	4.0×10^{-4}	5.0×10^{-4}	5.2×10^{-4}
	%AARD	0.13	0.10	0.10	0.19	0.23
PC-SAFT	$\hat{a}$	8.0×10^{-4}	1.1×10^{-3}	5.0×10^{-4}	5.2×10^{-4}	5.2×10^{-4}
	%AARD	0.20	0.27	0.03	0.15	0.21
NP		9	9	33	21	8

$$\%\ AARD = \frac{100}{NP}\sum_{i=1}^{NP}\left|\frac{T_i^{calculated} - T_i^{experimental}}{T_i^{experimental}}\right|$$

where NP is the number of experimental data points and T_i is the equilibrium temperature.

Comparing the results of the advanced-fit solid-phase model with the advanced solid-phase model, we observe that there is a general reduction of the % AARD between experiments and calculations with both EoS. The only exception is the CH_4 - *n*-$C_{24}H_{50}$ mixture correlation with PC-SAFT which presents a slightly higher % AARD than the prediction of the EoS with the advanced solid-phase model. However, by taking into account the reduction of the % AARD in all the other mixtures, it is asserted that the new solid-phase model is a successful modification of the one discussed in the previous section. Furthermore, the new model presents systematically lower deviations compared to the previous one, when coupled with the PR EoS. The highest deviations in the equilibrium temperature between experiments and models are presented in the mixtures of CH_4 with *n*-$C_{16}H_{34}$ and *n*-$C_{17}H_{36}$ with PC-SAFT EoS and their values are below 2 K.

In terms of % AARD, PR EoS is more accurate than PC-SAFT for the mixtures of CH_4 with *n*-$C_{16}H_{34}$ and *n*-$C_{17}H_{36}$, while PC-SAFT is more accurate for the mixtures of CH_4 with *n*-$C_{20}H_{42}$, *n*-$C_{24}H_{50}$ and *n*-$C_{30}H_{62}$. However, PC-SAFT predicts a lower UCEP compared to experimental data for these mixtures, as shown in Figure 8.15. PR EoS correlates with excellent accuracy the liquid-phase composition and the equilibrium temperature for the mixtures of CH_4 with *n*-$C_{16}H_{34}$ and *n*-$C_{17}H_{36}$, even near the critical composition, without any significant over-estimation of the UCEP. For the mixtures presented in Figure 8.15, PR EoS presents a slightly higher % AARD value than PC-SAFT, but taking into account the very accurate correlation of the UCEP, we can assert that the cubic EoS correlates more accurately the SLGE line overall. It is also observed that the values for the adjustable parameter $\hat{a}$ for the mixtures of CH_4 with *n*-$C_{20}H_{42}$, *n*-$C_{24}H_{50}$ and *n*-$C_{30}H_{62}$ are relatively similar for both EoS and more distinct values are obtained for the mixtures of CH_4 with *n*-$C_{16}H_{34}$ and *n*-$C_{17}H_{36}$. A mean value of the adjustable parameter can be also used for each EoS to eliminate the fitting process for other similar mixtures and reliable results should be expected.

8.3.5. Global Phase Diagrams

Figures 15 through 17 refer to the calculated global phase diagrams of selected CH_4 mixtures considered in this work with the adopted and proposed models. As it has already been discussed in a previous section, the k_{ij} parameters had to be adjusted to lower values than those regressed for the two cubic EoS in the CH_4 - *n*-C_6H_{14} mixture, so that the correct type of phase behavior is reproduced.

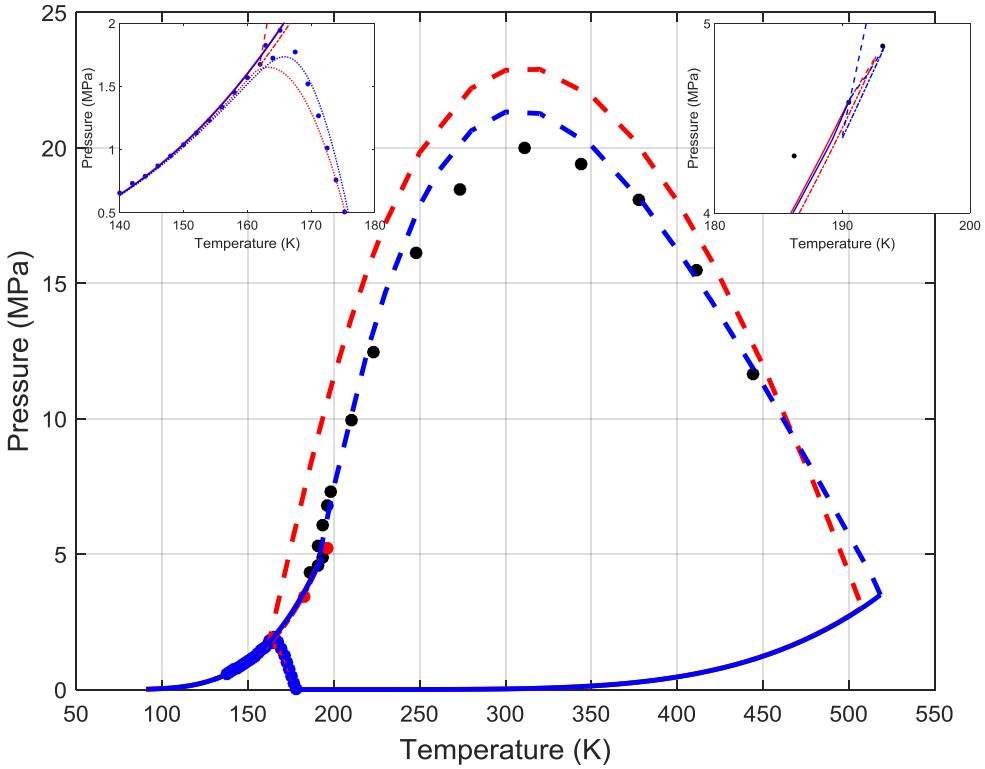

Figure 8.16: Global phase diagram of the CH_4 - *n*-C_6H_{14} mixture. Experimental SLGE data [244, 245] are represented by blue data points. Experimental VLE / GLE critical points [254, 255] are represented by black points. Experimental LCEP and UCEP are represented by red data points. Red lines correspond to PR and blue to PC-SAFT EoS. All calculations were performed with k_{ij} parameters fitted to experimental binary VLE data. Solid lines correspond to pure component vapor pressure calculations. Dashed lines correspond to VL / GL critical point calculations. Dash-dot lines correspond to VLLE / GLLE calculations. Dotted lines correspond to SLGE calculations. SLGE calculations were performed with the basic solid-phase model.

As it can be seen in Figure 8.16, PR EoS reproduces correctly the type V behavior of the CH_4 - *n*-C_6H_{14} mixture, with the calculated major critical line being connected to the LCEP of a VLLE / GLLE line. Their intersection lies very closely to the SLGE line but no quadruple point is formed. The VLLE / GLLE line terminates at a UCEP which is connected to the pure CH_4 critical point through a minor critical line. The use of a lower k_{ij} value with PR EoS would shift the major critical line to lower pressures and this would result in a better correlation of the VL / GL experimental critical points. Moreover, the VLLE / GLLE line would be shorter and would lie further away from the SLGE line. However, in this way the SLGE prediction would be worse, since the calculated SLGE pressures would be also lower. On the other hand, PC-SAFT EoS predicts with remarkable accuracy the global phase behavior of the CH_4 - *n*-C_6H_{14}

mixture. The most distinct inaccuracy is the very short VLLE / GLLE line predicted by the model, as shown in Figure 8.16.

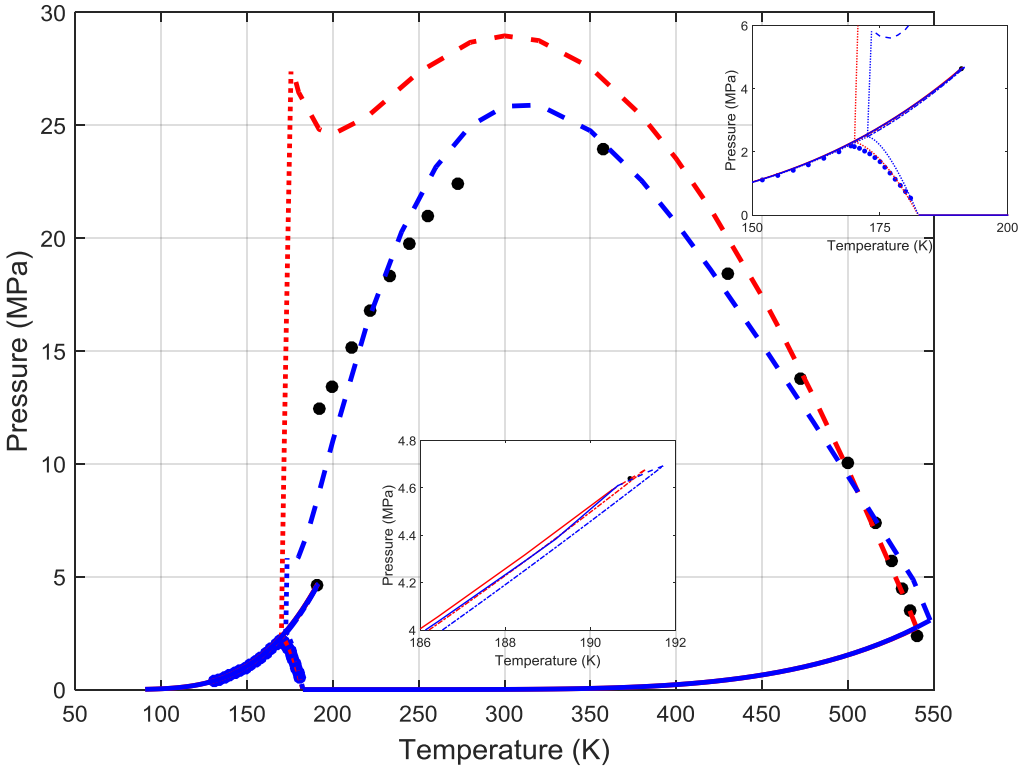

Figure 8.17: Global phase diagram of the CH_4 - n-C_7H_{16} mixture. Experimental SLGE data [246] are represented by blue data points. Experimental VLE / GLE critical points [256, 257] are represented by black points. Red lines correspond to PR and blue to PC-SAFT EoS. All calculations were performed with k_{ij} parameters fitted to experimental binary VLE data. Solid lines correspond to pure component vapor pressure calculations. Dashed lines correspond to VL / GL critical point calculations. Dash-dot lines correspond to VLLE / GLLE calculations. Dotted lines correspond to SLGE and SLLE calculations. SLGE and SLLE calculations were performed with the basic solid-phase model.

A similar adjustment of the k_{ij} parameter had to be done for PC-SAFT EoS in order to reproduce correctly the type of phase behavior of the CH_4 - n-C_7H_{16} mixture. As it has been mentioned, this mixture exhibits a type III phase behavior, but the major critical line is interrupted by an SLLE line before it reaches very high pressures. This phenomenon is reproduced with relatively high accuracy by PC-SAFT EoS as presented in Figure 8.17. The quadruple point formation is also predicted, while a VLLE / GLLE line extends from the Q point until terminated by a UCEP, which is connected to the pure CH_4 critical point through a minor critical line. This global phase behavior is also qualitatively reproduced by PR EoS, while the SLGE is predicted with higher accuracy

than PC-SAFT. However, the EoS significantly overestimates the major critical line, which results also in a SLLE line that extends to very high pressures.

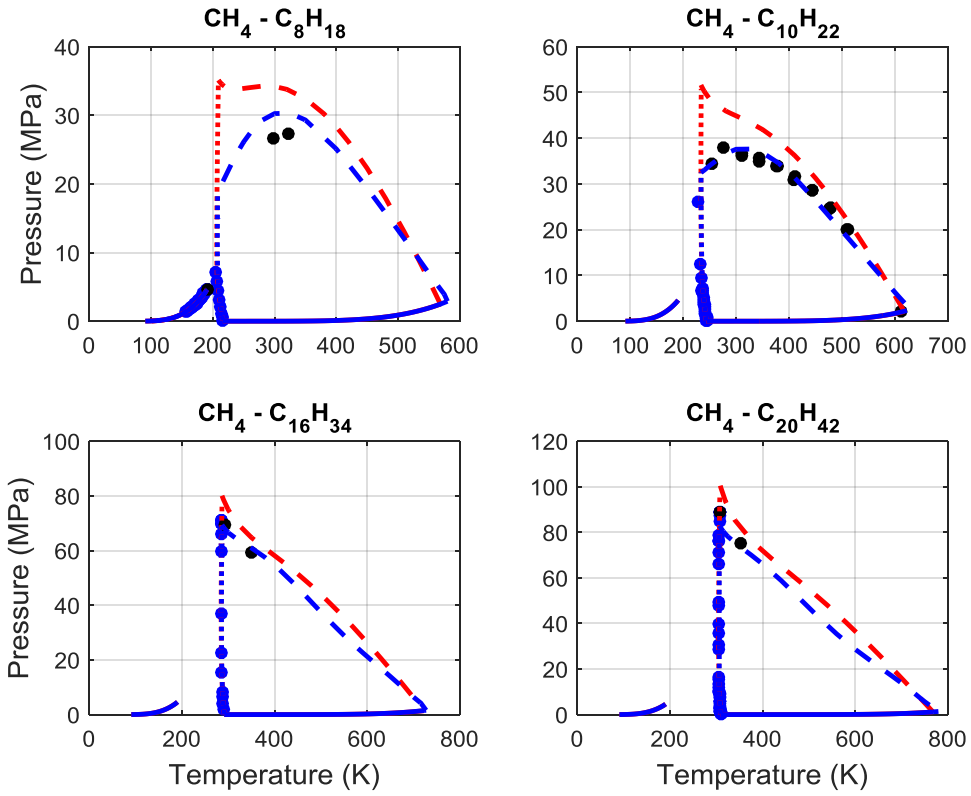

Figure 8.18: Global phase diagrams of various binary CH_4 mixtures. Experimental SLGE data [193, 198, 206, 242, 247, 248] are represented by blue points. Experimental VLE / GLE critical points [194, 242, 251, 258] are represented by black points. Red lines correspond to PR and blue to PC-SAFT EoS. All calculations were performed with k_{ij} parameters fitted to experimental binary VLE data. Solid lines correspond to pure component vapor pressure calculations. Dashed lines correspond to VL / GL critical point calculations. Dotted lines correspond to SLGE calculations. The CH_4 - *n*-C_8H_{18} SLGE was calculated with the basic solid-phase model. The CH_4 - *n*-$C_{10}H_{22}$ SLGE was calculated with the advanced solid-phase model. The CH_4 - *n*-$C_{16}H_{34}$ and CH_4 - *n*-$C_{20}H_{42}$ SLGE were calculated with the advanced-fit solid-phase model.

In Figure 8.18, four cases of type III mixtures are presented, in which the SLGE line that stems from the pure solid-former melting point interrupts the major critical line at high pressures. A second SLGE line is also present but it lies very closely to the pure CH_4 vapor pressure line and usually it is not determined experimentally. One exception is the CH_4 - *n*-C_8H_{18} mixture in which experimental data for the low temperature SLGE line exist and calculations were performed in this work, as presented in the previous sections. For the mixtures of CH_4 with *n*-C_8H_{18} and *n*-$C_{10}H_{22}$, PC-SAFT EoS correlates more accurately the experimental GL critical points than PR EoS, predicting also a lower pressure UCEP. The two EoS critical point predictions are qualitatively more similar for

the mixtures of CH_4 with *n*-$C_{16}H_{34}$ and *n*-$C_{20}H_{42}$, with PC-SAFT underestimating the UCEP.

8.4. Conclusions

Two cubic (SRK, PR) and a higher order (PC-SAFT) EoS were coupled with a solid-phase thermodynamic model to calculate the SLGE behavior of binary CH_4 mixtures with *n*-alkanes. Several aspects of each combined model were assessed and the effect of specific terms of the solid-phase modeling approach was systematically validated against available experimental data. It is concluded that the use of k_{ij} parameters is imperative for the correct qualitative and improved quantitative prediction of the SLGE for all the binary mixtures considered. Temperature independent k_{ij} parameters should preferably be fitted to experimental VLE / GLE data at temperatures close to the SLGE conditions of each mixture, so that the predictive nature of the models is retained and accurate description of the fluid phases is obtained at the relevant range of conditions. The basic solid-phase model in combination with the fluid-phase EoS considered and the regressed BIPs provides accurate predictions of the SLGE until pressures around 20 MPa.

Accurate results for the high pressure SLGE of asymmetric CH_4 mixtures with *n*-alkanes were obtained by taking into account the pressure dependency of the liquid molar volume in the Poynting correction of the solid-phase model, through the fluid-phase EoS. Implementation of the model with cubic EoS requires the use of volume-translated versions of them as proposed in this work. PC-SAFT EoS in its original form provides accurate low and high pressure results, since it reproduces more accurately the liquid molar volumes.

The newly proposed advanced-fit solid-phase model provides excellent correlation of the high-pressure SLGE for the mixtures considered, both with PR and PC-SAFT EoS. Combined with the new solid-phase model, PC-SAFT is more accurate in terms of % AARD from experimental data, but PR predicts with higher accuracy the UCEP resulting in a better description of the SLGE line overall. Global phase diagrams were also calculated for specific mixtures to showcase the ability of the adopted and proposed models in reproducing the global phase behavior. Generally, PC-SAFT predictions are in better agreement with experimental data when a wide range of conditions and different types of phase behavior are taken into account.

9. Vapor-Liquid Equilibrium and Physical Properties of C_2H_4 Mixtures

9.1. Introduction

The aim of this Chapter is to investigate the accuracy of widely used EoS by industry and academia towards the prediction and correlation of a broad range of thermodynamic properties of C_2H_4 and C_2H_4 mixtures without a re-parameterization of the EoS for pure components, unless needed. The PR EoS, and two versions of SAFT EoS, namely the PC-SAFT and SAFT-VR Mie are used to model the physical properties (density, heat capacity, speed of sound, Joule-Thomson coefficient, and isothermal compressibility) of pure C_2H_4. The comparison between the three EoS is based on pure C_2H_4 data. Furthermore, the VLE of binary C_2H_4 mixtures is modeled with the same EoS and BIPs are fitted using the available experimental phase equilibrium data to optimize the performance of each EoS. Finally, the VLE of ternary C_2H_4 mixtures is predicted, using the regressed BIPs and a thorough comparison between the three EoS is reported.

9.2. Results and Discussion

9.2.1. Pure Component Properties

Successful modeling of an ethylene pipeline depressurization process relies significantly on the accurate prediction of the physical properties of the system under study which is comprised mainly of C_2H_4 (>99 % mol). Consequently, the first step is the evaluation of the accuracy of every EoS in predicting the pure C_2H_4 physical properties.

The pure component parameters for the PR, PC-SAFT and SAFT-VR Mie EoS are summarized in Table C.1, Table C.2 and Table C.3 in Appendix C. The critical properties and the acentric factor needed for the PR EoS were taken from DIPPR [175] database, while the PC-SAFT parameters were gathered from literature [15, 18, 87, 259]. The SAFT-VR Mie parameters were taken from Dufal et al. [260], except for H_2, for which parameters were regressed in this work using supercritical data for density and speed of sound taken from NIST [261]. Table F.1 summarizes the % AARD between experimental data and SAFT-VR Mie predictions for density, isobaric heat capacity, speed of sound and Joule-Thomson coefficient for H_2 with the regressed set of

parameters. No speed of sound data were available in the literature for *1*-C_4H_8 and as a result calculations including this component were not performed with SAFT-VR Mie. Parameters for *1*-C_4H_8 could have been regressed without the inclusion of the missing data, but this approach was not followed, so that consistency is kept with the procedure proposed in the literature [34, 260].

Two sets of PC-SAFT parameters were available in the literature for C_2H_4; one proposed by Gross and Sadowski [18] (abbreviated as set 1) and one proposed by Xu et al. [87] (abbreviated as set 2). The accuracy of both PC-SAFT parameter sets was evaluated against pure C_2H_4 vapor pressure and physical property data from NIST [261]. Comparison between the two parameter sets showed that set 2 is more accurate in predicting the liquid density of C_2H_4 along the saturation line and in the supercritical region, while the prediction of all the other properties is of comparable accuracy. As a result, set 2 was chosen as the C_2H_4 parameter set for PC-SAFT in this work for all mixture calculations.

The three different EoS predictions are validated against C_2H_4 vapor pressure and physical property data at saturated and supercritical conditions from NIST [261]. Table 9.1 summarizes the %AARD between experiments and EoS predictions at saturated conditions. The vapor pressure is predicted with higher accuracy by SAFT-VR Mie EoS (% AARD = 0.55), while PC-SAFT shows a deviation of % AARD = 1.28. PR presents the highest deviation in the prediction of vapor pressure with % AARD = 3.92, although the higher deviations presented by PR are located in the lower temperature region from 105 to 180 K. Moreover, PR is more accurate than the two SAFT EoS close to the critical point, since the experimental critical properties are used by design to calculate the pure component parameters. When saturated densities are considered, PC-SAFT is the most accurate EoS for both the liquid and the vapor phase. Both SAFT EoS are much more accurate than PR (% AARD = 6.80) in describing the liquid phase density, but this is something to be expected taking into account the fitting process for the pure component parameters. In terms of the saturated isobaric heat capacity, PC-SAFT gives the most accurate prediction for the liquid phase (% AARD = 5.66), while PR gives the least accurate prediction (% AARD = 10.57). Nevertheless, for the vapor phase, PR is the most accurate EoS (% AARD = 8.39), while SAFT-VR Mie gives the least accurate prediction (% AARD = 15.0). For the speed of sound, PC-SAFT is the relatively most accurate EoS for the liquid phase (% AARD = 6.77), followed by SAFT-VR Mie (% AARD = 9.95). Despite the relatively large % AARD, it has to be noted that

the two SAFT EoS provide a qualitatively correct description of the data, while PR fails to catch the trend. Interestingly, PR predicts with very high accuracy the speed of sound of the vapor phase (% AARD = 0.36), even more accurately than PC-SAFT (% AARD = 0.51), while worth noticing is the even higher deviation of SAFT-VR Mie, although the fitting process of the pure component parameters includes speed of sound data. The speed of sound predictions with the three EoS are presented in Figure 9.1. Finally, for the Joule-Thomson coefficient, PC-SAFT is the most accurate in both liquid (% AARD = 8.03) and vapor (% AARD = 22.83) phase, while PR gives the least accurate prediction for the saturated liquid Joule-Thomson coefficient (% AARD = 72.09) and SAFT-VR Mie gives the least accurate prediction for the saturated vapor Joule-Thomson coefficient (% AARD = 28.42). Experimental data and model calculations for the Joule-Thomson coefficient are shown in Figure 9.2.

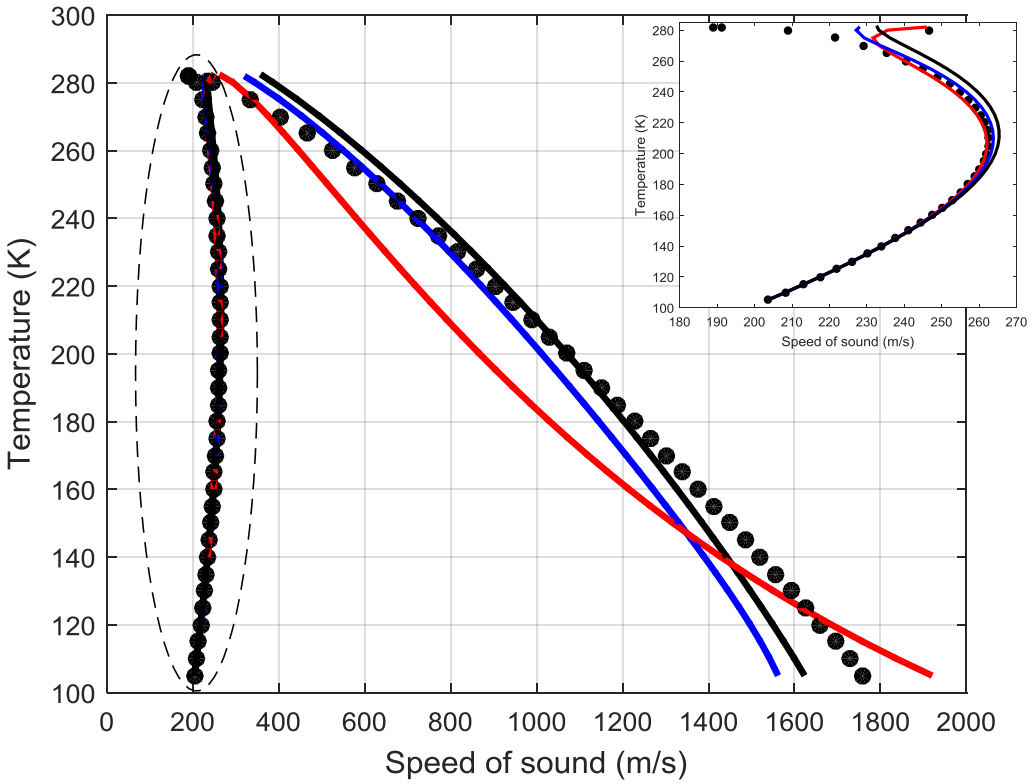

Figure 9.1: Speed of sound along the saturation curve of C_2H_4. NIST data [261] are represented by data points and calculations by lines. Red lines correspond to PR, blue lines to PC-SAFT and black lines to SAFT-VR Mie EoS.

Table 9.1: %AARD between experimental data at saturated conditions taken from NIST [261] and EoS predictions for C_2H_4. The ideal gas heat capacity is calculated using a correlation from DIPPR [175].

	% AARD									T (K)	NP
EoS	P^{sat} (MPa)	ρ^L (kg/m^3)	ρ^V (kg/m^3)	${c_p}^L$ (J/mol K)	${c_p}^V$ (J/mol K)	${v_s}^L$ (m/s)	${v_s}^V$ (m/s)	${\mu_{JT}}^L$ (K/kPa)	${\mu_{JT}}^V$ (K/kPa)		
PR	3.92	6.80	4.33	10.57	8.39	12.96	0.36	72.09	23.73	105 - 282	37
PC-SAFT	1.28	0.42	2.37	5.66	9.84	6.77	0.51	8.03	22.83		
SAFT-VR Mie	0.55	0.87	3.77	8.26	15.0	9.95	2.04	22.3	28.42		

$$\%\ AARD = \frac{100}{NP}\sum_{i=1}^{NP}\left|\frac{P_i^{calculated} - P_i^{experimental}}{P_i^{experimental}}\right|$$

where NP is the number of experimental data points and P_i is the respective property.

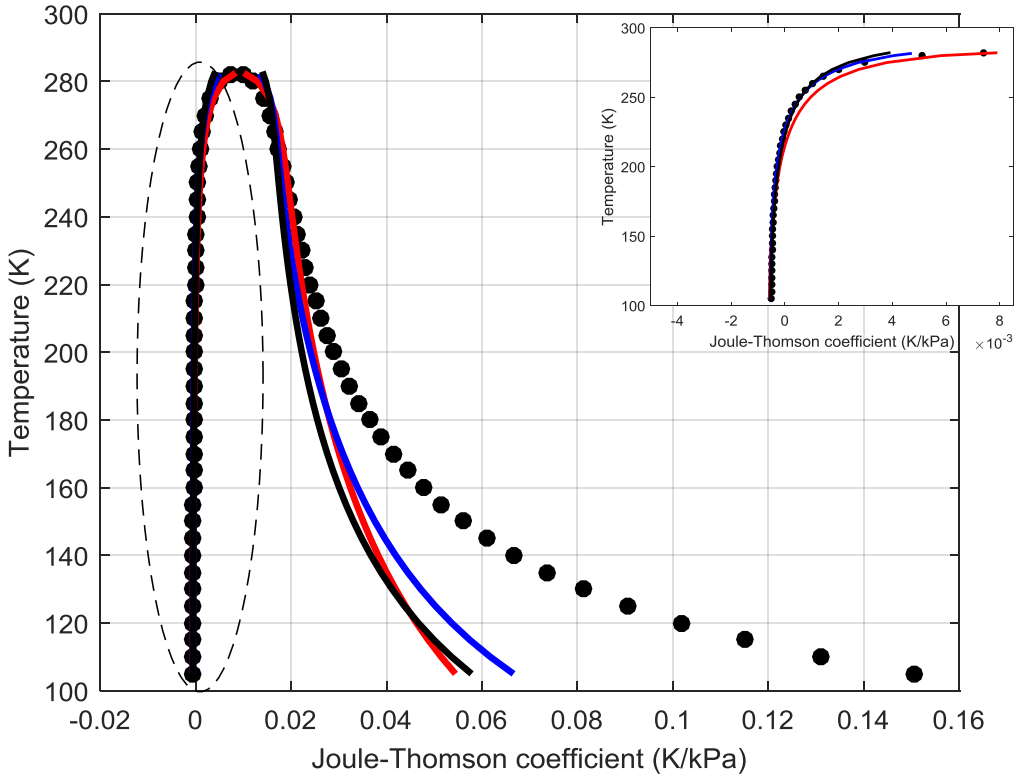

Figure 9.2: Joule-Thomson coefficient along the saturation curve of C_2H_4. NIST data [261] are represented by data points and calculations by lines. The color code is the same as in Figure 9.1

Table 9.2: %AARD between experimental data at supercritical conditions taken from NIST [261] and EoS predictions for C_2H_4. The ideal gas heat capacity is calculated using a correlation from DIPPR [175].

	% AARD					T (K)	P (MPa)	NP
EoS	ρ (kg/m^3)	c_p (J/mol K)	v_s (m/s)	μ_{JT} (K/kPa)	k_T (1/kPa)			
PR	3.05	2.04	8.22	101.03	16.93	285 - 405	1 - 40	560
PC-SAFT	1.24	3.18	2.90	53.15	7.23			
SAFT-VR Mie	1.98	3.24	1.88	69.4	5.11	290 - 405		520

$$\%\ AARD = \frac{100}{NP}\sum_{i=1}^{NP}\left|\frac{P_i^{calculated} - P_i^{experimental}}{P_i^{experimental}}\right|$$

where NP is the number of experimental data points and P_i is the respective property.

The C_2H_4 physical properties in the supercritical region were also calculated using the three EoS. Table 9.2 summarizes the % AARD between NIST data and EoS predictions at supercritical conditions. The supercritical density is predicted with high accuracy by the two SAFT EoS, with PC-SAFT being the most accurate (% AARD = 1.24), while PR is less accurate (% AARD = 3.05) with the higher deviations being prevalent at isotherms close to the critical isotherm and high pressures. The density predictions are presented in Figure 9.3.

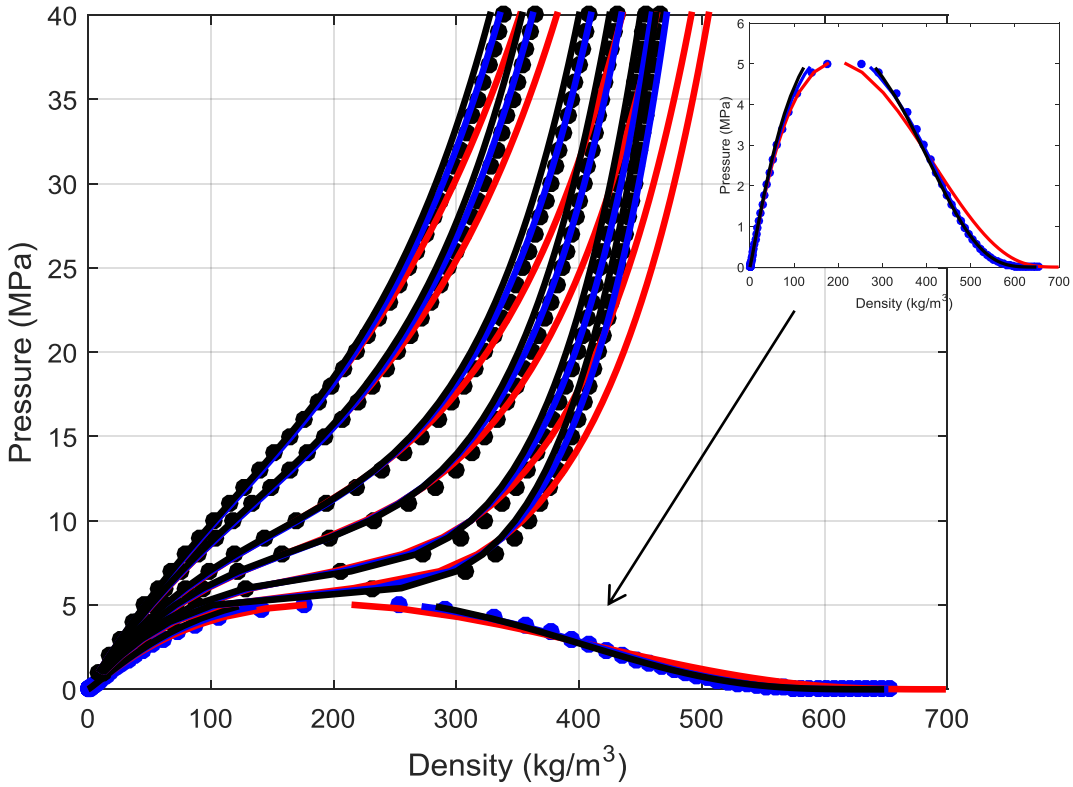

Figure 9.3: Saturated and supercritical density of C_2H_4. Supercritical temperature range (from right to left: $1.027T_r$, $1.062T_r$, $1.133T_r$, $1.204T_r$, $1.345T_r$, $1.434T_r$) spans $1.027T_r$ to $1.434T_r$. NIST data [261] are represented by data points and calculations by lines. The color code is the same as in Figure 9.1.

All three EoS are much more accurate in predicting the total isobaric heat capacity at supercritical conditions when compared to the saturated ones, but still they present relatively large deviations at high pressures (>20 MPa). Total supercritical heat capacity predictions at four isotherms with the three EoS are presented in Figure F.1. SAFT-VR Mie predicts with very satisfying accuracy the supercritical speed of sound (% AARD = 1.88), while PC-SAFT is ~1% less accurate. PR fails to provide a quantitatively satisfying prediction of the supercritical speed of sound (% AARD = 8.22), although the trend is qualitatively correct (Figure 9.4).

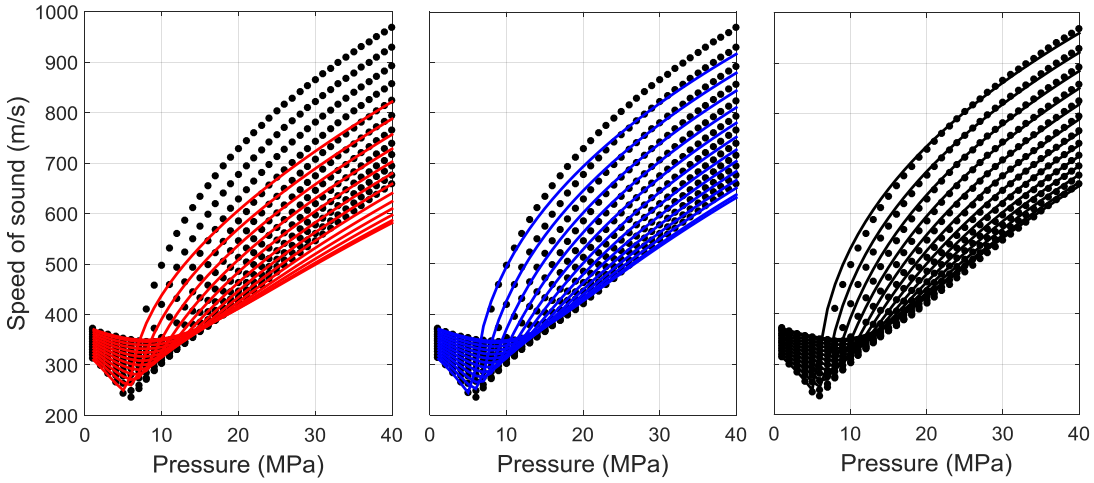

Figure 9.4: Supercritical speed of sound of C_2H_4. Supercritical temperature range spans $1.027T_r$ to $1.434T_r$. NIST data [261] are represented by data points and calculations by lines. The color code is the same as in Figure 9.1.

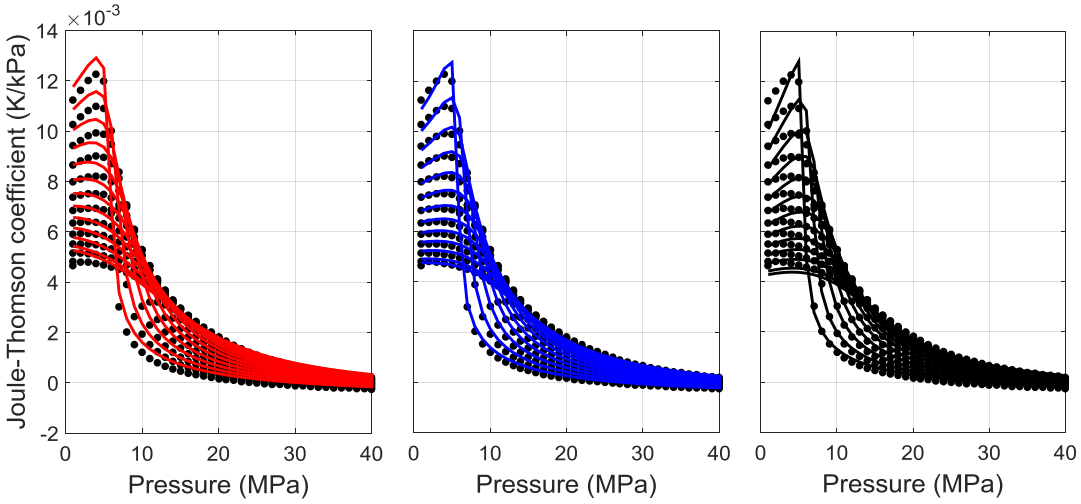

Figure 9.5: Supercritical Joule-Thomson coefficient of C_2H_4. Supercritical temperature range spans $1.027T_r$ to $1.434T_r$. NIST data [261] are represented by data points and calculations by lines. The color code is the same as in Figure 9.1.

Joule-Thomson coefficient predictions by the three EoS present very large deviations from NIST data. PC-SAFT is more accurate than the other two models and the high deviations are located in isotherms close to the critical one and pressures higher than 10 MPa. SAFT-VR Mie and PR EoS show large deviations from the experimental data even at low pressures (Figure 9.5), but all three models provide a satisfactory description of the Joule-Thomson coefficient at temperatures far from the critical one, even at high pressures. The isothermal compressibility is predicted accurately by SAFT-

VR Mie (% AARD = 5.11), while PC-SAFT is ~2% less accurate and PR presents the largest deviation (% AARD = 16.93) among the three EoS.

In summary, SAFT-VR Mie provides the most accurate prediction of the pure C_2H_4 vapor pressure, followed by PC-SAFT, while PR is the least accurate. For the physical properties along the saturation line, PC-SAFT is the most accurate EoS overall. SAFT-VR Mie is superior to PR in predicting all the saturated liquid phase properties and saturated vapor phase density, but inferior to PR when the other vapor phase properties are considered. Both SAFT EoS are superior to PR in the supercritical region except for the total isobaric heat capacity. PC-SAFT predicts more accurately than SAFT-VR Mie the supercritical density, isobaric heat capacity and the Joule-Thomson coefficient, while the opposite happens for the supercritical speed of sound and isothermal compressibility coefficient. In general, the performance of the two SAFT EoS is comparable, with none being clearly superior to the other.

9.2.2. Vapor-Liquid Equilibrium of Binary Mixtures

In Table 9.3 the temperature and pressure ranges for all the experimental VLE data considered in this work are presented. k_{ij} values were fitted by minimizing the root-mean-square deviation of the bubble pressure values between experimental data and EoS calculations. A temperature dependent k_{ij} was used for the case of H_2 - C_2H_4 mixture, to improve agreement with experimental data. A quadratic function was used for PR EoS:

$$k_{ij} = k_{ij,0} + k_{ij,1}T + k_{ij,2}T^2 \quad 9.1$$

Regarding the two SAFT EoS, a linear relationship with inverse temperature was employed:

$$k_{ij} = k_{ij,0} + \frac{k_{ij,1}}{T} \quad 9.2$$

In Eqs. 9.1 and 9.2, T is expressed in K.

Table 9.4 and Table 9.5 summarize the % AARD between the experimental VLE data and the EoS calculations for each mixture and the corresponding k_{ij} values. Only the experimental bubble pressure values are considered in the calculation of % AARD, since the mole fractions of the vapor phase were unavailable for some systems, *e.g.*, C_2H_4 - C_3H_6, and C_2H_4 - C_3H_8. In general, both PC-SAFT and SAFT-VR Mie proved to be much more sensitive to the k_{ij} values than PR, hence very small values of k_{ij} were obtained for the SAFT equations. This is also a manifestation that the Lorentz-Berthelot combining rule for energy is appropriate for these mixtures. In this Chapter, indicative

results for the binary and ternary mixtures VLE are presented, mainly with the use of the regressed BIPs. The complete set of calculations can be found in the publication of Nikolaidis et al. [262] and its respective Supporting Information.

Table 9.3: Experimental binary VLE data from literature modeled in this work.

Temperature (K)	Pressure (MPa)	Ref
H_2 - C_2H_4		
199.81	1.72 - 55.15	[263]
123.15 - 248.15	2.02 - 8.11	[264]
276.6 - 282.3	5.02 - 8.44	[118]
114.15 - 247.15	4.03 - 599.83	[265]
CH_4 - C_2H_4		
103.94 - 115.77	0.009 - 0.14	[266]
150.00 - 190.00	0.027 - 4.52	[267]
198.15 - 248.15	1.02 - 6.08	[264]
C_2H_4 - CO_2		
263.14 - 298.15	2.64 - 6.91	[268]
243.00 - 295.75	2.02 - 6.07	[269]
223.15 - 293.15	0.67 - 6.49	[270]
C_2H_4 - C_2H_6		
198.15 - 278.15	0.19 - 2.69	[271]
161.39	0.023 - 0.061	[272]
140.00 - 175.00	0.004 - 0.12	[273]
263.15 - 293.15	1.85 - 4.85	[274]
277.59 - 288.7	3.19 - 4.92	[275]
C_2H_4 - C_3H_8		
199.83 - 273.06	0.14 - 3.92	[276]
C_2H_4 - C_3H_6		
283.15 - 298.15	1.03 - 5.38	[277]
263.07 - 293.29	0.42 - 5.34	[278]
283.15 - 348.15	0.78 - 5.14	[279]
C_2H_4 - C_4H_8		
273.14 - 293.35	0.13 - 5.49	[278]
293.10 - 374.80	0.60 - 6.64	[117]

Table 9.4: %AARD between experimental VLE data and EoS calculations for the mixture bubble pressure and corresponding k_{ij} values.

EoS			H_2 - C_2H_4	CH_4 - C_2H_4	C_2H_4 - CO_2	C_2H_4 - C_2H_6	C_2H_4 - C_3H_8	C_2H_4 - C_3H_6	C_2H_4 - *1*-C_4H_8
PR	Pr.	%AARD	44.28	7.94	6.79	2.22	3.65	1.62	3.63
	Cor.	%AARD	32.48	1.50	0.29	0.36	0.63	1.43	3.68
		k_{ij}	-0.013	0.030	0.053	0.015	0.018	0.007	-0.005
PC-SAFT	Pr.	%AARD	46.11	5.85	10.90	2.57	4.48	1.88	3.88
	Cor.	%AARD	34.72	1.55	0.42	0.33	0.64	1.50	3.42
		k_{ij}	0.145	0.016	0.053	0.011	0.014	0.006	0.002
SAFT-VR Mie	Pr.	%AARD	28.3	3.77	2.63	2.33	1.09	1.83	-
	Cor.	%AARD	21.5	1.22	0.44	0.54	0.80	1.82	-
		k_{ij}	-0.0264	0.0095	0.0108	0.0092	0.0028	0.0006	-
NP			173[a]	91	84	159	34	113	70

$$\%\ AARD = \frac{100}{NP}\sum_{i=1}^{NP}\left|\frac{P_i^{calculated} - P_i^{experimental}}{P_i^{experimental}}\right|$$

where NP is the number of experimental data points and P_i is the bubble pressure.

"Pr." refers to predictions ($k_{ij} = 0$), whereas "Cor." refers to correlations (calculations with $k_{ij} \neq 0$).

[a]144 for SAFT-VR Mie

Table 9.5: %AARD between experimental VLE data and EoS calculations for the mixture bubble pressure and corresponding k_{ij} values, calculated as a temperature dependent function.

EoS			H_2 - C_2H_4
PR	Pr.	%AARD	44.28
	Cor.	%AARD	23.23
		$k_{ij,0}$	0.828
		$k_{ij,1}$ / K^{-1}	-0.011
		$k_{ij,2}$ / K^{-2}	0.0000353
PC-SAFT	Pr.	%AARD	46.11
	Cor.	%AARD	18.95
		$k_{ij,0}$	-0.489
		$k_{ij,1}$ / K	106.28
SAFT-VR Mie	Pr.	%AARD	28.30[a]
	Cor.	%AARD	7.60[a]
		$k_{ij,0}$	-0.244
		$k_{ij,1}$ / K	34.20
NP			173

$$\%\ AARD = \frac{100}{NP}\sum_{i=1}^{NP}\left|\frac{P_i^{calculated} - P_i^{experimental}}{P_i^{experimental}}\right|$$

where NP is the number of experimental data points and P_i is the bubble pressure.

"Pr." refers to predictions ($k_{ij} = 0$)

"Cor." refers to correlations (calculations with $k_{ij} \neq 0$).

[a]These values were calculated with the same experimental data range considered in the k_{ij} fitting.

The most challenging system in terms of thermodynamic modeling, among all the systems studied in this work, is certainly the mixture of C_2H_4 with H_2. Figure 9.6 and Figure 9.7 show the P-x,y diagrams for the binary mixture at different temperatures with all the calculations considering a temperature-dependent k_{ij}. The bubble pressures close to the critical point are very high and very unlikely to be found in the industrial

processes. Excluding the experimental values close to the critical point from the fitting procedure, a good fitting with SAFT-VR Mie is obtained, but with PC-SAFT an anomalous behavior was found for the predictions close to the critical point. Therefore, in the comparison that follows, the range of pressures is different for various mixtures in order to guarantee the maximum performance of each EoS in the description of a particular mixture. In general, we should stress that both PC-SAFT and SAFT-VR Mie significantly overestimate the critical pressure of the mixture, especially at lower temperatures as can be seen in Figure 9.6. PR EoS provides much more accurate values of the critical pressures in the temperature range from 158.15 to 205.15 K; albeit for one considering solely the low pressure range, the SAFT EoS seem to be better choices overall. Furthermore, from 220.15 to 247.15 K, PR EoS presents also a significant overestimation of the critical point of the mixture. Between PC-SAFT and SAFT-VR Mie, the latter performs better than the former as can be quantitatively assessed by the % AARD value in Table 9.5.

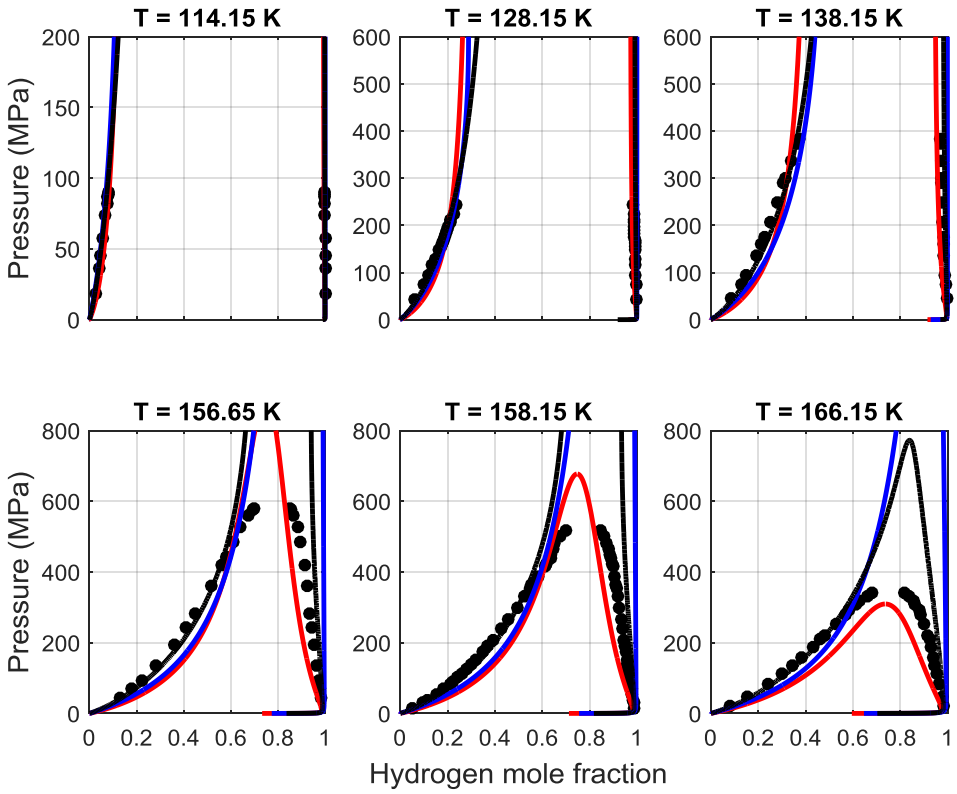

Figure 9.6: Pressure - composition VLE phase diagrams for the H_2 - C_2H_4 mixture at temperatures from 114.15 to 166.15 K. Experimental data [265] are represented by data points and calculations by lines. The color code is the same as in Figure 9.1. Calculations were performed with temperature-dependent k_{ij}.

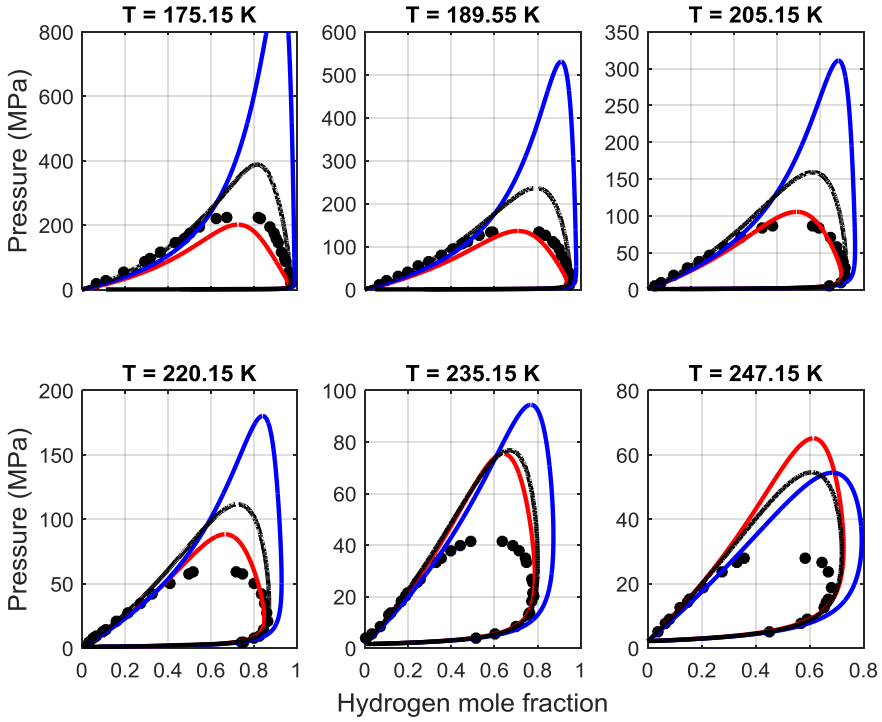

Figure 9.7: Pressure - composition VLE phase diagrams for the H_2 - C_2H_4 mixture at temperatures from 175.15 to 247.15 K. Experimental data [265] are represented by data points and calculations by lines. The color code is the same as in Figure 9.1. Calculations were performed with temperature-dependent k_{ij}.

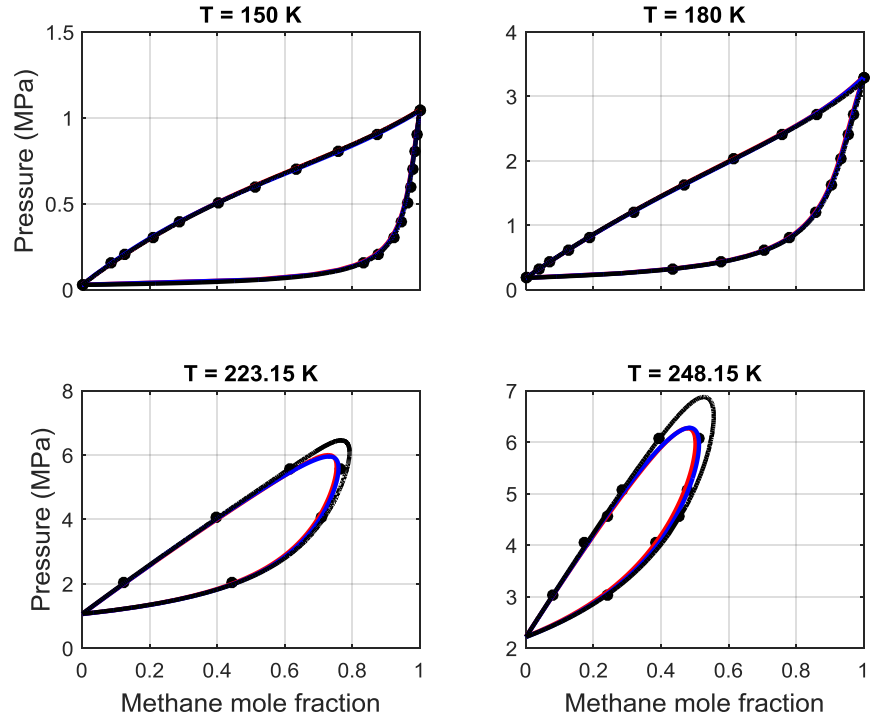

Figure 9.8: Pressure - composition VLE phase diagrams for the CH_4 - C_2H_4 mixture at various temperatures. Experimental data [264, 267] are represented by data points and calculations by lines. The color code is the same as in Figure 9.1. Calculations were performed with $k_{ij} \neq 0$.

For the CH_4 - C_2H_4 mixture, Figure 9.8 presents experimental data and EoS calculations performed at four different temperatures: two below CH_4 critical temperature (150 and 180 K), and two above CH_4 critical temperature (223.15 and 248.15 K). All the three EoS correlate very accurately the experimental data (with an AARD lower than 2 %). SAFT-VR Mie, however, performs slightly better than PR and PC-SAFT.

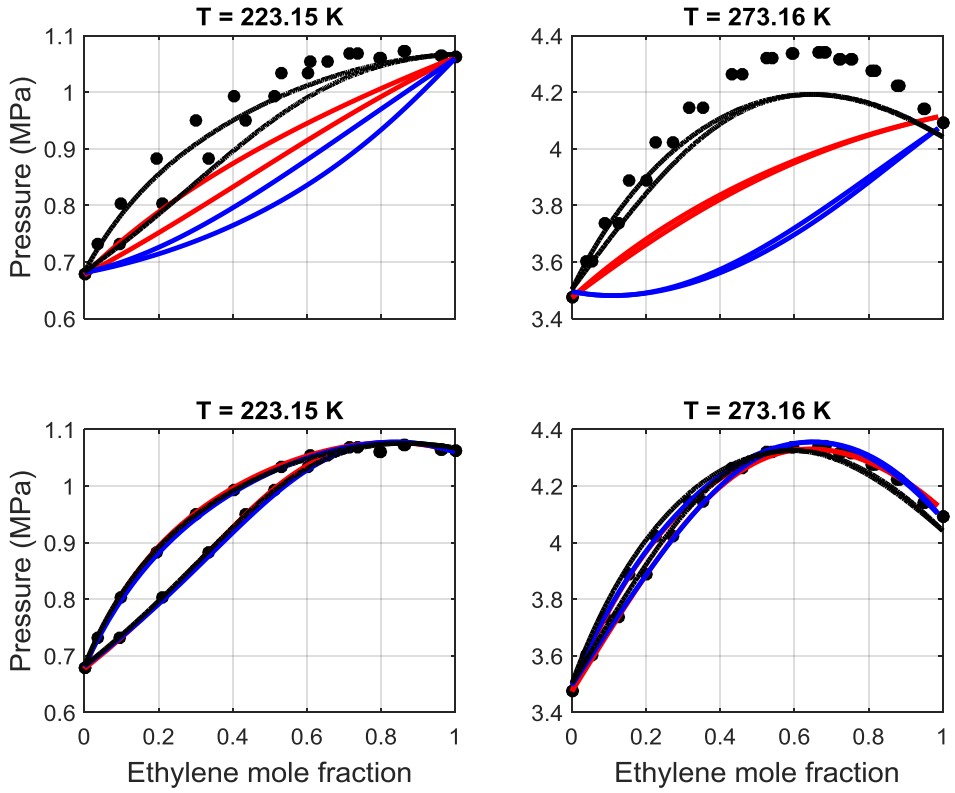

Figure 9.9: Pressure - composition VLE phase diagrams for the C_2H_4 - CO_2 mixture at various temperatures. Experimental data [268, 270] are represented by data points and calculations by lines. The color code is the same as in Figure 9.1. Top panels show predictions ($k_{ij} = 0$), while bottom panels show correlations ($k_{ij} \neq 0$).

Figure 9.9 shows the P-x,y diagrams for the C_2H_4 - CO_2 mixture at 223.15 K and at 273.16 K. For both temperatures, this mixture presents an azeotrope (maximum pressure). The upper two plots show the predicted phase diagram with $k_{ij} = 0$. SAFT-VR Mie gives a far better prediction for this system than PR or PC-SAFT. Interestingly, PC-SAFT predicts an inverse azeotrope behavior (minimum pressure) than the one experimentally observed. Nevertheless, when fitted k_{ij} parameters are used, all three EoS provide a good correlation of the phase diagrams, with PR being the most accurate one followed by PC-SAFT and SAFT-VR Mie, as shown in Table 9.4. SAFT-VR Mie sensitiveness to k_{ij} values proves to reduce its flexibility to correlate the experimental

data. While providing better results with $k_{ij} = 0$, SAFT-VR Mie is the least accurate, compared to PR and PC-SAFT, for fitted k_{ij}.

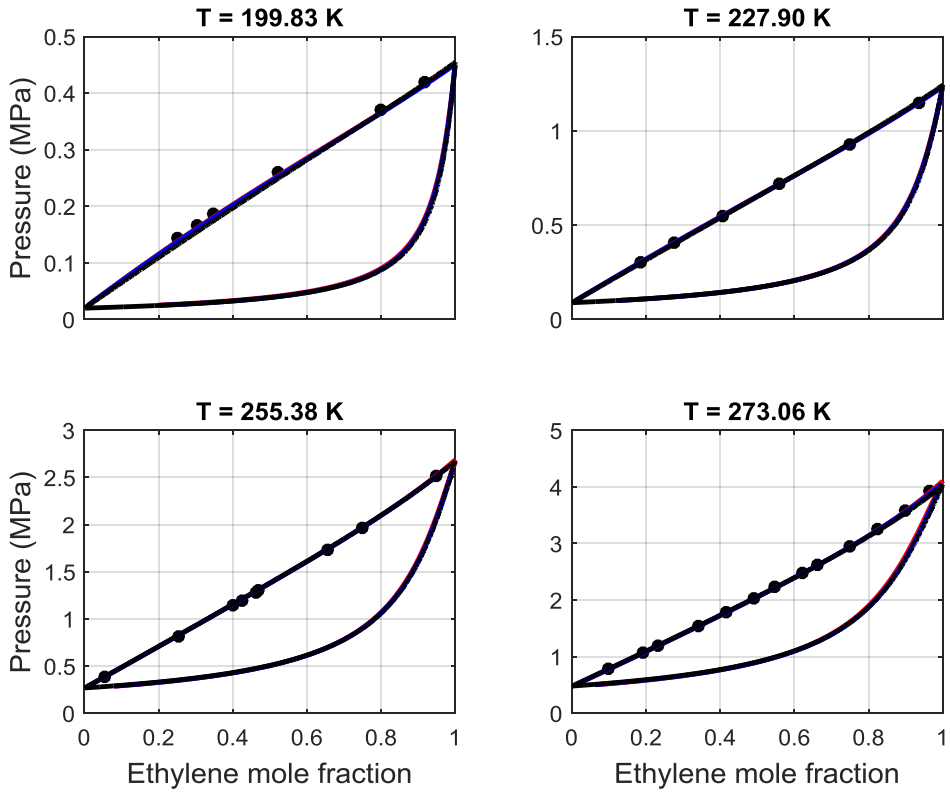

Figure 9.10: Pressure - composition VLE phase diagrams for the C_2H_4 - C_3H_8 mixture at various temperatures. Experimental data [276] are represented by data points and calculations by lines. The color code is the same as in Figure 9.1. Calculations were performed with $k_{ij} \neq 0$.

Figure 9.10 presents the P-x,y diagrams for the C_2H_4 - C_3H_8 mixture with calculations performed with fitted k_{ij} at four different temperatures, all of them lower than the C_2H_4 critical temperature. The C_2H_4 - C_3H_8 mixture behaves quite ideally with respect to Raoult's law. No mole fractions of the vapor phase were available for this binary mixture. As expected for such an ideal mixture, the three EoS perform very well.

Figure 9.11 shows the P-x,y diagrams for C_2H_4 - C_3H_6 mixture at four different temperatures with calculations performed with fitted k_{ij}. All three EoS capture the correct behavior and provide a very accurate correlation of the experimental data, although both PC-SAFT and SAFT-VR Mie predict a higher critical pressure for the mixture than PR.

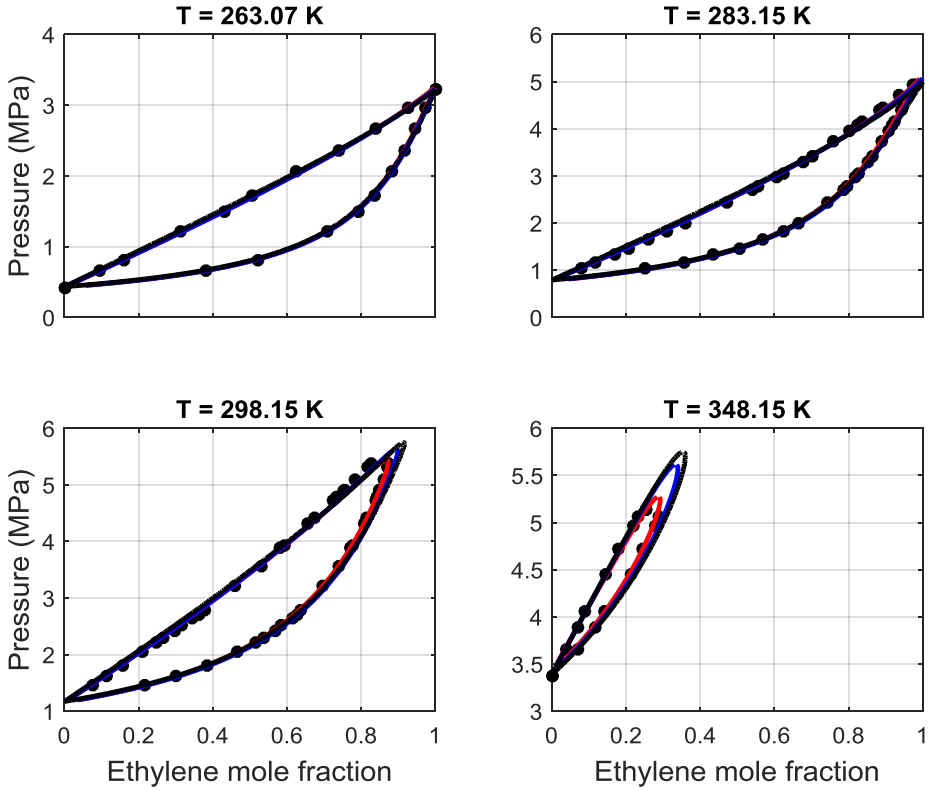

Figure 9.11: Pressure - composition VLE phase diagrams for the C_2H_4 - C_3H_6 mixture at various temperatures. Experimental data [277-279] are represented by data points and calculations by lines. The color code is the same as in Figure 9.1. Calculations were performed with $k_{ij} \neq 0$.

The three binary mixtures, C_2H_4 - C_2H_6, C_2H_4 - C_3H_8, and C_2H_4 - C_3H_6, consist of similar molecules in terms of chemical nature. Naturally, one expects a quite ideal behavior for the phase diagrams, and all EoS should be able to accurately correlate the experimental data. For the case of $k_{ij} = 0$, *i.e.*, in a pure prediction calculation by taking into account the non-ideal mixture behavior, SAFT-VR Mie proves to be by far the most accurate, as one can see by the % AARD values in Table 9.4, which shows that such an EoS has significant predictive capability, probably due to its strong theoretical basis. Nonetheless, upon k_{ij} fitting, both PR and PC-SAFT become much more accurate in terms of the experimental data correlation. Furthermore, although a thorough study on the computational efficiency in the use of these three EoS is out of the scope of the present article, we can point out that SAFT-VR Mie is the most computationally expensive amongst the three EoS studied here.

The last binary mixture investigated is C_2H_4 - *1*-C_4H_8. Figure 13 shows the P-x,y diagrams with calculations performed with fitted k_{ij} at four different temperatures. Both PR and PC-SAFT provide a reasonable correlation of the experimental data.

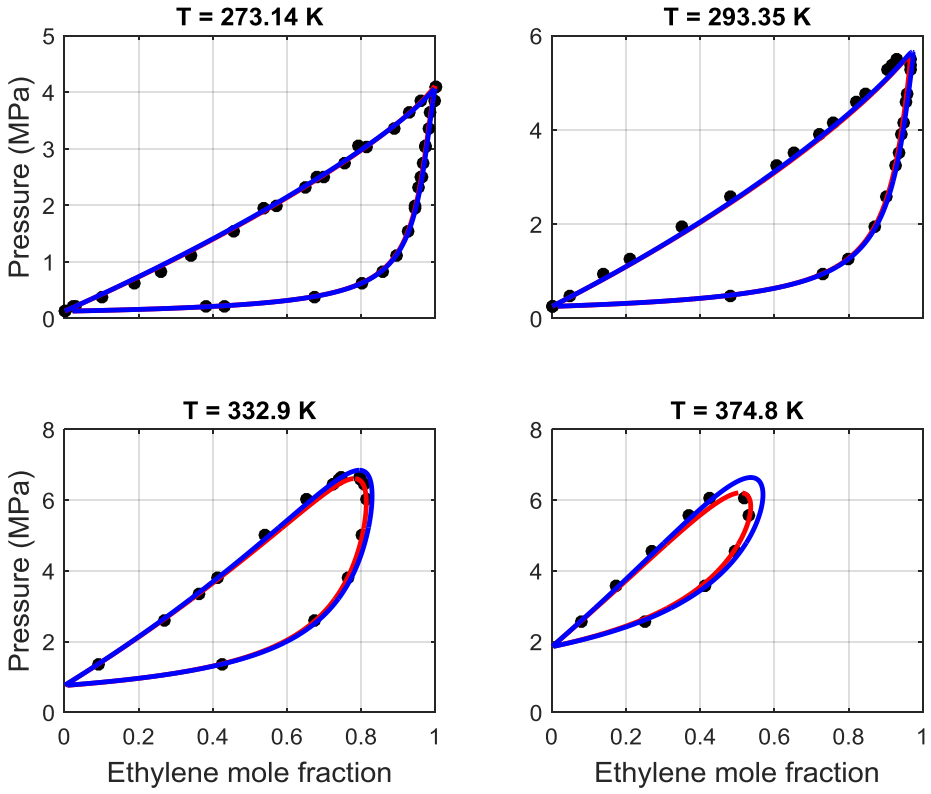

Figure 9.12: Pressure - composition VLE phase diagrams for the C_2H_4 - *1*-C_4H_8 mixture at various temperatures. Experimental data [117, 278] are represented by data points and calculations by lines. The color code is the same as in Figure 9.1. Calculations were performed with $k_{ij} \neq 0$.

9.2.3. Vapor-Liquid Equilibrium of Ternary Mixtures

Table 9.6 refers to the ternary mixtures studied in this work, with the temperature and pressure ranges of the experimental data. All the calculations presented here were carried out with a k_{ij} fitted to the respective binary mixtures. Therefore, all the ternary phase diagrams are predictions in the sense than no fitting was employed in the calculations. All the plots show the binodal lines and the tie lines for some specific points calculated with the three studied EoS and the experimental data obtained from the literature.

Table 9.6: Experimental ternary VLE data from literature modeled in this work.

Temperature (K)	Pressure (MPa)	Ref
H_2 - CH_4 - C_2H_4		
123.15 - 248.15	2.02 - 8.11	[264]
H_2 - C_2H_4 - C_2H_6		
148.15 - 223.15	2.02 - 8.11	[264]
H_2 - C_2H_4 - C_3H_8		
173.15 - 248.15	2.02 - 8.11	[280]
H_2 - C_2H_4 - C_3H_6		
199.817	6.89 - 55.16	[263]
CH_4 - C_2H_4 - C_2H_6		
169.15 - 273.15	0.51 - 5.06	[281]

The first ternary system examined is H_2 - CH_4 - C_2H_4. Figure 9.13(a), Figure 9.13(b) and Figure 9.13(c) show the phase diagrams for this system at 123.15 K and 2.0265 MPa, at 198.15 K and 8.106 MPa and at 248.15 K and 8.106 MPa, respectively. The predictions obtained with all EoS are in excellent agreement with the experimental data for both phases at 123.15 K and 2.0265 MPa. Figure 9.13(b), however, shows that at 198.15 K and 8.106 MPa, PR is more accurate for the vapor phase, while PC-SAFT and SAFT-VR Mie are more accurate for the liquid phase. As the temperature increases even further to 248.15 K, above H_2 and CH_4 critical temperatures, all three EoS fail to provide a satisfactory prediction of the phase diagram, as depicted in Figure 9.13(c).

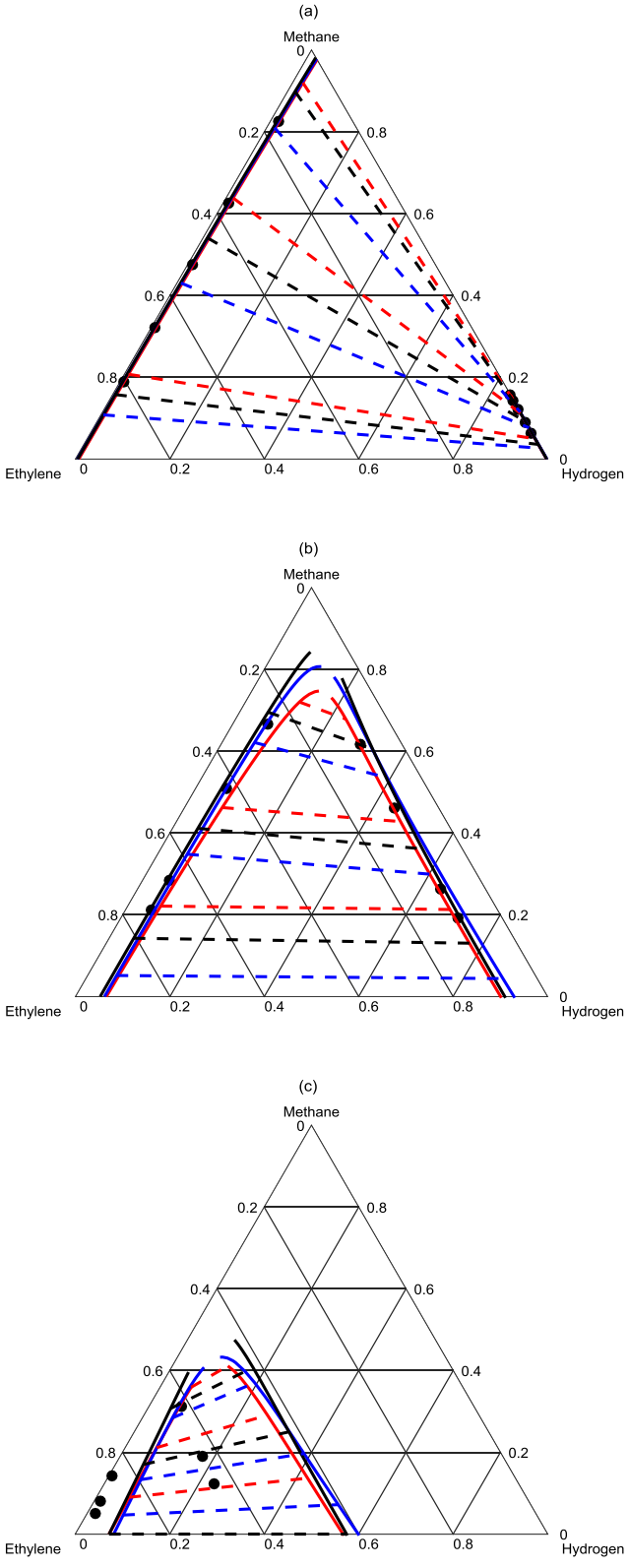

Figure 9.13: Ternary phase diagrams for the H_2 - CH_4 - C_2H_4 mixture at (a) T= 123.15 K and P= 2.0265 MPa, (b) T= 198.15 K and P= 8.106 MPa and (c) T= 248.15 K and P= 8.106 MPa. Experimental data [264] are represented by data points and calculations by lines. The color code is the same as in Figure 9.1. Calculations were performed with $k_{ij} \neq 0$.

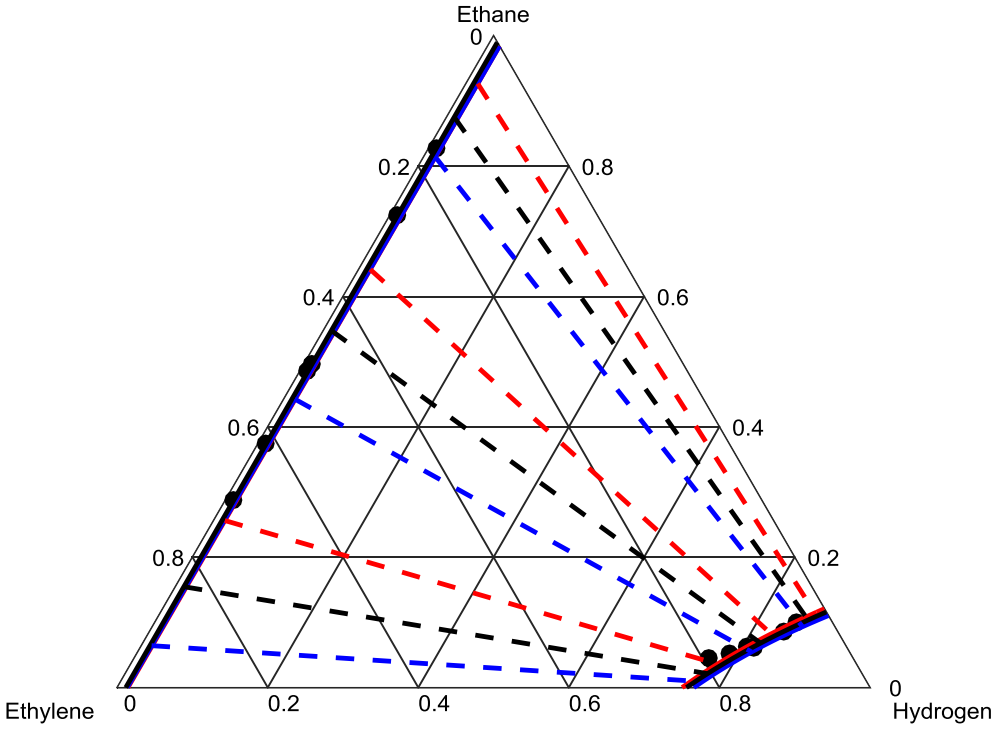

Figure 9.14: Ternary phase diagram for the H_2 - C_2H_4 - C_2H_6 mixture at T= 198.15 K and P= 2.0265 MPa. Experimental data [264] are represented by data points and calculations by lines. The color code is the same as in Figure 9.1. Calculations were performed with $k_{ij} \neq 0$.

For the H_2 - C_2H_4 - C_2H_6 and H_2 - C_2H_4 - C_3H_8 mixtures, Figure 9.14 and Figure 9.15 provide the phase diagrams at 198.15 K and 2.0265 MPa, and at 248.15 K and 2.0265 MPa, respectively. For both mixtures, the three EoS are very accurate in describing the phase boundaries. Nevertheless, for the former mixture, the predicted curvature for the vapor line is somehow the opposite of the one observed with the experimental data. Since one expects an uncertainty in the experimental measurement, an observation on whether something is intrinsically wrong in the modeling or not remains inconclusive.

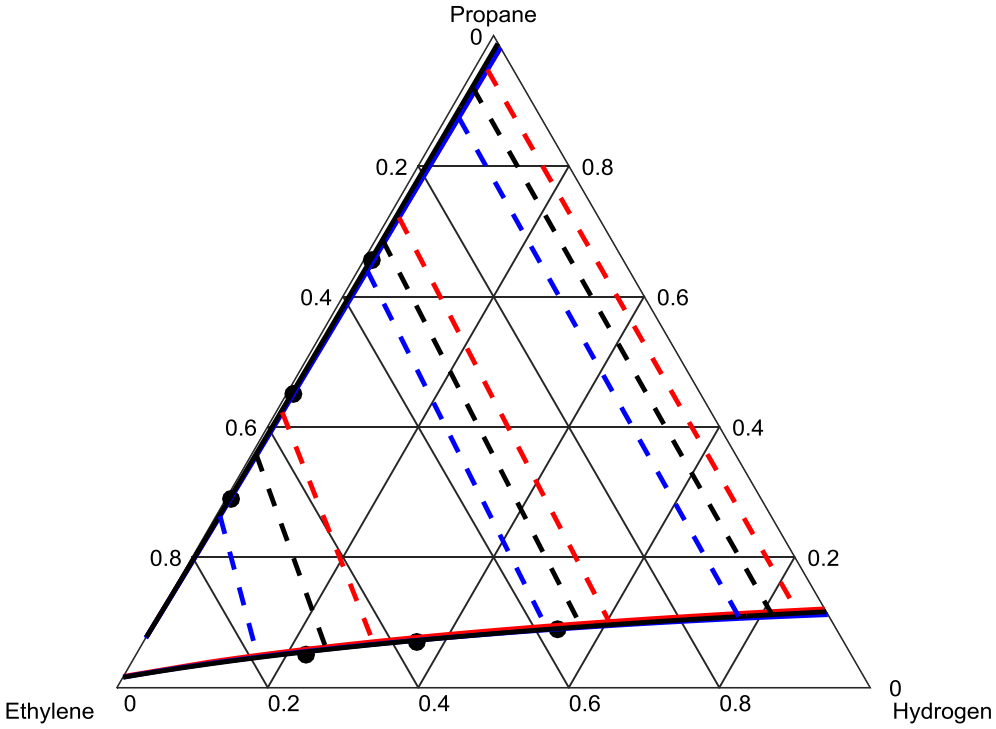

Figure 9.15: Ternary phase diagram for the H_2 - C_2H_4 - C_3H_8 mixture at T= 248.15 K and P= 2.0265 MPa. Experimental data [280] are represented by data points and calculations by lines. The color code is the same as in Figure 9.1. Calculations were performed with $k_{ij} \neq 0$.

Figure 9.16(a) and Figure 9.16(b) refer to the ternary phase diagrams for CH_4 - C_2H_4 - C_2H_6 mixture at 169.15 K and 0.50663 MPa, and at 273.15 K and 5.06625 MPa, respectively. For the system at lower temperatures and pressures, all three EoS agree with each other, but differ from the experimental binodal lines, especially for the vapor phase, for which they predict a much richer phase in terms of methane mole fraction than what is experimentally observed. At a pressure ten times higher and at a temperature higher than the methane critical temperature, the narrower phase boundary is reasonably well predicted by all three EoS, with PR being the most accurate for the vapor phase, and with SAFT-VR Mie performing slightly better than the others for the liquid phase.

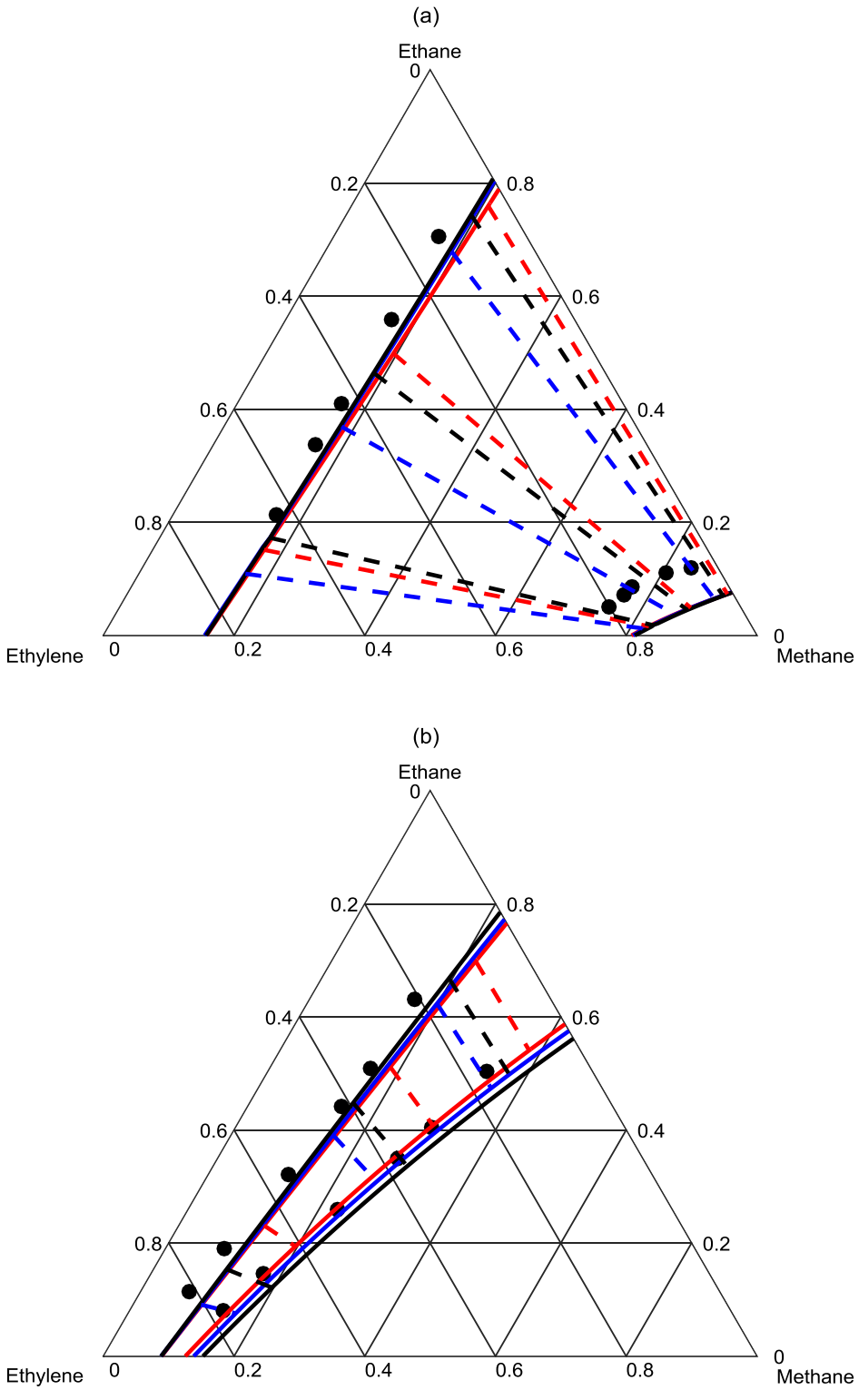

Figure 9.16: Ternary phase diagrams for the CH_4 - C_2H_4 - C_2H_6 mixture at (a) T= 169.15 K and P= 0.50663 MPa and (b) T= 273.15 K and P= 5.06625 MPa. Experimental data [281] are represented by data points and calculations by lines. The color code is the same as in Figure 9.1. Calculations were performed with $k_{ij} \neq 0$.

9.3. Conclusions

One cubic (PR) and two higher order EoS (PC-SAFT, SAFT-VR Mie) were used to model the pure C_2H_4 physical properties, as well as the binary and ternary C_2H_4 mixture VLE with components associated with C_2H_4 pipeline transportation.

The two SAFT EoS proved to be more accurate, when compared to PR EoS, in predicting the pure C_2H_4 physical properties, with the most prevalent differences being in the speed of sound and the Joule-Thomson coefficient calculations. PC-SAFT EoS proved to be the most accurate overall, when the physical properties along the saturation line were considered. SAFT-VR Mie predicted with higher accuracy the speed of sound and the isothermal compressibility coefficient in the supercritical region, but in general, the performance of the two SAFT EoS is of comparable accuracy.

Regarding the binary mixtures VLE modeling, SAFT-VR Mie proved to be the most accurate EoS in terms of prediction. The % AARD presented by SAFT-VR Mie was systematically lower than the other two EoS, except for the mixtures of C_2H_4 with C_2H_6 and C_3H_6, where PR was the most accurate, but the difference in accuracy was really small. It is worth noting that PR was more accurate than PC-SAFT for every mixture, except for the CH_4 - C_2H_4 mixture with zero BIPs. With the use of the regressed BIPs, the performance of all EoS is of comparable accuracy, apart from the H_2 - C_2H_4 mixture, where SAFT-VR Mie is clearly superior. At this point, it has to be stressed out that the equilibrium pressure of this mixture reaches extremely high values which are of very limited industrial interest. For the pressure range relevant to industrial applications, all three EoS are suitable, with the two SAFT EoS being more accurate. Finally, it should be noted that all the mixtures considered in this work are comprised of low molecular weight hydrocarbons and gaseous components, for which the vapor phase composition is correlated better with the PR EoS in the region where the pressure maximum of the P-x,y diagrams corresponds to a critical point. SAFT type EoS correlate more accurately the liquid phase composition, in expense of the critical point overshooting and the deterioration of the vapor phase description. It should be emphasized that for mixtures of more polar compounds and/or compounds of larger size, the accuracy of PR and SAFT EoS may not be the same.

With the use of the BIPs regressed from the binary mixture data, all EoS successfully predict the ternary mixture VLE considered in this work, while the differences between their predictions are minor. A general trend observed is that PR EoS tends to predict more accurately the vapor phase composition, while the two SAFT EoS

are more accurate in predicting the liquid one. This observation is in agreement with the binary mixtures VLE discussion.

10. Efficient Coupling of Thermodynamic Calculations with Models for Two-Phase Flow Simulation

10.1. Introduction

This PhD was executed, among others, in the framework of the CO_2QUEST project funded by the European Commission 7th Framework Programme and an NPRP project funded by the Qatar National Research Fund, which had as main objectives the quantitative assessment of the hazards of CO_2 and C_2H_4 mixtures releases from pressurized pipelines respectively. Such types of outflow are predicted using mathematical models based on CFD simulations. One of the project partners in University College London has developed a specialized computational model for performing these types of simulations. A collaborative research work was performed, the target of which was the efficient coupling of the thermodynamic models developed and validated in this thesis with the flow models. The thermodynamic models provide the physical properties (density, speed of sound, Joule-Thomson coefficient etc.) and the phase equilibria calculations for the associated mixtures, while the flow models are applied to predict the outflow. The techniques that are going to be discussed next were developed to be used in conjunction with the Homogeneous Equilibrium Model (HEM) for one-dimensional, transient state simulations. One of the assumptions of the model is the treatment of the multiple phases that may form as an effective one-phase fluid, the physical properties of which are calculated as weighted averages of the properties of the corresponding phases. For more details about the model the reader is referred to Brown et al. [282].

10.2. Pipeline Releases of CO_2 Mixtures

10.2.1. Interpolation Technique

As it has already been mentioned in Chapter 2, the coupling of thermodynamic properties calculated from EoS with models for fluid-flow simulation is complicated by the fact that the free variables in such simulations are the density and the internal energy, with which we must compute the system pressure and temperature. On the other hand, EoS are most commonly formulated using T and P or T and v as natural variables and all the other properties are calculated using specific thermodynamic relations. Furthermore, phase equilibrium calculations are usually performed at specified T, P and total

composition of a non-stable mixture and while the calculation can be formulated with other specifications, such as density and internal energy (ρ, U), these formulations lack the computational efficiency of the P-T flash formulation.

To overcome this, the construction of two interpolation grids is introduced, one of which is constructed using the T and P as free variables, denoted $\{T, P\}$, and the other using the density ρ and the specific internal energy e, denoted by $\{\rho, e\}$. For the composition in question, these two pairs of variables correspond to different state functions, i.e. T and P are the state variables of the specific Gibbs free energy while ρ and e are the state variables of the specific entropy. Consequently, by definition, a one-to-one and onto map exists between the considered grids which provide the means for rapidly computing the thermodynamic properties and phase equilibria during flow simulations. Furthermore, mapping $\{T, P\}$ to other property pairs, such as entropy and total sonic enthalpy (sum of enthalpy and kinetic energy at sonic flow) has important applications as it will be shown later.

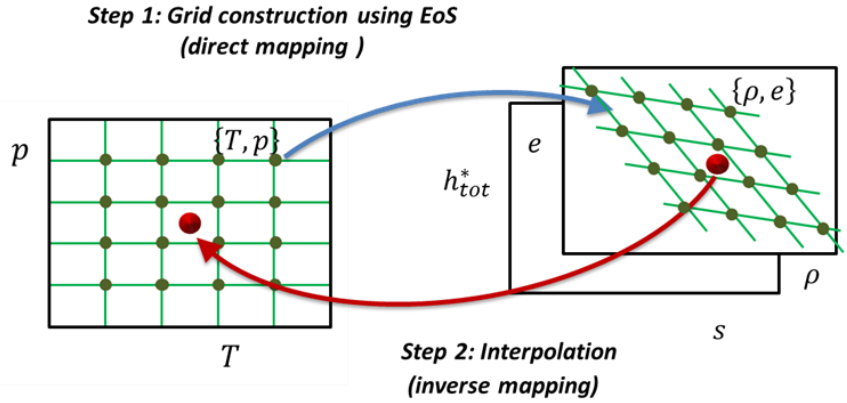

Figure 10.1: Sampling the $\{T, P\}$ grid and evaluating the corresponding $\{\rho, e\}$, or another property pair ($\{s, h_{tot}\}$ for example) (Step 1). Reinterpret the grid to return the inverse maps $P(\rho, e)$ and $T(\rho, e)$ (Step 2).

The construction begins by defining the bounds of the $\{T, P\}$ grid using the fluid conditions required for the simulation (i.e. the intervals $[T_{min}, T_{max}]$ and $[P_{min}, P_{max}]$). Grid points are sampled along isotherms which are uniformly distributed within the temperature range. Typically, for the pressure ranges of interest for CO_2 pipeline decompression, the isotherms will intersect the dew and bubble points and hence pass through the phase envelope. As a result, an interpolant has to be developed which can resolve the abrupt changes of the fluid properties with pressure and temperature within the phase coexistence regions, and in particular near the equilibrium lines. In practice this

means that the points selected for building the interpolant cannot be uniformly distributed along the isotherm, but must be chosen so as to resolve the region around, and within, the phase envelope of the mixture, which is known a priori given the composition of the fluid.

In order to address this problem and improve the mapping, a non-uniform sampling along each isotherm is adopted, resulting in an increased density of points close to the dew and bubble point pressures (P_d and P_b respectively) and within the phase envelope itself. The set of N_P points along each isotherm are selected as follows:

a. If $P_{max} \leq P_d$ or $P_b \leq P_{min}$, *i.e.* a permanently single-phase fluid, the points are uniformly distributed in $[P_{min}, P_{max}]$:

$$P_i = P_{min} + (i-1)\frac{P_{max} - P_{min}}{N_P - 1} \tag{10.1}$$

b. If $P_{min} \leq P_d \leq P_b \leq P_{max}$ *i.e.* the interval $[P_{min}, P_{max}]$ encompasses the two-phase region, N_d points are distributed in $[P_{min}, P_d - \Delta]$ to increase the point density close to the dew point line using:

$$P_i = P_{min} + (P_d - \Delta - P_{min}) f\left(\frac{i-1}{N_d}\right) \tag{10.2}$$

N_b points are distributed in $[P_b + \Delta, P_{max}]$ to increase the point density close to the bubble point line using:

$$P_i = (P_b + \Delta - P_{min}) + (P_{max} - P_b - \Delta) f\left(\frac{i-1}{N_b}\right) \tag{10.3}$$

while the remaining N_{VLE} points are distributed using the mapping function which increases the point density inside the VLE region and near phase boundary lines:

$$P_i = (P_d - \Delta) + (P_b - P_d + 2\Delta) f\left(\frac{i-1}{N_{VLE}}\right) \tag{10.4}$$

with

$$f(x) = \frac{1 + erf(X_{P1}x - X_{P2})}{2} \tag{10.5}$$

If $P_{min} \leq P_d \leq P_{max} \leq P_b$ or $P_d \leq P_{min} \leq P_b \leq P_{max}$, i.e. the interval $[P_{min}, P_{max}]$ contains part of the two-phase region a variant of the points distribution described in case b is applied. For example if $P_{min} \leq P_d \leq P_{max} \leq P_b$, the points are distributed according to Eqs. 10.2 and 10.4, with the exception that in Eq. 10.4 P_{max} is taken as the upper limit.

In case b, which is the most general, the number of points inside the VLE region (N_{VLE}) is taken as 70% of the total number of points (N_P), while N_d and N_b are each taken as 15% of N_P. The total number of points, as well as the distribution function parameters Δ, X_{P1}, X_{P2} are tuned to optimize the grid's quality. In this study X_{P1} and X_{P2} were set equal to 4.4 and 2.2 respectively while the values used for N_P and Δ are reported in later sections.

At each of these points, using T and P as the independent variables, the other thermodynamic properties are calculated from the EoS. In other words, at these points the maps $e(T,P)$ and $\rho(T,P)$ are established. Using these same points the grid is re-interpreted to return the inverse maps $P(\rho,e)$ and $T(\rho,e)$ and hence a $\{\rho,e\}$ grid.

In order to increase the accuracy of this new grid across the ranges of densities and internal energies covered, the points along an isotherm map $T(\rho,e)$ are redistributed, by taking uniform steps in ρ. The corresponding values of e at the new density points along an isotherm are calculated by interpolation. Then, the initial and the interpolated isothermal paths are expressed as mono-parametric curves $(e(\lambda),\rho(\lambda))$ with $0 \leq \lambda \leq 1$, where λ is length along the isotherm curve (arc length), calculated at multiple segments (ρ,e). Using the values of λ along the initial and the interpolated isotherms, the desired properties (T, P, vapor fraction, etc.) at the new (ρ,e) points are calculated as functions of λ by interpolating the corresponding functions using univariate Akima splines [283]. Eventually a uniform $\{\rho,e\}$ grid is produced for each property of interest and by fitting the bivariate Akima spline, accurate interpolations can be performed at the relevant range of conditions that were sampled initially.

Using the established $\{\rho,e\}$ grids, the thermodynamic calculations are decoupled from the actual simulation of the flow, increasing not only the efficiency but also the reliability of the proposed approach.

10.2.2. Interpolation Technique Consistency

Prior to its application to flow simulations the consistency of the interpolation method's predictions with those obtained with the underlying thermodynamic model must be assessed. The PC-SAFT EoS was used in this work. For the subsequent analysis, two mixtures are chosen; a simple binary mixture 95.96% (vol./vol) CO_2 - 4.04% N_2 and a more complex 5-component mixture of 91.03% (vol./vol) CO_2 - 1.15% H_2 - 1.87% O_2 - 4.0% N_2 - 1.95% CH_4. The construction of the interpolation tables used a total of 100 isotherms along which N_P was taken to be 200, while Δ was set equal to zero. It has to be

also noted, that the smoothening procedure using a uniform density distribution along each isotherm was not used in the following examples, since the adaptive sampling of the $\{T, P\}$ grid was enough to result in a uniform $\{\rho, e\}$ grid. One reason is that the critical region of the mixtures is not taken into account in the calculations, since the initial conditions of the depressurization process exclude this region. As it will be shown in section 10.3, inclusion of the critical and supercritical regions requires more detailed treatment, apart from a non-uniform sampling in T-P space.

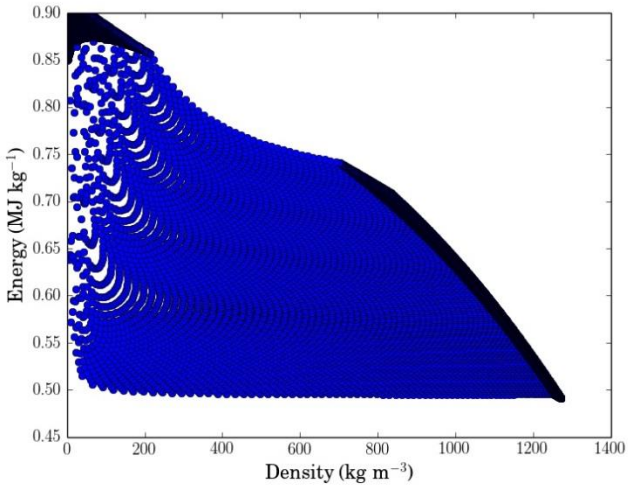

Figure 10.2: $\{\rho, e\}$ grid distribution with a uniform sampling for the binary 95.96% (vol./vol) CO_2 - 4.04% N_2 mixture. Calculations were performed with the PC-SAFT EoS.

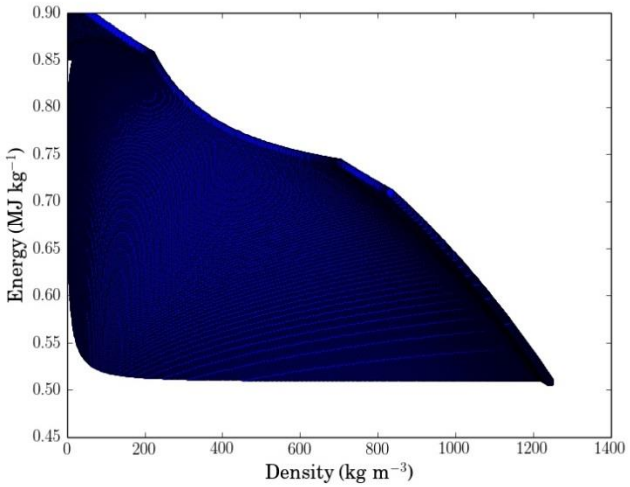

Figure 10.3: $\{\rho, e\}$ grid distribution with the proposed adaptive sampling for the binary 95.96% (vol./vol) CO_2 - 4.04% N_2 mixture. Calculations were performed with the PC-SAFT EoS.

Figure 10.2 and Figure 10.3 respectively show the points sampled for the $\{\rho, e\}$ distribution for the binary mixture using a uniform $\{T, P\}$ grid and using the methodology

developed above. The $\{T, P\}$ grid that corresponds to Figure 10.3 is shown in Figure 10.4. As shown in Figure 10.2, the "uniform sampling strategy" produces a much sparser weighting of the points through the phase envelope, as compared to the one presented in Figure 10.3, where the redistribution of the points is applied.

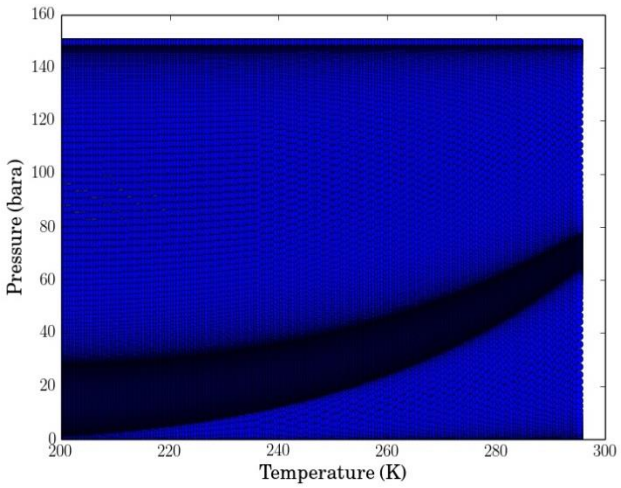

Figure 10.4: $\{T, P\}$ grid distribution with the proposed adaptive sampling for the binary 95.96% (vol./vol) CO_2 - 4.04% N_2 mixture. Calculations were performed with the PC-SAFT EoS.

In order to quantify the deviations of the predictions obtained from the interpolation grids and the actual values calculated from the underlying EoS, 10,000 random samples were taken in the relevant P-T domain. From these samples, the $e(T, P)$ and $\rho(T, P)$ functions were evaluated using the EoS and then the interpolation grids were applied using these values to compare with the original points. It should be noted that the grid produced from the uniform $\{T, P\}$ sampling failed to provide predictions for all of the points used in this comparison and so is omitted. This procedure is schematically shown in Figure 10.5.

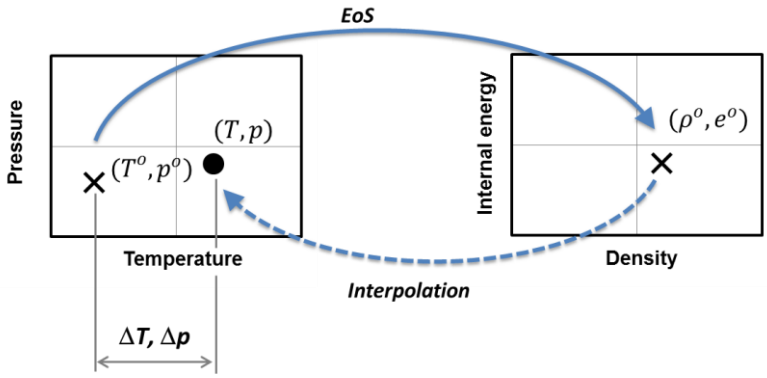

Figure 10.5: The temperature and pressure interpolation errors, ΔT and ΔP, due to a mismatch between the (T^o, P^o) data corresponding to the interpolation point (ρ^o, e^o) and the results of the interpolation (T, P).

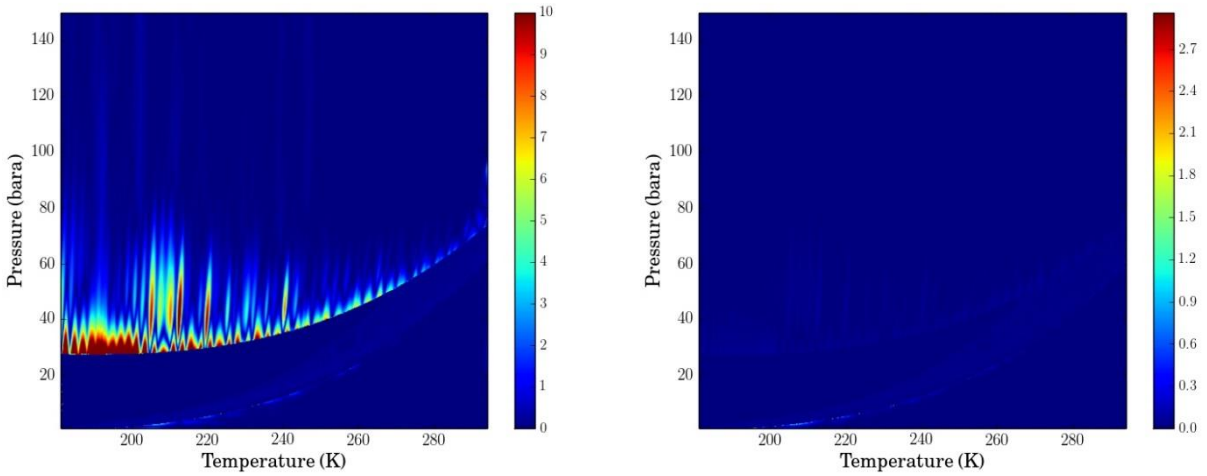

(a) (b)

Figure 10.6: %AARD interpolation errors observed in (a) pressure and (b) temperature across the relevant region in the P-T phase diagram for the binary mixture. Calculations were performed with the PC-SAFT EoS.

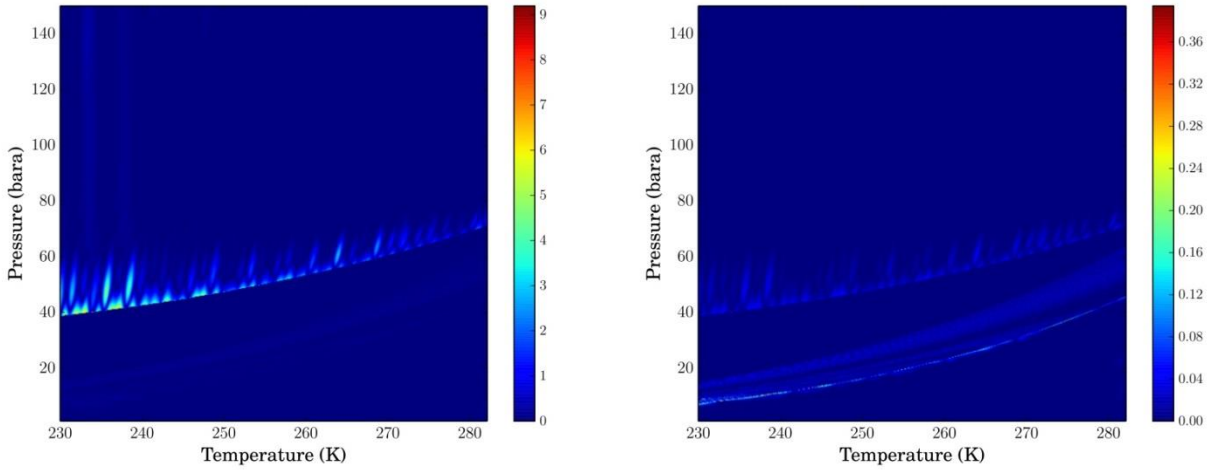

(a) (b)

Figure 10.7: %AARD interpolation errors observed in (a) pressure and (b) temperature across the relevant region in the P-T phase diagram for the 5-component mixture. Calculations were performed with the PC-SAFT EoS.

Figure 10.6(a) and Figure 10.6(b) show the %AARD contours of the predicted pressure and temperature respectively for the binary mixture. Figure 10.7(a) and Figure 10.7(b) show the same data for the 5-component mixture. As can be seen from both sets of Figures, the error observed in the prediction of the pressure is substantially higher in places (reaching up to 10%) than for the temperature, which is less than 0.5% throughout; nevertheless, the regions of high error are restricted to low temperatures above the bubble point line which has limited physical interest. It should further be

noted that this region also corresponds to conditions where solid-phase formation may be expected, which however is not accounted for in the current model.

10.2.3.Full-Bore Rupture Simulation of CO_2 Pipeline

In this section, simulation results with the HEM model combined with the proposed interpolation technique are presented for pipeline releases of CO_2 mixtures. Results are presented here for one set of data obtained from Full-Bore Rupture (FBR) releases of CO_2 from a 144 m long, 150 mm internal diameter section of pipeline using the binary mixture introduced earlier and originally presented in Cosham et al. [284]. For details regarding the initial conditions and simulation details, the reader is referred to Brown et al. [282]. Furthermore, decompression results for the 5-component mixture can be found in Brown et al. [282].

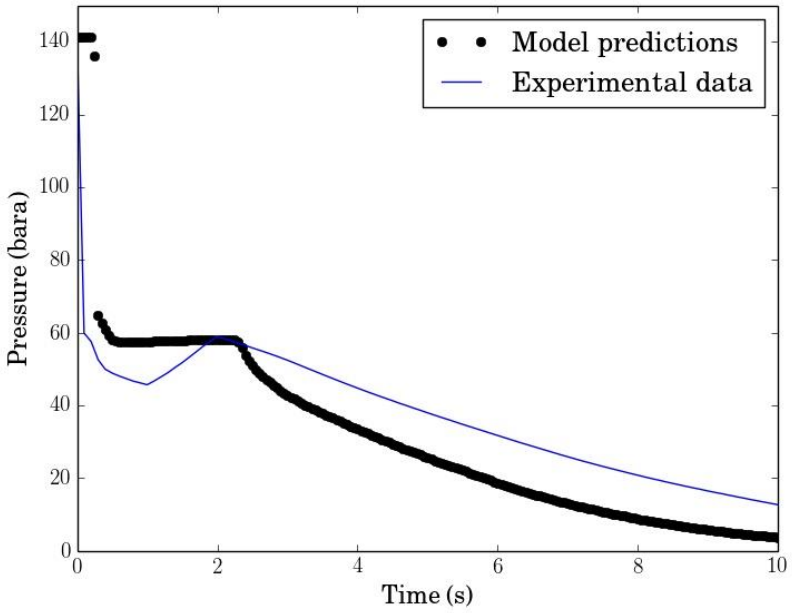

Figure 10.8: Comparison of the predicted and measured variation of pressure with time at the closed end of the pipeline following the initiation of decompression for the binary mixture.

Figure 10.8 shows a comparison of the predicted and measured variation of the pressure at the closed end of the section of pipeline following the initiation of the decompression. As may be observed in the predicted results, the pressure remains initially constant but falls rapidly at ca. 0.2 s. Following this, a pressure plateau of ca. 58 bara is predicted, until ca. 2.5 s at which point the pressure begins to fall again towards the ambient. In comparison, after the initial pressure drop, the experimental pressure is

observed to fall more slowly to a minimum at ca. 1 s before recovering to a pressure very close to the plateau pressure predicted by the model. Following this the pressure again drops, but at a slower rate than that predicted. As noted by various authors [285, 286] this later behavior is largely due to frictional and heat transfer effects, the modeling of which is outside of this study.

Figure 10.9 shows the thermodynamic trajectory at the closed end of the pipeline section during the decompression relative to the dew and bubble lines. As noted above, during the initial decompression the fluid drops almost instantaneously along the isentrope into the phase envelope where it descends towards the dew line at low temperatures.

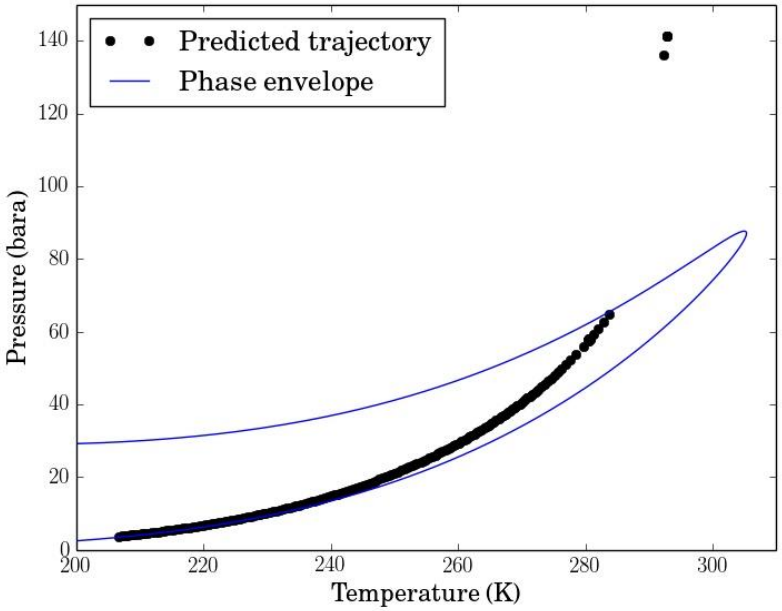

Figure 10.9: Thermodynamic trajectory of the decompression relative to the binary mixture phase envelope at the closed end of the pipeline following the initiation of decompression.

10.3. Pipeline Releases of C_2H_4 Mixtures

One of the advantages of the proposed interpolation technique is that it can readily be adopted to any fluid, the properties of which can be accurately predicted using dedicated models. Despite the fact that highly accurate computational models have been developed for the simulation of discharge of flashing fluids and condensable gases from pipelines, these have not been applied to simulate the failure of ethylene pipelines. The previous studies of small leaks [287, 288] and full-bore rupture [289] of ethylene pipelines, were performed based on simplified modeling assumptions and have not been fully validated against experimental data for ethylene.

In this section, the proposed technique for the coupling of thermodynamic calculations with flow models is going to be applied in combination with the HEM to model the experimental decompression of an ethylene pipeline. The density, the specific internal energy, the entropy, the heat capacity and the speed of sound of the vapor and liquid phases of a multicomponent ethylene mixture, as well as the vapor-liquid composition of the fluid are calculated with PC-SAFT EoS and the BIPs regressed in Chapter 9. The dynamic viscosity coefficient is calculated with the friction theory model [290], coupled with PC-SAFT EoS and pure component parameters regressed in this work. The thermal conductivity is approximated using NIST correlations for pure ethylene [291]. For more details regarding the flow model the reader is referred to Martynov et al. [292].

10.3.1. Physical Properties of the Chemical System

The chemical system involved in the simulations is a ternary 99.5% (mole) C_2H_4 - 0.2% CH_4 - 0.3% N_2 mixture, which approximates a real mixture for which experimental decompression data are available.

Figure 10.10 shows the P-T phase envelope of the mixture along with the saturation line of pure C_2H_4, as predicted by PC-SAFT EoS [262]. The mixture bubble and dew lines are very close to each other (the difference in the dew and bubble point pressures pressure is less than 0.02 MPa), resulting to the VLE region being very narrow. This is something to be expected, since both CH_4 and N_2 are in very low concentrations. Closer examination of the critical point region reveals a relatively large shift in the critical point from pure ethylene to the ternary mixture. While the accuracy of the EoS predictions of the phase equilibria near the critical point of multicomponent mixtures is uncertain, the errors of the VLE predictions in this region may only impact the

predictions of pipeline decompression when the thermodynamic decompression trajectory crosses this region.

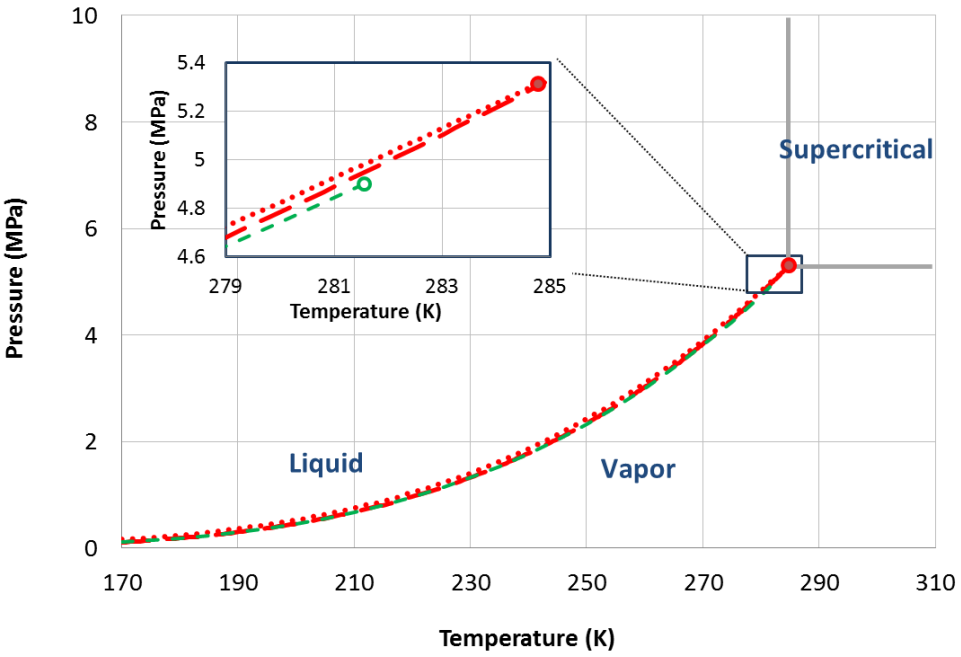

Figure 10.10: P-T phase envelope for the 99.5% (mole) C_2H_4 - 0.2% CH_4 - 0.3% N_2 mixture. The red line marks the VLE boundary for the mixture, while the green dashed line represents the VLE boundary for pure C_2H_4. The dots on the VLE boundaries represent the critical points. Calculations were performed with the PC-SAFT EoS.

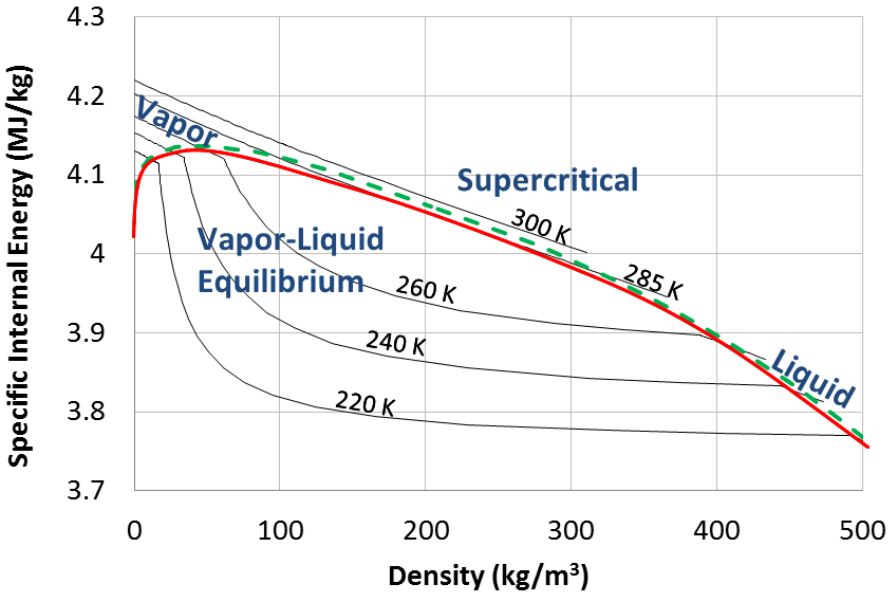

Figure 10.11: Density-specific internal energy phase diagram for the 99.5% (mole) C_2H_4 - 0.2% CH_4 - 0.3% N_2 mixture. The red line marks the VLE boundary for the mixture, while the green dashed line represents the VLE boundary for pure C_2H_4. The dots on the VLE boundaries represent the critical points. Calculations were performed with the PC-SAFT EoS.

Figure 10.11 shows the density-specific internal energy phase diagram, along with isotherms calculated with the PC-SAFT EoS. Calculations for the ternary ethylene mixture and for pure ethylene are shown. The density and specific internal energy data are obtained for the range of pressures from 0.01 MPa to 10 MPa and temperatures from 170 to 370 K.

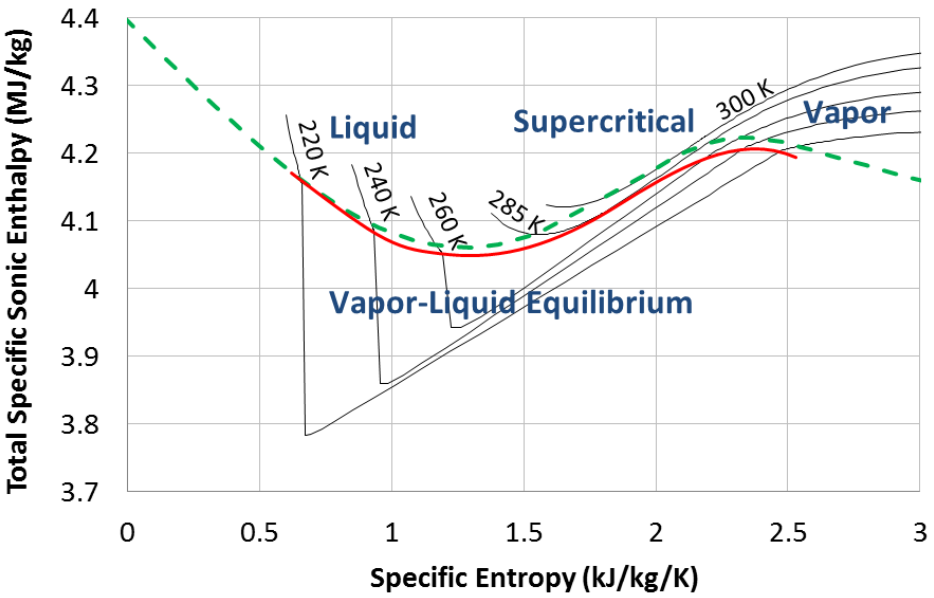

Figure 10.12: The entropy-total sonic enthalpy phase diagram for the 99.5% (mole) C_2H_4 - 0.2% CH_4 - 0.3% N_2 mixture. The red line marks the VLE boundary for the mixture, while the green dashed line represents the VLE boundary for pure C_2H_4. The dots on the VLE boundaries represent the critical points. Calculations were performed with the PC-SAFT EoS.

Figure 10.12 shows the entropy-total sonic enthalpy phase diagram along with isotherms calculated with the PC-SAFT EoS. Calculations for the ternary ethylene mixture and for pure ethylene are shown. This diagram is useful for the evaluation of the properties of the fluid upon choked flow conditions. Examination of the isotherms in Figure 10.12 shows that they are smooth and do not intersect, which is important feature guaranteeing a unique $\{T, P\} \leftrightarrow \{s, h^*_{tot}\}$ mapping.

10.3.2.Construction and Accuracy of the Interpolation Grids

Following the methodology developed in the previous section, the $\{T, P\}$ grid is created initially and using the EoS and the other property models, the various properties needed for the simulation are calculated. The direct maps $\{T, P\} \rightarrow \{\rho, e\}$ and $\{T, P\} \rightarrow \{s, h^*_{tot}\}$ are established and subsequently they are inverted, as discussed in the previous section.

The $\{T, P\}$ interpolation grids are sampled in the domain covering pressures from 0.1 MPa to 10 MPa and temperatures from 170 K to 370 K. For the sake of simplicity, the study is performed using the $\{T, P\}$ grids with equal number of isotherms N_T and pressure points N_P. The total number of points $N_{TOTAL} = N_T \times N_P$, was varied between 50 × 50 and 300 × 300. As described in Chapter 10.2.1, the pressure points are sampled non-uniformly along each isotherm, using the respective equations.

Contrary to the test-cases with CO_2 mixtures, the ethylene pipeline working conditions lie in the supercritical region of the ternary mixture examined. Consequently, the thermodynamic trajectory following a sudden decompression will most likely pass closely to the critical region of the mixture. This necessitates that the complete phase envelope of the mixture has to be calculated and the sampling in P-T space must include the critical and the supercritical regions. At the critical point, the density changes abruptly with pressure ($\left(\frac{d\rho}{dP}\right|_{critical} = \infty$) and this behavior extends to supercritical temperatures closely to the critical isotherm.

In order to form uniform $\{\rho, e\}$ and $\{s, h_{tot}^*\}$ grids, the N_T isotherms are distributed non-uniformly within the given temperature range, with higher concentration around the fluid cricondentherm point, using the same functions reported for pressure in Chapter 10.2.1. Furthermore, the pressure points have to be non-uniformly sampled in the supercritical region close to the critical point. Consequently, the equilibrium pressures in the dew and bubble lines close to the cricondentherm point are linearly extrapolated in the supercritical region in order to set upper and lower bounds, similar to the VLE regions, for the non-uniform distribution of the pressure points. Finally, the smoothening procedure based on a uniform distribution of density points along each isotherm was necessarily applied in order to finally get high quality $\{\rho, e\}$ and $\{s, h_{tot}^*\}$ grids.

After the sampling of the $\{T, P\}$ grid, the corresponding properties, including the density, the specific internal energy, the entropy and the total sonic enthalpy are calculated using the PC-SAFT EoS.

Figure 10.13, Figure 10.14 and Figure 10.15 show the resulting $\{T, P\}$, $\{\rho, e\}$ and $\{s, h_{tot}^*\}$ grids with 150 × 150 points sampled in the P-T domain by using the non-uniform sampling and smoothening procedures mentioned above. As can be seen from Figure 10.13, a relatively small fraction of points is seeded along isotherms in the liquid phase region. This is done in favor of the vapor and VLE regions, which are better resolved to ensure more accurate prediction of properties along decompression

trajectories passing across these regions. Figure 10.14 and Figure 10.15 show that the vapor and VLE regions are well covered by the grid points in both the ρ-e and s-h^*_{tot} domains.

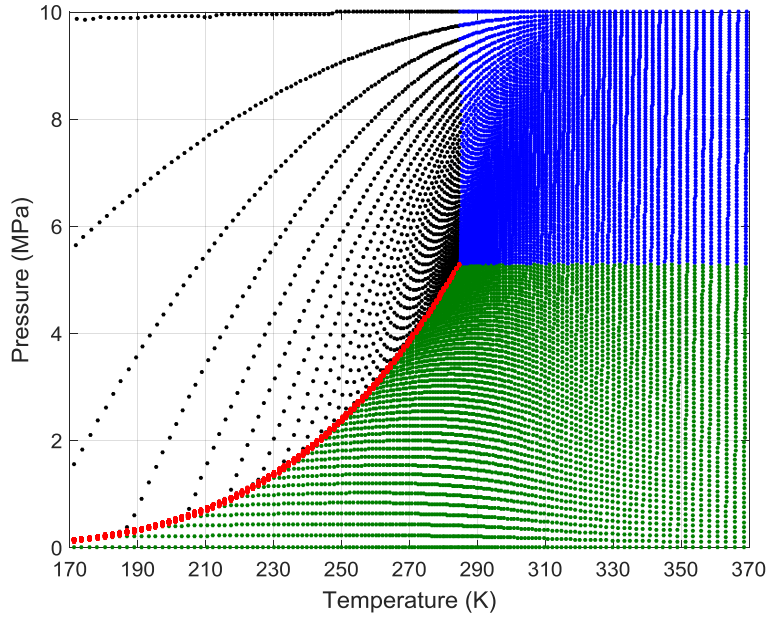

Figure 10.13: The P-T diagram of the 99.5% (mole) C_2H_4 - 0.2% CH_4 - 0.3% N_2 mixture with 150 × 150 points sampled in T-P space. Results are shown with the non-uniform sampling and smoothening procedures. Calculations were performed with the PC-SAFT EoS.

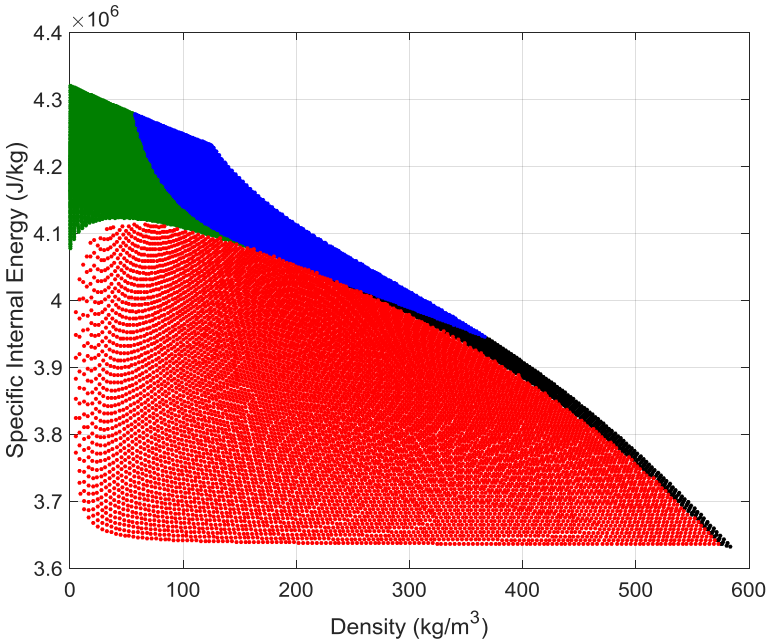

Figure 10.14: The ρ-e diagram of the 99.5% (mole) C_2H_4 - 0.2% CH_4 - 0.3% N_2 mixture with 150 × 150 points sampled in T-P space. Results are shown with the non-uniform sampling and smoothening procedures. Calculations were performed with the PC-SAFT EoS.

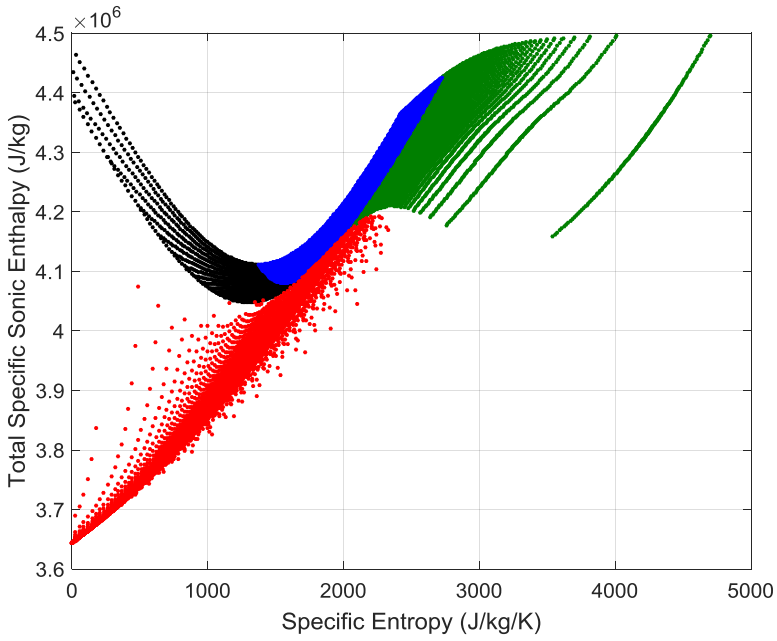

Figure 10.15: The s-h^*_{tot} diagram of the 99.5% (mole) C_2H_4 - 0.2% CH_4 - 0.3% N_2 mixture with 150 × 150 points sampled in T-P space. Results are shown with the non-uniform sampling and smoothening procedures. Calculations were performed with the PC-SAFT EoS.

The accuracy of the interpolation method is assessed on various sizes of grids at reference points $\{T^o, P^o\}$ sampled in P-T space, for which the corresponding $\{\rho^o, e^o\}$ and $\{s^o, h^*_{tot}{}^o\}$ data are calculated using the PC-SAFT EoS. For the sake of example, the accuracy of pressure and temperature interpolation is evaluated based on the $\{\rho, e\}$ grid, as shown schematically in Figure 10.5. The interpolation errors are calculated % AARD in temperature and pressure in the various regions.

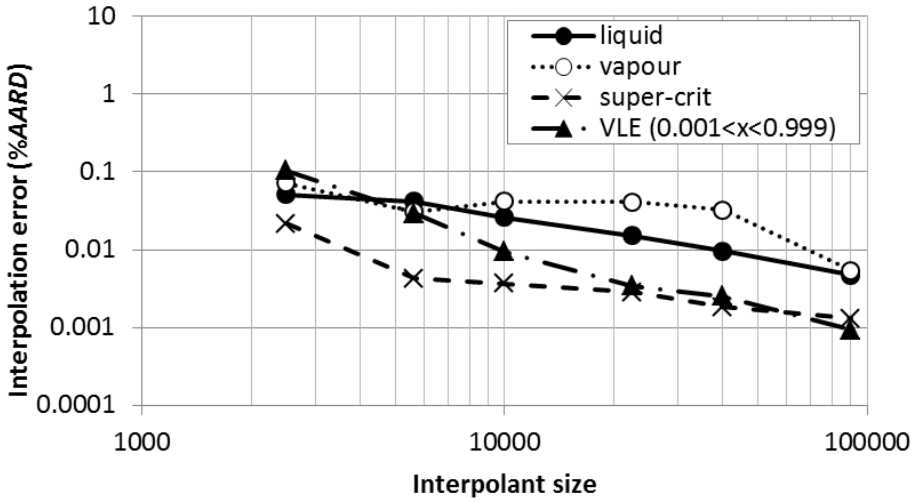

Figure 10.16: % AARD interpolation errors observed in pressure as functions of the grid size.

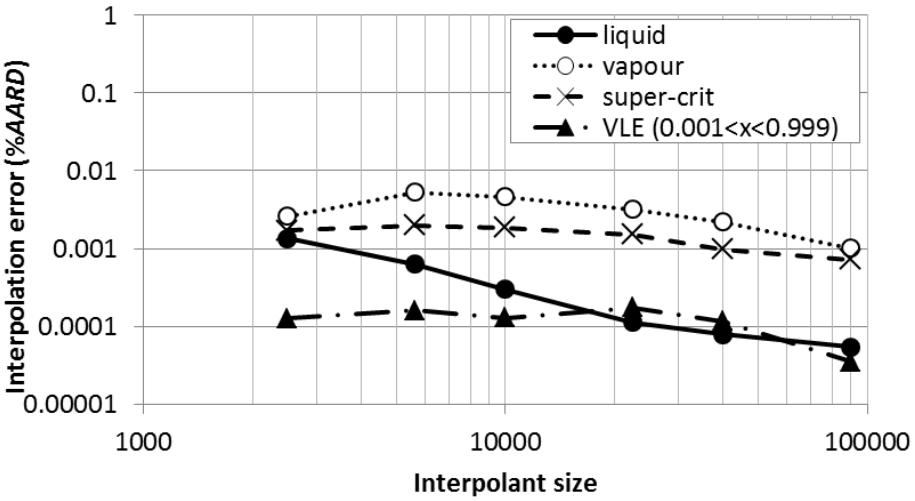

Figure 10.17: % AARD interpolation errors observed in temperature as functions of the grid size.

Figure 10.16 and Figure 10.17 show the calculated % AARD for pressure and temperature, plotted as functions of the grid size for the liquid, vapor and supercritical phases, as well as the VLE phase region. The results show that the temperature and pressure interpolation errors generally decrease as the grid size increases from 2,500 to 40,000 points. Remarkably, the temperature interpolation errors are about 10 times smaller than the errors of pressure interpolation. This behavior was qualitatively observed also in the case of CO_2 mixtures.

In order to relate errors in the interpolated (T, P) data to errors in density and energy, the error propagation is studied, as shown in Figure 10.18.

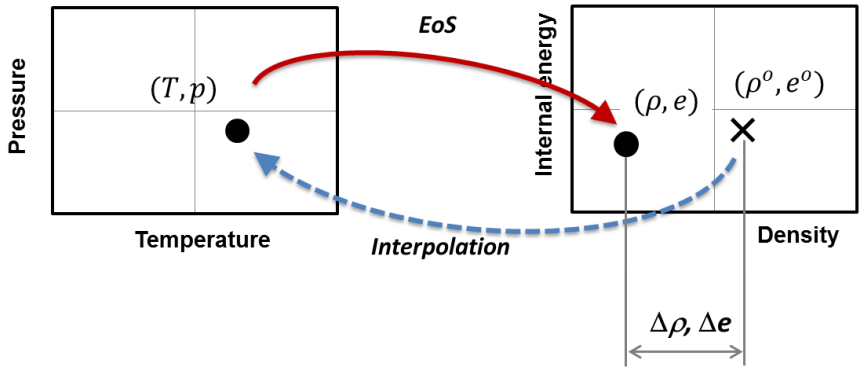

Figure 10.18: The density and internal energy errors, $\Delta\rho$ and Δe, resulting from propagation of interpolation errors carried from (T, P) data, into (ρ, e) data predicted using the PC-SAFT EoS.

The EoS is applied to obtain the (ρ, e) data at the interpolated (T, P) points. The difference between (ρ, e) and the original data (ρ^o, e^o) characterizes the accuracy of the interpolation method, expressed as % AARD.

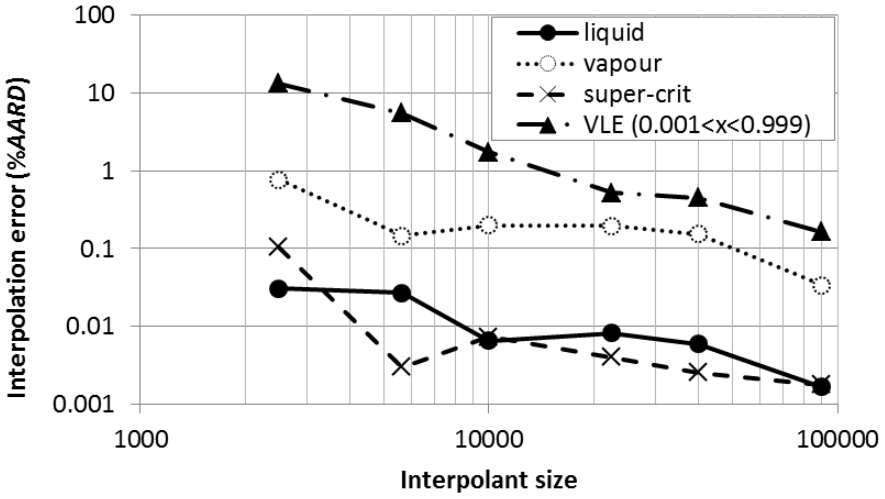

Figure 10.19: % AARD interpolation errors observed in density as functions of the grid size, using the interpolated temperature and pressure input data.

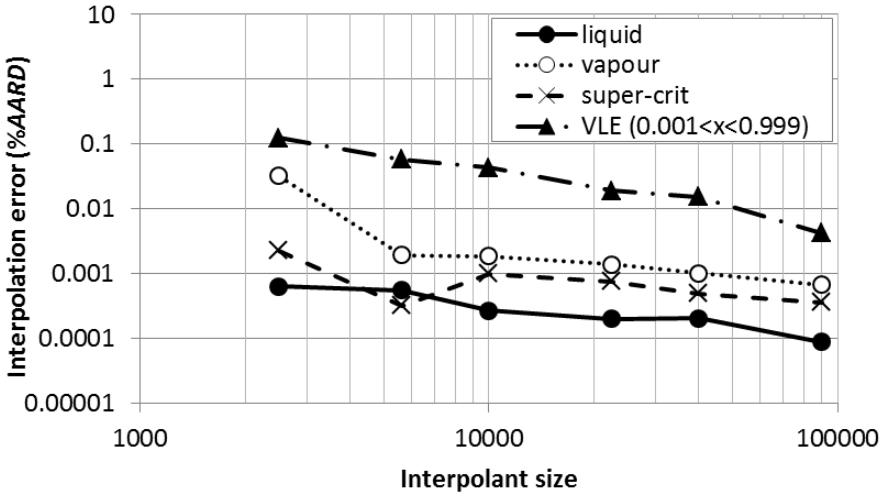

Figure 10.20: % AARD interpolation errors observed in specific internal energy as functions of the grid size, using the interpolated temperature and pressure input data.

Figure 10.19 and Figure 10.20 show the relative errors for the density and specific internal energy as functions of the number of the grid points. Comparison of the data shows that the internal energy is interpolated about 50 times more accurately than the density. Similar to the trend observed in Figure 10.16 and Figure 10.17, increasing the number of the interpolation points up to 40,000, generally improves accuracy of the method.

The density interpolation errors can be directly compared with the accuracy of the EoS. In particular, as follows from Figure 10.19, using a grid size with 10,000 (100 × 100) points results in density interpolation errors of approximately 0.2% for the vapor phase, and 0.01% for the liquid phase and the supercritical fluid. These errors are of the order of magnitude smaller than the accuracy of the PC-SAFT EoS, which was reported to be 2.37%, 0.42% and 1.24% for the saturated vapor, the saturated liquid and the supercritical fluid, respectively in Chapter 9. As such, it can be concluded that using a grid with 100 × 100 to 200 × 200 grid points guarantees density interpolation within the accuracy of the PC-SAFT EoS.

10.3.3.Full-bore Rupture Simulation of C_2H_4 pipeline

This section describes the simulation results with the HEM model combined with the interpolation method described above, using $\{\rho, e\}$ and $\{s, h^*_{tot}\}$ grids. The results are compared against data from an ethylene pipeline decompression experiment which are presented in Martynov et al. [292].

The fluid initial density and internal energy were obtained using the PC-SAFT EoS at 291 K and 7.7 MPa, while the initial velocity was set to zero. For the numerical solution of the flow model equations, the pipeline was discretised into 250 equally-spaced control volumes. This level of discretisation was shown to be sufficient to guarantee accurate and mesh-independent results [293]. The base-case study was performed using grids that contained 150 × 150 points, to ensure high accuracy and computational efficiency of the interpolation method.

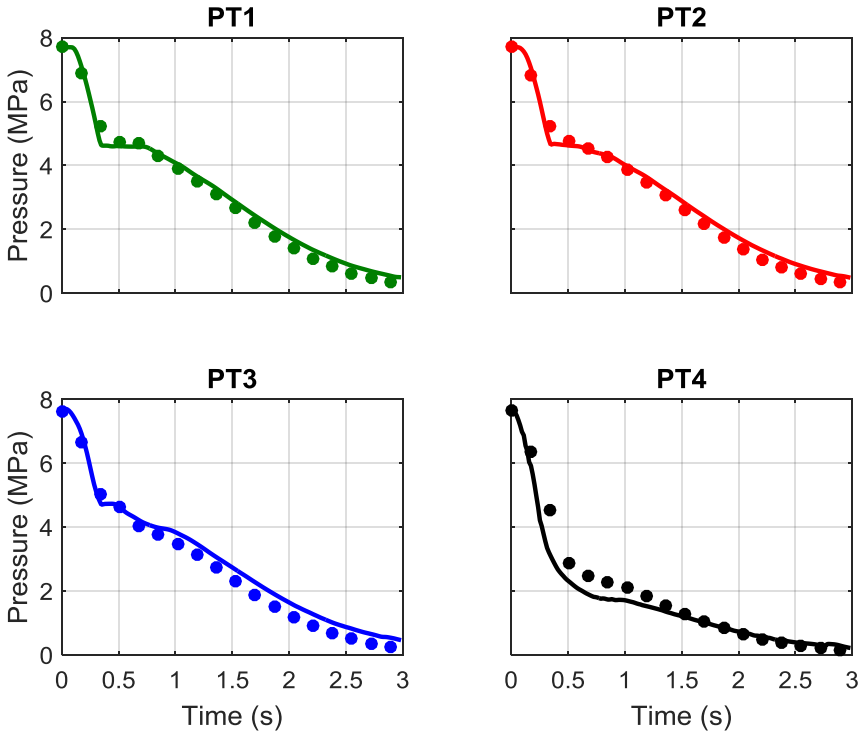

Figure 10.21: The time variation of pressure, as predicted by the decompression model at different locations on the pipeline (PT1, PT2, PT3, PT4), in comparison with the measurements from the pipeline discharge experiment. Experimental data are represented by data points and model predictions by lines.

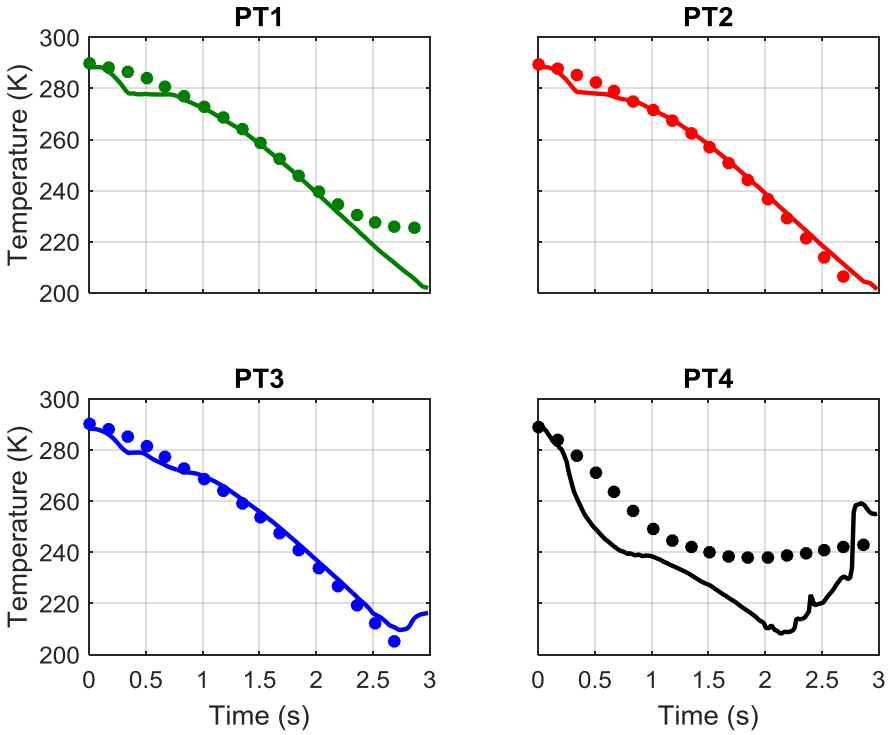

Figure 10.22: The time variation of temperature, as predicted by the decompression model at different locations on the pipeline (PT1, PT2, PT3, PT4), in comparison with the measurements from the pipeline discharge experiment. Experimental data are represented by data points and model predictions by lines.

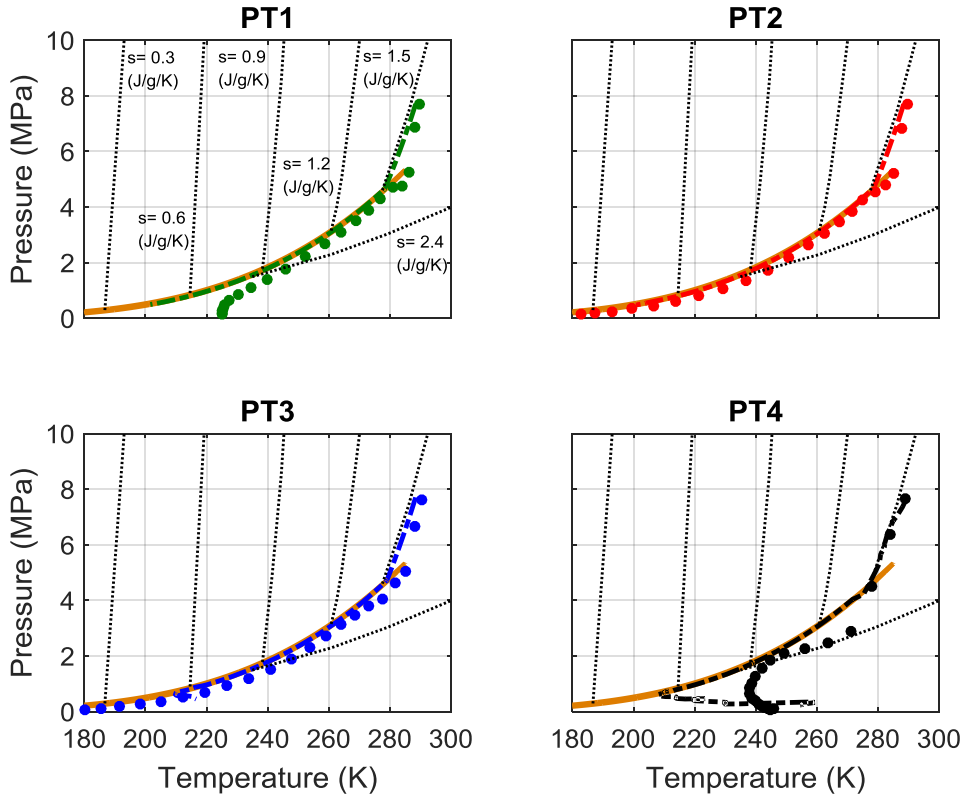

Figure 10.23: The thermodynamic trajectories plotted in T-P space, as predicted by the decompression model at different locations on the pipeline (PT1, PT2, PT3, PT4), in comparison with the measurements from the pipeline discharge experiment. Experimental data are represented by data points. Solid orange lines correspond to the P-T phase envelope of the 99.5% (mole) C_2H_4 - 0.2% CH_4 - 0.3% N_2 mixture, calculated with the PC-SAFT EoS. Dash-dot lines correspond to the decompression model predictions and dotted lines correspond to isentropes, calculated with the PC-SAFT EoS.

Figure 10.21 and Figure 10.22 show the pressure and temperature variation with time corresponding to predictions by the flow model and experimental measurements at specific locations on the pipeline. The fluid pressure predicted by the model is in good agreement with the measured data. In particular, at the beginning of release, both the predicted and measured pressures are rapidly decreasing everywhere in the pipe, from 7.7 MPa at time t = 0 s, to approximately 5 MPa at 0.4 s. At this stage the fluid (initially in the supercritical state) rapidly and near-isentropically (as can be seen in Figure 10.23) accelerates to reach chocked flow conditions at the release valve. As the pressure drops to approximately 5 MPa, the fluid starts flashing (see Figure 10.23) where its vapor content builds up. Figure 10.22 shows the temperature variation in the pipe as predicted by the model and measured in the test at the four locations. Similar to the trends discussed for pressure, the predicted temperatures demonstrate rapid decrease during the first 0.4 s, followed by temporary stabilization.

10.4. Conclusions

The development and application of a robust interpolation technique for the efficient coupling of thermodynamic calculations in flow models was presented. The technique is proposed as an alternative to using computationally demanding iterative algorithms for phase equilibrium calculations at specifications, other than T, P. The accuracy and computational cost of computing the physical properties and phase equilibria of mixtures greatly affects the overall accuracy and computational runtime of multiphase flow simulations. Thus, the adaption of this technique has significant impact on the ability to perform sophisticated CFD simulations at reasonable cost without significant loss of accuracy. The higher order PC-SAFT EoS was used for the accurate calculation of physical properties.

The interpolation tables used in the proposed method are built based on grid points which are non-uniformly sampled in the P-T domain to ensure accurate resolution of the fluid properties in the two-phase region. Furthermore, a smoothening procedure is applied by uniformly distributing the points along isotherms based on density. The optimal size of the grid was determined considering both the accuracy and the computational runtime of the properties interpolation.

Based on the case study for an ethylene-rich fluid it was shown that the method with a grid size of 150 × 150 results in low interpolation errors, regarding the reproduction of the initial (T, P) points that were used to sample it. An error propagation study showed also that the method predicts the fluid density as accurately as PC-SAFT EoS.

The method was coupled with the HEM model for two-phase simulations and was used for the simulation pipeline releases of CO_2-rich and C_2H_4-rich mixtures transported through high pressure pipelines. The results of the simulations were validated against full-bore rupture experimental data and reasonable agreement with the experiments was achieved.

11. Conclusions

In this thesis, efficient and robust methods were presented for the direct calculation of bubble and dew points of binary and multicomponent mixtures, based on the stability criterion of Gibbs. It was shown that a change of variables can be used to obtain optimal scaling in the minimization problem that is nested in all the methods presented. A simple and widely used initialization method was used in all calculations and specific guidelines and implementation details were given for each type of calculation. The proposed methods are not dependent on the EoS employed and can be used with cubic or higher order ones. The problem of multiplicity of solutions in the retrograde region of phase diagrams was targeted by designing each method to be able to calculate only one of the possible solutions. The proposed methods were tested in calculating saturation points of binary and multicomponent mixtures using cubic and non-cubic EoS at challenging conditions and proved to be very efficient and robust.

New Euler-Newton predictor-corrector methods were presented for the sequential construction of constant composition phase envelopes of binary and multicomponent mixtures and P-x,y, T-x,y phase diagrams of binary mixtures. The various variable sets that were proposed for direct saturation point calculations were used in the different formulations for the calculation of constant composition phase envelopes. In most cases all the proposed methods were able to trace the constant composition phase envelopes of various mixtures. The test cases included mixtures with similar composition to natural gas and gas condensate mixtures that are of interest to the oil and gas industry, as well as unusual phase envelopes exhibiting double retrograde behavior or open-ended phase envelopes extending to high pressures. The variable set that showed the best conditioning was used as the basis to construct methods for the calculation of P-x,y and T-x,y phase diagrams of binary mixtures. Several combinations of equations were proposed, each one possessing different independent and specification variables. The comparison between the methods was based on the conditioning of each method and the ability to trace different types of binary mixture phase diagrams.

Three solid-phase thermodynamic models of different complexity were coupled with three fluid-phase EoS (SRK, PR, PC-SAFT) to model the SFE of pure CO_2 and binary mixtures of CO_2 with other compounds. Scarcity of experimental data for two-phase SFE of CO_2 mixtures relevant to CCS applications, led to the evaluation of the performance of each combined model on SLGE experimental data from literature. The calculations showed that a model that successfully reproduces the pure solid-former

triple or normal melting point will predict more accurately the SLGE locus of the mixture.

A predictive methodology was developed for the calculation of the VLE of multicomponent hydrocarbon mixtures with high asymmetry, combining molecular simulations and EoS. GEMC simulations were used for the calculation of the VLE of binary CH_4 mixtures with *n*-alkanes, to be used as a pseudo-experimental dataset, for a consistent fitting of the BIPs of various EoS (SRK, PR, PC-SAFT). Simulations with the TraPPE-UA force field were validated with experimental VLE data for the binary mixtures considered and it was shown that accurate predictions can be retrieved even in very asymmetric mixtures, rendering the simulation data suitable for fitting BIPs of thermodynamic models. It was shown that the use of a dataset that spans a wide range of temperatures and pressures consistently affects the k_{ij} values, while the BIPs regressed from GEMC simulation data lead to equally accurate modeling results for multicomponent mixtures, compared to those regressed from experimental binary mixture data. Consequently, molecular simulations using accurate force fields can be used to generate precise VLE data for binary mixtures of CH_4 with *n*-alkanes, in the absence of experimental data.

The three EoS mentioned in the previous paragraph were coupled with the most accurate and flexible solid-phase thermodynamic model that occurred from the relevant CO_2 study. The combined models were used to calculate the SLGE behavior of binary CH_4 mixtures with *n*-alkanes. Several aspects of each combined model were assessed and the effect of specific terms of the solid-phase modeling approach was systematically validated against available experimental data. It is concluded that the use of k_{ij} parameters is imperative for the correct qualitative and improved quantitative prediction of the SLGE for all the binary mixtures considered. Temperature independent k_{ij} parameters should preferably be fitted to experimental VLE / GLE data at temperatures close to the SLGE conditions of each mixture, so that the predictive nature of the models is retained and accurate description of the fluid phases is obtained at the relevant range of conditions. The basic solid-phase model in combination with the fluid-phase EoS considered and the regressed BIPs provides accurate predictions of the SLGE until pressures around 20 MPa. Accurate results for the high pressure SLGE of asymmetric CH_4 mixtures with *n*-alkanes were obtained by taking into account the pressure dependency of the liquid molar volume in the Poynting correction of the solid-phase model, through the fluid-phase EoS. Implementation of the model with cubic EoS

requires the use of volume-translated versions of them as proposed in this thesis. PC-SAFT EoS in its original form provides accurate results at low and high pressures, since it reproduces more accurately the liquid molar volumes. Furthermore, a new solid-phase model was proposed, which provides excellent correlation of the high-pressure SLGE for the mixtures considered, both with PR and PC-SAFT EoS. Global phase diagrams were also calculated for specific mixtures to showcase the ability of the adopted and proposed models in reproducing the global phase behavior.

The PR, PC-SAFT and SAFT-VR Mie EoS were used to model the pure C_2H_4 physical properties, as well as the binary and ternary C_2H_4 mixture VLE with components associated with C_2H_4 pipeline transportation. The two SAFT EoS proved to be more accurate, when compared to PR EoS, in predicting the pure C_2H_4 physical properties, with the most prevalent differences being in the speed of sound and the Joule-Thomson coefficient calculations. PC-SAFT EoS proved to be the most accurate overall, when the physical properties along the saturation line were considered. SAFT-VR Mie predicted with higher accuracy the speed of sound and the isothermal compressibility coefficient in the supercritical region, but in general, the performance of the two SAFT EoS is of comparable accuracy. Regarding the binary mixtures VLE modeling, SAFT-VR Mie proved to be the most accurate EoS in terms of prediction. With the use of the regressed BIPs, the performance of all EoS is of comparable accuracy, apart from the H_2 - C_2H_4 mixture, where SAFT-VR Mie is clearly superior. With the use of the BIPs regressed from the binary mixture data, all EoS successfully predict the ternary mixture VLE considered in this work, while the differences between their predictions are minor. A general trend observed is that PR EoS tends to predict more accurately the vapor phase composition, while the two SAFT EoS are more accurate in predicting the liquid one. This observation is in agreement with the binary mixtures VLE discussion.

A technique for the rapid interpolation of thermodynamic properties of mixtures for the purposes of simulating two-phase flow was developed. The technique is proposed as an alternative to using computationally demanding iterative algorithms for phase equilibrium calculations at specifications, other than T, P. It was shown that the adaption of this technique has significant impact on the ability to perform sophisticated CFD simulations at reasonable cost without significant loss of accuracy. The method was coupled with the HEM model for two-phase flow simulations and was used for the simulation of pipeline releases of CO_2-rich and C_2H_4-rich mixtures transported through

high pressure pipelines. The results of the simulations were validated against full-bore rupture experimental data and reasonable agreement with the experiments was achieved.

12. Future Work

Future work that can be conducted as follow-up to this thesis is to investigate the possibility of extending the algorithms for direct saturation point calculations to VLLE. Probably this will require a second iterative loop in addition to the one already proposed, that will minimize the modified TPD function with respect to the new phase composition. The feed phase should be used as reference phase for the two incipient phases that occur and two minimization loops should be applied. Furthermore, the correction of temperature or pressure should probably be performed using the proposed equations, but taking into account the effect of both incipient phases. In addition, the continuation methods that were proposed for the sequential construction of two-phase diagrams can be readily extended to trace VLLE branches by adding the respective equations for an additional phase and again use the same feed phase as reference phase. Furthermore, it is possible to perform the direct saturation point calculation as an optimization problem of an objective function, but the stationary point is probably a saddle point. In that case, the numerical problem can be solved using nested iterations and perform the calculation as a min/max optimization problem.

Very limited experimental data are available in the open literature for CO_2 mixtures associated with CCS processes at SFE and SLGE conditions. Experimental data for the mixtures CO_2 with Ar and O_2 for example at SLGE conditions can help to validate further the developed models. Moreover, extension of the already available experimental data to higher pressures can help illuminate the capabilities and limitations of the examined models and approaches.

The combination of molecular simulations and EoS as proposed in this thesis, proved to be a successful approach for the prediction of multicomponent hydrocarbon mixtures VLE, even when very asymmetric mixtures are considered. However, the mixtures that were studied included only *n*-alkanes and CH_4, while in real reservoir fluids many more components are present, like branched-chain alkanes, alkenes, aromatic compounds etc. An extensive research work, incorporating a significant amount of GEMC simulations for binary mixtures that include the compounds mentioned previously and covers a wide range of conditions can be used to tune the interaction parameters of thermodynamic models consistently. In this way, multicomponent mixture predictions can be performed with higher consistency in evaluating the performance of the examined models and possibly advance the existing ones.

The SLGE modeling of binary CH_4 mixtures with *n*-alkanes can be readily extended to evaluate the performance of the applied and developed approaches to ternary mixtures in which only one component solidifies and the other two act as solvents in the fluid mixture. Furthermore, calculations can be extended in cases in which more than one component solidifies and multiple pure solid phases are formed. Moreover, the possibility of the formation of solid phases that include more than one component is worth investigating. As it was discussed in section 2.3, the modeling of solidification for mixtures with multiple solid-formers has been approached in the open literature in two ways. The first approach considers the formation of impure solid phases, while the second one assumes the formation of multiple pure solid phases. A research study that compares the two approaches against experimental data can give some insight on the matter.

For the C_2H_4 mixtures investigated in this thesis, no experimental data are available for binary and multicomponent mixture physical properties, such as density, speed of sound, heat capacity etc. Experimental measurements for these types of properties will give the opportunity to further validate the models considered in this work, which is important when these models are incorporated in flow simulators.

Finally, a research study that compares the sensitivity of flow simulations to the physical properties and phase equilibria calculated with various simple and complex EoS could give some quantitative insight on how much the accuracy of the thermodynamic models affects the final results and which properties are the most important. This insight could help the developers of new models target more efficiently the modifications that should be performed in existing models in order to enhance the prediction of specific properties that are important for engineering applications.

Appendix A: Flowcharts and Supporting Information for the Methods Presented in Chapter 4

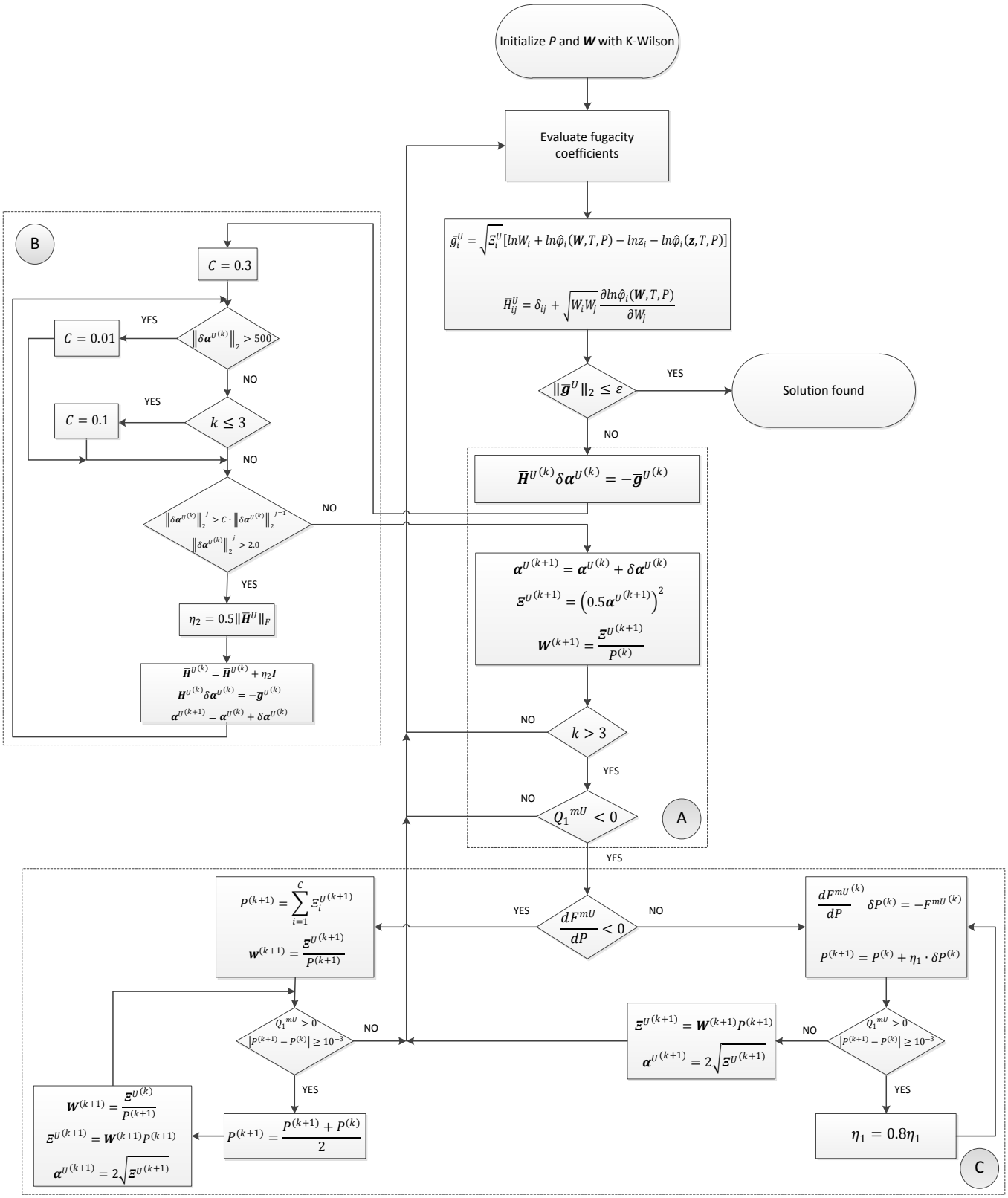

Figure A.1: Flow diagram of the implementation algorithm for method 2U.

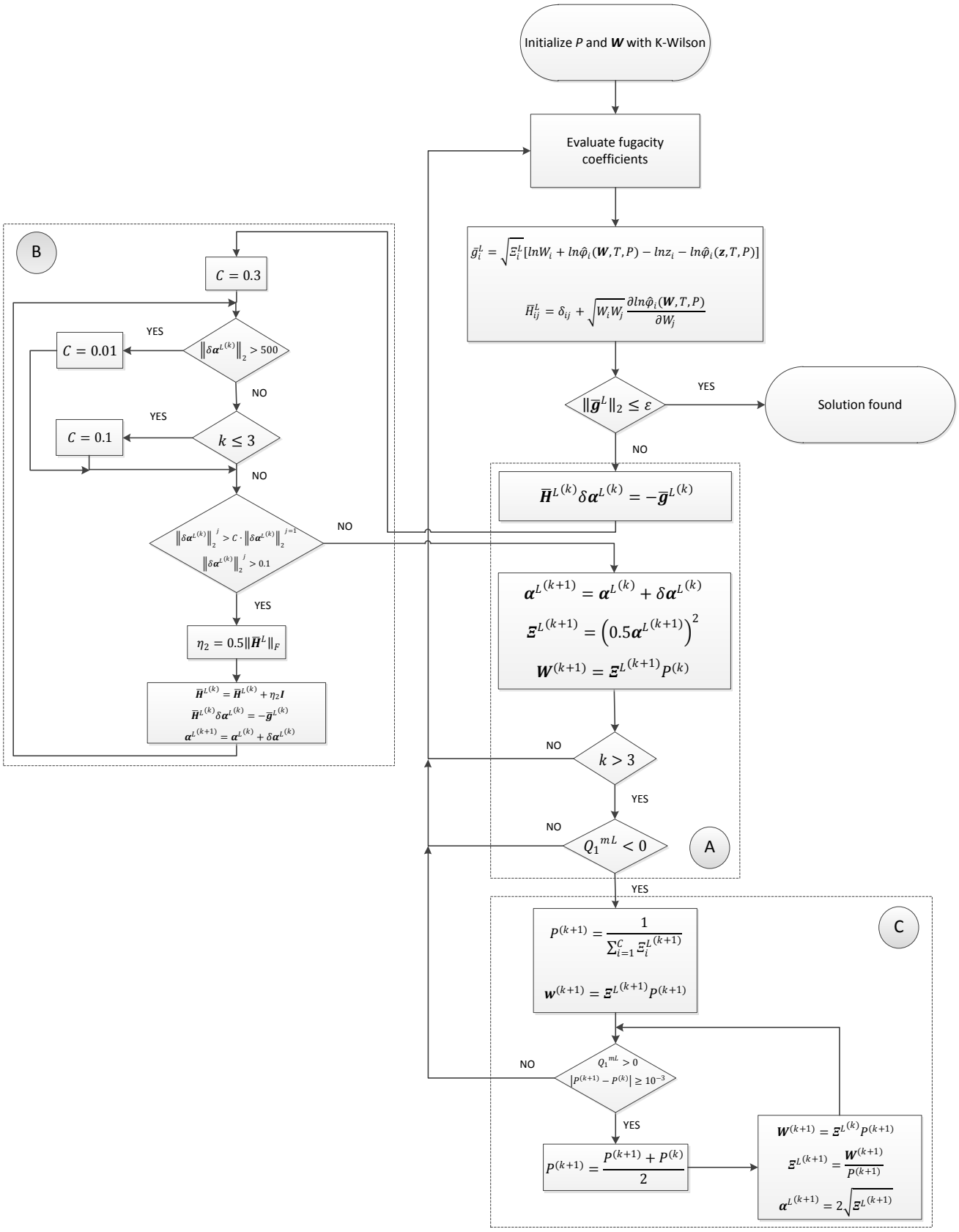

Figure A.2: Flow diagram of the implementation algorithm for method 1L.

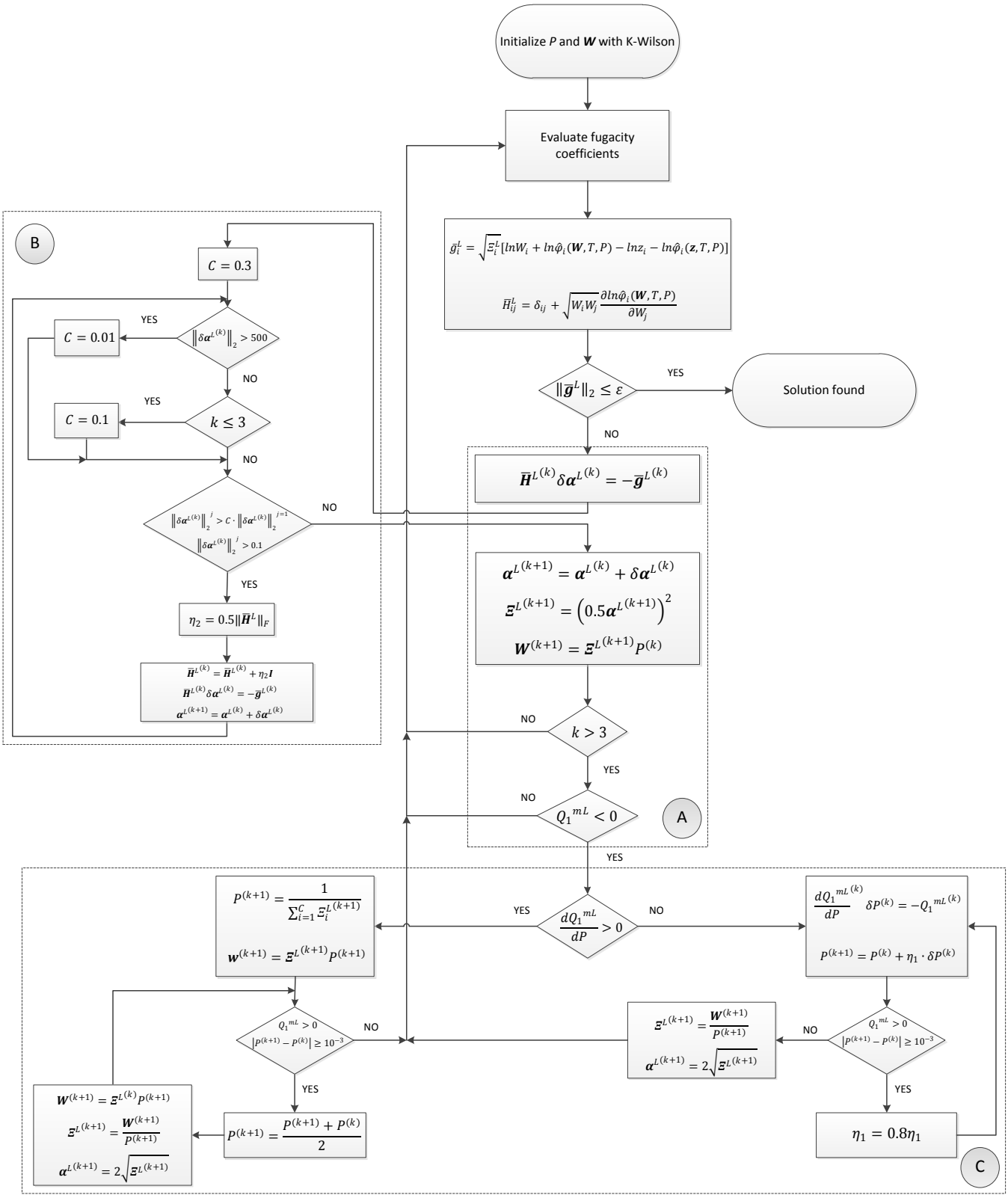

Figure A.3: Flow diagram of the implementation algorithm for method 3L.

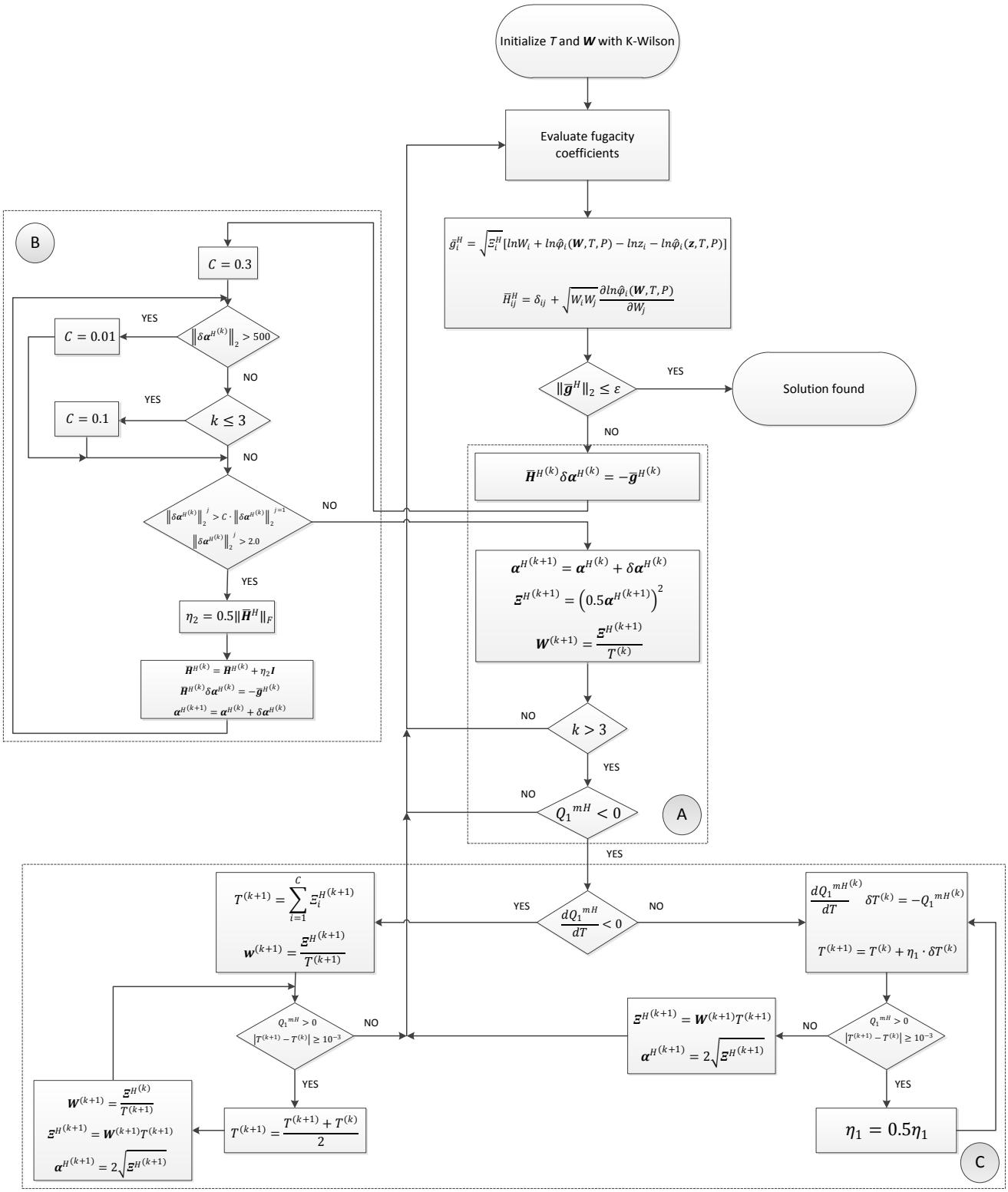

Figure A.4: Flow diagram of the implementation algorithm for method 3H.

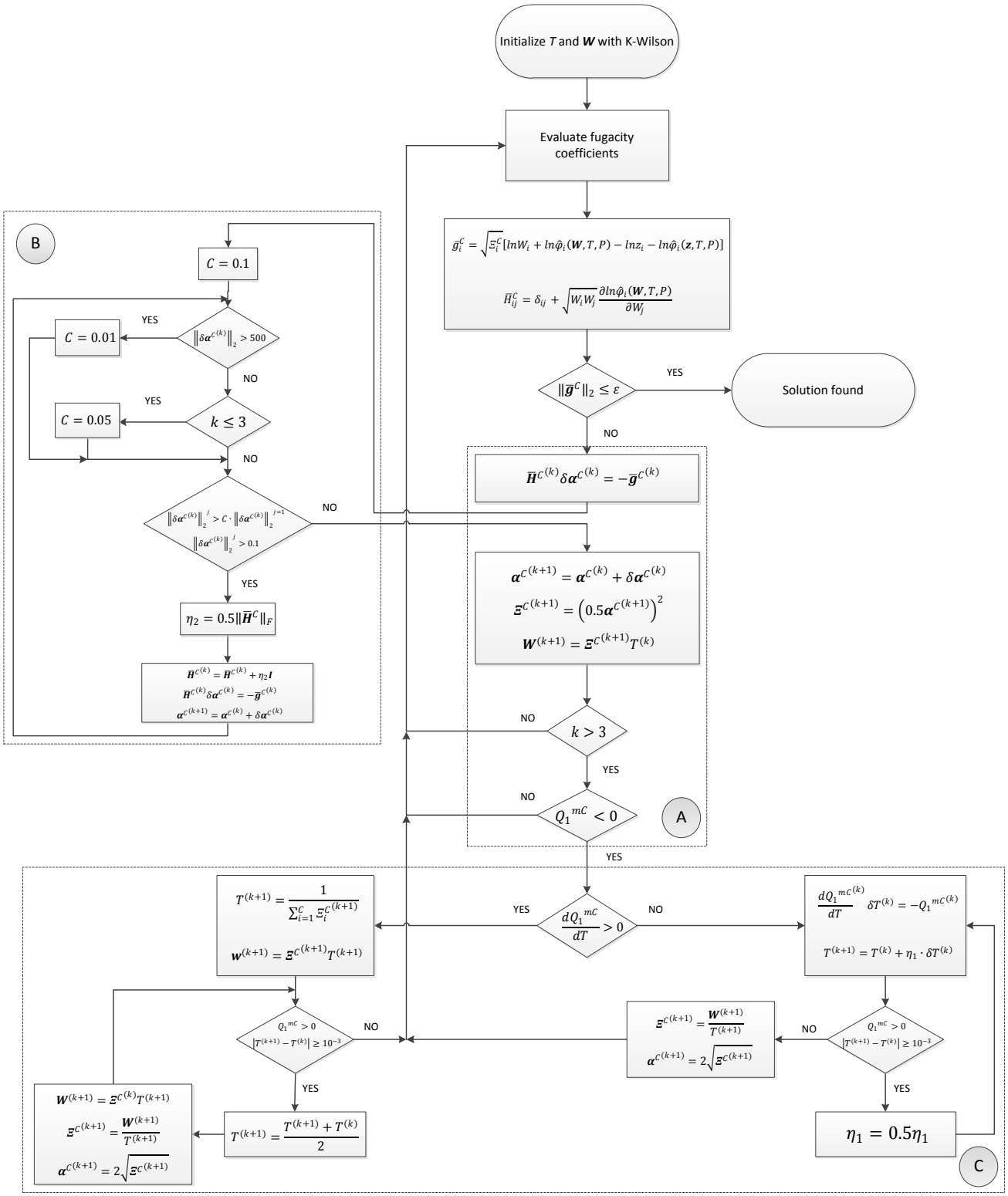

Figure A.5: Flow diagram of the implementation algorithm for method 3C.

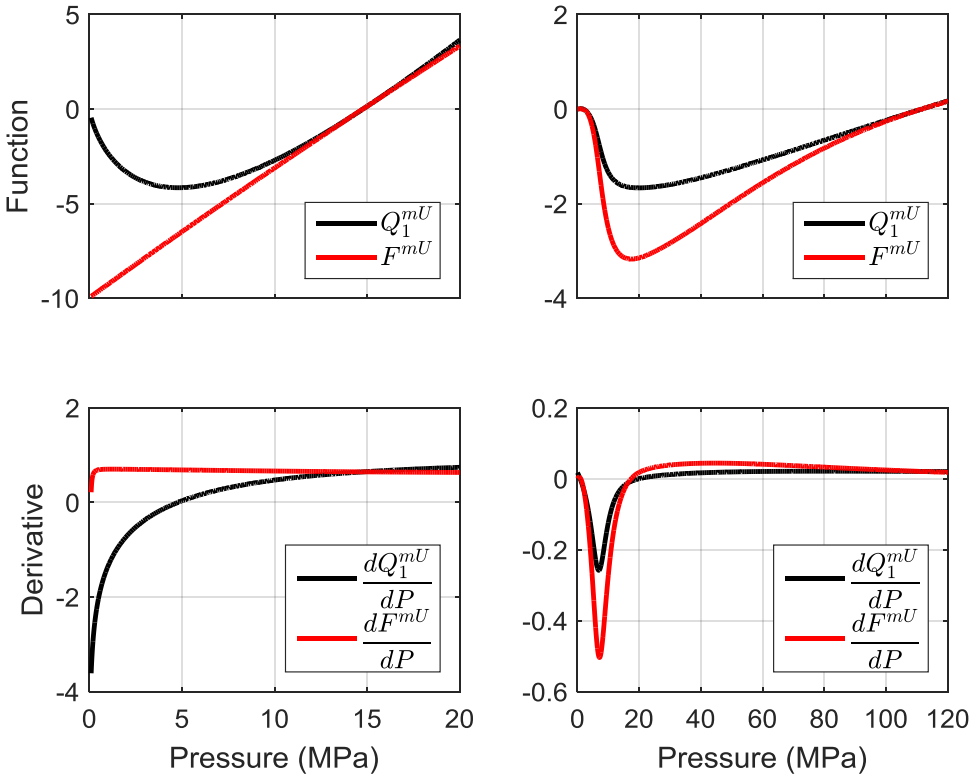

Figure A.6: Variation of ${Q_1}^{mU}, \frac{d{Q_1}^{mU}}{dP}, F^{mU}, \frac{dF^{mU}}{dP}$ with pressure for the CH_4 - *n*-$C_{36}H_{74}$ mixture (mix3) at T= 373 K. Left panels were calculated at $\boldsymbol{z}$ = (0.509,0.491) (liquid phase) and $\boldsymbol{W}$ = (0.99999993,0.00000007) (vapor phase), while right panels were calculated at $\boldsymbol{z}$ = (0.949,0.051) (liquid phase) and $\boldsymbol{W}$ = (0.984112372,0.015887628) (vapor phase). The calculations were performed with PC-SAFT EoS and $k_{ij} = 0.0282$ taken from Nikolaidis et al. [170] (Chapter 8).

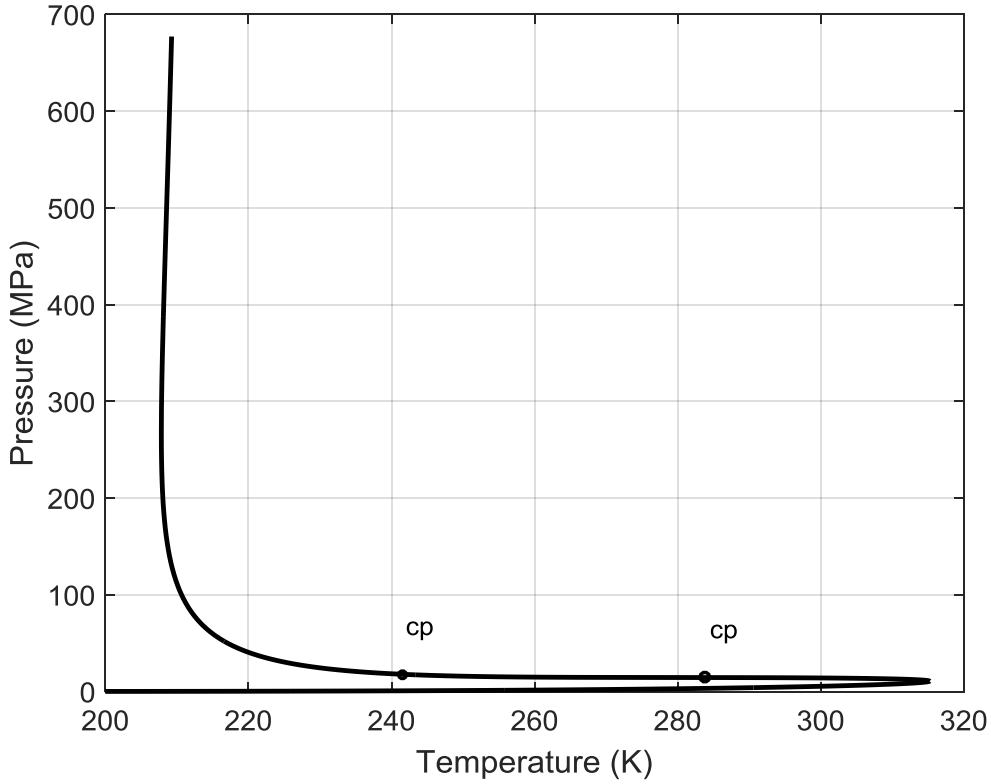

Figure A.7: Constant composition VLE phase envelope of a 50% (mole) CH_4 - 50% H_2S mixture (mix5). Calculations were performed with SRK EoS and $k_{ij} = 0.08$ taken from Nikolaidis et al [62].

Appendix B: Equations and Jacobian Matrices for the Methods Presented in Chapter 5

Method X1L

The stability criterion, under constant T and P, can be expressed by a modified TPD function, with an unconstrained formulation and using as independent variables $\Xi_i^L = W_i/P$. The corresponding TPD function is:

$$Q_1{}^{mL}(\boldsymbol{\Xi}^L) = \sum_{i=1}^{C} \Xi_i^L \left(\ln W_i + \ln\hat{\varphi}_i(\boldsymbol{W},T,P) - \ln z_i - \ln\hat{\varphi}_i(\boldsymbol{z},T,P)\right) + \frac{1}{P} - \sum_{i=1}^{C} \Xi_i^L \qquad \text{B.1}$$

Using as independent variables $\mathrm{X^L} = (\ln\Xi_1^L, \ldots, \ln\Xi_C^L, \ln T, \ln P)$, the nonlinear equation set for the phase envelope calculation takes the form:

$$g_i^L = \ln\Xi_i^L + \ln\hat{\varphi}_i(\boldsymbol{W},T,P) - \ln z_i - \ln\hat{\varphi}_i(\boldsymbol{z},T,P) + \ln P = 0;\ i = 1,2 \ldots C \qquad \text{B.2}$$

$$g_{C+1}^L = \sum_{i=1}^{C} \Xi_i^L - \frac{1}{P} = 0 \qquad \text{B.3}$$

$$g_{C+2}^L = X_S^L - S = 0 \qquad \text{B.4}$$

The elements of the Jacobian matrix of the equation set mentioned above are:

$$J_{ij}^L = \frac{\partial g_i^L}{\partial \ln\Xi_j^L} = \delta_{ij} + W_j \frac{\partial \ln\hat{\varphi}_i(\boldsymbol{W},T,P)}{\partial W_j};\ i,j = 1,2 \ldots C \qquad \text{B.5}$$

$$J_{i,C+1}^L = \frac{\partial g_i^L}{\partial \ln T} = T\left(\frac{\partial \ln\hat{\varphi}_i(\boldsymbol{W},T,P)}{\partial T} - \frac{\partial \ln\hat{\varphi}_i(\boldsymbol{z},T,P)}{\partial T}\right);\ i = 1,2 \ldots C \qquad \text{B.6}$$

$$J_{i,C+2}^L = \frac{\partial g_i^L}{\partial \ln P} = P\left(\frac{\partial \ln\hat{\varphi}_i(\boldsymbol{W},T,P)}{\partial P} - \frac{\partial \ln\hat{\varphi}_i(\boldsymbol{z},T,P)}{\partial P}\right) + 1;\ i = 1,2 \ldots C \qquad \text{B.7}$$

$$J_{C+1,j}^L = \frac{\partial g_{C+1}^L}{\partial \ln\Xi_j^L} = \Xi_j^L;\ j = 1,2 \ldots C \qquad \text{B.8}$$

$$J^L_{C+1,C+1} = \frac{\partial g^L_{C+1}}{\partial \ln T} = 0 \tag{B.9}$$

$$J^L_{C+1,C+2} = \frac{\partial g^L_{C+1}}{\partial \ln P} = \frac{1}{P} \tag{B.10}$$

$$J^L_{C+2,j} = \frac{\partial g^L_{C+2}}{\partial X^L_j} = \delta_{jS};\ j = 1,2 \dots C+2 \tag{B.11}$$

$$\boldsymbol{W}^{(k+1)} = \boldsymbol{\Xi}^{L\,(k+1)} P^{(k+1)} \tag{B.12}$$

The corresponding relations for the determination of the pressure and temperature maxima of the phase envelope are given by:

$$\left(\frac{\partial {Q_1}^{mL}}{\partial T}\right)_P = \sum_{i=1}^{C} \Xi^L_i \left(\frac{\partial \ln \hat{\varphi}_i(\boldsymbol{W},T,P)}{\partial T} - \frac{\partial \ln \hat{\varphi}_i(\boldsymbol{z},T,P)}{\partial T}\right) \tag{B.13}$$

and

$$\begin{aligned}\left(\frac{\partial {Q_1}^{mL}}{\partial P}\right)_T = -\frac{1}{P^2}\Bigg[\sum_{i=1}^{C} W_i\big(\ln W_i + \ln \hat{\varphi}_i(\boldsymbol{W},T,P) - \ln z_i - \ln \hat{\varphi}_i(\boldsymbol{z},T,P)\big) + 1 \\ - \sum_{i=1}^{C} W_i\Bigg] + \sum_{i=1}^{C} \Xi^L_i \left(\frac{\partial \ln \hat{\varphi}_i(\boldsymbol{W},T,P)}{\partial P} - \frac{\partial \ln \hat{\varphi}_i(\boldsymbol{z},T,P)}{\partial P}\right)\end{aligned} \tag{B.14}$$

Method X1H

The stability criterion, under constant T and P, can be expressed by a modified TPD function, with an unconstrained formulation and using as independent variables $\Xi^H_i = W_i T$. The corresponding TPD function is:

$${Q_1}^{mH}(\boldsymbol{\Xi}^H) = \sum_{i=1}^{C} \Xi^H_i \big(\ln W_i + \ln \hat{\varphi}_i(\boldsymbol{W},T,P) - \ln z_i - \ln \hat{\varphi}_i(\boldsymbol{z},T,P)\big) + T - \sum_{i=1}^{C} \Xi^H_i \tag{B.15}$$

Using as independent variables $\boldsymbol{X}^H = (\ln \Xi^H_1, \dots, \ln \Xi^H_C, \ln T, \ln P)$, the nonlinear equation set for the phase envelope calculation takes the form:

$$g_i^H = \ln\Xi_i^H + \ln\hat{\varphi}_i(\boldsymbol{W},T,P) - \ln z_i - \ln\hat{\varphi}_i(\boldsymbol{z},T,P) - \ln T = 0;\ i = 1,2 \dots C \quad \text{B.16}$$

$$g_{C+1}^H = \sum_{i=1}^{C} \Xi_i^H - T = 0 \quad \text{B.17}$$

$$g_{C+2}^H = X_S^H - S = 0 \quad \text{B.18}$$

The elements of the Jacobian matrix of the equation set mentioned above are:

$$J_{ij}^H = \frac{\partial g_i^H}{\partial \ln \Xi_j^H} = \delta_{ij} + W_j \frac{\partial \ln\hat{\varphi}_i(\boldsymbol{W},T,P)}{\partial W_j};\ i,j = 1,2 \dots C \quad \text{B.19}$$

$$J_{i,C+1}^H = \frac{\partial g_i^H}{\partial \ln T} = T\left(\frac{\partial \ln\hat{\varphi}_i(\boldsymbol{W},T,P)}{\partial T} - \frac{\partial \ln\hat{\varphi}_i(\boldsymbol{z},T,P)}{\partial T}\right) - 1;\ i = 1,2 \dots C \quad \text{B.20}$$

$$J_{i,C+2}^H = \frac{\partial g_i^H}{\partial \ln P} = P\left(\frac{\partial \ln\hat{\varphi}_i(\boldsymbol{W},T,P)}{\partial P} - \frac{\partial \ln\hat{\varphi}_i(\boldsymbol{z},T,P)}{\partial P}\right);\ i = 1,2 \dots C \quad \text{B.21}$$

$$J_{C+1,j}^H = \frac{\partial g_{C+1}^H}{\partial \ln \Xi_j^H} = \Xi_j^H;\ j = 1,2 \dots C \quad \text{B.22}$$

$$J_{C+1,C+1}^H = \frac{\partial g_{C+1}^H}{\partial \ln T} = -T \quad \text{B.23}$$

$$J_{C+1,C+2}^H = \frac{\partial g_{C+1}^H}{\partial \ln P} = 0 \quad \text{B.24}$$

$$J_{C+2,j}^H = \frac{\partial g_{C+2}^H}{\partial X_j^H} = \delta_{jS};\ j = 1,2 \dots C+2 \quad \text{B.25}$$

$$\boldsymbol{W}^{(k+1)} = \frac{\boldsymbol{\Xi}^{H\,(k+1)}}{T^{(k+1)}} \quad \text{B.26}$$

The corresponding relations for the determination of the pressure and temperature maxima of the phase envelope are given by:

$$\left(\frac{\partial {Q_1}^{mH}}{\partial T}\right)_P = \sum_{i=1}^{C} W_i\left(\ln W_i + \ln\hat{\varphi}_i(\boldsymbol{W},T,P) - \ln z_i - \ln\hat{\varphi}_i(\boldsymbol{z},T,P)\right) + 1 - \sum_{i=1}^{C} W_i + \sum_{i=1}^{C} \Xi_i^H \left(\frac{\partial \ln\hat{\varphi}_i(\boldsymbol{W},T,P)}{\partial T} - \frac{\partial \ln\hat{\varphi}_i(\boldsymbol{z},T,P)}{\partial T}\right) \quad \text{B.27}$$

and

$$\left(\frac{\partial {Q_1}^{mH}}{\partial P}\right)_T = \sum_{i=1}^{C} \Xi_i^H \left(\frac{\partial \ln\hat{\varphi}_i(\boldsymbol{W},T,P)}{\partial P} - \frac{\partial \ln\hat{\varphi}_i(\boldsymbol{z},T,P)}{\partial P}\right) \quad \text{B.28}$$

Method X1C

The stability criterion, under constant T and P, can be expressed by a modified TPD function, with an unconstrained formulation and using as independent variables $\Xi_i^C = W_i/T$. The corresponding TPD function is:

$${Q_1}^{mC}(\boldsymbol{\Xi}^C) = \sum_{i=1}^{C} \Xi_i^C\left(\ln W_i + \ln\hat{\varphi}_i(\boldsymbol{W},T,P) - \ln z_i - \ln\hat{\varphi}_i(\boldsymbol{z},T,P)\right) + \frac{1}{T} - \sum_{i=1}^{C} \Xi_i^C \quad \text{B.29}$$

Using as independent variables $\boldsymbol{X}^C = (\ln\Xi_1^C, \dots, \ln\Xi_C^C, \ln T, \ln P)$, the nonlinear equation set for the phase envelope calculation takes the form:

$$g_i^C = \ln\Xi_i^C + \ln\hat{\varphi}_i(\boldsymbol{W},T,P) - \ln z_i - \ln\hat{\varphi}_i(\boldsymbol{z},T,P) + \ln T = 0;\ i = 1,2 \dots C \quad \text{B.30}$$

$$g_{C+1}^C = \sum_{i=1}^{C} \Xi_i^C - \frac{1}{T} = 0 \quad \text{B.31}$$

$$g_{C+2}^C = X_S^C - S = 0 \quad \text{B.32}$$

The elements of the Jacobian matrix of the equation set mentioned above are:

$$J_{ij}^C = \frac{\partial g_i^C}{\partial \ln\Xi_j^C} = \delta_{ij} + W_j \frac{\partial \ln\hat{\varphi}_i(\boldsymbol{W},T,P)}{\partial W_j};\ i,j = 1,2 \dots C \quad \text{B.33}$$

$$J_{i,C+1}^{C} = \frac{\partial g_i^C}{\partial \ln T} = T\left(\frac{\partial \ln\hat{\varphi}_i(\boldsymbol{W},T,P)}{\partial T} - \frac{\partial \ln\hat{\varphi}_i(\boldsymbol{z},T,P)}{\partial T}\right) + 1;\ i = 1,2 \dots C \qquad \text{B.34}$$

$$J_{i,C+2}^{C} = \frac{\partial g_i^C}{\partial \ln P} = P\left(\frac{\partial \ln\hat{\varphi}_i(\boldsymbol{W},T,P)}{\partial P} - \frac{\partial \ln\hat{\varphi}_i(\boldsymbol{z},T,P)}{\partial P}\right);\ i = 1,2 \dots C \qquad \text{B.35}$$

$$J_{C+1,j}^{C} = \frac{\partial g_{C+1}^C}{\partial \ln \Xi_j^C} = \Xi_j^C;\ j = 1,2 \dots C \qquad \text{B.36}$$

$$J_{C+1,C+1}^{C} = \frac{\partial g_{C+1}^C}{\partial \ln T} = \frac{1}{T} \qquad \text{B.37}$$

$$J_{C+1,C+2}^{C} = \frac{\partial g_{C+1}^C}{\partial \ln P} = 0 \qquad \text{B.38}$$

$$J_{C+2,j}^{C} = \frac{\partial g_{C+2}^C}{\partial X_j^C} = \delta_{jS};\ j = 1,2 \dots C+2 \qquad \text{B.39}$$

$$\boldsymbol{W}^{(k+1)} = \boldsymbol{\Xi}^{C\,(k+1)} T^{(k+1)} \qquad \text{B.40}$$

The corresponding relations for the determination of the pressure and temperature maxima of the phase envelope are given by:

$$\left(\frac{\partial {Q_1}^{mC}}{\partial T}\right)_P = -\frac{1}{T^2}\left[\sum_{i=1}^{C} W_i\left(\ln W_i + \ln\hat{\varphi}_i(\boldsymbol{W},T,P) - \ln z_i - \ln\hat{\varphi}_i(\boldsymbol{z},T,P)\right) + 1 - \sum_{i=1}^{C} W_i\right] + \sum_{i=1}^{C} \Xi_i^C\left(\frac{\partial \ln\hat{\varphi}_i(\boldsymbol{W},T,P)}{\partial T} - \frac{\partial \ln\hat{\varphi}_i(\boldsymbol{z},T,P)}{\partial T}\right) \qquad \text{B.41}$$

and

$$\left(\frac{\partial {Q_1}^{mC}}{\partial P}\right)_T = \sum_{i=1}^{C} \Xi_i^C\left(\frac{\partial \ln\hat{\varphi}_i(\boldsymbol{W},T,P)}{\partial P} - \frac{\partial \ln\hat{\varphi}_i(\boldsymbol{z},T,P)}{\partial P}\right) \qquad \text{B.42}$$

Method 1m

(P-x,y) Diagrams

The vector of independent variables is $\boldsymbol{X}^{m1} = (\ln\Xi_1^{UW}, \ln\Xi_2^{UW}, \ln W_1, \ln W_2, \ln Z_1, \ln Z_2, \ln P)$ and the nonlinear equation set has the form:

$$g_i^{m1} = \ln\Xi_i^{UW} + \ln\hat{\varphi}_i(\boldsymbol{W}, T, P) - \ln Z_i - \ln\hat{\varphi}_i(\boldsymbol{Z}, T, P) - \ln P = 0;\ i = 1, C \quad \text{B.43}$$

$$g_{C+i}^{m1} = \Xi_i^{UW} - W_i P = 0;\ i = 1, C \quad \text{B.44}$$

$$g_{2C+1}^{m1} = W_1 + W_2 - 1 = 0 \quad \text{B.45}$$

$$g_{2C+2}^{m1} = Z_1 + Z_2 - 1 = 0 \quad \text{B.46}$$

$$g_{2C+3}^{m1} = X_S^{m1} - S = 0 \quad \text{B.47}$$

The elements of the Jacobian matrix are:

$$J_{ij}^{m1} = \frac{\partial g_i^{m1}}{\partial \ln\Xi_j^{UW}} = \delta_{ij};\ i, j = 1, C \quad \text{B.48}$$

$$J_{i,C+j}^{m1} = \frac{\partial g_i^{m1}}{\partial \ln W_j} = W_j \frac{\partial \ln\hat{\varphi}_i(\boldsymbol{W}, T, P)}{\partial W_j};\ i, j = 1, C \quad \text{B.49}$$

$$J_{i,2C+j}^{m1} = \frac{\partial g_i^{m1}}{\partial \ln Z_j} = -\delta_{ij} - Z_j \frac{\partial \ln\hat{\varphi}_i(\boldsymbol{Z}, T, P)}{\partial Z_j};\ i, j = 1, C \quad \text{B.50}$$

$$J_{i,3C+1}^{m1} = \frac{\partial g_i^{m1}}{\partial \ln P} = P\left(\frac{\partial \ln\hat{\varphi}_i(\boldsymbol{W}, T, P)}{\partial P} - \frac{\partial \ln\hat{\varphi}_i(\boldsymbol{Z}, T, P)}{\partial P}\right) - 1;\ i = 1, C \quad \text{B.51}$$

$$J_{C+i,j}^{m1} = \frac{\partial g_{C+i}^{m1}}{\partial \ln\Xi_j^{UW}} = \delta_{ij}\Xi_j^{UW};\ i, j = 1, C \quad \text{B.52}$$

$$J_{C+i,C+j}^{m1} = \frac{\partial g_{C+i}^{m1}}{\partial \ln W_j} = -\delta_{ij} W_j P;\ i, j = 1, C \quad \text{B.53}$$

$$J_{C+i,2C+j}^{m1} = \frac{\partial g_{C+i}^{m1}}{\partial \ln Z_j} = 0.0;\ i, j = 1, C \quad \text{B.54}$$

$$J^{m1}_{C+i,3C+1} = \frac{\partial g^{m1}_{C+i}}{\partial \ln P} = -W_i P;\ i = 1, C \tag{B.55}$$

$$J^{m1}_{2C+1,j} = \frac{\partial g^{m1}_{2C+1}}{\partial \ln \Xi^{UW}_j} = 0.0;\ j = 1, C \tag{B.56}$$

$$J^{m1}_{2C+1,C+j} = \frac{\partial g^{m1}_{2C+1}}{\partial \ln W_j} = W_j;\ j = 1, C \tag{B.57}$$

$$J^{m1}_{2C+1,2C+j} = \frac{\partial g^{m1}_{2C+1}}{\partial \ln Z_j} = 0.0;\ j = 1, C \tag{B.58}$$

$$J^{m1}_{2C+1,3C+1} = \frac{\partial g^{m1}_{2C+1}}{\partial \ln P} = 0.0; \tag{B.59}$$

$$J^{m1}_{2C+2,j} = \frac{\partial g^{m1}_{2C+2}}{\partial \ln \Xi^{UW}_j} = 0.0;\ j = 1, C \tag{B.60}$$

$$J^{m1}_{2C+2,C+j} = \frac{\partial g^{m1}_{2C+2}}{\partial \ln W_j} = 0.0;\ j = 1, C \tag{B.61}$$

$$J^{m1}_{2C+2,2C+j} = \frac{\partial g^{m1}_{2C+2}}{\partial \ln Z_j} = Z_j;\ j = 1, C \tag{B.62}$$

$$J^{m1}_{2C+2,3C+1} = \frac{\partial g^{m1}_{2C+2}}{\partial \ln P} = 0.0; \tag{B.63}$$

$$J^{m1}_{2C+3,j} = \frac{\partial g^{m1}_{2C+3}}{\partial X^{m1}_j} = \delta_{jS};\ j = 1,2,(3C+1) \tag{B.64}$$

(T-x,y) Diagrams

The vector of independent variables is $\boldsymbol{X}^{m1} = (\ln \Xi^{UW}_1, \ln \Xi^{UW}_2, \ln W_1, \ln W_2, \ln Z_1, \ln Z_2, \ln T)$. The same nonlinear equation set is used. The elements of the Jacobian matrix are the same as the ones for the P-x,y diagram calculation, except for those mentioned below:

$$J^{m1}_{i,3C+1} = \frac{\partial g^{m1}_i}{\partial \ln T} = T\left(\frac{\partial \ln \hat{\varphi}_i(\boldsymbol{W}, T, P)}{\partial T} - \frac{\partial \ln \hat{\varphi}_i(\boldsymbol{Z}, T, P)}{\partial T}\right);\ i = 1, C \tag{B.65}$$

$$J^{m1}_{C+i,3C+1} = \frac{\partial g^{m1}_{C+i}}{\partial \ln T} = 0.0;\ i = 1, C \tag{B.66}$$

Method 2m

(P-x,y) Diagrams

The vector of independent variables is $\boldsymbol{X}^{m2} = (\ln\Xi_1^{UW}, \ln\Xi_2^{UW}, \ln W_1, \ln W_2, \ln Z_1, \ln Z_2, \ln P)$ and the nonlinear equation set has the form:

$$g_i^{m2} = \ln\Xi_i^{UW} + \ln\hat{\varphi}_i(\boldsymbol{W}, T, P) - \ln Z_i - \ln\hat{\varphi}_i(\boldsymbol{Z}, T, P) - \ln P = 0;\ i = 1, C \tag{B.67}$$

$$g^{m2}_{C+i} = \Xi_i^{UW} - W_i P = 0;\ i = 1, C \tag{B.68}$$

$$g^{m2}_{2C+1} = \Xi_1^{UW} + \Xi_2^{UW} - P = 0 \tag{B.69}$$

$$g^{m2}_{2C+2} = Z_1 + Z_2 - 1 = 0 \tag{B.70}$$

$$g^{m2}_{2C+3} = X_S^{m2} - S = 0 \tag{B.71}$$

The elements of the Jacobian matrix are the same as in method 1m for constant temperature (P-x,y) diagrams, except for the 2C+1 row of the matrix in which:

$$J^{m2}_{2C+1,j} = \frac{\partial g^{m2}_{2C+1}}{\partial \ln\Xi_j^{UW}} = \Xi_j^{UW};\ j = 1, C \tag{B.72}$$

$$J^{m2}_{2C+1,C+j} = \frac{\partial g^{m2}_{2C+1}}{\partial \ln W_j} = 0.0;\ j = 1, C \tag{B.73}$$

$$J^{m2}_{2C+1,2C+j} = \frac{\partial g^{m2}_{2C+1}}{\partial \ln Z_j} = 0.0;\ j = 1, C \tag{B.74}$$

$$J^{m2}_{2C+1,3C+1} = \frac{\partial g^{m2}_{2C+1}}{\partial \ln P} = -P; \tag{B.75}$$

(T-x,y) Diagrams

The vector of independent variables is $\boldsymbol{X}^{m2} = (\ln\Xi_1^{UW}, \ln\Xi_2^{UW}, \ln W_1, \ln W_2, \ln Z_1, \ln Z_2, \ln T)$. The same nonlinear equation set is used. The elements of the Jacobian matrix are the same as the ones for the P-x,y diagram calculation, except for those mentioned below:

$$J_{i,3C+1}^{m2} = \frac{\partial g_i^{m2}}{\partial \ln T} = T\left(\frac{\partial \ln \hat{\varphi}_i(\boldsymbol{W},T,P)}{\partial T} - \frac{\partial \ln \hat{\varphi}_i(\boldsymbol{Z},T,P)}{\partial T}\right);\ i = 1,C \quad \text{B.76}$$

$$J_{C+i,3C+1}^{m2} = \frac{\partial g_{C+i}^{m2}}{\partial \ln T} = 0.0;\ i = 1,C \quad \text{B.77}$$

$$J_{2C+1,3C+1}^{m2} = \frac{\partial g_{2C+1}^{m2}}{\partial \ln T} = 0.0; \quad \text{B.78}$$

Method 3m

(P-x,y) Diagrams

$\boldsymbol{X}^{m3} = (\ln \Xi_1^{UW}, \ln \Xi_2^{UW}, \ln \Xi_1^{UZ}, \ln \Xi_2^{UZ}, \ln W_1, \ln W_2, \ln Z_1, \ln Z_2, \ln P)$ is the vector of independent variables and the nonlinear equation set has the form:

$$g_i^{m3} = \ln \Xi_i^{UW} + \ln \hat{\varphi}_i(\boldsymbol{W},T,P) - \ln \Xi_i^{UZ} - \ln \hat{\varphi}_i(\boldsymbol{Z},T,P) = 0;\ i = 1,C \quad \text{B.79}$$

$$g_{C+i}^{m3} = \Xi_i^{UW} - W_i P = 0;\ i = 1,C \quad \text{B.80}$$

$$g_{2C+i}^{m3} = \Xi_i^{UZ} - Z_i P = 0;\ i = 1,C \quad \text{B.81}$$

$$g_{3C+1}^{m3} = \Xi_1^{UW} + \Xi_2^{UW} - P = 0 \quad \text{B.82}$$

$$g_{3C+2}^{m3} = \Xi_1^{UZ} + \Xi_2^{UZ} - P = 0 \quad \text{B.83}$$

$$g_{3C+3}^{m3} = X_S^{m3} - S = 0 \quad \text{B.84}$$

The elements of the Jacobian matrix are:

$$J_{ij}^{m3} = \frac{\partial g_i^{m3}}{\partial \ln \Xi_j^{UW}} = \delta_{ij};\ i,j = 1,C \quad \text{B.85}$$

$$J_{i,C+j}^{m3} = \frac{\partial g_i^{m3}}{\partial \ln \Xi_j^{UZ}} = -\delta_{ij};\ i,j = 1,C \quad \text{B.86}$$

$$J_{i,2C+j}^{m3} = \frac{\partial g_i^{m3}}{\partial \ln W_j} = W_j \frac{\partial \ln \hat{\varphi}_i(\boldsymbol{W},T,P)}{\partial W_j};\ i,j = 1,C \quad \text{B.87}$$

$$J_{i,3C+j}^{m3} = \frac{\partial g_i^{m3}}{\partial \ln Z_j} = -Z_j \frac{\partial \ln \hat{\varphi}_i(\boldsymbol{Z}, T, P)}{\partial Z_j};\ i,j = 1,C \tag{B.88}$$

$$J_{i,4C+1}^{m3} = \frac{\partial g_i^{m3}}{\partial \ln P} = P\left(\frac{\partial \ln \hat{\varphi}_i(\boldsymbol{W}, T, P)}{\partial P} - \frac{\partial \ln \hat{\varphi}_i(\boldsymbol{Z}, T, P)}{\partial P}\right);\ i = 1,C \tag{B.89}$$

$$J_{C+i,j}^{m3} = \frac{\partial g_{C+i}^{m3}}{\partial \ln \Xi_j^{UW}} = \delta_{ij}\Xi_j^{UW};\ i,j = 1,C \tag{B.90}$$

$$J_{C+i,C+j}^{m3} = \frac{\partial g_{C+i}^{m3}}{\partial \ln \Xi_j^{UZ}} = 0.0;\ i,j = 1,C \tag{B.91}$$

$$J_{C+i,2C+j}^{m3} = \frac{\partial g_{C+i}^{m3}}{\partial \ln W_j} = -\delta_{ij}W_j P;\ i,j = 1,C \tag{B.92}$$

$$J_{C+i,3C+j}^{m3} = \frac{\partial g_{C+i}^{m3}}{\partial \ln Z_j} = 0.0;\ i,j = 1,C \tag{B.93}$$

$$J_{C+i,4C+1}^{m3} = \frac{\partial g_{C+i}^{m3}}{\partial \ln P} = -W_i P;\ i = 1,C \tag{B.94}$$

$$J_{2C+i,j}^{m3} = \frac{\partial g_{2C+i}^{m3}}{\partial \ln \Xi_j^{UW}} = 0.0;\ i,j = 1,C \tag{B.95}$$

$$J_{2C+i,C+j}^{m3} = \frac{\partial g_{2C+i}^{m3}}{\partial \ln \Xi_j^{UZ}} = \delta_{ij}\Xi_j^{UZ};\ i,j = 1,C \tag{B.96}$$

$$J_{2C+i,2C+j}^{m3} = \frac{\partial g_{2C+i}^{m3}}{\partial \ln W_j} = 0.0;\ i,j = 1,C \tag{B.97}$$

$$J_{2C+i,3C+j}^{m3} = \frac{\partial g_{2C+i}^{m3}}{\partial \ln Z_j} = -\delta_{ij}Z_j P;\ i,j = 1,C \tag{B.98}$$

$$J_{2C+i,4C+1}^{m3} = \frac{\partial g_{2C+i}^{m3}}{\partial \ln P} = -Z_i P;\ i = 1,C \tag{B.99}$$

$$J^{m3}_{3C+1,j} = \frac{\partial g^{m3}_{3C+1}}{\partial \ln \Xi^{UW}_j} = \Xi^{UW}_j;\ j = 1, C \quad \text{B.100}$$

$$J^{m3}_{3C+1,C+j} = \frac{\partial g^{m3}_{3C+1}}{\partial \ln \Xi^{UZ}_j} = 0.0;\ i, j = 1, C \quad \text{B.101}$$

$$J^{m3}_{3C+1,2C+j} = \frac{\partial g^{m3}_{3C+1}}{\partial \ln W_j} = 0.0;\ j = 1, C \quad \text{B.102}$$

$$J^{m3}_{3C+1,3C+j} = \frac{\partial g^{m3}_{3C+1}}{\partial \ln Z_j} = 0.0;\ j = 1, C \quad \text{B.103}$$

$$J^{m3}_{3C+1,4C+1} = \frac{\partial g^{m3}_{3C+1}}{\partial \ln P} = -P; \quad \text{B.104}$$

$$J^{m3}_{3C+2,j} = \frac{\partial g^{m3}_{3C+2}}{\partial \ln \Xi^{UW}_j} = 0.0;\ j = 1, C \quad \text{B.105}$$

$$J^{m3}_{3C+2,C+j} = \frac{\partial g^{m3}_{3C+2}}{\partial \ln \Xi^{UZ}_j} = \Xi^{UZ}_j;\ j = 1, C \quad \text{B.106}$$

$$J^{m3}_{3C+2,2C+j} = \frac{\partial g^{m3}_{3C+2}}{\partial \ln W_j} = 0.0;\ j = 1, C \quad \text{B.107}$$

$$J^{m3}_{3C+2,3C+j} = \frac{\partial g^{m3}_{3C+2}}{\partial \ln Z_j} = 0.0;\ j = 1, C \quad \text{B.108}$$

$$J^{m3}_{3C+2,4C+1} = \frac{\partial g^{m3}_{3C+2}}{\partial \ln P} = -P; \quad \text{B.109}$$

$$J^{m3}_{3C+3,j} = \frac{\partial g^{m3}_{3C+3}}{\partial X^{m3}_j} = \delta_{jS};\ j = 1,2,(3C+3) \quad \text{B.110}$$

(T-x,y) Diagrams

$\boldsymbol{X}^{m3} = (\ln \Xi^{UW}_1, \ln \Xi^{UW}_2, \ln \Xi^{UZ}_1, \ln \Xi^{UZ}_2, \ln W_1, \ln W_2, \ln Z_1, \ln Z_2, \ln T)$ is the vector of independent variables. The same nonlinear equation set is used. The elements of the Jacobian matrix are the same as the ones for the P-x,y diagram calculation, except for those mentioned below:

$$J_{i,4C+1}^{m3} = \frac{\partial g_i^{m3}}{\partial \ln T} = T\left(\frac{\partial \ln \hat{\varphi}_i(\boldsymbol{W},T,P)}{\partial T} - \frac{\partial \ln \hat{\varphi}_i(\boldsymbol{Z},T,P)}{\partial T}\right);\ i = 1,C \tag{B.111}$$

$$J_{C+i,4C+1}^{m3} = \frac{\partial g_{C+i}^{m3}}{\partial \ln T} = 0.0;\ i = 1,C \tag{B.112}$$

$$J_{2C+i,4C+1}^{m3} = \frac{\partial g_{2C+i}^{m3}}{\partial \ln T} = 0.0;\ i = 1,C \tag{B.113}$$

$$J_{3C+1,4C+1}^{m3} = \frac{\partial g_{3C+1}^{m3}}{\partial \ln T} = 0.0; \tag{B.114}$$

$$J_{3C+2,4C+1}^{m3} = \frac{\partial g_{3C+2}^{m3}}{\partial \ln P} = 0.0; \tag{B.115}$$

Method 4m

(P-x,y) Diagrams

$\boldsymbol{X}^{m4} = (\ln\overline{K_1}, \ln\overline{K_2}, \ln\Xi_1^{UW}, \ln\Xi_2^{UW}, \ln\Xi_1^{UZ}, \ln\Xi_2^{UZ}, \ln P)$ is the vector of independent variables and the nonlinear equation set has the form:

$$g_i^{m4} = \ln\overline{K}_i + \ln\hat{\varphi}_i(\boldsymbol{W},T,P) - \ln\hat{\varphi}_i(\boldsymbol{Z},T,P) = 0;\ i = 1,C \tag{B.116}$$

$$g_{C+i}^{m4} = \Xi_i^{UW} - \overline{K}_i\Xi_i^{UZ} = 0;\ i = 1,C \tag{B.117}$$

$$g_{2C+1}^{m4} = \Xi_1^{UW} + \Xi_2^{UW} - P = 0 \tag{B.118}$$

$$g_{2C+2}^{m4} = \Xi_1^{UZ} + \Xi_2^{UZ} - P = 0 \tag{B.119}$$

$$g_{2C+3}^{m4} = X_S^{m4} - S = 0 \tag{B.120}$$

The elements of the Jacobian matrix are:

$$J_{ij}^{m4} = \frac{\partial g_i^{m4}}{\partial \ln\overline{K}_j} = \delta_{ij};\ i,j = 1,C \tag{B.121}$$

$$J_{i,C+j}^{m4} = \frac{\partial g_i^{m4}}{\partial \ln\Xi_j^{UW}} = W_j\frac{\partial \ln\hat{\varphi}_i(\boldsymbol{W},T,P)}{\partial W_j};\ i,j = 1,C \tag{B.122}$$

$$J_{i,2C+j}^{m4} = \frac{\partial g_i^{m4}}{\partial \ln \Xi_j^{UZ}} = -Z_j \frac{\partial \ln \hat{\varphi}_i(\boldsymbol{Z}, T, P)}{\partial Z_j};\ i, j = 1, C \quad \text{B.123}$$

$$J_{i,3C+1}^{m4} = \frac{\partial g_i^{m4}}{\partial \ln P} = P\left(\frac{\partial \ln \hat{\varphi}_i(\boldsymbol{W}, T, P)}{\partial P} - \frac{\partial \ln \hat{\varphi}_i(\boldsymbol{Z}, T, P)}{\partial P}\right);\ i = 1, C \quad \text{B.124}$$

$$J_{C+i,j}^{m4} = \frac{\partial g_{C+i}^{m4}}{\partial \ln \bar{K}_j} = -\delta_{ij} \bar{K}_j \Xi_j^{UZ};\ i, j = 1, C \quad \text{B.125}$$

$$J_{C+i,C+j}^{m4} = \frac{\partial g_{C+i}^{m4}}{\partial \ln \Xi_j^{UW}} = \delta_{ij} \Xi_j^{UW};\ i, j = 1, C \quad \text{B.126}$$

$$J_{C+i,2C+j}^{m4} = \frac{\partial g_{C+i}^{m4}}{\partial \ln \Xi_j^{UZ}} = -\delta_{ij} \bar{K}_j \Xi_j^{UZ};\ i, j = 1, C \quad \text{B.127}$$

$$J_{C+i,3C+1}^{m4} = \frac{\partial g_{C+i}^{m4}}{\partial \ln P} = 0.0;\ i = 1, C \quad \text{B.128}$$

$$J_{2C+1,j}^{m4} = \frac{\partial g_{2C+1}^{m4}}{\partial \ln \bar{K}_j} = 0.0;\ j = 1, C \quad \text{B.129}$$

$$J_{2C+1,C+j}^{m4} = \frac{\partial g_{2C+1}^{m4}}{\partial \ln \Xi_j^{UW}} = \Xi_j^{UW};\ j = 1, C \quad \text{B.130}$$

$$J_{2C+1,2C+j}^{m4} = \frac{\partial g_{2C+1}^{m4}}{\partial \ln \Xi_j^{UZ}} = 0.0;\ j = 1, C \quad \text{B.131}$$

$$J_{2C+1,3C+1}^{m4} = \frac{\partial g_{2C+1}^{m4}}{\partial \ln P} = -P; \quad \text{B.132}$$

$$J_{2C+2,j}^{m4} = \frac{\partial g_{2C+2}^{m4}}{\partial \ln \bar{K}_j} = 0.0;\ j = 1, C \quad \text{B.133}$$

$$J_{2C+2,C+j}^{m4} = \frac{\partial g_{2C+2}^{m4}}{\partial \ln \Xi_j^{UW}} = 0.0;\ j = 1, C \quad \text{B.134}$$

$$J^{m4}_{2C+2,2C+j} = \frac{\partial g^{m4}_{2C+2}}{\partial \ln \Xi^{UZ}_j} = \Xi^{UZ}_j;\ j = 1, C \tag{B.135}$$

$$J^{m4}_{2C+2,3C+1} = \frac{\partial g^{m4}_{2C+2}}{\partial \ln P} = -P; \tag{B.136}$$

$$J^{m4}_{2C+3,j} = \frac{\partial g^{m4}_{2C+3}}{\partial X^{m4}_j} = \delta_{jS};\ j = 1,2,(3C+1) \tag{B.137}$$

(T-x, y) Diagrams

$\boldsymbol{X}^{m4} = (\ln\overline{K_1}, \ln\overline{K_2}, \ln\Xi^{UW}_1, \ln\Xi^{UW}_2, \ln\Xi^{UZ}_1, \ln\Xi^{UZ}_2, \ln T)$ is the vector of independent variables. The same nonlinear equation set is used. The elements of the Jacobian matrix are the same as the ones for the P-x,y diagram calculation, except for those mentioned below:

$$J^{m4}_{i,3C+1} = \frac{\partial g^{m4}_i}{\partial \ln T} = T\left(\frac{\partial \ln \hat{\varphi}_i(\boldsymbol{W}, T, P)}{\partial T} - \frac{\partial \ln \hat{\varphi}_i(\boldsymbol{Z}, T, P)}{\partial T}\right);\ i = 1, C \tag{B.138}$$

$$J^{m4}_{2C+1,3C+1} = \frac{\partial g^{m4}_{2C+1}}{\partial \ln T} = 0.0; \tag{B.139}$$

$$J^{m4}_{2C+2,3C+1} = \frac{\partial g^{m4}_{2C+2}}{\partial \ln T} = 0.0; \tag{B.140}$$

Appendix C: Pure Component Parameters

Table C.1: Critical Temperature (T_c), Critical Pressure (P_c) and Acentric Factor (ω) values for the components studied in this work.

Component	T_c (K)	P_c(MPa)	ω	Ref
H_2	33.1900	1.313	-0.2160	[175]
N_2	126.200	3.399	0.0377	[175]
CH_4	190.564	4.599	0.0115	[175]
C_2H_4	282.340	5.040	0.0865	[175]
CO_2	304.210	7.383	0.2236	[175]
C_2H_6	305.320	4.872	0.0995	[175]
C_3H_6	365.570	4.665	0.1398	[175]
C_3H_8	369.830	4.248	0.1523	[175]
1-C_4H_8	419.950	4.043	0.1905	[175]
n-C_4H_{10}	425.120	3.796	0.2002	[175]
i-C_5H_{12}	460.430	3.381	0.2275	[175]
n-C_5H_{12}	469.700	3.370	0.2515	[175]
n-C_6H_{14}	507.600	3.025	0.3013	[175]
n-C_7H_{16}	540.200	2.740	0.3495	[175]
n-C_8H_{18}	568.700	2.490	0.3996	[175]
n-$C_{10}H_{22}$	617.700	2.110	0.4923	[175]
n-$C_{12}H_{26}$	658.000	1.820	0.5764	[175]
n-$C_{16}H_{34}$	723.000	1.400	0.7174	[175]
n-$C_{17}H_{36}$	736.000	1.340	0.7697	[175]
n-$C_{20}H_{42}$	768.000	1.160	0.9069	[175]
n-$C_{24}H_{50}$	804.000	0.980	1.0710	[175]
n-$C_{30}H_{62}$	844.000	0.800	1.3072	[175]
n-$C_{36}H_{74}$	888.000	0.580	1.5260	[294]

Table C.2: PC-SAFT EoS parameters for the components studied in this work.

Component	m	σ (Å)	ε/k_B (K)	Ref
H_2	0.8285	2.9730	12.53	[259]
N_2	1.2053	3.313	90.96	[15]
CH_4	1.0000	3.7039	150.03	[18]
C_2H_4	1.5440	3.4470	180.361	[87]
CO_2	2.6037	2.555	151.04	[15]
C_2H_6	1.6069	3.5206	191.42	[18]
C_3H_6	1.9597	3.5356	207.19	[18]
C_3H_8	2.0020	3.6184	208.11	[18]
1-C_4H_8	2.2864	3.6431	222.00	[18]
n-C_4H_{10}	2.3316	3.7086	222.88	[18]
i-C_5H_{12}	2.5620	3.8296	230.75	[18]
n-C_5H_{12}	2.6896	3.7729	231.20	[18]
n-C_6H_{14}	3.0576	3.7983	236.77	[18]
n-C_7H_{16}	3.4831	3.8049	238.40	[18]
n-C_8H_{18}	3.8176	3.8373	242.78	[18]
n-$C_{10}H_{22}$	4.6627	3.8384	243.87	[18]
n-$C_{12}H_{26}$	5.3060	3.8959	249.21	[18]
n-$C_{16}H_{34}$	6.6485	3.9552	254.70	[18]
n-$C_{17}H_{36}$	6.9809	3.9675	255.65	[18]
n-$C_{20}H_{42}$	7.9849	3.9869	257.75	[18]
n-$C_{24}H_{50}$	9.6836	3.9709	254.69	[234]
n-$C_{30}H_{62}$	11.7391	3.9762	256.367	This work
n-$C_{36}H_{74}$	14.332	3.8836	252.89	[234]

Table C.3: SAFT-VR Mie EoS parameters for the components studied in this work taken from Dufal et al. [260].

Component	m	σ (Å)	ε/k_B (K)	λ_r	λ_a
H_2[a]	1.0000	3.1586	18.355	7.813	6.0
CH_4	1.0000	3.7366	151.45	12.319	6.0
C_2H_4	1.7972	3.2991	142.64	9.6463	6.0
CO_2	1.6936	3.0465	235.73	18.067	6.0
C_2H_6	1.7230	3.4763	164.27	10.121	6.0
C_3H_6	2.0060	3.5392	190.13	10.643	6.0
C_3H_8	1.8068	3.7943	221.96	12.106	6.0

[a] These values were fitted to supercritical data (100 to 400 K and 5 to 400 MPa).

Table C.4: Thermodynamic integration model parameters for the solid-phase forming components studied in this work.

Component	T_{0i}^{SL} (K)	Δh_{0i}^{SL} (J/mol)	v_{0i}^{S}(cm^3/mol)	$v_{0i}^{L^*}$(cm^3/mol)	P^+(MPa)	Ref
CO_2	216.580	8875 [163]	29.069	37.27	0.52	[175]
n-C_6H_{14}	177.830	13080	101.73	131.36	0.1	[175]
n-C_7H_{16}	182.570	14050	116.02	147.02	0.1	[175]
n-C_8H_{18}	216.380	20740	130.57	162.50	0.1	[175]
n-$C_{10}H_{22}$	243.510	28710	158.76	185.44	0.1	[175]
n-$C_{16}H_{34}$	291.308	53358	251.07	294.21	0.1	[175]
n-$C_{17}H_{36}$	295.134	40206[a]	277.39	310.94	0.1	[175]
n-$C_{20}H_{42}$	309.580	69870	312.21	366.39	0.1	[175]
n-$C_{24}H_{50}$	323.750	54894	369.71	434.94	0.1	[175]
n-$C_{30}H_{62}$	338.650	68827	482.86	540.50	0.1	[175]
n-$C_{36}H_{74}$	349.050	83656	527.56	648.43	0.1	[175]

[a] Interpolated from *n*-alkanes with odd number of carbon atoms.

Table C.5: Empirical correlations for pure CO_2 solid-vapor and solid-liquid saturation pressures [129].

SVE	$P^{sat}(\text{MPa}) = P_{tr} \cdot \exp\left[\left(\frac{T_{tr}}{T}\right) \cdot \left(-14.740846\left(1-\frac{T}{T_{tr}}\right) + 2.4327015\left(1-\frac{T}{T_{tr}}\right)^{1.9} - 5.3061778\left(1-\frac{T}{T_{tr}}\right)^{2.9}\right)\right]$
SLE	$P^{sat}(\text{MPa}) = P_{tr} \cdot \left[1 + 1955.5390\left(\frac{T}{T_{tr}}-1\right) + 2055.4593\left(\frac{T}{T_{tr}}-1\right)^{2}\right]$
	$T_{tr} = 216.592\ \text{K}$
	$P_{tr} = 0.51795\ \text{MPa}$

Appendix D: Monte Carlo Simulation Details and Results

Advanced simulation techniques such as CBMC [216-218] or CFCMC [219, 220] can be used to increase the acceptance probability of the molecule exchange trial move in MC simulations. In CFCMC, the interactions of a fractional molecule are scaled with a scaling parameter, λ, and molecules are gradually inserted / removed, allowing the surrounding molecules to adapt their configuration. A recent formulation of CFCMC by Poursaeidesfahni et al. [222, 295] allows for the direct calculation of the chemical potential of all components, which can be used to verify the chemical equilibrium between the two phases. It should be noted that simulations in the Gibbs ensemble using CBMC or CFCMC or no advanced methods lead to identical results [296]. Simulations using CBMC are more straight forward and easier to manage, especially when a large number of simulations, for various mixtures at several conditions should be performed. However, at high densities the conventional methods for calculating the chemical potential using CBMC might fail [296]. Contrary to CBMC, CFCMC simulations do not rely on occurrence of spontaneous cavities and therefore, have higher acceptance probabilities for the molecule exchange trial moves.

The TraPPE united atom (TraPPE-UA) force field was used for all the *n*-alkanes [182]. In the TraPPE-UA, CH_4, CH_3 and CH_2 groups are modeled as pseudo-atoms with no charges. The non-bonded intra- and intermolecular interactions between the pseudo-atoms are represented by the 12-6 Lennard-Jones (LJ) potential:

$$u_{nb}(r_{ij}) = 4\varepsilon_{ij}\left[\left(\frac{\sigma_{ij}}{r_{ij}}\right)^{12} - \left(\frac{\sigma_{ij}}{r_{ij}}\right)^{6}\right] \qquad \text{D.1}$$

where $\varepsilon_{ij}, \sigma_{ij}$ and r_{ij} are LJ energy parameter, the LJ size parameter and the distance between pseudoatoms *i* and *j*, respectively. In the TraPPE-UA, the intramolecular 1-4 interactions are excluded. The interactions between dissimilar pseudoatoms were described by the Lorentz-Berthelot mixing rules [185]. As required by the TraPPE-UA force field, the Lennard-Jones (LJ) interactions were truncated at 14 Å and analytic tail corrections were applied. Bond lengths are fixed to 1.54 Å. The bond-angle bending and torsional potentials are calculated from:

$$u_{bend}(\theta) = 31250k_B(\theta - 114)^2 \qquad \text{D.2}$$

$$u_{torsion}(\varphi) = k_B(335.03[1 + cos\,\varphi] - 68.19[1 - cos\,2\varphi] + 791.32[1 + cos\,3\varphi]) \quad \text{D.3}$$

where θ and φ are the bond-angle and dihedral angle, respectively.

Initially 50,000 Monte Carlo cycles were performed in every simulation to equilibrate the system, followed by 600,000 production cycles. The number of Monte Carlo steps per cycle equals the total number of molecules initially in the system, with a minimum of 20. The system size used was in the range of 500 - 1200 CH_4 molecules in total (in liquid and vapor phase) and 200 - 500 long-chain *n*-alkanes molecules in total. These ranges correspond to simulation boxes of 40 - 50 Å for the liquid phase and 90 - 100 Å for the vapor phase. The total production run was divided into five blocks and the standard deviation of the block average was used for the calculation of the error in computed properties.

Table D.1: CH_4 - *n*-$C_{10}H_{22}$ mixture Gibbs Ensemble Monte Carlo simulation data. The statistical uncertainty in the last digit is given in parentheses (*i.e.*, 0.503(3) is 0.503±0.003).

Temperature (K)	Pressure (MPa)	CH_4 mole fraction liquid phase	CH_4 mole fraction vapor phase
244	10.01	0.503(3)	0.997(1)
244	15.02	0.59(1)	0.997(1)
244	19.97	0.66(2)	0.992(2)
244	25.05	0.72(3)	0.984(2)
244	30.03	0.76(2)	0.973(3)
244	35.02	0.81(2)	0.95(1)
255	1.00	0.065(3)	0.962(1)
255	9.99	0.464(5)	0.9971(1)
255	25.05	0.72(1)	0.988(3)
255	30.02	0.77(1)	0.976(4)
255	34.98	0.81(1)	0.957(6)
277	0.99	0.054(3)	0.962(1)
277	5.03	0.244(8)	0.9926(1)
277	10.03	0.42(1)	0.9966(2)

277	20.03	0.628(5)	0.992(1)
277	25.00	0.70(1)	0.985(1)
277	30.02	0.75(3)	0.97(1)
277	35.02	0.80(2)	0.96(2)
283	1.00	0.051(2)	0.961(1)
283	5.01	0.242(3)	0.9923(1)
283	10.01	0.40(1)	0.9966(1)
283	13.60	0.502(6)	0.9985(1)
283	17.39	0.577(1)	0.9962(6)
283	24.07	0.68(1)	0.984(5)
283	30.04	0.75(3)	0.96(1)
283	34.97	0.81(4)	0.96(2)
303	1.00	0.048(2)	0.960(1)
303	5.07	0.221(4)	0.9918(1)
303	10.03	0.380(2)	0.9962(1)
303	14.86	0.501(5)	0.9973(2)
303	25.13	0.67(1)	0.98(1)
303	31.49	0.77(4)	0.95(2)
310	1.00	0.045(2)	0.958(1)
310	4.97	0.212(6)	0.9915(2)
310	15.52	0.505(3)	0.9965(4)
310	17.27	0.541(5)	0.9956(7)
310	18.96	0.571(6)	0.9937(6)
310	20.66	0.603(7)	0.991(1)
310	22.47	0.63(1)	0.989(2)
310	24.17	0.65(1)	0.98(1)
310	25.82	0.68(1)	0.979(6)
310	27.53	0.71(1)	0.96(1)
310	29.26	0.73(1)	0.95(1)
310	32.77	0.78(1)	0.94(2)
310	34.45	0.8(1)	0.95(5)
450	4.99	0.167(5)	0.948(4)
450	9.97	0.308(3)	0.956(2)

450	14.99	0.433(3)	0.950(1)
450	19.95	0.544(3)	0.933(4)
450	24.97	0.73(4)	0.84(4)
550	5.02	0.156(3)	0.652(2)
550	9.98	0.40(7)	0.659(8)
550	11.07	0.47(8)	0.655(9)
550	13.01	0.56(6)	0.65(4)

Table D.2: CH_4 - *n*-$C_{12}H_{26}$ mixture Gibbs Ensemble Monte Carlo simulation data. The statistical uncertainty in the last digit is given in parentheses.

Temperature (K)	Pressure (MPa)	CH_4 mole fraction liquid phase	CH_4 mole fraction vapor phase
283	1.00	0.056(4)	0.961(1)
283	5.02	0.242(6)	0.9927(1)
283	9.99	0.398(7)	0.9967(1)
283	15.03	0.51(1)	0.9979(1)
283	21.03	0.606(8)	0.997(2)
283	29.46	0.701(9)	0.98(1)
283	35.39	0.76(3)	0.98(2)
303	1.00	0.051(5)	0.960(2)
303	5.03	0.223(4)	0.9921(1)
303	10.04	0.37(1)	0.9963(1)
303	21.95	0.606(4)	0.996(1)
303	30.03	0.705(8)	0.988(3)
303	35.27	0.75(1)	0.983(4)
303	40.24	0.82(3)	0.971(5)
323	1.00	0.045(3)	0.958(1)
323	4.98	0.206(4)	0.9914(1)
323	9.98	0.354(7)	0.9959(1)
323	20.01	0.560(5)	0.997(2)
323	24.99	0.632(5)	0.994(6)
323	30.04	0.69(1)	0.98(1)

323	34.96	0.75(1)	0.97(2)
323	40.00	0.81(2)	0.96(1)
373	1.01	0.039(1)	0.9523(8)
373	5.02	0.184(2)	0.9900(1)
373	9.98	0.325(4)	0.9951(1)
373	15.01	0.442(3)	0.9962(3)
373	20.00	0.536(3)	0.9935(3)
373	25.02	0.615(4)	0.9892(8)
373	30.05	0.683(6)	0.981(1)
373	35.00	0.75(2)	0.96(1)
373	40.00	0.85(4)	0.92(3)
400	5.00	0.181(3)	0.9955(5)
400	10.00	0.314(5)	0.9948(5)
400	15.00	0.433(2)	0.9934(5)
400	20.00	0.524(5)	0.9895(7)
400	25.00	0.608(7)	0.983(1)
400	30.00	0.68(1)	0.971(5)
400	32.00	0.72(2)	0.964(5)
400	35.00	0.78(2)	0.93(1)
400	37.00	0.82(4)	0.91(3)
450	5.00	0.1717	0.9811
450	10.00	0.3119	0.9830
450	15.00	0.4311	0.9813
450	20.00	0.5241	0.9738
450	25.00	0.6094	0.9591
450	26.00	0.637(2)	0.960(2)
450	28.00	0.669(7)	0.949(4)
500	1.04	0.033(1)	0.79(1)
500	5.00	0.170(3)	0.942(2)
500	10.00	0.312(4)	0.952(2)
500	15.00	0.43(1)	0.947(5)
500	20.00	0.53(1)	0.933(7)
500	21.00	0.573(3)	0.933(2)

500	23.00	0.611(1)	0.923(1)
500	25.00	0.67(7)	0.89(2)
550	0.99	0.021(1)	0.46(2)
550	2.00	0.061(2)	0.70(1)
550	5.00	0.167(2)	0.84(1)
550	8.00	0.263(5)	0.876(5)
550	10.00	0.327(8)	0.88(1)
550	15.00	0.45(7)	0.85(4)
550	16.00	0.50(4)	0.83(2)
550	17.00	0.56(6)	0.79(5)
550	18.00	0.60(2)	0.75(2)
550	19.00	0.64(2)	0.68(4)
600	1.05	0.0056(1)	0.067(2)
600	2.54	0.073(2)	0.45(2)
600	5.11	0.210(5)	0.50(3)

Table D.3: CH_4 - *n*-$C_{16}H_{34}$ mixture Gibbs Ensemble Monte Carlo simulation data. The statistical uncertainty in the last digit is given in parentheses.

Temperature (K)	Pressure (MPa)	CH_4 mole fraction liquid phase	CH_4 mole fraction vapor phase
340	0.99	0.049(5)	1.0000(1)
340	4.98	0.210(5)	1.0000(1)
340	10.01	0.359(2)	1.0000(1)
340	15.03	0.463(8)	0.9971(1)
340	19.97	0.545(5)	0.9978(1)
340	24.56	0.602(2)	0.9984(1)
340	36.42	0.719(4)	0.9943(2)
340	53.30	0.85(1)	0.9697(5)
400	1.00	0.042(3)	0.9490(4)
400	4.98	0.186(3)	0.9890(1)
400	10.01	0.329(3)	0.9945(5)
400	15.02	0.436(5)	0.9964(3)

400	20.04	0.5243(6)	0.9973(2)
400	30.06	0.659(5)	0.9947(1)
462	2.08	0.083(1)	0.9934(1)
462	5.09	0.186(2)	0.9960(1)
462	10.29	0.331(2)	0.9960(1)
462	14.96	0.433(4)	0.9949(1)
462	20.08	0.526(7)	0.9928(4)
462	25.58	0.61(2)	0.989(2)
500	1.00	0.039(2)	0.952(1)
500	4.98	0.182(3)	0.9896(1)
500	9.95	0.323(3)	0.9900(1)
500	15.09	0.440(4)	0.988(1)
500	19.96	0.532(3)	0.9855(1)
500	29.95	0.683(4)	0.972(1)
500	35.00	0.77(2)	0.94(1)
550	1.00	0.0384(3)	0.878(6)
550	4.98	0.184(1)	0.963(1)
550	9.97	0.331(3)	0.971(1)
550	15.07	0.451(6)	0.968(3)
550	20.05	0.556(5)	0.963(3)
600	1.00	0.0323(7)	0.65(1)
600	4.98	0.190(3)	0.901(4)
600	9.96	0.348(1)	0.927(3)
600	14.97	0.48(1)	0.91(2)
600	20.02	0.69(7)	0.86(4)
623	2.14	0.079(1)	0.731(2)
623	3.23	0.126(2)	0.81(1)
623	5.13	0.207(3)	0.86(1)
623	10.03	0.38(2)	0.87(2)
670	1.00	0.012(2)	0.14(1)
670	3.00	0.107(1)	0.531(9)
670	5.02	0.202(3)	0.66(2)
670	6.98	0.30(3)	0.71(3)

Table D.4: CH_4 - *n*-$C_{20}H_{42}$ mixture Gibbs Ensemble Monte Carlo simulation data. The statistical uncertainty in the last digit is given in parentheses.

Temperature (K)	Pressure (MPa)	CH_4 mole fraction liquid phase	CH_4 mole fraction vapor phase
323	1.01	0.06(1)	1.0000(1)
323	5.02	0.25(1)	1.0000(1)
323	10.00	0.399(8)	0.9954(1)
323	15.02	0.50(1)	0.9970(1)
323	20.02	0.575(1)	0.9978(1)
323	25.01	0.62(1)	0.9982(1)
323	34.95	0.70(1)	0.9978(1)
323	39.99	0.73(1)	0.9980(1)
323	44.94	0.76(1)	0.9963(1)
323	62.76	0.83(1)	0.9892(4)
323	71.42	0.863(8)	0.9839(4)
323	79.87	0.91(2)	0.9674(4)
323	83.20	0.931(1)	0.956(6)
323	83.41	0.934(4)	0.953(3)
353	1.00	0.051(2)	0.9505(3)
353	4.99	0.22(1)	0.9896(1)
353	10.01	0.369(8)	0.9950(1)
353	14.98	0.47(1)	0.9967(1)
353	20.00	0.550(6)	0.9975(1)
353	24.99	0.611(7)	0.9980(1)
353	29.98	0.659(9)	0.9974(1)
353	35.04	0.701(3)	0.9977(1)
353	40.08	0.730(2)	0.9959(1)
353	45.11	0.765(8)	0.9945(4)
353	58.92	0.84(2)	0.987(1)
353	66.07	0.86(1)	0.982(1)
353	72.88	0.90(2)	0.968(6)
353	75.40	0.92(1)	0.960(4)
423	15.01	0.447(2)	0.9959(1)

423	20.05	0.533(2)	0.9969(1)
423	25.02	0.598(3)	0.9975(2)
423	35.08	0.706(5)	0.9973(4)
423	44.94	0.779(6)	0.992(2)
423	50.08	0.81(1)	0.987(3)
423	55.00	0.84(1)	0.978(5)
423	60.01	0.87(1)	0.970(1)
500	0.99	0.042(2)	0.9391(1)
500	5.04	0.195(4)	0.985(1)
500	10.07	0.336(6)	0.9928(2)
500	14.96	0.449(5)	0.9968(4)
500	20.05	0.53(1)	0.9956(6)
500	25.01	0.612(4)	0.9940(6)
500	30.07	0.67(1)	0.991(1)
500	34.96	0.728(8)	0.987(3)
500	40.05	0.780(8)	0.983(2)
500	45.04	0.83(2)	0.95(1)
550	1.00	0.043(2)	0.926(2)
550	5.05	0.199(5)	0.9848(1)
550	10.10	0.346(4)	0.9921(2)
550	14.93	0.462(5)	0.9908(4)
550	20.07	0.55(1)	0.9875(6)
550	25.07	0.629(4)	0.9847(6)
550	30.04	0.69(1)	0.977(1)
550	35.03	0.788(7)	0.952(3)
600	0.99	0.043(1)	0.890(8)
600	5.04	0.207(2)	0.969(8)
600	10.08	0.361(5)	0.975(2)
600	15.11	0.485(6)	0.975(1)
600	20.07	0.579(5)	0.970(1)
600	24.98	0.666(3)	0.962(4)
650	5.00	0.212(1)	0.917(2)
650	8.00	0.316(3)	0.935(1)

650	10.00	0.373(2)	0.935(1)
650	12.00	0.428(7)	0.94(1)
650	15.00	0.49(3)	0.93(1)
700	1.00	0.027(1)	0.35(1)
700	5.11	0.227(3)	0.78(1)
700	10.05	0.416(5)	0.83(1)
700	12.04	0.57(9)	0.79(1)

Table D.5: CH_4 - *n*-$C_{24}H_{50}$ mixture Gibbs Ensemble Monte Carlo simulation data. The statistical uncertainty in the last digit is given in the parentheses.

Temperature (K)	Pressure (MPa)	CH_4 mole fraction liquid phase	CH_4 mole fraction vapor phase
330	10.02	0.43(1)	1.0000
330	15.01	0.52(2)	1.0000
330	20.00	0.597(5)	1.0000
330	30.03	0.68(1)	1.0000
330	35.01	0.71(1)	1.0000
330	40.04	0.73(1)	1.0000
330	44.97	0.76(1)	1.0000
330	49.96	0.78(2)	1.0000
330	59.55	0.817(4)	0.9951(1)
330	69.51	0.84(2)	0.9924(7)
330	83.10	0.88(1)	0.9870(6)
330	97.09	0.93(1)	0.965(5)
350	5.01	0.26(2)	1.0000
350	10.02	0.41(1)	1.0000
350	15.02	0.50(1)	1.0000
350	19.99	0.57(1)	1.0000
350	25.01	0.62(1)	1.0000
350	29.96	0.67(1)	1.0000
350	35.05	0.71(1)	1.0000
350	39.96	0.740(6)	1.0000

350	45.00	0.76(1)	1.0000
350	57.29	0.81(1)	0.9949(2)
350	66.08	0.84(1)	0.9920(6)
350	78.04	0.88(1)	0.986(1)
350	90.14	0.94(1)	0.965(13)
374	0.90	0.060(1)	1.0000
374	5.05	0.242(6)	1.0000
374	10.02	0.38(1)	1.0000
374	15.01	0.48(1)	1.0000
374	19.98	0.56(1)	1.0000
374	25.02	0.62(1)	1.0000
374	30.00	0.67(1)	1.0000
374	35.00	0.70(1)	1.0000
374	39.97	0.736(8)	1.0000
374	45.04	0.765(5)	1.0000
374	49.98	0.79(1)	1.0000
374	55.15	0.815(6)	0.9946(4)
374	60.17	0.837(7)	0.9930(1)
374	71.07	0.873(7)	0.9874(3)
374	80.21	0.914(8)	0.976(6)
374	84.30	0.94(1)	0.963(4)
400	4.99	0.22(1)	0.9130(1)
400	10.04	0.393(6)	0.9323(2)
400	15.02	0.50(1)	0.9336(2)
400	19.97	0.570(6)	0.9504(4)
400	25.04	0.622(6)	0.962(1)
400	30.02	0.673(3)	0.9658(5)
400	35.03	0.71(1)	0.972(1)
400	40.07	0.74(1)	0.979(4)
400	45.04	0.77(1)	0.994(3)
400	50.01	0.797(6)	0.992(1)
400	55.06	0.835(4)	0.9898(6)
450	10.00	0.343(1)	0.9950(5)

450	20.00	0.544(3)	0.9983(1)
450	30.00	0.652(4)	0.9972(2)
450	40.00	0.74(1)	0.9911(1)
450	50.00	0.83(2)	0.9575(1)
500	0.98	0.048(2)	0.9983(1)
500	10.05	0.35(1)	0.9992(1)
500	15.03	0.46(1)	0.9990(1)
500	20.12	0.55(1)	0.9983(2)
500	25.03	0.62(1)	0.9977(3)
500	30.08	0.677(7)	0.996(1)
500	35.03	0.72(1)	0.995(1)
500	40.10	0.77(1)	0.992(3)
500	45.02	0.806(7)	0.987(5)
500	50.02	0.84(2)	0.97(1)
550	5.00	0.213(2)	0.9971(1)
550	10.00	0.36(1)	0.9973(1)
550	20.00	0.564(7)	0.9581(2)
550	30.00	0.694(4)	0.9932(4)
550	35.00	0.74(1)	0.989(1)
600	1.04	0.050(7)	0.963(7)
600	10.21	0.377(6)	0.990(1)
600	15.05	0.494(4)	0.990(1)
600	19.99	0.588(6)	0.988(2)
600	25.07	0.661(4)	0.985(2)
600	30.05	0.733(8)	0.981(3)
700	1.03	0.047(1)	0.71(1)
700	5.22	0.249(6)	0.916(8)
700	10.17	0.423(3)	0.937(3)
700	15.01	0.549(7)	0.93(1)
750	1.08	0.038(3)	0.38(4)
750	5.01	0.255(4)	0.78(2)
750	7.40	0.37(2)	0.80(4)
750	9.98	0.52(9)	0.82(3)

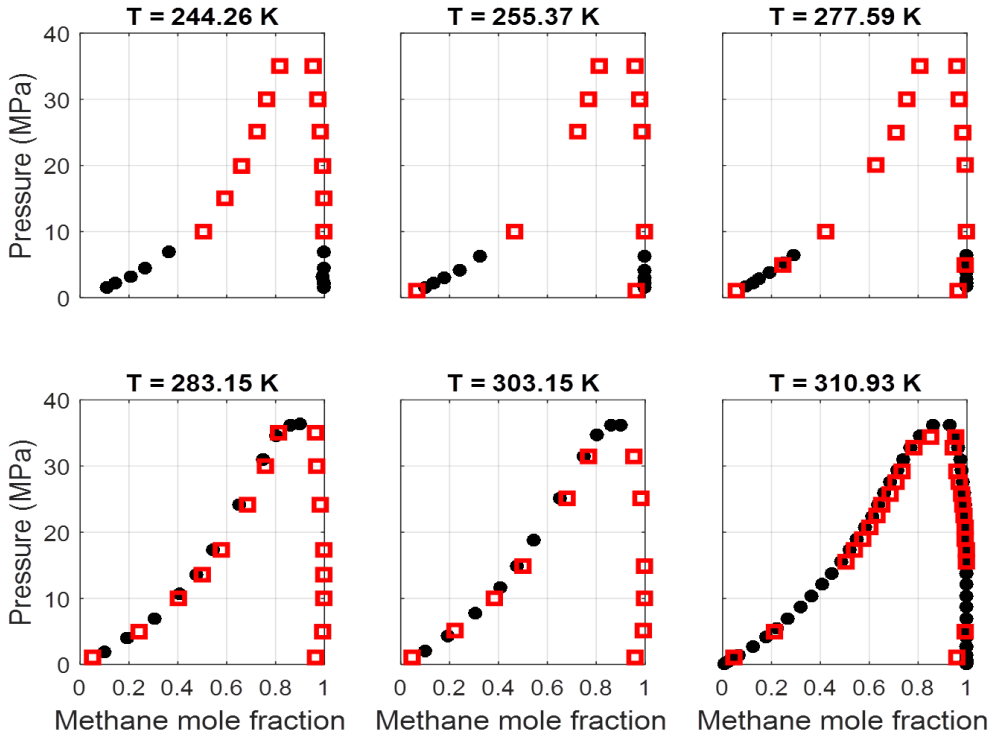

Figure D.1: Pressure - composition VLE phase diagrams for the CH_4 - *n*-$C_{10}H_{22}$ mixture at various temperatures. Experimental data [189, 190, 194] are represented by black data points. GEMC simulation data are represented by red squares.

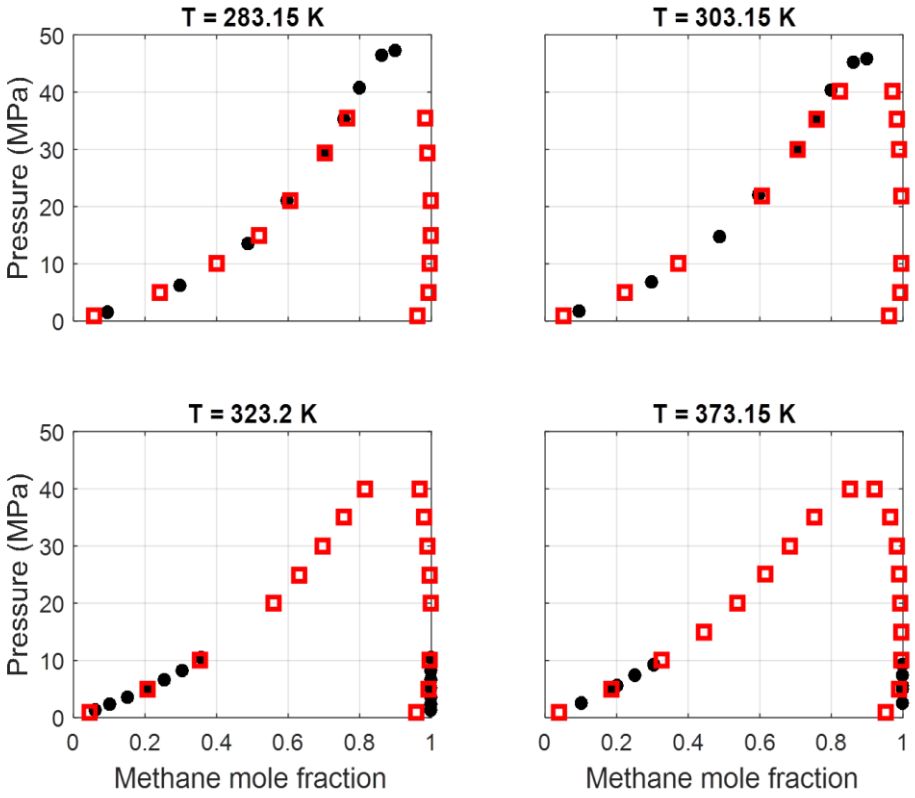

Figure D.2: Pressure - composition VLE phase diagrams for the CH_4 - *n*-$C_{12}H_{26}$ mixture at various temperatures. Experimental data [191, 196] are represented by black data points. GEMC simulation data are represented by red squares.

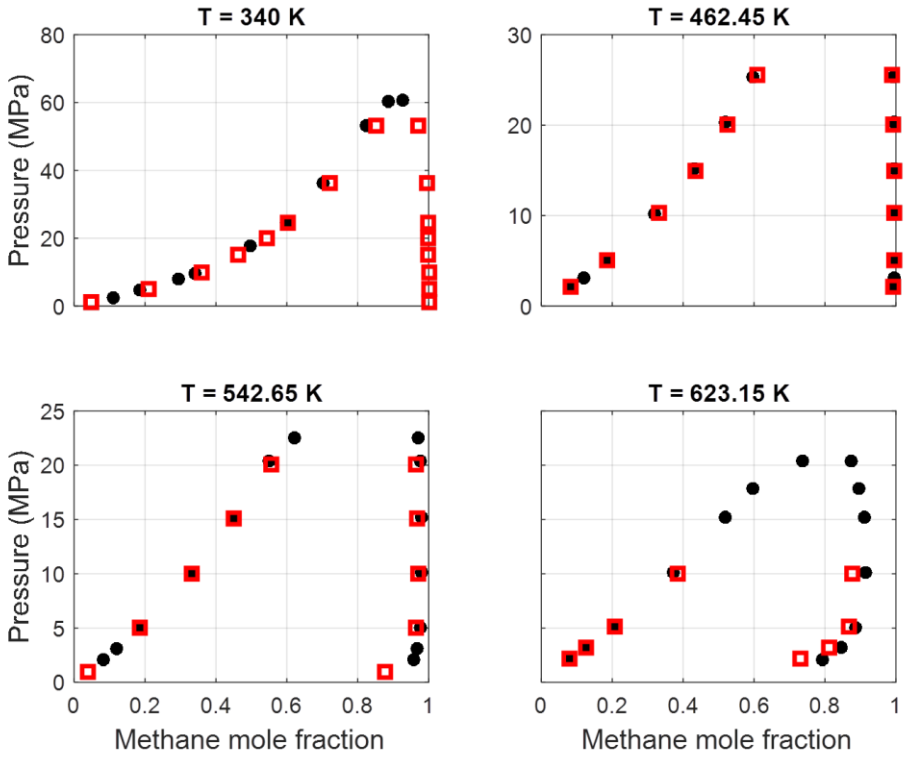

Figure D.3: Pressure - composition VLE phase diagrams for the CH_4 - *n*-$C_{16}H_{34}$ mixture at various temperatures. Experimental data [198, 202] are represented by black data points. GEMC simulation data are represented by red squares.

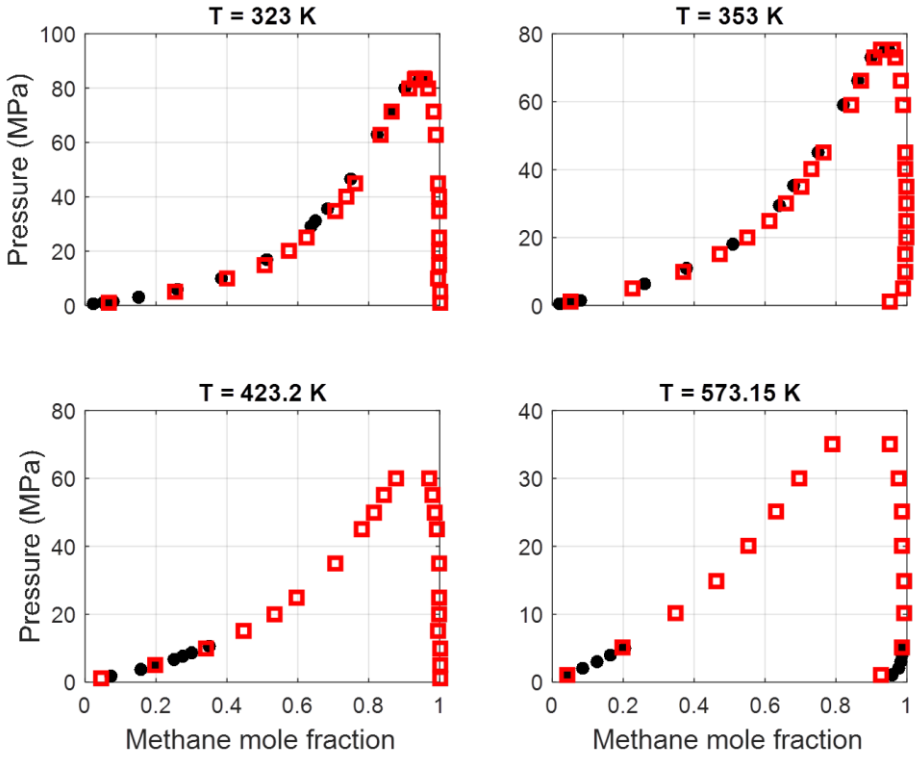

Figure D.4: Pressure - composition VLE phase diagrams for the CH_4 - *n*-$C_{20}H_{42}$ mixture at various temperatures. Experimental data [205-207] are represented by black data points. GEMC simulation data are represented by red squares.

Appendix E: CH_4 - *n*-Alkane Mixtures VLE and SLGE

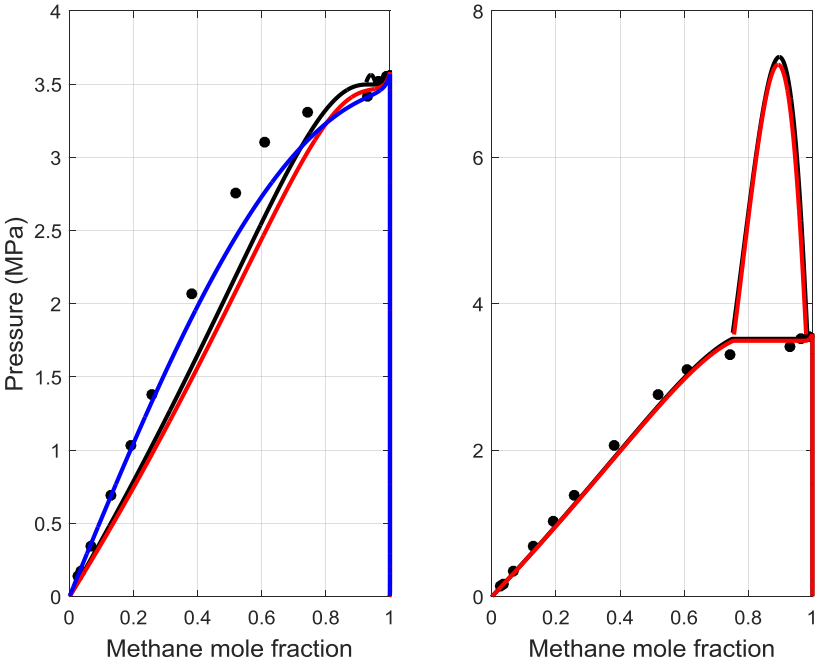

Figure E.1: Pressure - composition VLE phase diagrams for the CH_4 - *n*-C_6H_{14} mixture at T= 182.46 K. Experimental data [240] are represented by data points and calculations by lines. Black lines correspond to SRK, red to PR and blue to PC-SAFT EoS. Left panel shows predictions ($k_{ij} = 0$), while right panel shows correlations ($k_{ij} \neq 0$).

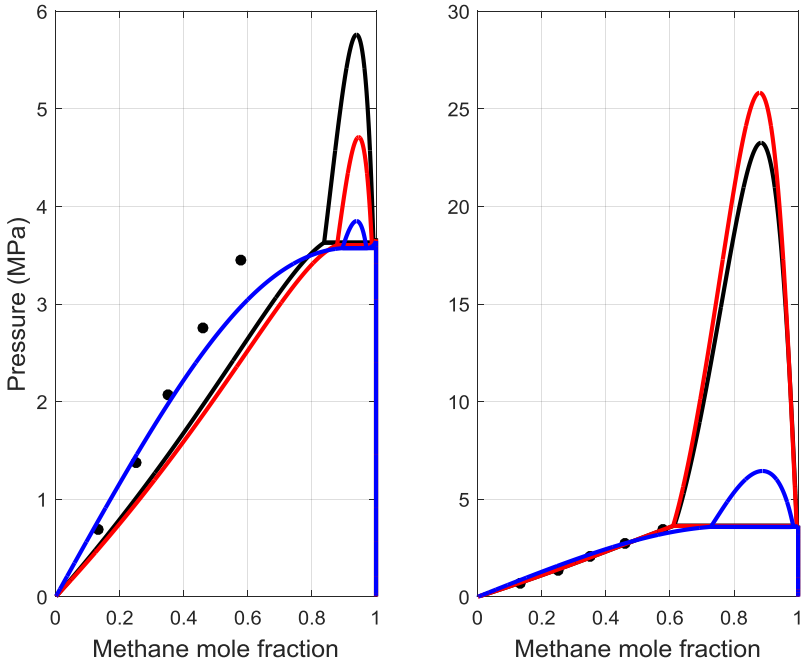

Figure E.2: Pressure - composition VLE phase diagrams for the CH_4 - *n*-C_7H_{16} mixture at T= 183.15 K. Experimental data [241] are represented by data points and calculations by lines. The color code is the same as in Figure E.1. Left panel shows predictions ($k_{ij} = 0$), while right panel shows correlations ($k_{ij} \neq 0$).

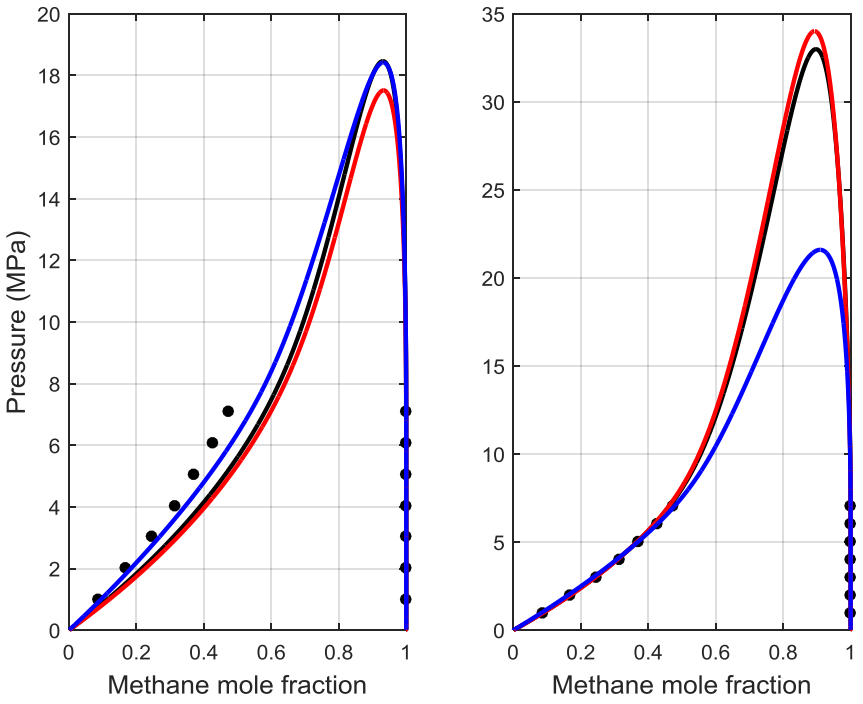

Figure E.3: Pressure - composition VLE phase diagrams for the CH_4 - *n*-C_8H_{18} mixture at T= 223.15 K. Experimental data [242] are represented by data points and calculations by lines. The color code is the same as in Figure E.1. Left panel shows predictions ($k_{ij} = 0$), while right panel shows correlations ($k_{ij} \neq 0$).

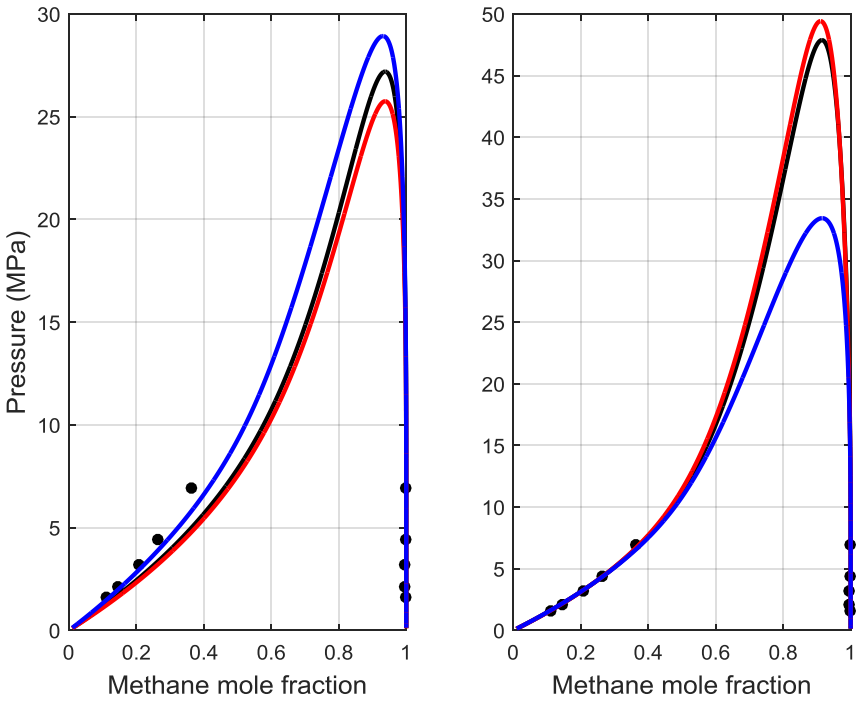

Figure E.4: Pressure - composition VLE phase diagrams for the CH_4 - *n*-$C_{10}H_{22}$ mixture at T= 244.26 K. Experimental data [189] are represented by data points and calculations by lines. The color code is the same as in Figure E.1. Left panel shows predictions ($k_{ij} = 0$), while right panel shows correlations ($k_{ij} \neq 0$).

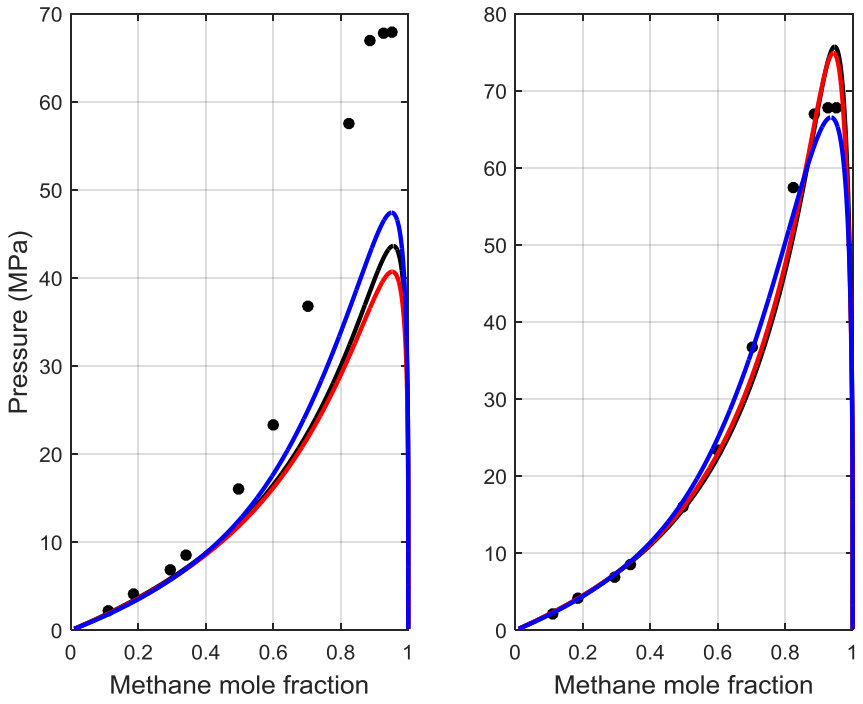

Figure E.5: Pressure - composition VLE phase diagrams for the CH_4 - *n*-$C_{16}H_{34}$ mixture at T= 300 K. Experimental data [198] are represented by data points and calculations by lines. The color code is the same as in Figure E.1. Left panel shows predictions ($k_{ij} = 0$), while right panel shows correlations ($k_{ij} \neq 0$).

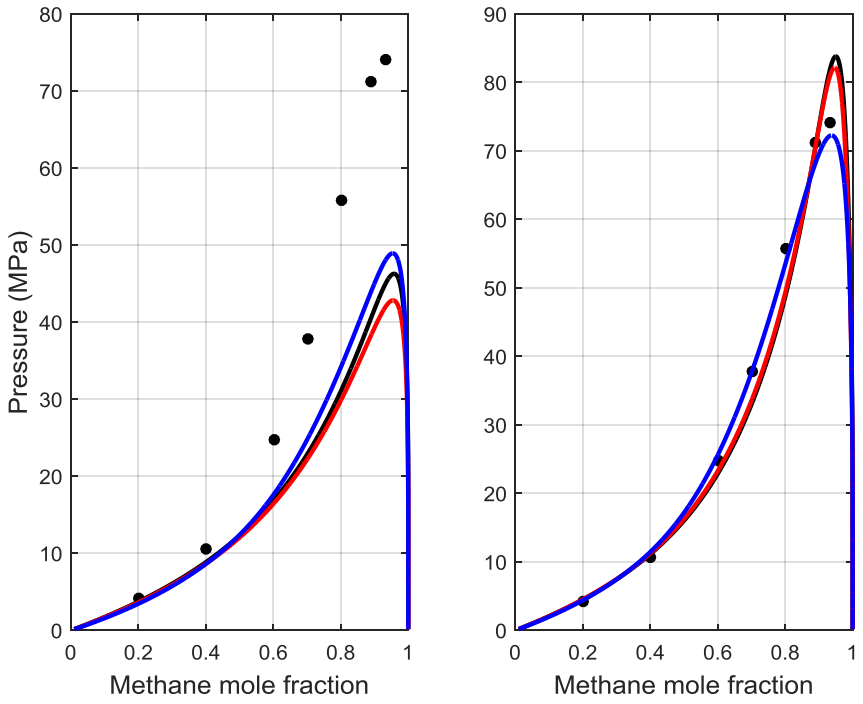

Figure E.6: Pressure - composition VLE phase diagrams for the CH_4 - *n*-$C_{17}H_{36}$ mixture at T= 300 K. Experimental data [24] are represented by data points and calculations by lines. The color code is the same as in Figure E.1. Left panel shows predictions ($k_{ij} = 0$), while right panel shows correlations ($k_{ij} \neq 0$).

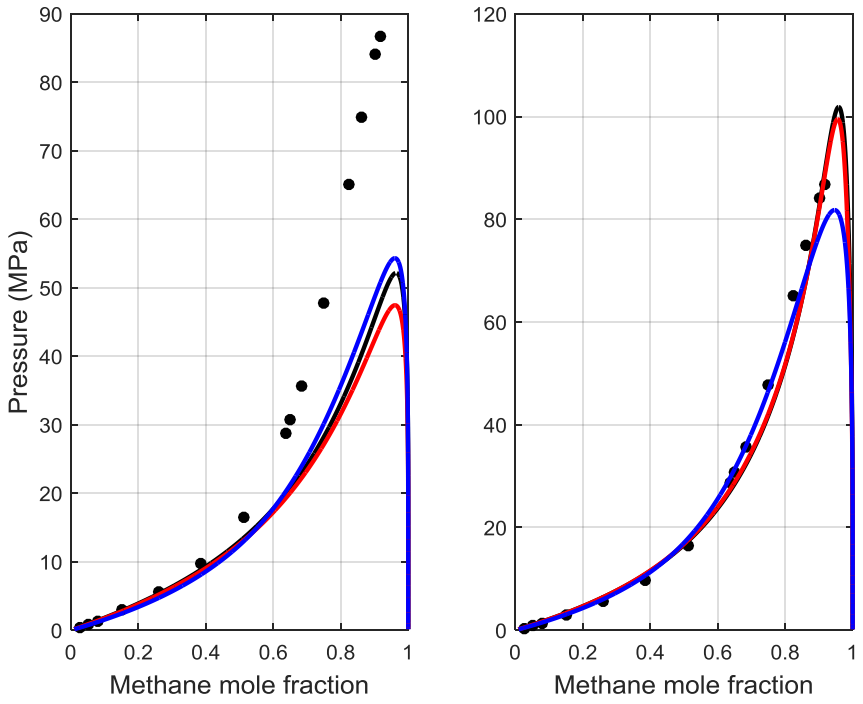

Figure E.7: Pressure - composition VLE phase diagrams for the CH_4 - *n*-$C_{20}H_{42}$ mixture at T= 310 K. Experimental data [206] at temperatures close to 310 K are represented by data points and calculations by lines. The color code is the same as in Figure E.1. Left panel shows predictions ($k_{ij} = 0$), while right panel shows correlations ($k_{ij} \neq 0$).

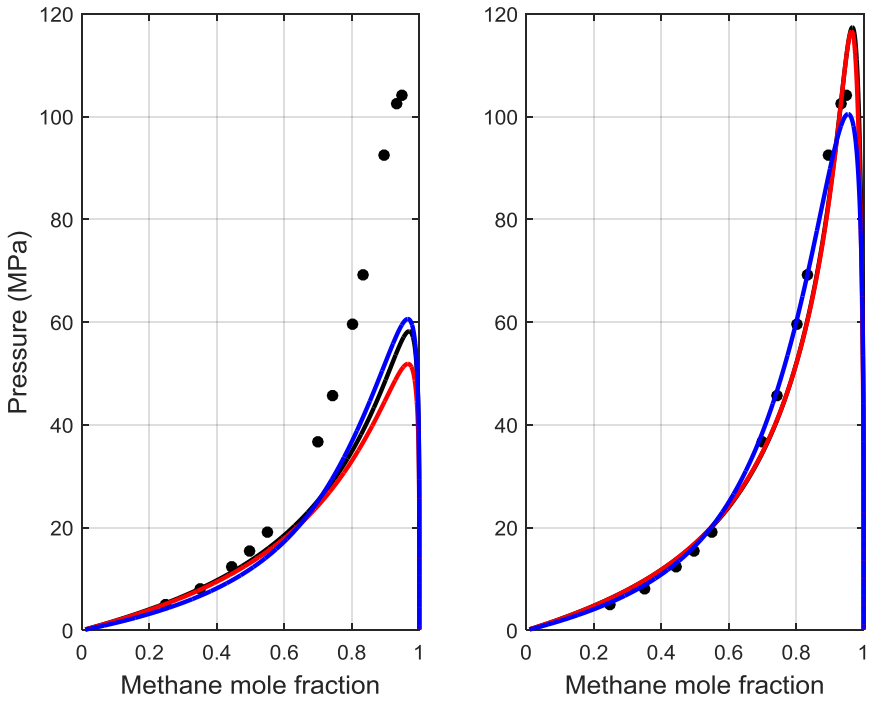

Figure E.8: Pressure - composition VLE phase diagrams for the CH_4 - *n*-$C_{24}H_{50}$ mixture at T= 323 K. Experimental data [208] at temperatures close to 323 K are represented by data points and calculations by lines. The color code is the same as in Figure E.1. Left panel shows predictions ($k_{ij} = 0$), while right panel shows correlations ($k_{ij} \neq 0$).

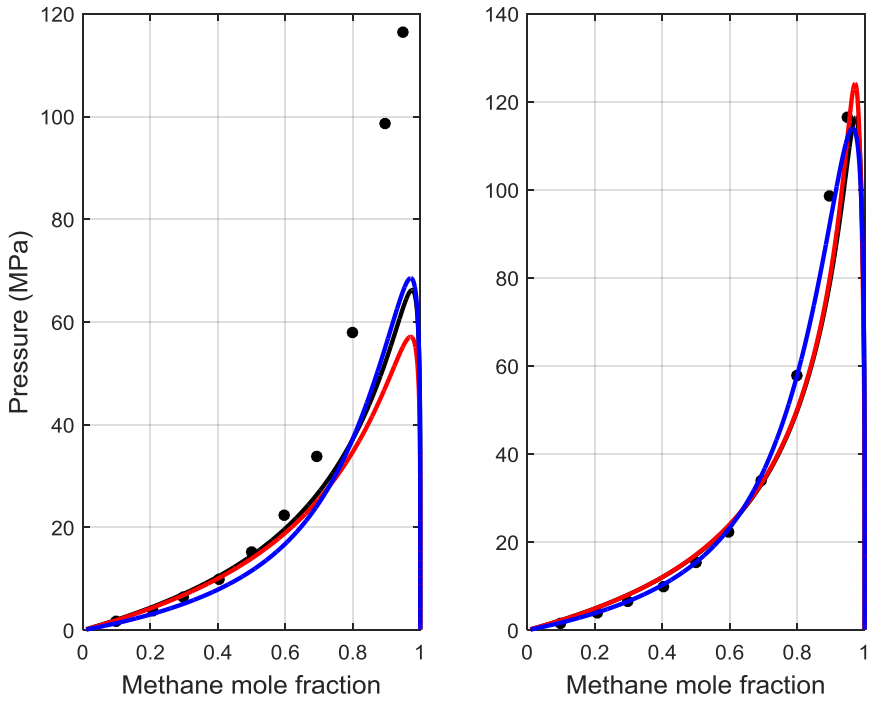

Figure E.9: Pressure - composition VLE phase diagrams for the CH_4 - *n*-$C_{30}H_{62}$ mixture at T= 345 K. Experimental data [20] at temperatures from 338 to 350 K are represented by data points and calculations by lines. The color code is the same as in Figure E.1. Left panel shows predictions ($k_{ij} = 0$), while right panel shows correlations ($k_{ij} \neq 0$).

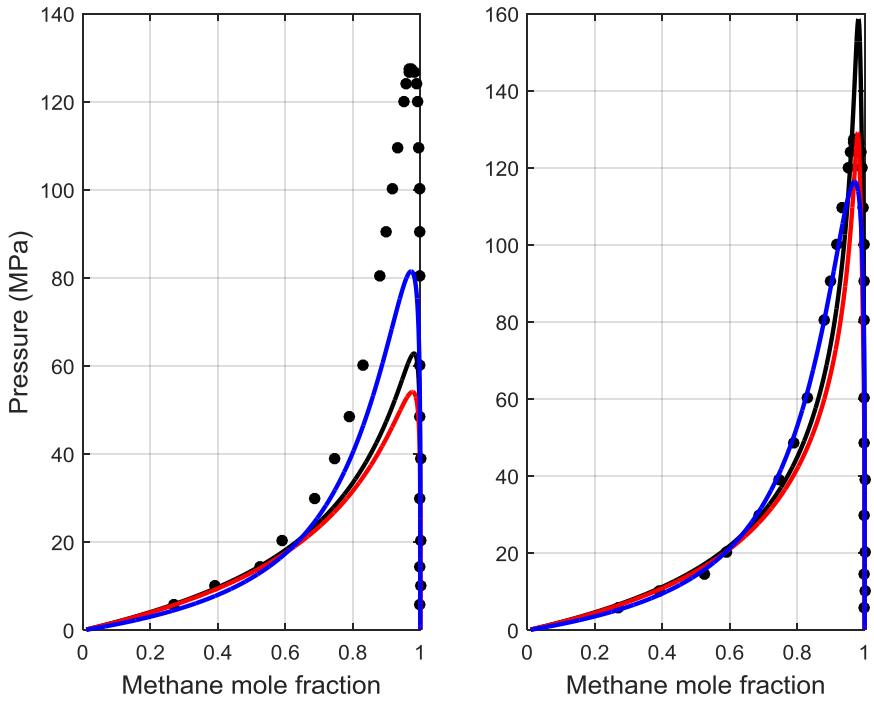

Figure E.10: Pressure - composition VLE phase diagrams for the CH_4 - *n*-$C_{36}H_{74}$ mixture at T= 373 K. Experimental data [243] are represented by data points and calculations by lines. The color code is the same as in Figure E.1. Left panel shows predictions ($k_{ij} = 0$), while right panel shows correlations ($k_{ij} \neq 0$).

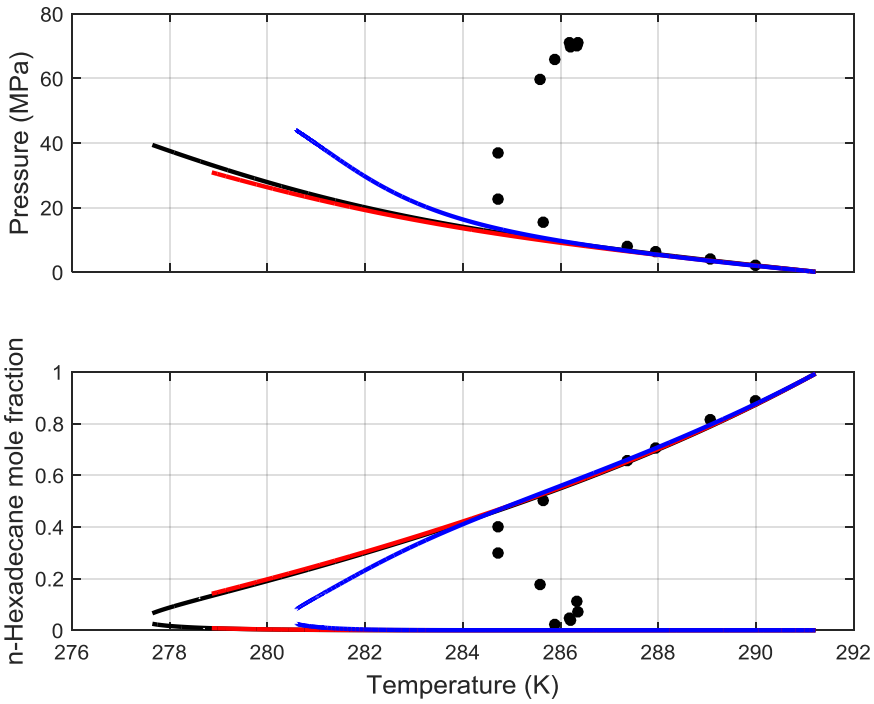

Figure E.11: Prediction of the SLGE curve of the CH_4 - *n*-$C_{16}H_{34}$ mixture with the basic solid-phase model and $k_{ij} = 0$. Experimental data [198] are represented by data points and calculations by lines. The color code is the same as in Figure E.1. The *n*-$C_{16}H_{34}$ mole fraction refers to the liquid and vapor phases along the SLGE curve.

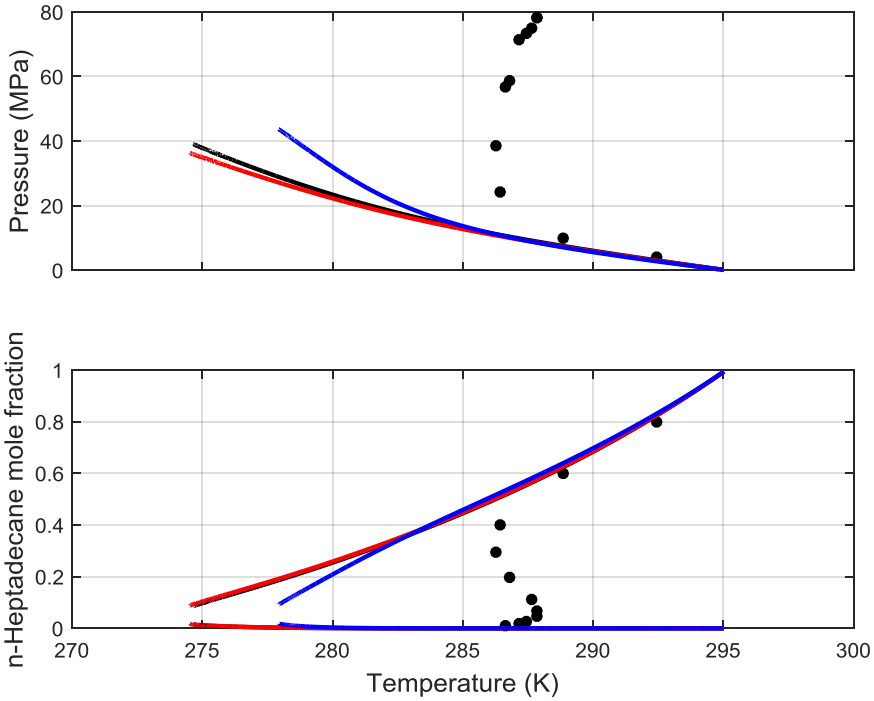

Figure E.12: Prediction of the SLGE curve of the CH_4 - *n*-$C_{17}H_{36}$ mixture with the basic solid-phase model and $k_{ij} = 0$. Experimental data [24] are represented by data points and calculations by lines. The color code is the same as in Figure E.1. The *n*-$C_{17}H_{36}$ mole fraction refers to the liquid and vapor phases along the SLGE curve.

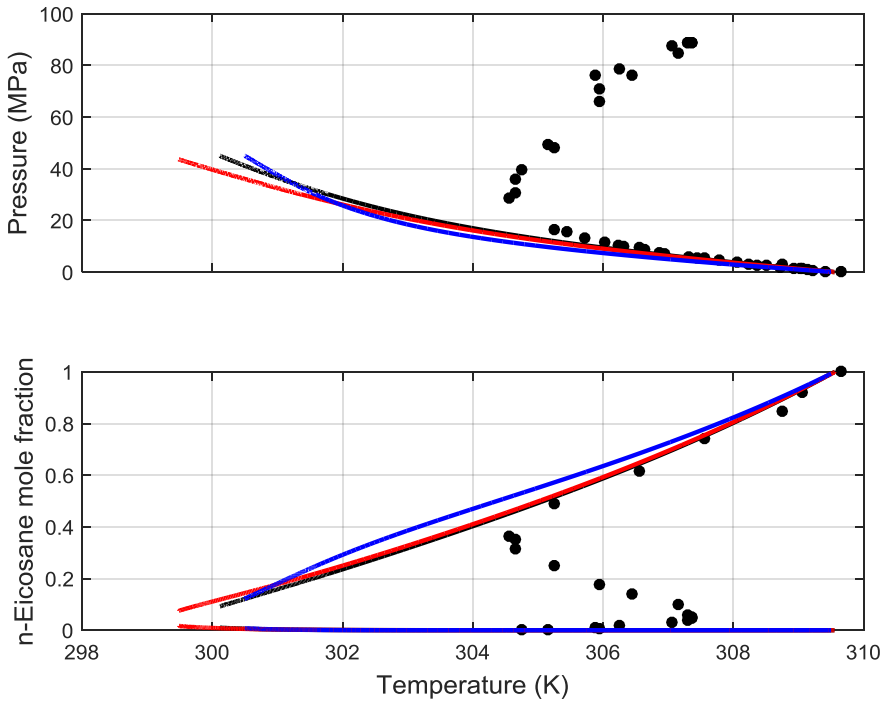

Figure E.13: Prediction of the SLGE curve of the CH_4 - *n*-$C_{20}H_{42}$ mixture with the basic solid-phase model and $k_{ij} = 0$. Experimental data [206] are represented by data points and calculations by lines. The color code is the same as in Figure E.1. The *n*-$C_{20}H_{42}$ mole fraction refers to the liquid and vapor phases along the SLGE curve.

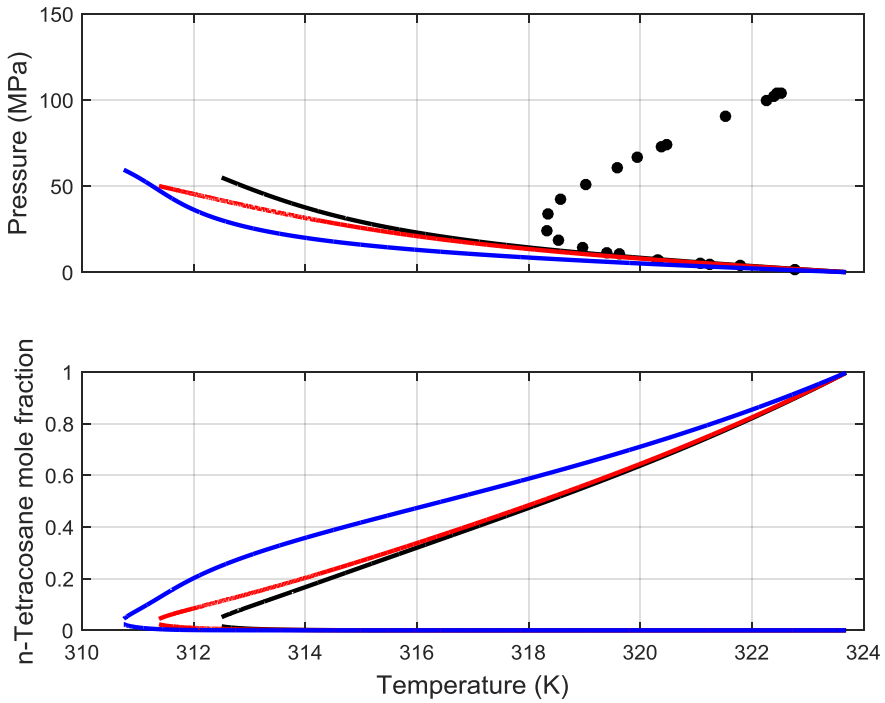

Figure E.14: Prediction of the SLGE curve of the CH_4 - *n*-$C_{24}H_{50}$ mixture with the basic solid-phase model and $k_{ij} = 0$. Experimental data [208] are represented by data points and calculations by lines. The color code is the same as in Figure E.1. The *n*-$C_{24}H_{50}$ mole fraction refers to the liquid and vapor phases along the SLGE curve.

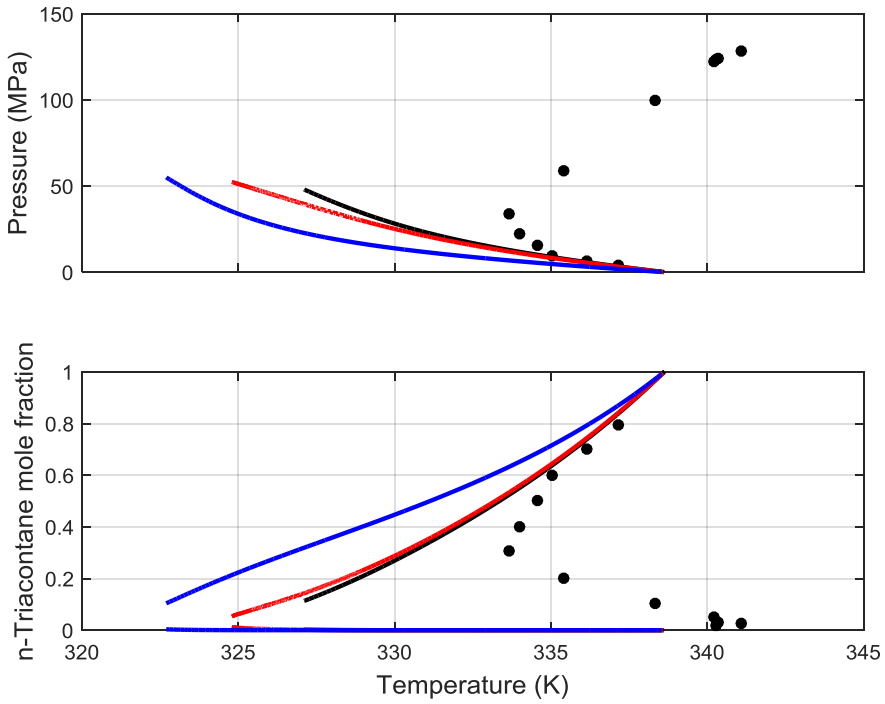

Figure E.15: Prediction of the SLGE curve of the CH_4 - *n*-$C_{30}H_{62}$ mixture with the basic solid-phase model and $k_{ij} = 0$. Experimental data [20] are represented by data points and calculations by lines. The color code is the same as in Figure E.1. The *n*-$C_{30}H_{62}$ mole fraction refers to the liquid and vapor phases along the SLGE curve.

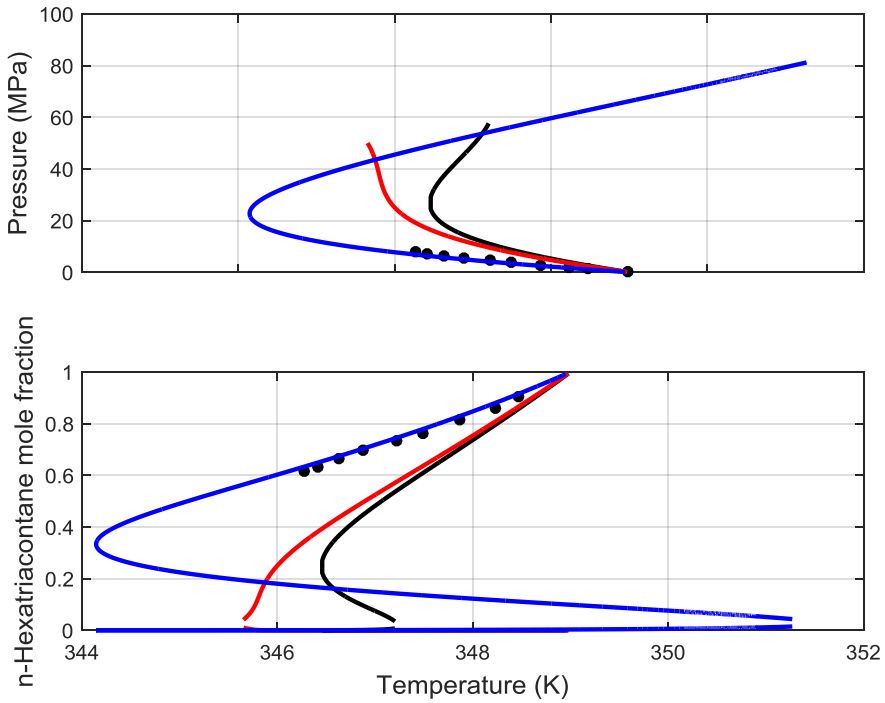

Figure E.16: Prediction of the SLGE curve of the CH_4 - *n*-$C_{36}H_{74}$ mixture with the basic solid-phase model and $k_{ij} = 0$. Experimental data [249] are represented by data points and calculations by lines. The color code is the same as in Figure E.1. The *n*-$C_{36}H_{74}$ mole fraction refers to the liquid and vapor phases along the SLGE curve.

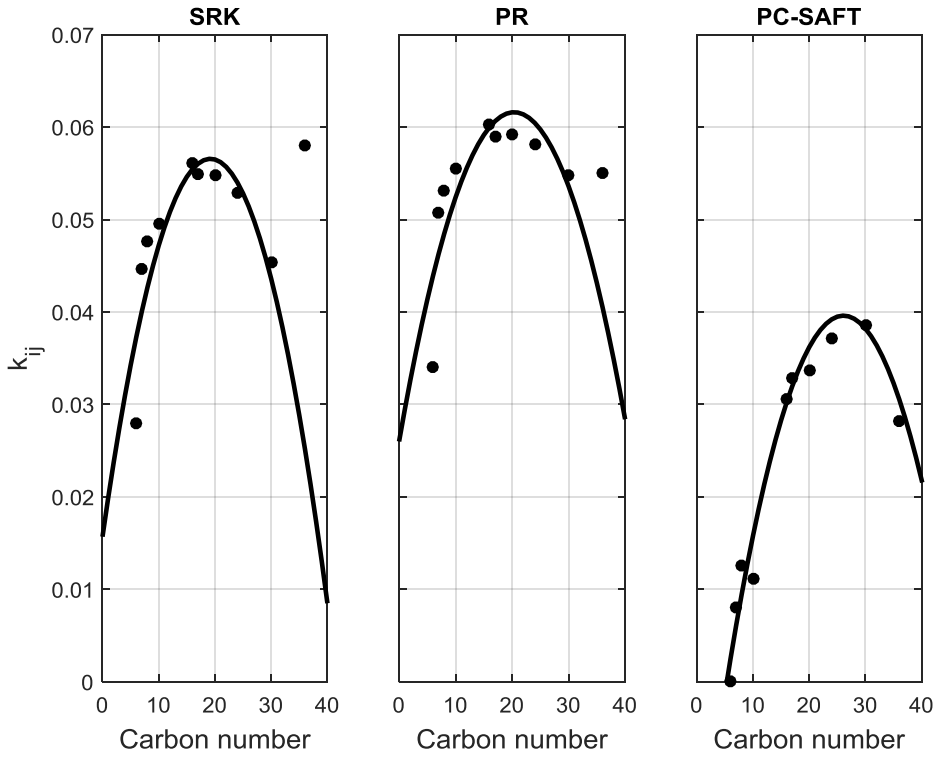

Figure E.17: k_{ij} values for the individual CH_4 - *n*-alkane mixtures and the quadratic function fitted to these values. The k_{ij} values for the CH_4 - *n*-$C_{36}H_{74}$ mixture are not taken into account in the fitting for the cubic EoS correlations.

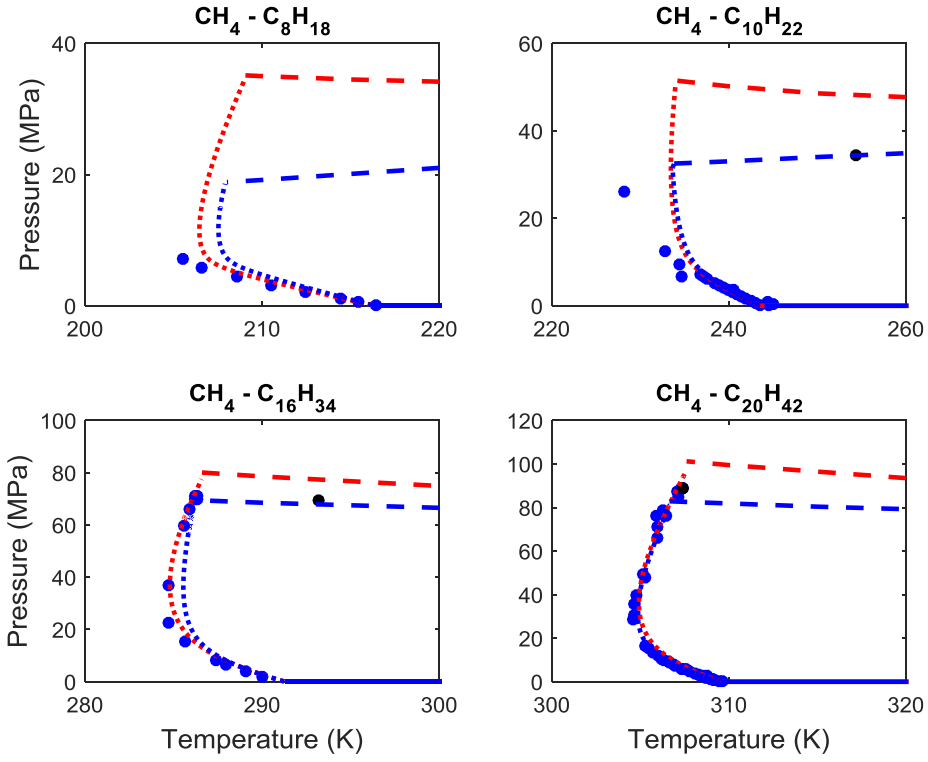

Figure E.18: Global phase diagrams of various binary CH_4 mixtures (Enlarged version of Figure 8.18).

Table E.1: Volume translation parameters for the two cubic EoS for the components studied in this work. The translation parameters are calculated as the difference between the liquid molar volumes of Table C.4 and the predicted volumes of the untranslated cubic EoS at the reported temperature and pressure conditions (normal melting point of pure components).

Component	T (K)	P (MPa)	c_{SRK} (cm^3/mol)	c_{PR} (cm^3/mol)
n-$C_{10}H_{22}$	243.510	0.1	43.556	19.031
n-$C_{16}H_{34}$	291.308	0.1	105.922	63.480
n-$C_{17}H_{36}$	295.134	0.1	113.324	68.453
n-$C_{20}H_{42}$	309.580	0.1	142.437	88.959
n-$C_{24}H_{50}$	323.750	0.1	191.868	126.494
n-$C_{30}H_{62}$	338.650	0.1	260.006	177.389
n-$C_{36}H_{74}$	349.050	0.1	505.328	387.383

Table E.2: Coefficients of the quadratic functions of k_{ij} parameters with the carbon number of *n*-alkanes for CH_4 binary mixtures. It is: $k_{ij} = k_{ij,0} + k_{ij,1}CN + k_{ij,2}CN^2$

EoS	$k_{ij,0}$	$k_{ij,1}$	$k_{ij,2}$
SRK	0.0157	0.00426	-1.11e-04
PR	0.0260	0.00350	-8.6e-05
PC-SAFT	-0.0230	0.00480	-9.2e-05

Table E.3: %AARD between experimental SLGE data and model predictions using k_{ij} parameters calculated from the proposed correlations. %AARD is calculated for the equilibrium temperature or pressure of each mixture.

EoS		CH_4 - *n*-C_6H_{14}	CH_4 - *n*-C_7H_{16}	CH_4 - *n*-C_8H_{18}	CH_4 - *n*-$C_{10}H_{22}$	CH_4 - *n*-$C_{16}H_{34}$	CH_4 - *n*-$C_{17}H_{36}$	CH_4 - *n*-$C_{20}H_{42}$	CH_4 - *n*-$C_{24}H_{50}$	CH_4 - *n*-$C_{30}H_{62}$	CH_4 - *n*-$C_{36}H_{74}$
PR	Bsc. Cor.	3.0	3.7	1.2, 0.2	-	-	-	-	-	-	-
	Adv. Cor.	-	-	-	0.3	0.2	0.9	0.2	0.4	0.4	0.3
PC-SAFT	Bsc. Cor.	6.7	10.9	1.0, 0.5	-	-	-	-	-	-	-
	Adv. Cor.	-	-	-	0.5	0.2	0.7	0.1	0.1	1.1	0.04
NP		23	26	34	22	8	9	33	19	7	10

$$\%\ AARD = \frac{100}{NP}\sum_{i=1}^{NP}\left|\frac{X_i^{calculated} - X_i^{experimental}}{X_i^{experimental}}\right|$$

where NP is the number of experimental data points and X_i is the equilibrium temperature or pressure.

"Bsc. Cor" refers to predictions with the basic solid-phase model and k_{ij} parameters calculated from the proposed correlations.

"Adv. Cor" refers to predictions with the advanced solid-phase model and k_{ij} parameters calculated from the proposed correlations.

% AARD is calculated for the equilibrium pressure in the mixtures CH_4 - *n*-C_6H_{14}, CH_4 - *n*-C_7H_{16}, CH_4 - *n*-C_8H_{18} (first number). For all the other mixtures and CH_4 - *n*-C_8H_{18} (second number) is calculated for the equilibrium temperature.

Appendix F: Supporting Information for Chapter 9

Table F.1: %AARD between experimental data at supercritical conditions taken from NIST [261] and SAFT-VR Mie predictions for H_2. The ideal gas heat capacity is calculated using a correlation from DIPPR [175].

	% AARD			
EoS	ρ (kg/m^3)	C_p (J/mol K)	v_s (m/s)	μ_{JT} (K/kPa)
SAFT-VR Mie	0.27	5.59	1.23	10.01

$$\%\ AARD = \frac{100}{NP}\sum_{i=1}^{NP}\left|\frac{P_i^{calculated} - P_i^{experimental}}{P_i^{experimental}}\right|$$

where NP is the number of experimental data points and P_i is the respective property.

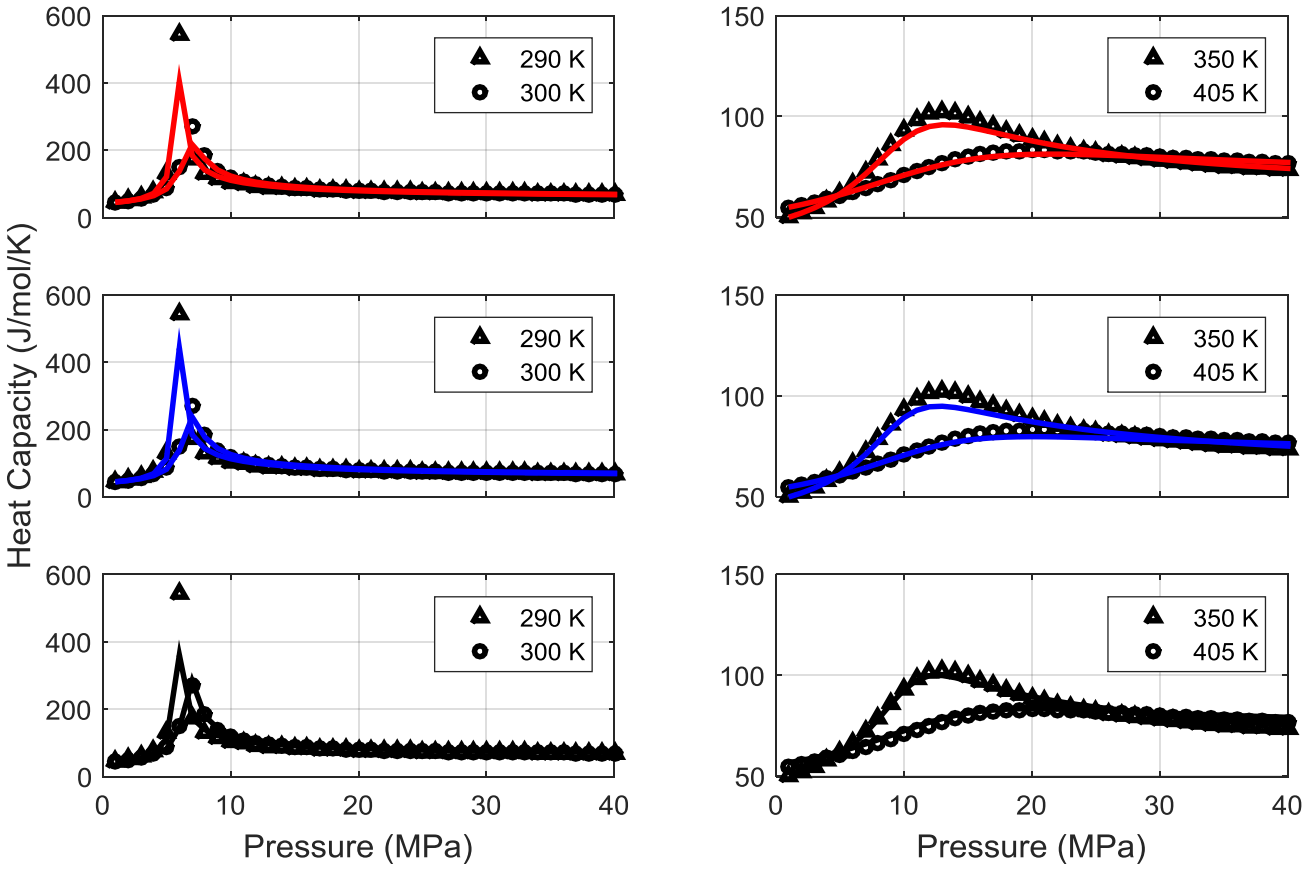

Figure F.1: Supercritical isobaric heat capacity of C_2H_4. Experimental data [261] are represented by data points and calculations by lines. Red lines correspond to PR, blue lines to PC-SAFT and black lines to SAFT-VR Mie EoS.

References

[1] B. Petroleum, BP Statistical Review of World Energy, in, 2018.

[2] I.M. Mujtaba, R. Srinivasan, N.O. Elbashir, The Water-Food-Energy Nexus: Processes, Technologies, and Challenges, CRC Press, 2017.

[3] www.co2.earth. Accessed: 2019 (1 June).

[4] Meeting the energy challenge: A white paper on energy, in, www.berr.gov.uk/files/file39387.pdf, UK Department of Trade and Industry, 2007.

[5] P. Alivizatos, M. Buchanan, Basic research needs for carbon capture: beyond 2020, in: www.sc.doe.gov/bes/reports/files/CCB2020_rpt.pdf, US Department of Energy, 2010.

[6] N. MacDowell, N. Florin, A. Buchard, J. Hallett, A. Galindo, G. Jackson, C.S. Adjiman, C.K. Williams, N. Shah, P. Fennell, An overview of CO2 capture technologies, Energy & Environmental Science, 3 (11) (2010) 1645-1669.

[7] B. Metz, O. Davidson, H. de Coninck, M. Loos, L. Meyer, IPCC, 2006: IPCC Special Report of Carbon Dioxide Capture and Storage. Prepared by Working Group III of the Intergovernmental Panel on Climate Change, in, New York, , 2005.

[8] ExxonMobil, 2018 Outlook for energy: A View to 2040, in, 2018.

[9] U.C.I. Agency, Length and types of pipelines for transporting products like natural gas, crude oil, or petroleum products, The world factbook, (2013).https://www.cia.gov/library/publications/the-world-factbook/fields/2117.html. Accessed: 2014 (11 November).

[10] H. Montiel, J.A. Vílchez, J. Arnaldos, J. Casal, Historical analysis of accidents in the transportation of natural gas, Journal of Hazardous Materials, 51 (1) (1996) 77-92.

[11] H. Montiel, J.A. Vílchez, J. Casal, J. Arnaldos, Mathematical modelling of accidental gas releases, Journal of Hazardous Materials, 59 (2) (1998) 211-233.

[12] R.M. Woolley, M. Fairweather, C.J. Wareing, C. Proust, J. Hebrard, D. Jamois, V.D. Narasimhamurthy, I.E. Storvik, T. Skjold, S.A.E.G. Falle, S. Brown, H. Mahgerefteh, S. Martynov, S.E. Gant, D.M. Tsangaris, I.G. Economou, G.C. Boulougouris, N.I. Diamantonis, An integrated, multi-scale modelling approach for the simulation of multiphase dispersion from accidental CO2 pipeline releases

in realistic terrain, International Journal of Greenhouse Gas Control, 27 (0) (2014) 221-238.

[13] N.I. Diamantonis, G.C. Boulougouris, E. Mansoor, D.M. Tsangaris, I.G. Economou, Evaluation of Cubic, SAFT, and PC-SAFT Equations of State for the Vapor–Liquid Equilibrium Modeling of CO2 Mixtures with Other Gases, Industrial & Engineering Chemistry Research, 52 (10) (2013) 3933-3942.

[14] N.I. Diamantonis, G.C. Boulougouris, D.M. Tsangaris, M.J.E. Kadi, H. Saadawi, S. Negahban, I.G. Economou, Thermodynamic and transport property models for carbon capture and sequestration (CCS) processes with emphasis on CO2 transport, Chemical Engineering Research and Design, 91 (10) (2013) 1793-1806.

[15] N.I. Diamantonis, I.G. Economou, Evaluation of Statistical Associating Fluid Theory (SAFT) and Perturbed Chain-SAFT Equations of State for the Calculation of Thermodynamic Derivative Properties of Fluids Related to Carbon Capture and Sequestration, Energy & Fuels, 25 (7) (2011) 3334-3343.

[16] S.H. Huang, M. Radosz, Equation of state for small, large, polydisperse, and associating molecules, Industrial & Engineering Chemistry Research, 29 (11) (1990) 2284-2294.

[17] S.H. Huang, M. Radosz, Equation of state for small, large, polydisperse, and associating molecules: extension to fluid mixtures, Industrial & Engineering Chemistry Research, 30 (8) (1991) 1994-2005.

[18] J. Gross, G. Sadowski, Perturbed-Chain SAFT: An Equation of State Based on a Perturbation Theory for Chain Molecules, Industrial & Engineering Chemistry Research, 40 (4) (2001) 1244-1260.

[19] J. Gross, G. Sadowski, Application of the Perturbed-Chain SAFT Equation of State to Associating Systems, Industrial & Engineering Chemistry Research, 41 (22) (2002) 5510-5515.

[20] J.J.B. Machado, T.W. de Loos, Liquid–vapour and solid–fluid equilibria for the system methane + triacontane at high temperature and high pressure, Fluid Phase Equilibria, 222–223 (2004) 261-267.

[21] G. De Bruijn, C. Skeates, R. Greenaway, D. Harrision, M. Parris, S. James, F. Mueller, S. Ray, M. Riding, L. Temple, K. Wutherich, High-Pressure, High-Temperature Technologies, in: Oilfield Review, Schlumberger, 2008, pp. 46-60.

[22] P. Ungerer, B. Faissat, C. Leibovici, H. Zhou, E. Behar, G. Moracchini, J.P. Courcy, High pressure-high temperature reservoir fluids: investigation of

synthetic condensate gases containing a solid hydrocarbon, Fluid Phase Equilibria, 111 (2) (1995) 287-311.

[23] A. Shariati, E.J.M. Straver, L.J. Florusse, C.J. Peters, Experimental phase behavior study of a five-component model gas condensate, Fluid Phase Equilibria, 362 (2014) 147-150.

[24] J. Pauly, J. Coutinho, J.-L. Daridon, High pressure phase equilibria in methane + waxy systems: 1. Methane + heptadecane, Fluid Phase Equilibria, 255 (2) (2007) 193-199.

[25] H. Pan, A. Firoozabadi, P. Fotland, Pressure and Composition Effect on Wax Precipitation: Experimental Data and Model Results.

[26] J. Pauly, J.A.P. Coutinho, J.-L. Daridon, High pressure phase equilibria in methane+waxy systems. 2. Methane+waxy ternary mixture, Fluid Phase Equilibria, 297 (1) (2010) 149-153.

[27] C.A. Gärtner, A.C. van Veen, J.A. Lercher, Oxidative Dehydrogenation of Ethane: Common Principles and Mechanistic Aspects, ChemCatChem, 5 (11) (2013) 3196-3217.

[28] P.M. Plehiers, G.C. Reyniers, G.F. Froment, Simulation of the run length of an ethane cracking furnace, Industrial & Engineering Chemistry Research, 29 (4) (1990) 636-641.

[29] G.P. Froment, B.O. Van de Steene, P.S. Van Damme, S. Narayanan, A.G. Goossens, Thermal Cracking of Ethane and Ethane-Propane Mixtures, Industrial & Engineering Chemistry Process Design and Development, 15 (4) (1976) 495-504.

[30] M.S. Shokrollahi Yancheshmeh, S. Seifzadeh Haghighi, M.R. Gholipour, O. Dehghani, M.R. Rahimpour, S. Raeissi, Modeling of ethane pyrolysis process: A study on effects of steam and carbon dioxide on ethylene and hydrogen productions, Chemical Engineering Journal, 215–216 (2013) 550-560.

[31] R.B. Eldridge, Olefin/paraffin separation technology: a review, Industrial & Engineering Chemistry Research, 32 (10) (1993) 2208-2212.

[32] G. Soave, Equilibrium constants from a modified Redlich-Kwong equation of state, Chemical Engineering Science, 27 (6) (1972) 1197-1203.

[33] D.-Y. Peng, D.B. Robinson, A New Two-Constant Equation of State, Industrial & Engineering Chemistry Fundamentals, 15 (1) (1976) 59-64.

[34] T. Lafitte, A. Apostolakou, C. Avendaño, A. Galindo, C.S. Adjiman, E.A. Müller, G. Jackson, Accurate statistical associating fluid theory for chain molecules formed from Mie segments, The Journal of Chemical Physics, 139 (15) (2013) 154504.

[35] P.H.V. Konynenburg, R.L. Scott, Critical Lines and Phase Equilibria in Binary Van Der Waals Mixtures, Philosophical Transactions of the Royal Society of London. Series A, 298 (1442) (1980) 495-540.

[36] M. Cismondi, M. Michelsen, Automated calculation of complete Pxy and Txy diagrams for binary systems, Fluid Phase Equilibria, 259 (2) (2007) 228-234.

[37] G. Venkatarathnam, Density Marching Method for Calculating Phase Envelopes, Industrial & engineering chemistry research, 53 (9) (2014) 3723-3730.

[38] G. Venkatarathnam, Density Marching Method for Calculating Phase Envelopes. 2. Three-Phase Envelopes, Industrial & engineering chemistry research, 53 (30) (2014) 12122-12128.

[39] G. Venkatarathnam, Density Marching Method for Drawing Phase Envelopes. 3. P-xy Diagrams of Binary Mixtures, Industrial & Engineering Chemistry Research, 56 (46) (2017) 13894-13904.

[40] J.W. Gibbs, On the Equilibrium of Heterogeneous Substances., III (1876 - 1878) 108-248, 343-524.

[41] M.L. Michelsen, The isothermal flash problem. Part I. Stability, Fluid Phase Equilibria, 9 (1) (1982) 1-19.

[42] M.L. Michelsen, The isothermal flash problem. Part II. Phase-split calculation, Fluid Phase Equilibria, 9 (1) (1982) 21-40.

[43] S.T. Harding, C.A. Floudas, Phase stability with cubic equations of state: Global optimization approach, AIChE Journal, 46 (7) (2000) 1422-1440.

[44] M.N. Ammar, H. Renon, The isothermal flash problem: New methods for phase split calculations, AIChE Journal, 33 (6) (1987) 926-939.

[45] D.V. Nichita, S. Gomez, E. Luna, Multiphase equilibria calculation by direct minimization of Gibbs free energy with a global optimization method, Computers & Chemical Engineering, 26 (12) (2002) 1703-1724.

[46] D.V. Nichita, S. Gomez, E. Luna, Phase stability analysis with cubic equations of state by using a global optimization method, Fluid Phase Equilibria, 194–197 (2002) 411-437.

[47] D.V. Nichita, M. Petitfrere, Phase equilibrium calculations with quasi-Newton methods, Fluid Phase Equilibria, 406 (2015) 194-208.

[48] L. Asselineau, G. Bogdanic, J. Vidal, A versatile algorithm for calculating vapour—liquid equilibria, Fluid Phase Equilibria, 3 (4) (1979) 273-290.

[49] T.F. Anderson, J.M. Prausnitz, Computational Methods for High-Pressure Phase Equilibria and Other Fluid-Phase Properties Using a Partition Function. 2. Mixtures, Industrial & Engineering Chemistry Process Design and Development, 19 (1) (1980) 9-14.

[50] D.V. Nichita, C.F. Leibovici, Improved solution windows for the resolution of the Rachford-Rice equation, Fluid Phase Equilibria, 452 (2017) 69-73.

[51] M. Petitfrere, D.V. Nichita, On a choice of independent variables in Newton iterations for multiphase flash calculations, Fluid Phase Equilibria, 427 (2016) 147-151.

[52] Y.S. Teh, G.P. Rangaiah, A Study of Equation-Solving and Gibbs Free Energy Minimization Methods for Phase Equilibrium Calculations, Chemical Engineering Research and Design, 80 (7) (2002) 745-759.

[53] H.H. Rachford, Jr., J.D. Rice, Procedure for Use of Electronic Digital Computers in Calculating Flash Vaporization Hydrocarbon Equilibrium, SPE-952327-G, 4 (10) (1952) 19-13.

[54] M. Petitfrere, D.V. Nichita, A comparison of conventional and reduction approaches for phase equilibrium calculations, Fluid Phase Equilibria, 386 (2015) 30-46.

[55] C. McDonald, C. Floudas, Decomposition based and branch and bound global optimization approaches for the phase equilibrium problem, J Glob Optim, 5 (3) (1994) 205-251.

[56] M. Petitfrere, D.V. Nichita, Robust and efficient Trust-Region based stability analysis and multiphase flash calculations, Fluid Phase Equilibria, 362 (0) (2014) 51-68.

[57] M.L. Michelsen, J.M. Mollerup, Thermodynamic Models: Fundamentals & Computational Aspects, 2nd ed., Tie-Line Publications, Denmark, 2007.

[58] R. Privat, J.-N. Jaubert, Y. Privat, A simple and unified algorithm to solve fluid phase equilibria using either the gamma–phi or the phi–phi approach for binary and ternary mixtures, Computers & Chemical Engineering, 50 (2013) 139-151.

[59] L.E. Baker, K.D. Luks, Critical Point and Saturation Pressure Calculations for Multipoint Systems (includes associated paper 8871), (1980).

[60] M.L. Michelsen, Saturation point calculations, Fluid Phase Equilibria, 23 (2–3) (1985) 181-192.

[61] M.L. Michelsen, Calculation of phase envelopes and critical points for multicomponent mixtures, Fluid Phase Equilibria, 4 (1–2) (1980) 1-10.

[62] I.K. Nikolaidis, I.G. Economou, G.C. Boulougouris, L.D. Peristeras, Calculation of the phase envelope of multicomponent mixtures with the bead spring method, AIChE Journal, 62 (3) (2016) 868-879.

[63] S.E. Quiñones-Cisneros, U.K. Deiters, An efficient algorithm for the calculation of phase envelopes of fluid mixtures, Fluid Phase Equilibria, 329 (0) (2012) 22-31.

[64] N.R. Nagarajan, A.S. Cullick, A. Griewank, New strategy for phase equilibrium and critical point calculations by thermodynamic energy analysis. Part I. Stability analysis and flash, Fluid Phase Equilibria, 62 (3) (1991) 191-210.

[65] U.K. Deiters, Differential equations for the calculation of fluid phase equilibria, Fluid Phase Equilibria, 428 (2016) 164-173.

[66] U.K. Deiters, Differential equations for the calculation of isopleths of multicomponent fluid mixtures, Fluid Phase Equilibria, 447 (2017) 72-83.

[67] D.V. Nichita, Density-based phase envelope construction, Fluid Phase Equilibria, 478 (2018) 100-113.

[68] D.V. Nichita, Volume-based phase stability testing at pressure and temperature specifications, Fluid Phase Equilibria, 458 (2018) 123-141.

[69] D.V. Nichita, A volume-based approach to phase equilibrium calculations at pressure and temperature specifications, Fluid Phase Equilibria, 461 (2018) 70-83.

[70] F.E. Pereira, G. Jackson, A. Galindo, C.S. Adjiman, A duality-based optimisation approach for the reliable solution of (P, T) phase equilibrium in volume-composition space, Fluid Phase Equilibria, 299 (1) (2010) 1-23.

[71] F.E. Pereira, G. Jackson, A. Galindo, C.S. Adjiman, The HELD algorithm for multicomponent, multiphase equilibrium calculations with generic equations of state, Computers & Chemical Engineering, 36 (2012) 99-118.

[72] L.X. Nghiem, Y.-K. Li, R.A. Heidemann, Application of the tangent plane criterion to saturation pressure and temperature computations, Fluid Phase Equilibria, 21 (1–2) (1985) 39-60.

[73] E. Khodapanah, S.A. Tabatabaei-Nejad, A consistent method for simultaneous calculation of upper and lower dew point pressures of gas condensate fluids, Journal of Natural Gas Science and Engineering, 21 (0) (2014) 556-567.

[74] G. Wilson, A modified Redlich-Kwong equation of state, application to general physical data calculations, in: The AIChE 65th National Meeting, Cleveland, Ohio, 1969.

[75] C. Coquelet, A. Valtz, F. Dieu, D. Richon, P. Arpentinier, F. Lockwood, Isothermal P, x, y data for the argon + carbon dioxide system at six temperatures from 233.32 to 299.21 K and pressures up to 14 MPa, Fluid Phase Equilibria, 273 (1–2) (2008) 38-43.

[76] H. Li, J. Yan, Evaluating cubic equations of state for calculation of vapor–liquid equilibrium of CO2 and CO2-mixtures for CO2 capture and storage processes, Applied Energy, 86 (6) (2009) 826-836.

[77] A. Chapoy, C. Coquelet, H. Liu, A. Valtz, B. Tohidi, Vapour–liquid equilibrium data for the hydrogen sulphide (H2S)+carbon dioxide (CO2) system at temperatures from 258 to 313 K, Fluid Phase Equilibria, 356 (0) (2013) 223-228.

[78] C. Coquelet, A. Valtz, P. Arpentinier, Thermodynamic study of binary and ternary systems containing CO2 + impurities in the context of CO2 transportation, Fluid Phase Equilibria, 382 (0) (2014) 205-211.

[79] S.F. Westman, H.G.J. Stang, S.W. Løvseth, A. Austegard, I. Snustad, S.Ø. Størset, I.S. Ertesvåg, Vapor–liquid equilibrium data for the carbon dioxide and nitrogen (CO2 + N2) system at the temperatures 223, 270, 298 and 303 K and pressures up to 18 MPa, Fluid Phase Equilibria, 409 (2016) 207-241.

[80] S.F. Westman, H.G.J. Stang, S.W. Løvseth, A. Austegard, I. Snustad, I.S. Ertesvåg, Vapor-liquid equilibrium data for the carbon dioxide and oxygen (CO2 + O2) system at the temperatures 218, 233, 253, 273, 288 and 298 K and pressures up to 14 MPa, Fluid Phase Equilibria, 421 (2016) 67-87.

[81] S. Lasala, P. Chiesa, R. Privat, J.-N. Jaubert, VLE properties of CO2 – Based binary systems containing N2, O2 and Ar: Experimental measurements and modelling results with advanced cubic equations of state, Fluid Phase Equilibria, (2016).

[82] M. Ahmad, J. Gernert, E. Wilbers, Effect of impurities in captured CO2 on liquid–vapor equilibrium, Fluid Phase Equilibria, 363 (0) (2014) 149-155.

[83] S. Blanco, C. Rivas, R. Bravo, J. Fernandez, M. Artal, I. Velasco, Discussion of the Influence of CO and CH4 in CO2 Transport, Injection, and Storage for CCS Technology, Environmental science & technology, 48 (18) (2014) 10984-10992.

[84] S. Blanco, C. Rivas, J. Fernandez, M. Artal, I. Velasco, Influence of Methane in CO2 Transport and Storage for CCS Technology, Environmental science & technology, 46 (23) (2012) 13016-13023.

[85] A. Chapoy, M. Nazeri, M. Kapateh, R. Burgass, C. Coquelet, B. Tohidi, Effect of impurities on thermophysical properties and phase behaviour of a CO2-rich system in CCS, International Journal of Greenhouse Gas Control, 19 (0) (2013) 92-100.

[86] J. Ke, N. Suleiman, Y. Sanchez-Vicente, T.S. Murphy, J. Rodriguez, A. Ramos, M. Poliakoff, M.W. George, The phase equilibrium and density studies of the ternary mixtures of CO2 + Ar + N2 and CO2 + Ar + H2, systems relevance to CCS technology, International Journal of Greenhouse Gas Control, 56 (2017) 55-66.

[87] X. Xu, R. Privat, J.-N. Jaubert, V. Lachet, B. Creton, Phase equilibrium of CCS mixtures: Equation of state modeling and Monte Carlo simulation, The Journal of Supercritical Fluids, 119 (2017) 169-202.

[88] T. Regueira, Y. Liu, A.A. Wibowo, M. Ashrafi, F. Varzandeh, G. Pantelide, E.H. Stenby, W. Yan, High pressure phase equilibrium of ternary and multicomponent alkane mixtures in the temperature range from (283 to 473) K, Fluid Phase Equilibria, 449 (2017) 186-196.

[89] W. Yan, F. Varzandeh, E.H. Stenby, PVT modeling of reservoir fluids using PC-SAFT EoS and Soave-BWR EoS, Fluid Phase Equilibria, 386 (2015) 96-124.

[90] N. von Solms, M.L. Michelsen, G.M. Kontogeorgis, Computational and Physical Performance of a Modified PC-SAFT Equation of State for Highly Asymmetric and Associating Mixtures, Industrial & Engineering Chemistry Research, 42 (5) (2003) 1098-1105.

[91] G.S. Soave, An effective modification of the Benedict–Webb–Rubin equation of state, Fluid Phase Equilibria, 164 (2) (1999) 157-172.

[92] N. Novak, V. Louli, S. Skouras, E. Voutsas, Prediction of dew points and liquid dropouts of gas condensate mixtures, Fluid Phase Equilibria, 457 (2018) 62-73.

[93] E. Voutsas, V. Louli, C. Boukouvalas, K. Magoulas, D. Tassios, Thermodynamic property calculations with the universal mixing rule for EoS/GE models: Results with the Peng–Robinson EoS and a UNIFAC model, Fluid Phase Equilibria, 241 (1–2) (2006) 216-228.

[94] J.M. Prausnitz, R.N. Lichtenthaler, E.G. de Azevedo, Molecular Thermodynamics of Fluid-Phase Equilibria, 3rd ed., Prentice-Hall, New Jersey, 1999.

[95] K.W. Won, Thermodynamics for solid solution-liquid-vapor equilibria: wax phase formation from heavy hydrocarbon mixtures, Fluid Phase Equilibria, 30 (1986) 265-279.

[96] J.H. Hansen, A. Fredenslund, K.S. Pedersen, H.P. Rønningsen, A thermodynamic model for predicting wax formation in crude oils, AIChE Journal, 34 (12) (1988) 1937-1942.

[97] K. Schou Pedersen, P. Skovborg, H.P. Roenningsen, Wax precipitation from North Sea crude oils. 4. Thermodynamic modeling, Energy & Fuels, 5 (6) (1991) 924-932.

[98] J.A.P. Coutinho, S.I. Andersen, E.H. Stenby, Evaluation of activity coefficient models in prediction of alkane solid-liquid equilibria, Fluid Phase Equilibria, 103 (1) (1995) 23-39.

[99] C. Lira-Galeana, A. Firoozabadi, J.M. Prausnitz, Thermodynamics of wax precipitation in petroleum mixtures, AIChE Journal, 42 (1) (1996) 239-248.

[100] J.A.P. Coutinho, K. Knudsen, S.I. Andersen, E.H. Stenby, A local composition model for paraffinic solid solutions, Chemical Engineering Science, 51 (12) (1996) 3273-3282.

[101] J.A.P. Coutinho, V. Ruffier-Méray, Experimental Measurements and Thermodynamic Modeling of Paraffinic Wax Formation in Undercooled Solutions, Industrial & Engineering Chemistry Research, 36 (11) (1997) 4977-4983.

[102] N. Lindeloff, S.I. Andersen, E.H. Stenby, R.A. Heidemann, Phase-Boundary Calculations in Systems Involving More than Two Phases, with Application to Hydrocarbon Mixtures, Industrial & Engineering Chemistry Research, 38 (3) (1999) 1107-1113.

[103] C.H. Twu, An internally consistent correlation for predicting the critical properties and molecular weights of petroleum and coal-tar liquids, Fluid Phase Equilibria, 16 (2) (1984) 137-150.

[104] J. Pauly, J.-L. Daridon, J.A.P. Coutinho, N. Lindeloff, S.I. Andersen, Prediction of solid–fluid phase diagrams of light gases–heavy paraffin systems up to 200 MPa using an equation of state–GE model, Fluid Phase Equilibria, 167 (2) (2000) 145-159.

[105] C. Boukouvalas, N. Spiliotis, P. Coutsikos, N. Tzouvaras, D. Tassios, Prediction of vapor-liquid equilibrium with the LCVM model: a linear combination of the Vidal and Michelsen mixing rules coupled with the original UNIF, Fluid Phase Equilibria, 92 (1994) 75-106.

[106] L. Lundgaard, J.M. Mollerup, The influence of gas phase fugacity and solubility on correlation of gas-hydrate formation pressure, Fluid Phase Equilibria, 70 (2) (1991) 199-213.

[107] A. Péneloux, E. Rauzy, R. Fréze, A consistent correction for Redlich-Kwong-Soave volumes, Fluid Phase Equilibria, 8 (1) (1982) 7-23.

[108] P. Morawski, J.A.P. Coutinho, U. Domańska, High pressure (solid + liquid) equilibria of n-alkane mixtures: experimental results, correlation and prediction, Fluid Phase Equilibria, 230 (1–2) (2005) 72-80.

[109] E. Ghanaei, F. Esmaeilzadeh, J.F. Kaljahi, A new predictive thermodynamic model in the wax formation phenomena at high pressure condition, Fluid Phase Equilibria, 254 (1) (2007) 126-137.

[110] K. Nasrifar, M. Fani Kheshty, Effect of pressure on the solid–liquid equilibria of synthetic paraffin mixtures using predictive methods, Fluid Phase Equilibria, 310 (1) (2011) 111-119.

[111] E. Ghanaei, F. Esmaeilzadeh, J. Fathikalajahi, High pressure phase equilibrium of wax: A new thermodynamic model, Fuel, 117 (2014) 900-909.

[112] M. Ameri Mahabadian, A. Chapoy, B. Tohidi, A New Thermodynamic Model for Paraffin Precipitation in Highly Asymmetric Systems at High Pressure Conditions, Industrial & Engineering Chemistry Research, 55 (38) (2016) 10208-10217.

[113] J.-N. Jaubert, F. Mutelet, VLE predictions with the Peng–Robinson equation of state and temperature dependent kij calculated through a group contribution method, Fluid Phase Equilibria, 224 (2) (2004) 285-304.

[114] H.-Y. Ji, B. Tohidi, A. Danesh, A.C. Todd, Wax phase equilibria: developing a thermodynamic model using a systematic approach, Fluid Phase Equilibria, 216 (2) (2004) 201-217.

[115] J.-N. Jaubert, R. Privat, Relationship between the binary interaction parameters (kij) of the Peng–Robinson and those of the Soave–Redlich–Kwong equations of state: Application to the definition of the PR2SRK model, Fluid Phase Equilibria, 295 (1) (2010) 26-37.

[116] V. Machát, T. Boublík, Vapour—liquid equilibrium at elevated pressures from the back equation of state. II. Binary systems, Fluid Phase Equilibria, 21 (1) (1985) 11-24.

[117] S. Laugier, D. Richon, H. Renon, Ethylene + Olefin Binary Systems: Vapor-Liquid Equilibrium Experimental Data and Modeling, Journal of Chemical & Engineering Data, 39 (2) (1994) 388-391.

[118] Z.-h. Chen, Z. Yao, F.-j. Zhu, K. Cao, Y. Li, Z.-m. Huang, Gas−Liquid Critical Properties of Ethylene + Hydrogen and Propylene + Hydrogen Binary Mixtures, Journal of Chemical & Engineering Data, 55 (5) (2010) 2004-2007.

[119] T. Holderbaum, J. Gmehling, PSRK: A Group Contribution Equation of State Based on UNIFAC, Fluid Phase Equilibria, 70 (2) (1991) 251-265.

[120] J.-W. Qian, J.-N. Jaubert, R. Privat, Prediction of the phase behavior of alkene-containing binary systems with the PPR78 model, Fluid Phase Equilibria, 354 (2013) 212-235.

[121] M.L. Michelsen, State function based flash specifications, Fluid Phase Equilibria, 158-160 (Supplement C) (1999) 617-626.

[122] M. Castier, Solution of the isochoric–isoenergetic flash problem by direct entropy maximization, Fluid Phase Equilibria, 276 (1) (2009) 7-17.

[123] M. Castier, R. Kanes, L.N. Véchot, Flash calculations with specified entropy and stagnation enthalpy, Fluid Phase Equilibria, 408 (2016) 196-204.

[124] D.V. Nichita, New unconstrained minimization methods for robust flash calculations at temperature, volume and moles specifications, Fluid Phase Equilibria, 466 (2018) 31-47.

[125] R. Zaydullin, D.V. Voskov, S.C. James, H. Henley, A. Lucia, Fully compositional and thermal reservoir simulation, Computers & Chemical Engineering, 63 (2014) 51-65.

[126] A. Iranshahr, D. Voskov, H.A. Tchelepi, Generalized negative-flash method for multiphase multicomponent systems, Fluid Phase Equilibria, 299 (2) (2010) 272-284.

[127] M. Dumbser, U. Iben, C.-D. Munz, Efficient implementation of high order unstructured WENO schemes for cavitating flows, Computers & Fluids, 86 (2013) 141-168.

[128] Y. Fang, M. De Lorenzo, P. Lafon, S. Poncet, Y. Bartosiewicz, An Accurate and Efficient Look-up Table Equation of State for Two-Phase Compressible Flow Simulations of Carbon Dioxide, Industrial & Engineering Chemistry Research, 57 (22) (2018) 7676-7691.

[129] R. Span, W. Wagner, A New Equation of State for Carbon Dioxide Covering the Fluid Region from the Triple- Point Temperature to 1100 K at Pressures up to 800 MPa, Journal of Physical and Chemical Reference Data, 25 (6) (1996) 1509-1596.

[130] Ø. Wilhelmsen, G. Skaugen, M. Hammer, P.E. Wahl, J.C. Morud, Time Efficient Solution of Phase Equilibria in Dynamic and Distributed Systems with Differential Algebraic Equation Solvers, Industrial & Engineering Chemistry Research, 52 (5) (2013) 2130-2140.

[131] E. Aursand, S. Dumoulin, M. Hammer, H.I. Lange, A. Morin, S.T. Munkejord, H.O. Nordhagen, Fracture propagation control in CO2 pipelines: Validation of a coupled fluid–structure model, Engineering Structures, 123 (2016) 192-212.

[132] M. Hammer, Å. Ervik, S.T. Munkejord, Method Using a Density–Energy State Function with a Reference Equation of State for Fluid-Dynamics Simulation of Vapor–Liquid–Solid Carbon Dioxide, Industrial & Engineering Chemistry Research, 52 (29) (2013) 9965-9978.

[133] S. Martynov, S. Brown, H. Mahgerefteh, V. Sundara, S. Chen, Y. Zhang, Modelling three-phase releases of carbon dioxide from high-pressure pipelines, Process Safety and Environmental Protection, 92 (1) (2014) 36-46.

[134] I.K. Nikolaidis, G.C. Boulougouris, L.D. Peristeras, I.G. Economou, Equation-of-State Modeling of Solid–Liquid–Gas Equilibrium of CO2 Binary Mixtures, Industrial & Engineering Chemistry Research, 55 (21) (2016) 6213-6226.

[135] J.D. Van der Waals, On the continuity of the gas and liquid state, Leiden, (1873), PhD Thesis.

[136] G.M. Kontogeorgis, G.K. Folas, Thermodynamic Models for Industrial Applications, John Wiley & Sons, Ltd, 2010.

[137] G. Jackson, W.G. Chapman, K.E. Gubbins, Phase equilibria of associating fluids, Molecular Physics, 65 (1) (1988) 1-31.

[138] W.G. Chapman, G. Jackson, K.E. Gubbins, Phase equilibria of associating fluids, Molecular Physics, 65 (5) (1988) 1057-1079.

[139] W.G. Chapman, K.E. Gubbins, G. Jackson, M. Radosz, New reference equation of state for associating liquids, Industrial & Engineering Chemistry Research, 29 (8) (1990) 1709-1721.

[140] M.S. Wertheim, Fluids with highly directional attractive forces. I. Statistical thermodynamics, J Stat Phys, 35 (1-2) (1984) 19-34.

[141] M.S. Wertheim, Fluids with highly directional attractive forces. II. Thermodynamic perturbation theory and integral equations, J Stat Phys, 35 (1-2) (1984) 35-47.

[142] M.S. Wertheim, Fluids with highly directional attractive forces. III. Multiple attraction sites, J Stat Phys, 42 (3-4) (1986) 459-476.

[143] M.S. Wertheim, Fluids with highly directional attractive forces. IV. Equilibrium polymerization, J Stat Phys, 42 (3-4) (1986) 477-492.

[144] H. Guérin, A new simple analytic equation of state for square-well chain fluids with variable width, $1.1<\lambda<2$, based on perturbation theory and an analytic representation of the hard-sphere radial distribution function gHS(r), Journal of Molecular Liquids, 156 (2) (2010) 179-183.

[145] J. Li, H. He, C. Peng, H. Liu, Y. Hu, A new development of equation of state for square-well chain-like molecules with variable width $1.1\leq\lambda\leq3$, Fluid Phase Equilibria, 276 (1) (2009) 57-68.

[146] B.H. Patel, H. Docherty, S. Varga, A. Galindo, G.C. Maitland, Generalized equation of state for square-well potentials of variable range, Molecular Physics, 103 (1) (2005) 129-139.

[147] H. Adidharma, M. Radosz, Prototype of an Engineering Equation of State for Heterosegmented Polymers, Industrial & Engineering Chemistry Research, 37 (11) (1998) 4453-4462.

[148] A. Gil-Villegas, A. Galindo, P.J. Whitehead, S.J. Mills, G. Jackson, A.N. Burgess, Statistical associating fluid theory for chain molecules with attractive potentials of variable range, The Journal of Chemical Physics, 106 (10) (1997) 4168-4186.

[149] A. Galindo, L.A. Davies, A. Gil-Villegas, G. Jackson, The thermodynamics of mixtures and the corresponding mixing rules in the SAFT-VR approach for potentials of variable range, Molecular Physics, 93 (2) (1998) 241-252.

[150] F.J. Blas, L.F. Vega, Thermodynamic behaviour of homonuclear and heteronuclear Lennard-Jones chains with association sites from simulation and theory, Molecular Physics, 92 (1) (1997) 135-150.

[151] F.J. Blas, L.F. Vega, Prediction of Binary and Ternary Diagrams Using the Statistical Associating Fluid Theory (SAFT) Equation of State, Industrial & Engineering Chemistry Research, 37 (2) (1998) 660-674.

[152] T. Kraska, K.E. Gubbins, Phase Equilibria Calculations with a Modified SAFT Equation of State. 1. Pure Alkanes, Alkanols, and Water, Industrial & Engineering Chemistry Research, 35 (12) (1996) 4727-4737.

[153] J.K. Johnson, E.A. Mueller, K.E. Gubbins, Equation of State for Lennard-Jones Chains, The Journal of Physical Chemistry, 98 (25) (1994) 6413-6419.

[154] W.G. Chapman, Prediction of the thermodynamic properties of associating Lennard-Jones fluids: Theory and simulation, The Journal of Chemical Physics, 93 (6) (1990) 4299-4304.

[155] S.S. Chen, A. Kreglewski, Applications of the Augmented van der Waals Theory of Fluids.: I. Pure Fluids, Berichte der Bunsengesellschaft für physikalische Chemie, 81 (10) (1977) 1048-1052.

[156] T. Lafitte, D. Bessieres, M.M. Piñeiro, J.-L. Daridon, Simultaneous estimation of phase behavior and second-derivative properties using the statistical associating fluid theory with variable range approach, The Journal of Chemical Physics, 124 (2) (2006) 024509.

[157] T. Lafitte, M.M. Piñeiro, J.-L. Daridon, D. Bessières, A Comprehensive Description of Chemical Association Effects on Second Derivative Properties of Alcohols through a SAFT-VR Approach, The Journal of Physical Chemistry B, 111 (13) (2007) 3447-3461.

[158] A.J. de Villiers, C.E. Schwarz, A.J. Burger, G.M. Kontogeorgis, Evaluation of the PC-SAFT, SAFT and CPA equations of state in predicting derivative properties of selected non-polar and hydrogen-bonding compounds, Fluid Phase Equilibria, 338 (Supplement C) (2013) 1-15.

[159] I. Polishuk, Addressing the issue of numerical pitfalls characteristic for SAFT EOS models, Fluid Phase Equilibria, 301 (1) (2011) 123-129.

[160] M.A. McHugh, J.J. Watkins, B.T. Doyle, V.J. Krukonis, High-pressure naphthalene-xenon phase behavior, Industrial & Engineering Chemistry Research, 27 (6) (1988) 1025-1033.

[161] I. Kikic, M. Lora, A. Bertucco, A Thermodynamic Analysis of Three-Phase Equilibria in Binary and Ternary Systems for Applications in Rapid Expansion of a Supercritical Solution (RESS), Particles from Gas-Saturated Solutions (PGSS), and Supercritical Antisolvent (SAS), Industrial & Engineering Chemistry Research, 36 (12) (1997) 5507-5515.

[162] M. Seiler, J. Groß, B. Bungert, G. Sadowski, W. Arlt, Modeling of Solid/Fluid Phase Equilibria in Multicomponent Systems at High Pressure, Chemical Engineering & Technology, 24 (6) (2001) 607-612.

[163] A. Jäger, R. Span, Equation of State for Solid Carbon Dioxide Based on the Gibbs Free Energy, Journal of Chemical & Engineering Data, 57 (2) (2012) 590-597.

[164] M.L. Michelsen, Phase equilibrium calculations. What is easy and what is difficult?, Computers & Chemical Engineering, 16 (1992) S19-S29.

[165] D.V. Nichita, Phase stability testing near the stability test limit, Fluid Phase Equilibria, 426 (2016) 25-36.

[166] R.A. Heidemann, M.L. Michelsen, Instability of Successive Substitution, Industrial & Engineering Chemistry Research, 34 (3) (1995) 958-966.

[167] D.V. Nichita, Fast and robust phase stability testing at isothermal-isochoric conditions, Fluid Phase Equilibria, 447 (2017) 107-124.

[168] J. Nocedal, S.J. Wright, Numerical Optimization, 2nd ed., Springer, New York, 2006.

[169] I.K. Nikolaidis, A. Poursaeidesfahani, Z. Csaszar, M. Ramdin, T.J.H. Vlugt, I.G. Economou, O.A. Moultos, Modeling the phase equilibria of asymmetric hydrocarbon mixtures using molecular simulation and equations of state, AIChE Journal, 65 (2) (2019) 792-803.

[170] I.K. Nikolaidis, V.S. Samoili, E.C. Voutsas, I.G. Economou, Solid–Liquid–Gas Equilibrium of Methane–n-Alkane Binary Mixtures, Industrial & Engineering Chemistry Research, 57 (25) (2018) 8566-8583.

[171] C. Jarne, S. Avila, S.T. Blanco, E. Rauzy, S. Otín, I. Velasco, Thermodynamic Properties of Synthetic Natural Gases. 5. Dew Point Curves of Synthetic Natural Gases and Their Mixtures with Water and with Water and Methanol:

Measurement and Correlation, Industrial & Engineering Chemistry Research, 43 (1) (2004) 209-217.

[172] N.I. Diamantonis, I.G. Economou, Modeling the phase equilibria of a H2O–CO2 mixture with PC-SAFT and tPC-PSAFT equations of state, Molecular Physics, 110 (11-12) (2012) 1205-1212.

[173] N.I. Diamantonis, Mathematical modeling of thermophysical properties and phase equilibria of pure carbon dioxide and multicomponent mixtures, National Technical University of Athens, (2013), PhD thesis.

[174] J.S. Chickos, W.E. Acree, Enthalpies of Sublimation of Organic and Organometallic Compounds. 1910–2001, Journal of Physical and Chemical Reference Data, 31 (2) (2002) 537-698.

[175] DIPPR 801, Evaluated Standards Thermophysical Property Values, in, American Institute of Chemical Engineers, New York, 2015.

[176] O. Fandiño, J.P.M. Trusler, D. Vega-Maza, Phase behavior of (CO2 + H2) and (CO2 + N2) at temperatures between (218.15 and 303.15) K at pressures up to 15 MPa, International Journal of Greenhouse Gas Control, 36 (2015) 78-92.

[177] H.G. Donnelly, D.L. Katz, Phase Equilibria in the Carbon Dioxide–Methane System, Industrial & Engineering Chemistry, 46 (3) (1954) 511-517.

[178] J.A. Davis, N. Rodewald, F. Kurata, Solid-liquid-vapor phase behavior of the methane-carbon dioxide system, AIChE Journal, 8 (4) (1962) 537-539.

[179] G.-i. Kaminishi, T. Taturo, Vapor-liquid equilibria in the systems: CO2-CO,CO2-CO-H2 and CO2-CH4, The Review of Physical Chemistry of Japan, 38 (1) (1968) 79-84.

[180] A. Kreglewski, K.R. Hall, Phase equilibria calculated for the systems N2 + CO2, CH4 + CO2 and CH4 + H2S, Fluid Phase Equilibria, 15 (1) (1983) 11-32.

[181] D. Frenkel, B. Smit, Understanding molecular simulation: from algorithms to applications, 2nd ed., Academic Press, San Diego, California, 2002.

[182] M.G. Martin, J.I. Siepmann, Transferable Potentials for Phase Equilibria. 1. United-Atom Description of n-Alkanes, The Journal of Physical Chemistry B, 102 (14) (1998) 2569-2577.

[183] V.K. Michalis, O.A. Moultos, I.N. Tsimpanogiannis, I.G. Economou, Molecular dynamics simulations of the diffusion coefficients of light n-alkanes in water over a wide range of temperature and pressure, Fluid Phase Equilibria, 407 (2016) 236-242.

[184] O.A. Moultos, I.N. Tsimpanogiannis, A.Z. Panagiotopoulos, J.P.M. Trusler, I.G. Economou, Atomistic Molecular Dynamics Simulations of Carbon Dioxide Diffusivity in n-Hexane, n-Decane, n-Hexadecane, Cyclohexane, and Squalane, The Journal of Physical Chemistry B, 120 (50) (2016) 12890-12900.

[185] M.P. Allen, D.J. Tildesley, Computer simulation of liquids, Oxford University Press, New York, 1989.

[186] A.Z. Panagiotopoulos, Direct Determination of Fluid Phase Equilibria by Simulation in the Gibbs Ensemble: A Review, Molecular Simulation, 9 (1) (1992) 1-23.

[187] A.Z. Panagiotopoulos, Molecular simulation of phase equilibria: simple, ionic and polymeric fluids, Fluid Phase Equilibria, 76 (1992) 97-112.

[188] M. Dinpajooh, P. Bai, D.A. Allan, J.I. Siepmann, Accurate and precise determination of critical properties from Gibbs ensemble Monte Carlo simulations, The Journal of Chemical Physics, 143 (11) (2015) 114113.

[189] K.T. Koonce, R. Kobayashi, A Method for Determining the Solubility of Gases in Relatively Nonvolatile Liquids: Solubility of Methane in n-Decane, Journal of Chemical & Engineering Data, 9 (4) (1964) 490-494.

[190] M.P.W.M. Rijkers, M. Malais, C.J. Peters, J. de Swaan Arons, Measurements on the phase behavior of binary hydrocarbon mixtures for modelling the condensation behavior of natural gas: Part I. The system methane + decane, Fluid Phase Equilibria, 71 (1) (1992) 143-168.

[191] S. Srivastan, N.A. Darwish, K.A.M. Gasem, R.L. Robinson, Solubility of methane in hexane, decane, and dodecane at temperatures from 311 to 423 K and pressures to 10.4 MPa, Journal of Chemical & Engineering Data, 37 (4) (1992) 516-520.

[192] H.-M. Lin, H.M. Sebastian, J.J. Simnick, K.-C. Chao, Gas-liquid equilibrium in binary mixtures of methane with N-decane, benzene, and toluene, Journal of Chemical & Engineering Data, 24 (2) (1979) 146-149.

[193] J.M. Beaudoin, J.P. Kohn, Multiphase and volumetric equilibria of the methane-n-decane binary system at temperatures between -36.degree. and 150.degree, Journal of Chemical & Engineering Data, 12 (2) (1967) 189-191.

[194] H.H. Reamer, R.H. Olds, B.H. Sage, W.N. Lacey, Phase Equilibria in Hydrocarbon Systems, Industrial & Engineering Chemistry, 34 (12) (1942) 1526-1531.

[195] T. Regueira, G. Pantelide, W. Yan, E.H. Stenby, Density and phase equilibrium of the binary system methane + n-decane under high temperatures and pressures, Fluid Phase Equilibria, 428 (Supplement C) (2016) 48-61.

[196] M.P.W.M. Rijkers, V.B. Maduro, C.J. Peters, J. de Swaan Arons, Measurements on the phase behavior of binary mixtures for modeling the condensation behavior of natural gas: Part II. The system methane + dodecane, Fluid Phase Equilibria, 72 (Supplement C) (1992) 309-324.

[197] J.-F. Arnaud, Caractérisation des propriétés physiques et thermodynamiques des fluides pétroliers à haute pression, Universite de Pau, (1995), PhD thesis.

[198] M. Glaser, C.J. Peters, H.J. Van Der Kooi, R.N. Lichtenthaler, Phase equilibria of (methane + n-hexadecane) and (p, Vm, T) of n-hexadecane, The Journal of Chemical Thermodynamics, 17 (9) (1985) 803-815.

[199] M.P.W.M. Rijkers, C.J. Peters, J. de Swaan Arons, Measurements on the phase behavior of binary mixtures for modeling the condensation behavior of natural gas: Part III. The system methane + hexadecane, Fluid Phase Equilibria, 85 (Supplement C) (1993) 335-345.

[200] C.E.P. Siqueira Campos, J.R. Penello, F.L. Pellegrini Pessoa, A.M. Cohen Uller, Experimental Measurement and Thermodynamic Modeling for the Solubility of Methane in Water and Hexadecane, Journal of Chemical & Engineering Data, 55 (7) (2010) 2576-2580.

[201] S. Le Roy, E. Behar, P. Ungerer, Vapour-liquid equilibrium data for synthetic hydrocarbon mixtures. Application to modelling of migration from source to reservoir rocks, Fluid Phase Equilibria, 135 (1) (1997) 63-82.

[202] H.-M. Lin, H.M. Sebastian, K.-C. Chao, Gas-liquid equilibrium in hydrogen + n-hexadecane and methane + n-hexadecane at elevated temperatures and pressures, Journal of Chemical & Engineering Data, 25 (3) (1980) 252-254.

[203] A. Cohen, D. Richon, New apparatus for simultaneous determination of phase equilibria and rheological properties of fluids at high pressures: Its application to coal pastes studies up to 773 K and 30 MPa, Review of Scientific Instruments, 57 (6) (1986) 1192-1195.

[204] S. Puri, J.P. Kohn, Solid-liquid-vapor equilibrium in the methane-n-eicosane and ethane-n-eicosane binary systems, Journal of Chemical & Engineering Data, 15 (3) (1970) 372-374.

[205] N.A. Darwish, J. Fathikalajahi, K.A.M. Gasem, R.L. Robinson, Solubility of methane in heavy normal paraffins at temperatures from 323 to 423 K and pressures to 10.7 MPa, Journal of Chemical & Engineering Data, 38 (1) (1993) 44-48.

[206] H.J. van der Kooi, E. Flöter, T.W.d. Loos, High-pressure phase equilibria of {(1−x)CH4+xCH3(CH2)18CH3}, The Journal of Chemical Thermodynamics, 27 (8) (1995) 847-861.

[207] S.H. Huang, H.M. Lin, K.C. Chao, Solubility of carbon dioxide, methane, and ethane in n-eicosane, Journal of Chemical & Engineering Data, 33 (2) (1988) 145-147.

[208] E. Flöter, T.W. de Loos, J. de Swaan Arons, High pressure solid-fluid and vapour-liquid equilibria in the system (methane + tetracosane), Fluid Phase Equilibria, 127 (1–2) (1997) 129-146.

[209] C.-P. Huang, D.-S. Jan, F.-N. Tsai, Modeling of Methane Solubility in Heavy n-Paraffins, Journal of Chemical Engineering of Japan, 25 (2) (1992) 182-186.

[210] J.F. Arnaud, P. Ungerer, E. Behar, G. Moracchini, J. Sanchez, Excess volumes and saturation pressures for the system methane + n-tetracosane at 374 K. Representation by improved EOS mixing rules, Fluid Phase Equilibria, 124 (1) (1996) 177-207.

[211] A.M. Ferrenberg, R.H. Swendsen, New Monte Carlo Technique for Studying Phase Transitions, Physical Review Letters, 63 (15) (1989) 1658-1658.

[212] K.S. Rane, S. Murali, J.R. Errington, Monte Carlo Simulation Methods for Computing Liquid–Vapor Saturation Properties of Model Systems, Journal of Chemical Theory and Computation, 9 (6) (2013) 2552-2566.

[213] D.A. Kofke, Gibbs-Duhem integration: a new method for direct evaluation of phase coexistence by molecular simulation, Molecular Physics, 78 (6) (1993) 1331-1336.

[214] M. Mehta, D.A. Kofke, Coexistence diagrams of mixtures by molecular simulation, Chemical Engineering Science, 49 (16) (1994) 2633-2645.

[215] T. Spyriouni, I.G. Economou, D.N. Theodorou, Phase Equilibria of Mixtures Containing Chain Molecules Predicted through a Novel Simulation Scheme, Physical Review Letters, 80 (20) (1998) 4466-4469.

[216] S. Consta, T.J.H. Vlugt, J.W. Hoeth, B. Smit, D. Frenkel, Recoil growth algorithm for chain molecules with continuous interactions, Molecular Physics, 97 (12) (1999) 1243-1254.

[217] J.I. Siepmann, A method for the direct calculation of chemical potentials for dense chain systems, Molecular Physics, 70 (6) (1990) 1145-1158.

[218] J.I. Siepmann, S. Karaborni, B. Smit, Vapor-liquid equilibria of model alkanes, Journal of the American Chemical Society, 115 (14) (1993) 6454-6455.

[219] W. Shi, E.J. Maginn, Continuous Fractional Component Monte Carlo: An Adaptive Biasing Method for Open System Atomistic Simulations, Journal of Chemical Theory and Computation, 3 (4) (2007) 1451-1463.

[220] W. Shi, E.J. Maginn, Improvement in molecule exchange efficiency in Gibbs ensemble Monte Carlo: Development and implementation of the continuous fractional component move, Journal of Computational Chemistry, 29 (15) (2008) 2520-2530.

[221] A. Poursaeidesfahani, R. Hens, A. Rahbari, M. Ramdin, D. Dubbeldam, T.J.H. Vlugt, Efficient Application of Continuous Fractional Component Monte Carlo in the Reaction Ensemble, Journal of Chemical Theory and Computation, 13 (9) (2017) 4452-4466.

[222] A. Poursaeidesfahani, A. Torres-Knoop, D. Dubbeldam, T.J.H. Vlugt, Direct Free Energy Calculation in the Continuous Fractional Component Gibbs Ensemble, Journal of Chemical Theory and Computation, 12 (4) (2016) 1481-1490.

[223] J.J. Potoff, J.R. Errington, A.Z. Panagiotopoulos, Molecular simulation of phase equilibria for mixtures of polar and non-polar components, Molecular Physics, 97 (10) (1999) 1073-1083.

[224] J. Vrabec, J. Fischer, Vapor–liquid equilibria of the ternary mixture CH4 + C2H6 + CO2 from molecular simulation, AIChE Journal, 43 (1) (1997) 212-217.

[225] J. Delhommelle, A. Boutin, A.H. Fuchs, Molecular Simulation of Vapour-Liquid Coexistence Curves for Hydrogen Sulfide-Alkane and Carbon Dioxide-Alkane Mixtures, Molecular Simulation, 22 (6) (1999) 351-368.

[226] B. Neubauer, B. Tavitian, A. Boutin, P. Ungerer, Molecular simulations on volumetric properties of natural gas1Partly presented at the CECAM (Centre Européen de Calcul Atomique et Moléculaire) workshop, Lyon, France, April 26–28, 1998.1, Fluid Phase Equilibria, 161 (1) (1999) 45-62.

[227] P. Ungerer, C. Nieto-Draghi, V. Lachet, A. Wender, A. di Lella, A. Boutin, B. Rousseau, A.H. Fuchs, Molecular simulation applied to fluid properties in the oil and gas industry, Molecular Simulation, 33 (4-5) (2007) 287-304.

[228] P. Ungerer, C. Nieto-Draghi, B. Rousseau, G. Ahunbay, V. Lachet, Molecular simulation of the thermophysical properties of fluids: From understanding toward quantitative predictions, Journal of Molecular Liquids, 134 (1) (2007) 71-89.

[229] D. Dubbeldam, S. Calero, D.E. Ellis, R.Q. Snurr, RASPA: molecular simulation software for adsorption and diffusion in flexible nanoporous materials, Molecular Simulation, 42 (2) (2016) 81-101.

[230] D. Dubbeldam, A. Torres-Knoop, K.S. Walton, On the inner workings of Monte Carlo codes, Molecular Simulation, 39 (14-15) (2013) 1253-1292.

[231] B. Chen, J.I. Siepmann, Transferable Potentials for Phase Equilibria. 3. Explicit-Hydrogen Description of Normal Alkanes, The Journal of Physical Chemistry B, 103 (25) (1999) 5370-5379.

[232] D.S. Abrams, J.M. Prausnitz, Statistical thermodynamics of liquid mixtures: A new expression for the excess Gibbs energy of partly or completely miscible systems, AIChE Journal, 21 (1) (1975) 116-128.

[233] J. Gmehling, P. Rasmussen, A. Fredenslund, Vapor-liquid equilibriums by UNIFAC group contribution. Revision and extension. 2, Industrial & Engineering Chemistry Process Design and Development, 21 (1) (1982) 118-127.

[234] Scienomics, MAPS platform, v4.0, 2016.

[235] A.G. Perez, C. Coquelet, P. Paricaud, A. Chapoy, Comparative study of vapour-liquid equilibrium and density modelling of mixtures related to carbon capture and storage with the SRK, PR, PC-SAFT and SAFT-VR Mie equations of state for industrial uses, Fluid Phase Equilibria, 440 (2017) 19-35.

[236] L.E. Urlic, L.J. Florusse, E.J.M. Straver, S. Degrange, C.J. Peters, Phase and Interfacial Tension Behavior of Certain Model Gas Condensates: Measurements and Modeling, Transport in Porous Media, 52 (2) (2003) 141-157.

[237] F. Gozalpour, A. Danesh, A.C. Todd, D.H. Tehrani, B. Tohidi, Vapour–liquid equilibrium volume and density measurements of a five-component gas condensate at 278.15–383.15 K, Fluid Phase Equilibria, 206 (1) (2003) 95-104.

[238] M.R. Jensen, P. Ungerer, B. de Weert, E. Behar, Crystallisation of heavy hydrocarbons from three synthetic condensate gases at high pressure, Fluid Phase Equilibria, 208 (1) (2003) 247-260.

[239] E. Bertakis, I. Lemonis, S. Katsoufis, E. Voutsas, R. Dohrn, K. Magoulas, D. Tassios, Measurement and thermodynamic modeling of solid–liquid–gas equilibrium of some organic compounds in the presence of CO2, The Journal of Supercritical Fluids, 41 (2) (2007) 238-245.

[240] Y.-N. Lin, R.J.J. Chen, P.S. Chappelear, R. Kobayashi, Vapor-liquid equilibrium of the methane-n-hexane system at low temperature, Journal of Chemical & Engineering Data, 22 (4) (1977) 402-408.

[241] J.P. Kohn, Heterogeneous phase and volumetric behavior of the methane n-heptane system at low temperatures, AIChE Journal, 7 (3) (1961) 514-518.

[242] J.P. Kohn, W.F. Bradish, Multiphase and Volumetric Equilibria of the Methane-n-Octane System at Temperatures between -110 and 150 C, Journal of Chemical & Engineering Data, 9 (1) (1964) 5-8.

[243] P. Marteau, P. Tobaly, V. Ruffier-Meray, J.C. de Hemptinne, High-Pressure Phase Diagrams of Methane + Squalane and Methane + Hexatriacontane Mixtures, Journal of Chemical & Engineering Data, 43 (3) (1998) 362-366.

[244] J. Shim, J.P. Kohn, Multiphase and Volumetric Equilibria of Methane-n-Hexane Binary System at Temperatures Between -110° and 150° C, Journal of Chemical & Engineering Data, 7 (1) (1962) 3-8.

[245] K.D. Luks, J.D. Hottovy, J.P. Kohn, Three-phase solid-liquid-vapor equilibriums in the binary hydrocarbon systems methane-n-hexane and methane-benzene, Journal of Chemical & Engineering Data, 26 (4) (1981) 402-403.

[246] D.L. Tiffin, K.D. Luks, J.P. Kohn, Solubility Enhancement of Solid Hydrocarbons in Liquid Methane due to the Presence of Ethane, in: K.D. Timmerhaus (Ed.) Advances in Cryogenic Engineering, Springer US, Boston, MA, 1978, pp. 538-543.

[247] J.P. Kohn, K.D. Luks, P.H. Liu, D.L. Tiffin, Three-phase solid-liquid-vapor equilibriums of the binary hydrocarbon systems methane-n-octane and methane-cyclohexane, Journal of Chemical & Engineering Data, 22 (4) (1977) 419-421.

[248] F.I. Stalkup, R. Kobayashi, High-pressure phase-equilibrium studies by gas-liquid partition chromatography, AIChE Journal, 9 (1) (1963) 121-128.

[249] S.-P. Hong, K.A. Green, K.D. Luks, Phase equilibria of the mixtures methane + n-hexane + n-hexatriacontane, methane + toluene + naphthalene, and methane + n-hexane + naphthalene, Fluid Phase Equilibria, 87 (2) (1993) 255-272.

[250] H. Quinteros-Lama, F. Llovell, Global phase behaviour in methane plus n-alkanes binary mixtures, The Journal of Supercritical Fluids, 111 (2016) 151-161.

[251] M. Cismondi Duarte, M.V. Galdo, M.J. Gomez, N.G. Tassin, M. Yanes, High pressure phase behavior modeling of asymmetric alkane+alkane binary systems with the RKPR EOS, Fluid Phase Equilibria, 362 (Supplement C) (2014) 125-135.

[252] I. Polishuk, J. Wisniak, H. Segura, Prediction of the critical locus in binary mixtures using equation of state: I. Cubic equations of state, classical mixing rules, mixtures of methane–alkanes, Fluid Phase Equilibria, 164 (1) (1999) 13-47.

[253] D.C. Garcia, K.D. Luks, Patterns of solid–fluid phase equilibria: new possibilities?, Fluid Phase Equilibria, 161 (1) (1999) 91-106.

[254] R.S. Poston, J.J. McKetta, Vapor-Liquid Equilibrium in the Methane-n-Hexane System, Journal of Chemical & Engineering Data, 11 (3) (1966) 362-363.

[255] R.J.J. Chen, P.S. Chappelear, R. Kobayashi, Dew-point loci for methane-n-hexane and methane-n-heptane binary systems, Journal of Chemical & Engineering Data, 21 (2) (1976) 213-219.

[256] H.H. Reamer, B.H. Sage, W.N. Lacey, Phase Equilibria in Hydrocarbon Systems. Volumetric and Phase Behavior of the Methane-n-Heptane System, Industrial & Engineering Chemistry Chemical & Engineering Data Series, 1 (1) (1956) 29-42.

[257] H.L. Chang, L.J. Hurt, R. Kobayashi, Vapor- liquid equilibria of light hydrocarbons at low temperatures and high pressures: The methane- n- heptane system, AIChE Journal, 12 (6) (1966) 1212-1216.

[258] H.C. Wiese, H.H. Reamer, B.H. Sage, Phase equilibriums in hydrocarbon systems. Phase behavior in the methane-propane-n-decane system, Journal of Chemical & Engineering Data, 15 (1) (1970) 75-82.

[259] Aspen Polymer Plus V7.1 Database.

[260] S. Dufal, T. Lafitte, A. Galindo, G. Jackson, A.J. Haslam, Developing intermolecular-potential models for use with the SAFT-VRMie equation of state, AIChE Journal, 61 (9) (2015) 2891-2912.

[261] E.W. Lemmon, M.O. McLinden, D.G. Friend, Thermophysical Properties of Fluid Systems, in: P.J. Linstrom, W.G. Mallard (Eds.) NIST Chemistry WebBook,

NIST Standard Reference Database Number 69, National Institute of Standards and Technology, Gaithersburg MD, 20899, 2017.

[262] I.K. Nikolaidis, L.F.M. Franco, L.N. Vechot, I.G. Economou, Modeling of physical properties and vapor – liquid equilibrium of ethylene and ethylene mixtures with equations of state, Fluid Phase Equilibria, 470 (2018) 149-163.

[263] R.B. Williams, D.L. Katz, Vapor-Liquid Equilibria in Binary Systems. Hydrogen with Ethylene, Ethane, Propylene, and Propane, Industrial & Engineering Chemistry, 46 (12) (1954) 2512-2520.

[264] H. Sagara, Y. Arai, S. Saito, Vapor-Liquid Equilibria of Binary and Ternary Systems Containing Hydrogen and Light Hydrocarbons, Journal of Chemical Engineering of Japan, 5 (4) (1972) 339-348.

[265] A. Heintz, W.B. Streett, Phase Equilibria in the H2/C2H4 System at Temperatures from 114.1 to 247.1 K and Pressures to 600 MPa, Berichte der Bunsengesellschaft für physikalische Chemie, 87 (4) (1983) 298-303.

[266] J.C.G. Calado, V.A.M. Soares, Thermodynamics of liquid mixtures of methane and ethene, Journal of the Chemical Society, Faraday Transactions 1: Physical Chemistry in Condensed Phases, 73 (0) (1977) 1271-1280.

[267] R.C. Miller, A.J. Kidnay, M.J. Hiza, Liquid + vapor equilibria in methane + ethene and in methane + ethane from 150.00 to 190.00 K, The Journal of Chemical Thermodynamics, 9 (2) (1977) 167-178.

[268] H.K. Bae, K. Nagahama, M. Hirata, Isothermal vapor-liquid equilibriums for the ethylene-carbon dioxide system at high pressure, Journal of Chemical & Engineering Data, 27 (1) (1982) 25-27.

[269] G.G. Haselden, F.A. Holland, M.B. King, R.F. Strickland-Constable, Two-Phase Equilibrium in Binary and Ternary Systems. X. Phase Equilibria and Compressibility of the Systems Carbon Dioxide/Propylene, Carbon Dioxide/Ethylene and Ethylene/Propylene, and an Account of the Thermodynamic Functions of the System Carbon Dioxide/Propylene, Proceedings of the Royal Society of London. Series A. Mathematical and Physical Sciences, 240 (1220) (1957) 1-28.

[270] J. Mollerup, Vapour/liquid equilibrium in ethylene + carbon dioxide and ethane + carbon dioxide, Journal of the Chemical Society, Faraday Transactions 1: Physical Chemistry in Condensed Phases, 71 (0) (1975) 2351-2360.

[271] D.A. Barclay, J.L. Flebbe, D.B. Manley, Relative volatilities of the ethane-ethylene system from total pressure measurements, Journal of Chemical & Engineering Data, 27 (2) (1982) 135-142.

[272] J.C.G. Calado, E.J.S.G. de Azevedo, P. Clancy, K.E. Gubbins, Thermodynamic study of liquid mixtures of ethane and ethene, Journal of the Chemical Society, Faraday Transactions 1: Physical Chemistry in Condensed Phases, 79 (11) (1983) 2657-2667.

[273] A.M. Clark, F. Din, Equilibria between solid, liquid and gaseous phases at low temperatures. The system carbon dioxide + ethane + ethylene, Discussions of the Faraday Society, 15 (1953) 202-207.

[274] A. Fredenslund, J. Mollerup, K.R. Hall, Vapor-liquid equilibrium data for the systems ethylene + ethane and carbon dioxide + ethylene + ethane, Journal of Chemical & Engineering Data, 21 (3) (1976) 301-304.

[275] J.L. McCurdy, D.L. Katz, Phase Equilibria in the System Ethane-Ethylene-Acetylene, Industrial & Engineering Chemistry, 36 (7) (1944) 674-680.

[276] I.M. Elshayal, B.C.Y. Lu, Measurement of total pressures for ethylene — propane mixtures, The Canadian Journal of Chemical Engineering, 53 (1) (1975) 83-87.

[277] K. Ohgaki, S. Nakai, S. Nitta, T. Katayama, Isothermal vapor-liquid equilibria for the binary systems propylene-carbon dioxide, propylene-ethylene and propylene-ethane at high pressure, Fluid Phase Equilibria, 8 (2) (1982) 113-122.

[278] H.K. Bae, K. Nagahama, M. Hirata, Measurement and Correlation of High Pressure Vapor-Liquid Equilibria for the Systems Ethylene-1-Butene and Ethylene-Propylene, Journal of Chemical Engineering of Japan, 14 (1) (1981) 1-6.

[279] H. Kubota, H. Inatome, Y. Tanaka, T. Makita, Vapor-Liquid Equilibria of the Ethylene-Propylene System under High Pressure, Journal of Chemical Engineering of Japan, 16 (2) (1983) 99-103.

[280] H. Sagara, S. Mihara, Y. Arai, S. Saito, Vapor-Liquid Equilibria and Henry's Constants for Ternary Systems Containing Hydrogen and Light Hydrocarbons, Journal of Chemical Engineering of Japan, 8 (2) (1975) 98-104.

[281] M. Guter, D.M. Newitt, M. Ruhemann, Two-Phase Equilibrium in Binary and Ternary Systems. II. The System Methane-Ethylene. III. The System Methane-Ethane-Ethylene, Proceedings of the Royal Society of London. Series A. Mathematical and Physical Sciences, 176 (964) (1940) 140-152.

[282] S. Brown, L.D. Peristeras, S. Martynov, R.T.J. Porter, H. Mahgerefteh, I.K. Nikolaidis, G.C. Boulougouris, D.M. Tsangaris, I.G. Economou, Thermodynamic interpolation for the simulation of two-phase flow of non-ideal mixtures, Computers & Chemical Engineering, 95 (2016) 49-57.

[283] H. Akima, Algorithm 761: Scattered-data surface fitting that has the accuracy of a cubic polynomial, ACM Trans. Math. Softw., 22 (3) (1996) 362-371.

[284] A. Cosham, D.G. Jones, K. Armstrong, D. Allason, J. Barnett, The Decompression Behaviour of Carbon Dioxide in the Dense Phase, (45141) (2012) 447-464.

[285] H. Mahgerefteh, S. Brown, S. Martynov, A study of the effects of friction, heat transfer, and stream impurities on the decompression behavior in CO2 pipelines, Greenhouse Gases: Science and Technology, 2 (5) (2012) 369-379.

[286] S.T. Munkejord, J.P. Jakobsen, A. Austegard, M.J. Mølnvik, Thermo- and fluid-dynamical modelling of two-phase multi-component carbon dioxide mixtures, International Journal of Greenhouse Gas Control, 4 (4) (2010) 589-596.

[287] G. Saville, S.M. Richardson, P. Barker, Leakage in Ethylene Pipelines, Process Safety and Environmental Protection, 82 (1) (2004) 61-68.

[288] G. Geiger, B. Bollermann, R. Tetzner, Leak Monitoring of an Ethylene Gas Pipeline, in: PSIG Annual Meeting, Pipeline Simulation Interest Group, Palm Springs, California, 2004, pp. 30.

[289] P.S. Cumber, Outflow from fractured pipelines transporting supercritical ethylene, Journal of Loss Prevention in the Process Industries, 20 (1) (2007) 26-37.

[290] S.E. Quiñones-Cisneros, C.K. Zéberg-Mikkelsen, J. Fernández, J. García, General friction theory viscosity model for the PC-SAFT equation of state, AIChE Journal, 52 (4) (2006) 1600-1610.

[291] M.J. Assael, A. Koutian, M.L. Huber, R.A. Perkins, Reference Correlations of the Thermal Conductivity of Ethene and Propene, Journal of Physical and Chemical Reference Data, 45 (3) (2016) 033104.

[292] S. Martynov, I.K. Nikolaidis, J. Hebrard, I.G. Economou, H. Mahgerefteh, Efficient Interpolation of Thermodynamic Properties of Ethylene for Use in a Computational Model of Pipeline Decompression, Submitted, (2019).

[293] S. Brown, S. Martynov, H. Mahgerefteh, C. Proust, A homogeneous relaxation flow model for the full bore rupture of dense phase CO2 pipelines, International Journal of Greenhouse Gas Control, 17 (2013) 349-356.

[294] E.D. Nikitin, A.P. Popov, Critical temperatures and pressures of C40, C44, and C60 normal alkanes measured by the pulse-heating technique, Fluid Phase Equilibria, 379 (2014) 191-195.

[295] A. Poursaeidesfahani, A. Rahbari, A. Torres-Knoop, D. Dubbeldam, T.J.H. Vlugt, Computation of thermodynamic properties in the continuous fractional component Monte Carlo Gibbs ensemble, Molecular Simulation, 43 (3) (2017) 189-195.

[296] A. Rahbari, A. Poursaeidesfahani, A. Torres-Knoop, D. Dubbeldam, T.J.H. Vlugt, Chemical potentials of water, methanol, carbon dioxide and hydrogen sulphide at low temperatures using continuous fractional component Gibbs ensemble Monte Carlo, Molecular Simulation, 44 (5) (2018) 405-414.

Short CV

Ilias Nikolaidis is a PhD candidate in the Molecular Thermodynamics and Modeling of Materials Laboratory (MTMML) at the National Center for Scientific Research "Demokritos" in Athens, Greece. He holds a Diploma in Chemical Engineering from the National Technical University of Athens, Greece (2013) and a MSc (2015) in "Computational Mechanics" from the same institution. His main scientific interest is the use of classical (cubic) and advanced (SAFT-based) equations of state to model the physical properties of fluids and perform multiphase equilibrium calculations that can also include solid phases. Furthermore, he works on developing new efficient algorithms for the calculation of phase equilibria. He has been involved in the EU funded project CO_2QUEST (2013 - 2016), which is associated with the thermodynamic modeling of CO_2 mixtures relevant to Carbon Capture, Transport and Sequestration and in the European Union Horizon 2020 Research and Innovation Programme, ShaleXenvironmenT (2017). He has also been a scholar (2017 - 2018) of the General Secretariat for Research and Technology Hellas (GSRT) and the Hellenic Foundation for Research and Innovation (HFRI). His academic experience includes working as a Research Assistant in the Chemical Engineering department of Texas A&M at Qatar (2015) as a visiting PhD student and in the NPRP grant number 8-1339-2-569 (2016 - 2017) from the Qatar National Research Fund in the same institution. He has also been a visiting PhD student in TU Delft in the context of research collaboration with the thermodynamics group at the institution.

Publications

Journal Publications

1. Brown S, Peristeras LD, Martynov SB, et al. Thermodynamic interpolation for the simulation of two-phase flow of non-ideal mixtures. Computers & Chemical Engineering. 2016;95:49-57.
2. Nikolaidis IK, Boulougouris GC, Peristeras LD, Economou IG. Equation-of-State Modeling of Solid–Liquid–Gas Equilibrium of CO2 Binary Mixtures. Industrial & Engineering Chemistry Research. 2016;55:6213-6226.
3. Porter RTJ, Mahgerefteh H, Brown S, et al. Techno-economic assessment of CO2 quality effect on its storage and transport: CO2QUEST: An overview of aims, objectives and main findings. International Journal of Greenhouse Gas Control. 2016;54, Part 2:662-681.
4. Nikolaidis IK, Samoili VS, Voutsas EC, Economou IG. Solid–Liquid–Gas Equilibrium of Methane–*n*-Alkane Binary Mixtures. Industrial & Engineering Chemistry Research. 2018;57:8566-8583.
5. Nikolaidis IK, Franco LFM, Vechot LN, Economou IG. Modeling of physical properties and vapor – liquid equilibrium of ethylene and ethylene mixtures with equations of state. Fluid Phase Equilibria. 2018;470:149-163.
6. Nikolaidis IK, Poursaeidesfahani A, Csaszar Z, et al. Modeling the phase equilibria of asymmetric hydrocarbon mixtures using molecular simulation and equations of state. AIChE Journal. 2019;65:792-803.
7. Nikolaidis IK, Boulougouris GC, Peristeras LD, Economou IG. Efficient and Robust Methods for Direct Saturation Point Calculations. Submitted.
8. Nikolaidis IK, Boulougouris GC, Peristeras LD, Economou IG. Construction of Phase Envelopes for Binary and Multicomponent Mixtures with Euler-Newton Predictor-Corrector Methods. Submitted.
9. Martynov SB, Nikolaidis IK, Hebrard J, Economou IG, Mahgerefteh H. Efficient Interpolation of Thermodynamic Properties of Ethylene for Use in a Computational Model of Pipeline Decompression. Submitted.

Book Chapters

1. Mahgerefteh H, Porter RTJ, Brown S, et al. Carbon capture: Whole system experimental and theoretical modeling investigation of the optimal CO2 stream composition in the carbon capture and sequestration chain. In The Water-Food-Energy Nexus: Processes, Technologies and Challenges, Mutjaba IM, Srinivasan R, Elbashir NO Eds. Green Chemistry and Chemical Engineering. pgs. 553-602, Taylor & Francis (2017).

Conference Presentations

1. Nikolaidis IK, Boulougouris GC, Tsangaris DM, Peristeras LD, Economou IG. Modeling solid-fluid equilibria with application to CO_2 mixtures. 28th European Symposium on Applied Thermodynamics, Athens, Greece, 11 - 14 June 2015.
2. Nikolaidis IK, Boulougouris GC, Peristeras LD, Economou IG. Calculation of bubble and dew points of mixtures with minimization of the tangent plain distance to a modified Gibbs free energy surface. 29th European Symposium on Applied Thermodynamics, Bucharest, Romania, 18 - 21 May 2017.
3. Nikolaidis IK, Poursaeidesfahani A, Csaszar Z, Ramdin M, Vlugt TJH, Economou IG, Moultos OA. Predictive modeling of the phase behavior of asymmetric hydrocarbon mixtures via Molecular Simulations and Equations of State. 30th European Symposium on Applied Thermodynamics, Prague, Czech Republic, 11 - 14 June 2018.